



**NAM**

# **Experimental campaign on cavity walls systems representative of the Groningen building stock**

---

**Alberto Pavese, Francesco Graziotti and Guido Magenes**

**Eucentre**

(European Centre for Training and Research in Earthquake Engineering)

Date June 2016

Editors Jan van Elk & Dirk Doornhof



## General Introduction

For the modeling of the seismic response of unreinforced masonry buildings, knowledge of the properties of building material is essential. An experimental program to test the properties of the building materials used in the Groningen area was therefore executed. This included measurements of material in existing buildings (Ref. 1) and in laboratories (Ref. 2 and 3).

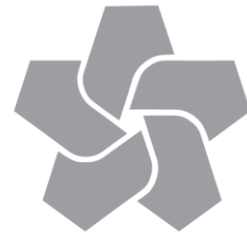
This report described experiments carried out in Eucentre, Pavia, for the characterization of replicated masonry wall elements and of larger wall units of calcium silicate and clay bricks and the shake-table test of a typical Groningen terraced house.

The tests on replicated wall elements and larger walls are complemented by cyclic test carried out by TU Delft on slender and wide wall units (Ref. 4 and 5). Both wide and slender walls have been tested. Test set-up and testing procedures are presented and results discussed. Much attention was given to recording of the failure (crack) pattern in the walls.

The results of these experiments, response of wall units, has been used in the calibration for modelling of the seismic response of masonry buildings (Ref. 7 and 8).

## References

1. In-situ testing of URM houses (building unit: Loppersum, Zijlvest 25), Eucentre (F. Graziotti, A. Rossi, I. Senaldi, S. Peloso), 5<sup>th</sup> December 2014.
2. Material Characterisation – Version 1.3, Eucentre, P&P, TU-Delft, TU-Eindhoven, October 2015.
3. Summary report for the characterisation of original Groningen masonry, TU Delft (S. Safari, J. Rots), 18<sup>th</sup> December 2015.
4. Tests for the characterisation of replicated masonry and wall ties, TU Delft (R. Esposito, F. Messali, J. Rots), 18<sup>th</sup> April 2016
5. In-plane tests of replicated masonry walls, TU Delft (G. Ravenshorst, F. Messali), 18<sup>th</sup> April 2016
6. URM Modelling and Analysis Cross Validation – Arup, Eucentre, TU Delft, Reference 229746\_032.0\_REP127\_Rev.0.03 April 2015.
7. Eucentre Shake-table Test of Terraced House Modelling Predictions and Analysis Cross Validation, staff from ARUP, Eucentre (Pavia) and TU Delft, November 2015 [this document also includes; (1) Instruments full-scale test-house Eucentre Laboratory, (2) Protocol for Shaking Table Test on Full Scale Building (Eucentre) V\_1, and (3) Selection of Acceleration Time-Series for Shake Table Testing of Groningen Masonry Building at the EUCENTRE, Pavia, all three by staff from Eucentre (Pavia)].
8. Laboratory component testing: Modelling post-test predictions and analysis cross-validation, ARUP, TU Delft and Eucentre (several staff members from all three institutions), 16<sup>th</sup> February 2016.



**NAM**

<b>Title</b>	<b>Experimental campaign on cavity walls systems representative of the Groningen building stock</b>		<b>Date</b>	June 2016
			<b>Initiator</b>	NAM
<b>Autor(s)</b>	<b>Alberto Pavese, Francesco Graziotti and Guido Magenes</b>	<b>Editors</b>	Jan van Elk and Dirk Doornhof	
<b>Organisation</b>	Eucentre in Pavia (European Centre for Training and Research in Earthquake Engineering)	<b>Organisation</b>	NAM	
<b>Place in the Study and Data Acquisition Plan</b>	<p><u>Study Theme:</u> Seismic Response of Buildings (URM)</p> <p><u>Comment:</u>  For the modeling of the seismic response of unreinforced masonry buildings, knowledge of the properties of building material is essential. An experimental program to test the properties of the building materials used in the Groningen area was therefore executed. This included measurements of material in existing buildings (Ref. 1) and in laboratories (Ref. 2 and 3).  This report described experiments carried out in Eucentre, Pavia, for the characterization of replicated masonry wall elements and of larger wall units of calcium silicate and clay bricks and the shake-table test of a typical Groningen terraced house.  The tests on replicated wall elements and larger walls are complemented by cyclic test carried out by TU Delft on slender and wide wall units (Ref. 4 and 5). Both wide and slender walls have been tested. Test set-up and testing procedures are presented and results discussed. Much attention was given to recording of the failure (crack) pattern in the walls.  The results of these experiments, response of wall units, has been used in the calibration for modelling of the seismic response of masonry buildings (Ref. 7 and 8).</p>			
<b>Directly linked research</b>	(1) Building Material properties (2) Shake table tests (3) Fragility curves for building typologies (URM) (4) Risk Assessment			
<b>Used data</b>	Experiments			
<b>Associated organisation</b>	NAM			
<b>Assurance</b>	Eucentre			

Nederlandse Aardolie Maatschappij B.V.

Schepersmaat 2, Postbus 28000, 9400 HH Assen

# Experimental campaign on cavity walls systems representative of the Groningen building stock



**EUCENTRE**

European Centre for Training and Research in Earthquake Engineering

Via Ferrata 1, 27100 Pavia, Italy

Tel. +39.0382.516911 Fax. +39.0382.529131

<http://www.eucentre.it>

email: [info@eucentre.it](mailto:info@eucentre.it)

LAB AND TESTS RESPONSIBLE	DOCUMENT AUTHOR	REVIEWER
Prof. Alberto Pavese	Dr. Francesco Graziotti	Prof. Guido Magenes
Signature	Signature	Signature
Issue: 30/10/2015	Document type:  <b>Technical report</b> pages: 345	File name: EUC318_2015U.pdf
Revision: 06/11/2015		Protocol EUC318/2015U
Revision: 13/04/2016		
Revision: 16/06/2016		

According to law, EUCENTRE Foundation trademark cannot be reproduced, copied or utilized, without the written permission of the EUCENTRE Foundation, which is the owner, except in accordance with established contract conditions pertaining to the production of this document.



Cite as:

- Report

Graziotti, F., Tomassetti, U., Rossi, A., Kallioras, S., Mandirola, M., Cenja, E., Penna, A., Magenes G. (2015): *Experimental campaign on cavity-wall systems representative of the Groningen building stock*. Report, EUC318/2015U, EUCENTRE, Pavia, Italy.

- Papers

Graziotti, F., Rossi, A., Mandirola, M., Penna, A., Magenes, G. (2016) “Experimental Characterization of Calcium-Silicate Brick Masonry for Seismic Assessment”, *Brick and Block Masonry: Trends, Innovations and Challenges - Proceedings of the 16th International Brick and Block Masonry Conference, IBMAC 2016*, pp. 1619-1628.

Graziotti, F., Tomassetti, U., Penna, A., Magenes, G. (2016) “Out-of-plane shaking table tests on URM single leaf and cavity walls”, *Engineering Structures*, 125, 455-470, DOI:10.1016/j.engstruct.2016.07.011.

Graziotti, F., Tomassetti, U., Kallioras, S., Penna, A., Magenes, G. (2017) “Shaking table test on a full-scale URM cavity wall building”, *Bulletin of Earthquake Engineering*, (in-press) DOI: 10.1007/s10518-017-0185-8.



## Table of Contents

---

Table of Contents.....	3
1 Introduction.....	6
1.1 Description of the test programme.....	6
2 Nomenclature.....	10
3 Test for materials characterization.....	11
3.1 Compressive strength of masonry unit.....	12
3.2 Flexural and compressive strength of mortar.....	15
3.2.1 Tests on mortar of component specimens .....	19
3.2.2 Tests on mortar of full-scale building.....	25
3.2.3 Mortar sampled from full-scale building specimen ( <i>HE</i> ).....	31
3.3 Compressive strength of masonry.....	33
3.3.1 Compressive strength of C.S. masonry - EC_MAT_11 .....	33
3.3.2 Compressive strength of clay masonry - EC_MAT_21 .....	41
3.3.3 Compressive strength of C.S. masonry - EC_MAT_H_11 .....	49
3.3.4 Compressive strength of clay masonry - EC_MAT_H_21.....	57
3.4 Bond strength of masonry .....	65
3.4.1 Results of bond strength of C.S. masonry - EC_MAT_15.....	67
3.4.2 Results of bond strength of clay masonry - EC_MAT_25 .....	70
3.4.3 Results of bond strength of C.S. masonry - EC_MAT_H_15 .....	72
3.4.4 Results of bond strength of clay masonry - EC_MAT_H_25 .....	75
3.5 Shear strength of masonries .....	77
3.5.1 Triplet Test Result for C.S. masonry - EC_MAT_16.....	81
3.5.2 Triplet Test Result for C.S. masonry - EC_MAT_H_16.....	84
3.5.3 Triplet Test Result for clay masonry - EC_MAT_H_26.....	88
3.6 Tensile Strength of ties .....	92
3.7 Summary table .....	93
4 In-Plane Component Tests.....	94
4.1 Test Specimens .....	94
4.2 Test set-up and instrumentation .....	97
4.2.1 Test set-up.....	97
4.2.2 Instrumentation .....	99
4.3 Testing procedure.....	103



4.3.1	Cantilever boundary conditions.....	103
4.3.2	Double fixed boundary conditions.....	104
4.3.3	Execution of the test and horizontal loading history .....	105
4.4	Experimental Results .....	110
4.4.1	EC_COMP_2.....	110
4.4.2	EC_COMP_1.....	114
4.4.3	EC_COMP_3.....	125
4.4.4	Bilinear envelopes .....	138
5	Out-of-Plane Component Tests .....	142
5.1	Test specimens .....	142
5.2	Test set-up and instrumentation .....	147
5.2.1	Test setup.....	147
5.2.2	Instrumentation .....	153
5.3	Test procedure.....	155
5.3.1	Dynamic input .....	155
5.3.2	Testing Sequence .....	159
5.4	Test Results.....	163
5.4.1	EC_COMP_4.....	163
5.4.2	EC_COMP_5.....	172
5.4.3	EC_COMP_6.....	184
5.4.4	EC_COMP_7.....	196
5.4.5	Deformed shapes .....	208
5.4.6	Damage Pattern.....	211
5.4.7	Summary of the results .....	214
6	Full-Scale Building Test, terraced house.....	218
6.1	Geometry of specimen .....	219
6.1.1	Construction details .....	230
6.2	Instrumentation and acquisition system.....	245
6.2.1	Identification of the position of the accelerometers .....	245
6.2.2	Identification of the position of the displacement transducers .....	249
6.3	Test procedure.....	252
6.3.1	Dynamic Input Typologies .....	252
6.3.2	Applied Dynamic Input Sequence .....	255
6.4	Test Results.....	256
6.4.1	Damage pattern evolution.....	256



6.4.2	Test #2_25%_EQ1_024.....	292
6.4.3	Test #4_50%_EQ1_050.....	296
6.4.4	Test #6*_50%_4xEQ1_050 (Rigid roof).....	299
6.4.5	Test #7_100%_EQ1_100.....	302
6.4.6	Test #9_150%_EQ1_150.....	305
6.4.7	Test #11,#12,#13_30%_EQ2_050.....	308
6.4.8	Test #14_50%_EQ2_080.....	311
6.4.9	Test #16_100%_EQ2_160.....	314
6.4.10	Test #18_50%_EQ2_080.....	317
6.4.11	Test #19_125%_EQ2_200.....	320
6.4.12	Test #21_150%_EQ2_240.....	323
6.4.13	Test #23_200%_EQ2_320.....	326
6.4.14	Test #26*, #27*, #28*_30%_EQ2_050 (Rigid roof).....	329
6.4.15	Test #29*_60%_EQ2_100 (Rigid roof).....	332
6.4.16	Summary of the results.....	335
6.4.17	Evolution of dynamic properties.....	339
	References.....	346

# 1 Introduction

## 1.1 Description of the test programme

As part of the NAM data acquisition and analysis programme aimed at developing a seismic hazard and risk model for induced seismicity in the Groningen area, laboratory tests were performed on full-scale structural members and a two-storey unreinforced masonry building, representative of a structural typology very common in the region. The work presented in this report is part of a coordinated experimental programme also involving complementary tests carried out at the Technical University of Delft (Figure 1).

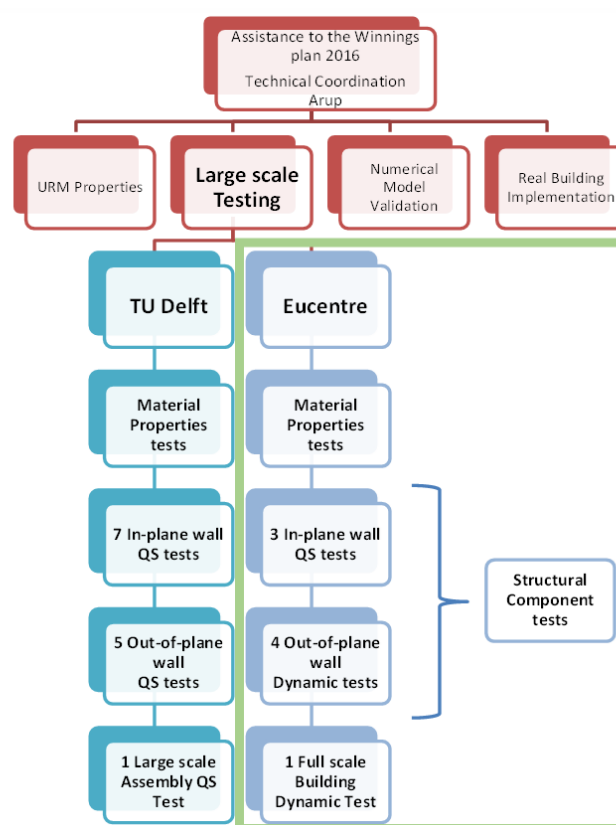


Figure 1. Scheme of the testing campaign.

This experimental research aimed at investigating the seismic behaviour of a specific typology of Dutch residential buildings usually identified as terraced houses. Terraced house in general are expected to be of at least 8 different types including 2 RC buildings. In particular, the full-scale specimen has been design according to a recurrent family of masonry terraced house typical of the late 70's in the Groningen region. These structures are usually built with masonry cavity walls, with an inner loadbearing masonry wall and an outer veneer mostly with aesthetic and insulating functions.



This document describes the testing campaign performed at the laboratory of the European Centre for Training and Research in Earthquake Engineering (EUCENTRE) in 2015. Some of the tests were also conducted by EUCENTRE staff at the DICAR Laboratory of University of Pavia (UNIPV). The experimental programme included:

- Characterization tests on units, mortar and small masonry assemblies;
- In-plane quasi static tests on full-scale masonry piers;
- Dynamic (shaking-table) out-of-plane tests on full-scale cavity masonry walls;
- Shaking table tests on a full-scale two-storey masonry building specimen with cavity walls ideally representative of the end structural unit of a terraced house.

The complete list of the tests carried out at the EUCENTRE laboratory is reported in Table 1.

*Table 1. Summary table of tests and dates*

Company	Activity Name	Test type	Day of Test
UNIPV	BRICK-CLAY-SPEC	Compression Brick	4/5/2015
UNIPV	BRICK-CS-SPEC	Compression Brick	4/5/2015
UNIPV	BRICK-CLAY-SPEC-HOUSE	Compression Brick	1/10/2015
UNIPV	BRICK-CS-SPEC-HOUSE	Compression Brick	1/10/2015
UNIPV	MOR-CLAY-SPEC	Mortar	21-23/4/2015
UNIPV	MOR-CS-SPEC	Mortar	27/2/2015-23/4/2015
UNIPV	MOR-CLAY-HOUSE	Mortar	29/7/2015-26/8/2015
UNIPV	MOR-CS-HOUSE	Mortar	22/7/2015-26/8/2015
UNIPV	MOR-CS-HOUSE-IN-SITU	Mortar	29-30/9/2015
UNIPV	EC-MAT-CLAY-SPEC	Compression	10-29/6/2015
UNIPV	EC-MAT-CS-SPEC	Compression	22/4/2015-4/5/2015



UNIPV	EC-MAT-CLAY-HOUSE	Compression	29/9/2015- 1/10/2015
UNIPV	EC-MAT-CS- HOUSE	Compression	23-28/9/2015
UNIPV	EC-MAT-CS-SPEC	Shear	5-26/6/2015
UNIPV	EC-MAT-CLAY-HOUSE	Shear	9-15/10/2015
UNIPV	EC-MAT-CS- HOUSE	Shear	3-18/11/2015
UNIPV	EC-MAT-CLAY-SPEC	Bond Wrench	8-10/7/2015
UNIPV	EC-MAT-CS-SPEC	Bond Wrench	8/5/2015- 10/7/2015
UNIPV	EC-MAT-CLAY-HOUSE	Bond Wrench	27-31/8/2015
UNIPV	EC-MAT-CS- HOUSE	Bond Wrench	26-27/8/2015
EUCENTRE	EC-COMP-1	In Plane	22/05/2015
EUCENTRE	EC-COMP-2	In Plane	14/05/2015
EUCENTRE	EC-COMP-3	In Plane	24/07/2015
EUCENTRE	EC-COMP-4	OOP-DYN	11/06/2015
EUCENTRE	EC-COMP-5	OOP-DYN	18/06/2015
EUCENTRE	EC-COMP-6	OOP-DYN	09/07/2015
EUCENTRE	EC-COMP-7	OOP-DYN	03/07/2015
EUCENTRE	<i>EUC-BUILD</i>	SHAKE- TABLE	07-15/09/2015

Tests on materials and components were performed in order to fully characterize the masonry adopted for all the tests on components (structural members) and on the building specimen. Tests on materials, tests on components and tests on sub-assemblies allowed obtaining this basic information relevant for the interpretation of all the tests carried out on larger specimens and for the verification of the representativeness of the experimental results with respect to the masonry properties in real buildings in the area.

The masonry types subjected to characterization are those composing the cavity wall system adopted for the full-scale specimens, i.e. calcium silicate brick masonry for the loadbearing walls and clay brick masonry for the outer veneer. Tests on small masonry assemblies, including compression tests, bond wrench tests and shear tests on triplets, allowed determining the mechanical parameters of these two brick masonry types.



Three quasi-static tests were performed to assess the in-plane shear behaviour of calcium silicate brick masonry piers. To this aim, in-plane cyclic shear-compression tests were carried out on full-scale 10 cm thick masonry walls with different aspect ratios and subjected to different boundary and loading conditions. These tests provided the validation of strength criteria related to different failure modes, the direct assessment of hysteretic energy dissipation and the identification of displacement limit states.

Since no dynamic tests on cavity walls were found in the literature, four out-of-plane tests were conducted on full-scale masonry assemblies reproducing four different wall configurations. Three of them were cavity walls with different ties distributions and one single-wythe wall made of calcium silicate brick masonry. The setup allowed testing the specimens under different time histories and loading conditions. This report presents all the outcomes of these tests, including deformed shapes, damping estimates and the other specific features of the observed dynamic behaviour.

The shaking table tests on the two-storey full-scale unreinforced masonry building was performed at the EUCENTRE laboratory in September 2015. The building was meant to be representative of the end unit of an existing cavity wall masonry terraced house system without any particular aseismic detailing. In the tested specimen, the loadbearing masonry was composed by calcium silicate bricks sustaining two 6-meter-long reinforced concrete floors. The same masonry structure composed two gable walls supporting a pitched timber roof. The outer veneer was made by clay bricks connected to the inner masonry by metallic ties as in the common construction practice.

The shaking table tests were performed applying uniaxial acceleration time-histories oriented parallel to the longitudinal axis of the terraced house, i.e. along its weaker direction. The applied strong motions were carefully selected to be consistent with the expected induced seismicity hazard in the region. An incremental dynamic test series was carried out up to the near collapse limit state of the specimen. This report presents the results obtained during the shaking table tests, illustrating the response of the structure, the observed damage mechanisms and their evolution in the different testing phases.



## 2 Nomenclature

Symbol	Material property
$\rho$	Density
$f_c$	Compressive strength of mortar
$f_t$	Flexural strength of mortar
$f_b$	Compressive strength of masonry unit
$f_m$	Compressive strength of masonry in the direction perpendicular to bed joints
$E_{m,1}$	Elastic modulus of masonry in the direction perpendicular to bed joints (E1) - (30% $f_m$ )
$E_{m,2}$	Elastic modulus of masonry in the direction perpendicular to bed joints (E2) - (10% $f_m$ )
$E_{m,3}$	Elastic modulus of masonry in the direction perpendicular to bed joints given by the secant line passing through the points (30% $f_m, \epsilon_{30\% f_m}$ ) and (10% $f_m, \epsilon_{10\% f_m}$ ) (E3)
$\nu_m$	Poisson ratio of masonry in the direction perpendicular to bed joints
$f_w$	Flexural bond strength
$f_{v0}$	Masonry (bed joint) initial shear strength
$\mu$	Masonry (bed joint) shear friction coefficient
$F_t$	Tensile load capacity of ties
$f_{t,t}$	Tensile strength of ties



### 3 Test for materials characterization

---

This entire testing campaign aims to investigate the seismic behavior of a particular typology of Dutch residential building called terraced houses, typical of the late 70's in the Groningen region. These structures are usually built with cavity walls. These are usually composed by an inner loadbearing wall and an outer wall having aesthetic and insulating functions. In particular, the structural system considered as a reference in this campaign has the loadbearing walls made of calcium silicate (CS) brick masonry and the outer walls made of clay brick masonry.

The final goal of the characterization tests is to study the mechanical characteristics of all the component (mortar and bricks) as well as the mechanical properties of the two masonries. In particular test on compressive and tensile strength of mortar, compressive strength of bricks, compression tests on masonry wallettes, bond wrench test and shear test on masonry triplets were conducted.

Due to different environmental condition between the construction of the specimen for test on components (in plane quasi-static test and out of plane dynamic test) and the construction of the full scale specimen for dynamic shake table test, two different full sets of specimens for mechanical characterization were built and then tested. In this way there was the opportunity to have specific mechanical parameters for each type of full scale test.

### 3.1 Compressive strength of masonry unit

The two components of the masonry (mortar and bricks) have been tested in order to characterize their mechanical properties, according to EN 772-1.

The bricks used to build the full-scale test and the others specimens were tested in compression (compressive strength of masonry unit  $f_b$ ). TUD tested the same unit in flexion in order to determine the tensile strength of the units.

Four series of test were performed at the DICAr Laboratory of University of Pavia:

1. Compression test on five calcium silicate (C.S.) bricks from the same batch used to cast the walls tested both in-plane and out of plane; These specimens are named "CS\_#".
2. Compression test on five calcium silicate (C.S.) bricks from the same batch used to build the full-scale test-house; These specimens are named "CS\_H\_#".
3. Compression test on five clay bricks, from the same batch used to cast the walls tested out of plane; These specimens are named "CLAY\_#".
4. Compression test on five clay bricks, from the same batch used to build the full-scale test-house; These specimens are named "CLAY\_H\_#".

The following figure shows the two bricks typologies.

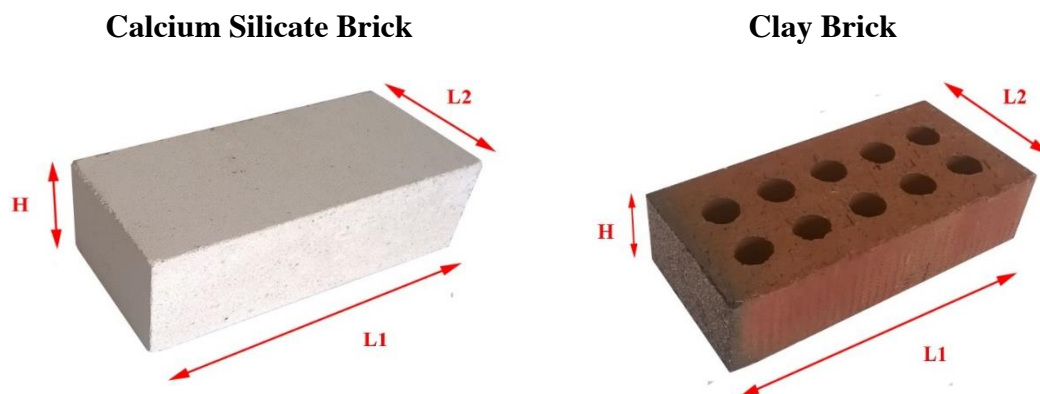


Figure 2. View of CS Bricks and Clay Bricks.

The specimens were tested in compression till the attainment of failure. The following Tables and Figure summarise the ultimate compression load reached by specimens before failure, as well as their dimensions and weight.

The void percentage of clay bricks is 17%.

The compressive strength has been computed considering the gross area =  $L1 \cdot L2$ .

In order to obtain the normalized compressive strength,  $f_b$ , the compressive strength of masonry units is multiplied by a shape factor  $d$ , depending on the width and height of the masonry unit.



Table 2. Test Results - CS bricks used to cast specimens and build the walls.

Test #	Date	Dimensions (mm)			Weight [kg]	$\rho$ [kg/m <sup>3</sup> ]	Ultimate Load		d [-]	f <sub>b</sub> [MPa]
		L1 [mm]	L2 [mm]	H [mm]			[t]	[MPa]		
CS_1	04/05/2015	212.8	102.3	70.8	2.81	1823	37.60	16.94	0.87	14.82
CS_2	04/05/2015	212.5	103.6	70.8	2.96	1899	48.00	21.39	0.87	18.71
CS_3	04/05/2015	212.7	102.3	70.8	2.84	1843	39.40	17.76	0.87	15.54
CS_4	04/05/2015	212.4	102.6	70.9	2.8	1812	36.00	16.21	0.88	14.18
CS_5	04/05/2015	212.6	103.8	70.8	2.94	1882	47.30	21.03	0.87	18.40
					<b>mean</b>	<b>1852</b>	41.66	18.67	0.87	<b>16.33</b>
					<b>c.o.v.</b>	<b>0.02</b>	0.13	0.13	0.00	<b>0.13</b>

Table 3. Test Results - CS bricks used to build the test-house.

Test #	Date	Dimensions (mm)			Weight [kg]	$\rho$ [kg/m <sup>3</sup> ]	Ultimate Load		d [-]	f <sub>b</sub> [MPa]
		L1 [mm]	L2 [mm]	H [mm]			[t]	[MPa]		
CS_H_1	01/10/2015	212	103	71	2.9617	1910	38.00	17.07	0.88	14.95
CS_H_2	01/10/2015	212	103	70	3.0078	1968	50.90	22.87	0.87	19.93
CS_H_3	01/10/2015	212	102	70	2.8053	1853	38.20	17.33	0.87	15.10
CS_H_4	01/10/2015	212	102	70	2.8568	1887	41.90	19.01	0.87	16.56
CS_H_5	01/10/2015	212	102	70	2.9011	1917	49.00	22.23	0.87	19.37
					<b>mean</b>	<b>1907</b>	43.60	19.70	0.87	<b>17.18</b>
					<b>c.o.v.</b>	<b>0.02</b>	0.14	0.14	0.00	<b>0.14</b>

Table 4. Test Results - Clay bricks used to cast specimens and build the walls and the house.

Test #	Date	Dimensions (mm)			Weight [kg]	$\rho$ [kg/m <sup>3</sup> ]	Ultimate Load		d [-]	f <sub>b</sub> [MPa]
		L1 [mm]	L2 [mm]	H [mm]			[t]	[MPa]		
CLAY_1	04/05/2015	212	100.8	50.2	1.73	1613	97.00	44.53	0.75	33.40
CLAY_2	04/05/2015	211.1	98.2	50	1.71	1650	97.00	45.90	0.75	34.43
CLAY_3	04/05/2015	211.1	100.6	49.8	1.7	1607	104.60	48.32	0.75	36.24
CLAY_4	04/05/2015	211.2	100.6	50.3	1.75	1637	99.00	45.71	0.75	34.28
CLAY_5	04/05/2015	211	99.1	50.2	1.66	1581	95.00	44.57	0.75	33.43
CLAY_H_1	01/10/2015	210	100	50	1.69	1614	92.40	43.16	0.75	32.37
CLAY_H_2	01/10/2015	209	100	49	1.70	1656	97.00	45.53	0.75	34.15
CLAY_H_3	01/10/2015	208	100	49	1.71	1676	60.50	28.53	0.75	21.40
CLAY_H_4	01/10/2015	209	100	50	1.70	1627	96.00	45.06	0.75	33.80
CLAY_H_5	01/10/2015	209	100	49	1.70	1655	88.00	41.31	0.75	30.98

<b>mean</b>	<b>1631</b>	92.65	43.26	0.75	<b>32.45</b>
<b>c.o.v.</b>	<b>0.02</b>	0.13	0.13	0.00	<b>0.13</b>

The following Table and Figure summarize the value of compressive strength,  $f_b$ , for each series of tested specimens.

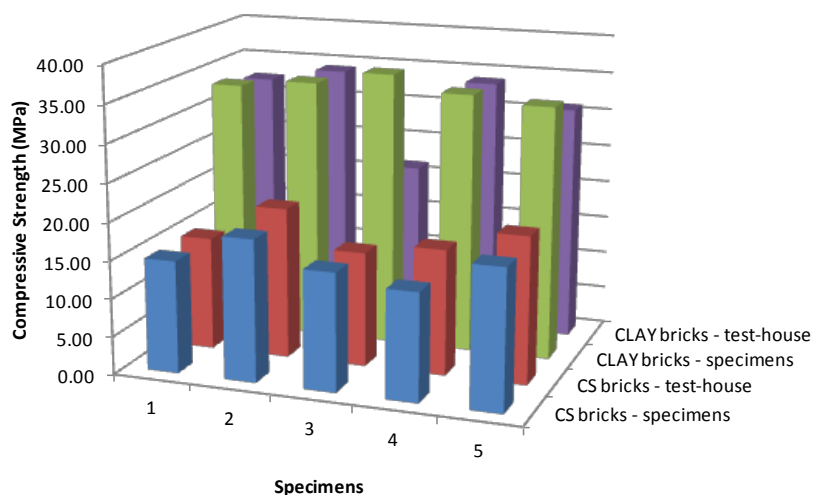


Figure 3. Summary of Test Results.

Table 5. Test Results – Compressive strength of CS and clay and bricks

<i>Compressive strength</i>	$f_b$ [MPa]	<i>c.o.v.</i> [-]
<i>CS bricks - specimens</i>	16.33	0.13
<i>CS bricks - test-house</i>	17.18	0.14
<i>CLAY bricks</i>	34.35	0.13

### 3.2 Flexural and compressive strength of mortar

The mechanical properties of the mortar are fundamental to evaluate the overall behaviour of the masonry. Hence, the mortar used to cast the specimens and to build the test-house was tested in order to determine its flexural and compressive strength.

There are three sets of tests:

1. the first series of test is relative to the mortar casted during the construction of the specimens used for the tests on the single masonry components (e.g. masonry wallettes, triplets, walls);
2. the second series is relative to the mortar casted during the construction of the full-scale test-house.
3. The last series is relative to the mortar sampled "in-situ" from the test-house. After the full-scale test on the shacking table, during the demolition phase, a series of samples of intact mortar bedjoints of the calcium silicate walls were extracted.

#### *Testing Procedure for 1. and 2.*

The tests were conducted in accordance with EN 1015-11 at DICAr Laboratory of University of Pavia.

Each specimen has dimensions 160x40x40 mm. The framework used to cast the specimens is represented in Figure 4.

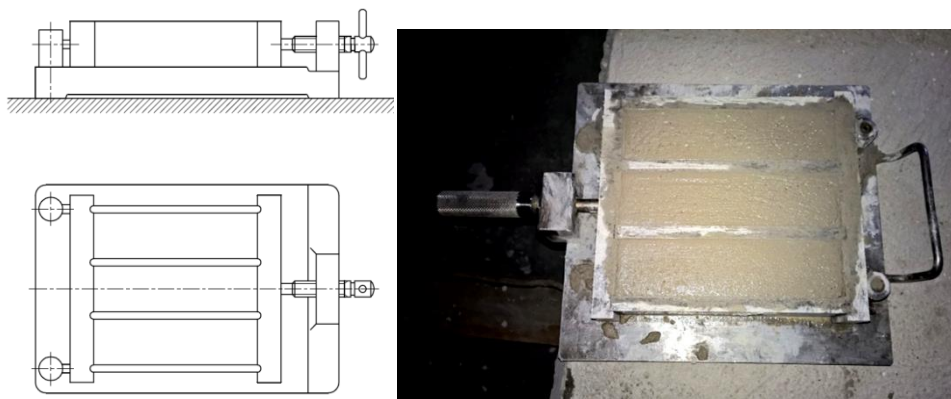


*Figure 4. View of the formwork to cast the specimen.*

The specimens were loaded in bending and the resulting two broken parts were subsequently loaded in compression.

The setup of the bending test for the determination of the flexural strength of the mortar is shown in Figure 5. The load "1" is applied with a constant velocity in between 100 N/s and 50 N/s, in order to obtain the failure of the specimen after a time in between 30 and 90 seconds.

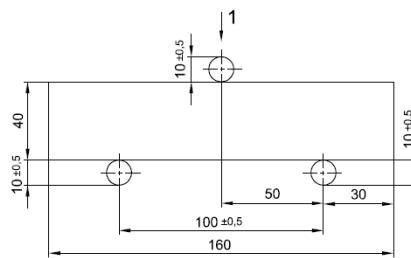


Figure 5. Setup of flexural test on the mortar specimen.

The flexural strength,  $f_t$  is given by the formula:

$$f_t = (3/2) \cdot F \cdot l / (b \cdot d^2)$$

$F$ : maximum load applied to the specimen

$l$ : distance between the rollers = 100 mm

$b$ : width of the specimen = 40 mm

$d$ : thickness of the specimen = 40 mm

After the flexural test the specimen results to be divided in two parts (almost identical) that are tested in compression.

The compressive load must be applied with a constant velocity in between 50 N/s and 500 N/s, in order to obtain the failure of the specimen after a time in between 30 and 90 seconds.

### **Testing Procedure for 3.**

Due to the very high temperature during the construction of the full scale house specimen, the maturation of the mortar in the C.S. masonry was different than the one in the standard metallic formwork. This could be due to the high water absorption of the C.S. bricks that do not guarantee a good hydration of the mortar during its maturation. After the test on the shaking table of the full-scale test-house, in the demolition phase, a series of samples of mortar were extracted from the specimen. These samples (named *HE*) came from courses of calcium silicate masonry that appear to be still intact after the dynamic test.

The raw pieces of mortar were cut in order to obtain a series of small samples. Their dimensions are about 10 cm of length, 4 cm of width and 1 cm of thickness. The following Figure shows the sampling phase. This sampling procedure can be applied to existing buildings if the mortar is not too weak and its layering is regular.

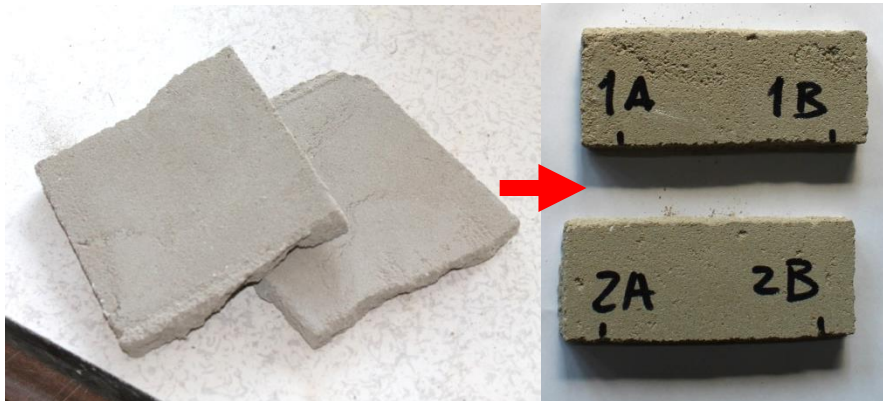


*Figure 6 Specimen sampling of the mortar for CS bricks taken "in-situ".*

The specimens were loaded in bending and the resulting two broken parts were subsequently loaded in compression, adapting the procedure of the EN 1015-11 to this geometry.



*Figure 7. Bending Test on the mortar specimens taken "in-situ".*



*Figure 8. Compressive Test on half specimen of the mortar taken "in-situ".*

The bending test on the samples gives information on the tensile strength, while the compression test allow to compute the compressive strength of the mortar.

### Materials and Water Content

The mortar used of the calcium silicate bricks is different from the one used for the clay bricks.

The following Figure shows the identification code of these two materials.

Mortar for C.S. bricks	Mortar for clay bricks
0920150102 t.h.t.: 19-08-2016 705 ITALY	1401151030 t.h.t.: 28-09-2016 705 BM2 PAVIA/DELFT

Figure 9. Mortar types.

Due to the fact that the two materials are different, also the water content is not the same. Table 6 shows the percentage of water that was used as a fraction of the weight of the mortar.

Table 6. Mortar water content.

	WATER	MORTAR	W/M
	[kg]	[kg] – 1 bag	[%]
<b>Mortar for CS bricks</b>	2.9	25	12%
<b>Mortar for Clay bricks</b>	3.75	25	15%

### 3.2.1 Tests on mortar of component specimens

#### Sampling of specimens

The samples of mortar were casted during the constructions of masonry walls and specimens used for the in-plane and out-of-plane tests as well as others tests on smaller specimens (e.g. wallettes for the compressive test on the masonry).



Figure 10. View of the mortar specimens.

#### Test Results

The following Tables and Figures show the results of the test carried out after 10 and 20 days. These test were performed in order to obtain a relationship between the days of maturation and the mechanical properties of the mortar.

Table 7. Specimen ID - mortar for C.S. masonry, test after 10 days.

#	mortar for	casting date	test date	maturation [days]	weight [g]	$f_c$ [MPa]	$f_t$ [MPa]
CS-10-1	CS	27/02/2015	09/03/2015	10	412.7	5.36	1.72
CS-10-2	CS	27/02/2015	09/03/2015	10	423	5.47	2.53
CS-10-3	CS	27/02/2015	09/03/2015	10	413.6	5.15	1.66
CS-10-4	CS	27/02/2015	09/03/2015	10	424.7	5.00	2.25
CS-10-5	CS	27/02/2015	09/03/2015	10	419.5	5.43	1.20
CS-10-6	CS	27/02/2015	09/03/2015	10	420.4	5.44	2.12
					<b>mean</b>	<b>5.31</b>	<b>1.91</b>

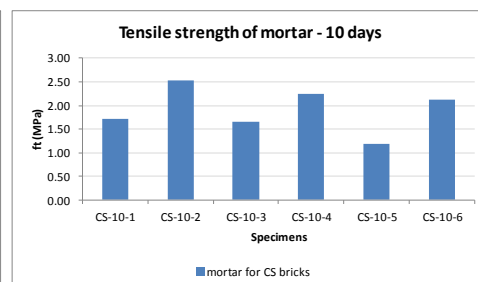
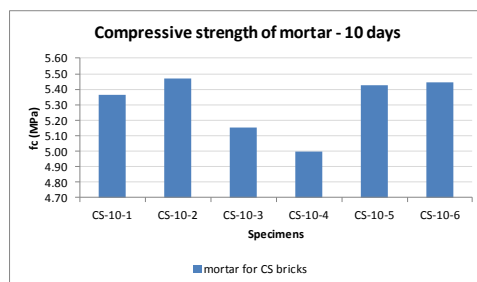


Figure 11. Results of Tests on mortar for C.S. masonry, test after 10 days.

Table 8. Results of Tests on mortar for C.S. masonry, test after 20 days.

#	mortar for	relative masonry specimen	casting date	test date	[day]	weight [g]	$f_c$ [MPa]	$f_t$ [MPa]
CS-20-1	CS	shove wall	24/03/2015	13/04/2015	20	408.7	7.30	2.39
CS-20-2	CS	EUC-COMP-1, shove wall	25/03/2015	13/04/2015	19	395.2	7.17	2.53
CS-20-3	CS	EUC-COMP-1, shove wall	25/03/2015	13/04/2015	19	389.1	7.05	2.76
CS-20-5	CS	compression specimens	25/03/2015	13/04/2015	19	405.3	5.33	2.07
CS-20-6	CS	EUC-COMP-1&2	26/03/2015	15/04/2015	20	415.8	8.15	3.10
CS-20-7	CS	EUC-COMP-3	26/03/2015	15/04/2015	20	415.6	8.78	3.40
CS-20-8	CS	EUC-COMP-3	27/03/2015	15/04/2015	19	417.6	8.02	2.76
CS-20-9	CS	EUC-COMP-4	27/03/2015	15/04/2015	19	393.1	5.70	1.79
CS-20-10	CS	EUC-COMP-4	27/03/2015	15/04/2015	19	420.9	6.93	2.58
<b>mean</b>						<b>406.8</b>	<b>7.16</b>	<b>2.60</b>

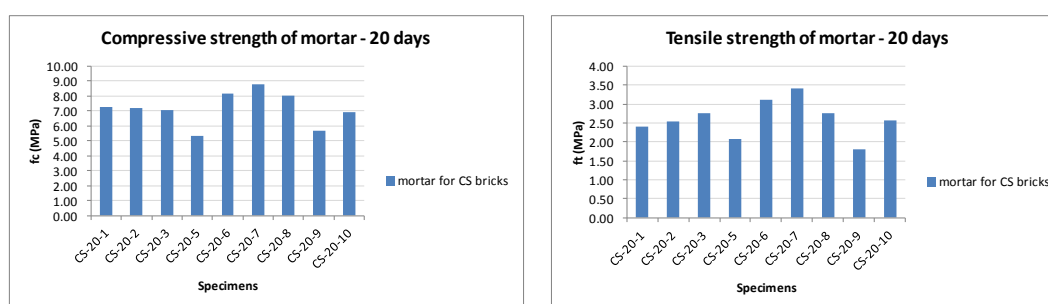


Figure 12. Results of Test on mortar for C.S. masonry, test after 20 days.

The following Table and Figure show the results of the test carried out on mortar with the masonry constituted by calcium silicate bricks after 28 days.

Table 9. Results of Test on mortar for C.S. masonry, test after 28 days.

#	morta r for	relative masonry specimen	casting date	test date	Maturation [days]	weight [g]	$f_c$ [MPa]	$f_t$ [MPa]
CS-28-1	CS	shove wall	24/03/2015	21/04/2015	28	416	7.88	3.03
CS-28-1	CS	shove wall	24/03/2015	21/04/2015	28	414.1	8.52	2.71
CS-28-2	CS	EUC-COMP-1, shove wall	25/03/2015	21/04/2015	27	400.7	6.94	2.67
CS-28-2	CS	EUC-COMP-1, shove wall	25/03/2015	21/04/2015	27	394	6.58	2.12
CS-28-3	CS	EUC-COMP-1, shove wall	25/03/2015	21/04/2015	27	392.7	7.45	2.44
CS-28-3	CS	EUC-COMP-1, shove wall	25/03/2015	21/04/2015	27	388.6	5.95	2.30
CS-28-5	CS	compression specimens	25/03/2015	21/04/2015	27	412.9	7.13	2.71
CS-28-5	CS	compression specimens	25/03/2015	21/04/2015	27	398.9	6.84	2.64
CS-28-6	CS	EUC-COMP-1&2	26/03/2015	23/04/2015	28	416	8.29	2.85
CS-28-6	CS	EUC-COMP-1&2	26/03/2015	23/04/2015	28	412.8	7.63	2.90
CS-28-7	CS	EUC-COMP-3	26/03/2015	23/04/2015	28	415.5	8.65	2.81
CS-28-7	CS	EUC-COMP-3	26/03/2015	23/04/2015	28	411.4	8.46	2.99
CS-28-8	CS	EUC-COMP-3	27/03/2015	23/04/2015	27	423.3	7.85	3.54
CS-28-8	CS	EUC-COMP-3	27/03/2015	23/04/2015	27	423.7	7.46	3.72
CS-28-9	CS	EUC-COMP-4	27/03/2015	23/04/2015	27	395.2	6.12	2.48
CS-28-9	CS	EUC-COMP-4	27/03/2015	23/04/2015	27	398	5.73	2.58
CS-28-10	CS	EUC-COMP-4	27/03/2015	23/04/2015	27	424.4	7.82	3.08
CS-28-10	CS	EUC-COMP-4	27/03/2015	23/04/2015	27	427.3	7.11	2.71

CS-28-11	CS	triplets	27/03/2015	23/04/2015	27	434.9	8.19	4.05
CS-28-11	CS	triplets	27/03/2015	23/04/2015	27	431.1	8.91	3.17
CS-28-11	CS	triplets	27/03/2015	23/04/2015	27	427.4	9.20	3.77
CS-28-12	CS	bond wrench specimens	27/03/2015	23/04/2015	27	423	7.14	3.17
CS-28-12	CS	bond wrench specimens	27/03/2015	23/04/2015	27	415.4	6.64	2.60
CS-28-12	CS	bond wrench specimens	27/03/2015	23/04/2015	27	427.3	7.84	3.03
CS-28-OOP-5	CS	EC_comp_6	22/04/2015	26/05/2015	34	417.7	6.53	2.81
CS-28-OOP-5	CS	EC_comp_6	22/04/2015	26/05/2015	34	420.7	5.00	3.54
CS-28-OOP-5	CS	EC_comp_6	22/04/2015	26/05/2015	34	409.8	6.35	2.58
CS-28-OOP-1	CS	EC_comp_7	21/04/2015	26/05/2015	35	410.1	7.54	2.85
CS-28-OOP-1	CS	EC_comp_7	21/04/2015	26/05/2015	35	411.3	8.83	
CS-28-OOP-1	CS	EC_comp_7	21/04/2015	26/05/2015	35	407.8	6.90	2.99
CS-28-OOP-6	CS	EC_comp_7	22/04/2015	26/05/2015	34	409.6	7.42	2.62
CS-28-OOP-6	CS	EC_comp_7	22/04/2015	26/05/2015	34	403.9	6.87	2.53
CS-28-OOP-6	CS	EC_comp_7	22/04/2015	26/05/2015	34	411.1	7.14	2.71
CS-28-OOP-2	CS	EC_comp_5 + EC_comp_6	21/04/2015	26/05/2015	35	429.0	6.10	2.48
CS-28-OOP-2	CS	EC_comp_5 + EC_comp_6	21/04/2015	26/05/2015	35	423.0	6.04	3.03
CS-28-OOP-2	CS	EC_comp_5 + EC_comp_6	21/04/2015	26/05/2015	35	423.7	5.76	2.76
CS-28-OOP-8	CS	EC_comp_5 + EC_comp_6	23/04/2015	26/05/2015	33	409.7	7.02	2.76
CS-28-OOP-8	CS	EC_comp_5 + EC_comp_6	23/04/2015	26/05/2015	33	411.5	7.08	2.81
CS-28-OOP-8	CS	EC_comp_5 + EC_comp_6	23/04/2015	26/05/2015	33	413.4	7.30	2.58
<b>mean</b>						<b>413.8</b>	<b>7.24</b>	<b>2.87</b>

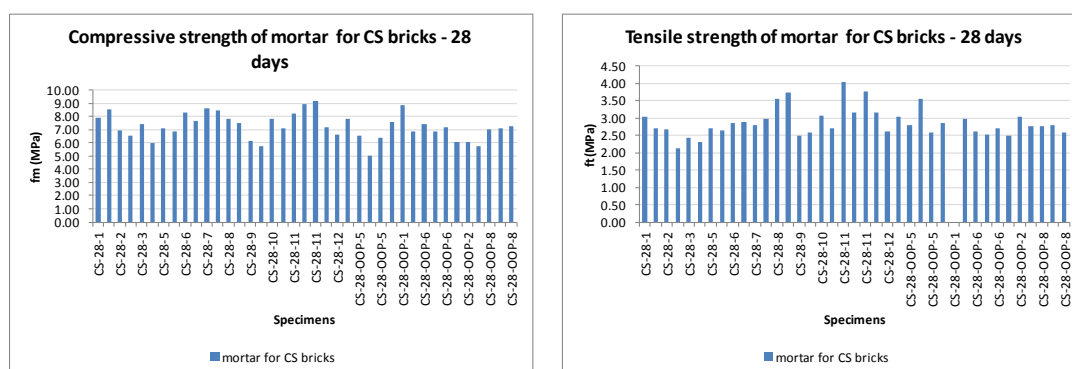


Figure 13. Results of Test on mortar for C.S. masonry, test after 28 days.

Figure 14 plots the distribution of tensile and compressive strength of mortar for C.S. masonry after 28 days of maturation.

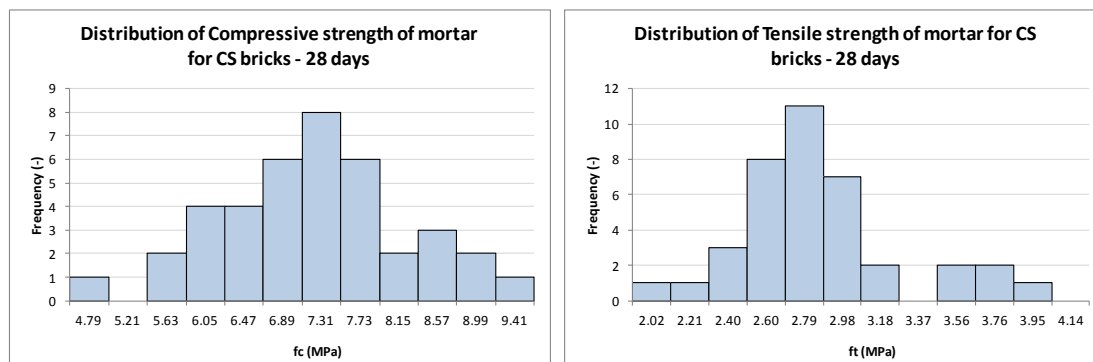


Figure 14. Distribution of strength relative to the mortar for C.S. masonry, test after 28 days.

It is possible to reorganize the results shown before of the test carried out on mortar with the masonry constituted by calcium silicate bricks after 28 days, by showing the values of compressive and tensile strength for each masonry specimen (Table 10).

Table 10. Results of Test on mortar for C.S. masonry, test after 28 days, divided per masonry specimens.

mortar for	relative masonry specimen	Compressive strength - $f_c$			Tensile strength - $f_t$		
		mean [MPa]	st. dv. [MPa]	c.o.v. -	mean [MPa]	st. dv. [MPa]	c.o.v. -
CS bricks	shove wall	7.22	0.93	0.13	2.54	0.33	0.13
CS bricks	compression specimens	6.98	0.21	0.03	2.68	0.05	0.02
CS bricks	EC-COMP-1&2	7.96	0.47	0.06	2.87	0.03	0.01
CS bricks	EC-COMP-3	8.10	0.55	0.07	3.26	0.44	0.13
CS bricks	EC-COMP-4	6.69	0.95	0.14	2.71	0.26	0.10
CS bricks	EC-COMP-5 & 6	6.35	0.73	0.11	2.82	0.32	0.11
CS bricks	EC-COMP-7	7.45	0.73	0.10	2.74	0.18	0.07

The following Table and Figure show the results of the test carried out on the mortar used for the masonry constituted by clay bricks after 28 days.

Table 11. Results of Test on mortar for clay masonry, test after 28 days.

#	mortar for	relative masonry specimen	casting date	test date	[days]	weight [g]	$f_c$ [MPa]	$f_t$ [MPa]
CL-28-4	CLAY bricks	Material test specimens	21/04/2015	26/05/2015	35	436.8	4.72	2.02
CL-28-4	CLAY bricks	Material test specimens	21/04/2015	26/05/2015	35	440.1	4.54	2.25
CL-28-4	CLAY bricks	Material test specimens	21/04/2015	26/05/2015	35	438.2	4.35	2.07
CL-28-3	CLAY bricks	EC_comp_7	22/04/2015	26/05/2015	34	457.0	4.35	1.61
CL-28-3	CLAY bricks	EC_comp_7	22/04/2015	26/05/2015	34	464.8	4.35	2.02
CL-28-3	CLAY bricks	EC_comp_7	22/04/2015	26/05/2015	34	467.2	4.51	1.75
CL-28-7	CLAY bricks	EC_comp_7	22/04/2015	26/05/2015	34	450.8	6.96	2.30
CL-28-7	CLAY bricks	EC_comp_7	22/04/2015	26/05/2015	34	453	7.14	2.71
CL-28-7	CLAY bricks	EC comp 7	22/04/2015	26/05/2015	34	452.3	7.20	2.16
CL-28-9	CLAY bricks	EC_comp_5 + EC_comp_6	23/04/2015	26/05/2015	33	447.6	7.30	1.84
CL-28-9	CLAY bricks	EC_comp_5 + EC_comp_6	23/04/2015	26/05/2015	33	448.2	7.02	2.71
CL-28-9	CLAY bricks	EC_comp 5 + EC_comp 6	23/04/2015	26/05/2015	33	452.1	6.62	2.12

CL-28-10	CLAY bricks	EC_comp_5 + EC_comp_6	23/04/2015	26/05/2015	33	457	5.61	1.47
CL-28-10	CLAY bricks	EC_comp_5 + EC_comp_6	23/04/2015	26/05/2015	33	452.8	6.78	2.39
CL-28-10	CLAY bricks	EC_comp_5 + EC_comp_6	23/04/2015	26/05/2015	33	456.8	5.33	1.29
<b>mean</b>						<b>451.6</b>	<b>5.79</b>	<b>2.05</b>

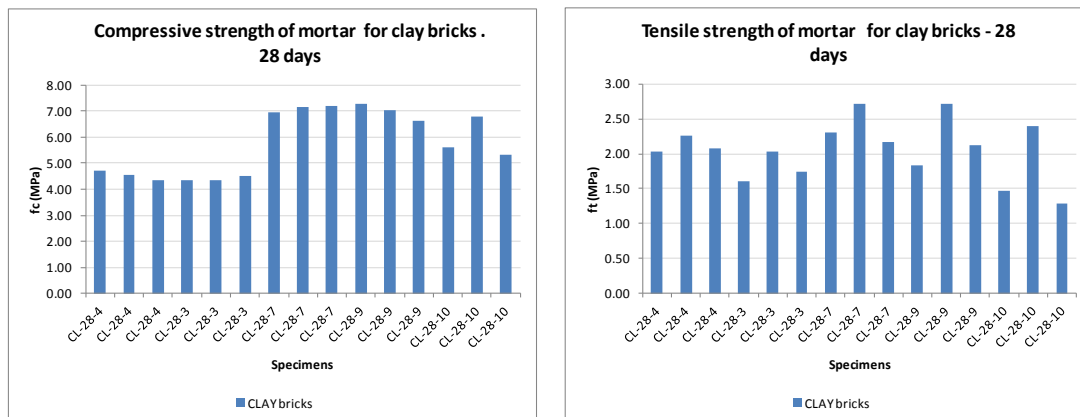


Figure 15. Results of Test on mortar for clay masonry, test after 28 days.

Figure 15 plots the distribution of tensile and compressive strength of mortar for clay masonry after 28 days of maturation.

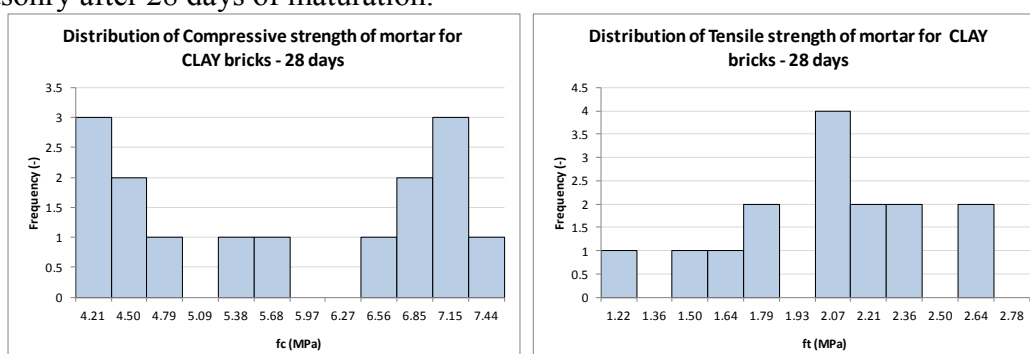


Figure 16. Distribution of strength relative to the mortar for clay masonry, test after 28 days.

It is possible to reorganize the results shown before of the test carried out on mortar with the masonry constituted by clay bricks after 28 days, by showing the values of compressive and tensile strength for each masonry specimen (Table 12).

Table 12. Results of Test on mortar for clay masonry, test after 28 days, divided per masonry specimens.

mortar for	relative masonry specimen	Compressive strength - $f_c$			Tensile strength - $f_t$		
		mean	st. dv.	c.o.v.	mean	st. dv.	c.o.v.
		[MPa]	[MPa]	-	[MPa]	[MPa]	-
CLAY bricks	compression specimens	4.54	0.18	0.04	2.12	0.12	0.06
CLAY bricks	EC-COMP-5 & 6	6.44	0.79	0.12	1.97	0.54	0.28
CLAY bricks	EC-COMP-7	5.75	1.48	0.26	2.09	0.40	0.19

All the results can be resumed in the following Tables:

*Table 13. Resume of Test results- comparison between the tests on the mortar relative to CS and clay masonries.*

	<i>Compressive strength - <math>f_c</math></i>			<i>Tensile strength - <math>f_t</math></i>		
	mean	st. dev.	c.o.v.	mean	st. dev.	c.o.v.
	[MPa]	[MPa]	-	[MPa]	[MPa]	-
Mortar for CS bricks	<b>7.24</b>	0.97	0.13	<b>2.87</b>	0.41	0.14
Mortar for Clay bricks	<b>5.79</b>	1.24	0.21	<b>2.05</b>	0.41	0.20

*Table 14. Resume of Test results - comparison between the tests on the mortar relative to CS masonry, after 10, 20 and 28 days.*

	<i>Compressive strength - <math>f_c</math></i>			<i>Tensile strength - <math>f_t</math></i>			
	mean	st. dev.	c.o.v.	mean	st. dev.	c.o.v.	
	[MPa]	[MPa]	-	[MPa]	[MPa]	-	
mortar for	[MPa]	[MPa]	-	[MPa]	[MPa]	-	
CS bricks	<b>5.31</b>	0.19	0.04	<b>1.91</b>	0.48	0.25	<i>after 10 days</i>
CS bricks	<b>7.16</b>	1.11	0.16	<b>2.60</b>	0.49	0.19	<i>after 20 days</i>
CS bricks	<b>7.24</b>	0.97	0.13	<b>2.87</b>	0.41	0.14	<i>after 28 days</i>

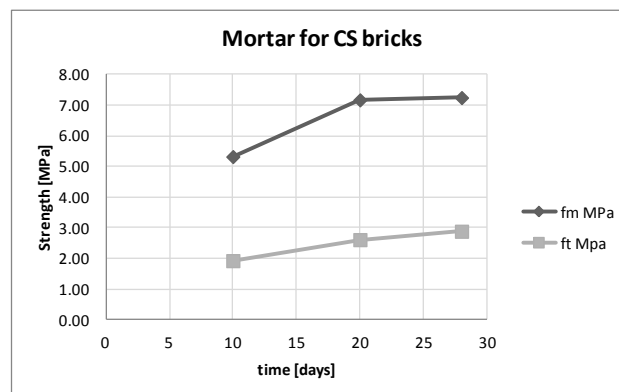


*Figure 17. Compressive and flexural strength of mortar for CS masonry, after 10, 20 and 28 days.*

### 3.2.2 Tests on mortar of full-scale building

#### Sampling of specimens

The samples of mortar were casted during the constructions of the full-scale building specimens

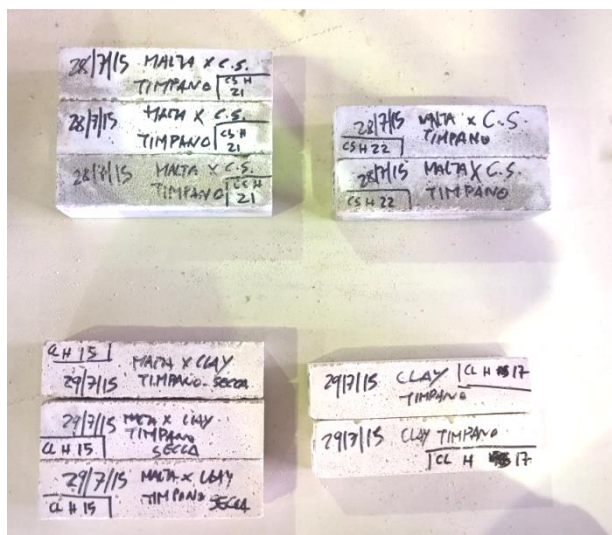


Figure 18. View of part of the specimens.

#### Test Results

The following Tables and Figures show the results of the test carried out on the mortar used to built the calcium silicate walls of the house, after 7, 11, 16 and after 28 days.

This was done in order to obtain also a relationship between the days of maturation and the mechanical properties of the mortar, and not only the raw value of the mechanical properties of the mortar after the prescribed time of maturation (*i.e.* 28 days).

Table 15. Specimen ID - mortar for C.S. house masonry, test after 7 days.

#	use	relative masonry specimen	test date	casting date	[days]	weight [g]	$f_c$ [MPa]	$f_t$ [MPa]
CS-H-01	CS	house	22/07/2015	15/07/2015	7	419.6	1.35	0.37
CS-H-02	CS	house	22/07/2015	15/07/2015	7	420.9	1.46	0.00
CS-H-03	CS	house	22/07/2015	15/07/2015	7	423.8	1.50	0.37
<b>mean</b>						421.4	<b>1.44</b>	<b>0.37</b>

Table 16. Specimen ID - mortar for C.S. house masonry, test after 11 days.

#	use	relative masonry specimen	test date	casting date	[days]	weight [g]	$f_c$ [MPa]	$f_t$ [MPa]
CS-H-4	CS	house	27/07/2015	16/07/2015	11	399.4	3.67	1.84
CS-H-5	CS	house	27/07/2015	16/07/2015	11	400	3.37	1.75
CS-H-6	CS	house	27/07/2015	16/07/2015	11	399.9	3.33	1.66
<b>mean</b>						399.8	<b>3.46</b>	<b>1.75</b>

Table 17. Specimen ID - mortar for C.S. house masonry, test after 16 days.

#	use	relative masonry specimen	test date	casting date	[days]	weight [g]	$f_c$ [MPa]	$f_t$ [MPa]
CS-H-10	CS	house	05/08/2015	20/07/2015	16	463.8	4.81	1.98
CS-H-10	CS	house	05/08/2015	20/07/2015	16	469.7	5.70	1.47
CS-H-10	CS	house	05/08/2015	20/07/2015	16	467.6	5.18	1.66
<b>mean</b>						467.0	<b>5.23</b>	<b>1.70</b>

Table 18. Specimen ID - mortar for C.S. house masonry, test after 28 days.

#	use	relative masonry specimen	test date	casting date	[days]	weight [g]	$f_c$ [MPa]	$f_t$ [MPa]
CS-H-11	CS	house	24/08/2015	21/07/2015	34	416.2	6.28	1.93
CS-H-11	CS	house	24/08/2015	21/07/2015	34	415.5	5.52	1.93
CS-H-11	CS	house	24/08/2015	21/07/2015	34	412.8	6.39	1.93
CS-H-12	CS	house	24/08/2015	21/07/2015	34	405	4.72	1.61
CS-H-12	CS	house	24/08/2015	21/07/2015	34	407.1	4.93	1.79
CS-H-12	CS	house	24/08/2015	21/07/2015	34	397.9	5.00	1.54
CS-H-13	CS	house	24/08/2015	21/07/2015	34	399.9	4.80	1.70
CS-H-13	CS	house	24/08/2015	21/07/2015	34	411.9	5.76	1.98
CS-H-13	CS	house	24/08/2015	21/07/2015	34	416.8	6.05	1.77
CS-H-14	CS	house	24/08/2015	21/07/2015	34	408.8	6.07	2.07
CS-H-14	CS	house	24/08/2015	21/07/2015	34	399.5	4.78	1.84
CS-H-14	CS	house	24/08/2015	21/07/2015	34	400.3	5.24	1.56
CS-H-15	CS	house	24/08/2015	22/07/2015	33	420.3	8.05	2.30
CS-H-15	CS	house	24/08/2015	22/07/2015	33	420.7	8.06	2.35
CS-H-15	CS	house	24/08/2015	22/07/2015	33	418	7.19	2.16
CS-H-16	CS	house	25/08/2015	23/07/2015	33	404.5	3.53	1.24
CS-H-16	CS	house	25/08/2015	23/07/2015	33	400.4	3.02	1.06
CS-H-16	CS	house	25/08/2015	23/07/2015	33	402.1	3.69	1.10
CS-H-18	CS	house	25/08/2015	24/07/2015	32	397.7	3.85	1.06
CS-H-18	CS	house	25/08/2015	24/07/2015	32	400.8	3.72	1.10
CS-H-18	CS	house	25/08/2015	24/07/2015	32	399.7	4.58	1.43
CS-H-19	CS	house	25/08/2015	27/07/2015	29	444.9	8.71	1.98
CS-H-19	CS	house	25/08/2015	27/07/2015	29	433.4	6.42	1.79
CS-H-19	CS	house	25/08/2015	27/07/2015	29	441.4	6.28	1.93
CS-H-20	CS	house	25/08/2015	27/07/2015	29	421	4.51	1.47
CS-H-20	CS	house	25/08/2015	27/07/2015	29	424.8	5.29	1.52
CS-H-20	CS	house	25/08/2015	27/07/2015	29	421.1	4.75	1.47
CS-H-21	CS	house	26/08/2015	28/07/2015	29	421.6	7.39	2.30
CS-H-21	CS	house	26/08/2015	28/07/2015	29	421.4	6.62	2.02
CS-H-21	CS	house	26/08/2015	28/07/2015	29	419.3	7.27	2.58
CS-H-22	CS	house	26/08/2015	28/07/2015	29	416	6.45	2.30
CS-H-22	CS	house	26/08/2015	28/07/2015	29	416.9	7.86	2.30
<b>mean</b>						413.7	<b>5.71</b>	<b>1.78</b>

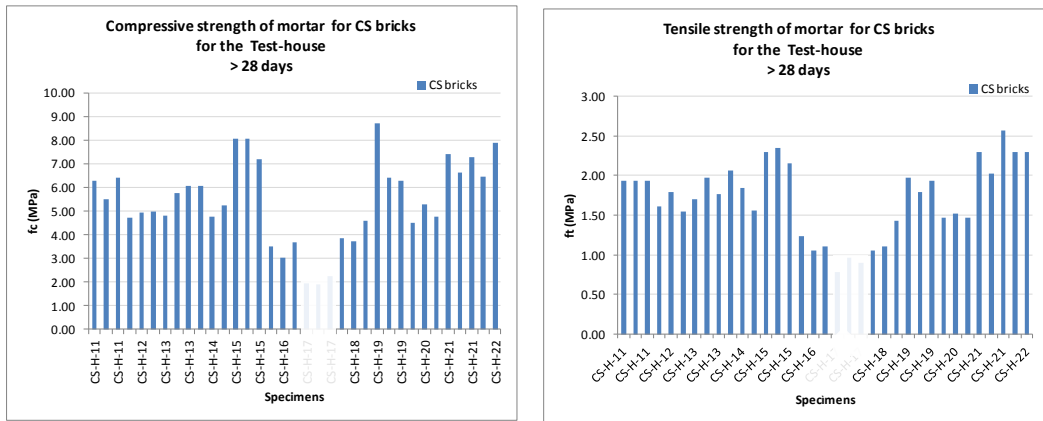


Figure 19. Tests Results on the mortar for C.S. house masonry, test after 28 days.

CS-H-17 specimens were considered not reliable, being not casted properly (too much time after the preparation, mortar too dry). This defect was noticed during the casting. It is possible to notice that the mortar casted the day 23/7/2016 (CS-H-16) exhibited lower values of compressive and flexural strengths. Maybe the low values of compressive strength could be associated to a casting procedure similar to CS-H-16. In any case no defects were noticed during this casting, for this reason these results were used in order to compute the average compressive strength. In particular, this mortar refers to the portion of masonry in between the mid-height and top-height of the piers of the second floor. As possible to notice from Figures of Chapter 6.4.1 this seemed not to affect the global behavior of the house (e.g. no unexpected cracks were noticed in this portion of specimen during the tests).

Figure 20 plots the distribution of tensile and compressive strength of the mortar for calcium silicate masonry used to build the full-scale test-house, after at least 28 days of maturation.

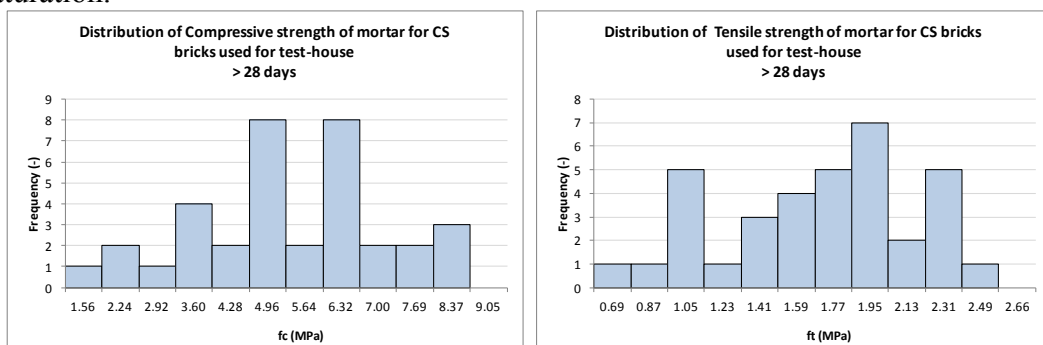


Figure 20. Distribution of strength relative to the mortar for C.S. house masonry, test after 28 days.

The following Tables and Figures show the results of the test carried out on the mortar used to build the clay walls of the house, after 13, 18 and after 28 days. This was done in order to obtain also a relationship between the days of maturation and the mechanical properties of the mortar.



Table 19. Specimen ID - mortar for clay house masonry, test after 13 days.

#	mortar for	masonry specimen	test date	casting date	[days]	weight [g]	$f_m$ MPa	ft Mpa
CL-H-01	CLAY	house	29/07/2015	16/07/2015	13	457.8	4.22	0.92
CL-H-02	CLAY	house	29/07/2015	16/07/2015	13	443.6	3.69	0.92
CL-H-03	CLAY	house	29/07/2015	16/07/2015	13	451.2	3.63	1.24
<b>mean</b>						450.9	<b>3.85</b>	<b>1.03</b>

Table 20. Specimen ID - mortar for clay house masonry, test after 18 days.

#	mortar for	masonry specimen	test date	casting date	[days]	weight [g]	$f_m$ MPa	ft Mpa
CL-H-5	CLAY	house	05/08/2015	18/07/2015	18	445	4.60	
CL-H-5	CLAY	house	05/08/2015	18/07/2015	18	443.3	5.46	2.02
CL-H-5	CLAY	house	05/08/2015	18/07/2015	18	437.2	4.60	1.70
<b>mean</b>						433.4	<b>3.72</b>	<b>1.33</b>

Table 21. Specimen ID - mortar for clay house masonry, test after at least 28 days.

#	use	Masonry specimen	test date	casting date	[days]	weight [g]	$f_c$ [MPa]	$f_t$ [MPa]
CL-H-6	CLAY	house	24/08/2015	20/07/2015	35	434.6	6.51	1.20
CL-H-6	CLAY	house	24/08/2015	20/07/2015	35	428.4	6.41	1.29
CL-H-6	CLAY	house	24/08/2015	20/07/2015	35	433.3	6.65	1.43
CL-H-7	CLAY	house	24/08/2015	22/07/2015	33	443.9	6.53	1.79
CL-H-7	CLAY	house	24/08/2015	22/07/2015	33	448.4	7.56	1.89
CL-H-7	CLAY	house	24/08/2015	22/07/2015	33	448.4	7.71	1.70
CL-H-8	CLAY	house	25/08/2015	23/07/2015	33	449.7	7.05	1.29
CL-H-8	CLAY	house	25/08/2015	23/07/2015	33	454.7	6.35	1.47
CL-H-8	CLAY	house	25/08/2015	23/07/2015	33	457.7	6.64	1.33
CL-H-9	CLAY	house	25/08/2015	24/07/2015	32	451.8	6.93	1.33
CL-H-9	CLAY	house	25/08/2015	24/07/2015	32	456.5	6.76	1.06
CL-H-9	CLAY	house	25/08/2015	24/07/2015	32	451.7	5.78	1.43
CL-H-10	CLAY	house	25/08/2015	25/07/2015	31	426.5	3.66	0.92
CL-H-10	CLAY	house	25/08/2015	25/07/2015	31	430.7	3.66	0.92
CL-H-10	CLAY	house	25/08/2015	25/07/2015	31	435.7	3.68	1.15
CL-H-11	CLAY	house	25/08/2015	25/07/2015	31	450.1	7.68	1.93
CL-H-11	CLAY br.	house	25/08/2015	25/07/2015	31	445.4	8.20	2.07
CL-H-11	CLAY br.	house	25/08/2015	25/07/2015	31	446.7	7.43	1.89
CL-H-12	CLAY br.	house	25/08/2015	25/07/2015	31	445.7	7.20	1.79
CL-H-12	CLAY br.	house	25/08/2015	25/07/2015	31	442.6	7.76	1.84
CL-H-12	CLAY br.	house	25/08/2015	25/07/2015	31	437.6	7.54	1.61
CL-H-13	CLAY br.	house	25/08/2015	27/07/2015	29	447.4	6.04	1.43
CL-H-13	CLAY br.	house	25/08/2015	27/07/2015	29	452.9	6.02	1.79
CL-H-13	CLAY br.	house	25/08/2015	27/07/2015	29	451.2	6.71	1.61
CL-H-15	CLAY br.	house	26/08/2015	29/07/2015	28	453.7	5.59	1.43
CL-H-15	CLAY br.	house	26/08/2015	29/07/2015	28	456.7	5.01	1.70
CL-H-15	CLAY br.	house	26/08/2015	29/07/2015	28	455.3	5.00	1.24
CL-H-17	CLAY br.	house	26/08/2015	29/07/2015	28	424.9	4.81	1.10

CL-H-17	CLAY br.	house	26/08/2015	29/07/2015	28	417.9	4.20	1.24
<b>mean</b>						<b>0.0</b>	<b>6.24</b>	<b>1.48</b>

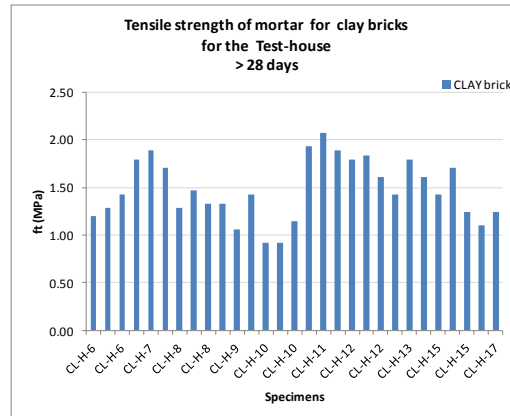
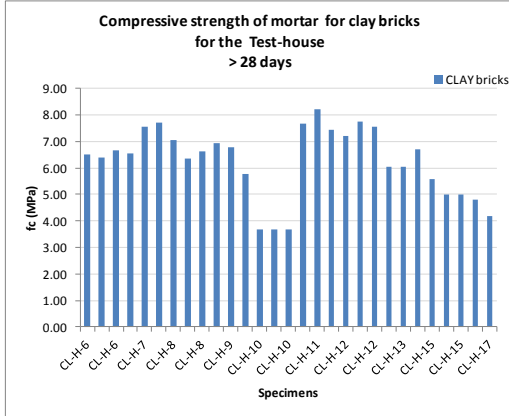


Figure 21. Tests Results on the mortar for clay house masonry, test after at least 28 days.

Figure 22 plots the distribution of tensile and compressive strength of the mortar for clay masonry used to build the full-scale test-house, after at least 28 days of maturation.

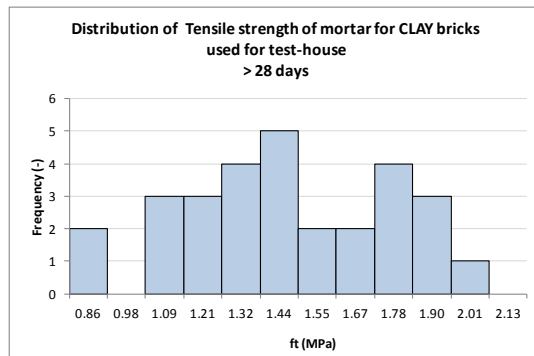
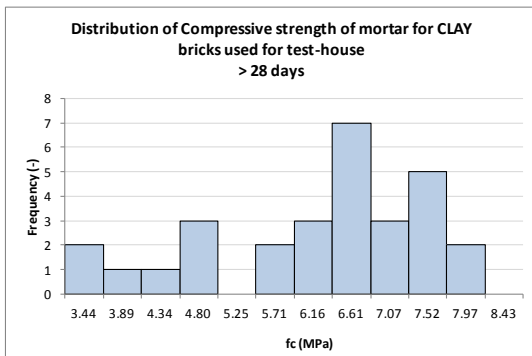


Figure 22. Distribution of strength relative to the mortar for clay house masonry, test after at least 28 days.

All the results can be resumed in the following Table:

Table 22. Resume of Test results- comparison between the tests on the mortar relative to CS and clay house masonry.

use	Compressive strength - $f_c$			Tensile strength - $f_t$			
	mean	st. dev.	c.o.v.	mean	st. dev.	c.o.v.	
	[MPa]	[MPa]	[-]	[MPa]	[MPa]	[-]	
CS	<b>1.44</b>	0.08	0.06	<b>0.37</b>	0.21	0.58	after 7 days
CS	<b>3.46</b>	0.19	0.05	<b>1.75</b>	0.09	0.05	after 11 days
CS	<b>5.23</b>	0.45	0.09	<b>1.70</b>	0.26	0.15	after 16 days
CS	<b>5.71</b>	1.46	0.25	<b>1.78</b>	0.41	0.23	> 28 days
CLAY	<b>3.85</b>	0.32	0.08	<b>1.03</b>	0.19	0.18	after 13 days
CLAY	<b>4.88</b>	0.50	0.10	<b>1.86</b>	0.23	0.12	after 18 days
CLAY	<b>6.24</b>	0.58	0.09	<b>1.48</b>	0.28	0.19	> 28 days

The following graph shows the dependence of the mechanical properties of the mortar on time of maturation. The mortar is the one used for the calcium silicate masonry. The dashed line is referred to the masonry relative to the constructions walls and specimens used for the in-plane and out-of-plane tests as well as others tests on smaller specimens (eg. wallettes for the compressive test on the masonry). The solid line is referred to the masonry relative to the full-scale test-house.

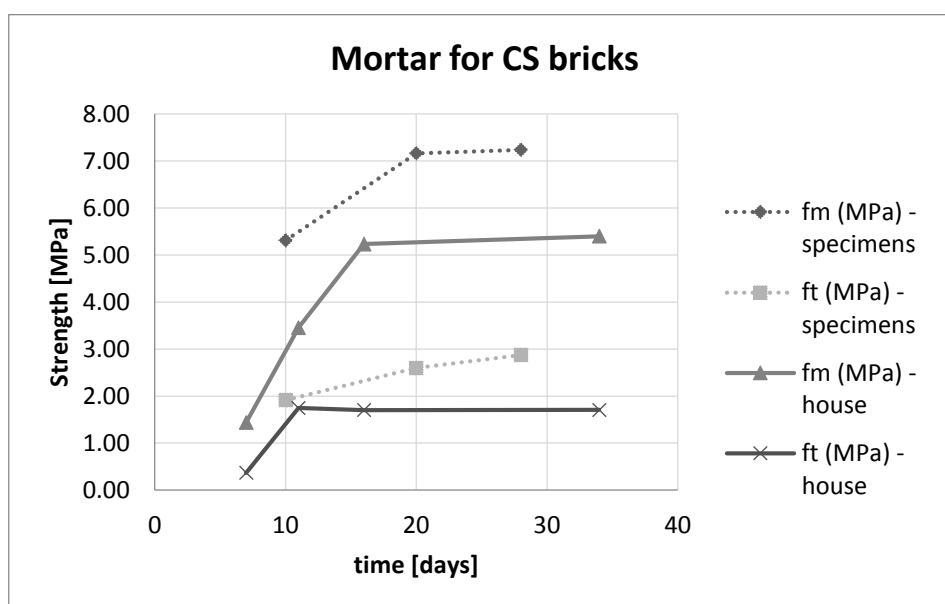


Figure 23. Dependence of Compressive and flexural strength of mortar for CS bricks on time of maturation.

### 3.2.3 Mortar sampled from full-scale building specimen (HE)

The specimen of mortar taken "in-situ", after the test on the shaking table of the full-scale test-house, were tested in flexion and compression by adapting the procedure of the EN 1015-11.

The mortar tested was extracted from the courses of calcium silicate masonry that appear to be still intact after the dynamic test. In particular, the mortar was taken from the last courses of masonry of the spandrels at the second floor (laid the 21<sup>st</sup> of July 2015).

The dimensions of the samples are about 10 cm of length, 4 cm of width and 1 cm of thickness. The scaling of the specimen should affect the results giving better results in terms of mechanical properties of the mortar. However, for this series of tests both compressive and flexural strength results to be lower respect the values obtained from the previous test campaign with the mortar casted in its proper formwork. Hence the values of  $f_c$  and  $f_t$  derived from the specimens taken in-situ can be assumed as a lower bound.

The following Table resumes the results obtained from this test.

*Table 23. Resume of Test results- ID #, dimensions, density, tensile and compressive strength of the mortar taken "in-situ" from the CS walls of the test-house*

Specimen	Geometry			Density $\rho$ [kg/m <sup>3</sup> ]	Strength		Test date
	L [mm]	B [mm]	t [mm]		Tensile $f_t$ [MPa]	Compressive $f_c$ [MPa]	
	1	100	40	12	1536	0.75	
2	100	40	12	1580	1.04	3.01	29/09/2015
3	100	44	11	1437	0.97	1.68	30/09/2015
4	100	44	12	1372	0.94	1.65	30/09/2015
5	99	40	12	1464	0.83	1.59	30/09/2015
6	100	41	11	1433	0.87	1.86	30/09/2015
7	102	44	10	1379	1.27	1.18	30/09/2015
8	99	42	10	1445	0.80	2.35	30/09/2015
9	102	41	13	1450	1.28	2.13	30/09/2015
10	101	41	12	1435	1.09	1.75	30/09/2015
11	100	41	12	1490	0.80	2.02	30/09/2015
12	100	41	11	1364	0.94	2.04	30/09/2015
13	100	42	11	1382	0.94	2.08	30/09/2015
<b>mean</b>				1444	<b>0.96</b>	<b>1.97</b>	
<b>st.dev.</b>				64.30	0.17	0.44	
<b>c.o.v.</b>				0.04	0.17	0.23	

It is possible to notice that the values of Tensile and Compressive Strength are much smaller than the ones obtained following the code procedure:



$f_{\bar{r}}=1.80$  MPa with a c.o.v = 0.10,

$f_c=5.46$  MPa with a c.o.v = 0.12.

These values refer to the mortar casted the 21<sup>st</sup> of July 2015 only.

### 3.3 Compressive strength of masonry

The reference code for the present experimental test is the European Norm EN 1052-1:1998. The tests were performed at the DICAr Laboratory of the University of Pavia in Italy. The compressive strength evaluated according to this procedure refers to the direction perpendicular to the bedjoints of the masonry specimens.

Four series of compression test on masonry wallettes were performed:

1. Compression test specimens made of calcium silicate (C.S.) masonry, with the same materials used to cast the walls tested both in-plane and out of plane; These specimens are named EC\_MAT\_11 plus a letter.
2. Compression test specimens made of clay masonry, with the same materials used to cast the walls tested out of plane; These specimens are named EC\_MAT\_21 plus a letter.
3. Compression test specimens made of calcium silicate masonry, with the same materials used to build the full-scale test-house; These specimens are named EC\_MAT\_H\_11 plus a letter.
4. Compression test specimens made of clay masonry, with the same materials used to build the full-scale test-house; These specimens are named EC\_MAT\_H\_21 plus a letter.

#### 3.3.1 Compressive strength of C.S. masonry - EC\_MAT\_11

The test specimens were composed by 6 Calcium silicate wallettes listed in following Table. The specimens were built with the same materials used to cast the walls tested both in-plane and out of plane; These specimens are named EC\_MAT\_11 plus a letter.

*Table 24. Specimen ID # and geometric properties*

<b>EC_MAT_11_a</b>	476 x 434 x 102 mm
<b>EC_MAT_11_b</b>	476 x 434 x 102 mm
<b>EC_MAT_11_c</b>	476 x 434 x 102 mm
<b>EC_MAT_11_d</b>	476 x 434 x 102 mm
<b>EC_MAT_11_e</b>	476 x 434 x 102 mm
<b>EC_MAT_11_g</b>	476 x 434 x 102 mm

Figure 4.1 shows the masonry wallets built by the Dutch masons in the DICAr laboratory.



Figure 24. View of the C.S. masonry wallettes

The date of construction of the masonry wallettes (Specimens EC\_MAT\_11\_a/b/c/d/e/g) was 25/3/2015. The compression tests were performed from 22<sup>nd</sup> April 2015 to 4<sup>th</sup> May 2015.

The masonry wallettes were composed by 6 layers of calcium silicate bricks; the specimen dimensions were chosen according to the UNI EN-1052-1 prescriptions (section 7.1); the section area of the specimens is equal to 44268 mm<sup>2</sup>. As shown in Figure 25, the masonry wallets are 476 mm high, 434 mm wide and 102 mm thick.

Figure 25 shows also the instrumentation adopted and the brick texture of Calcium silicate wallettes.

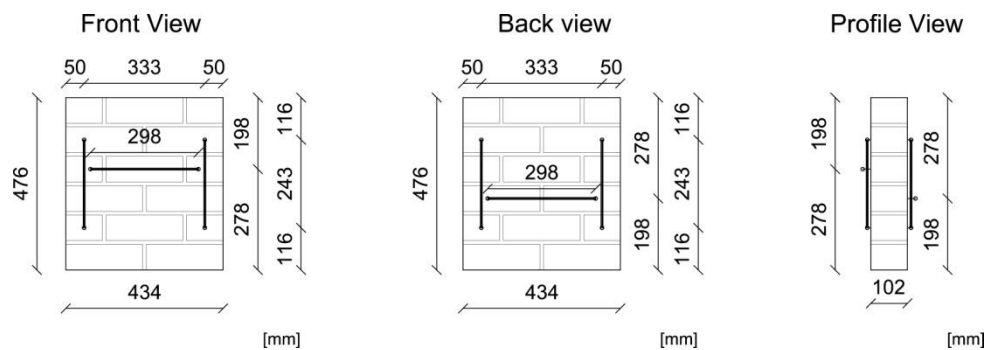


Figure 25. Geometry and Instrumentation of test specimen, C.S. wallettes.

The instrumentation in the front side of the specimen was composed by two vertical potentiometers of length equal to 243 mm spaced 333 mm and one horizontal potentiometer of length 298 mm positioned at the mid-height of the fourth layer of bricks. In the back side of the test specimen there were two vertical potentiometers of length equal to 243 mm spaced 333 mm and one horizontal potentiometer of length 298 mm positioned at the mid-height of the third layer of bricks. Figure 26 shows the ID number associated to each potentiometer.

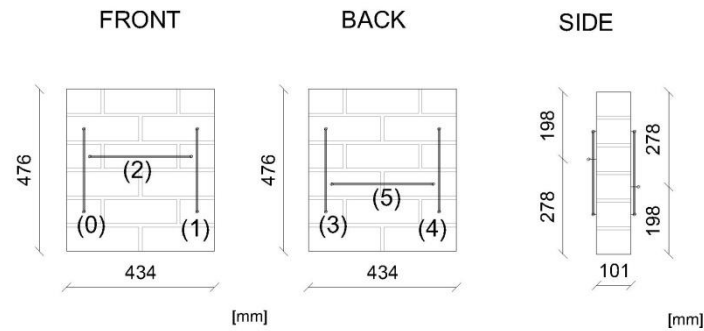


Figure 26. Potentiometer layout and identification, C.S. wallettes.

Figure 27 shows the test layout and the positioning of the test specimen on the testing machine.

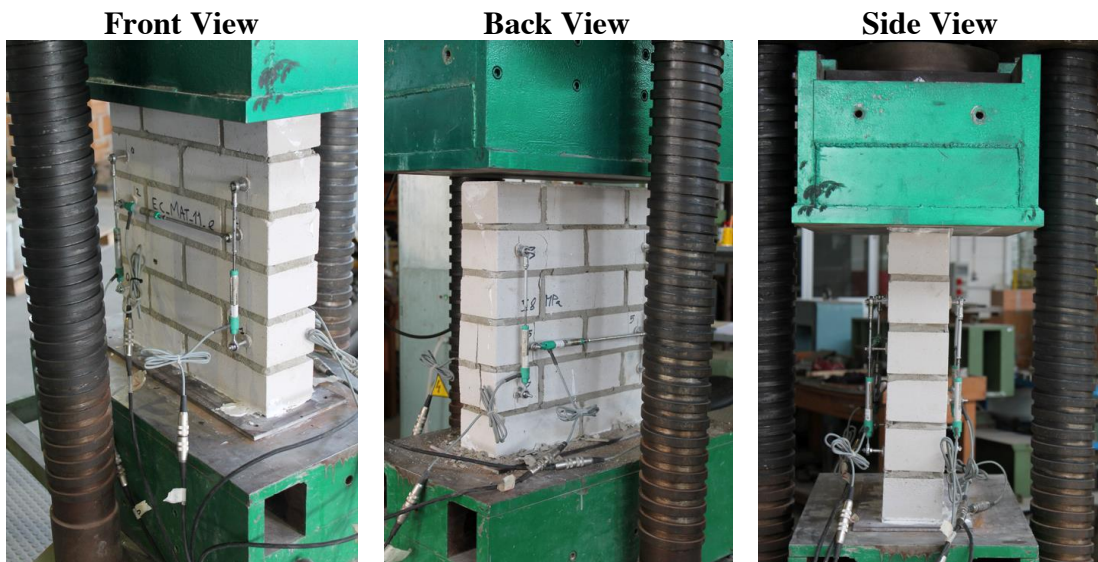


Figure 27. Setup of the compressive test on CS masonry wallettes.

### Experimental Procedure

The test envisaged the failure of the test specimens by means of vertical compression load applied at their top. This vertical compressive load is perpendicular to the bedjoints of the masonry specimens. The loading protocol consisted on series of 3 cycles of loading and unloading at constant force amplitude; the force amplitude was then increased progressively for the further cycles and the force increment is equal to 74 kN. The loading velocity is consistent with UNI EN-1052-1 prescriptions. Figure 4.5 shows the applied loading history.

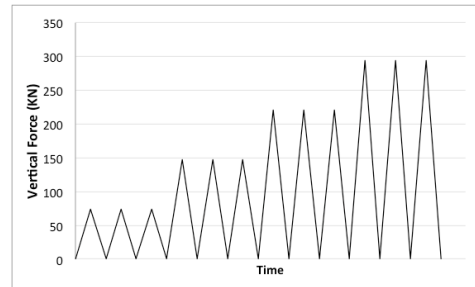


Figure 28. Loading history used for the compressive test on CS masonry wallettes.

### Test results

The vertical and horizontal deformations later shown were obtained averaging the deformation recorded by each vertical and horizontal potentiometer.

In particular, the vertical deformation is obtained averaging the deformation recorded by potentiometers number 0-1-3-4, while the horizontal deformation is obtained from the horizontal potentiometers 2 and 5.

Young Modulus ( $E_1$ ) is the secant elastic modulus at 33% of  $f_m$  and the origin (0,0).

Young Modulus ( $E_2$ ) was computed as the secant at 10% of  $f_m$  and the origin (0,0).

Young Modulus ( $E_3$ ) was computed as the secant at 30% of  $f_m$  and 10% of  $f_m$ .

Other calculation on elastic modulus (e.g. considering the unloading and reloading phase could be calculated if needed).

Looking at the envelope of the cyclic pressure-deformation curve it can be seen as specimens exhibit a non-linear behavior even for low level of vertical pressure. Figure 29 shows the pressure-deformation curve ( $\sigma - \epsilon$ ) of the specimen EC\_MAT\_11\_b. This seems to be associable to a peculiarity of the C.S. material.

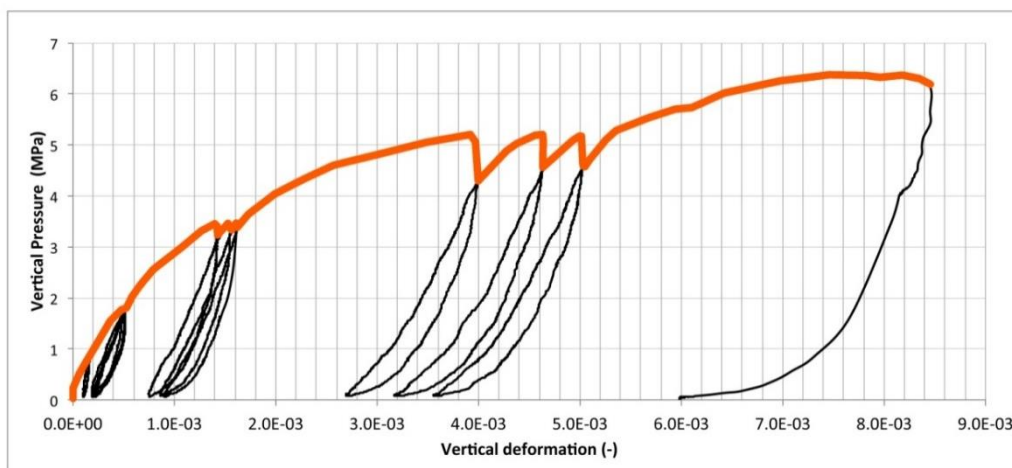


Figure 29. Vertical Deformations vs Vertical Pressure ( $\sigma - \epsilon$ ) of EC\_MAT\_11\_b Specimen.

It is not possible to individuate a linear branch of the envelope curve where the  $E$  modulus can be considered constant. The choice of the pressure level can affect the value of the Young Modulus  $E$ . Figure 30 underline such differences.

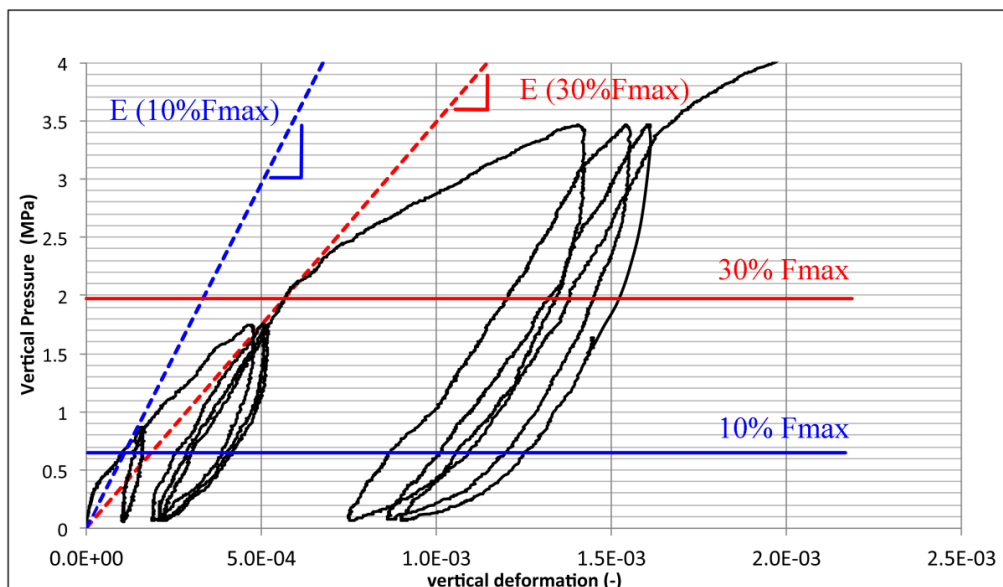


Figure 30. Influence on the  $E$  Modulus of the pressure level considered (EC\_MAT\_11\_b).

Following table summarizes the maximum pressure reached by each Specimen ( $f_m$ ), and the Young Modulus computed respectively with 33% ( $E_1$ ), 10% ( $E_2$ ) of the maximum pressure and the secant line passing through the points ( $33\%f_m, \epsilon_{33\%f_m}$ ) and ( $10\%f_m, \epsilon_{10\%f_m}$ ) representing the Modulus value termed  $E_3$ .

Table 25. Compressive strength and Elastic Moduli of the C.S. wallettes.

	$f_m$	$E_1(33\%f_m)$	$E_2(10\%f_m)$	$E_3$	
	[MPa]	[MPa]	[MPa]	[MPa]	date
EC_MAT_11_a	6.83	3833	4359	3645	22/04/2015
EC_MAT_11_b	6.38	3491	6395	2924	27/04/2015
EC_MAT_11_c	5.96	3703	4036	3577	28/04/2015
EC_MAT_11_d	5.92	2908	4407	2539	29/04/2015
EC_MAT_11_e	6.39	3486	3799	3365	24/04/2015
EC_MAT_11_g	5.72	2118	2097	3365	04/05/2015
<b>mean</b>	<b>6.20</b>	<b>3256</b>	<b>4182</b>	<b>3236</b>	
<b>st.dev.</b>	0.41	641.24	1377.97	424.33	
<b>c.o.v.</b>	0.07	0.20	0.33	0.13	

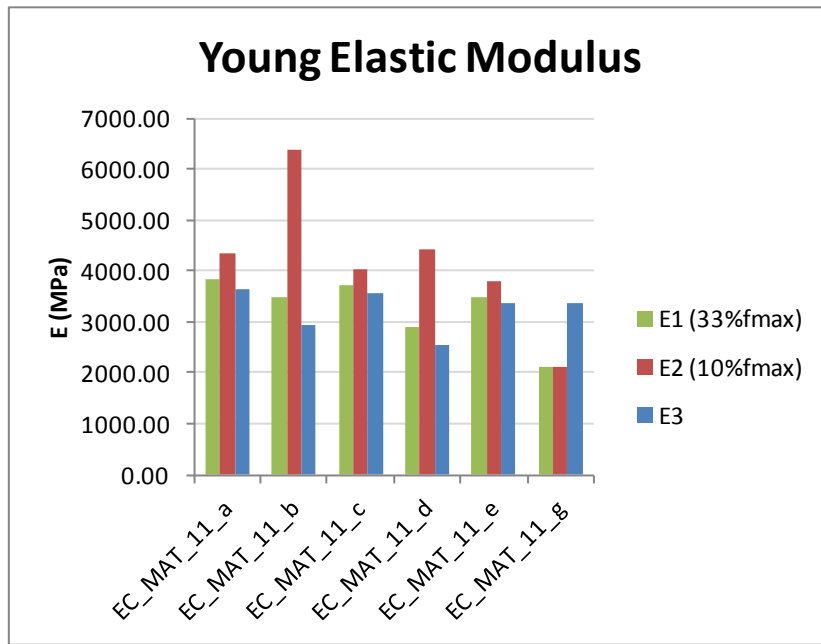


Figure 31. Elastic Moduli of C.S. wallettes.

Following Figures show the Vertical Deformation vs. Vertical Pressure (black solid line) and the Horizontal Deformation vs. Vertical Pressure (dashed red line) related to each specimen tested.

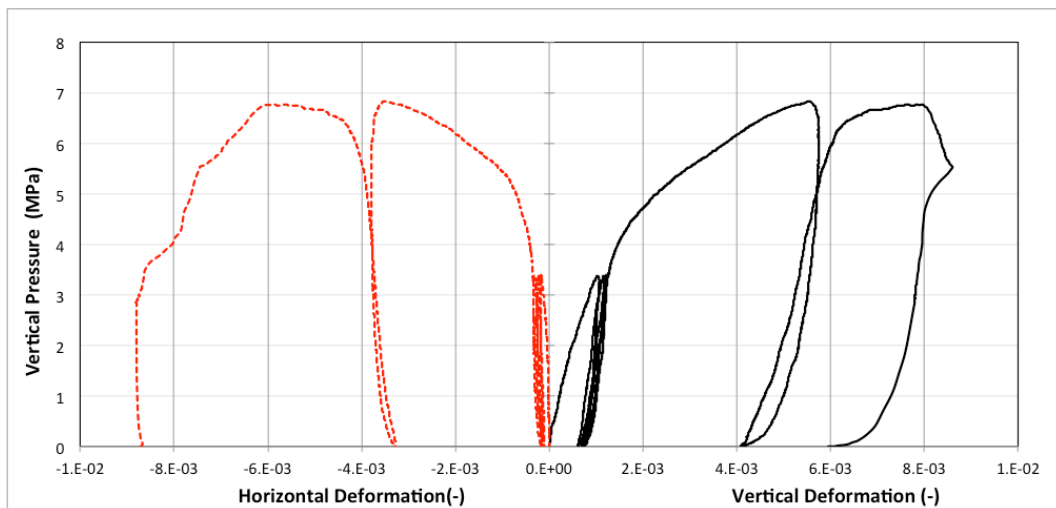


Figure 32. EC\_MAT\_11\_a: Vertical and Horizontal Deformations vs Vertical Pressure.

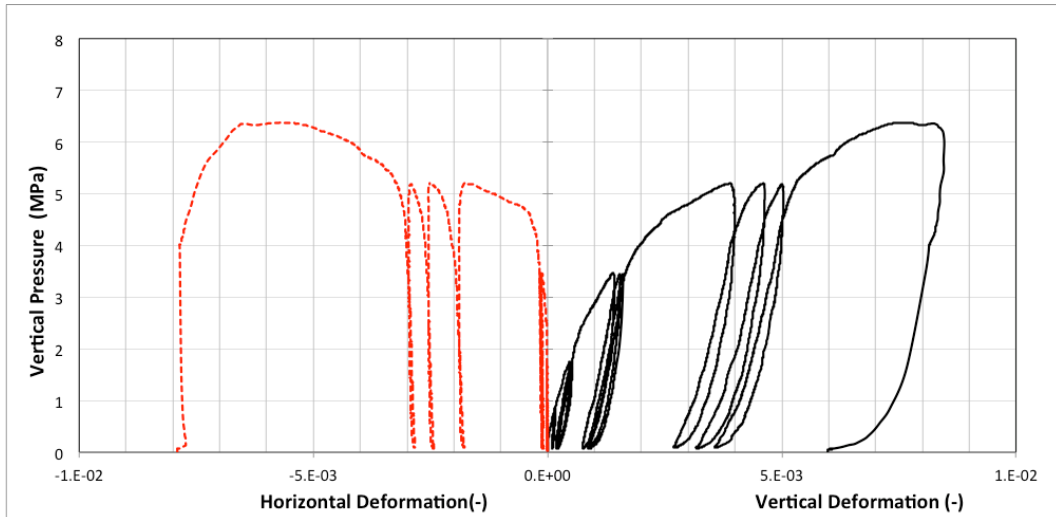


Figure 33. *EC\_MAT\_11\_b: Vertical and Horizontal Deformations vs Vertical Pressure.*

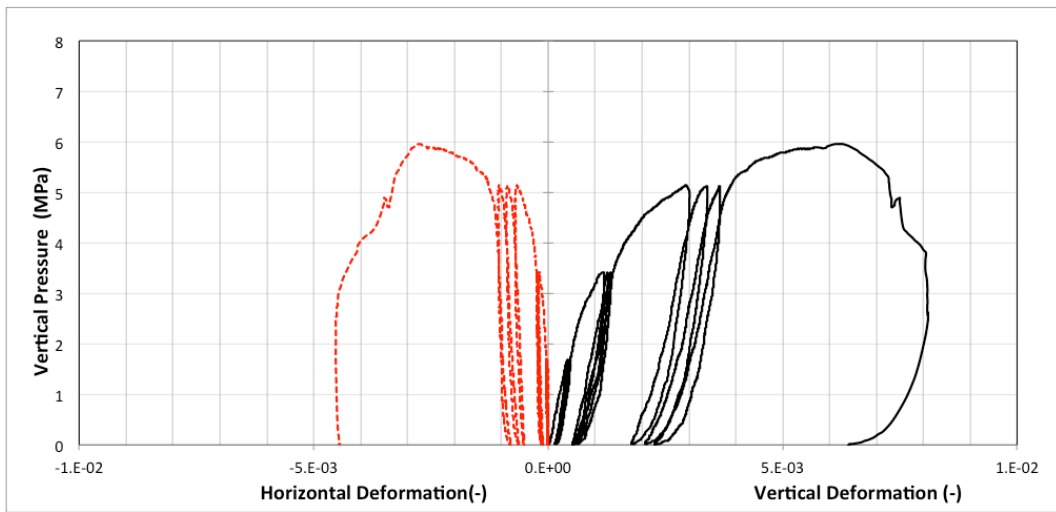


Figure 34. *EC\_MAT\_11\_c: Vertical and Horizontal Deformations vs Vertical Pressure.*

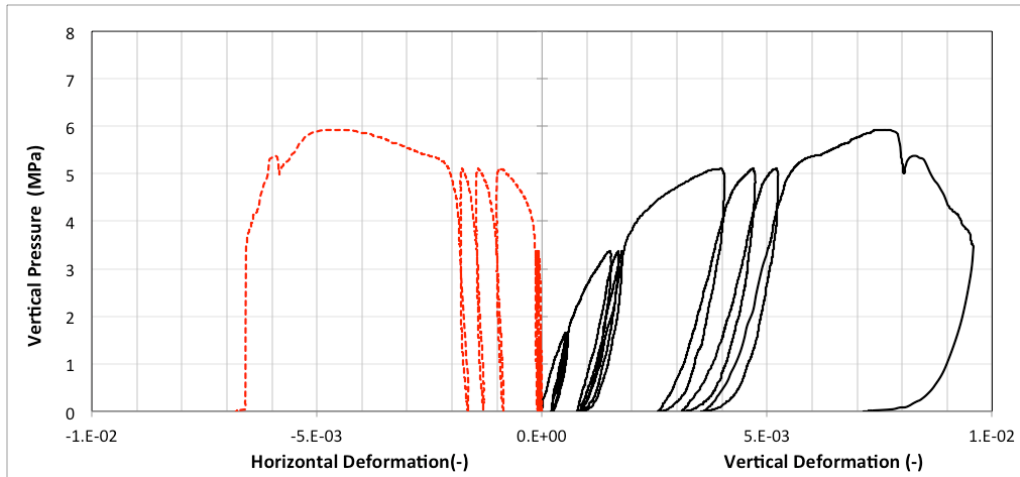


Figure 35. *EC\_MAT\_11\_d: Vertical and Horizontal Deformations vs Vertical Pressure.*

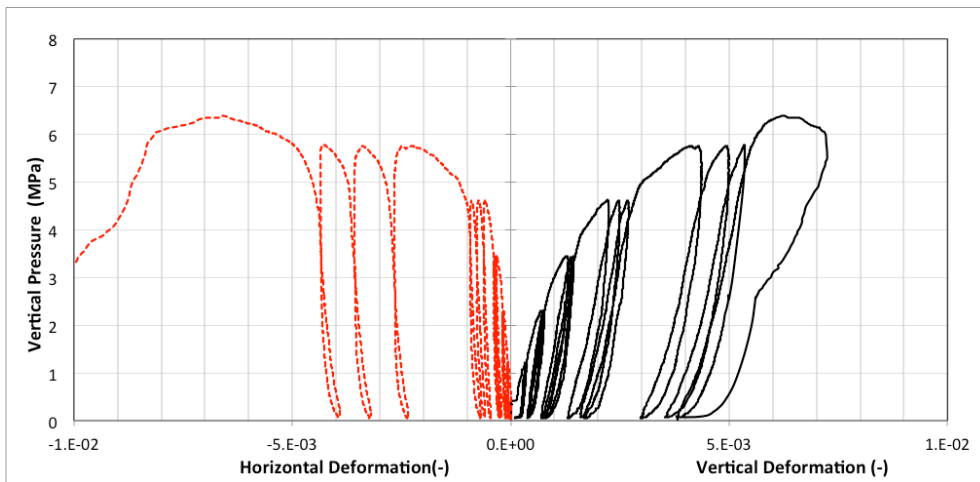


Figure 36. *EC\_MAT\_11\_e: Vertical and Horizontal Deformations vs Vertical Pressure.*

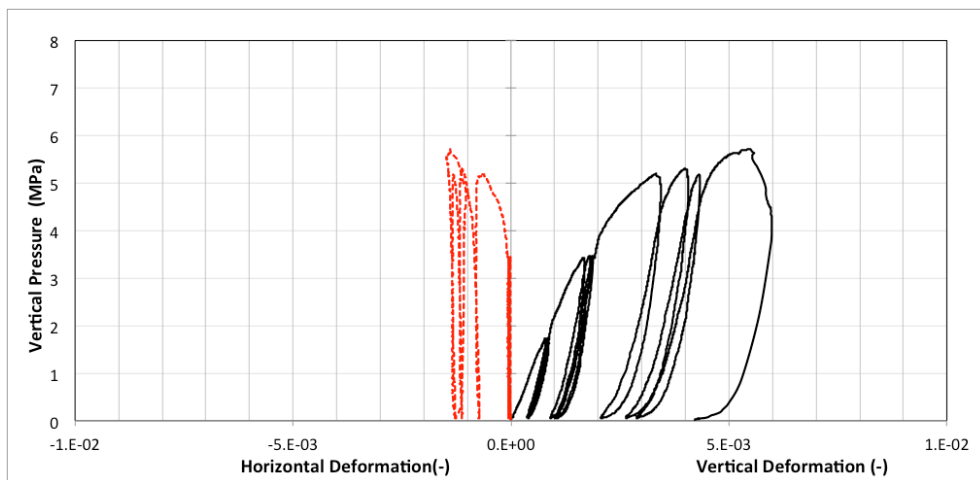


Figure 37. *EC\_MAT\_11\_g: Vertical and Horizontal Deformations vs Vertical Pressure.*

### 3.3.2 Compressive strength of clay masonry - EC\_MAT\_21

The test specimens were composed by 7 clay wallettes listed in Table 26. The specimens were built with the same materials used to cast the walls tested out of plane; These specimens are named EC\_MAT\_21 plus a letter.

Table 26. Specimen ID and geometric Properties

<b>EC_MAT_21_a</b>	485 x 430 x 100 mm
<b>EC_MAT_21_b</b>	485 x 436 x 99 mm
<b>EC_MAT_21_c</b>	485 x 435 x 99 mm
<b>EC_MAT_21_d</b>	485 x 434 x 99 mm
<b>EC_MAT_21_e</b>	486 x 434 x 96 mm
<b>EC_MAT_21_f</b>	485 x 432 x 100 mm
<b>EC_MAT_21_g</b>	486 x 434 x 99 mm

Figure 4.14 shows the masonry wallets built by the Dutch masons in the DICAr laboratory.



Figure 38. View of the Clay Masonry wallets (EC\_MAT\_21\_a/g).

The date of construction of the masonry wallets (Specimens EC\_MAT\_21\_a/g) was 21/4/2015. The compression tests were performed the 10-29/6/2015.

The masonry wallets were composed by 8 layers of clay bricks; the specimen dimensions were chosen according to the UNI EN-1052-1 prescriptions (section 7.1); the section area of the specimens is equal to 43000 mm<sup>2</sup>. As shown by figure 4.15, the masonry wallets are 485 mm high (the first layer of gypsum at the base of the wallette is about 15 mm), 430 mm wide and 100 mm thick.

Figure 38 shows also the instrumentation adopted and the brick texture of clay wallets.

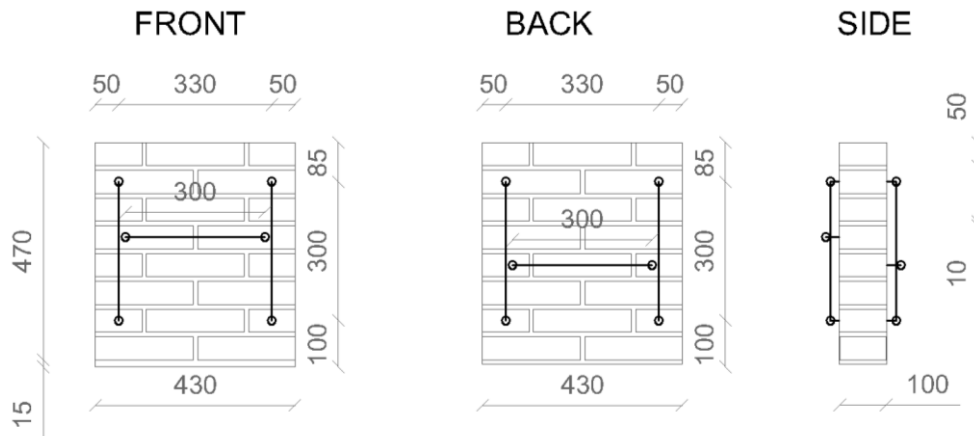


Figure 39. Geometry and Instrumentation of test specimen, clay. wallettes.

The instrumentation in the front side of the specimen was composed by two vertical potentiometer of length equal to 300 mm spaced 330 mm and one horizontal potentiometer of length 300 mm positioned at the mid-height of the fifth layer of bricks. Two vertical potentiometers were installed on one side of the specimen. Their length is equal to 300 mm spaced 330 mm and one horizontal potentiometer of length 300 mm positioned at the mid-height of the fourth layer of bricks. Figure 4.16 shows the ID number associated to each potentiometer.

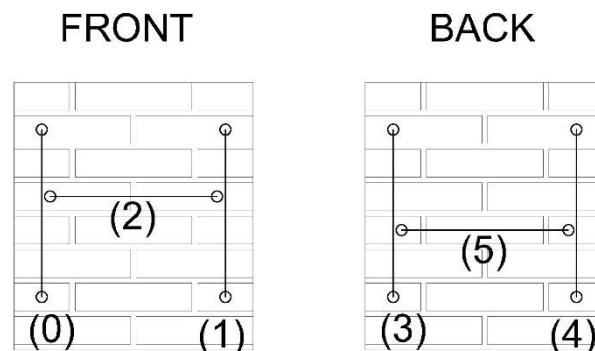


Figure 40. Potentiometer layout and identification, clay. wallettes.

Next figure shows the test layout and the positioning of the test specimen on the testing machine.

**Front View**

**Back View**

**Side View**



*Figure 41. Setup of the compressive test on clay masonry wallettes*

### ***Experimental Procedure***

The test envisaged the failure of the test specimens by means of vertical compression load applied at their top. The loading protocol consisted on series of 3 cycles of loading and unloading at constant force amplitude; the force amplitude was then increased progressively for the further cycles and the force increment is equal to 98 kN. The loading velocity is consistent with UNI EN-1052-1 prescriptions. Figure 42 shows the applied loading history.

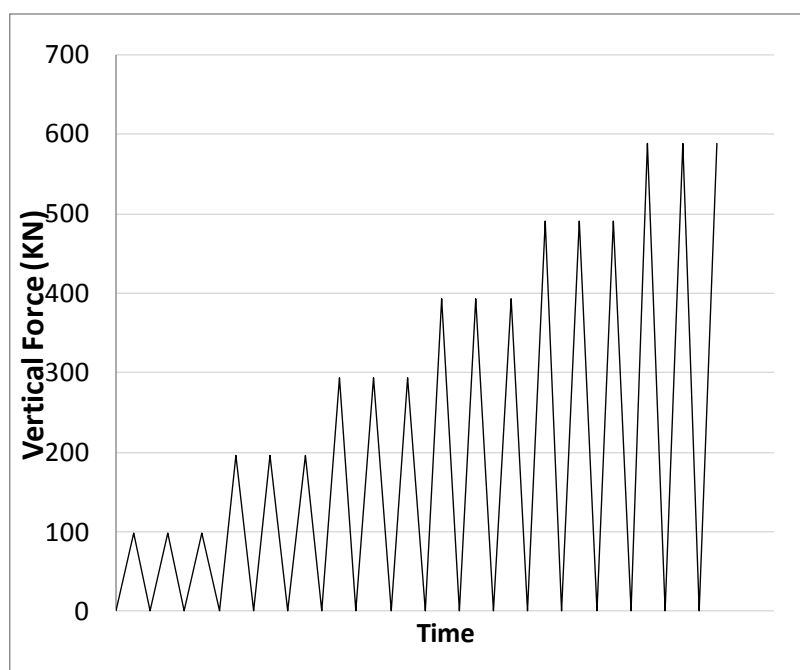


*Figure 42. Loading history used for the compressive test on clay masonry wallettes*

### ***Test results***

The vertical and horizontal deformations were obtained averaging the deformation recorded by each vertical and horizontal potentiometer.

In particular, the vertical deformation is obtained averaging the deformation recorded by potentiometers number 0-1-3-4, while the horizontal deformation is obtained from the horizontal potentiometers 2 and 5.

The Young Modulus ( $E_1$ ) is the secant elastic modulus at 33% of  $f_m$  and the origin (0,0).

The Young Modulus ( $E_2$ ) was computed as the secant at 10% of  $f_m$  and the origin (0,0).

The Young Modulus ( $E_3$ ) was computed as the secant at 30% of  $f_m$  and 10% of  $f_m$ .

Other calculation on elastic modulus (e.g. considering the unloading and reloading phase) are available if needed. Figure 4.19 shows the pressure-deformation curve ( $\sigma - \epsilon$ ) of the specimen EC\_MAT\_21\_a.

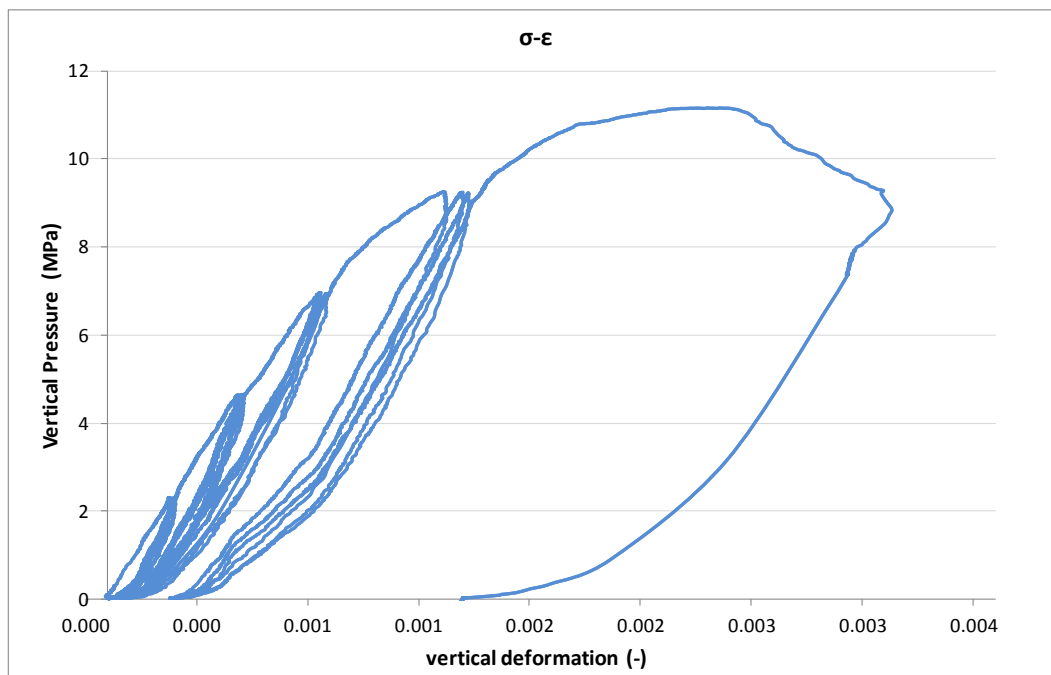


*Figure 43. Vertical Deformations vs Vertical Pressure ( $\sigma - \epsilon$ ) of EC\_MAT\_21\_a Specimen.*

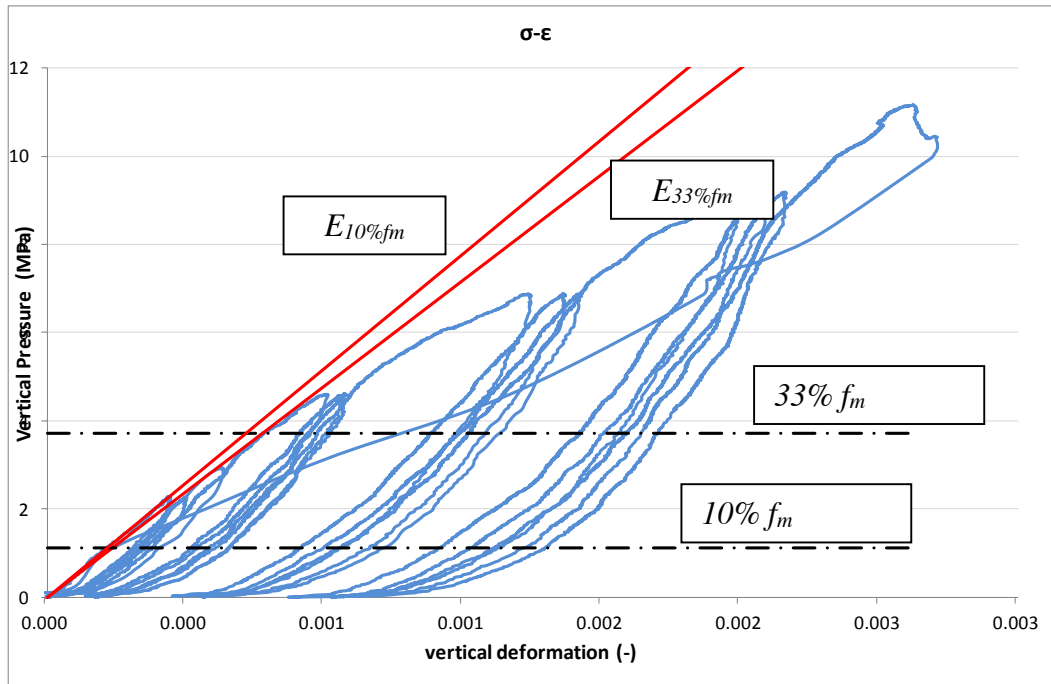


Figure 44. Influence on the E Modulus of the pressure level considered (EC\_MAT\_21\_b)

Table 27 summarizes the maximum pressure reached by each Specimen ( $f_m$ ), and the Young Modulus computed respectively with 30% ( $E_1$ ), 10% ( $E_2$ ) of the maximum pressure and the secant line passing through the points ( $33\%f_m, \epsilon_{33\%f_m}$ ) and ( $10\%f_m, \epsilon_{10\%f_m}$ ) representing the Modulus value termed E3.

Table 27. Compressive strength and Elastic Moduli of the clay wallettes.

	$f_m$	$E_1 (30\%f_m)$	$E_2 (10\%f_m)$	$E_3$	date
	[MPa]	[MPa]	[MPa]	[MPa]	
<b>EC_MAT_21_A</b>	11.17	7981	8004	7972	10/06/2015
<b>EC_MAT_21_B</b>	11.17	4799	5198	4647	11/06/2015
<b>EC_MAT_21_C</b>	10.49	5584	5382	5676	15/06/2015
<b>EC_MAT_21_D</b>	11.95	4284	5403	4991	15/06/2015
<b>EC_MAT_21_E</b>	12.36	7608	8130	8252	26/06/2015
<b>EC_MAT_21_F</b>	9.08	3792	3806	3979	26/06/2015
<b>EC_MAT_21_G</b>	13.05	6268	6309	6251	29/06/2015
<b>mean</b>	11.32	5760	6033	<b>5967</b>	
<b>st.dev.</b>	1.31	1613	1573	1636	
<b>c.o.v.</b>	0.12	0.28	0.26	0.27	

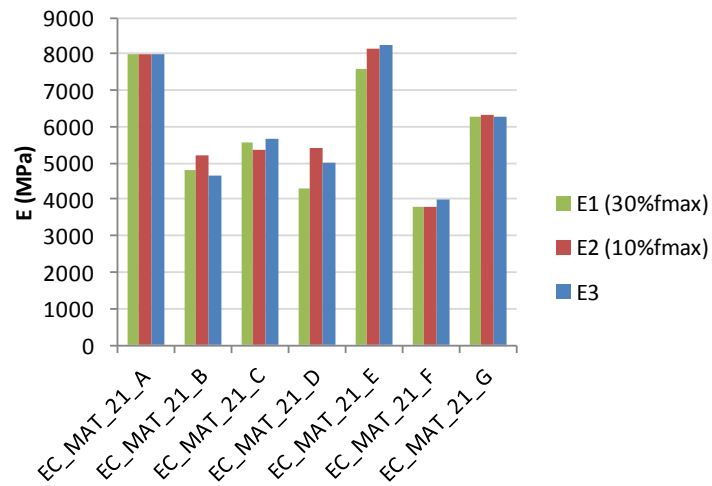


Figure 45. Elastic Moduli of clay wallettes.

Following Figures show the Vertical Deformation vs Vertical Pressure (black line) and the Horizontal Deformation vs. Vertical Pressure (red line) related to each specimen tested.

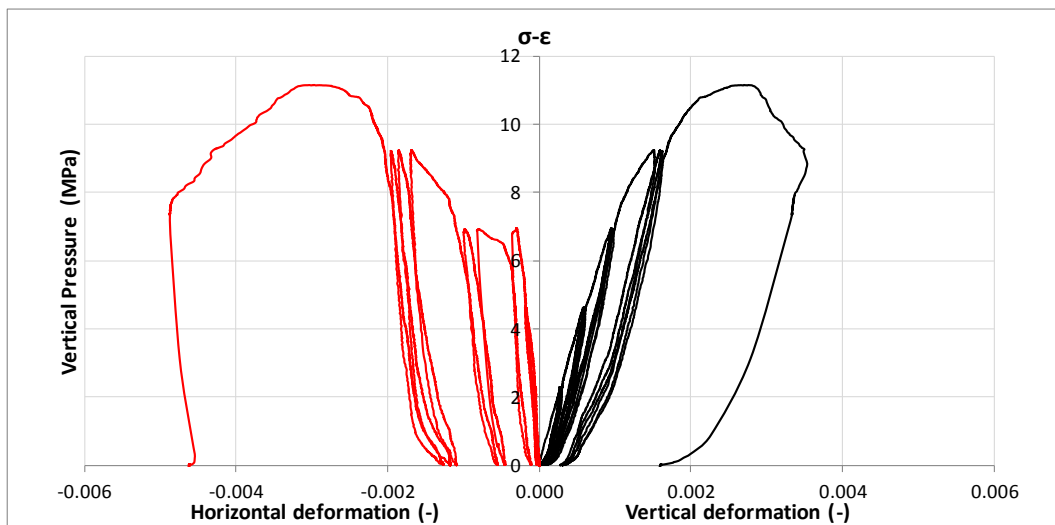


Figure 46. EC\_MAT\_21\_a: Vertical and Horizontal Deformations vs Vertical Pressure.

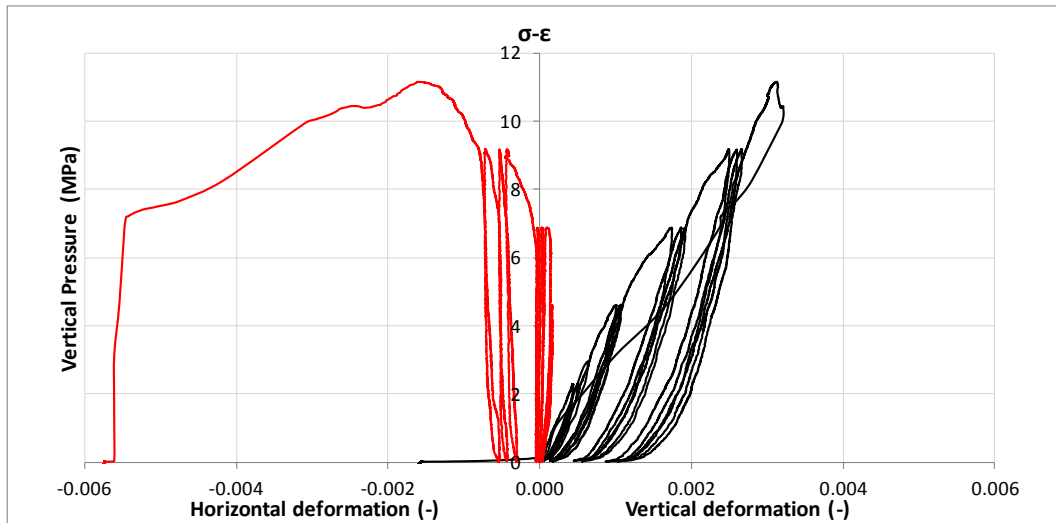


Figure 47. EC\_MAT\_21\_b: Vertical and Horizontal Deformations vs Vertical Pressure.

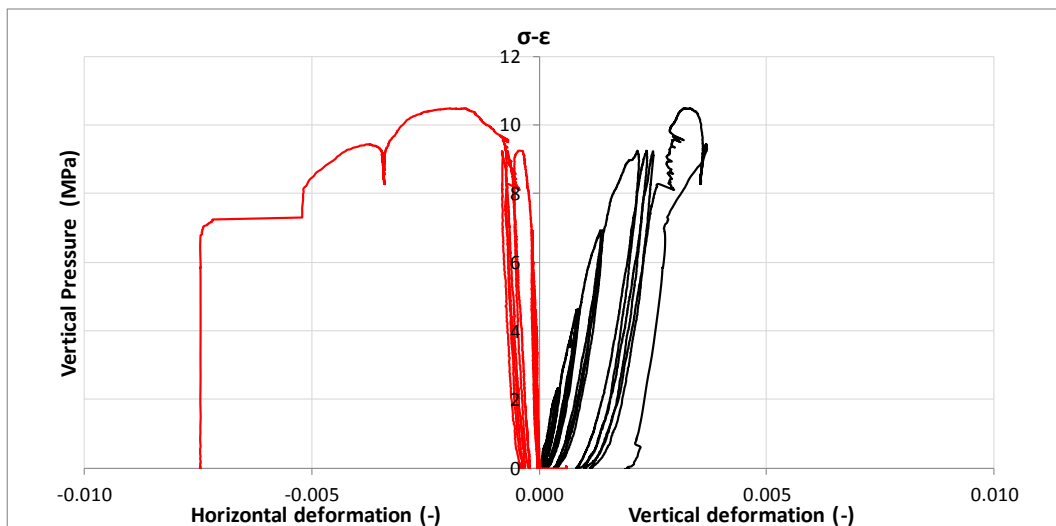


Figure 48. EC\_MAT\_11\_c: Vertical and Horizontal Deformations vs Vertical Pressure.

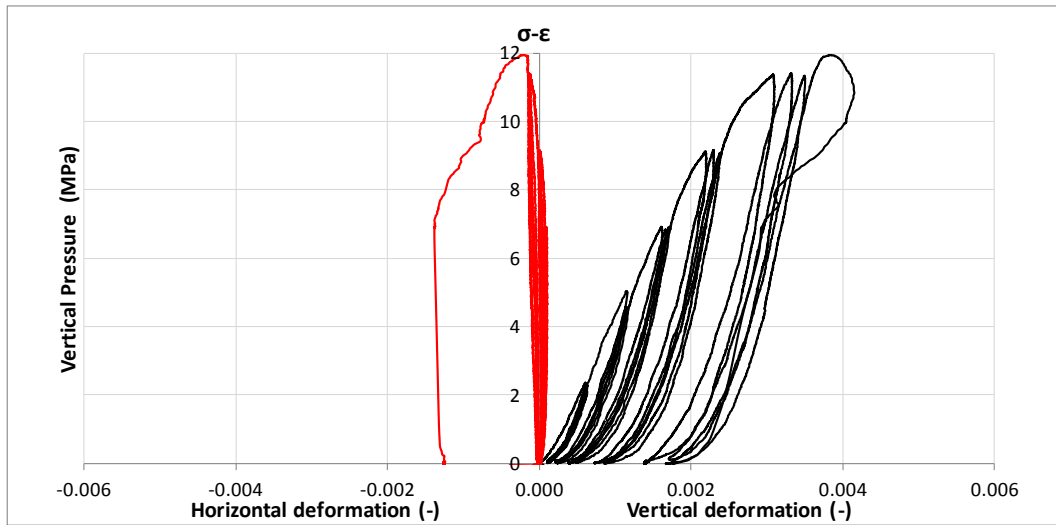


Figure 49. EC\_MAT\_11\_d: Vertical and Horizontal Deformations vs Vertical Pressure.

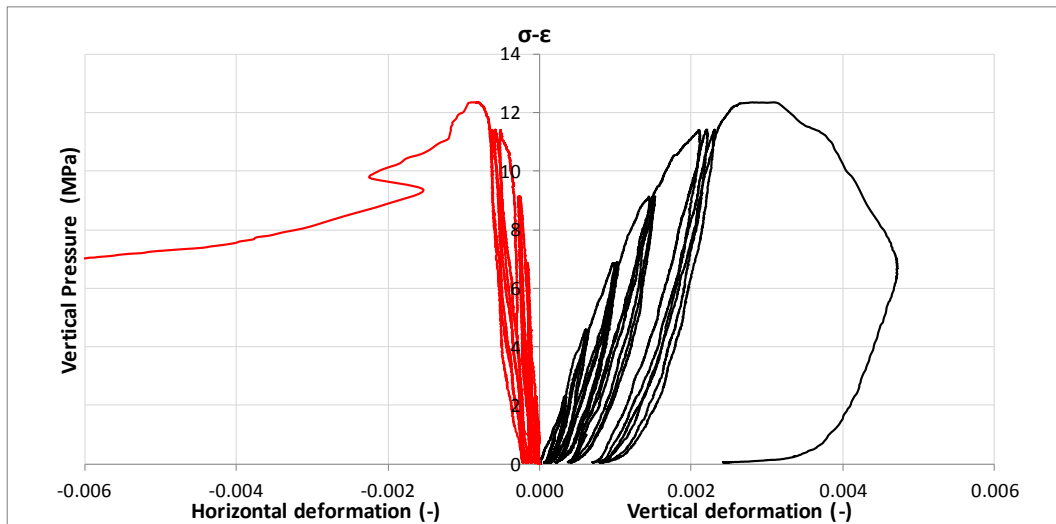


Figure 50. EC\_MAT\_11\_e: Vertical and Horizontal Deformations vs Vertical Pressure.

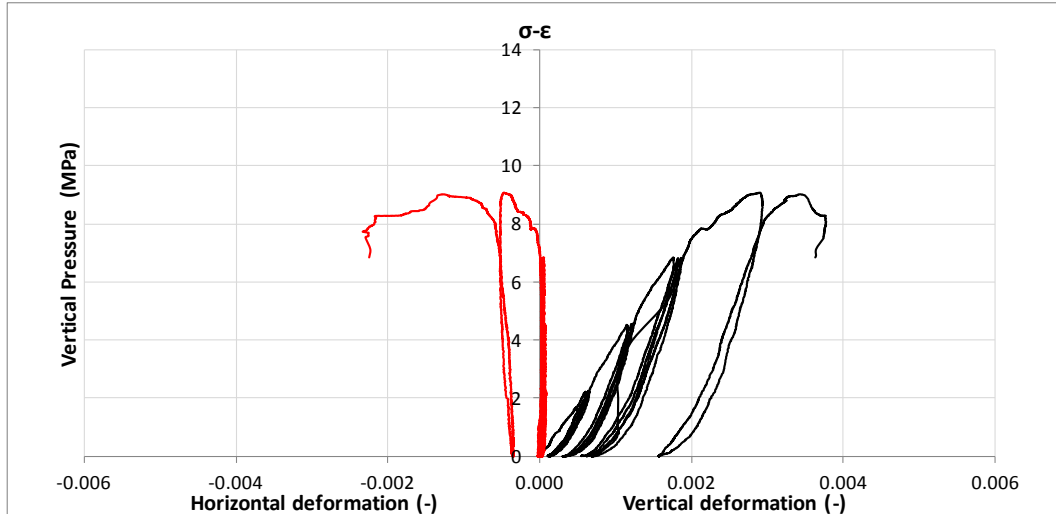


Figure 51. EC\_MAT\_11\_f: Vertical and Horizontal Deformations vs Vertical Pressure.

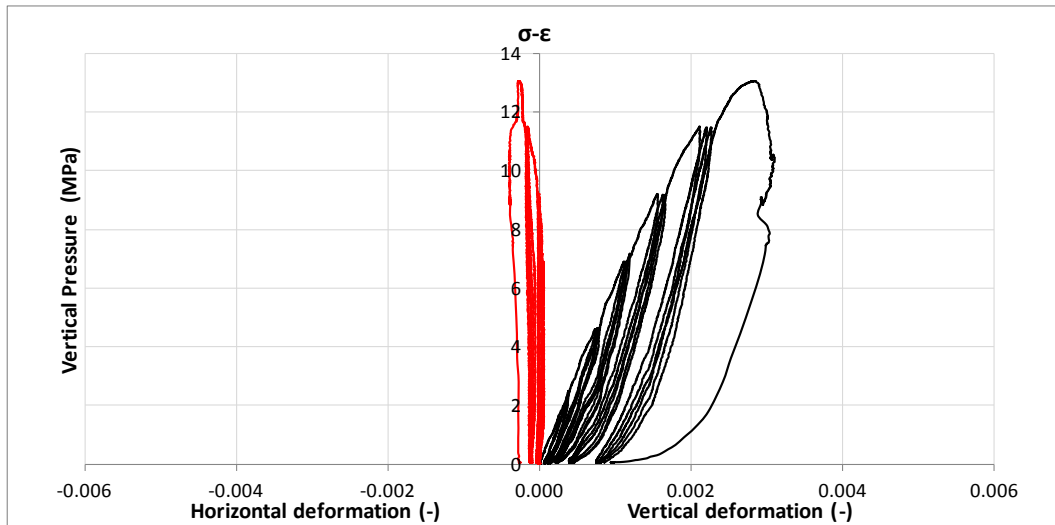


Figure 52. EC\_MAT\_11\_g: Vertical and Horizontal Deformations vs Vertical Pressure.

### 3.3.3 Compressive strength of C.S. masonry - EC\_MAT\_H\_11

The test specimens were composed by 6 Calcium silicate walleets listed in Table 28.

The specimens were made of the same bricks and mortar used to build the full-scale test-house: the materials come from the same batch. Also the environmental conditions were similar and the masons were the same.

Table 28. Specimen ID and geometric properties of C.S "house" walleets.

	<i>hs</i> (height)	<i>ls</i> (length)	<i>ts</i> (thickness)	Area	Weigth	density
	[mm]	[mm]	[mm]	[mm <sup>2</sup> ]	[kg]	[kg/m <sup>3</sup> ]
EC_MAT_H_11_a	480	440	102	44880	39.6	1838
EC_MAT_H_11_b	483	436	102	44472	39.8	1853
EC_MAT_H_11_c	487	439	102	44778	39.6	1816
EC_MAT_H_11_d	472	443	101	44743	38.5	1823
EC_MAT_H_11_f	481	434	101	43834	38.4	1821
EC_MAT_H_11_g	485	442	102	45084	40.6	1857
<b>mean</b>	481	439	102	44632	39.4	<b>1835</b>
<b>st.dev.</b>	5	3	1	439	0.8	17
<b>c.o.v.</b>	0.01	0.01	0.01	0.01	0.02	0.01

Figure 53 shows the masonry walleets built by the Dutch masons in the DICAr laboratory.



Figure 53. View of the Calcium Silicate Masonry “house” wallets.

The date of construction of the masonry wallets (Specimens EC\_MAT\_H\_11\_a/b/c/d/f/g) was 24/6/2015. The compression tests were performed between the 23- 28/9/2015.

The masonry wallets were composed by 6 layers of calcium silicate bricks; the specimen dimensions were chosen according to the UNI EN-1052-1 prescriptions (section 7.1); the section area of the specimens is equal to 44632 mm<sup>2</sup>. As shown by Table 4.5, the masonry wallets are about 481 mm high, 439 mm wide and 102 mm thick.

For what concerns properties and characteristic strength of the mortar and the brick see the dedicated report. Next Figure 54 shows also the instrumentation adopted and the brick texture of calcium silicate wallets.

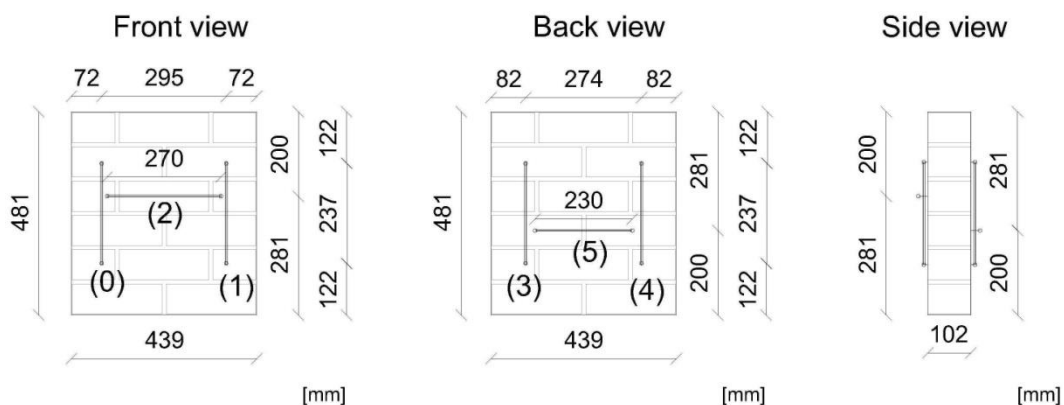


Figure 54. Geometry and Instrumentation of test specimen - CS "house" wallettes.

The instrumentation in the front side of the specimen was composed by two vertical potentiometer of length equal to 237 mm spaced 294 mm and 1 horizontal potentiometer of length 270 mm positioned at the mid-height of the fourth layer of bricks. In the back side of the test specimen there were two vertical potentiometer of length equal to 237 mm spaced 274 mm and 1 horizontal potentiometer of length 230 mm positioned at the mid-height of the third layer of bricks.

ID number associated to each potentiometer is shown in brackets in Figure 4.30.

The measures can slightly change from one test to one other.

Figure 55 shows the test layout and the positioning of the test specimen on the testing machine.



Figure 55. Setup of the compressive test on CS masonry wallettes.

### ***Experimental Procedure***

The test envisaged the failure of the test specimens by means of vertical compression load applied at their top. The loading protocol consisted on series of 3 cycles of loading and unloading at constant force amplitude; the force amplitude was then increased progressively for the further cycles and the force increment is about 75 kN. The loading velocity is consistent with UNI EN-1052-1 prescriptions. Figure 56 and Table 29 show the applied loading history.

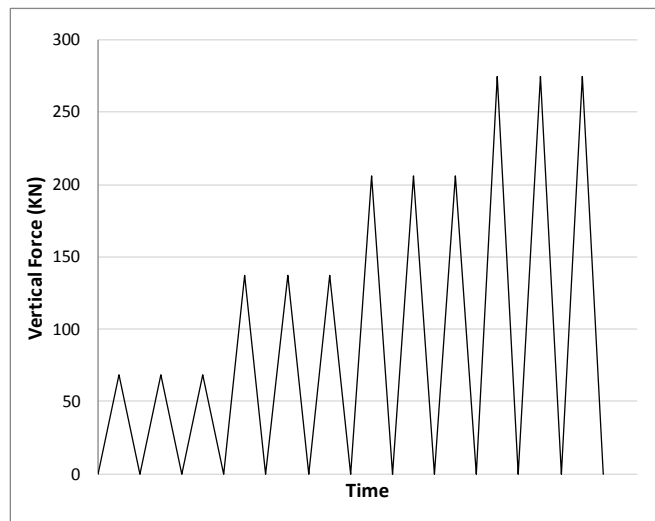


Figure 56. Example of loading history used for the compressive test on CS masonry wallettes.

Table 29. Loading history applied to each specimen, for the compressive test on CS masonry wallttes.

Test	Cycle 1 $F_{max}$ [t]	Cycle 2 $F_{max}$ [t]	Cycle 3 $F_{max}$ [t]	Cycle 4 $F_{max}$ [t]
EC_MAT_H_11_a	7	14	21	24
EC_MAT_H_11_b	7.5	15	22.5	29
EC_MAT_H_11_c	7.5	15	22.5	23.7
EC_MAT_H_11_d	7.5	15	22.5	Rupture at C3 at 19 t
EC_MAT_H_11_f	7	14	21	24.8
EC_MAT_H_11_g	7	14	21	24.7

### Test results

The vertical and horizontal deformations later shown were obtained averaging the deformation recorded by each vertical and horizontal potentiometer.

In particular, the vertical deformation is obtained averaging the deformation recorded by potentiometers 0, 1, 3 and 4, while the horizontal deformation is obtained from the horizontal potentiometers 2 and 5.

Looking at the envelope of the cyclic pressure-deformation curve it can be seen as the specimens exhibit a non-linear behaviour even for low level of vertical pressure. This seems to be associable to a peculiarity of the C.S. material. Figure 57 shows the pressure-deformation curve ( $\sigma - \epsilon$ ) of the specimen EC\_MAT\_H\_11\_c.

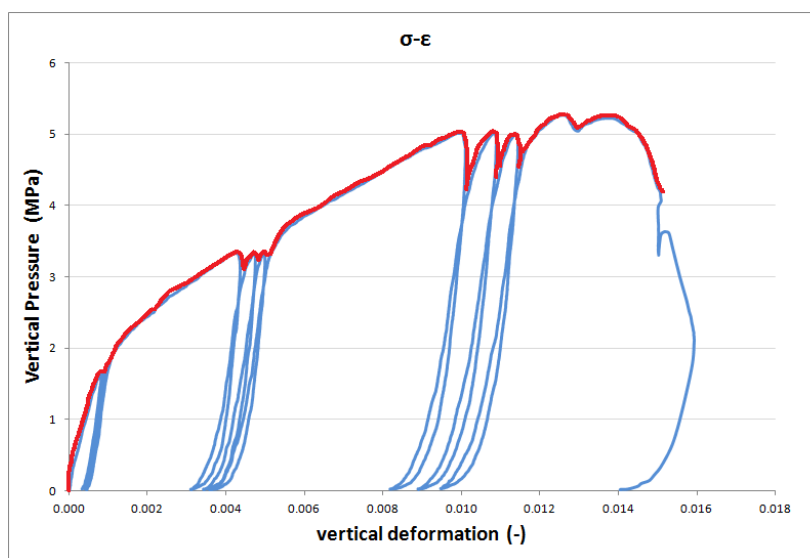


Figure 57. Vertical Deformations vs Vertical Pressure ( $\sigma - \epsilon$ ) of EC\_MAT\_H\_11\_c Specimen.

The Young Modulus  $E_1$  is the secant elastic modulus at 33% of  $f_m$ , the Young Modulus  $E_2$  is the secant elastic modulus at 10% of  $f_m$  and the Young Modulus  $E_3$  was computed as the secant line passing through the points ( $33\%f_m, \epsilon_{33\%f_m}$ ) and ( $10\%f_m, \epsilon_{10\%f_m}$ ).

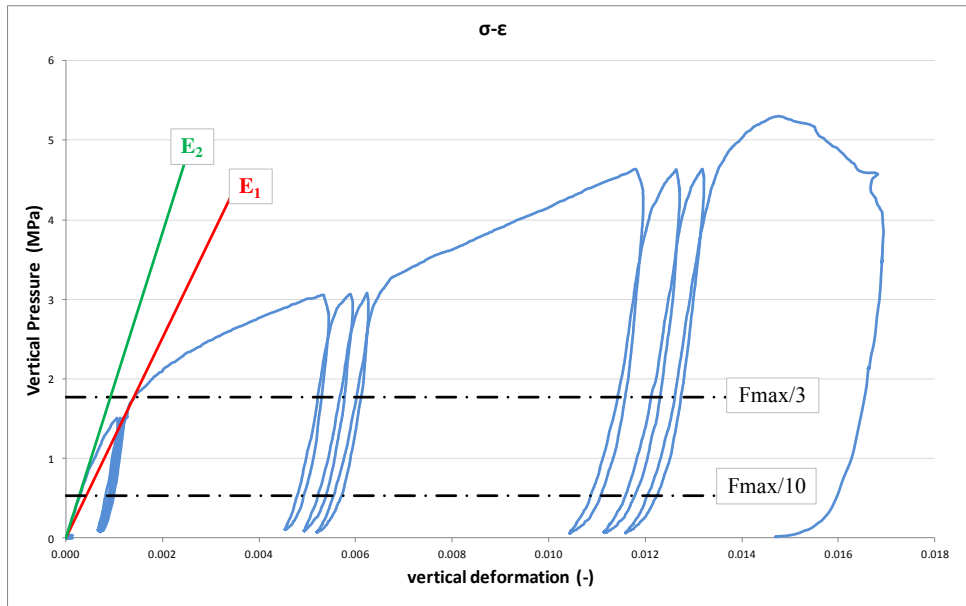


Figure 58. Influence on the E Modulus of the pressure level considered (EC\_MAT\_H\_11\_a).

Table 30 summarizes the maximum pressure reached by each Specimen ( $f_m$ ), and the Young Modulus computed respectively with 33% ( $E_1$ ), 10% ( $E_2$ ) of the maximum pressure and the secant line passing through the points ( $33\%f_m, \epsilon_{33\%f_m}$ ) and ( $10\%f_m, \epsilon_{10\%f_m}$ ) representing the Modulus value termed  $E_3$ .

Table 30. Compressive strength and Elastic Moduli of CS "house" wallettes.

	$f_m$	$E_1 (33\%f_m)$	$E_2 (10\%f_m)$	$E_3$	date
	[MPa]	[MPa]	[MPa]	[MPa]	
EC_MAT_H_11_a	5.30	1256	1916	1090	23/09/2015
EC_MAT_H_11_b	6.46	2197	2395	2123	23/09/2015
EC_MAT_H_11_c	5.26	1717	2664	1492	22/09/2015
EC_MAT_H_11_d	4.91	1128	2033	949	23/09/2015
EC_MAT_H_11_f	5.63	2104	2122	2096	25/09/2015
EC_MAT_H_11_g	5.41	2012	1662	2212	28/09/2015
<b>mean</b>	<b>5.49</b>	<b>1736</b>	<b>2132</b>	<b>1660</b>	
<b>st.dev.</b>	0.53	452.75	354.82	560.00	
<b>c.o.v.</b>	0.10	0.26	0.17	0.34	

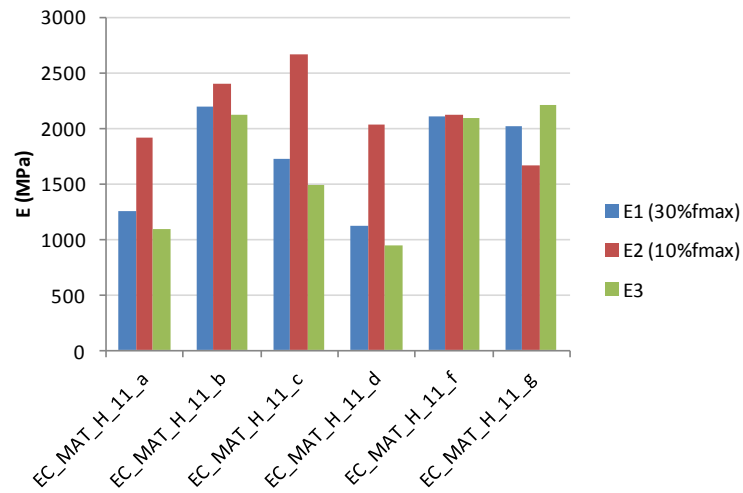


Figure 59. Elastic Moduli of CS "house" wallettes.

Following Figures show the Vertical Deformation vs Vertical Pressure (black solid line) and the Horizontal Deformation vs. Vertical Pressure (dashed red line) for each specimen tested.

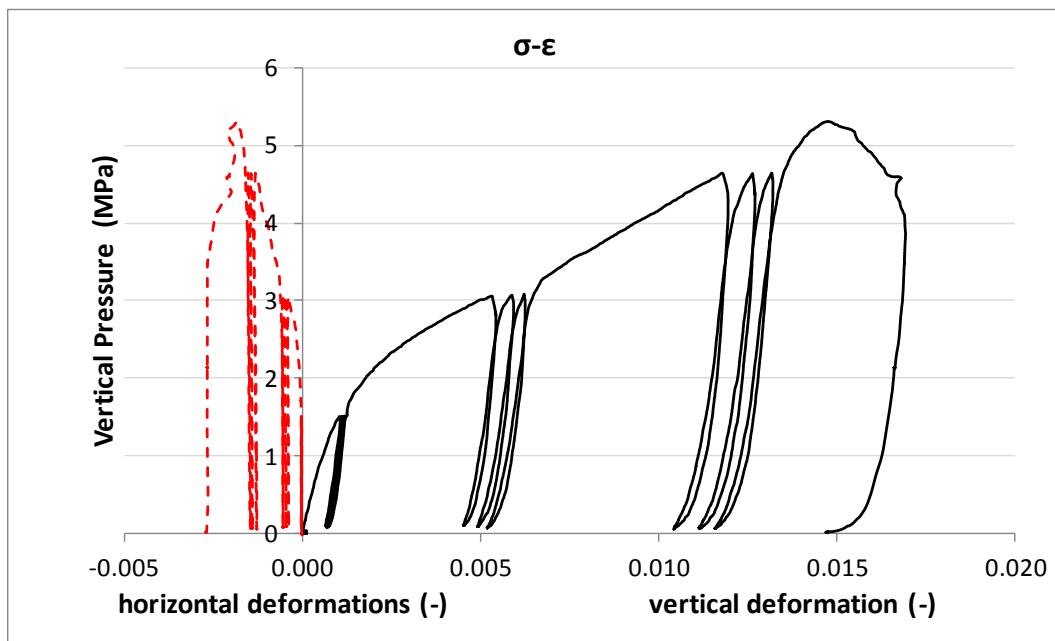


Figure 60. EC\_MAT\_H\_11\_a: Vertical and Horizontal Deformations vs Vertical Pressure.

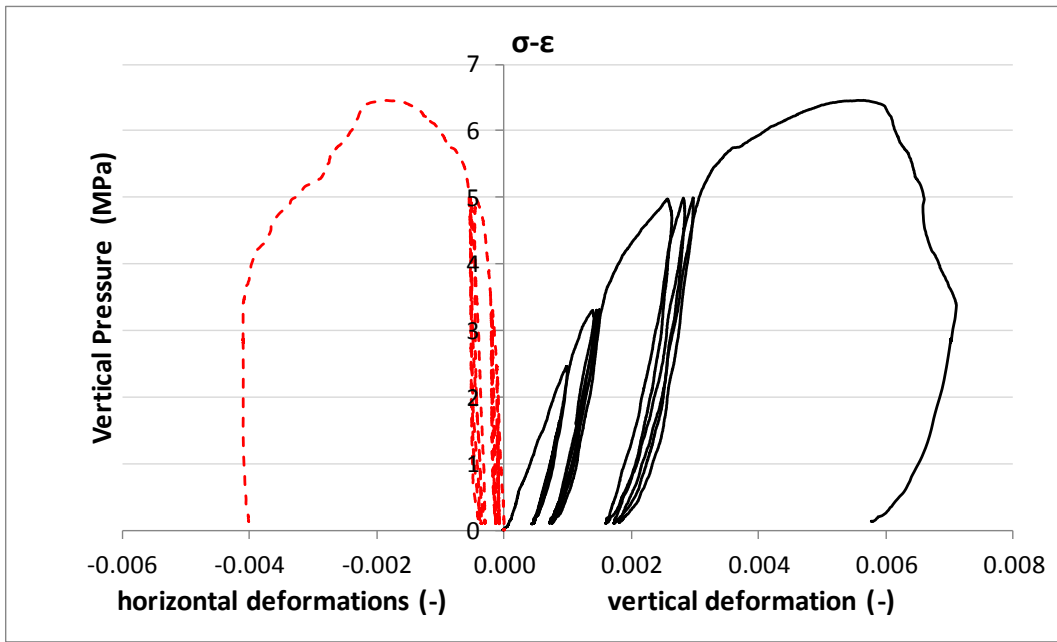


Figure 61. EC\_MAT\_H\_11\_b: Vertical and Horizontal Deformations vs Vertical Pressure.

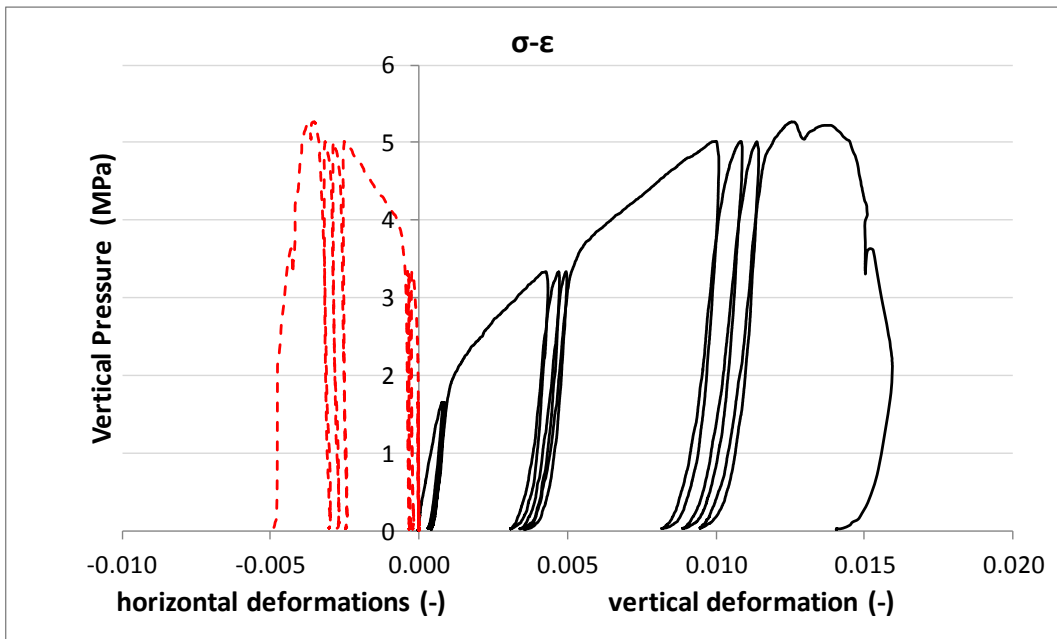


Figure 62. EC\_MAT\_H\_11\_c: Vertical and Horizontal Deformations vs Vertical Pressure.

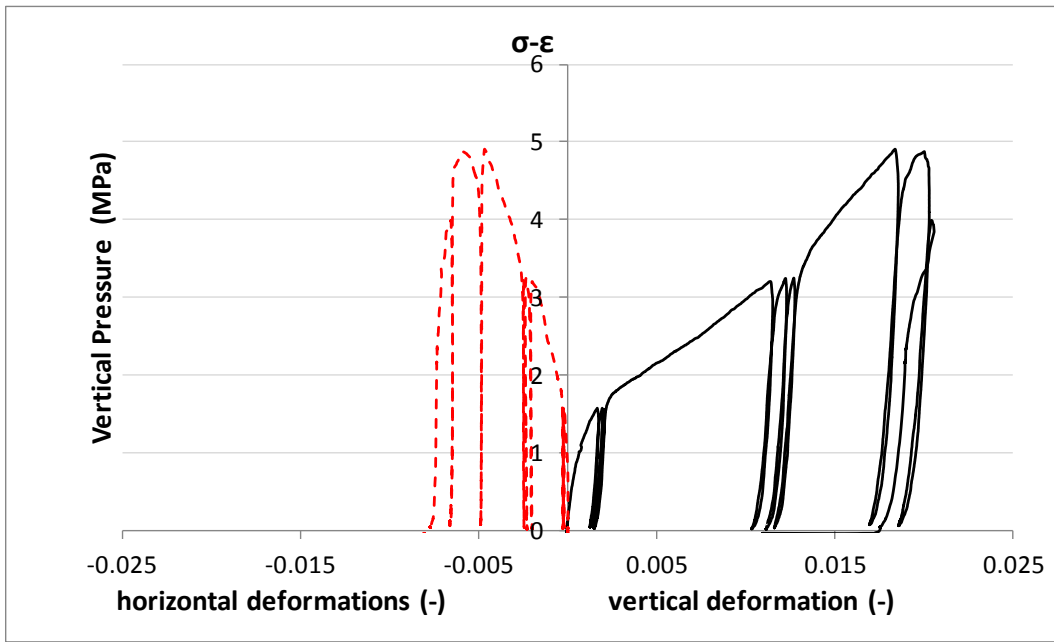


Figure 63. EC\_MAT\_H\_11\_d: Vertical and Horizontal Deformations vs Vertical Pressure.

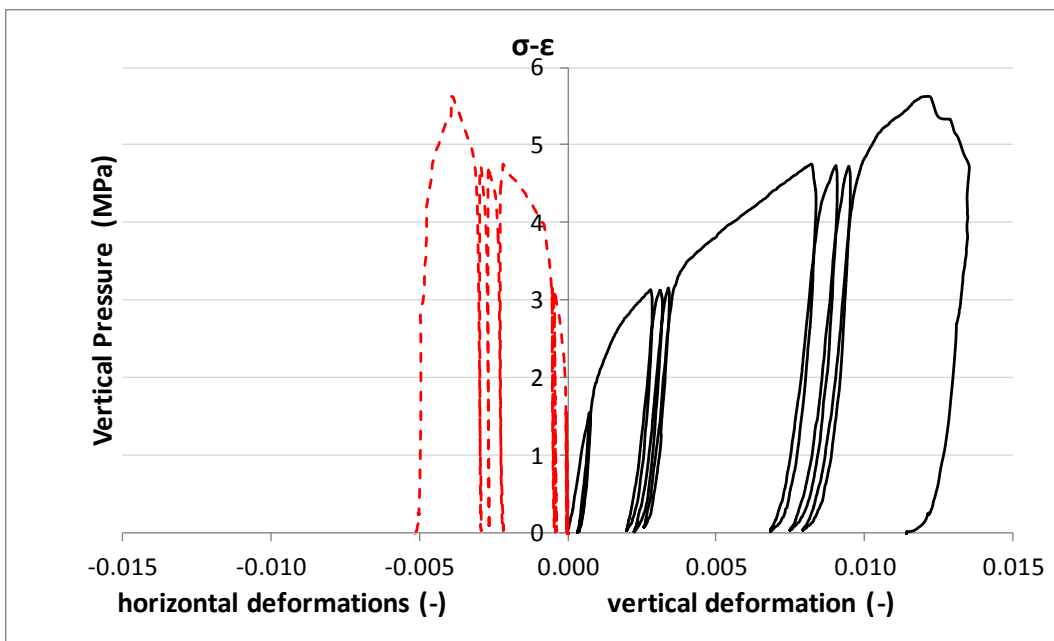


Figure 64. EC\_MAT\_H\_11\_f: Vertical and Horizontal Deformations vs Vertical Pressure.

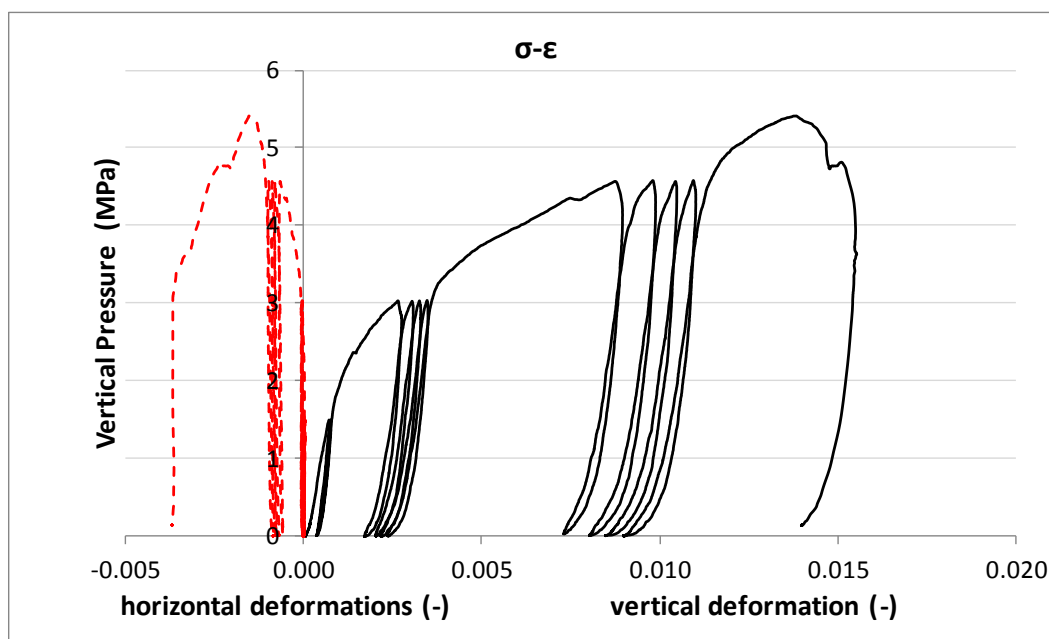


Figure 65. EC\_MAT\_H\_11\_g: Vertical and Horizontal Deformations vs Vertical Pressure.

### 3.3.4 Compressive strength of clay masonry - EC\_MAT\_H\_21

The test specimens were composed by 6 clay walleets listed in Table 4.8.

The specimens were made of the same bricks and mortar used to build the full-scale test-house: the materials come from the same batch. Also the environmental conditions were similar and the masons were the same.

Table 31. Specimen ID and geometric properties

	<i>hs</i> (height)	<i>ls</i> (length)	<i>ts</i> (thickness)	Area	Weight	density
	[mm]	[mm]	[mm]	[mm <sup>2</sup> ]	[kg]	[kg/m <sup>3</sup> ]
EC_MAT_H_21_b	473	430	99	42570	38.4	1907
EC_MAT_H_21_c	463	428	98	41944	37.2	1916
EC_MAT_H_21_d	466	429	96	41184	38	1980
EC_MAT_H_21_e	470	434	100	43400	37.4	1834
EC_MAT_H_21_f	469	428	98	41944	37.8	1922
EC_MAT_H_21_g	473	432	100	43200	38.2	1869
<b>mean</b>	469	430	99	42374	38	1905
<b>st.dev.</b>	4	2	2	844	0	50
<b>c.o.v.</b>	0.01	0.01	0.02	0.02	0.01	0.03

Figure 66 shows the masonry walleets built by the Dutch masons in the DICAr laboratory.



Figure 66. View of the clay masonry wallets, “house”.

The date of construction of the masonry wallets (Specimens EC\_MAT\_H\_21\_b/c/d/e/f/g) was 24/7/2015. The compression tests were performed between the 29/9-1/10/2015.

The masonry wallets were composed by 8 layers of clay bricks; the specimen dimensions were chosen according to the UNI EN-1052-1 prescriptions (section 7.1); the section area of the specimens is equal to 42374 mm<sup>2</sup>. The masonry wallets are about 469 mm high, 430 mm wide and 99 mm thick.

Figure 4.43 shows also the instrumentation adopted and the brick texture of Clay wallets.

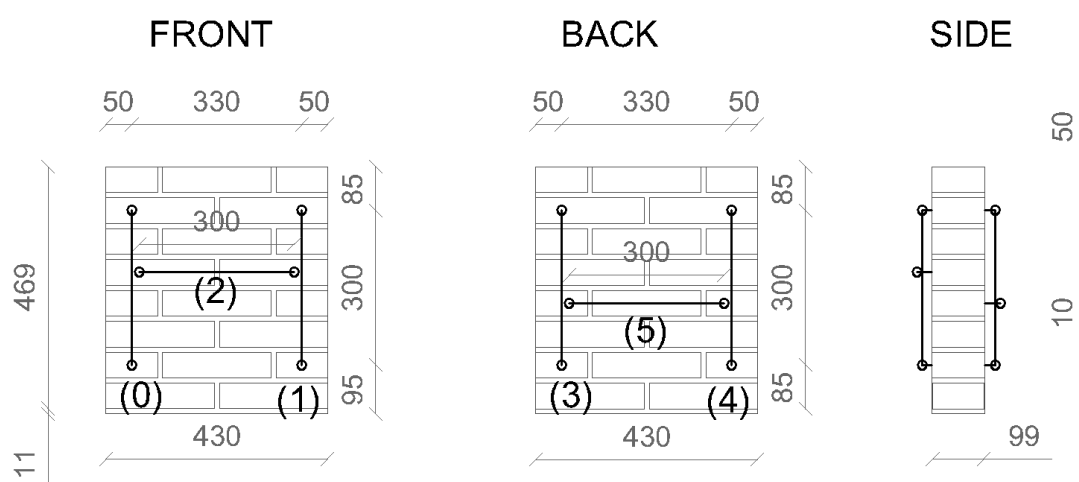


Figure 67. Geometry and Instrumentation of test specimen- clay "house" wallettes.

The instrumentation in the front side of the specimen was composed by two vertical potentiometers of length equal to 300 mm spaced 330 mm and one horizontal potentiometer of length 300 mm positioned at the mid-height of the fifth layer of bricks. In the back side of the test specimen there were two vertical potentiometer of length equal to 300 mm spaced 330 mm and one horizontal potentiometer of length 300 mm positioned at the mid-height of the fourth layer of bricks.

ID number associated to each potentiometer is shown in brackets in Figure 67.

The measures can slightly change from one test to one other.

Figure 68 shows the test layout and the positioning of the test specimen on the testing machine.



Figure 68. Setup of the compressive test on clay masonry wallettes.

### Experimental Procedure

The test envisaged the failure of the test specimens by means of vertical compression load applied at their top. The loading protocol consisted on series of 3 cycles of loading and unloading at constant force amplitude; the force amplitude was then increased progressively for the further cycles and the force increment is equal to 15 t. The loading velocity, consistent with UNI EN-1052-1 prescriptions, is about 15 t/m. Next plot shows the applied loading history.

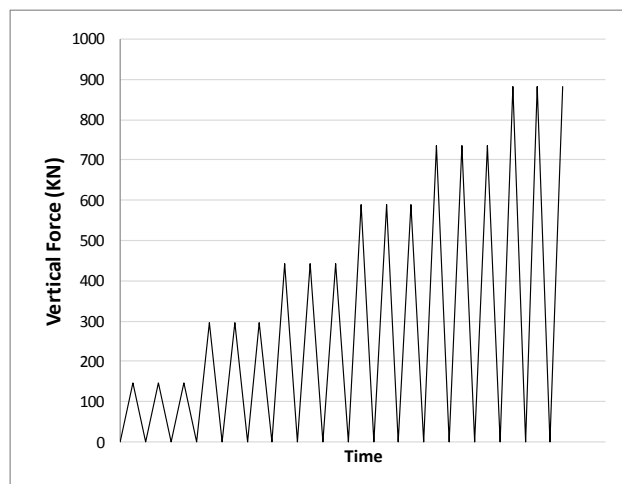


Figure 69. Example of loading history applied for the compressive test on clay masonry "house" wallettes

### Test results

The vertical and horizontal deformations later shown were obtained averaging the deformation recorded by each vertical and horizontal potentiometer.

In particular the vertical deformation is obtained averaging the deformation recorded by potentiometers 0, 1, 3 and 4, while the horizontal deformation is obtained from the horizontal potentiometers 2 and 5.

Figure 70 shows the pressure-deformation curve ( $\sigma - \varepsilon$ ) of the specimen EC\_MAT\_H\_21\_b.

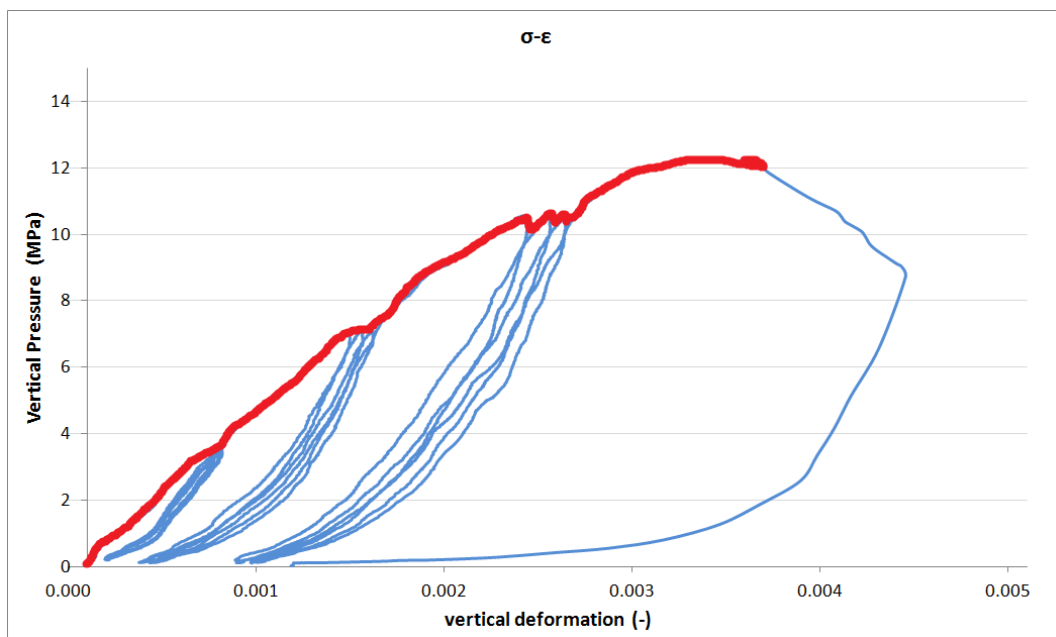


Figure 70. Vertical Deformations vs Vertical Pressure ( $\sigma - \varepsilon$ ) of EC\_MAT\_H\_21\_b Specimen.

The Young Modulus  $E_1$  is the secant elastic modulus at 33% of  $f_m$ , the Young Modulus  $E_2$  is the secant elastic modulus at 10% of  $f_m$  and the Young Modulus  $E_3$  was computed as the secant line passing through the points  $(33\%f_m, \varepsilon_{33\%f_m})$  and  $(10\%f_m, \varepsilon_{10\%f_m})$ .

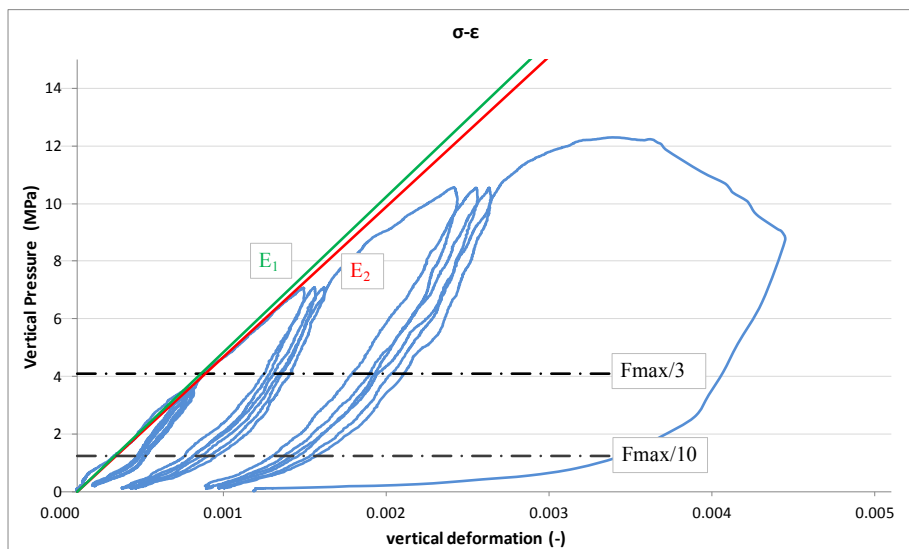


Figure 71. Influence on the E Modulus of the pressure level considered (EC\_MAT\_H\_21\_b).

Table 32 summarizes the maximum pressure reached by each Specimen ( $f_m$ ), and the Young Modulus computed respectively with 33% ( $E_1$ ), 10% ( $E_2$ ) of the maximum pressure and the secant line passing through the points ( $33\%f_m, \varepsilon_{33\%f_m}$ ) and ( $10\%f_m, \varepsilon_{10\%f_m}$ ) representing the Modulus value termed  $E_3$ .

Table 32. Compressive strength and Elastic Moduli of clay "house" wallettes.

	$f_m$	$E_1 (33\%f_m)$	$E_2 (10\%f_m)$	$E_3$	
	[MPa]	[MPa]	[MPa]	[MPa]	date
EC_MAT_H_21_b	12.30	5213	5394	5140	01/10/2015
EC_MAT_H_21_c	12.14	5143	4246	5656	29/09/2015
EC_MAT_H_21_d	15.95	3413	3009	3621	29/09/2015
EC_MAT_H_21_e	10.61	5169	4575	5472	30/09/2015
EC_MAT_H_21_f	13.61	5412	3708	6725	01/10/2015
EC_MAT_H_21_g	11.72	4102	2623	5418	30/09/2015
<b>mean</b>	<b>12.72</b>	<b>4742</b>	<b>3926</b>	<b>5339</b>	
<b>st.dev.</b>	1.85	798.80	1026.04	1003.56	
<b>c.o.v.</b>	0.15	0.17	0.26	0.19	

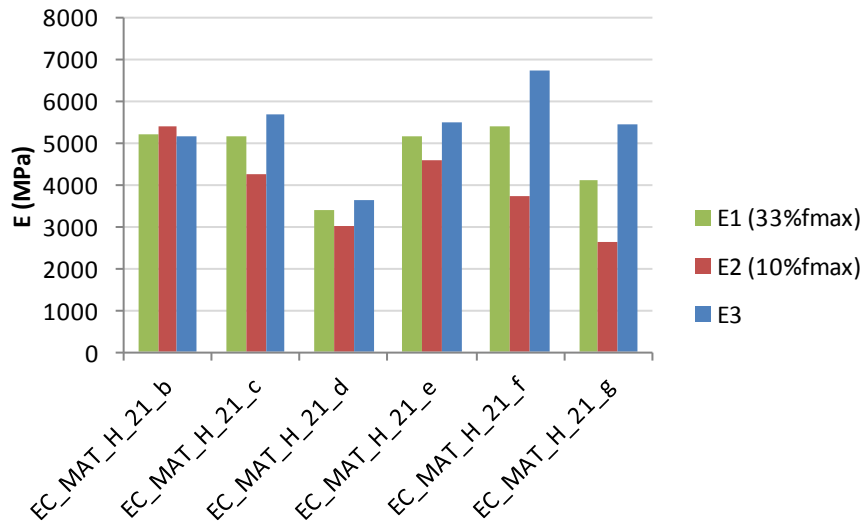


Figure 72. Elastic Moduli of clay "house" wallettes.

Following figures show the Vertical Deformation vs Vertical Pressure (black solid line) and the Horizontal Deformation vs Vertical Pressure (dashed red line) for each specimen tested.

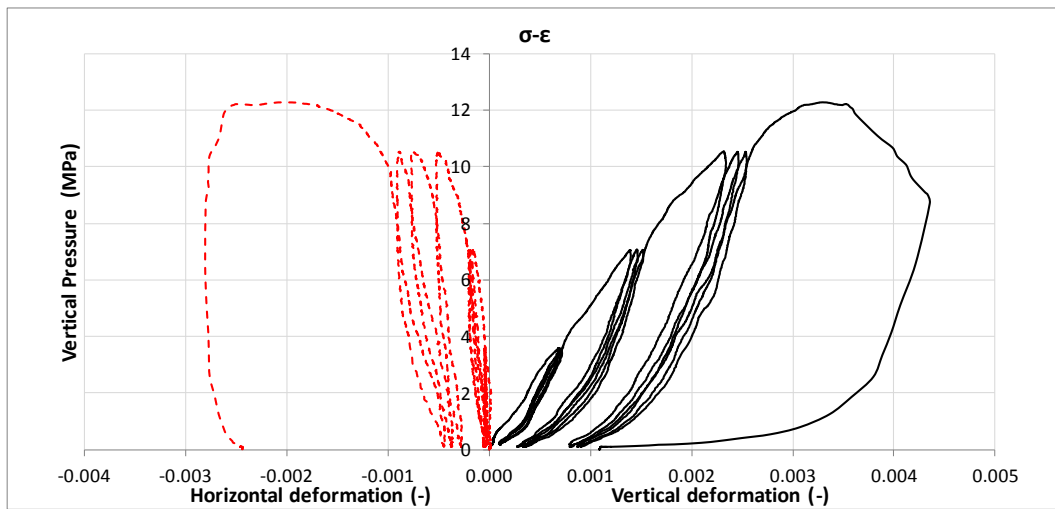


Figure 73. EC\_MAT\_H\_21\_b: Vertical and Horizontal Deformations vs Vertical Pressure.

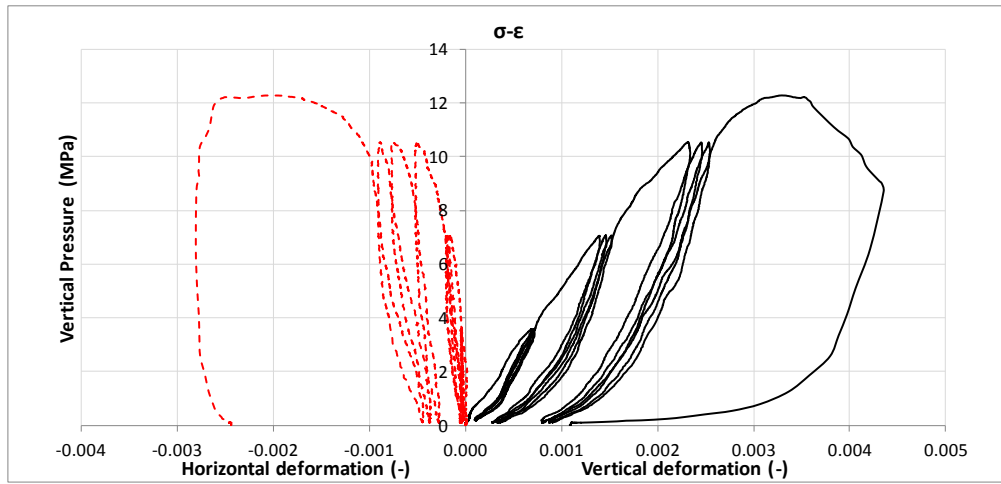


Figure 74. EC\_MAT\_H\_21\_c: Vertical and Horizontal Deformations vs Vertical Pressure.

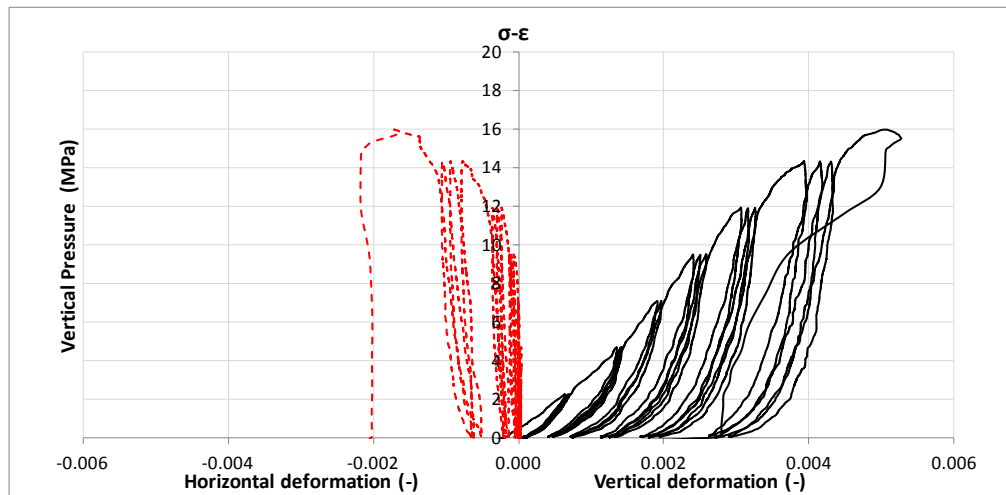


Figure 75. EC\_MAT\_H\_21\_d: Vertical and Horizontal Deformations vs Vertical Pressure.

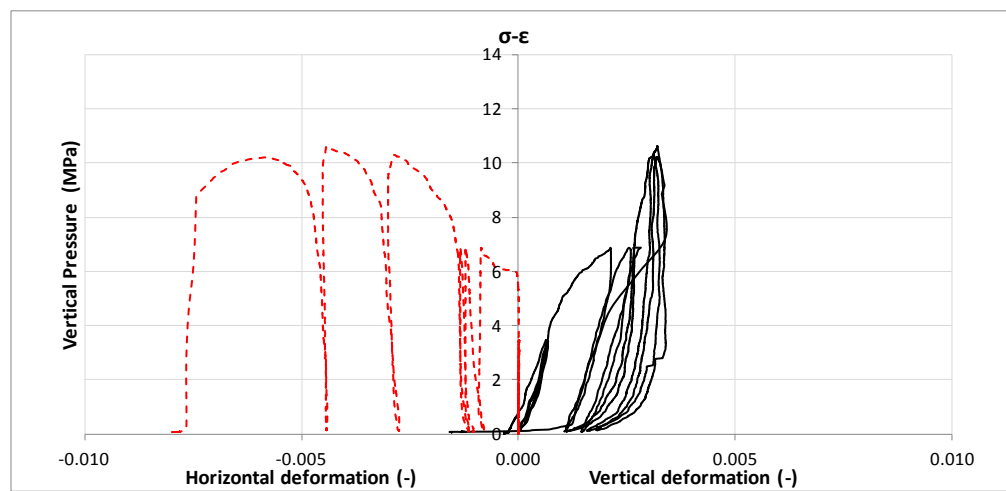


Figure 76. EC\_MAT\_H\_21\_e: Vertical and Horizontal Deformations vs Vertical Pressure.

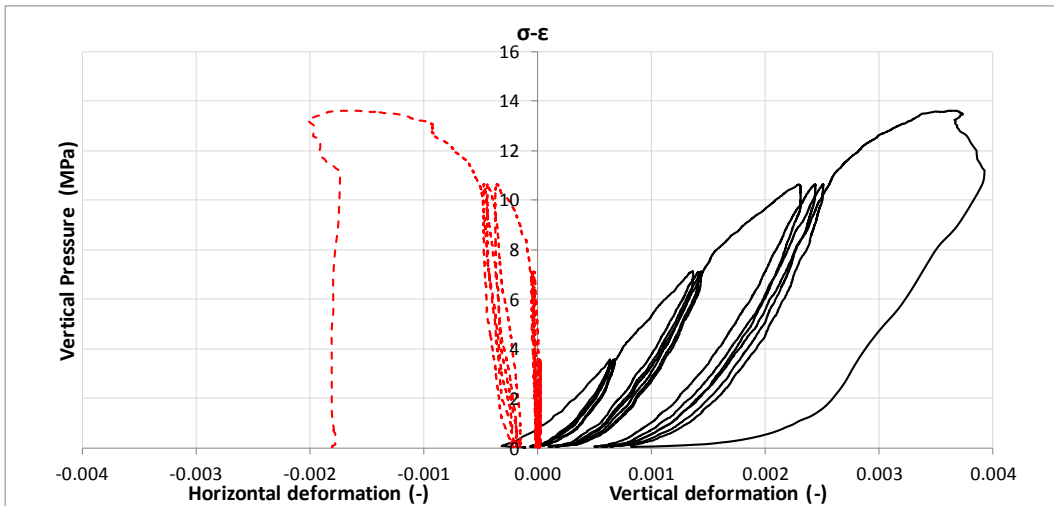


Figure 77. EC\_MAT\_H\_21\_f: Vertical and Horizontal Deformations vs Vertical Pressure.

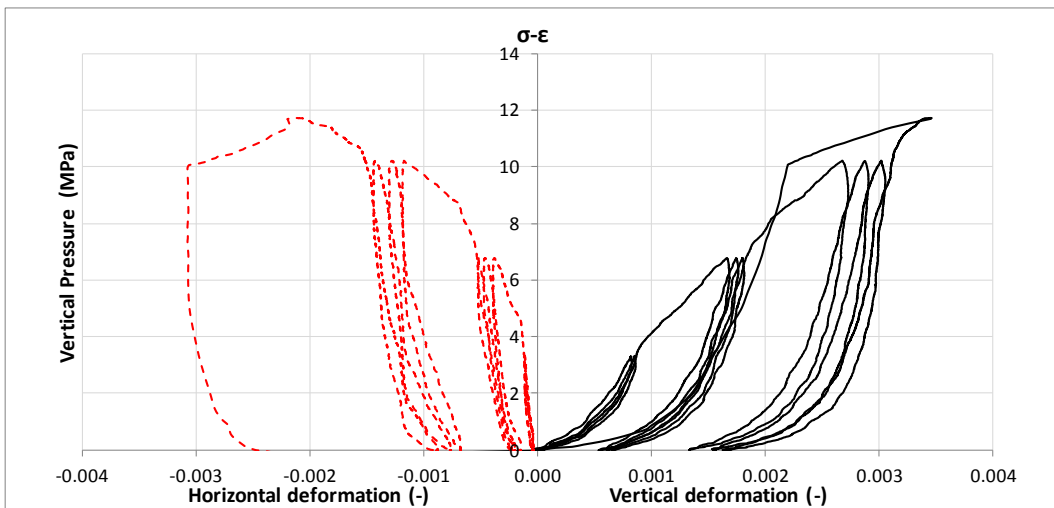


Figure 78. EC\_MAT\_H\_21\_g: Vertical and Horizontal Deformations vs Vertical Pressure.

### 3.4 Bond strength of masonry

The reference code for the present experimental test is the European Norm EN 1052-5 of October 2005: "Determination of bond strength by the bond wrench method".

The tests were performed at the DICAr Laboratory of the University of Pavia in Italy.

Four series of bond wrench test on masonry wallettes were performed:

1. Bond wrench test specimens made of calcium silicate (C.S.) masonry, with the same materials used to cast the walls tested both in-plane and out of plane; These specimens are named EC\_MAT\_15 plus a letter.
2. Bond wrench test specimens made of clay masonry, with the same materials used to cast the walls tested out of plane; These specimens are named EC\_MAT\_25 plus a letter.
3. Bond wrench test specimens made of calcium silicate masonry, with the same materials used to build the full-scale test-house; These specimens are named EC\_MAT\_H\_15 plus a letter.
4. Bond wrench test specimens made of clay masonry, with the same materials used to build the full-scale test-house; These specimens are named EC\_MAT\_H\_25 plus a letter.

The target of the present experimental work is to determine the bond strength of the horizontal bed joints of the masonry.

The test specimens were composed by 5 wallettes per each of the four series of tests, as shown in next Figure. Each specimen is made of by five bricks in line, as shown in figure.

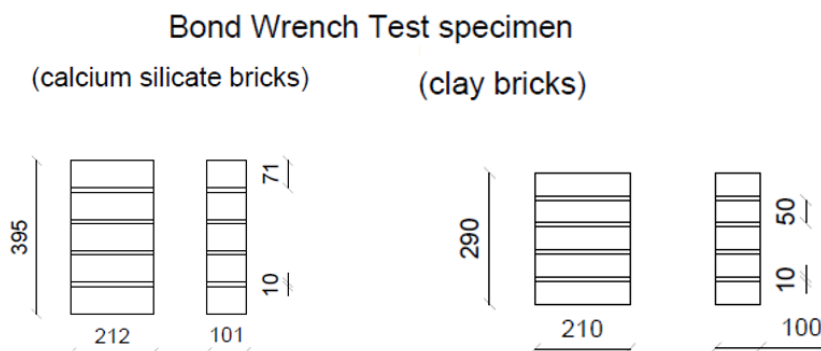


Figure 79. Geometry of the tested specimens.

Figure 80 shows the test layout. The top brick is subjected to a moment and compressive forces, results of the two forces F1 and F2, while the rest of the specimen is clamped. In particular the brick below the unit to test is fixed.

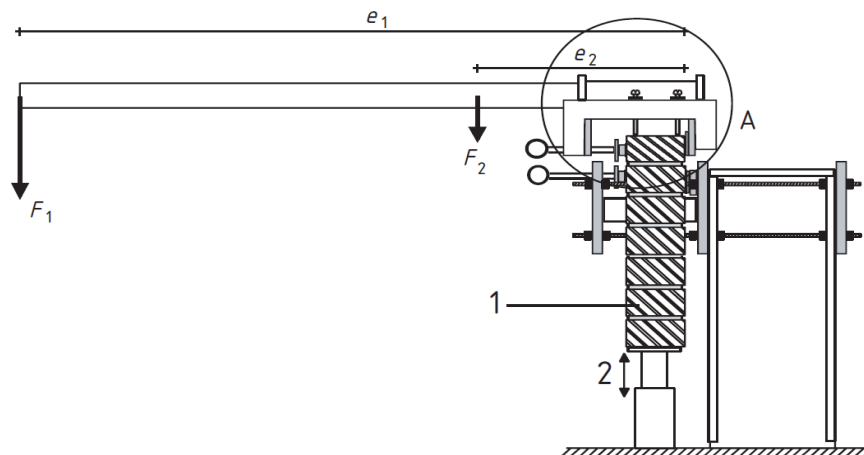


Figure 80. Layout of the Bond Wrench Test (EN 1052-5).

The test was repeated 3 times on the same specimen with the failure of the 2<sup>nd</sup>, 3<sup>rd</sup> and 4<sup>th</sup> mortar bed-joint.

The list of symbols is reported here (EN 1052-5)

- $h$  height of the specimen
- $e_1$  distance from the applied load to the tension face of the specimen in mm
- $e_2$  distance from the centre of gravity of the lever and upper clamp from the tension face of the specimen in mm. In the present case this distance is equal to half width of the brick because the upper clamp is perfectly balanced, *i.e.* its centre of mass is aligned vertically with the center of mass of the bricks.



Figure 81. Balanced upper clamp for bond wrench test.

- $W$  weight of masonry unit pulled of the specimen and any adherent mortar
- $F_1$  applied load
- $F_2$  weight of the bond wrench
- $f_w$  bond strength

- $d$  mean depth of the specimen
- $b$  mean width of the bed joint tested
- $Z$  section modulus of the projected plan area of the failure surface

Figure 82 represents the acceptable types of bed joint failure, according to the EN 1052-5, observed during the tests in the DICAr Laboratory.

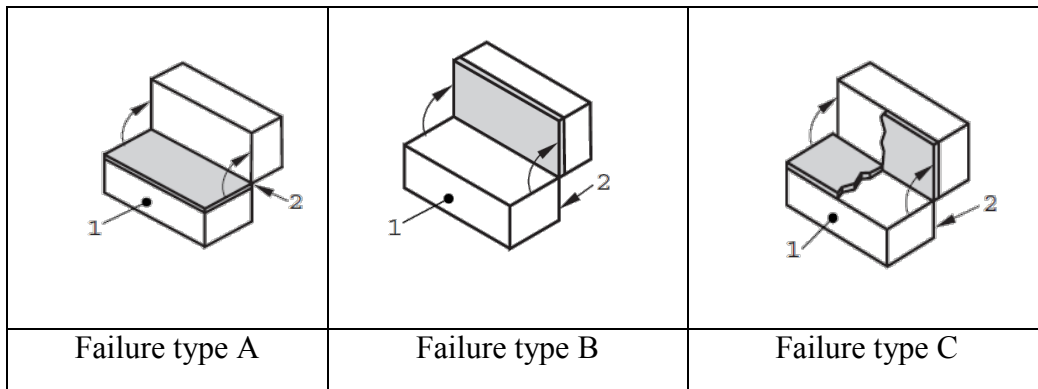


Figure 82. Type of acceptable failure observed during these tests.

### 3.4.1 Results of bond strength of C.S. masonry - EC\_MAT\_15

The following Table reports the output and the results of the test performed on the calcium silicate masonry specimens, with the same materials used to cast the walls tested both in-plane and out of plane; these specimens are named EC\_MAT\_15 plus a letter.

Table 33. ID and geometric Properties of the Test and Test Results - CS specimens.

EC_MAT_15_A		08/05/2015					
h	395	mm					
e1-d/2	470	mm					
b	212.4	mm					
d	102.4	mm					
e1	521.2	mm					
e2	95	mm					
Z	371196	mm <sup>3</sup>					
F2	53.955	N					
W	0.00	N					
				F1	F1	M	fwi
			Bedjoint	(kg)	(N)	(Nm)	(MPa)
			1	14.6	143.2	69.7	0.179
			2	19.5	191.3	92.5	0.238
			3	20.5	201.1	96.8	0.249
			4				
					mean	86	<b>0.222</b>
					st.dev.	14.588	0.038
					c.o.v.	17%	17%



EC_MAT_15_C			07/07/2015					
h	395	mm		F1	F1	M	fwi	
e1-d/2	395	mm	Bedjoint	(kg)	(N)	(Nm)	(MPa)	way of failure
b	212	mm	1	24	235.4	93.0	0.249	C
d	100	mm	2	25	245.3	96.9	0.259	A
e1	445	mm	3	22	215.8	85.2	0.228	A
e2	50	mm	4	24	235.4	93.0	0.249	A
Z	353333	mm <sup>3</sup>			mean	92	<b>0.246</b>	
F2	29.43	N			st.dev.	4.876	0.013	
W	28.15	N			c.o.v.	5%	5%	

EC_MAT_15_D			08/07/2015						
h	395	mm		W	F1	F1	M	fwi	
e1-d/2	395	mm	Bedjoint		(kg)	(N)	(Nm)	(MPa)	way of failure
b	212	mm	1	27	22	215.8	85.2	0.228	A
d	100	mm	2						
e1	445	mm	3						
e2	50	mm	4	30	19	186.4	73.6	0.197	A
Z	353333	mm <sup>3</sup>				mean	79	<b>0.213</b>	
F2	29.43	N				st.dev.	8.220	0.022	
W	28.15	N				c.o.v.	10%	11%	

EC_MAT_15_B			08/07/2015						
h	395	mm		W	F1	F1	M	fwi	
e1-d/2	395	mm	Bedjoint	(N)	(kg)	(N)	(Nm)	(MPa)	way of failure
b	212	mm	1	27	20	196.2	77.5	0.207	A
d	100	mm	2	31	24	235.4	93.0	0.249	A
e1	445	mm	3	61	22	215.8	85.2	0.227	A
e2	50	mm	4	32	24	235.4	93.0	0.249	A
Z	353333	mm <sup>3</sup>				mean	87	<b>0.233</b>	
F2	29.43	N				st.dev.	7.420	0.020	
W	28.15	N				c.o.v.	9%	9%	

EC_MAT_15_E			10/07/2015								
h	394	mm									
Z	367608	mm <sup>3</sup>									
F2	29.43	N									
	e1-d/2	b	d	e1	e2	W	F1	F1	M	fwi	
Bedjoint	mm	mm	mm	mm	mm	(N)	(kg)	(N)	(Nm)	(MPa)	way of failure
1	393	212	102	444	51	27	17	166.8	65.5	0.168	A
2	390.5	212	102	441.5	51	31	32	313.9	122.6	0.316	A
3	379.5	212	102	430.5	51	30	32.5	318.8	121.0	0.312	A
4	379.5	212	102	430.5	51	61	26	255.1	96.8	0.247	A
								mean	101	<b>0.261</b>	
								st.dev.	26.707	0.069	
								c.o.v.	26%	27%	



*Figure 83. Test performed on CS specimens.*

Table 34 resumes the results of all the tests, the bond strength of the mortar bedjoints, relative to the specimen series EC\_MAT\_15.

*Table 34. Flexural Bond Strength of CS masonry.*



C.S. masonry EC_MAT_15	Bond Strength $f_w$	Flexural Strength of mortar * $f_i$
Mean [MPa]	0.238	2.935
St.Dev. [MPa]	0.039	0.300
C.o.V. [%]	16%	10%

\*Reference value of flexural strength of the mortar relative to EC MAT 15

### 3.4.2 Results of bond strength of clay masonry - EC\_MAT\_25

The following Table reports the output and the results of the test performed on the clay masonry specimens, with the same materials used to cast the walls tested out of plane; these specimens are named EC\_MAT\_25 plus a letter.

Table 35. ID and geometric Properties of the Test and Test Results - clay specimens.

EC_MAT_25_A			08/07/2015									
h	293	mm										
Z	353333	mm <sup>3</sup>										
F2	29.43	N										
	e1-d/2	b	d	e1	e2	W	F1	F1	M	fwi		
Bedjoint	mm	mm	mm	mm	mm	(N)	(kg)	(N)	(Nm)	(MPa)	way of failure	
1	413	212	100	463	50	18	13	127.5	52.7	0.141	A	
2	413	212	100	463	50	23	9	88.3	36.5	0.097	A	
3	403	212	100	453	50	23	10	98.1	39.5	0.105	A	
4	405	212	100	455	50	28	7	68.7	27.8	0.073	A	
									mean	39	<b>0.104</b>	
									st.dev.	10.307	0.028	
									c.o.v.	26%	27%	

EC_MAT_25_B			09/07/2015									
h	293	mm										
Z	329315	mm <sup>3</sup>										
F2	29.43	N										
	e1-d/2	b	d	e1	e2	W	F1	F1	M	fwi		
Bedjoint	mm	mm	mm	mm	mm	(N)	(kg)	(N)	(Nm)	(MPa)	way of failure	
1	403	210	97	451.5	48.5	21	16	157.0	63.3	0.182	B	
2	403	210	97	451.5	48.5	23	24	235.4	94.9	0.274	B	
3	403	210	97	451.5	48.5	24	9	88.3	35.6	0.101	B	
4	403	210	97	451.5	48.5	23	24	235.4	94.9	0.274	B	
									mean	72	<b>0.208</b>	
									st.dev.	28.577	0.083	
									c.o.v.	40%	40%	

EC_MAT_25_C			09/07/2015				10/07/2015						
h	293	mm											
Z	332451	mm <sup>3</sup>											
F2	29.43	N											
	e1-d/2	b	d	e1	e2	W	F1	F1	M	fwi			
Bedjoint	mm	mm	mm	mm	mm	(N)	(kg)	(N)	(Nm)	(MPa)	way of failure		
1	395	212	97	443.5	48.5	22	7	68.7	27.1	0.076	B		
2	395	212	97	443.5	48.5	19	17	166.8	65.9	0.188	A		
									mean	46	<b>0.132</b>		
									st.dev.	27.400	0.079		
									c.o.v.	59%	60%		



EC_MAT_25_D			10/07/2015									
h	292	mm										
Z	350000	mm <sup>3</sup>										
F2	29.43	N										
	e1-d/2	b	d	e1	e2	W	F1	F1	M	fwi	way of failure	
Bedjoint	mm	mm	mm	mm	mm	(N)	(kg)	(N)	(Nm)	(MPa)		
1	382	210	100	432	50	23	9	88.3	33.7	0.090		B
2	381.5	210	100	431.5	50	23	9	88.3	33.7	0.090		B
3	373.5	210	100	423.5	50	24	14	137.3	51.3	0.137		B
4	390.5	210	100	440.5	50	23	5	49.1	19.2	0.050		B
									mean	34	<b>0.092</b>	
									st.dev.	13.151	0.036	
									c.o.v.	38%	39%	

EC_MAT_25_E			10/07/2015									
h	290	mm										
Z	350000	mm <sup>3</sup>										
F2	29.43	N										
	e1-d/2	b	d	e1	e2	W	F1	F1	M	fwi	way of failure	
Bedjoint	mm	mm	mm	mm	mm	(N)	(kg)	(N)	(Nm)	(MPa)		
1	379.5	210	100	429.5	50	18	32	313.9	119.1	0.323		A
2	389.5	210	100	439.5	50	42	23	225.6	87.9	0.237		A
3	389.5	210	100	439.5	50	28	8	78.5	30.6	0.081		B
4	379.5	210	100	429.5	50	19	33	323.7	122.9	0.333		A
									mean	90	<b>0.244</b>	
									st.dev.	42.680	0.117	
									c.o.v.	47%	48%	





Figure 84. Test performed on clay specimens.

Table 36 resumes the results of all the tests, the bond strength of the mortar bedjoints, relative to the specimen series EC\_MAT\_25.

Table 36. Flexural Bond Strength of clay masonry.

Clay masonry	Bond Strength	Flexural Strength of mortar *
EC_MAT_25	$f_w$	$f_t$
Mean [MPa]	0.158	2.115
St.Dev. [MPa]	0.092	0.122
C.o.V. [%]	58%	6%

\*Reference value of flexural strength of the mortar relative to EC MAT 25

### 3.4.3 Results of bond strength of C.S. masonry - EC\_MAT\_H\_15

The following Table reports the output and the results of the test performed on the C.S. masonry specimens, with the same materials used to build the full-scale test-house; these specimens are named EC\_MAT\_H\_15 plus a letter.

Table 37. ID and geometric Properties of the Test and Test Results - CS specimens.



EC_MAT_H_15_A			26/08/2015									
h	394	mm										
Z	358735	mm <sup>3</sup>										
F2	29.43	N										
	e1-d/2	b	d	e1	e2	W	F1	F1	M	fwi		
Bedjoint	mm	mm	mm	mm	mm	(N)	(kg)	(N)	(Nm)	(MPa)	way of failure	
1	407	211	101	457.5	50.5	27	3	29.4	12.0	0.029	A	
2	407	211	101	457.5	50.5	0	0				A	
3	407	211	101	457.5	50.5	0	0				A	
4	407	211	101	457.5	50.5	0	0				A	
									mean	12	<b>0.029</b>	
									st.dev.			
									c.o.v.			

EC_MAT_H_15_B			26/08/2015									
h	398	mm										
Z	374851	mm <sup>3</sup>										
F2	29.43	N										
	e1-d/2	b	d	e1	e2	W	F1	F1	M	fwi		
Bedjoint	mm	mm	mm	mm	mm	(N)	(kg)	(N)	(Nm)	(MPa)	way of failure	
1	407	212	103	458.5	51.5	29	3	29.4	12.0	0.028	A	
2	407	212	103	458.5	51.5	32	6	58.9	24.0	0.058	A	
3	407	212	103	458.5	51.5	32	4	39.2	16.0	0.038	A	
4	407	212	103	458.5	51.5	32	7	68.7	27.9	0.069	A	
									mean	20	<b>0.048</b>	
									st.dev.	7.290	0.019	
									c.o.v.	37%	38%	

EC_MAT_H_15_C			26/08/2015									
h	395	mm										
Z	367608	mm <sup>3</sup>										
F2	29.43	N										
	e1-d/2	b	d	e1	e2	W	F1	F1	M	fwi		
Bedjoint	mm	mm	mm	mm	mm	(N)	(kg)	(N)	(Nm)	(MPa)	way of failure	
1	407	212	102	458	51	28	4	39.2	16.0	0.039	A	
2	407	212	102	458	51	31	4	39.2	16.0	0.039	A	
3	407	212	102	458	51	0	0				A	
4	407	212	102	458	51	32	6	58.9	24.0	0.060	A	
									mean	19	<b>0.046</b>	
									st.dev.	4.610	0.012	
									c.o.v.	25%	26%	

EC_MAT_H_15_D			27/08/2015									
h	395	mm										
Z	367608	mm <sup>3</sup>										
F2	29.43	N										
	e1-d/2	b	d	e1	e2	W	F1	F1	M	fwi		
Bedjoint	mm	mm	mm	mm	mm	(N)	(kg)	(N)	(Nm)	(MPa)	way of failure	
1		212	102	51	51							
2	248	212	102	299	51	36	14	137.3	34.1	0.083	B	
3		212	102	51	51							
4		212	102	51	51							
									mean	34	<b>0.083</b>	
									st.dev.			
									c.o.v.			

EC_MAT_H_15_E			27/08/2015									
h	401	mm										
Z	367608	mm <sup>3</sup>										
F2	29.43	N										
	e1-d/2	b	d	e1	e2	W	F1	F1	M	fwi		
Bedjoint	mm	mm	mm	mm	mm	(N)	(kg)	(N)	(Nm)	(MPa)	way of failure	
1	407	212	102	458	51	27	7	68.7	27.9	0.070	A	
2	407	212	102	458	51	32	2	19.6	8.0	0.018	A	
3	407	212	102	458	51	31	10	98.1	39.9	0.101	A	
4	407	212	102	458	51	31	9	88.3	35.9	0.091	A	
									mean	28	<b>0.070</b>	
									st.dev.	14.210	0.037	
									c.o.v.	51%	53%	



Figure 85. Test performed on CS specimens.

Table 38 resumes the results of all the tests, the bond strength of the mortar bedjoints, relative to the specimen series EC\_MAT\_H\_15.

Table 38. Flexural Bond Strength of CS "house" masonry.

C.S. masonry EC_MAT_H_15	Bond Strength $f_w$	Flexural Strength of mortar * $f_t$
Mean [MPa]	0.056	1.707
St.Dev. [MPa]	0.026	0.248
C.o.V. [%]	47%	15%

\*Reference value of flexural strength of the mortar relative to EC MAT H 15



### 3.4.4 Results of bond strength of clay masonry - EC\_MAT\_H\_25

The following Table reports the output and the results of the test performed on the clay masonry specimens, with the same materials used to build the full-scale test-house; these specimens are named EC\_MAT\_H\_25 plus a letter.

Table 39. ID and geometric Properties of the Test and Test Results - clay specimens.

EC_MAT_H_25_A		27/08/2015									
h	298	mm									
Z	350000	mm <sup>3</sup>									
F2	29.43	N									
	e1-d/2	b	d	e1	e2	W	F1	F1	M	fwi	
Bedjoint	mm	mm	mm	mm	mm	(N)	(kg)	(N)	(Nm)	(MPa)	way of failure
1	407	210	100	457	50	22	5	49.1	20.0	0.052	B
2	407	210	100	457	50	23	4	39.2	16.0	0.041	B
3	397	210	100	447	50	23	9	88.3	35.1	0.093	B
4	395	210	100	445	50	23	4	39.2	15.5	0.040	B
									mean	22	<b>0.057</b>
									st.dev.	9.174	0.025
									c.o.v.	42%	44%

EC_MAT_H_25_B		27/08/2015									
h	290	mm									
Z	337741	mm <sup>3</sup>									
F2	29.43	N									
	e1-d/2	b	d	e1	e2	W	F1	F1	M	fwi	
Bedjoint	mm	mm	mm	mm	mm	(N)	(kg)	(N)	(Nm)	(MPa)	way of failure
1	397	211	98	446	49	17	6	58.9	23.4	0.064	A
2	392	211	98	441	49	23	8	78.5	30.8	0.085	A
3	400	211	98	449	49	23	13	127.5	51.0	0.142	A
4	397	211	98	446	49	22	5	49.1	19.5	0.053	A
									mean	31	<b>0.086</b>
									st.dev.	14.042	0.040
									c.o.v.	45%	46%

EC_MAT_H_25_E		27/08/2015									
h	290	mm									
Z	350000	mm <sup>3</sup>									
F2	29.43	N									
	e1-d/2	b	d	e1	e2	W	F1	F1	M	fwi	
Bedjoint	mm	mm	mm	mm	mm	(N)	(kg)	(N)	(Nm)	(MPa)	way of failure
1	407	210	100	457	50	17	8	78.5	31.9	0.085	A
2	400	210	100	450	50	25	22	215.8	86.3	0.234	C
3	407	210	100	457	50	21	22	215.8	87.8	0.238	A
4	407	210	100	457	50						A
									mean	69	<b>0.186</b>
									st.dev.	31.845	0.087
									c.o.v.	46%	47%

EC_MAT_H_25_C		31/08/2015									
h	292	mm									
Z	350000	mm <sup>3</sup>									
F2	29.43	N									
	e1-d/2	b	d	e1	e2	W	F1	F1	M	fwi	
Bedjoint	mm	mm	mm	mm	mm	(N)	(kg)	(N)	(Nm)	(MPa)	way of failure
1	401	210	100	451	50	22	23	225.6	90.5	0.245	A
2	401	210	100	451	50	19	33	323.7	129.8	0.353	A
3	406	210	100	456	50	22	25	245.3	99.6	0.270	A
4	405	210	100	455	50	22	26	255.1	103.3	0.281	A
									mean	106	<b>0.287</b>
									st.dev.	16.898	0.046
									c.o.v.	16%	16%

EC_MAT_H_25_D		31/08/2015										
h	286	mm										
Z	350000	mm <sup>3</sup>										
F2	29.43	N										
	e1-d/2	b	d	e1	e2	W	F1	F1	M	fwi	way of failure	
Bedjoint	mm	mm	mm	mm	mm	(N)	(kg)	(N)	(Nm)	(MPa)		
1	405	210	100	455	50	18	18	176.6	71.5	0.194		A
2	405	210	100	455	50	23	9	88.3	35.8	0.095		A
3		210	100	50	50							A
4	405	210	100	455	50	23	16	157.0	63.6	0.172	A	
									mean	57	<b>0.154</b>	
									st.dev.	18.776	0.052	
									c.o.v.	33%	34%	



Figure 86. Test performed on clay specimens - failure of the joint.

Table 40 resumes the results of all the tests, the bond strength of the mortar bedjoints, relative to the specimen series EC\_MAT\_H\_25.

Table 40. Flexural Bond Strength of clay "house" masonry.

Clay masonry	Bond Strength	Flexural Strength of mortar *
EC_MAT_H_25	$f_w$	$f_i$
Mean [MPa]	0.152	1.478
St.Dev. [MPa]	0.098	0.284
C.o.V. [%]	65%	19%

\*Reference value of flexural strength of the mortar relative to EC MAT H 25

### 3.5 Shear strength of masonries

The purpose of the test is to evaluate the shear resistance of the two horizontal bedjoints relative to a single unit block of the masonry.

The tests were performed at the DICAr Laboratory of the University of Pavia in Italy.

The specimens were made of the same bricks and mortar used to build the walls tested in-plane and out of plane and the full-scale test-house: the materials come from the same batch. Also the environmental conditions were similar during the casting of related specimens.

The reference code for the present experimental work is the European Norm EN 1052-3:2002 and its amendment EN 1052-3:200/A1:2007.

In the tests performed in DICAr Laboratory., the specimen type chosen is the "I": three bricks bonded with two layers of mortar, always according to EN 1052-3:2002 and EN 1052-3/A1:2007. The procedure "A" is the one adopted: at least three specimens must be tested at three different level of precompression.

Three series of triplet test are scheduled:

1. Triplet specimens made of calcium silicate (C.S.) masonry, with the same materials used to cast the walls tested both in-plane and out of plane.
2. Triplet specimens made of C.S. masonry, with the same materials used to build the full-scale test-house.
3. Triplet specimens made of Clay masonry, with the same materials used to build the full-scale test-house.

The specimen is composed by three masonry units and their two relative bedjoints, as shown in Figure 87.

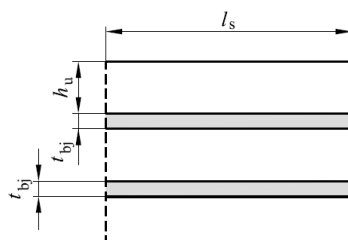


Figure 87. Specimen dimensions of Triplet Test (EN 1052-3:2002).

The average dimensions of bricks and specimens, shown in Figure 88, are equal to:

- C.S. bricks: 212x101x72 (mm),
- caly bricks: 210x100x50 (mm),
- Specimen made of C.S. bricks: 236x212x101 (mm),
- Specimen made of clay bricks: 170x210x100 (mm).

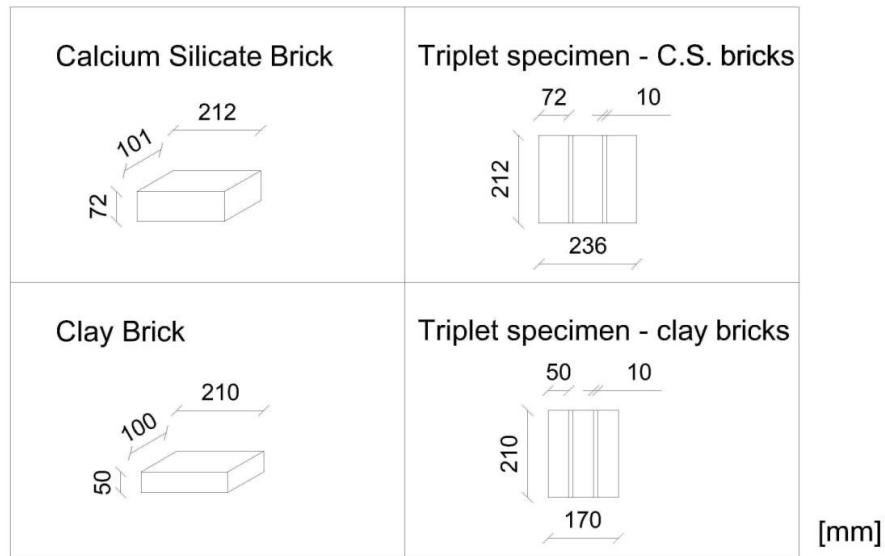


Figure 88. Brick and Specimen dimensions.

The length of the bricks is smaller than 300 mm in both cases, hence the length of the specimen is exactly equal to the length of the bricks.

The mortar bedjoints are 10 mm thick.

### Procedure

The tests were conducted in Force-control, their procedure is summarized in the following list:

1. Two layers of gypsum are applied on the external faces of the specimens;
2. The specimen is positioned and instrumented in the testing apparatus, between two steel plates, while it is supported by roller bearings;
3. Apply a compression,  $F_p$  at the two lateral faces of the specimen, as shown in Figure 89;

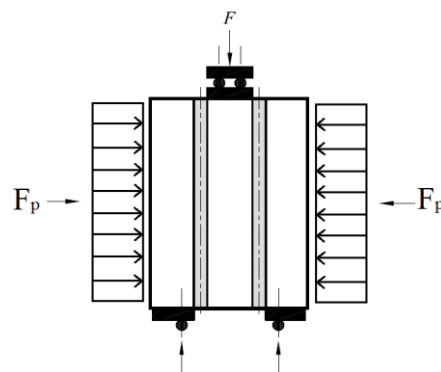


Figure 89. Triplet Test, load application.

4. For elements that have a compressive resistance greater than  $10 \text{ N/mm}^2$ , as in this case, the compressive load  $F_p$  must impose to the specimen a stress value of about  $0.2 \text{ N/mm}^2$ ,  $0.6 \text{ N/mm}^2$  and  $1.0 \text{ N/mm}^2$ . The compressive load, uniformly

distributed on the faces of the specimen, is maintained constant during the test; The triplet specimen tend to dilate during the test. This is due to the dilatancy phenomenon usually associated to this type of masonry (or more in general to the Coulomb mechanism). In order to accommodate displacement, a spring is positioned in series with the horizontal force. This guarantee a reduction of differential pressure at rupture.

5. A shear force  $F$  is applied vertically on the specimen with a velocity between  $0.1 \text{ N}/(\text{mm}^2/\text{min})$  and  $0.4 \text{ N}/(\text{mm}^2/\text{min})$ , till the mortar bedjoints are cracked;
6. Measures and recorded quantities:
  - A. the area of the transversal section  $A_i$ , of the specimens, parallel to the shear force
  - B. the maximum load applied  $F_{i,max}$
  - C. the compressive load  $F_{pi}$
7. In DICAr Laboratory, the values of the loads applied are real time recorded simultaneously with the displacements 0,1,2,3,4,5 by using LVDTs, as represented in Figure 90. In this case a proper self-centering screw is used;

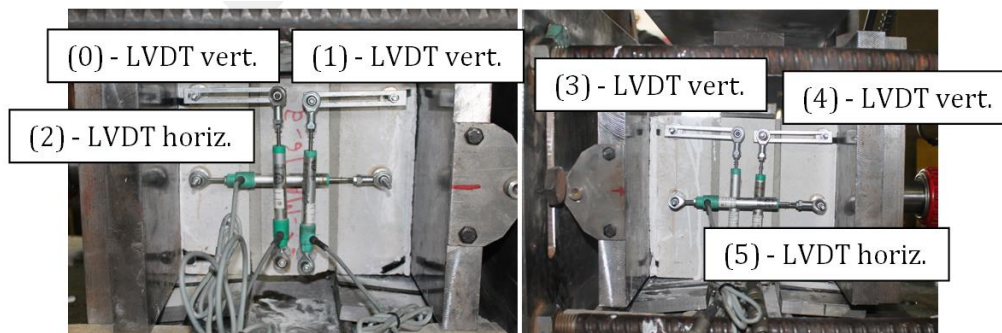


Figure 90. Triplet Test, LVDTs positions.

8. In DICAr Lab., if the specimen was not damaged too much, another test was performed on the same triplet at a different level of lateral compressive load, with the bedjoints already cracked. This data were recorded in order to evaluate the shear strength of the mortar bedjoints in the case in which only the friction contribution is acting, and not the cohesive strength.

### Test results

The shear strength,  $f_{vi}$ , of a specimen  $i$ , for a given compressive stress  $\sigma_i$  (imposed by the lateral load on the specimen,  $F_{pi}$ ), is equal to:

$$f_{vi} = \frac{F_{i,max}}{2A_i}$$

with:

$$\sigma_i = \frac{F_{pi}}{A_i}$$

$F_{i,max}$  maximum shear force

$F_{pi}$  compressive lateral load

$A_i$  transversal area of the specimens, parallel to the bedjoints

For each value of pressure  $F_{pi}$ , and then  $\sigma_i$ , there is a corresponding value of  $f_{vi}$ .

By plotting the couples  $(\sigma_i, f_{vi})$  it is possible to obtain a graph like the one shown as example in Figure 91.

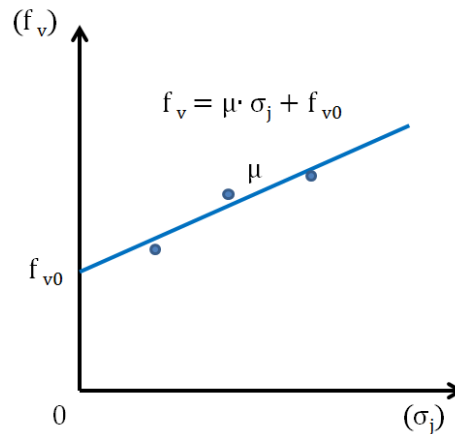


Figure 91. Triplet Test,  $\sigma$ - $f_v$  strength envelope

Coulomb's law resulted to be the more representative of the results. The shear strength of the mortar bedjoints of the specimens ( $f_v$ ) depends on three parameters: the cohesion, the friction coefficient and the transversal compression. The cohesion contributes to the strength only if the mortar bedjoints are not cracked, while the friction force acts also after the formations of the fractures, till there is contact between the two materials. The shear strength ( $f_v$ ), according to Coulomb's law is linear depending on the compression ( $\sigma$ ):

$$f_v = f_{v0} + \mu \cdot \sigma$$

with:

$f_{v0}$  cohesion (or adhesion stress)

$\mu$  coefficient of friction

### 3.5.1 Triplet Test Result for C.S. masonry - EC\_MAT\_16

The test specimens were composed by 16 triplets of C.S. masonry (Figure 92) built by Dutch masons in the DICAR laboratory, with the same materials used to cast the walls tested both in-plane and out of plane. Nevertheless, it was possible to test only ten of them.



Figure 92. View of the specimens (EC\_MAT\_16\_a/p) for Triplet Test.

The date of construction of the Triplets (Specimens EC\_MAT\_16\_a/p) was the 27/3/2015. The triplet shear tests were performed between 5-26/6/2015.

Figure 93 shows the results of the test:

- square-dots: represent all the couples  $(\sigma_l, f_{v1})$  relative to the maximum value of shear strength of mortar bedjoint. The contribution to shear strength is given by both cohesion and friction force, because the specimen, before the test, is intact. The values are shown in following Table.

Table 41. Results of Triplet Test on CS specimens:  $(\sigma_1, f_{v1})$  couples.

Specimen	$\sigma$ [MPa]	$f_{v0}$ [MPa]
<b>A</b>	0.23	0.36
<b>B</b>	0.95	0.66
<b>C</b>	0.26	0.35
<b>D</b>	0.92	0.61
<b>E</b>	0.21	0.25
<b>F</b>	0.94	0.56
<b>G</b>	0.48	0.42
<b>J</b>	-	-
<b>L</b>	0.46	0.40
<b>P</b>	0.52	0.41

- solid blue line: is the linear regression of all the couples  $(\sigma_1, \tau_1)$  relative to the maximum value of shear strength of mortar bedjoint.

After this clarification, it is possible to define the terms of the equation:  $f_v = f_{v0} + \mu \sigma$ .

- The cohesion,  $f_{v0}$ , is the Y-intercept of the linear regression line of all the points  $(\sigma_1, f_{v1})$  relative to the maximum value of shear strength of mortar bedjoint.
- The coefficient of friction,  $\mu$ , is the slope of the linear regression line of all the points  $(\sigma_1, f_{v1})$  relative to the maximum value of shear strength of mortar bedjoint.

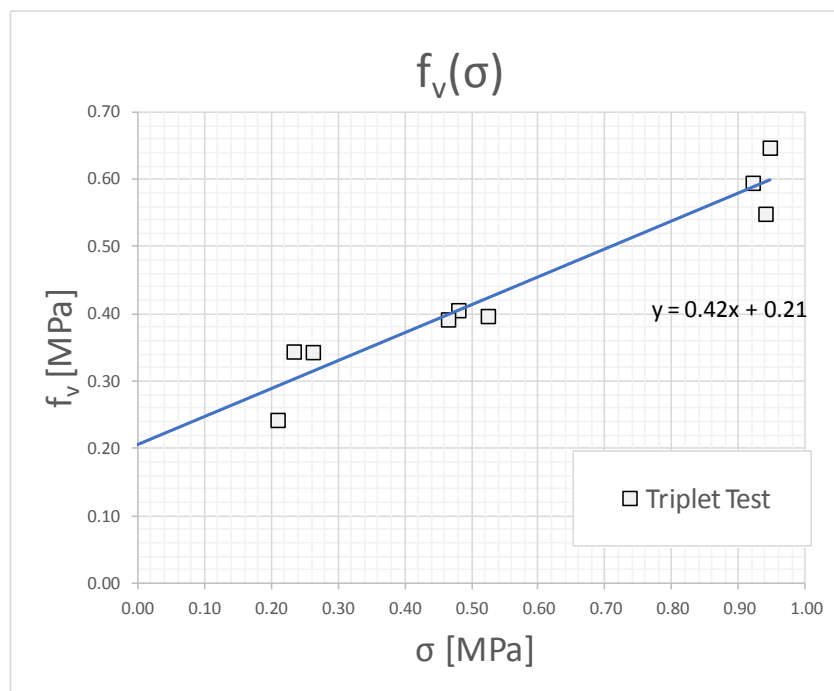


Figure 93. Triplet Test,  $\sigma$ - $f_v$  strength envelope



Hence the values of the wanted parameter are:

$$\text{Cohesion:} \quad f_{v0} = 0.21 \text{ [MPa]}$$

$$\text{Coefficient of friction:} \quad \mu = 0.42 \text{ [-]}$$

### 3.5.2 Triplet Test Result for C.S. masonry - EC\_MAT\_H\_16

The test specimens were composed by 15 triplets of C.S. masonry (Figure 94) built by Dutch masons in the DICAr laboratory, with the same materials used to build the full-scale test-house. Nevertheless 3 specimens were damaged during the preparation of the test, hence only 12 triplets were tested.



Figure 94. View of the specimens (EC\_MAT\_H\_16\_A/P) for Triplet Test.

The date of construction of the Triplets (Specimens EC\_MAT\_H\_16\_A/P) was the 24/7/2015. The triplet shear tests were performed between the 3rd and the 19th of November 2015.

Figure 95 shows the results of the test. The square-dots represent all the couples  $(\sigma_l, f_{vl})$  relative to the maximum value of shear strength of mortar bedjoint, and the dashed black line is their linear regression line. The values of the couples  $(\sigma_l, f_{vl})$  are shown in Table 42.

The contribution to shear strength is given by both cohesion and friction force, because the specimen, before the test, is intact.

As specified before, a Coulomb like criterion is appropriate to describe these results. Hence the terms of the equation  $f_v = f_{v0} + \mu \cdot \sigma$  are found to be equal to:

*Cohesion:*  $f_{v0} = 0.0$  [MPa]

Y-intercept of the linear regression line of the couples  $(\sigma_l, f_{vl})$  relative to the maximum value of shear strength of mortar bedjoints.

*Coefficient of friction:*  $\mu = 0.5$  [-]

Slope of the linear regression line of all the points  $(\sigma_l, f_{vl})$  relative to the maximum value of shear strength of mortar bedjoints.

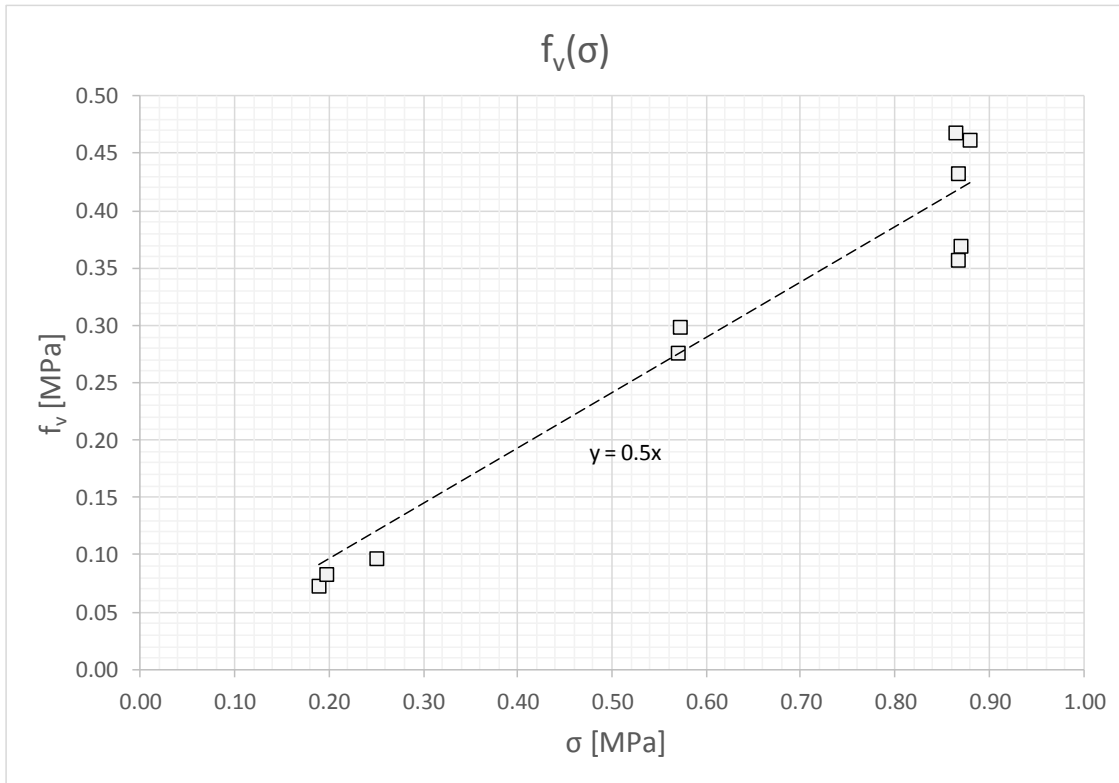


Figure 95. Triplet Test, C.S. specimens, series EC\_MAT\_H\_16;  $\sigma$ - $f_v$  strength envelope

Table 42. Triplet Test, C.S. specimens, series EC\_MAT\_H\_16;  $(\sigma_1, f_{v1})$  couples.

<i>specimen</i>	$\sigma$ [MPa]	$f_v$ [MPa]
A	-	-
B	-	-
C	0.19	0.07
D	0.20	0.08
E	0.57	0.28
F	0.57	0.30
G	0.87	0.36
H	0.86	0.47
I	0.87	0.37
L	0.25	0.10
M	0.87	0.43
N	0.88	0.46

The fact that the value of the cohesion determined by mean of the regression line of the couples  $(\sigma_l, f_{vl})$  is zero could be due to the sensibility of the method. A direct evaluation of the cohesion from each test will lead to a more representative result.

For this reason the different test on the triplets are analyzed separately. In fact from each of these test it is possible to obtain a value of cohesion and friction coefficient, always according to a Columb's like criterion.

The output of each test is the sequent:

- The couple of values  $(\sigma_I, f_{vI})$ : the shear strength  $f_{vI}$  at the first level of compression imposed on the specimen  $\sigma_I$ : both cohesion and friction contribute to shear strength;
- The couples of values  $(\sigma_{residual}, f_{v-residual})_i$ : the shear strength  $f_{v-residual}$  corresponding to the value of compression imposed on the specimen  $\sigma_{residual}$ , after the first shove of the central brick: only the friction contributes to shear strength, because the bedjoints of mortar are already cracked.

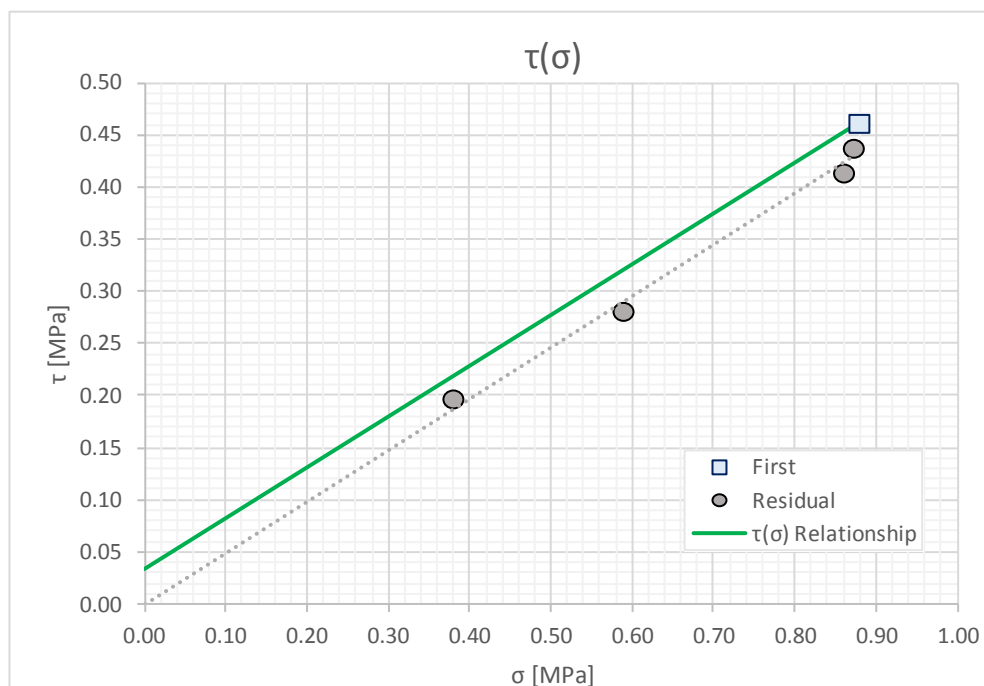


Figure 96. Triplet Test, Specimen EC\_MAT\_H\_16-N;  $\sigma$ - $f_v$  plot

Figure 96 shows the output of the tested specimen EC\_MAT\_H\_16-N. The squared dot is the couple  $(\sigma_I, f_{vI})$ , the circular dots are the couples  $(\sigma_{residual}, f_{v-residual})_i$ , the dashed line is the regression line of the couples  $(\sigma_{residual}, f_{v-residual})_i$  and the green solid line is the line passing through the first point  $(\sigma_I, f_{vI})$  and parallel to the other one.

The coefficient of friction,  $\mu$ , is the slope of the line relative to the linear regression of all the points  $(\sigma_{residual}, f_{v-residual})_i$ , from all the tests, except the ones corresponding to the first rupture.

The shear stress at zero nominal compressive stress,  $f_{v0}$  (cohesion or adhesion stress), is the Y-intercept of the line passing through the first point  $(\sigma_I, f_{vI})$  and with the slope equal to  $\mu$ .

Table 43 resume the values of cohesion and friction coefficient found per each test.

Table 43. Triplet Test, C.S. specimens, series EC\_MAT\_H\_16; values of cohesion and friction coefficient.

	$f_{v0}$	$\mu$
<i>Specimen</i>	[MPa]	[-]
EC-MAT-H-16- A	-	0.44
EC-MAT-H-16- B	-	0.58
EC-MAT-H-16- C	0.02	0.57
EC-MAT-H-16- D	0.02	0.56
EC-MAT-H-16- E	0.02	0.49
EC-MAT-H-16- F	0.03	0.55
EC-MAT-H-16- G	-	0.00
EC-MAT-H-16- H	0.06	0.48
EC-MAT-H-16- I	-	0.43
EC-MAT-H-16- L	0.02	0.44
EC-MAT-H-16- M	-	0.55
EC-MAT-H-16- N	0.03	0.49
<b>mean</b>	<b>0.03</b>	<b>0.51</b>
st.dev.	0.02	0.06
C.o.V.	55%	11%

The mean values of these parameters are:

*Cohesion:*  $f_{v0} = 0.03$  [MPa]

*Coefficient of friction:*  $\mu = 0.51$  [-]

It is possible to notice that the value of the friction coefficient is the same of the one found by considering the linear regression of all the couples ( $\sigma_l, f_{vl}$ ) only. This allow to consider the latter methodology reasonable.

The value of cohesion is still low but not null: 0.03 MPa.

### 3.5.3 Triplet Test Result for clay masonry - EC\_MAT\_H\_26

The test specimens were composed by 10 triplets of clay masonry (part of them are shown in the following Figure 97), built by Dutch masons in the DICAr laboratory, with the same materials used to build the full-scale test-house.



Figure 97. View of part of the specimens (EC\_MAT\_H\_26\_A/P) for Triplet Test.

The date of construction of the Triplets (Specimens EC\_MAT\_H\_26\_A/L) was the 24/7/2015. The triplet shear tests were performed between the 9<sup>th</sup> and the 27<sup>th</sup> of October 2015.

Figure 98 shows the results of the test. The square-dots represent all the couples  $(\sigma_l, f_{vl})$  relative to the maximum value of shear strength of mortar bedjoints, and the dashed black line is their linear regression line. The values of the couples  $(\sigma_l, f_{vl})$  are shown in Table 44.

The contribution to shear strength is given by both cohesion and friction force, because the specimen, before the test, is intact.

As specified before, a Coulomb like criterion is appropriate to describe these results. Hence the terms of the equation  $f_v = f_{v0} + \mu \cdot \sigma$  are found to be equal to:

*Cohesion:*  $f_v = 0.11$  [MPa]

Y-intercept of the linear regression line of the couples  $(\sigma_l, f_{vl})$  relative to the maximum value of shear strength of mortar bedjoint.

*Coefficient of friction:*  $\mu = 0.68$  [-]

Slope of the linear regression line of all the points  $(\sigma_1, f_{v1})$  relative to the maximum value of shear strength of mortar bedjoint.

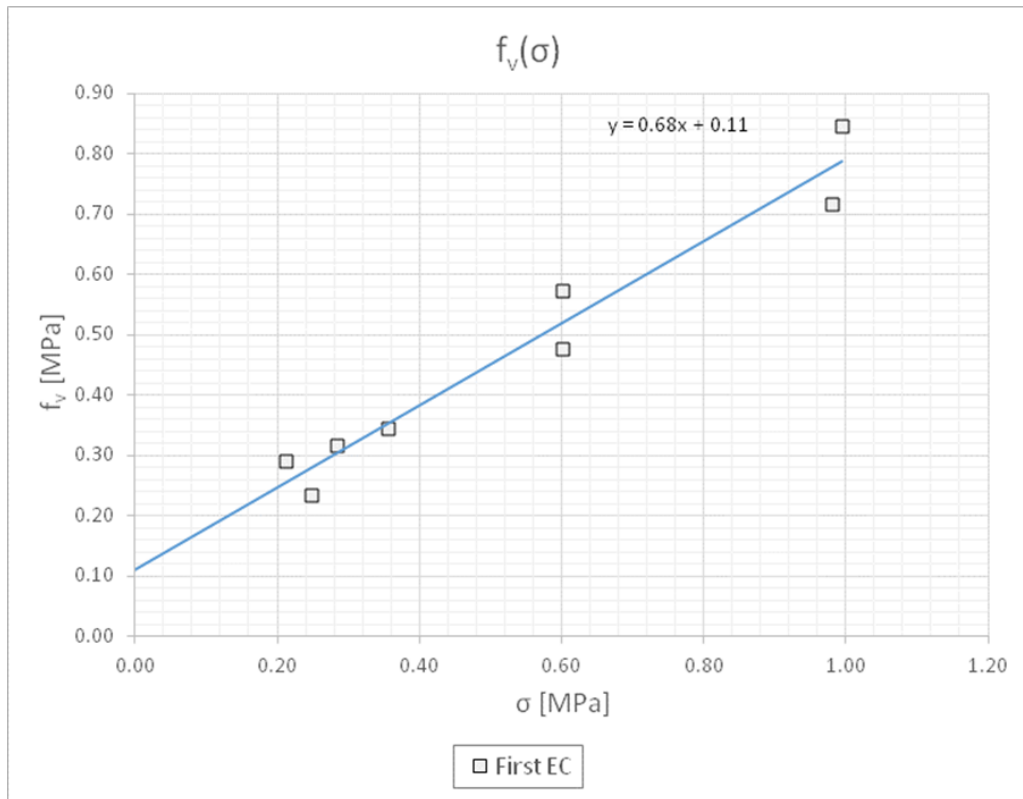


Figure 98. Triplet Test, Clay. specimens, series EC\_MAT\_H\_26;  $\sigma$ - $f_v$  strength envelope

Table 44. Triplet Test, Clay specimens, series EC\_MAT\_H\_26;  $(\sigma_1, f_{v1})$  couples.

<i>Specimen</i>	$\sigma$ [MPa]	$f_{v0}$ [MPa]
<b>A</b>	0.25	0.23
<b>B</b>	0.99	0.84
<b>C</b>	0.60	0.57
<b>D</b>	-	-
<b>E</b>	0.60	0.48
<b>F</b>	0.98	0.72
<b>G</b>	0.28	0.32
<b>H</b>	0.36	0.34
<b>I</b>	-	-
<b>L</b>	0.21	0.29

Considering this series of test few considerations have to be done:

- the results shows a significant dispersion
- because of the bricks present holes, the wet mortar, during the casting of the triplet, flow into the holes and create a sort of discontinues cylindrical bars along

the specimen. These mortar-bars complicate the interaction between the mortar bedjoints and the bricks, creating a sort of mechanical constrain.

For these reason the need to examine deeply the output of the tests is considered appropriate.

As for the case of triplet test on C.S. specimens cast during the construction of the full-scale test-house, the triplet test results are analyzed separately.

The output of each test, according to a Columb's like criterion, is the sequent:

- The couple of values  $(\sigma_I, f_{vI})$ : the shear strength  $f_{vI}$  at the first level of compression imposed on the specimen  $\sigma_I$ : both cohesion and friction contribute to shear strenght;
- The couples of values  $(\sigma_i, f_{vi})_{residual}$ : the shear strength  $f_{vi}$  corresponding to the value of compression imposed on the specimen  $\sigma_i$ , after the first shove of the central brick: only the friction contributes to shear strength, because the bedjoints of mortar are already cracked.

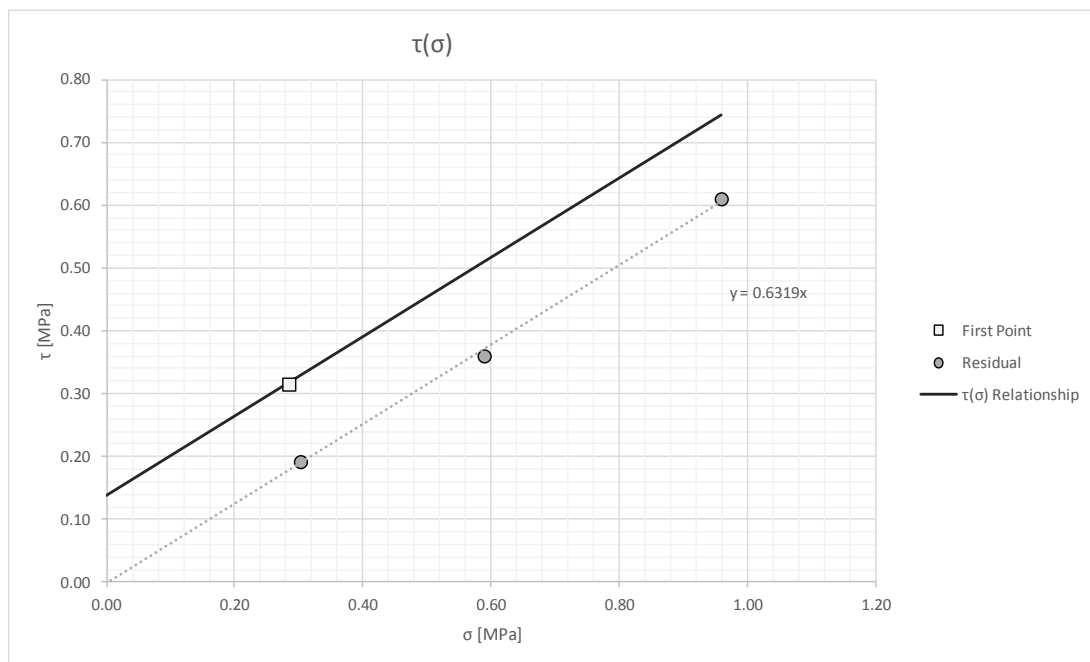


Figure 99. Triplet Test, Clay specimen EC\_MAT\_H\_26-G,  $\sigma$ - $f_v$  plot

Figure 99 shows the output of the tested specimen EC\_MAT\_H\_26-G. The square dot is the couple  $(\sigma_I, f_{vI})$ , the circle dots are the couples  $(\sigma_{residual}, f_{v-residual})_i$ , the dashed line is the regression line of the couples  $(\sigma_{residual}, f_{v-residual})_i$  and the black solid line is the line passing through the first point  $(\sigma_I, f_{vI})$  and parallel to the other one.

The coefficient of friction,  $\mu$ , is the slope of the line relative to the linear regression of all the points  $(\sigma_{residual}, f_{v-residual})_i$ , from all the tests, except the ones corresponding to the first rupture.

The shear stress at zero nominal compressive stress,  $f_{v0}$  (cohesion or adhesion stress), is the Y-intercept of the line passing through the first point  $(\sigma_1, f_{v1})$  and with the slope equal to  $\mu$ .

Table 45 resume the values of cohesion and friction coefficient found per each test.

*Table 45. Triplet Test, C.S. specimens, series EC\_MAT\_H\_26; values of cohesion and friction coefficient.*

<i>Specimen</i>	$f_{v0}$ [MPa]	$\mu$ [-]
EC-MAT-H-26- A	-	0.57
EC-MAT-H-26- B	0.25	0.60
EC-MAT-H-26- C	0.22	0.58
EC-MAT-H-26- D	-	0.56
EC-MAT-H-26- E	-	0.55
EC-MAT-H-26- F	0.14	0.59
EC-MAT-H-26- G	0.14	0.63
EC-MAT-H-26- H	-	0.53
EC-MAT-H-26- I	-	-
EC-MAT-H-26- L	-	-
<b>mean</b>	<b>0.19</b>	<b>0.58</b>
st.dev.	0.06	0.03
C.o.V.	30%	6%

The mean values of these parameters are:

*Cohesion:*  $f_{v0} = 0.19$  [MPa]

*Coefficient of friction:*  $\mu = 0.58$  [-]

These values differ significantly from the ones found by considering the linear regression of all the couples  $(\sigma_1, f_{v1})$  only.

This is a proof of the difficulties to interpret correctly the output of these tests when other mechanism of resistance (i.e. the little cylinder of mortar inside the specimens) interfere with the cohesion and friction between the bricks and the mortar.

At this stage it is suggested to use the values of cohesion and coefficient of friction found by considering the linear regression of all the couples  $(\sigma_1, f_{v1})$  only, as suggested by the EN 1052-3:2002:

### 3.6 Tensile Strength of ties

The purpose of the test is to evaluate the tensile strength of the steel ties utilized to connect the two leaves of the cavity walls. These elements were simply pulled in tension till their failure.

The tests were performed at the DICAr Laboratory of the University of Pavia in Italy.

The dimensions and the geometry of the ties are shown in the following Figure.

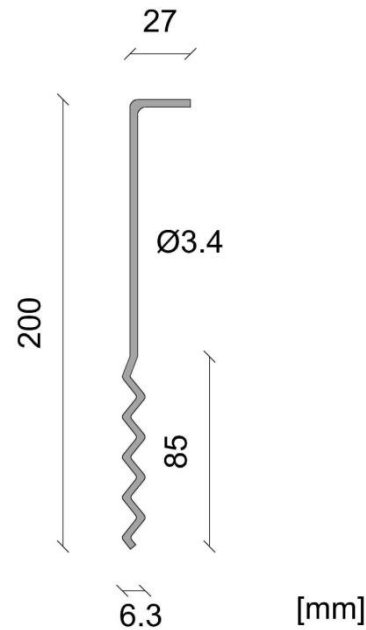


Figure 100. Metal ties geometry and dimensions.

The tensile load of ties results to be equal to:

$$F_t = 4.35 \text{ kN} \quad \text{with a } C.o.V. = 0.01.$$

The tensile strength capacity of ties is:

$$f_{t,t} = 479 \text{ MPa} \quad \text{with a } C.o.V. = 0.01.$$

### 3.7 Summary table

			<i>Calcium Silicate</i>		<i>Clay</i>	
<i>Material property</i>	<i>Symbol</i>	<i>UM</i>	<i>Average</i>	<i>C.o.V.</i>	<i>Average</i>	<i>C.o.V.</i>
Density	$\rho$	[kg/m <sup>3</sup> ]	1835 <sup>H</sup>	0.01 <sup>H</sup>	1905 <sup>H</sup>	0.03 <sup>H</sup>
Compressive strength of mortar	$f_c$	[MPa]	7.24	0.13	5.79	0.21
			5.71 <sup>H</sup>	0.25 <sup>H</sup>	6.24 <sup>H</sup>	0.09 <sup>H</sup>
Compressive strength of masonry unit	$f_b$	[MPa]	16.3	0.13	32.45	0.13
			17.18 <sup>H</sup>	0.14 <sup>H</sup>		
Flexural strength of mortar	$f_i$	[MPa]	2.87	0.14	2.05	0.20
			1.78 <sup>H</sup>	0.23 <sup>H</sup>	1.48 <sup>H</sup>	0.19 <sup>H</sup>
Compressive strength of masonry in the direction perpendicular to bed joints	$f_m$	[MPa]	6.20	0.07	11.32	0.12
			5.49 <sup>H</sup>	0.10 <sup>H</sup>	12.72 <sup>H</sup>	0.15 <sup>H</sup>
Elastic modulus of masonry in the direction perpendicular to bed joints (33% $f_m$ )	$E_{m-1}$	[MPa]	3256	0.20	5760	0.28
			1736 <sup>H</sup>	0.26 <sup>H</sup>	4742 <sup>H</sup>	0.17 <sup>H</sup>
Elastic modulus of masonry in the direction perpendicular to bed joints (10% $f_m$ )	$E_{m-2}$	[MPa]	4182	0.33	6033	0.26
			2132 <sup>H</sup>	0.17 <sup>H</sup>	3926 <sup>H</sup>	0.26 <sup>H</sup>
Elastic modulus of masonry in the direction perpendicular to bed joints given by the secant line passing through the points (33% $f_m$ , $\epsilon$ 33% $f_m$ ) and (10% $f_m$ , $\epsilon$ 10% $f_m$ )	$E_{m-3}$	[MPa]	3236	0.13	5967	0.27
			1660 <sup>H</sup>	0.34 <sup>H</sup>	5339 <sup>H</sup>	0.19 <sup>H</sup>
Flexural bond strength	$f_w$	[MPa]	0.238	0.163	0.158	0.582
			0.056 <sup>H</sup>	0.471 <sup>H</sup>	0.152 <sup>H</sup>	0.646 <sup>H</sup>
Masonry (bed joint) initial shear strength	$f_{v0}$	[MPa]	0.21 0.03 <sup>H</sup>	-	0.11 <sup>H</sup>	-
Masonry (bed joint) shear friction coefficient	$\mu$	[-]	0.42 0.5 <sup>H</sup>	-	0.68 <sup>H</sup>	-
Tensile load capacity of ties	$F_t$	[kN]	4.35	0.01		

*H*: values referred to the specimens casted with the same materials used to build the full-scale test-house.

*HE*: values referred to the specimens extracted from the full-scale test-house already built.

## 4 In-Plane Component Tests

The experimental test program administrated by EUCENTRE and carried out in the TREE Labs of Pavia, included three in-plane cyclic shear-compression tests on full scale calcium-silicate unreinforced masonry walls with different combinations of vertical compression, boundary conditions and slenderness ratios. Similar tests were performed in TUD. The study of the cyclic behaviour of different piers will be fundamental in order to calibrate reliable numerical models in term of force-displacement behaviour as well as define proper limit states.

Info on the test will be found in the following paper:

Graziotti F., Rossi A., Mandirola M., Penna A., Magenes G., (2016) *Experimental Characterization of Calcium-Silicate Brick Masonry for Seismic Assessment*, Proc. 16th IBMAC conference, Padua, Italy.

### 4.1 Test Specimens

The specimens tested are:

- 2 slender walls tested in double fixed boundary condition, with two different levels of vertical mean compression stress: 0.7 MPa (EC\_COMP\_2) and 0.52 MPa (EC\_COMP\_1).
- 1 squat wall tested in cantilever boundary condition, with a vertical mean compression stress of 0.3 MPa (EC\_COMP\_3).

The tested specimens with their characteristics are summarised in Table 46 and Figure 101.

Table 46. Tested Specimens: characteristics and dimensions.

Specimen Name	L [m]	t [m]	h [m]	$\sigma_v$ [MPa]	Unit size (lxtxh) [mm]	Unit # (hxlt) [-]	Boundary condition
EC_COMP_2	1.1	0.102	2.75	0.7	212x102x71	34x5x1	Double fixed
EC_COMP_1	1.1	0.102	2.75	0.52	212x102x71	34x5x1	Double fixed
EC_COMP_3	4	0.102	2.75	0.3	212x102x71	34x18x1	Cantilever

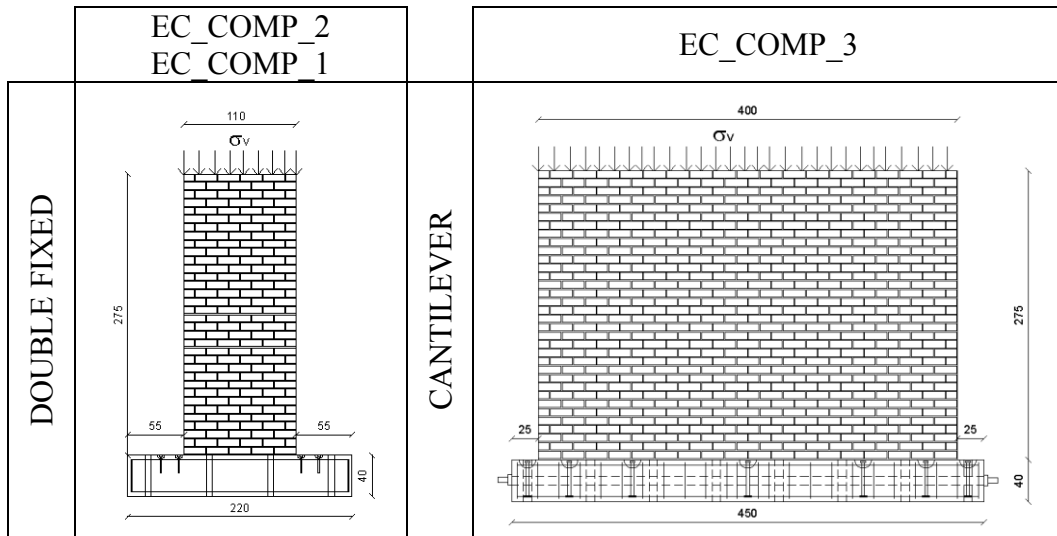


Figure 101. Experimental configurations considered.

The following pictures (Figure 102 to Figure 104) show the specimens during the construction phases.



Figure 102. Slender wall during the construction phases.



*Figure 103. Squat wall during the construction phases.*



*Figure 104. Specimens for In-Plane tests during the construction phases.*

## 4.2 Test set-up and instrumentation

### 4.2.1 Test set-up

The set-up adopted for the tests is shown in Figure 105. In particular it consists of:

- Horizontal servo-hydraulic actuator, able to apply a horizontal shear force at the top of the specimen equal to its maximum shear strength and a maximum displacement higher than 2 % of the height of the specimen; the actuator is fixed in order to guarantee a sufficiently rigid reaction in one end and it is connected to the top of the wall through a loading beam;
- Vertical servo-hydraulic actuators able to apply simultaneously a force equal to the required vertical load and a moment corresponding to the maximum resisting moment at the top section; the actuators are fixed in order to guarantee a sufficiently rigid vertical reaction in one end and they are connected to the loading beam;
- A restraining system to prevent out-of-plane deflection of the loading beam connected to the top of the specimen.

The horizontal servo-hydraulic actuator applies a horizontal shear force to the top of the wall through a composite steel/R.C. loading beam. The steel beam is stiffened with steel plates positioned orthogonally to the axis of the beam. A layer of self-levelling high strength shrinkage-controlled gypsum is placed between the steel/R.C. composite beam and the top of the masonry specimen, which can present an irregular surface, to allow a continuous and uniform support.

Two vertical servo-hydraulic actuators apply the vertical load on the wall, reacting on a steel frame fixed on a strong wall. The two vertical actuators allow to control the vertical load applied and to provide different boundary conditions (*e.g.* cantilever and double-fixed boundary conditions). The reinforced concrete footing is bolted to a strong floor. The horizontal actuator allows to apply horizontal forces and displacements according to the test protocol. The wall is restrained from out-of-plane deflections by a low-friction sliding restraining system.

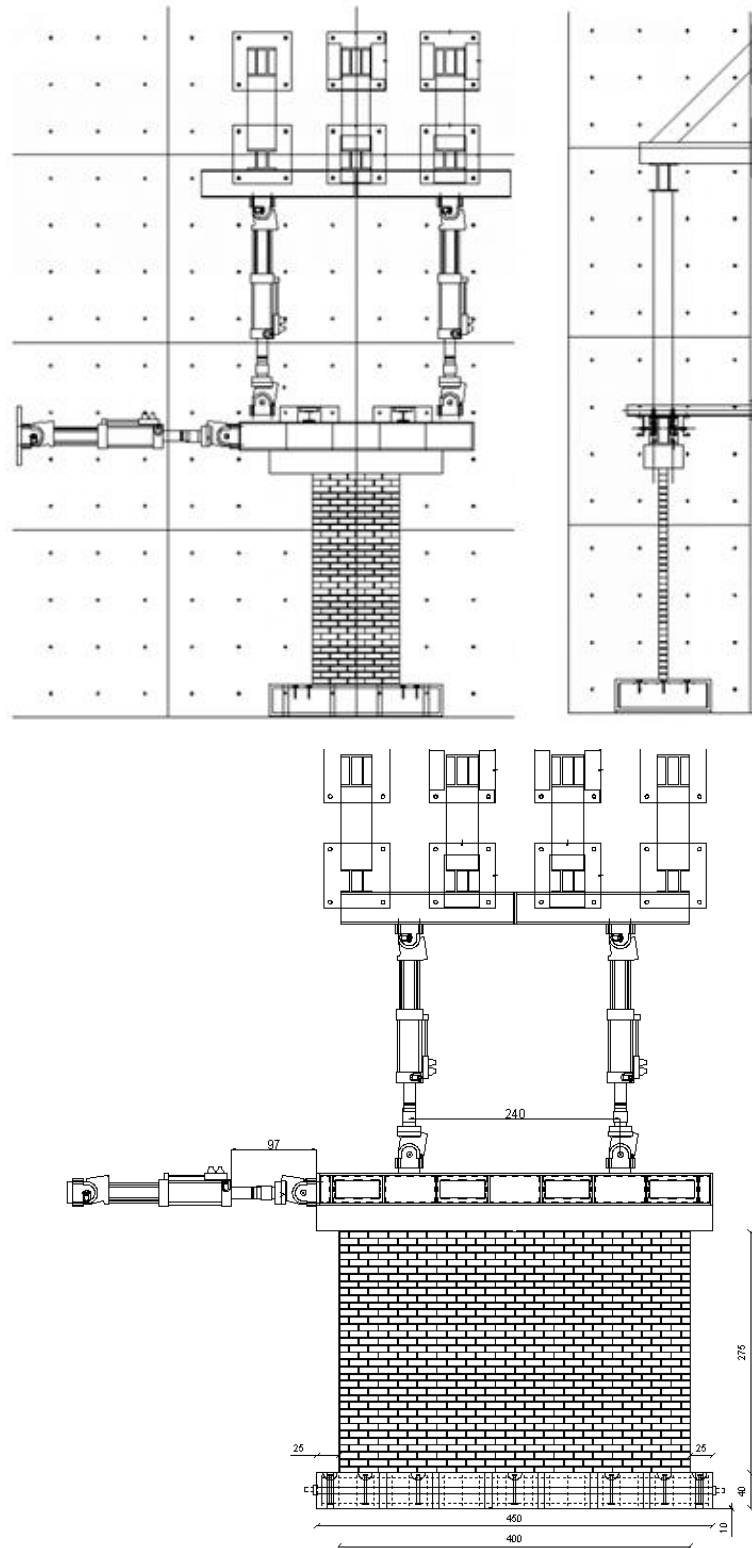


Figure 105. Test set-up.



### 4.2.2 Instrumentation

The instrumentation consist of a set of transducers, which guarantee an accurate measurement of the following quantities:

- forces in the actuators: horizontal and vertical forces applied to the top of the specimen;
- horizontal displacement of the beam on top of the specimen;
- vertical displacements of at least two different points of the top of the specimen, possibly symmetrical with respect to the central axis of the wall, in order to detect possible in-plane rotations;
- the relative out-of-plane displacement of the wall will be monitored by mean of potentiometers;
- possible sliding between the various mechanical parts involved in the test and possible sliding of the specimen with respect to the test apparatus (e.g. sliding of top beam or sliding with respect to the foundation).

The wall instrumentation for all the specimens is reported in the following figures (from Figure 106 to Figure 108). All the displacement transducers are mounted at middle stroke, fixed to the specimen with flat head nail anchored in the masonry and a plate with threaded rod is glued at the head of the nail. In this case, if the end scale of the transducer is reached, failure of the bonding of the two parts prevents the instrument from getting damaged. The instruments indicated with the letter “T” are spring-loaded potentiometers. The initial distance between the measure bases, with eventual extension of the transducers, has been measured after the installation of the instruments (for details refer to the Appendix A1 shared with the experimental raw data).

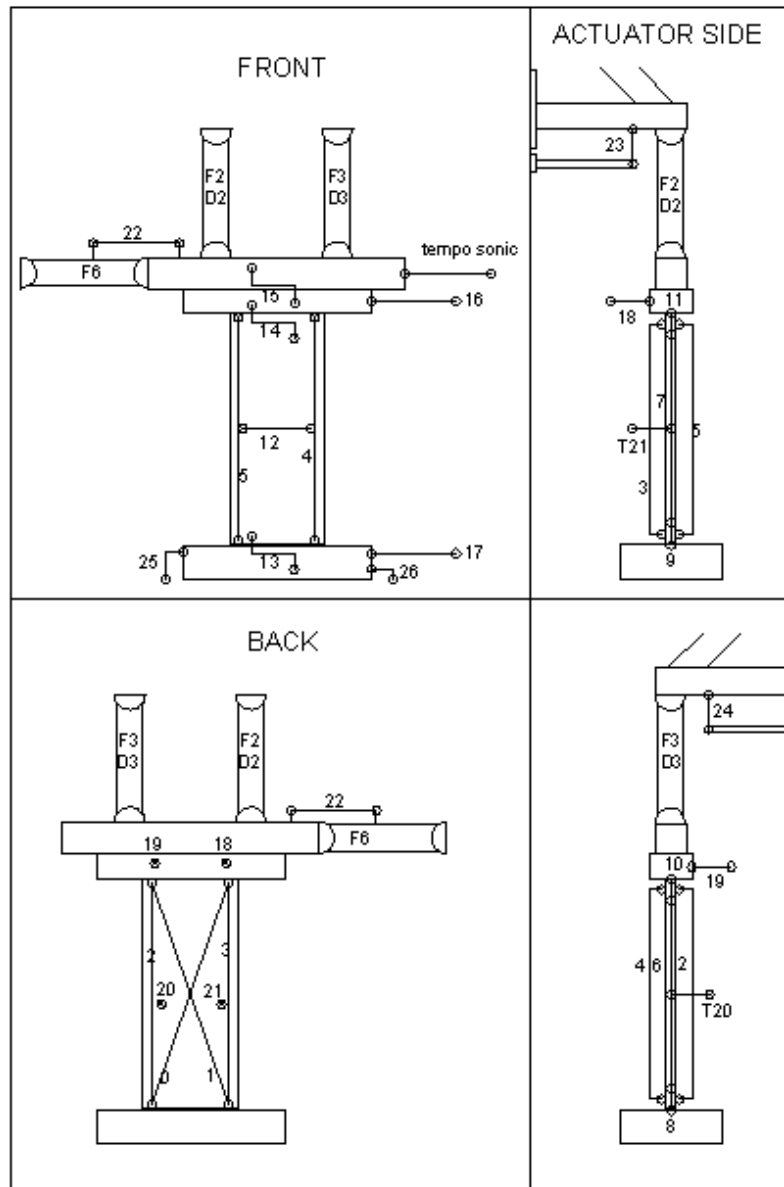


Figure 106. EC\_COMP\_2: Location of the instruments.

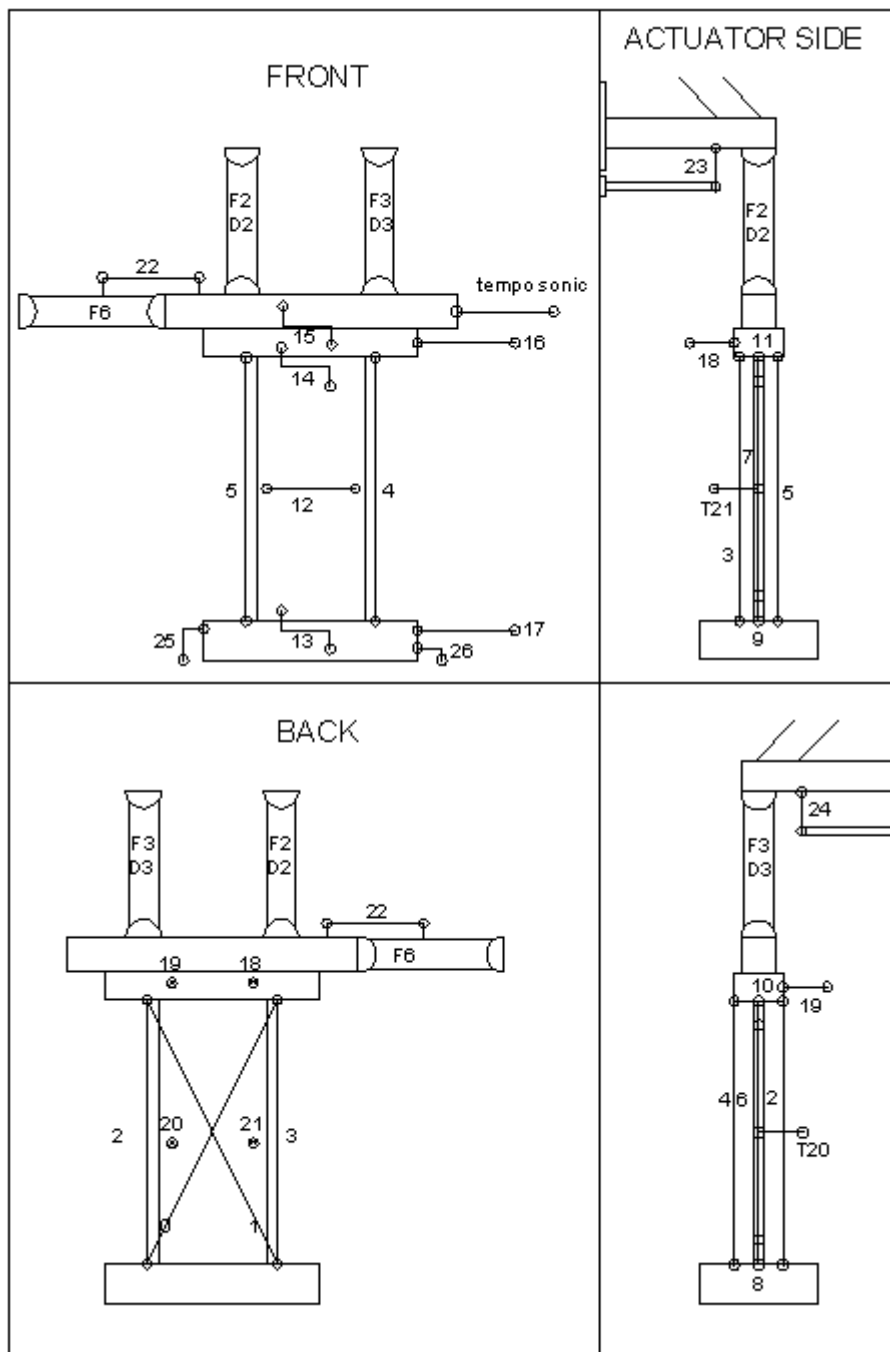


Figure 107. EC\_COMP\_1: Location of the instruments.

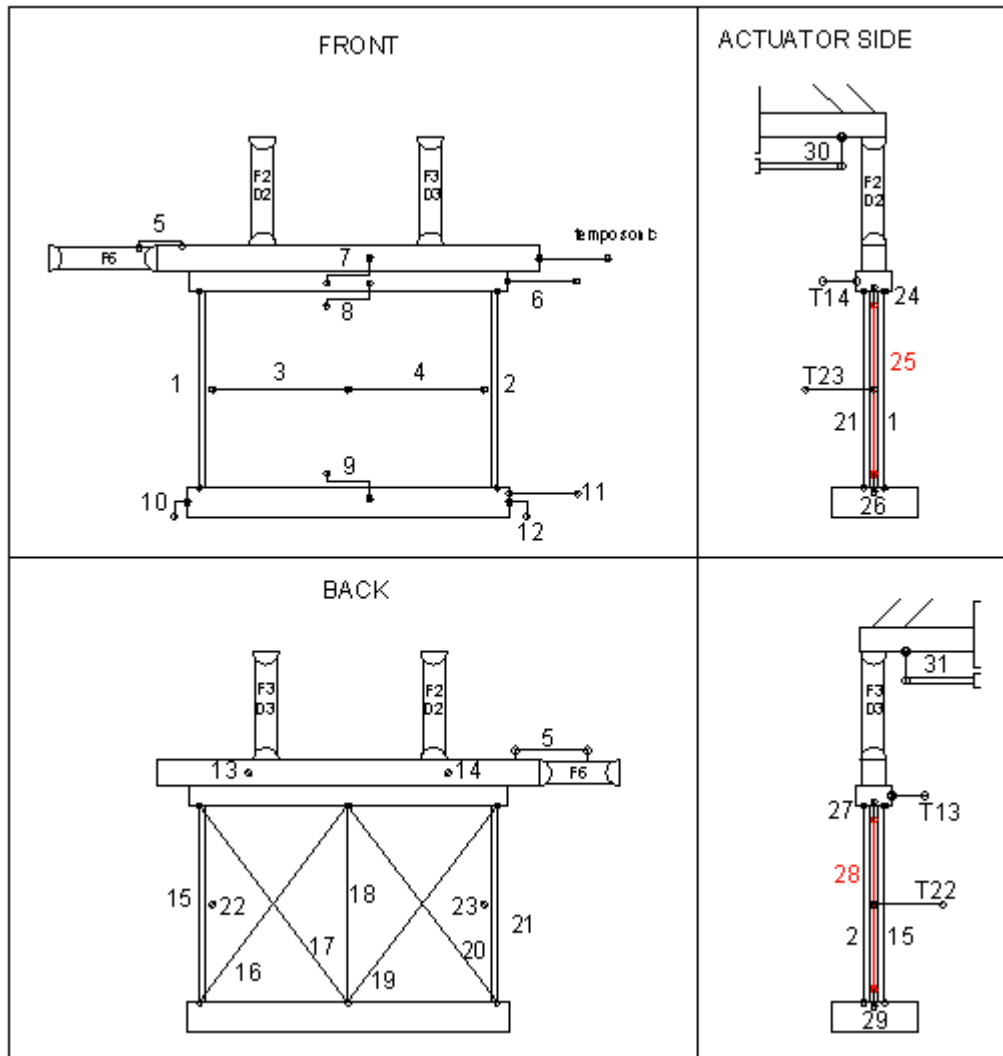


Figure 108. EC\_COMP\_3: Location of the instruments.

### 4.3 Testing procedure

The testing procedure envisaged two different boundary conditions: a “double fixed” system (rotation restrained at the top beam) and a “cantilever” system (free rotation at the top) with a constant vertical load.

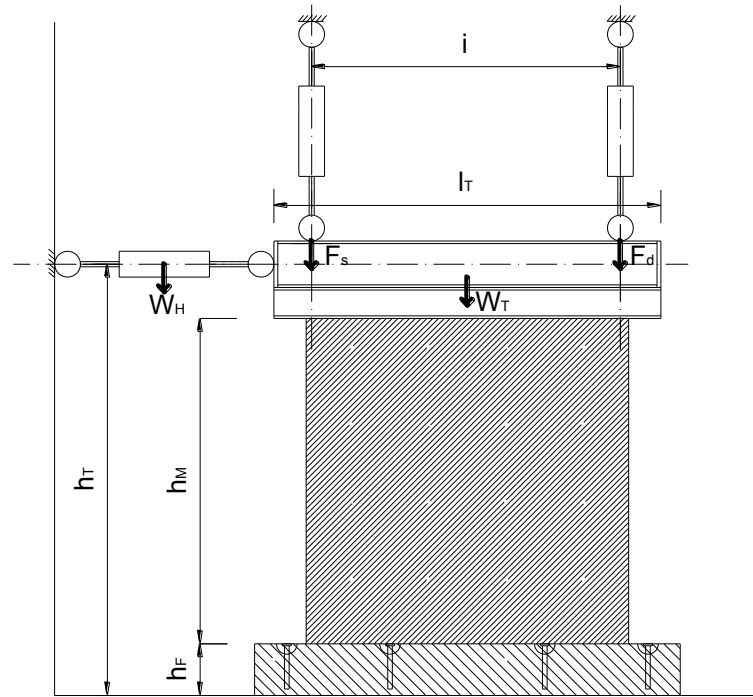


Figure 109. Scheme of the acting forces on the test set-up.

#### 4.3.1 Cantilever boundary conditions

In case of a cantilever system, both the forces of the right and left actuators are kept constant during the test and hence they are not dependent on the force and displacement of the horizontal actuator.

Therefore, the relationships between the actuator forces shall be as follows (see Figure 109 for notation):

$$\begin{cases} F_D + F_S + \frac{W_H}{2} + W_T = P \\ F_D \frac{i}{2} = F_S \frac{i}{2} + \frac{W_H l_T}{4} \end{cases}$$

where  $F_D$  and  $F_S$  are the applied vertical forces of the right and left actuator respectively;  $W_H$  is the weight of the horizontal actuator,  $W_T$  is the weight of the top beam,  $i$  is the horizontal distance between the 2 vertical actuators,  $l_T$  is the length of the top beam.

Therefore, independently from the imposed value of the horizontal displacement  $u_H$ , the transmitted forces of the vertical actuators are computed with the following expressions:

$$\begin{cases} F_S = \frac{P}{2} - \frac{W_T}{2} - \frac{W_H}{4} \left(1 + \frac{l_T}{i}\right) \\ F_D = \frac{P}{2} - \frac{W_T}{2} - \frac{W_H}{4} \left(1 - \frac{l_T}{i}\right) \end{cases}$$

### 4.3.2 Double fixed boundary conditions

The double fixed boundary conditions can be obtained by two alternative settings of the actuator control. The first one is based on a “static” criterion (force control), the second one consists of a “kinematic” criterion (mixed control). The “kinematic” criterion allows a better control of the tests and hence it is strongly recommended, provided the testing controller allows a mixed force-displacement control.

The “static criterion” consists in imposing the condition of zero bending moment at mid-height of the wall. Therefore, the following expressions are implemented in the test procedure:

$$\begin{cases} F_D + F_S = P - \frac{W_H}{2} - W_T \\ F_S - F_D = F_H \frac{2}{i} \left( h_H - \frac{h_M}{2} - h_F \right) - \frac{l_H W_H}{2i} \end{cases}$$

where  $F_D$  and  $F_S$  are the applied vertical forces of the right and left actuator respectively;  $F_H$  is the applied horizontal force of the horizontal actuator,  $W_H$  is the weight of the horizontal actuator,  $W_T$  is the weight of top beam,  $i$  is the horizontal distance between the 2 vertical actuators,  $l_T$  is the length of the top beam,  $h_H = h_T$  is the height of the axis of the horizontal actuator,  $h_M$  is the clear height of the wall,  $h_F$  is the height of the foundation.

The “kinematic” criterion involves a mixed force-displacement control, imposing both a constant vertical load and a condition of free translation with no rotation of the top beam.

Therefore, the following expressions are implemented in the test procedure:

$$\begin{cases} F_D + F_S + \frac{W_H}{2} + W_T = P \\ u_D = u_S \end{cases}$$

where  $u_D$  and  $u_S$  are the vertical displacements of the right and left actuator respectively,  $F_D$  and  $F_S$  are the applied forces of the right and on the left actuator respectively,  $W_H$  is the weight of the horizontal actuator,  $W_T$  is the weight of top beam,  $i$  is the horizontal distance between the 2 vertical actuators,  $l_T$  is the length of the top beam.

### 4.3.3 Execution of the test and horizontal loading history

Firstly, the horizontal actuator is kept unloaded and the vertical load is applied by the vertical actuators with constant velocity. The horizontal loading history is then applied in a displacement-controlled procedure. The duration of each cycle is kept constant, incrementing the actuator displacement rate proportionally to the cycle target displacement. The tests are stopped in case of critical damage conditions.

The cycles of horizontal displacement imposed to the top of the walls are summarised in the tables and figures below (from Table 47 to Table 49 and from Figure 110 to Figure 115).

#### EC\_COMP\_2

Table 47. EC\_COMP\_2: cycles of horizontal displacement imposed to the top of the wall.

N cycles	Drift [%]	Amplitude [mm]	Velocity [mm/s]
1_1	0.0125	0.35	0.025
1_2	0.025	0.69	0.025
1_3	0.0375	1.04	0.025
1_D	0.05	1.38	0.025
2_D	0.075	2.06	0.0375
3_D	0.1	2.75	0.05
4_D	0.15	4.13	0.0625
5_D	0.2	5.5	0.08
6_D	0.25	6.88	0.1

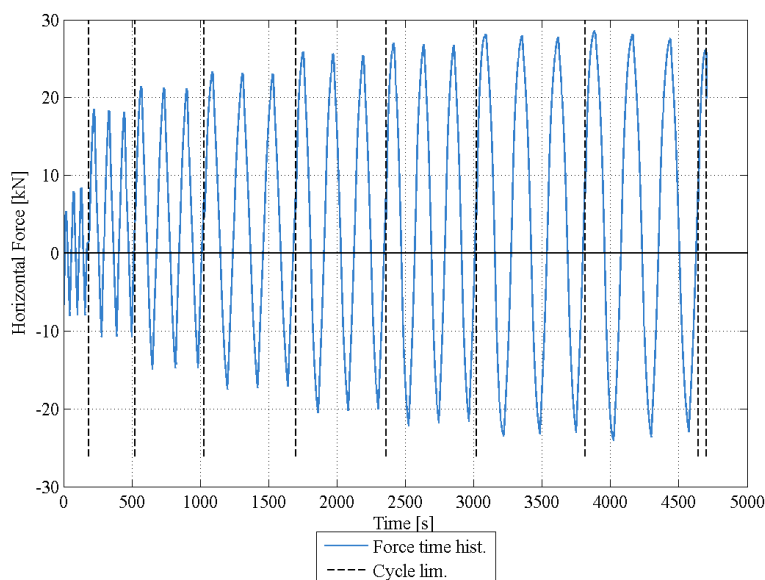


Figure 110. EC\_COMP\_2: Time history of the horizontal load.

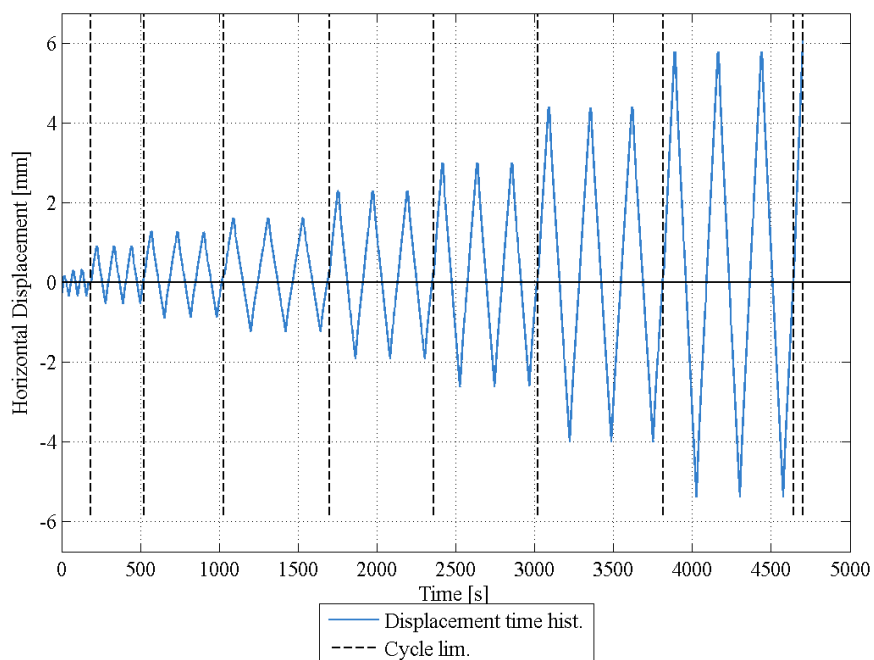


Figure 111. EC\_COMP\_2: Time history of the horizontal displacement.

### EC\_COMP\_1

Table 48. EC\_COMP\_1: cycles of horizontal displacement imposed to the top of the wall.

<b>N cycles</b>	<b>Drift [%]</b>	<b>Amplitude [mm]</b>	<b>Velocity [mm/s]</b>
1_1	0.0125	0.35	0.025
1_2	0.025	0.69	0.025
1_3	0.0375	1.04	0.025
1_D	0.05	1.38	0.025
2_D	0.075	2.06	0.0375
3_D	0.1	2.75	0.05
4_D	0.15	4.13	0.0625
5_D	0.2	5.5	0.08
6_D	0.25	6.88	0.1
7_D	0.3	8.25	0.12
8_D	0.4	11	0.16
9_D	0.5	13.75	0.2
10_D	0.6	16.5	0.24
12_D	0.8	22	0.32
13_D	1	27.5	0.4
14_D	1.25	34.38	0.5
15_D	1.5	41.25	0.5
17_D	2	55	0.5

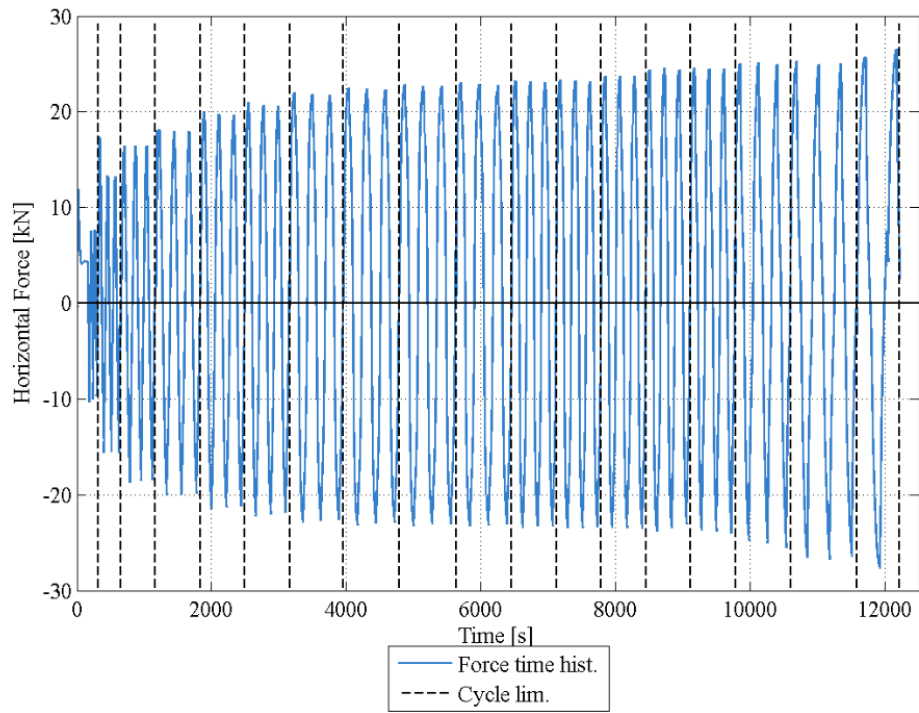


Figure 112. EC\_COMP\_1: Time history of the horizontal load.

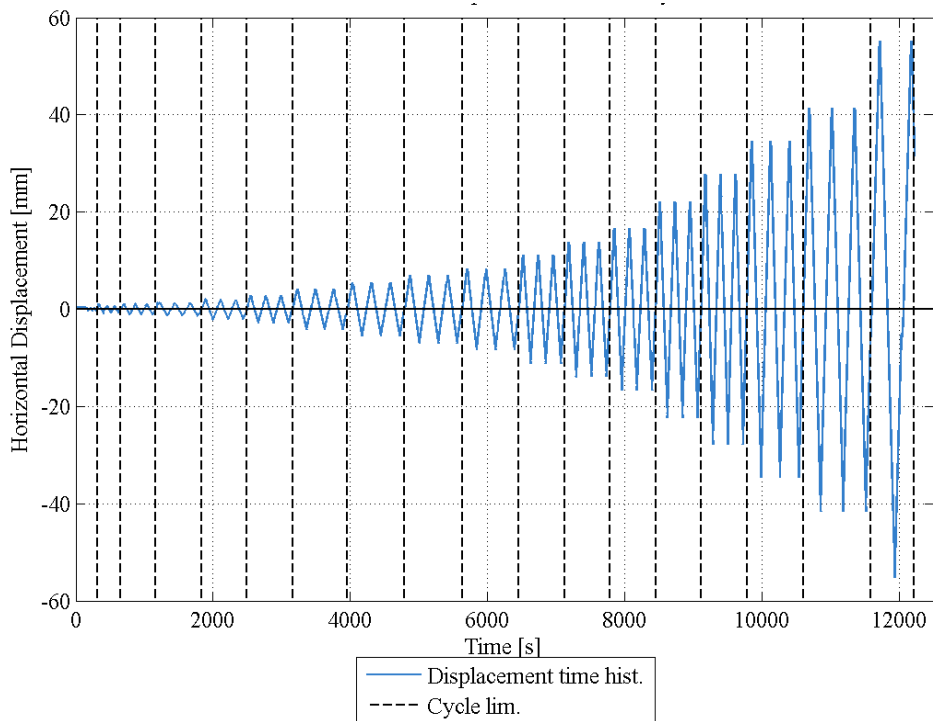


Figure 113. EC\_COMP\_1: Time history of the horizontal displacement.

### EC\_COMP\_3

Table 49. EC\_COMP\_3: cycles of horizontal displacement imposed to the top of the wall.

N cycles	Drift [%]	Amplitude [mm]	Velocity [mm/s]
1_1*	15 kN	0.09	0.5 kN/s
1_2	0.008	0.21	0.015
1_3	0.012	0.33	0.015
1_4	0.016	0.44	0.02
1_5	0.02	0.55	0.02
1_6	0.028	0.78	0.02
1_7	0.037	1.03	0.02
1_D	0.05	1.38	0.025
2_D	0.075	2.06	0.0375
3_D	0.1	2.75	0.05
4_D	0.15	4.13	0.0625
5_D	0.2	5.5	0.08
6_D	0.25	6.88	0.1
7_D	0.3	8.25	0.12

\*This cycle was conducted in force control

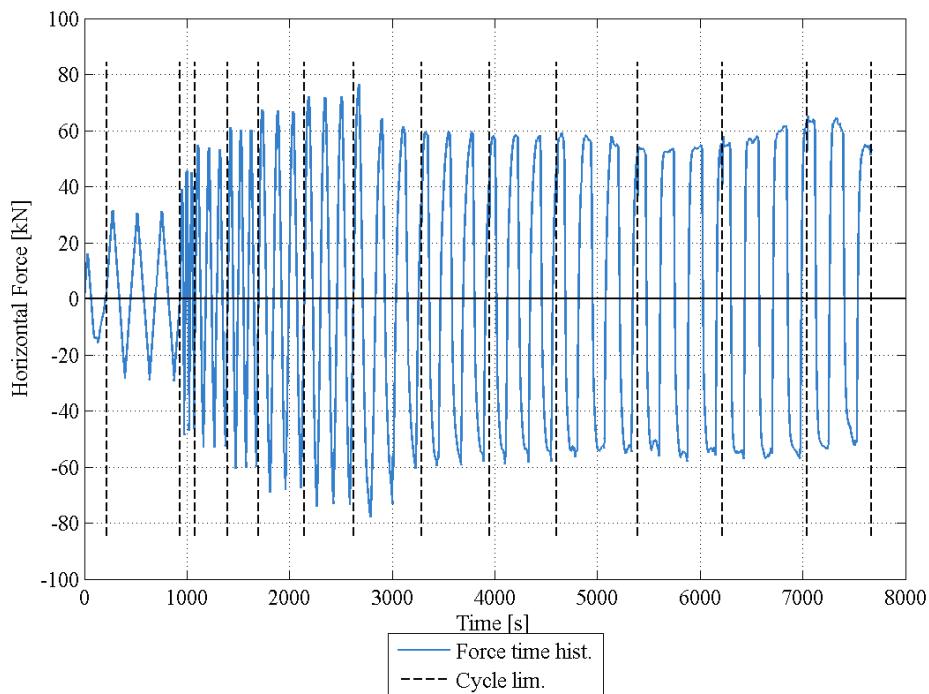


Figure 114. EC\_COMP\_3: Time history of the horizontal load.

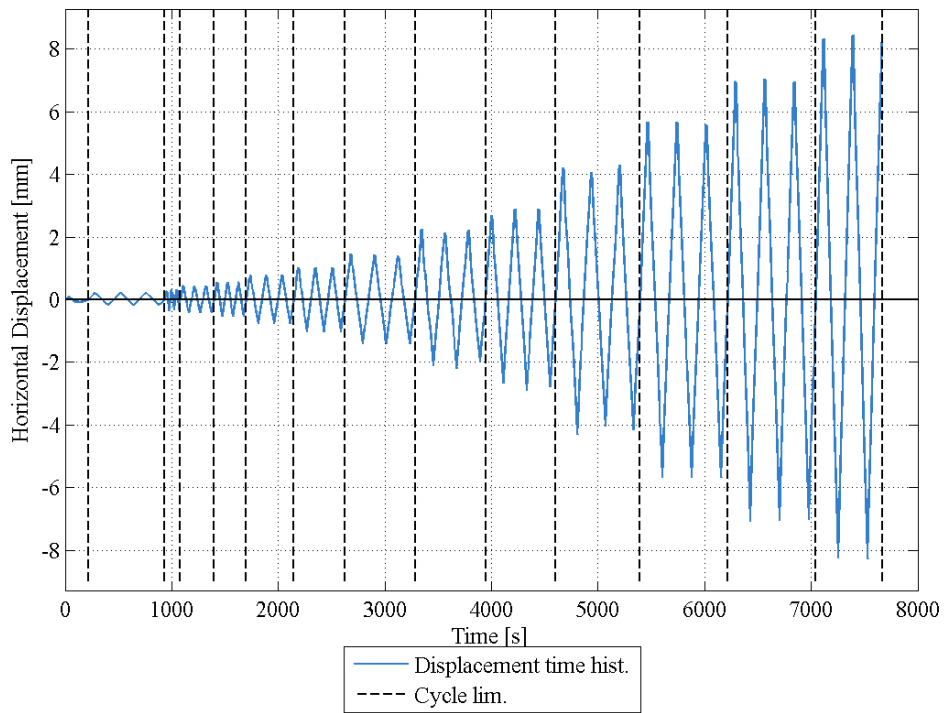


Figure 115. EC\_COMP\_3: Time history of the horizontal displacement.

## 4.4 Experimental Results

### 4.4.1 EC\_COMP\_2

EC\_COMP\_2 is the first of the three quasi-static in-plane tests performed (in double fixed conditions) in the TREE Labs of EUCENTRE. This specimen is 1.1 metres long and 2.75 metres high. The applied overburden stress is 0.7 MPa.

A picture of the test set-up is reported in Figure 116.

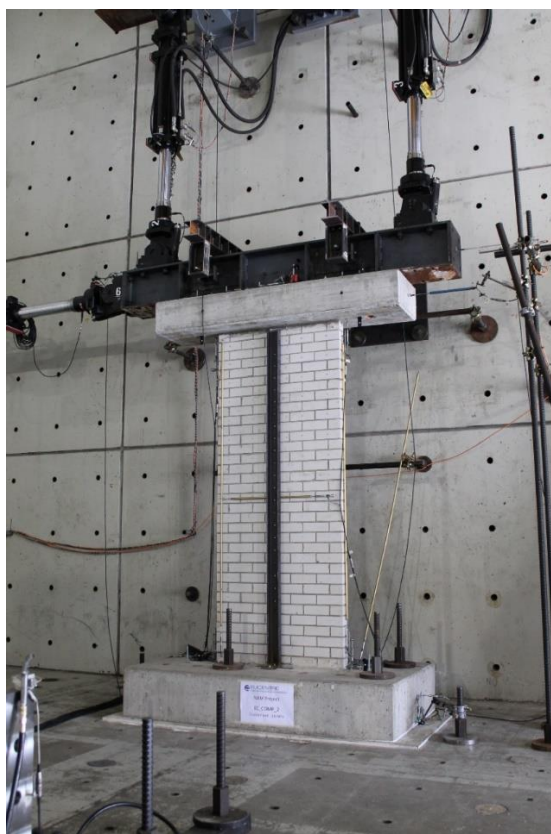


*Figure 116. EC\_COMP\_2: Test set-up.*

As expected the specimen exhibits a pure rocking behavior with cracks opening at the edges. No damaged were observed in the masonry panel.

The end of the test was reached for an early out-of-plane failure of the specimen 0.25% of drift. Due to very different in plane and out of plane slenderness of the specimen and due to the restrain conditions, the top beam began to rotate after 0.15% of drift. The hysteretic behavior is considered reliable up to that level of drift. The crack pattern is not specifically reported, two horizontal cracks opened at the base and under the upper brick as reported in Figure 117, that shows the failure mechanism.

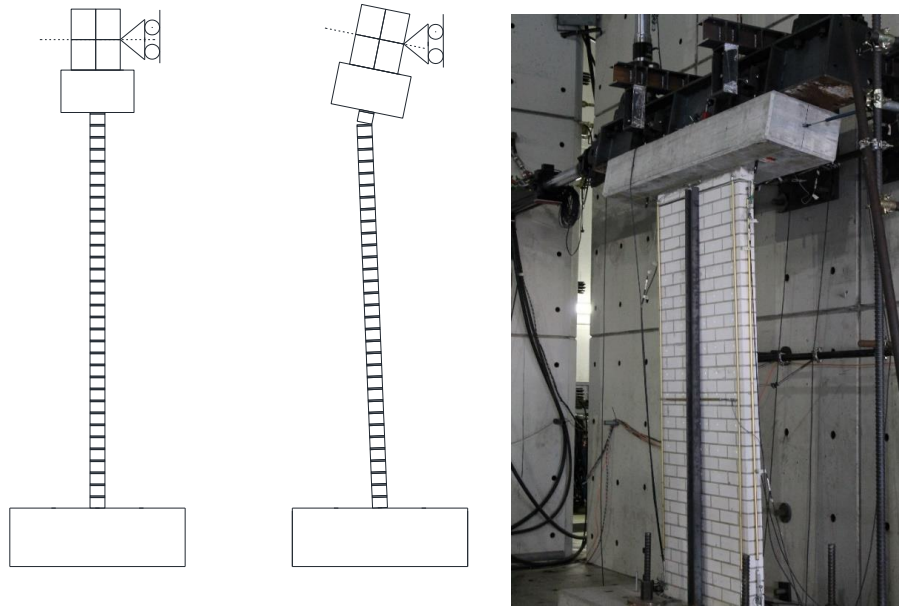


Figure 117. Failure mechanism of the specimen EC\_COMP\_2.

The hysteretic behavior of the specimen during the test is reported in Figure 118.

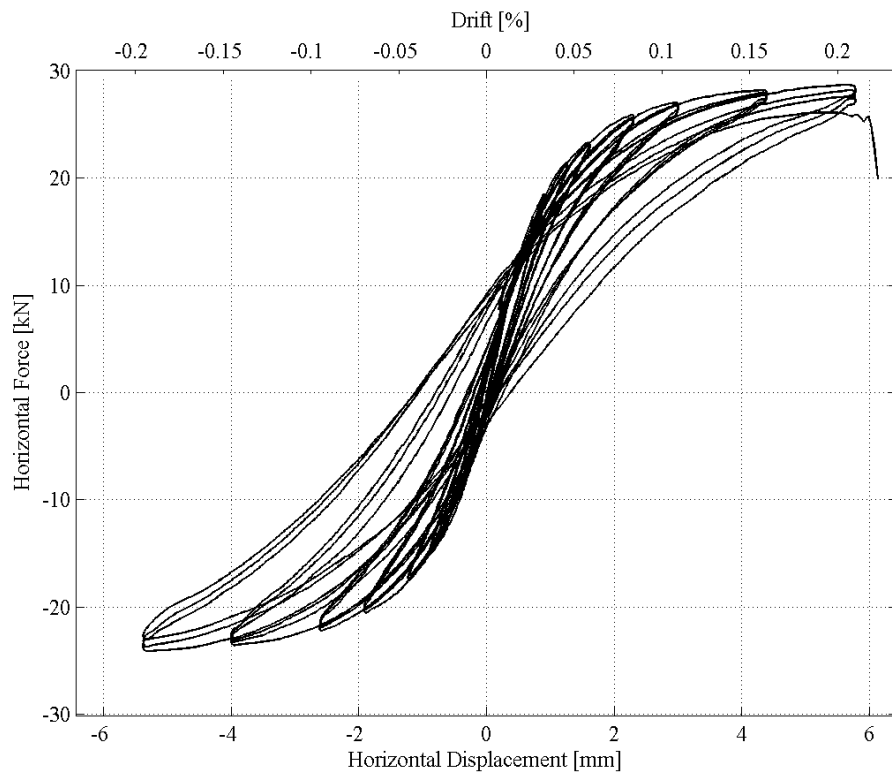


Figure 118. Hysteretic behaviour of specimen EC\_COMP\_2 during the test.

The initial elastic stiffness of the wall has been estimated according to the initial experimental curves as reported in Figure 119. It results equal to about 24 kN/mm.

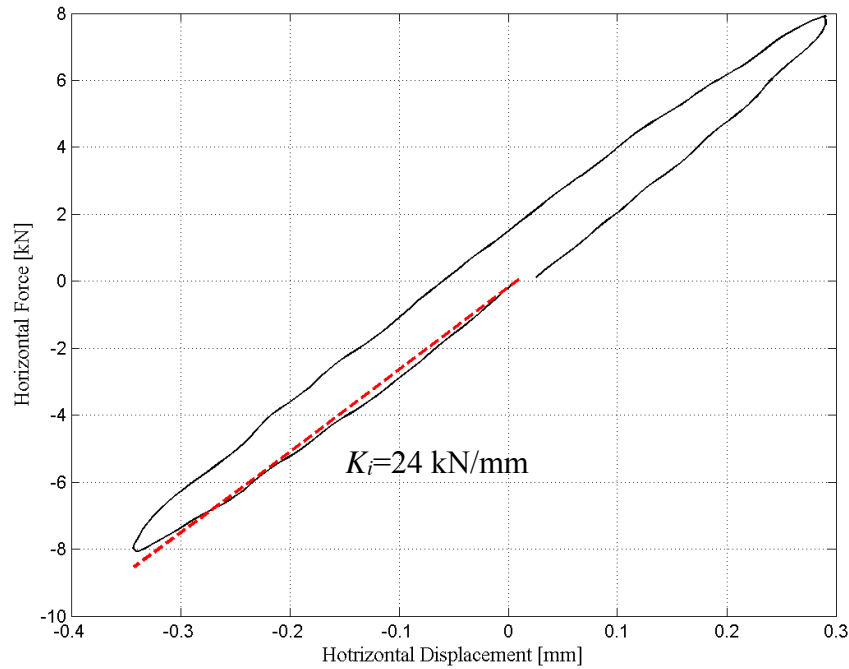


Figure 119. EC\_COMP\_2: Evaluation of the initial elastic stiffness.

A reference value for the initial stiffness can be calculated also theoretically by considering the Elastic Modulus of the masonry wall equal to  $E_{m-2-h} = 4182$  MPa. This value of  $E_{m-2-h}$  is the result of the compressive tests on wallettes built with the same masonry of the walls tested in-plane. The theoretical value of the elastic initial stiffness resulted to be equal to 18.45 kN/mm.

Figure 120 reports the total work computed during each cycles (the dashed curve represents the dissipated energy).

The dissipated hysteretic energy was evaluated also in terms of equivalent viscous damping coefficient:

$$\xi_{\text{hyst}} = A_h / (2\pi F_m \Delta_m)$$

where  $A_h$  is the area within one complete cycle of stabilized force-displacement response,  $F_m$  and  $\Delta_m$  are the maximum force and displacement achieved in the stabilized loops. The results of the calculated equivalent viscous damping are plotted in Figure 121 as a function of displacement ductility of each cycle.

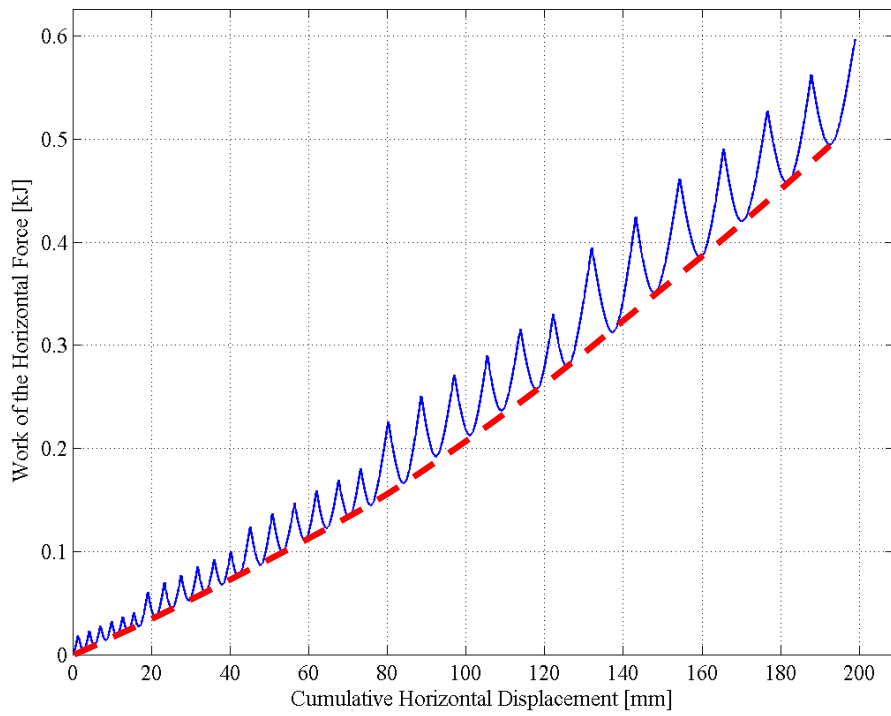


Figure 120. EC\_COMP\_2: Work and dissipated energy.

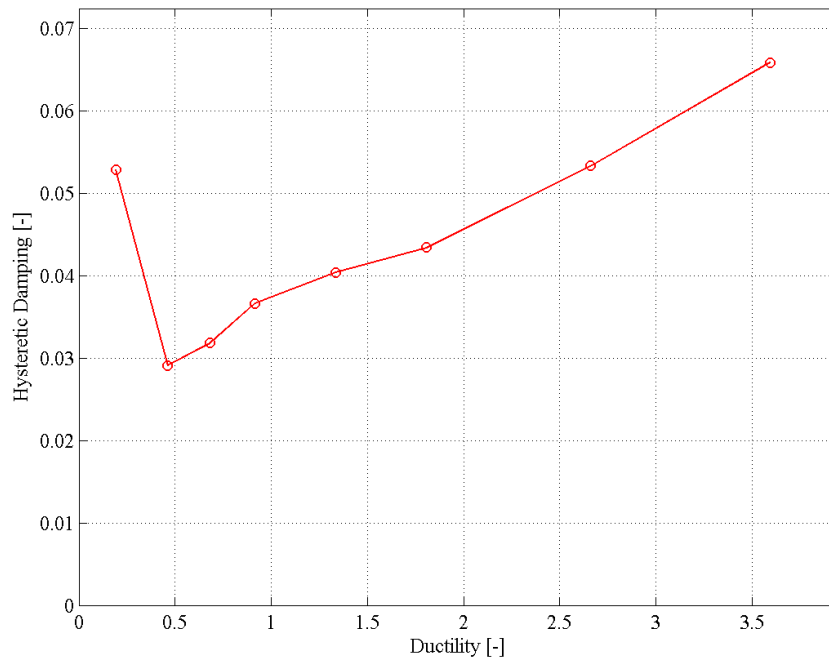


Figure 121. EC\_COMP\_2: Equivalent viscous damping ratio vs. displacement ductility.

#### 4.4.2 EC\_COMP\_1

EC\_COMP\_1 is the second of the three quasi-static in-plane tests performed (in double fixed conditions) in the TREE Labs of EUCENTRE. This specimen is 1.1 metres long and 2.75 metres high. The applied overburden stress is 0.52 MPa.

A picture of the test set-up is reported in Figure 122.



*Figure 122. EC\_COMP\_1: Test set-up.*

As expected the specimen exhibits a pure rocking behavior with cracks opening at the edges. A migration of the horizontal crack at the bottom was observed. Its location was at the interface up to a drift of 0.6%, above the first layer up to a drift of 1.5% and above the second layer during last cycle with a drift of 2%.

In particular, during CYCLE 5\_D (drift 0.2%) the specimen suffered slight damage and the formation of the first few cracks was observed (two horizontal cracks, one at the base of the wall and one on top of the wall) as shown in Figure 123.



Figure 123. EC\_COMP\_1: crack pattern after CYCLE 5\_D (drift 0.2%).

During CYCLE 7\_D (drift 0.3%) and CYCLE 12\_D (drift 0.8%) new horizontal cracks appeared at the top of the wall, while a widening of the existing cracks was noticed after each tests (Figure 124 and Figure 125, in red the cracks induced at current cycle and in black the pre-existing cracks).

The first cracks in the brick at the base of the wall have been observed during CYCLE 14\_D (drift 1.25%), as reported in Figure 126.

At the end of the test (CYCLE 17\_D, drift 2%) a toe crushing mechanism at the top and bottom of the wall was exhibited, with the expulsion of portions of brick and mortar (Figure 127, in red cracks induced at current cycle, in black the pre-existing cracks and in green the pieces of brick and mortar detached).

The end of the test was reached for the inability of the pier to sustain the imposed vertical load at a drift of 2% of drift.

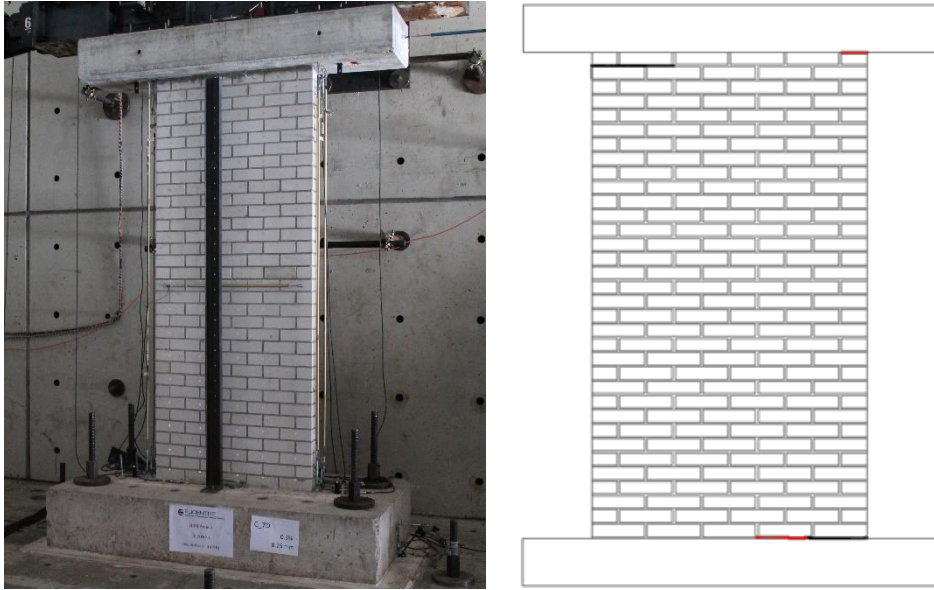


Figure 124. EC\_COMP\_1: crack pattern after CYCLE 7\_D (drift 0.3%).

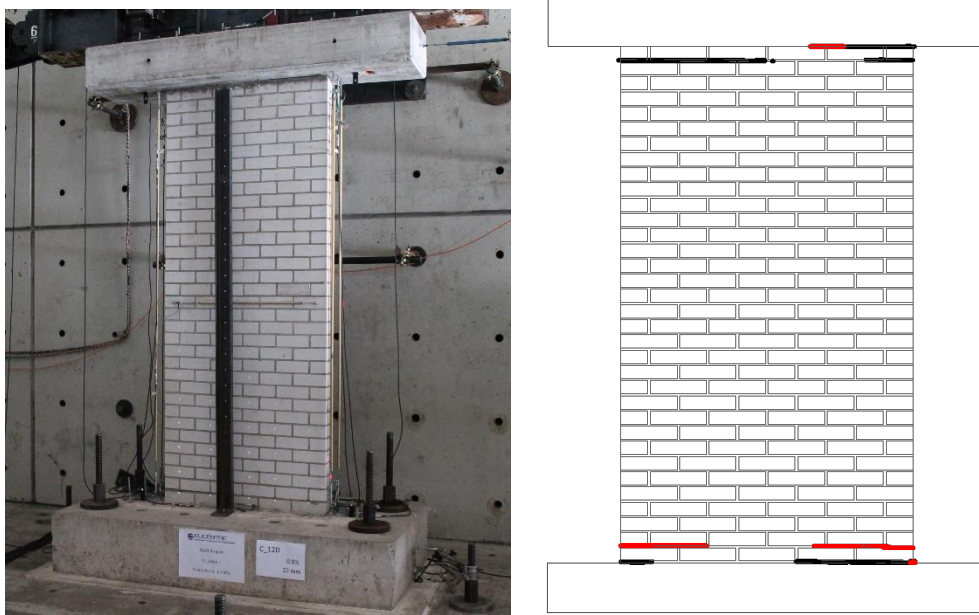


Figure 125. EC\_COMP\_1: crack pattern after CYCLE 12\_D (drift 0.8%).

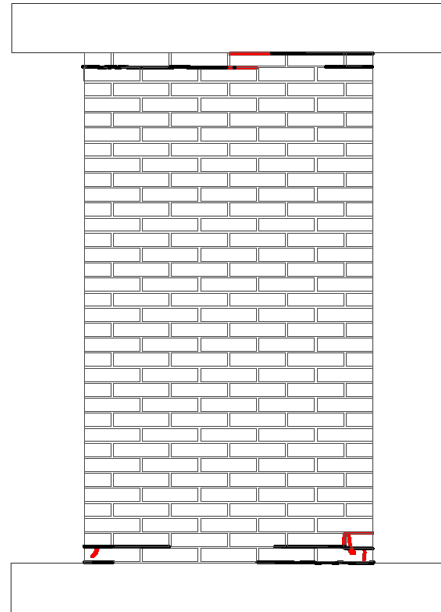


Figure 126. EC\_COMP\_1: crack pattern after CYCLE 14\_D (drift 1.25%).

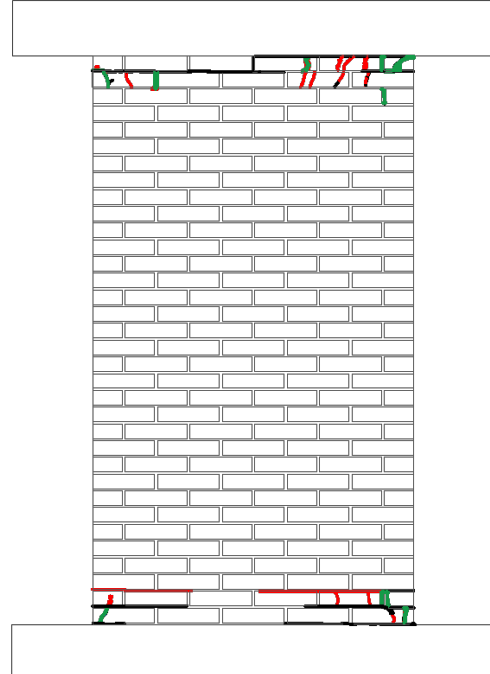


Figure 127. EC\_COMP\_1: crack pattern after CYCLE 17\_D (drift 2%).

Some pictures of the specimen at the end of the test are presented in the following figures (from Figure 128 to Figure 131).



*Figure 128. EC\_COMP\_1. Toe crushing mechanism at the base of the wall, after CYCLE 17\_D (drift 2%).*



*Figure 129. EC\_COMP\_1. Toe crushing mechanism at the top of the wall (actuator side), after CYCLE 17\_D (drift 2%).*



*Figure 130. Toe crushing mechanism at the top of the wall, after CYCLE 17\_D (drift 2%).*



*Figure 131. Expulsion of a portion of masonry due to toe crushing mechanism at the top of the wall, after CYCLE 17\_D (drift 2%).*

The hysteretic behavior of the specimen during the test is reported in Figure 132.

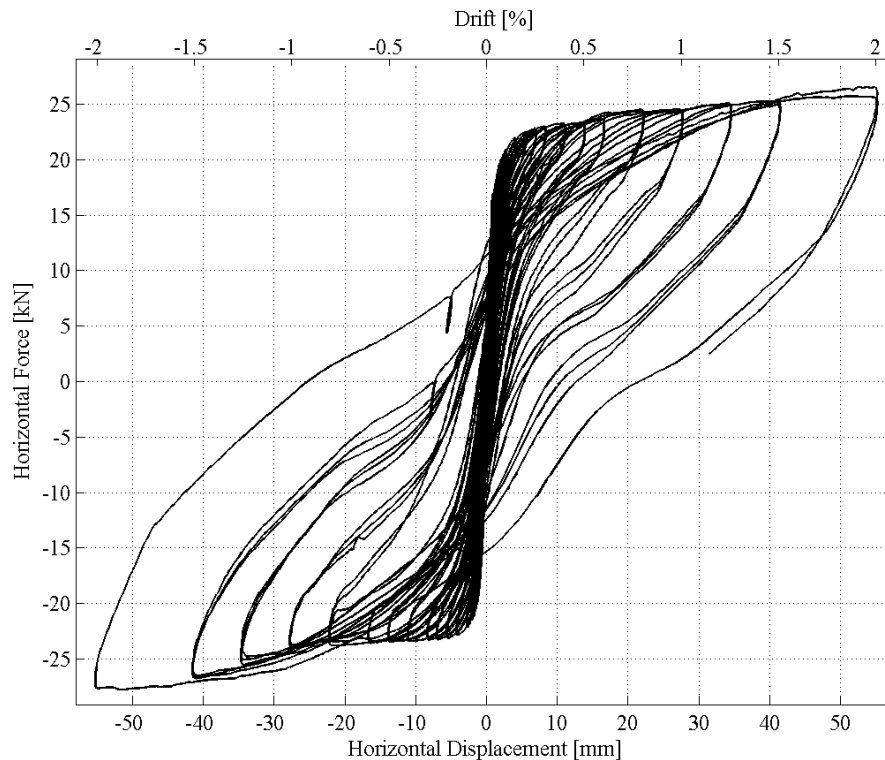


Figure 132. Hysteretic behaviour of the specimen *EC\_COMP\_1* during the test.

It is possible to observe a sort of hardening (e.g. increase of the Horizontal Force once reached the plateau phase) for drift higher than 0.8%. This is associated to the “migration” of the lower horizontal crack that create the effect of a squatter pier (with higher flexural capacity).

As for the previous test, the trend of the vertical displacement at the top of the wall has been investigated for all the cycles and the result is reported in Figure 133. This measure may be directly related to the toe (top and bottom) crushing. It is possible to observe how the top beam tends to be lifted due to rocking mechanism. For higher drift cycles and with their repetitions, the beam tends to be lower once the wall is pushed in rest condition). This phenomenon is particularly evident in Figure 134, representing the vertical displacement of the top of the wall vs. drift history. This phenomenon ends with the vertical collapse of the wall at a drift of 2%.

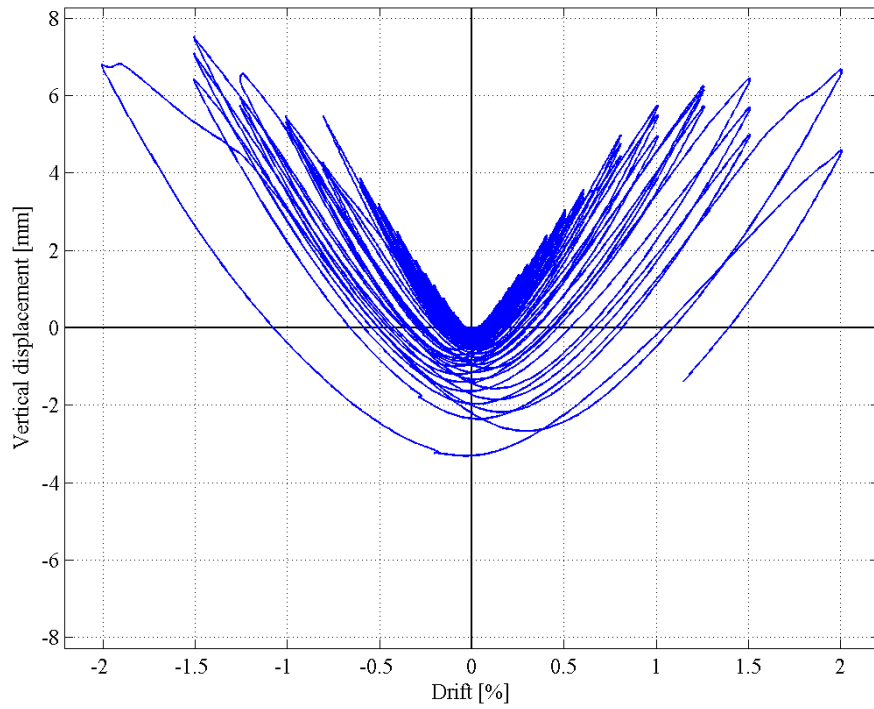


Figure 133. EC\_COMP\_1: vertical displacement of the top of the wall vs. drift.

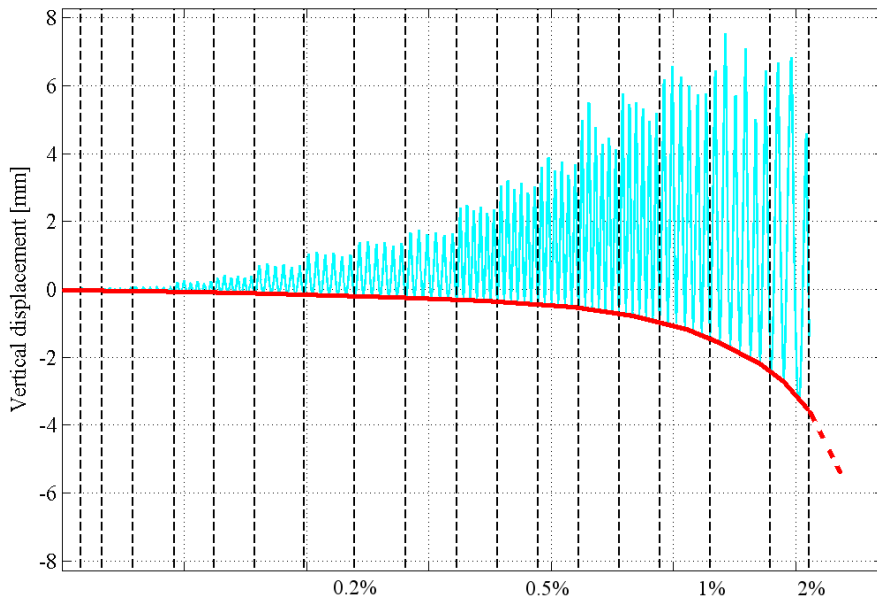


Figure 134. EC\_COMP\_1: vertical displacement of the top of the wall vs. drift history.

The initial elastic stiffness of the wall has been estimated according to the initial experimental curves as reported in Figure 135. It results equal to about 22.87 kN/mm.

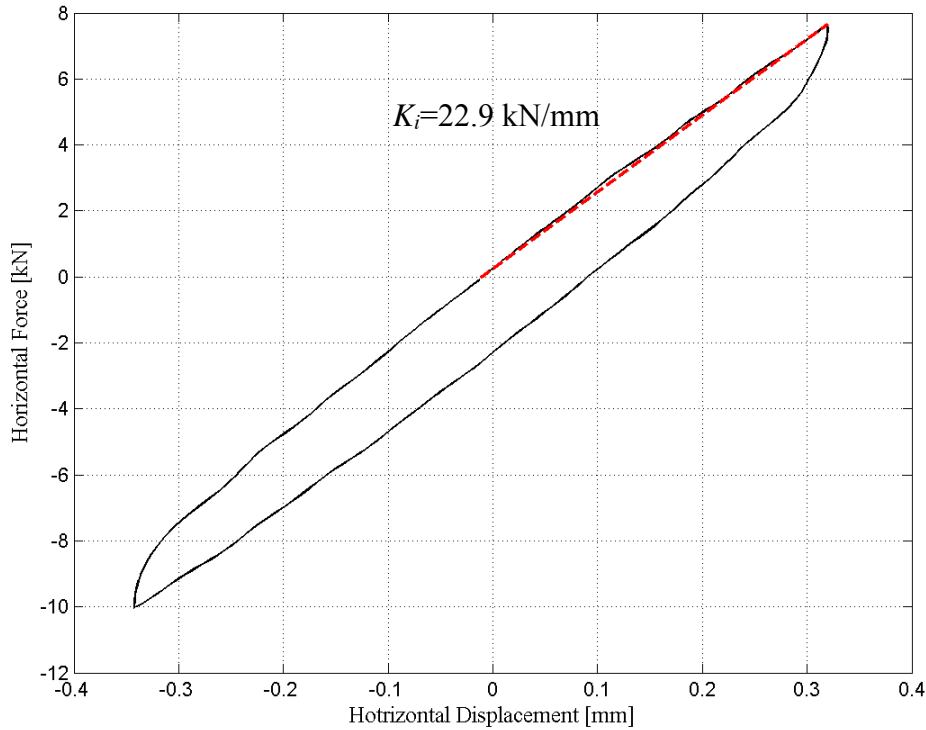


Figure 135. EC\_COMP\_1: Evaluation of the initial elastic stiffness.

The value of theoretical initial stiffness results to be equal to 18.45 kN/mm.

Figure 136 reports the total work computed during each cycles (the dashed curve represents the dissipated energy), while the equivalent viscous damping (as described for the previous test) is reported in Figure 138 as a function of displacement ductility of each cycle.

The relationship between the residual vertical displacement and the dissipated energy is plotted in Figure 137.

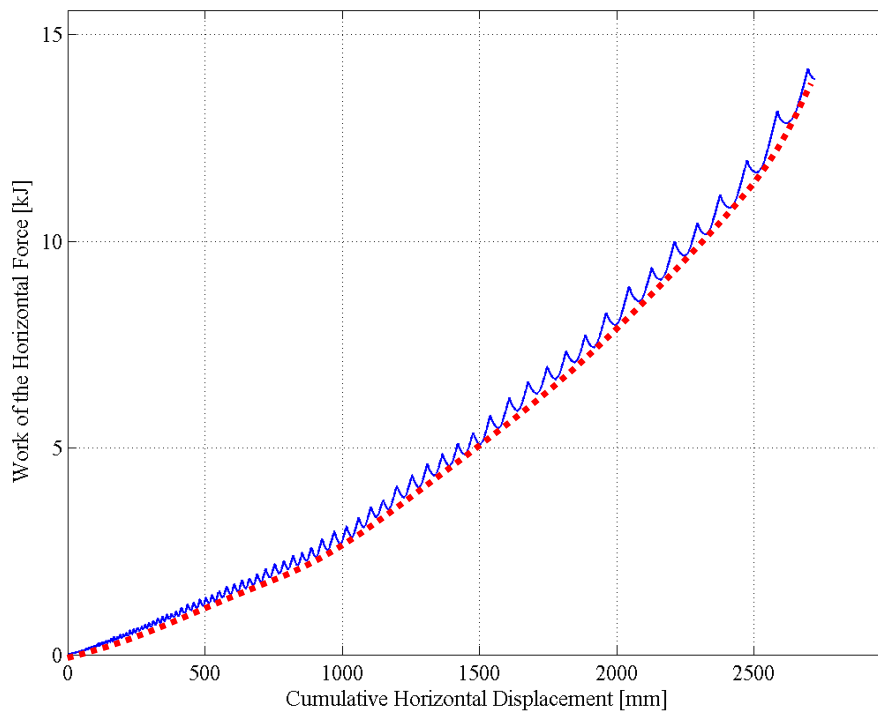


Figure 136. EC\_COMP\_1: Work and dissipated energy.

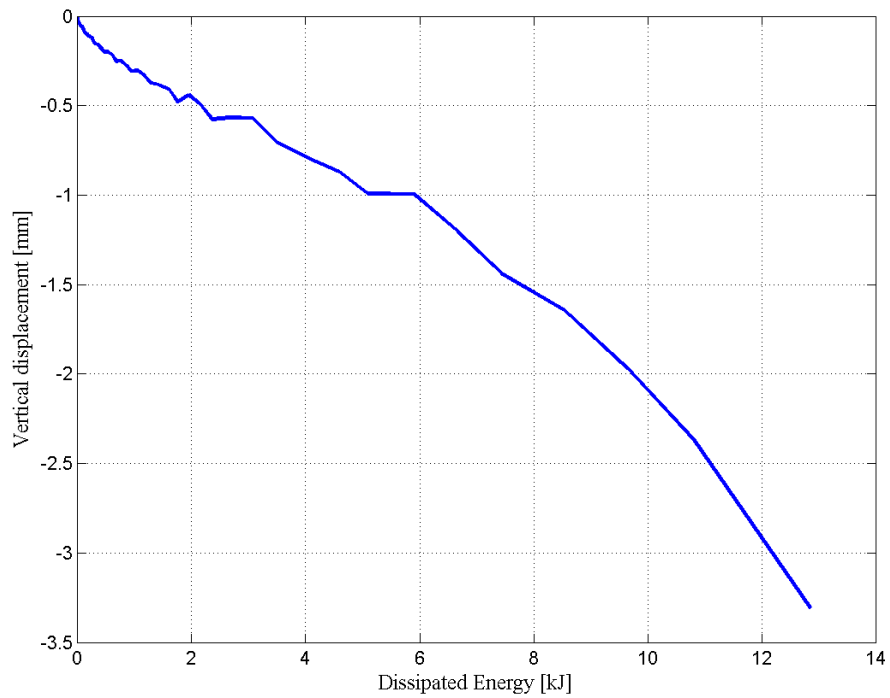


Figure 137. EC\_COMP\_1: Residual vertical displacement of the top of the wall vs. dissipated energy.

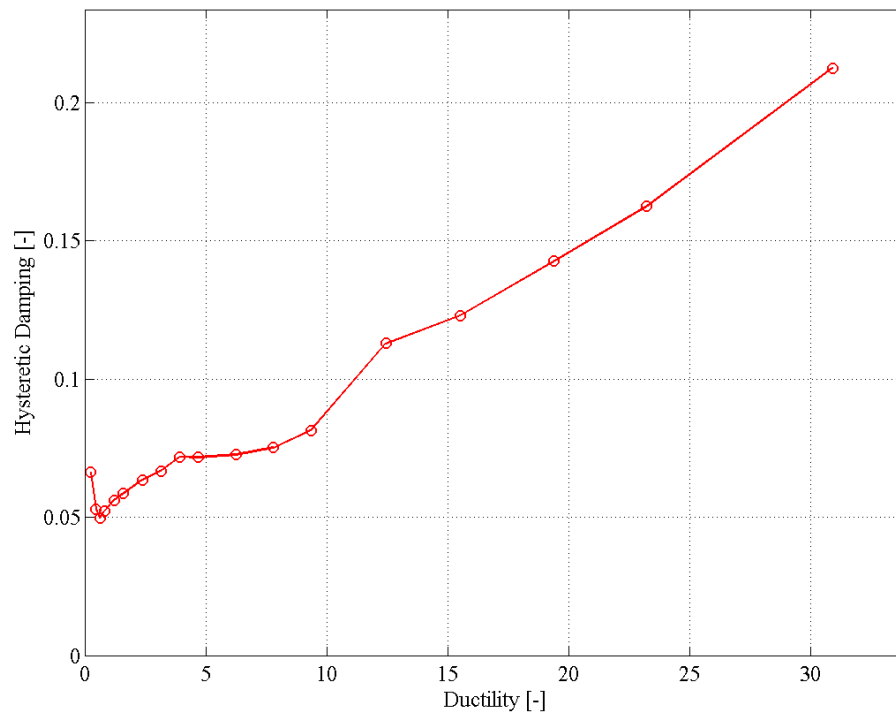
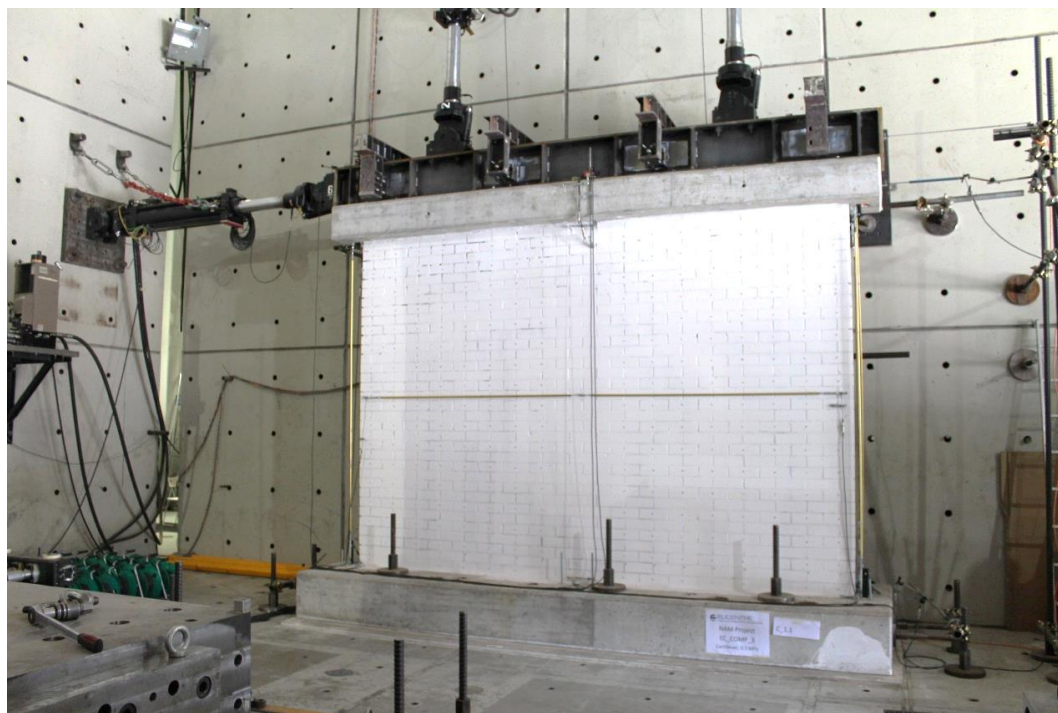


Figure 138. EC\_COMP\_1: Equivalent viscous damping ratio vs. displacement ductility.

### 4.4.3 EC\_COMP\_3

EC\_COMP\_3 is the third of the three quasi-static in-plane tests performed (in cantilever conditions) in the TREE Labs of EUCENTRE. This specimen is 4 metres long and 2.75 metres high. The applied overburden stress is 0.3 MPa.

A picture of the test set-up is reported in Figure 139.



*Figure 139. EC\_COMP\_3: Test set-up.*

As expected the specimen exhibits a shear behavior with X stepped cracks (mainly in the interface between mortar and bricks). The first cracks were created at a drift of 0.05% (Figure 140). During the higher deformation, the wall insisted on the same cracks increasing their width.

In particular, after the CYCLE C\_2D (drift 0.075%) the widening of the existing cracks is observed and the first cracks in the brick at the base of the wall appeared (Figure 141). The widening of the exiting cracks is observed also in CYCLE C\_4D (drift 0.15%) in addition to the comparison of new diagonal stepped cracks in the left portion of the wall (Figure 142, in red the cracks induced at current cycle and in black the pre-existing cracks).

During CYCLE C\_5D (drift 0.2%) the wall insisted on the same cracks increasing their width up to a partial disaggregation of the mortar joints. This mechanism will lead to partial collapse of the specimen, in subsequent tests (Figure 143, in green the portion of mortar detached).



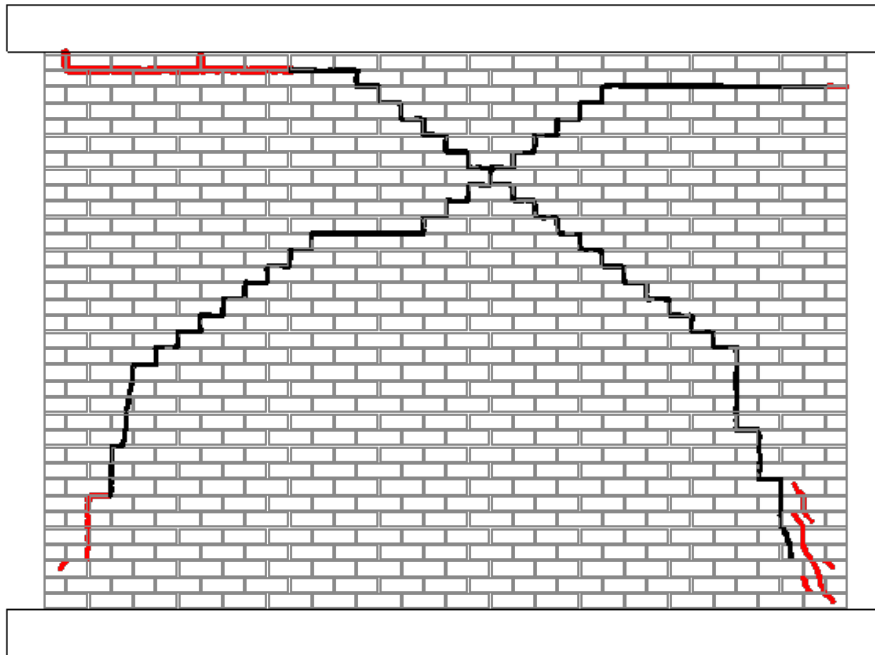
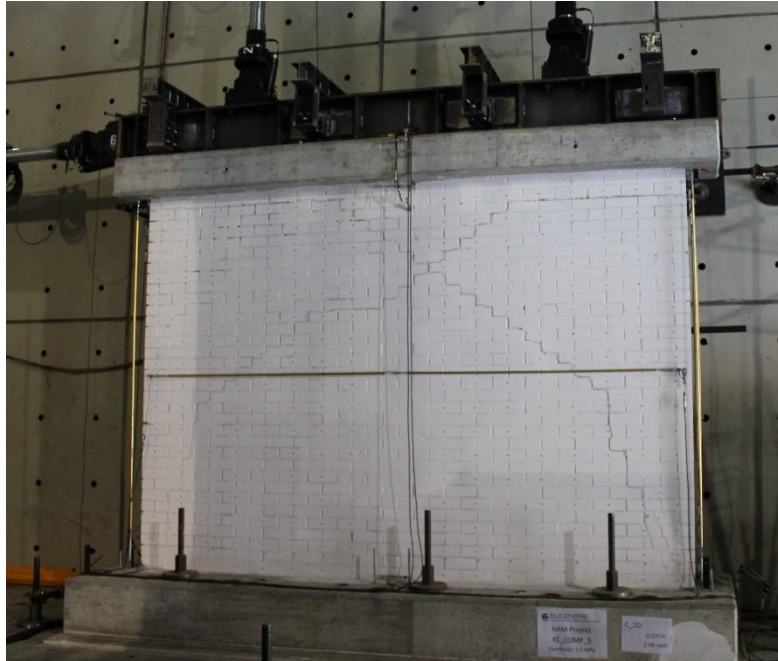


Figure 141. EC\_COMP\_3: crack pattern after CYCLE C\_2D (drift 0.075%).

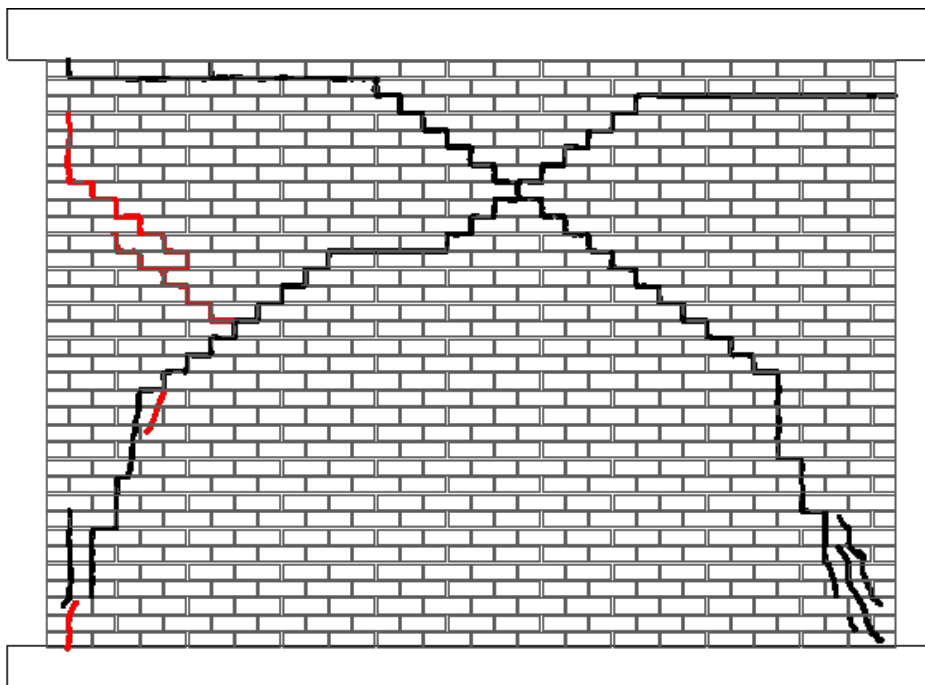


Figure 142. EC\_COMP\_3: crack pattern after CYCLE C\_4D (drift 0.15%).

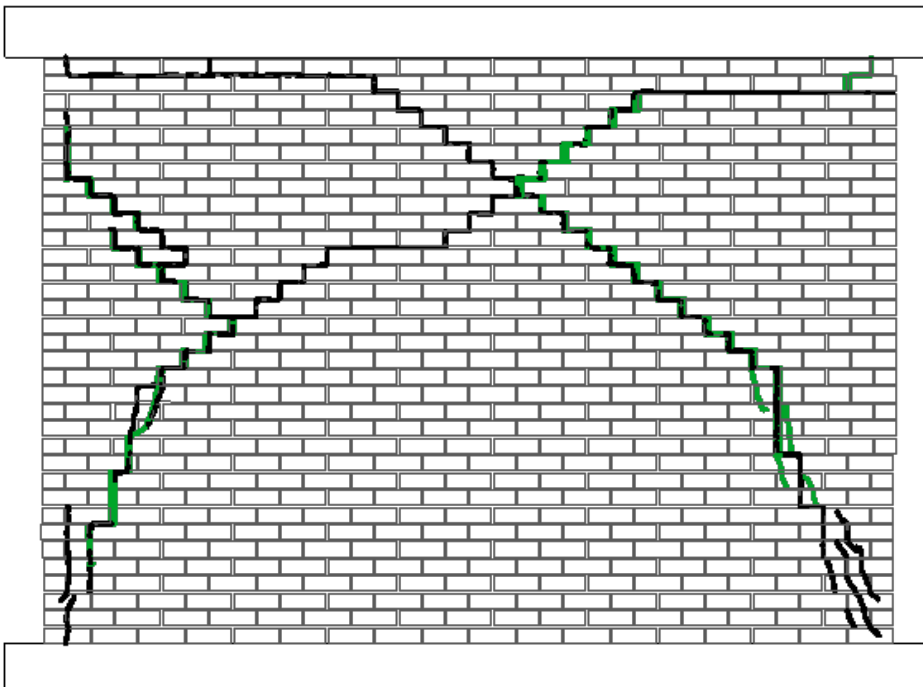
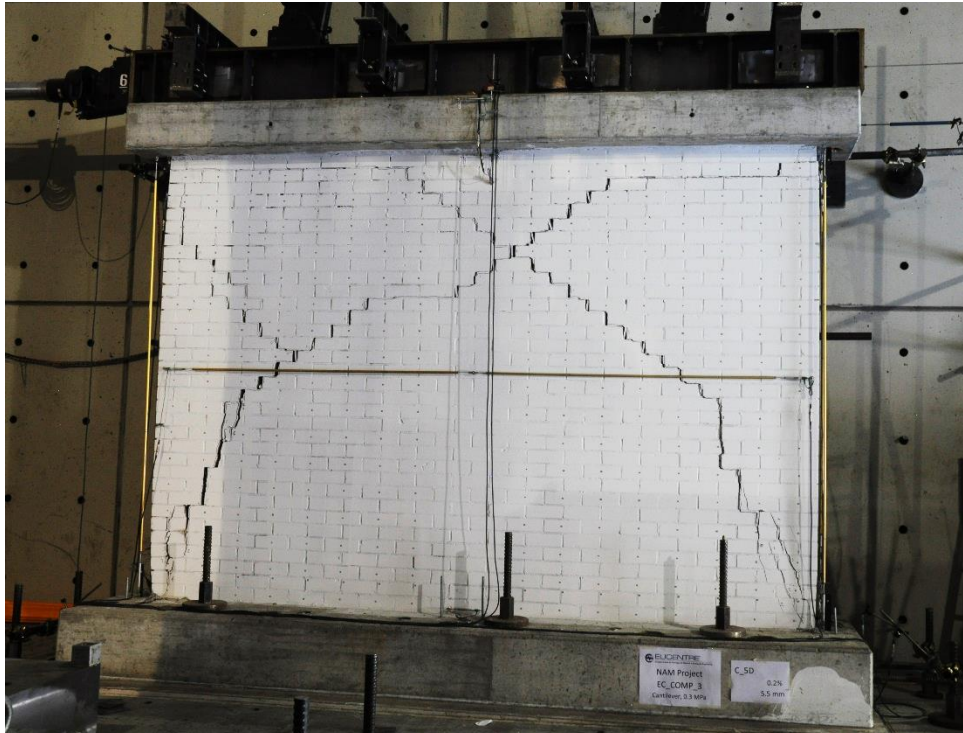


Figure 143. EC\_COMP\_3: crack pattern after CYCLE C\_5D (drift 0.2%).

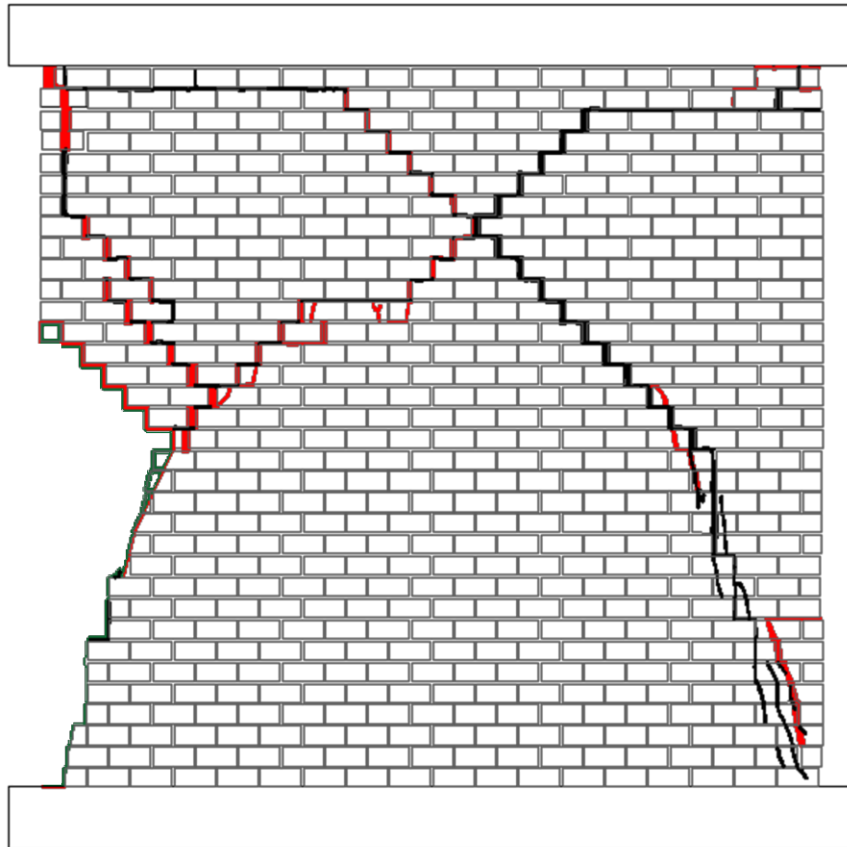
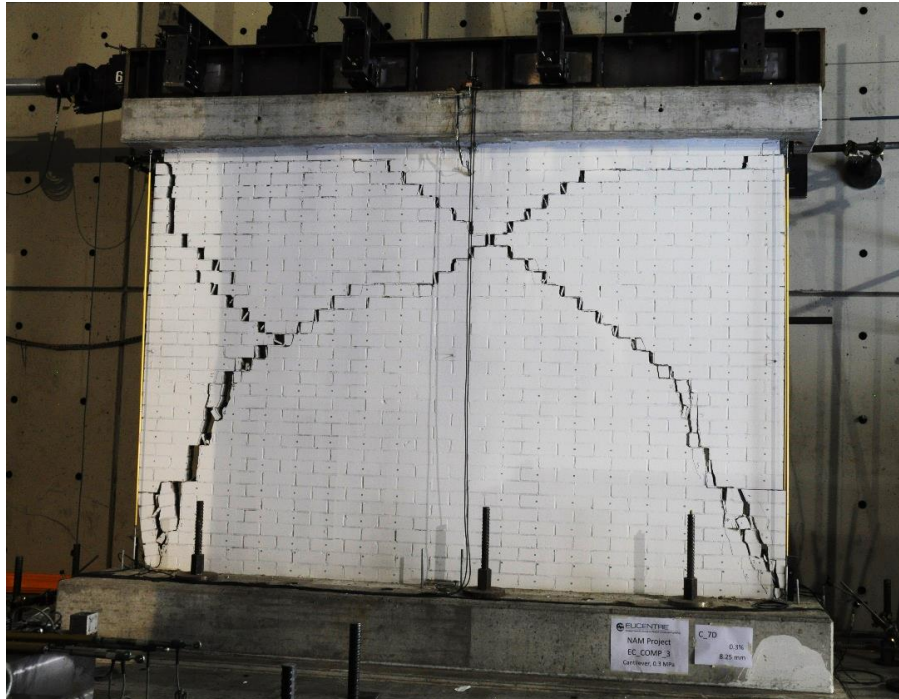


Figure 144. EC\_COMP\_3: crack pattern after CYCLE C\_7D (drift 0.3%).

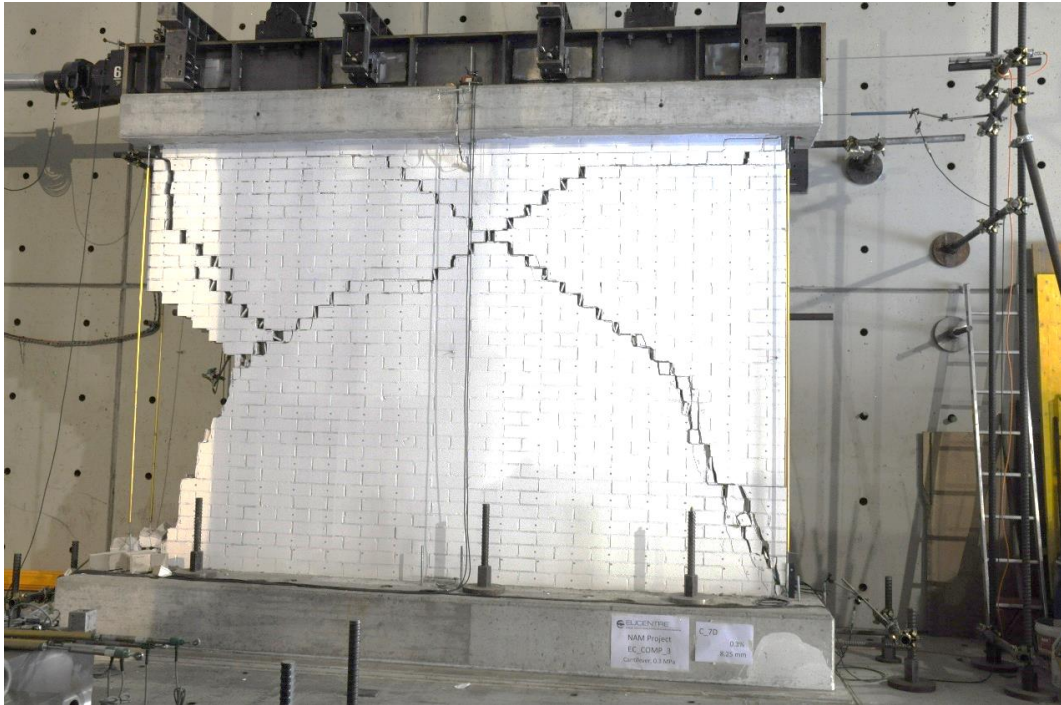


Figure 145. EC\_COMP\_3. Close to collapse condition of the wall, after CYCLE C\_7D (drift 0.3%).



Figure 146 EC\_COMP\_3. Back view of the partial collapse of the wall after CYCLE C\_7D (drift 0.3%).

The hysteretic behavior of the specimen during the test is reported in Figure 147.

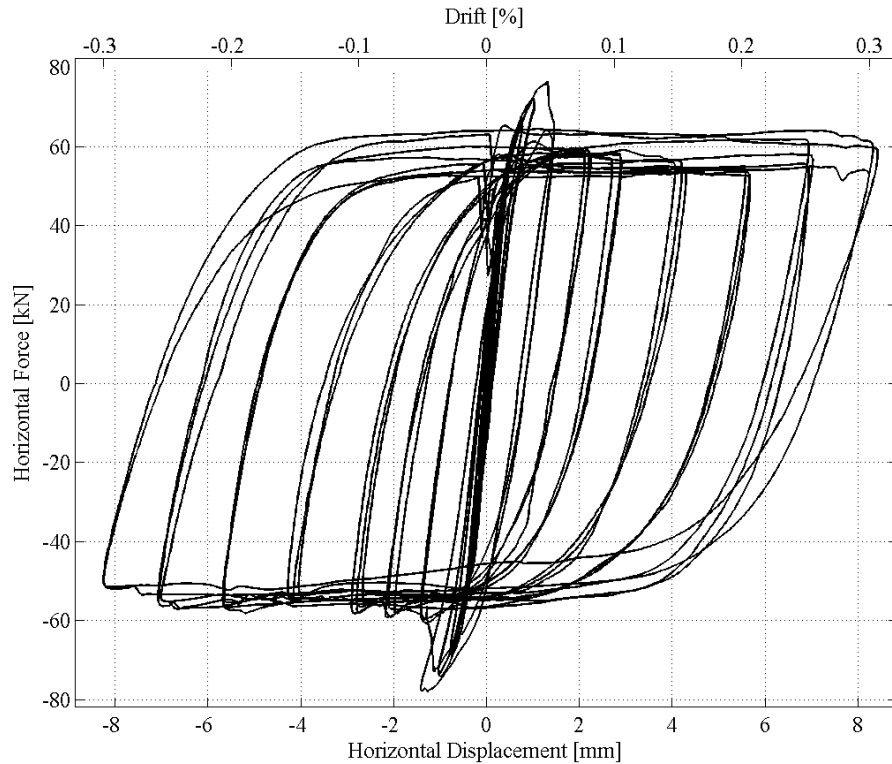


Figure 147. Hysteretic behaviour of the specimen EC\_COMP\_3 during the test.

As for the previous test, the trend of the vertical displacement at the top of the wall has been investigated for all the cycles and the result is reported in Figure 148.

An additional check on the rotation of the top beam has been computed and reported in Figure 149, Figure 151. It is possible to notice how the behaviour is symmetrical up to a drift of 0.15% (see Figure 151). Beyond this point the top beam maintains a residual positive rotation (clockwise). This residual rotation increased up to the collapse limit state reached at a drift of 0.3%.

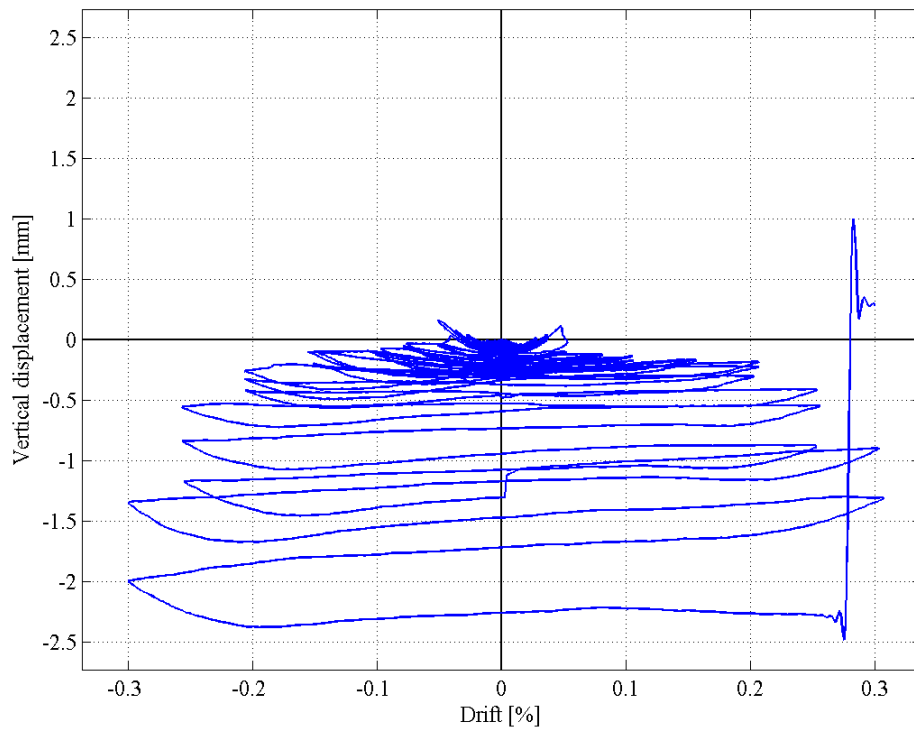


Figure 148. EC\_COMP\_3: vertical displacement of the top of the wall.

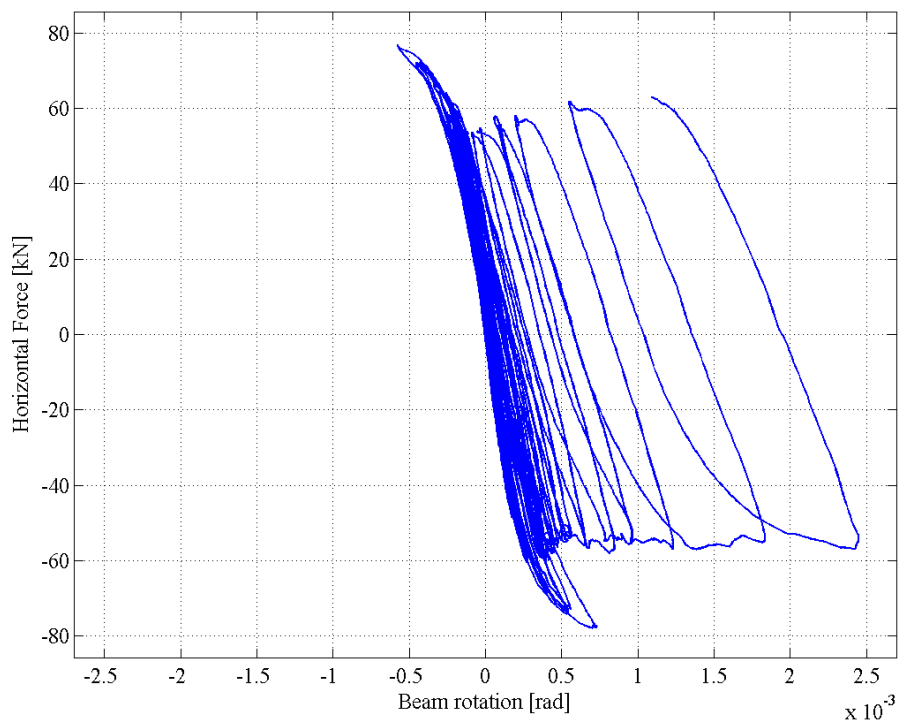


Figure 149. EC\_COMP\_3: Horizontal force Vs. Top Beam rotation.

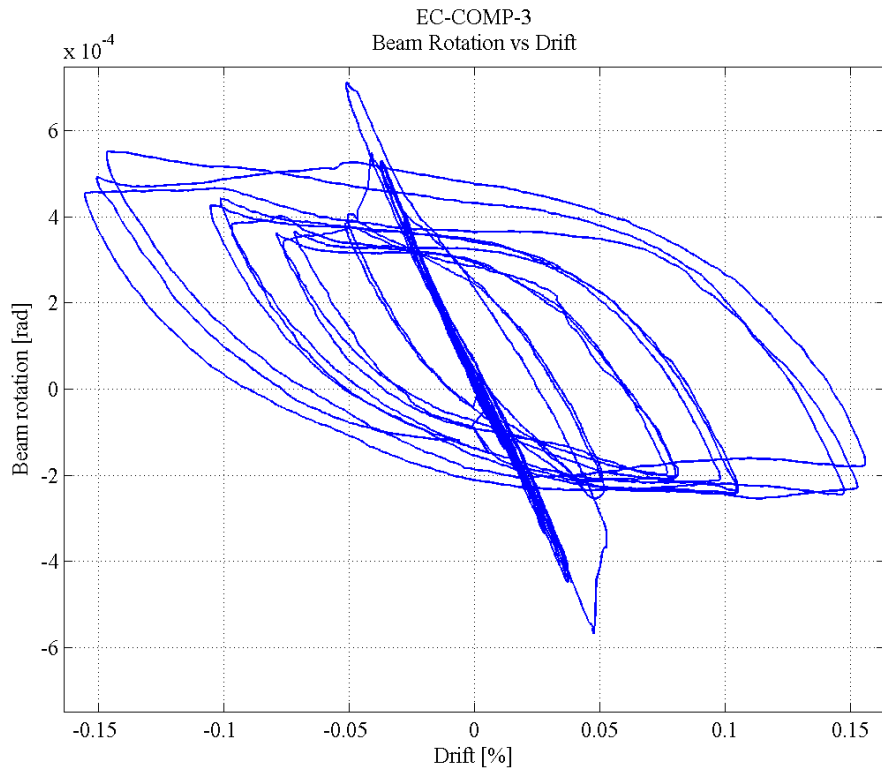


Figure 150. EC\_COMP\_3: Top Beam rotation Vs. Drift up to C\_4D (drift 0.15%).

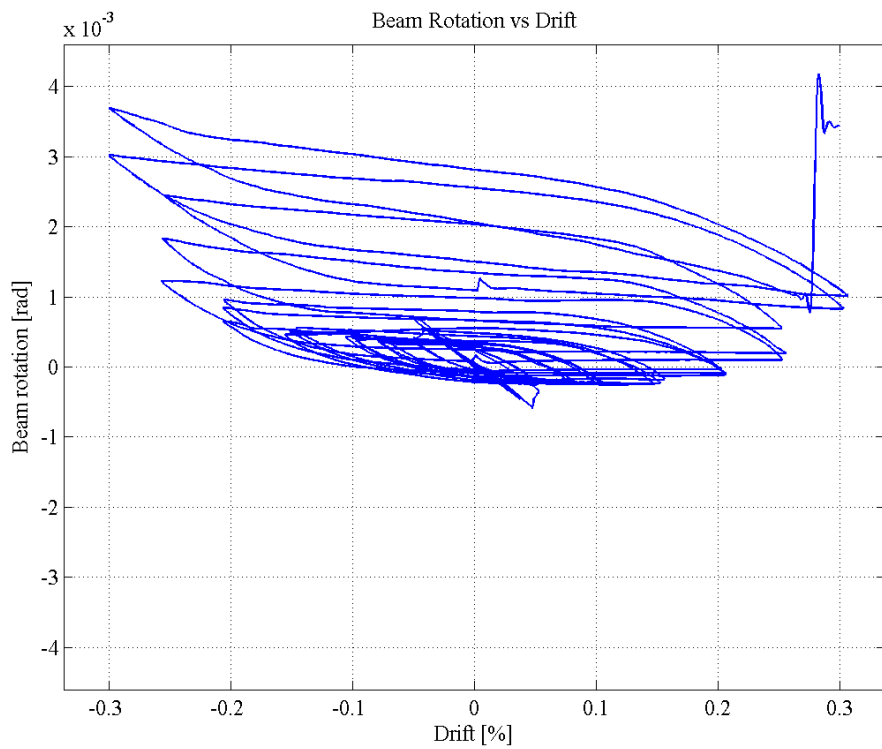
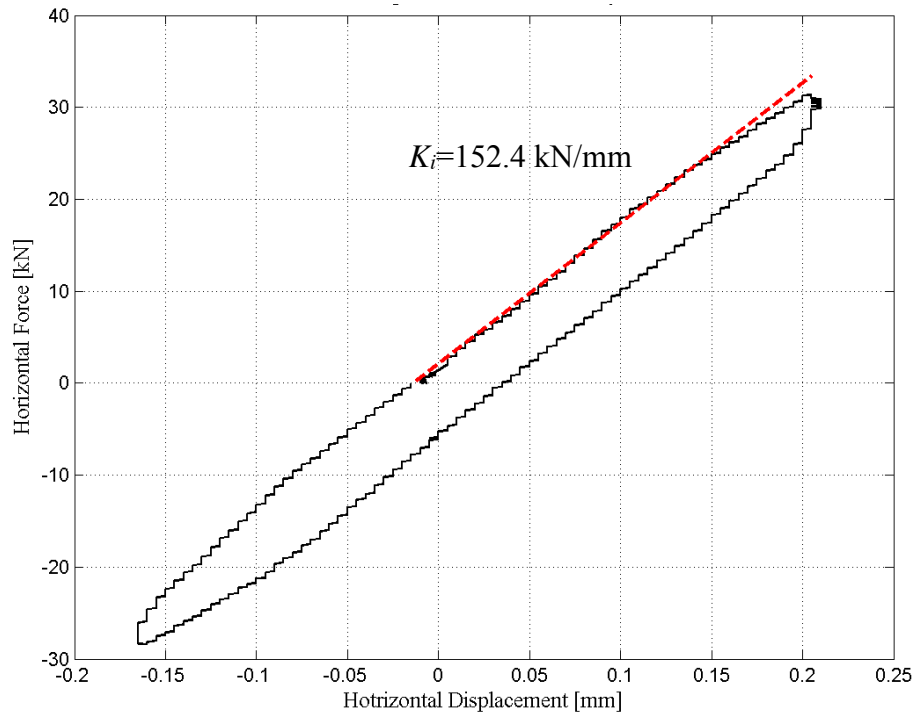


Figure 151. EC\_COMP\_3: Top Beam rotation Vs. Drift.

The initial elastic stiffness of the wall has been estimated according to the initial experimental curves as reported in Figure 152. It results equal to about 152.45 kN/mm.



*Figure 152. EC\_COMP\_3: Evaluation of the initial elastic stiffness.*

The value of the theoretical initial stiffness results to be equal to 126.87 kN/mm.

Figure 153 reports the total work computed during each cycles (the dashed curve represents the dissipated energy), while the equivalent viscous damping (as described for the previous test) is reported in Figure 154 as a function of displacement ductility of each cycle.

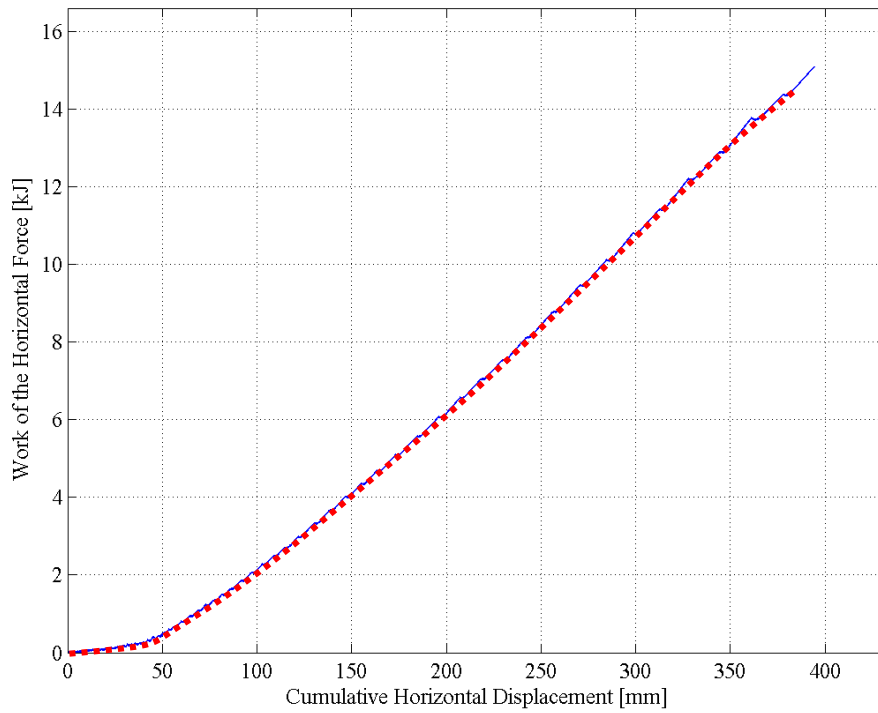


Figure 153. EC\_COMP\_3: Work and dissipated energy.

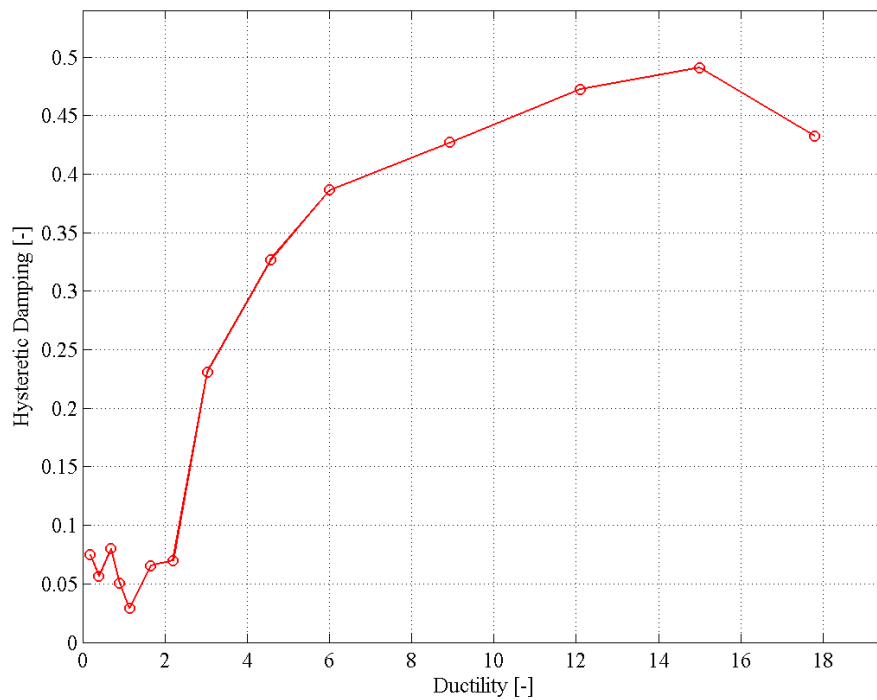


Figure 154. EC\_COMP\_3: Equivalent viscous damping ratio vs. displacement ductility.

Figure 155 reports the maximum residual opening of the cracks, while Figure 156 reports the shear deformation of the pier obtained during the test. It is observable how also this response is not symmetric. This is due to the permanent rotation of the top beam recorded and plotted in Figure 151.

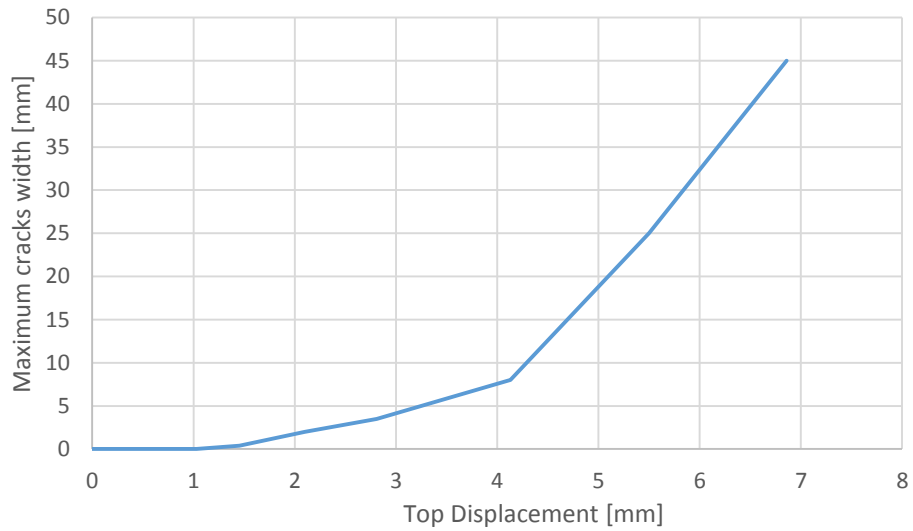


Figure 155. EC\_COMP\_3: Maximum residual opening of the cracks.

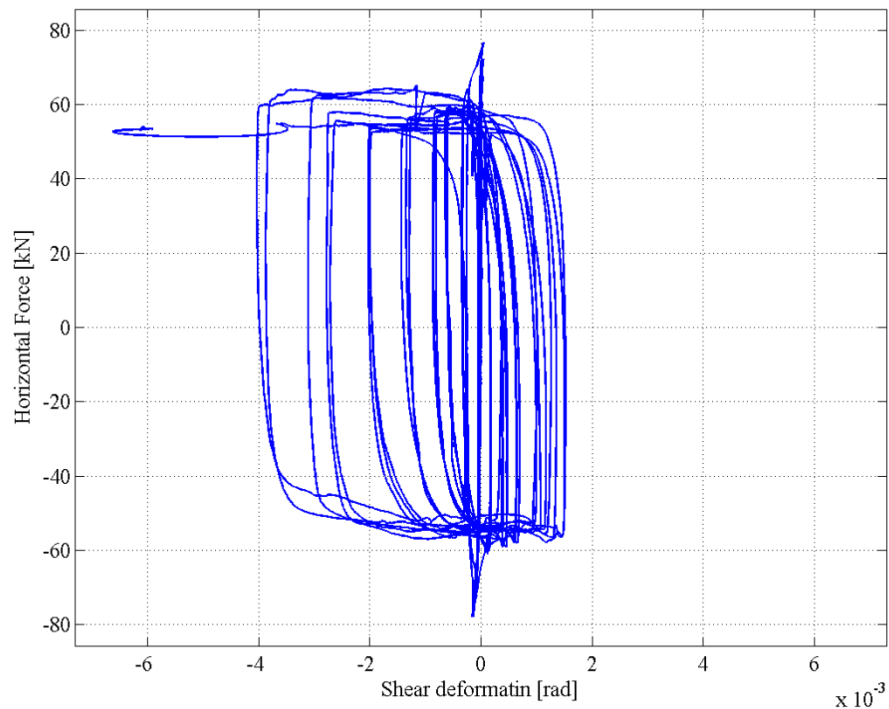


Figure 156. EC\_COMP\_3: Horizontal Force Vs. Shear deformation.

#### 4.4.4 Bilinear envelopes

A common approach to interpret the in-plane response of masonry walls is to idealize the cyclic envelope of the hysteresis loop with a bilinear envelope.

In Figure 157 a possible definition of the parameters of the bilinear curve is given. The elastic stiffness  $k_{el}$  is obtained by drawing the secant to the experimental envelope at  $0.70V_{max}$ , where  $V_{max}$  is the maximum shear of the envelope. The ultimate displacement  $\delta_u$  can be evaluated as the displacement corresponding to strength degradation equal to 20% of  $V_{max}$  or as the displacement corresponding to an inability of the wall to sustain the applied vertical load. The value of the shear  $V_u$  corresponding to the horizontal branch of the bilinear curve can be found by ensuring that the areas below the cyclic envelope curve and below the equivalent bilinear curve are equal. Knowing the elastic stiffness  $k_{el}$  and the value of  $V_u$  it is possible to evaluate the elastic displacement  $\delta_e$  as  $V_u/k_{el}$ . The ultimate ductility is defined as  $\mu_u = \delta_u/\delta_e$ .

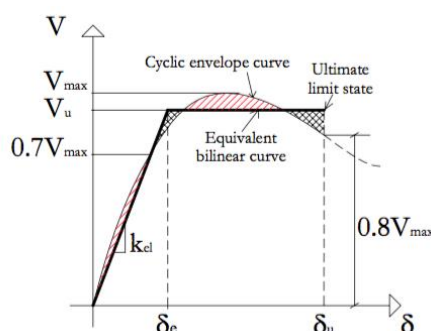


Figure 157. Bilinear idealisation of the hysteresis envelope.

The bilinear curves of the experimental global envelopes are reported in the following figures (Figure 158, Figure 159 and Figure 160). The values obtained for these parameters (computed from the envelope curve corresponding to the attainment of the maximum absolute value of the shear force considering both positive and negative directions) are summarized in Table 50 and plotted in Figure 161.

Table 50. Parameters of the equivalent bilinear curves.

<i>Test</i>	$V_{el}^+$ [kN]	$V_{el}^-$ [kN]	$V_u^+$ [kN]	$V_u^-$ [kN]	$K_{el}^+$ [kN/mm]	$K_{el}^-$ [kN/mm]	$\delta_{el}^+$ [mm]	$\delta_{el}^-$ [mm]
EC_COMP_1	24.7	25.4	26.5	27.6	12.5	15.8	1.967	1.605
EC_COMP_2*	27.4	23.0	28.6	24.1	18.8	15.1	1.452	1.524
EC_COMP_3	64.2	57.8	76.7	78.0	130.9	130.0	0.490	0.444
	$\delta_u^+$ [mm]	$\delta_u^-$ [mm]	$\mu_u^+$ [-]	$\mu_u^-$ [-]	$\mu_{u,min}$ [-]	$\delta_u^+/H$ [%]	$\delta_u^-/H$ [%]	$(\delta_u/H)_{min}$ [%]
EC_COMP_1	55.132	55.256	28.0	34.4	28.0	2.00	2.01	2.00
EC_COMP_2*	5.780	5.379	4.0	3.5	3.5	0.21	0.20	0.20
EC_COMP_3	8.430	8.256	17.2	18.6	17.2	0.31	0.30	0.30

\*Out-of-plane collapse

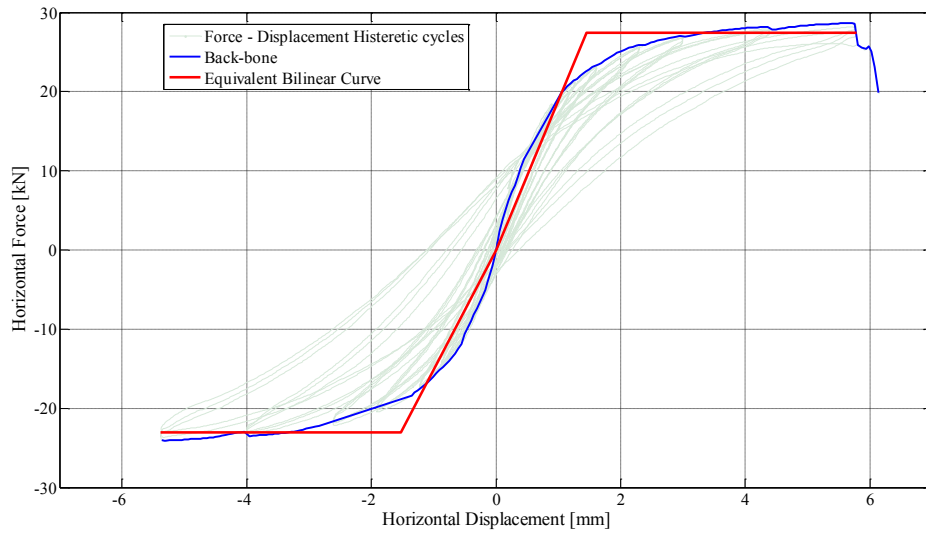


Figure 158. EC\_COMP\_2: Bilinear idealisation of the hysteresis envelope.

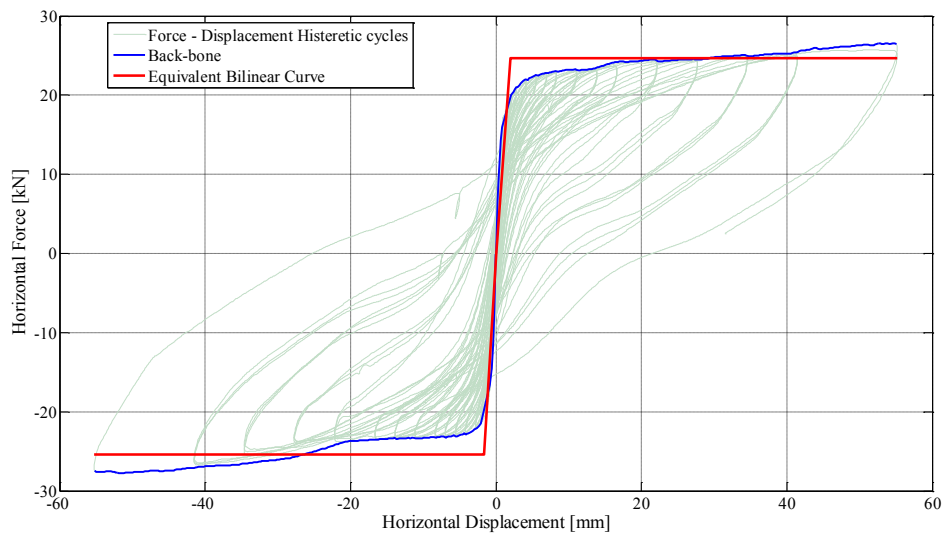


Figure 159. EC\_COMP\_1: Bilinear idealisation of the hysteresis envelope.

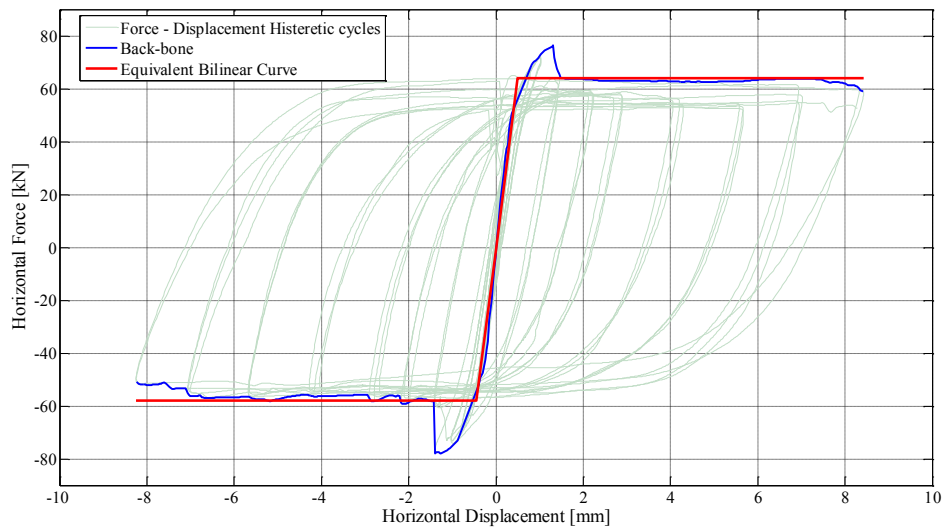


Figure 160. EC\_COMP\_3: Bilinear idealisation of the hysteresis envelope.

Figure 161 reports only the bilinear idealizations for EC\_COMP\_1 and EC\_COMP\_3, they were the only two comparable since EC\_COMP\_2 did not exploit the entire strength  $V_{max}$  due to an early OOP collapse.

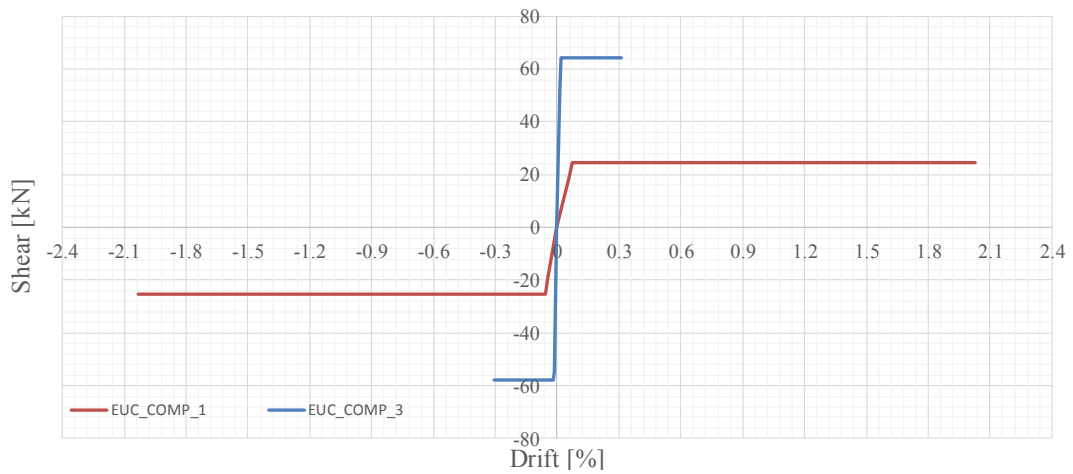


Figure 161. Bilinear idealisation for the two specimens exhibiting in plane failure.



## 5 Out-of-Plane Component Tests

As specified in previous chapters, the entire testing campaign aims to investigate the seismic behavior of a particular typology of Dutch residential building called terraced houses. These structures are usually built with cavity walls. These are usually composed by an inner loadbearing wall and an outer wall having aesthetic and insulating functions. In particular, the structural system considered as a reference in this campaign has the loadbearing walls made of calcium silicate (CS) brick masonry and the outer walls made of clay brick masonry.

Since no dynamic tests on cavity walls were found in literature, four out-of-plane tests were conducted on full scale masonry assemblages reproducing four different wall configurations. Three of them were cavity walls with different ties distributions and one single leaf calcium silicate wall. The setup allowed testing the specimens under different time histories and loading conditions. The document reports all the outcomes of these test, in particular the deformed shapes, the damping and the dynamic behavior were described.

### 5.1 Test specimens

The specimens tested in the out-of-plane one-way bending shake table test are:

- 1 single leaf URM wall made of calcium silicate bricks (EC\_COMP\_4);
- 2 cavity walls with the inner calcium silicate wall and the outer veneer clay wall with 2 ties/m<sup>2</sup> (EC\_COMP\_5/6);
- 1 cavity walls with the inner calcium silicate wall and the outer veneer clay wall with 4 ties/m<sup>2</sup> (EC\_COMP\_7).

Table 24 provides a list of the specimens and their dimensions.

*Table 51. Tested Specimens: characteristics and dimensions.*

Specimen Name	Wall Type	L [m]	t [m]	h [m]	$\sigma_v$ [MPa]
EC_COMP_4	Single-leaf wall	1.438	0.102	2.754	0.3-0.1
EC_COMP_5	CS inner wall	1.438	0.102	2.754	0.1
	Clay outer wall	1.425	0.100	2.700	-
EC_COMP_6	CS inner wall	1.438	0.102	2.754	0.3
	Clay outer wall	1.425	0.100	2.700	-
EC_COMP_7	CS inner wall	1.438	0.102	2.754	0.1
	Clay outer wall	1.425	0.100	2.700	-

The distance between the two leaves is about 8 centimeters and the connection is guaranteed by metal ties. Figure 162 shows the metal ties typology adopted to connect the two leaves and their position. The length of the tie embedded in the calcium silicate

mortar joint is about 8 centimeters while the length of the tie in the veneer wall is about 5 centimeters.

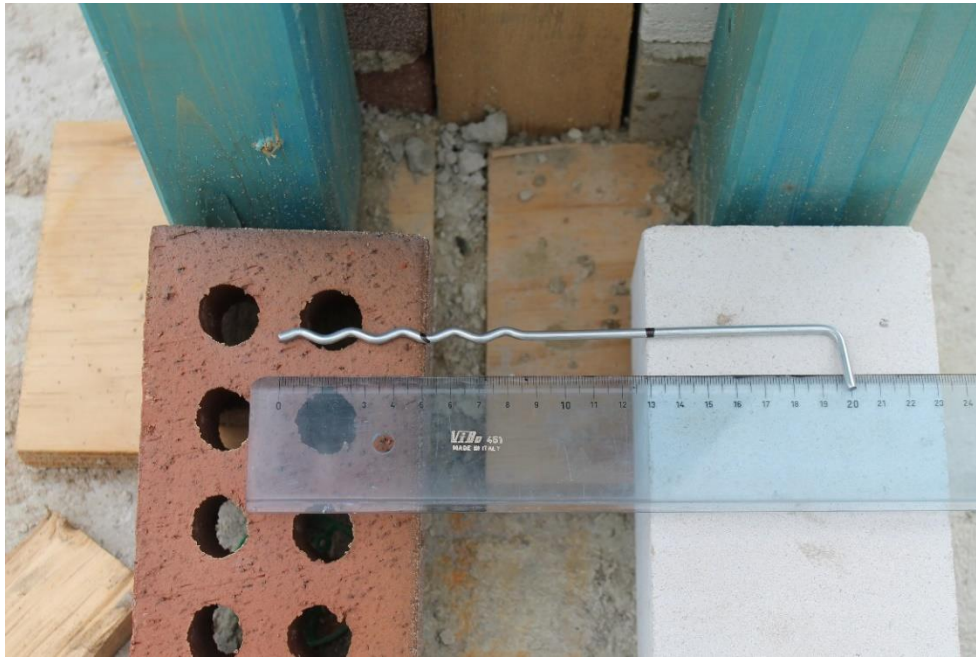


Figure 162. Metal ties typology and position.

Figure 163 shows a view of the specimens and their tie grid. A detailed view of the specimens is given in Figure 164. The EC\_COMP\_5 & 6 specimens have 2 ties/m<sup>2</sup> while EC\_COMP\_7 specimen has 4 ties/m<sup>2</sup>.

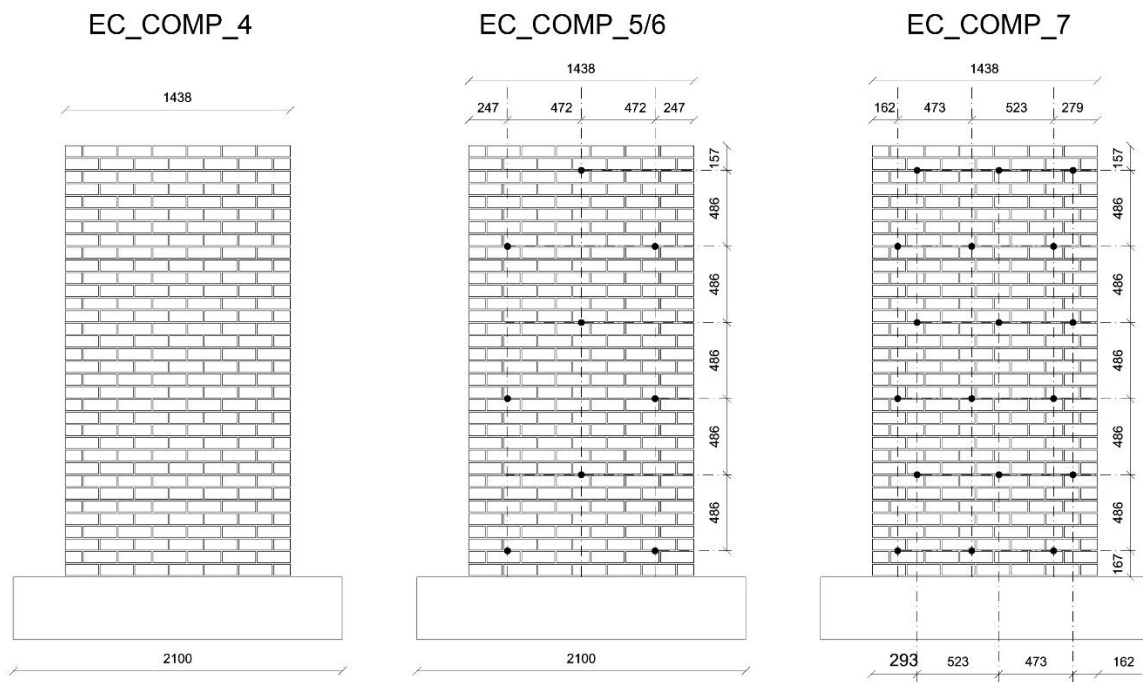
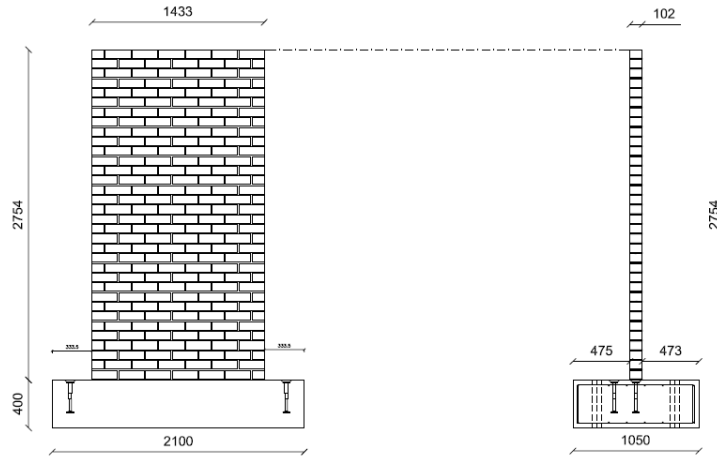
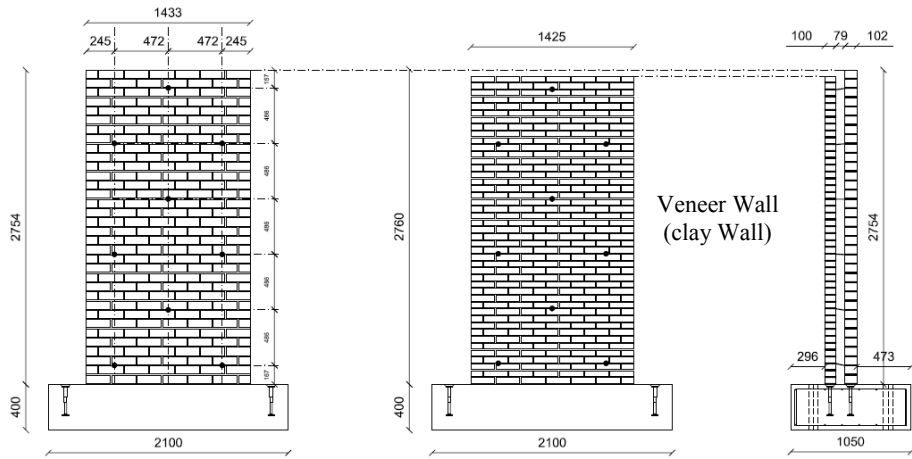


Figure 163. Specimens geometry and tie grid.

### EC\_COMP\_4



### EC\_COMP\_5-6



### EC\_COMP\_7

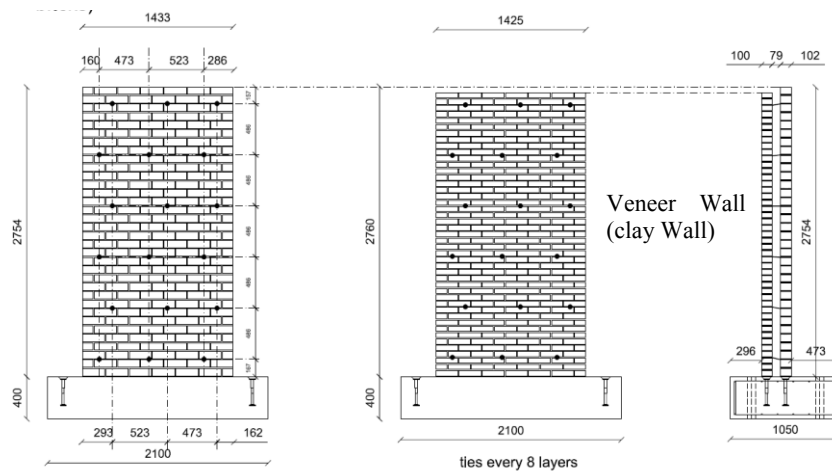


Figure 164. Specimens view and geometry.

The following pictures (Figure 165 to Figure 169) show the specimens in the construction phases.



*Figure 165. EC\_COMP\_7 Specimen during construction phases.*



*Figure 166. Cavity Wall Specimens during construction phases.*



*Figure 167. Detail of tie installed for the specimen transportation.*



*Figure 168. Cavity Wall Specimens (CS side).*



*Figure 169. Cavity Wall Specimens (Clay side).*

## 5.2 Test set-up and instrumentation

### 5.2.1 Test setup

The set-up and instrumentation used in the present test are composed of:

- One-directional shake table;
- Wire potentiometers, accelerometers and/or displacement/deformation measuring devices capable of describing the displacement/deformation field of the specimen during all the phases of the test;
- Rigid frame capable of transferring the shake table input without significant amplification at the top of the masonry specimens;
- A safety system to prevent the global out-of-plane failure of the specimens.

An example of a suitable test set-up is shown in Figure 170, which represents a side view of the test set-up; Figure 170 provides a lateral view for all the specimen tested: single leaf specimen and cavity wall specimens. It indicates also the position of all the instrumentation and the reference system adopted. A detailed view showing all the test set-up measures is given in Figure 171.

The structure is installed on a one-directional shake table test. The frame on the left guarantees the transfer of the dynamic input motion to the top of the wall with a negligible amplification effect. The specimens are anchored through the foundation to the shake table by means of screwed steel rods.

The specimens are pre-stressed at the desired initial pressure value by means of steel rods connecting a steel beam installed in the specimen top to the spring system anchored to the foundation. For what concerns cavity wall specimens, only the inner wall can be pre-stressed at the desired overburden pressure.

The initial static scheme of the wall specimens (inner wall in case of cavity) is a double fixed boundary condition. Such restrain condition is guaranteed in the top wall extremity by L steel profiles bolted to the top steel beam and screwed to the last brick layer. The bottom section of the wall specimen lies on a mortar bed-joint resting on the specimen foundation. For cavity wall specimens the outer leaf static scheme is a cantilever.

The connection between the frame and the top beam of the tested specimen is made by a couple of arms characterized by a mechanical hinge on the right extremity. The hinge system allows the rotation and the incoming uplift of the wall transferring the floor dynamic input simultaneously at the top of the specimen. The stiffness of the spring system guarantees that the increased force at collapse condition (when the wall height is maximum) is less than 5% of the static initial static pressure. These solutions guarantee a double fixed condition with almost constant overburden pressure.



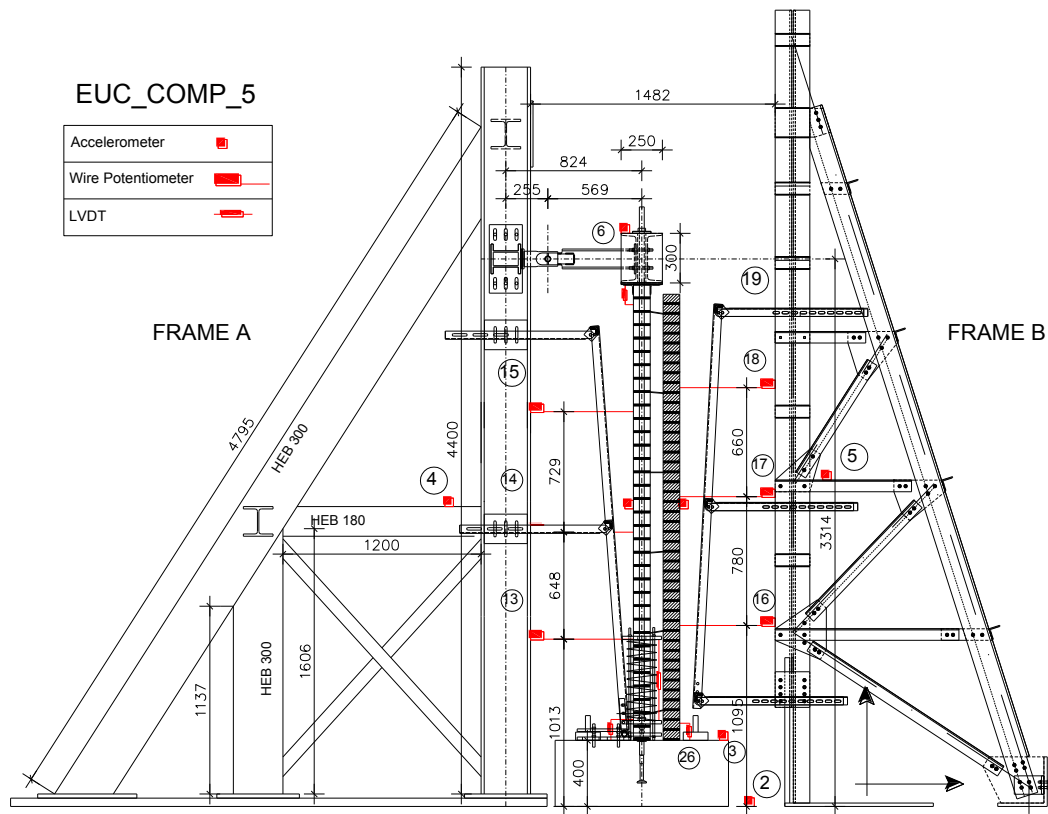


Figure 171. Test Layout and geometry for the EC\_COMP\_5 Specimen.

Table 52 summarises the spring properties:

Table 52. Spring Properties.

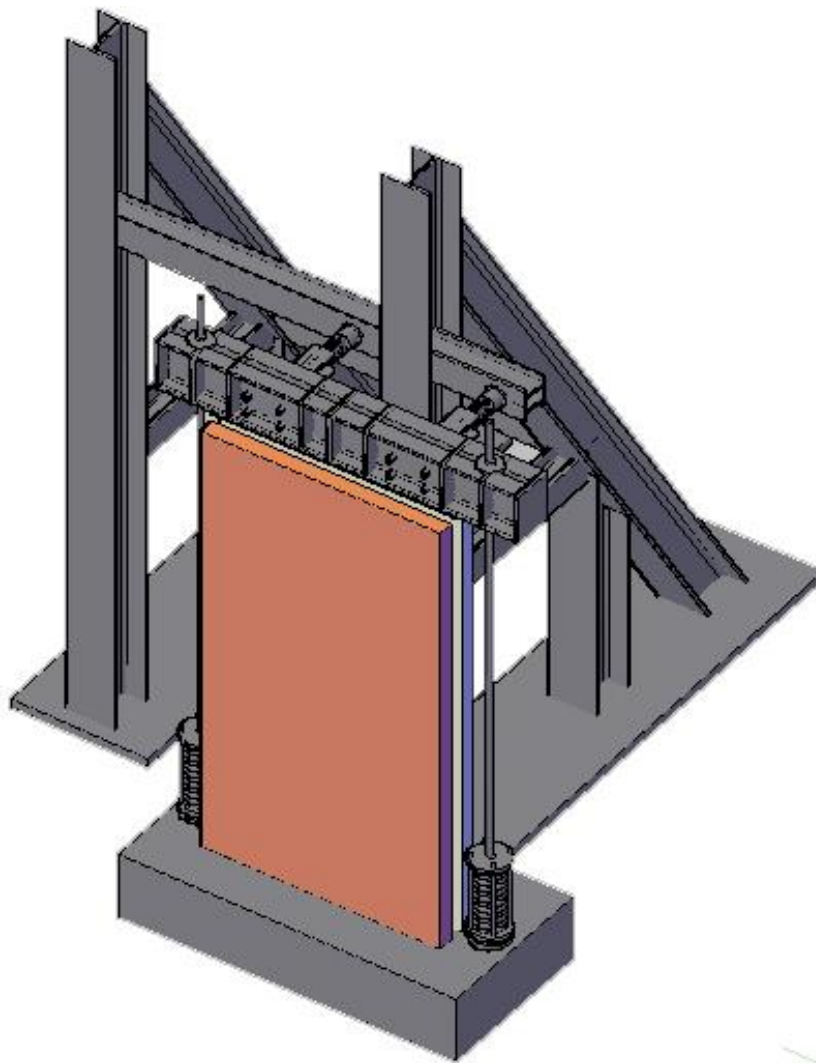
Spring	$O_v$ [MPa]	$F_{springs}$ [kN]	$F_0$ [kN]	$K_0$ [N/mm]	$L_0$ [mm]	$L_{test}$ [mm]	$\Delta L$ [mm]
Type 1	0.3	40.9	20.4	164.7	484	348	136
Type 2	0.1	11.6	5.8	53.5	391	268	123

where  $O_v$  is the desired overburden pressure and  $F_0$ , the force in each spring minus half of the weight of the top steel system. The weight of the steel beam (composed by two UPN 300 and stiffeners) plus the bottom steel plate (10 mm thick), the two L 60x5 profiles and half of the weight of the two braces is 315 kg (3.09 kN). Such weight should be subtracted from the total desired overburden force.  $L_0$  is the initial spring length while  $L_{test}$  the required length during the test;  $K_0$ , represents the spring stiffness necessary to limit the increased spring force due to wall uplift to less than 5% of the static spring force;  $\Delta_{z,max}$ , instead is the wall uplift at collapse limit state, which can be computed as

follow assuming a perfect rigid body behaviour for the two wall portions above and below the incipient mid-height crack:

$$\Delta_{z,max} = 2 \cdot \left( \sqrt{\frac{H_{wall}^2}{2} + t^2} - \frac{H_{wall}}{2} \right) = 7.6 \text{ mm}$$

where  $t$  is equal to the wall thickness and  $H_{wall}$  the wall height. A restraining system is installed to prevent the out-of-plane collapse of the specimens. It consisted in two adjustable steel frames sustaining transparent polycarbonate panels opportunely pierced to allow the installation of the wire potentiometers on the wall specimens. Figure 2 shows a 3D view of the test layout without the steel safety frames.



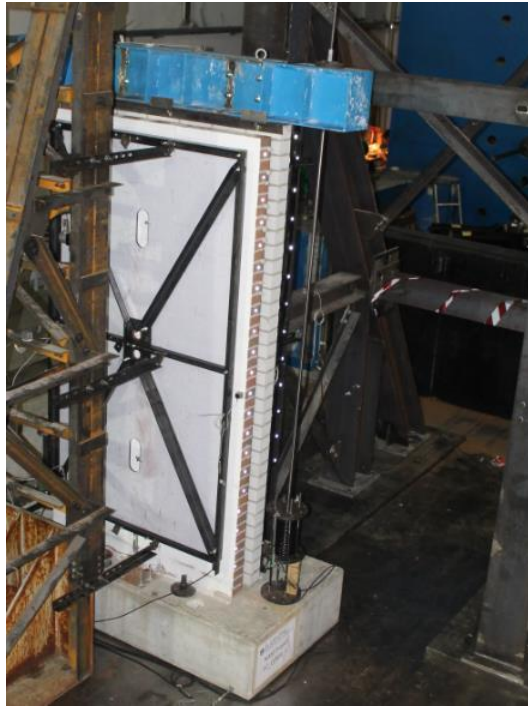
*Figure 172. 3D View of the test layout (without safety system).*

Figure 173 shows a picture of the testing layout for the EC\_COMP\_4 specimen.



*Figure 173. Testing layout for the EC\_COMP\_4 Specimen.*

Figure 174, Figure 175 and Figure 176 show picture of the testing layout for the EC\_COMP\_5 and EC\_COMP\_6 specimens respectively.



*Figure 174. Experimental layout EC\_COMP\_5 Test.*



*Figure 175. Experimental layout EC\_COMP\_6 Test.*



*Figure 176. Experimental layout EC\_COMP\_7 Test.*

### 5.2.2 Instrumentation

The entire set-up instrumentation consisted in accelerometers, wire potentiometers and traditional potentiometers. Figure 170 shows also the position of all the instruments installed. The accelerometers guaranteed at least an accurate measurement of the following quantities:

- Acceleration of the shake table;
- Top Accelerations on both frames;
- Top and mid-height horizontal acceleration of the wall specimens or of both walls (in case of cavity walls).

The instrumentation consisted also of a set of wire potentiometers, which guaranteed a measurement of the deformed shape of the wall specimen or of both walls (in case of cavity walls). The wire potentiometers have been installed at  $\frac{1}{4}$ ,  $\frac{1}{2}$  and  $\frac{3}{4}$  of the wall specimens recording the relative horizontal displacement with respect the two lateral frames.

Couples of potentiometers are also necessary to measure the vertical displacement related to each spring system (directly related to  $\sigma_v$ ). Potentiometers were installed to monitor the rocking behavior of the second layer of the specimen with respect the foundation. Potentiometers were installed also to monitor the rocking behaviour of the second last brick layer with respect the top steel beam.



Table 53 lists the entire set-up instrumentation required for tests on single leaf specimen and cavity wall specimens; the instrument number indicates also the column data related to each devices during each test. All the data related to each test, indeed, have been collected in matrix delivered in a “.txt” format. Table 53 provides also information about the columns of such matrix.

*Table 53. Instrument identifier and organisation of the Experimental Data Array.*

<b>Device Type</b>	<b>#/ Column</b>	<b>Description and position</b>
-	1	Time [s]
Accelerometer	2	Shake Table Acceleration [g]
Accelerometer	3	Foundation Acceleration [g]
Accelerometer	4	Frame A Acceleration [g]
Accelerometer*	5	Frame B Acceleration [g]
Accelerometer	6	Top Beam Acceleration [g]
Accelerometer	7	Mid-Height CS Wall Acceleration Side A [g]
Accelerometer	8	Mid-Height CS Wall Acceleration Side B [g]
Accelerometer*	9	Mid-Height Clay Wall Acceleration Side A [g]
Accelerometer*	10	Mid-Height Clay Wall Acceleration Side B [g]
Potentiometer	11	Shake Table Displacement 1 [g]
Table-Output	12	Shake Table Displacement 2 [g]
Wire Potentiometer	13	1/4 CS Wall Height Displacement [mm]
Wire Potentiometer	14	1/2 CS Wall Height Displacement [mm]
Wire Potentiometer	15	3/4 CS Wall Height Displacement [mm]
Wire Potentiometer*	16	1/4 Clay Wall Height Displacement [mm]
Wire Potentiometer*	17	1/2 Clay Wall Height Displacement [mm]
Wire Potentiometer*	18	3/4 Clay Wall Height Displacement [mm]
Wire Potentiometer*	19	4/4 Clay Wall Height Displacement [mm]
Potentiometer	20	Spring 1 Side A [mm]
Potentiometer	21	Spring 2 Side A [mm]
Potentiometer	22	'Spring 1 Side B [mm]'
Potentiometer	23	'Spring 2 Side B [mm]'
Potentiometer	24	'Rocking CS Bottom [mm]'
Potentiometer	25	'Rocking CS Top [mm]'
Potentiometer*	26	'Rocking Clay Bottom [mm]'

\* not present in EC\_COMP\_4 (single leaf specimen) Test.

## 5.3 Test procedure

### 5.3.1 Dynamic input

The following procedure have been applied for the out-of plane shake table testing of the specimens. Before the activation of the shake table the free vibration response of the specimen subjected to hammer blow have been recorded by the accelerometer positioned at the wall mid-height. A white noise test have been also performed in order to have data usefull to characterize the dynamic properties of the considered specimens.

The dynamic inputs have been chosen to be representative of Groningen seismicity according to the report “Selection of records for nonlinear dynamic analysis of Groningen buildings” by H. Crowley, J. Bommer and R. Pinho (Version 1.0, 13th May 2015). Table 54 clarifies the accelerogram typologies considered for the present test.

Table 54. Dynamic Input Typologies.

Type #	ID Input	Description
1	Gr_1	Groningen Record (7_EQ2WSE_H2.txt) (Crowley <i>et al.</i> )
2	Gr_2	Floor Accelerograms (FA) obtained with TREMURI program (Gr_1 input, PGA 0.2g) assuming T1_STAR Model in the flexible direction.
3	RWA	4 Hz Acceleration Pulse input

Once chosen the desired prestress level for the specimen, the sequence of dynamic test was:

- ‘Initial Phase’ Testing: incremental dynamic testing procedure till the attainment of close to cracking condition in the specimen with Type 1 accelerogram;
- ‘Pulse Phase’ Testing: Ricker Wave Acceleration Input (RWA): the shake table will observe precise acceleration pulses, ideal to calibrate numerical model on the specimen response;
- ‘Transient Excitation Phase Testing’: Type 2 accelerogram: to understand the specimen behaviour subjected to a floor motion out-of-plane condition.

Repetitions of the aforementioned sequence have been performed till the attainment of collapse limit state of the wall specimen. During the EC\_COMP\_4 experiment, the procedure have been suspended modifying the test setup in order to vary the prestressing overburden pressure acting on the specimen.

Figure 177 shows the acceleration time history of the Gr\_1 (100%) Input.

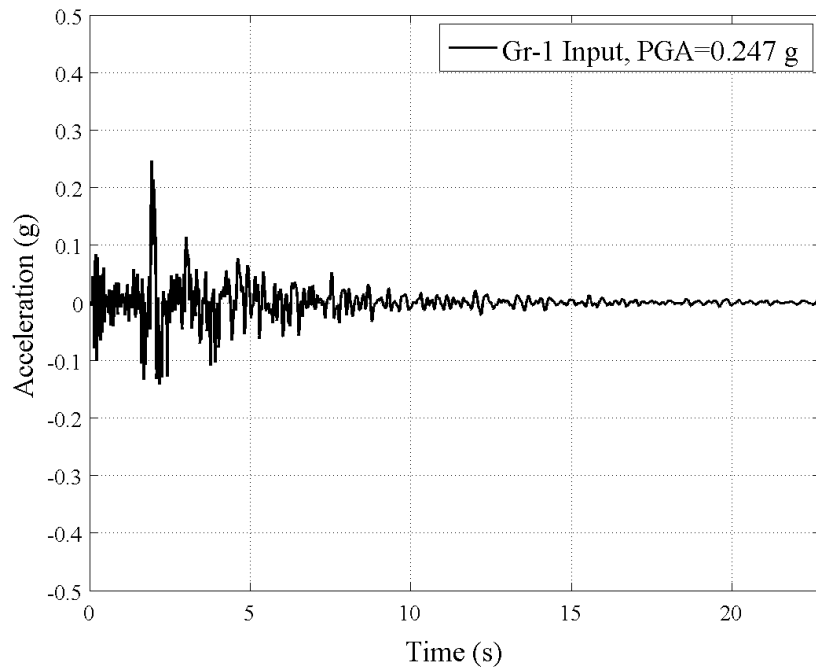


Figure 177. Gr\_1 Input Acceleration Time History.

Gr\_2 motion represents a floor motion of a typical Dutch terraced house. Since no dynamic tests were present in literature at the moment of the shaking table test herein reported, an artificial floor motion has been computed. In particular, one of the nonlinear numerical model (representing a two storeys cavity-walls terraced house, labeled T1\*) used for other scope in the same project were used in order to obtain an acceleration time history representative of the second floor motion. Figure 178 shows the force-displacement curve of a cyclic pushover performed with TREMURI program for the T1\* Model (total mass 99 t) in the X direction (weak direction); dynamic time histories analyses were run assuming as ground input the Gr\_1 earthquake to compute the floor accelerogram Gr\_2. This output was used as an input for the shaking table.

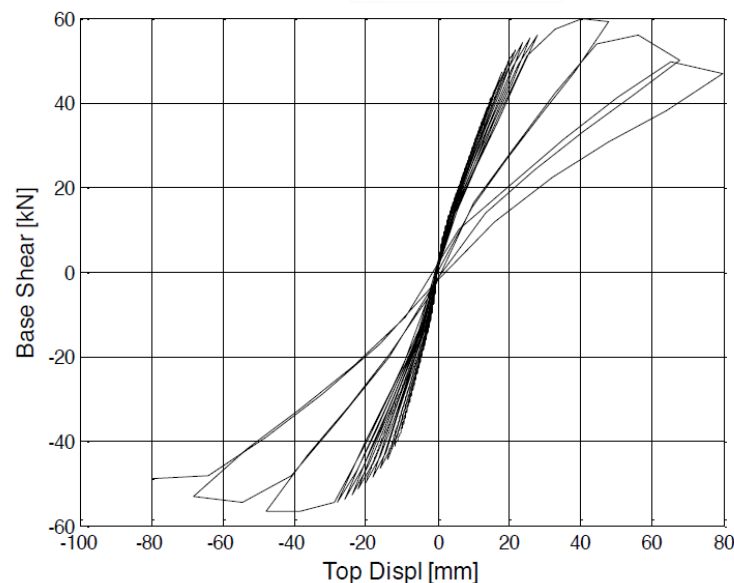


Figure 178. Cyclic Pushover Results of T1\* Model.

Figure 179 shows the acceleration time history of the Gr\_2 (100%) Input. As aforementioned it represents the floor accelerograms response of T1\* Model.

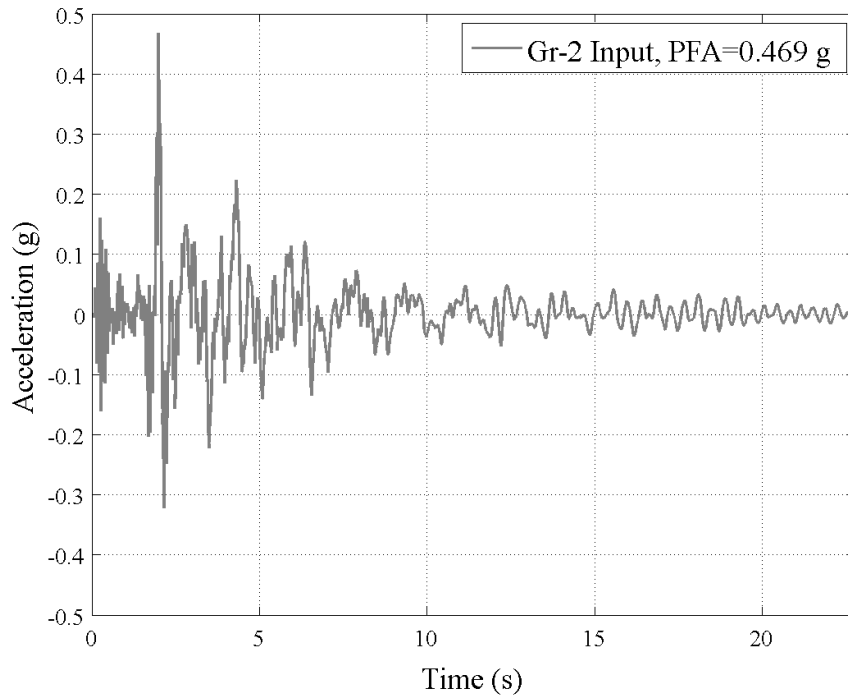


Figure 179. Gr\_2 Input Acceleration Time History.

Figure 180 shows the acceleration history related to a RWA input, scaled to a PGA equal to 0.1 g.

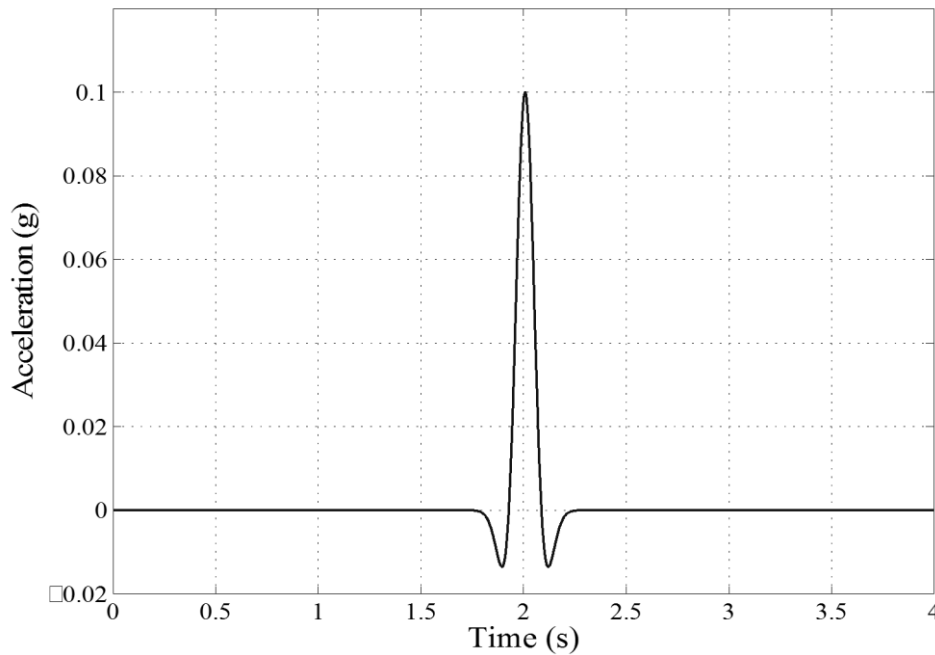


Figure 180. RWA Input Acceleration Time History.

Gr-1, Gr-2 and RWA 5% Acceleration (a) and Displacement (b) Response Spectrum are reported in following figures.

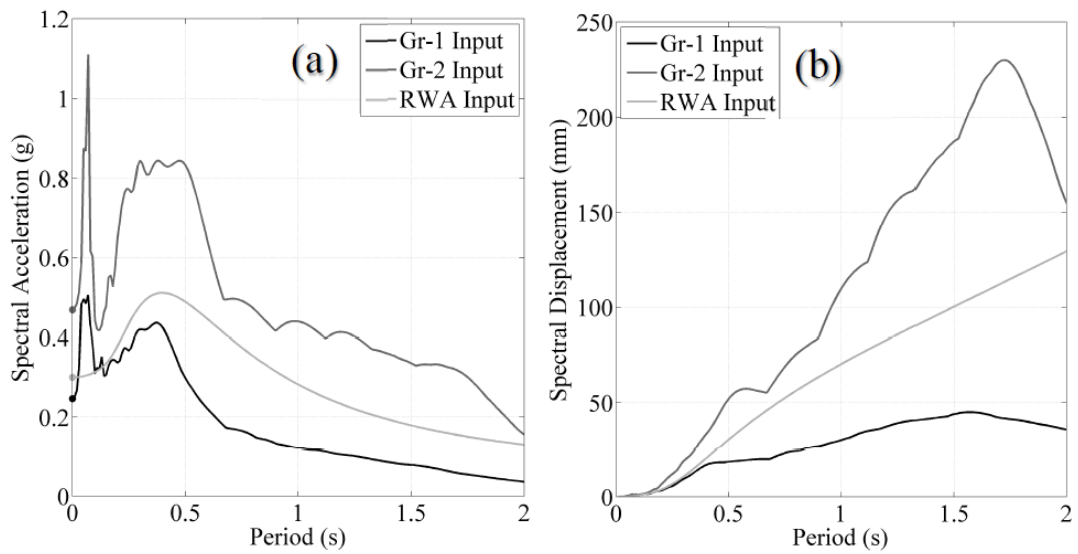


Figure 181. Gr-1, Gr-2 and RWA 5% Acceleration (a) and Displacement (b) Response Spectrum.

### 5.3.2 Testing Sequence

The following tables present the experimental dynamic testing sequence performed on each test specimen. Information about the global response of the specimen are included like the CS wall horizontal mid-height displacement response peak for both specimen typology: single leaf and cavity wall specimens.

Table 55, Table 56, Table 57 and Table 58 present the dynamic testing sequence correspondent to EC\_COMP\_4, EC\_COMP\_5, EC\_COMP\_6 and EC\_COMP\_7 specimens. The tables specify the testing phase, the test number, the N code (which is necessary to extract data), the dynamic input typology, its scaling factor and the PGA recorded during the test.

Table 55. EC\_COMP\_4 Testing Sequence.

Phase #	Test #	N #	Dynamic Input	Input Scaling	PGA [g]	Max CS ½ H Disp. [mm]
<b>Imposed Overburden Pressure: 0.3 MPa</b>						
1	1.1	1	Gr_1	20%	+0.04	+0
	1.2	2	Gr_1	40%	+0.09	+0.12
	1.3	3	Gr_1	80%	+0.16	+0.37
	1.4	4	Gr_1	100%	+0.20	+0.57
	1.5	5	Gr_1	160%	+0.32	+0.93
	1.6	6	Gr_1	200%	+0.42	+1.21
	1.7	7	Gr_1	250%	+0.53	+1.41
	1.8	8	Gr_1	350%	+0.74	+1.69
	1.9	9	Gr_1	450%	+0.96	+4.91
2	2.1	1	RWA 2Hz	-	-1.11	-1,97
	2.2	2	RWA 2Hz	-	-1.63	-9,62
	2.3	3	RWA 2Hz	-	-1.04	-2,68
	2.4	4	RWA 2Hz	-	-1.88	-14,09
<b>Imposed Overburden Pressure: 0.1 MPa</b>						
3	3.1	1	Gr_1	40%	+0.08	-0,35
	3.2	2	Gr_1	80%	+0.17	-0,73
	3.3	3	Gr_1	100%	+0.21	-0,92
	3.4	4	Gr_1	160%	+0.34	-1,29
	3.5	5	Gr_1	200%	+0.41	1,94
	3.6	6	Gr_1	250%	+0.51	-7,42
	3.7	7	Gr_1	300%	+0.60	-14,42
	3.8	8	Gr_1	350%	+0.73	-16,61
4	4.1	1	RWA 2Hz	-	-0.25	-0,38
	4.2	2	RWA 2Hz	-	-0.48	-1,92
	4.3	3	RWA 2Hz	-	-0.72	-16,05
	4.4	4	RWA 2Hz	-	-0.96	-52,99
5	5.1	1	Gr_2	100%	+0.44	2,88
	5.2	2	Gr_2	150%	+0.64	-9,87
	5.3	3	Gr_2	200%	+0.85	-failure



Table 56. EC\_COMP\_5 Testing Sequence.

Phase #	Test #	N	Dynamic Input	Input Scaling	PGA [g]	Max CS ½ H Disp. [mm]
0	0.1	-	Hammering	-	-	-
	0.2	-	White Noise	-	0.1	-
1	1.1	1	Gr_1	+20%	+0.04	0.00
	1.2	2	Gr_1	+40%	+0.09	0.12
	1.3	3	Gr_1	+60%	+0.12	0.19
	1.4	4	Gr_1	+80%	+0.17	0.31
	1.5	5	Gr_1	+100%	+0.23	0.36
	1.6	6	Gr_1	-40%	-0.086	-0.15
	1.7	7	Gr_1	-60%	-0.13	0.20
	1.8	8	Gr_1	-80%	-0.17	-0.40
	1.9	9	Gr_1	-100%	-0.23	-0.54
2	2.1	1	RWA	-	-0.22	-0.31
	2.2	2	RWA	-	-0.31	-0.67
3	3.1	1	Gr_2	+70%	+0.33	-0.74
	3.2	2	Gr_2	+100%	+0.50	2.44
	3.3	3	Gr_2	+150%	+0.60	-10.65
4	4.1	10	Gr_1	+300%	+0.63	-42.45
5	5.1	3	RWA	-	-0.31	-3.21
	5.2	4	RWA	-	-0.49	40.43
6	6.1	4	Gr_2	+150%	+0.65	-failure



Table 57. EC\_COMP\_6 Testing Sequence.

Phase #	Test #	N	Dynamic Input	Input Scaling	PGA [g]	Max CS ½ H Disp. [mm]
0	0.1	-	Hammering	-	-	-
	0.2	-	White Noise	-	0.1	-
1	1.1	1	Gr_1	-40%	-0.09	0.18
	1.2	2	Gr_1	-60%	-0.13	0.22
	1.3	3	Gr_1	-80%	-0.17	-0.15
	1.4	4	Gr_1	-100%	-0.22	-0.27
	1.5	5	Gr_1	+40%	+0.09	0.05
	1.6	6	Gr_1	+60%	+0.12	-0.12
	1.7	7	Gr_1	+80%	+0.17	0.12
	1.8	8	Gr_1	+100%	+0.21	0.14
2	2.1	1	RWA	-	-0.30	-0.64
	2.2	2	RWA	-	+0.29	+0.41
3	3.1	1	Gr_2	+70%	-0.32	-0.64
	3.2	2	Gr_2	+100%	-0.47	-1.00
	3.3	3	Gr_2	+150%	-0.66	-1.71
	3.4	4	Gr_2	+170%	-0.77	2.88
4	4.1	3	RWA	-	-0.49	-1.90
	4.2	4	RWA	-	+0.53	+1.99
5	5.1	5	Gr_2	+210%	-0.97	6.12
	5.2	6	Gr_2	+250%	-1.17	+ failure



Table 58. EC\_COMP\_7 Testing Sequence.

Phase #	Test #	N	Dynamic Input	Input Scaling	PGA [g]	Max CS ½ H Disp. [mm]
0	0.1	-	Hammering	-	-	-
	0.2	-	White Noise	-	0.1	-
1	1.1	1	Gr_1	-20%	-0.04	-0,05
	1.2	2	Gr_1	-40%	-0.09	0,07
	1.4	3	Gr_1	-60%	-0.13	0,17
	1.5	4	Gr_1	-80%	-0.18	0,26
	1.6	5	Gr_1	-100%	-0.23	-0,36
2	2.1	1	RWA	-	-0.31	-0.33
	2.2	2	RWA	-	+0.37	+0.50
3	3.1	1	Gr_2	-70%	-0.32	-0.61
	3.2	2	Gr_2	-100%	-0.45	-1.47
	3.3	3	Gr_2	-150%	-0.66	2.89
	3.4	4	Gr_2	-170%	-0.75	45.52
4	4.1	3	RWA	-	+0.33	+4.64
	4.2	4	RWA	-	-0.31	-2.25
	4.3	-	Hammering	-	-	-
	4.4	-	White Noise	-	-	-
	4.5	5	RWA	-	-0.50	+28.82
	4.6	6	RWA	-	+0.52	+45.27
5	5.1	5	Gr_2	-100%	-0.46	32,90
	5.2	6	Gr_2	-150%	-0.64	+failure
	5.3	7	Gr_2	+100%	+0.51	-47.09*
	5.4	8	Gr_2	+150%	+0.72	-failure

\*recorded on the Clay wall

## 5.4 Test Results

The present chapter reports the main outcome of the performed tests in terms of response and damage pattern.

More info could be found in the following two papers:

- Graziotti F., Tomassetti U., Penna A., Magenes G. (2016), Out-of-Plane Shaking Table Tests on URM Single Leaf and Cavity walls, *Engineering Structures*, (In press).
- Tomassetti U., Graziotti F., Penna A., Magenes G. (2016), Out-of-plane shaking table test on URM cavity walls, *Proc. 16<sup>th</sup> IBMAC conference*, Padua, Italy.

Some videos of the described test could be watched at:

[www.youtube.com/playlist?list=PLRDMVFxhFvQn8fGJNlvMzD5Q5bOCUS5t5](http://www.youtube.com/playlist?list=PLRDMVFxhFvQn8fGJNlvMzD5Q5bOCUS5t5)

### 5.4.1 EC\_COMP\_4

#### Testing phase 1

The testing phase 1 was carried out with an imposed overburden pressure equal to 0.3 MPa. Figure 182 shows the incremental experimental test results in term of maximum mid-height horizontal displacements achieved by the wall during the testing phase 1.

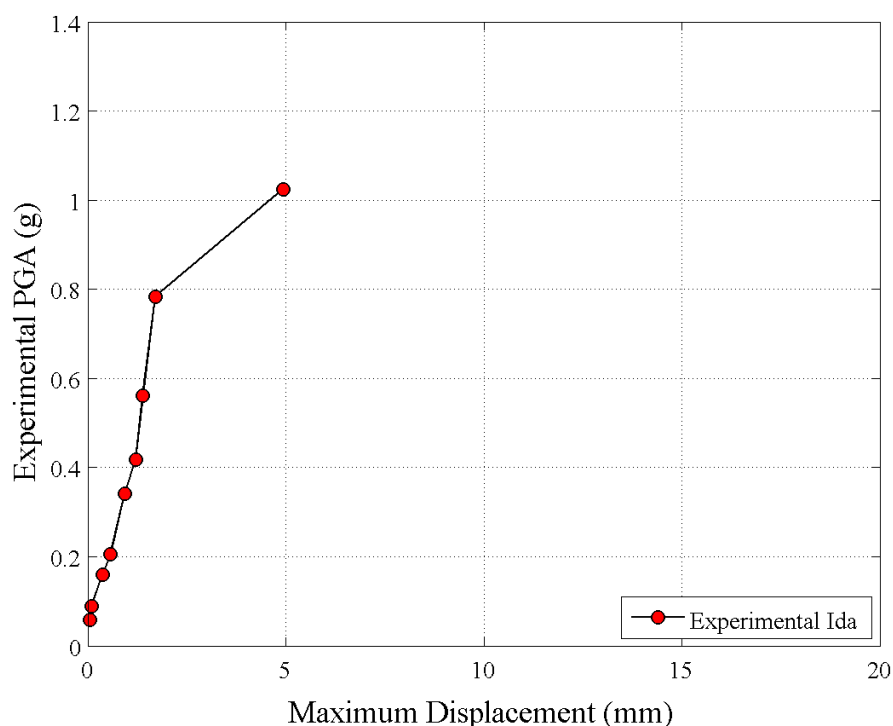


Figure 182. Experimental Tests Gr\_1 (PGA vs. Max response at mid-height).

### Testing phase 2

The testing phase 2 was carried out with an imposed overburden pressure equal to 0.3 MPa. The EC\_COMP\_4 specimen was subjected to Ricker Wave Acceleration input. Figure 183 and Figure 184 represent respectively displacement and acceleration histories of the shake table during the test 2.4.

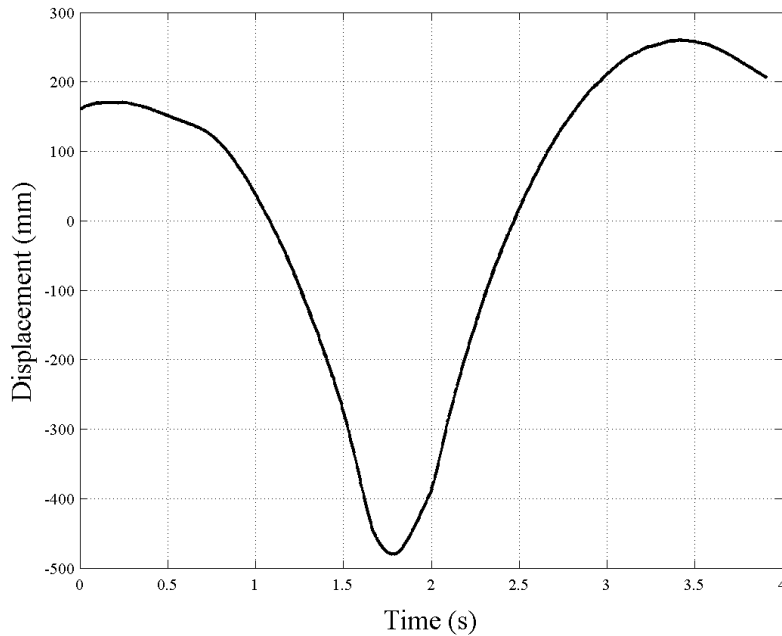


Figure 183. Shake-table Displacement History during test 2.4.

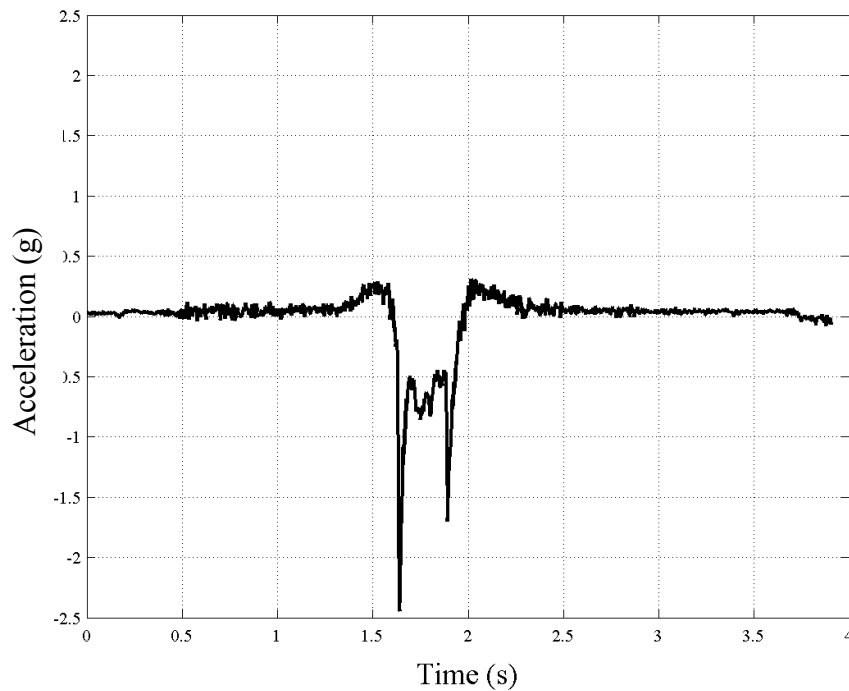


Figure 184. Shake-table Acceleration History during test 2.4.

Figure 185 shows the horizontal mid-height displacement history for the 2.4 test.

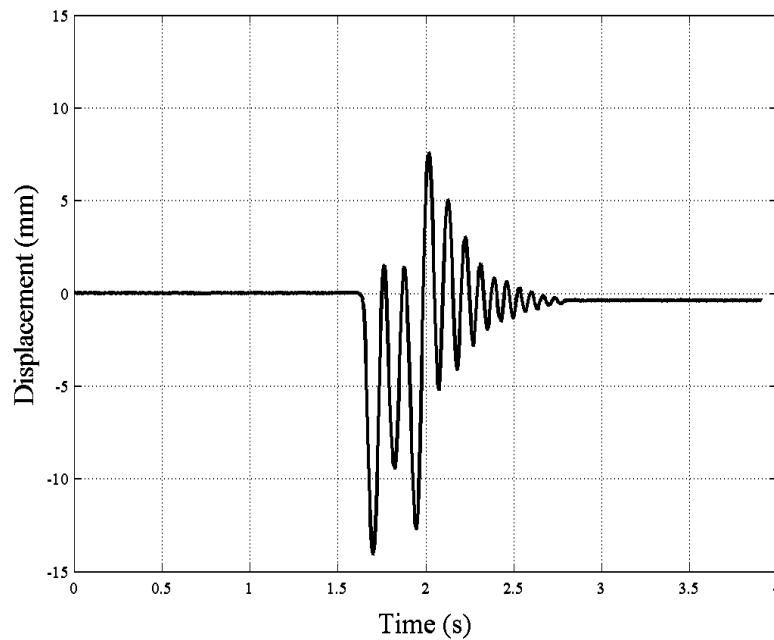


Figure 185. Specimen Horizontal Mid-height Displacement History during test 2.4.

### Testing Phase 3

The testing phase 3 was carried out with an imposed overburden pressure equal to 0.1 MPa. The EC\_COMP\_4 specimen was subjected to incremental experimental test adopting the Gr\_1 input. Figure 186 shows the incremental experimental test results in term of maximum mid-height horizontal displacements achieved by the wall during the testing phase 3.

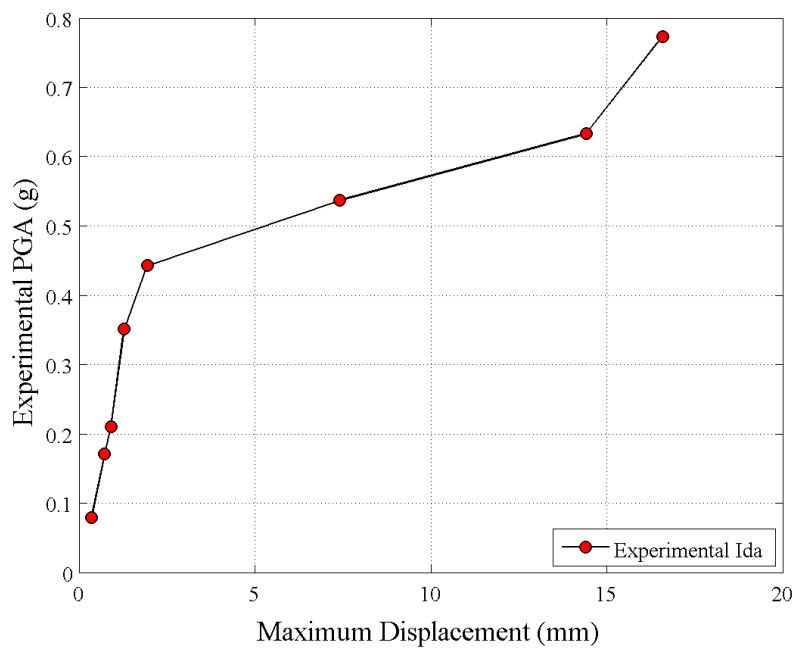


Figure 186. Experimental Tests Gr\_1 (PGA vs. Max response at mid-height).

### Testing Phase 4

The testing phase 4 was carried out with an imposed overburden pressure equal to 0.1 MPa. The EC\_COMP\_4 specimen was subjected to Ricker Wave Acceleration input. Figure 187 and Figure 188 represent respectively displacement and acceleration histories of the shake table during the test 4.3.

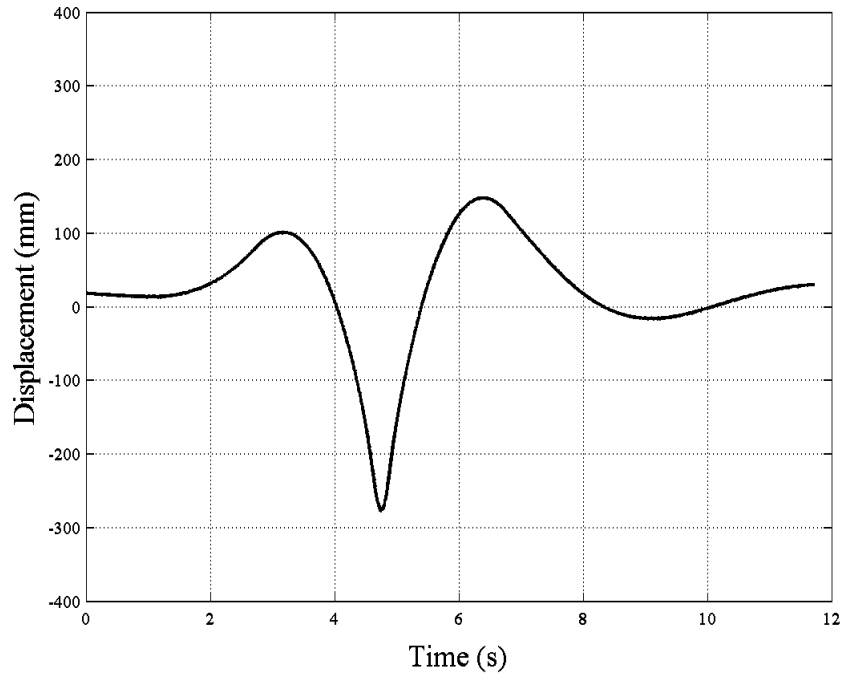


Figure 187. Shake-table Displacement History during test 4.3.

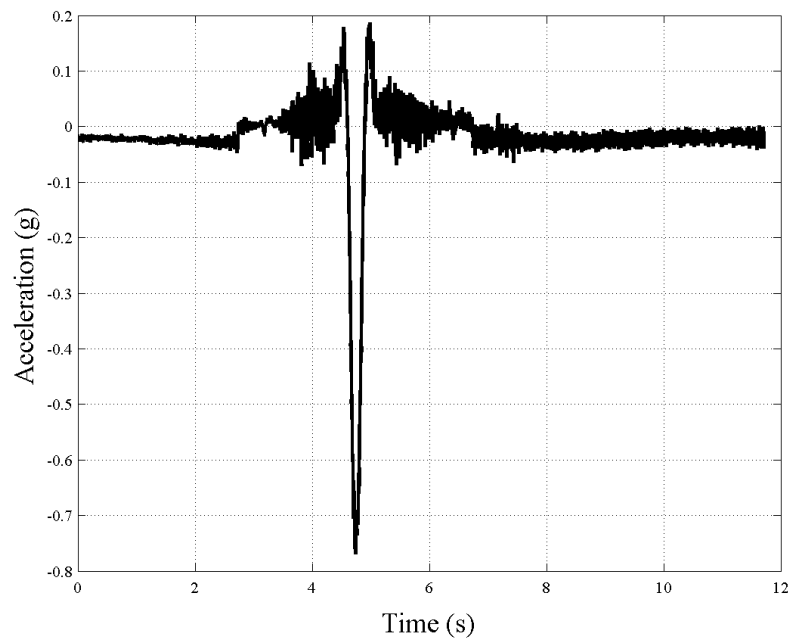


Figure 188. Shake-table Acceleration History during test 4.3.

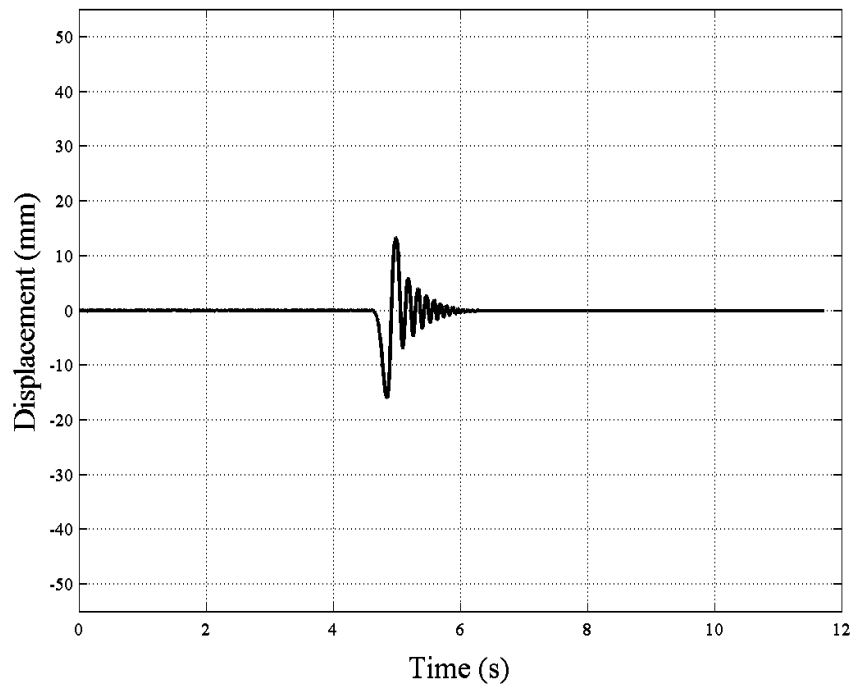


Figure 189. Shows the horizontal mid-height displacement history for the 4.3 test.

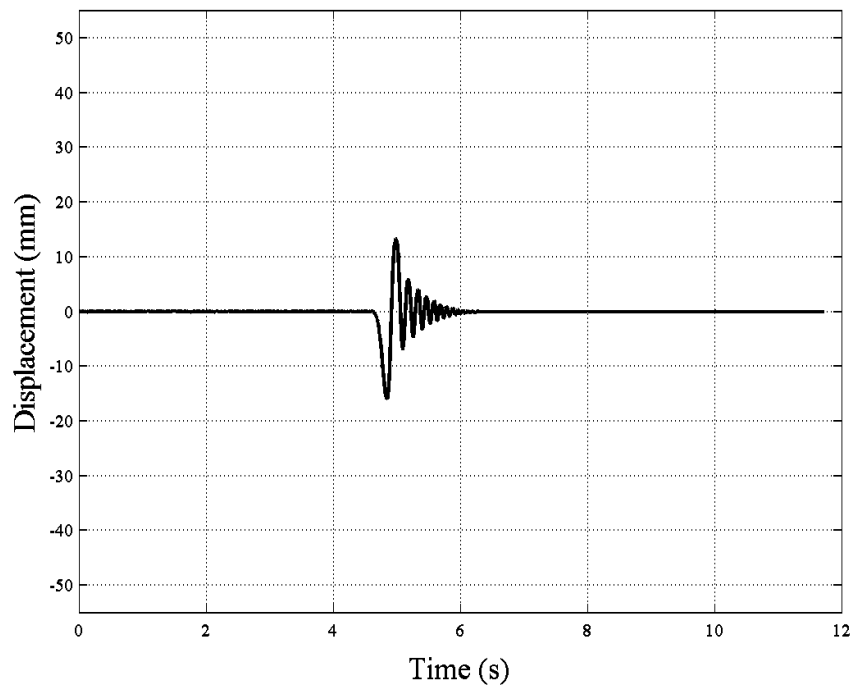


Figure 190. Specimen Horizontal mid-height Displacement History during test 4.3.

Figure 191 and Figure 192 represent respectively displacement and acceleration histories of the shake table during the test 4.4.

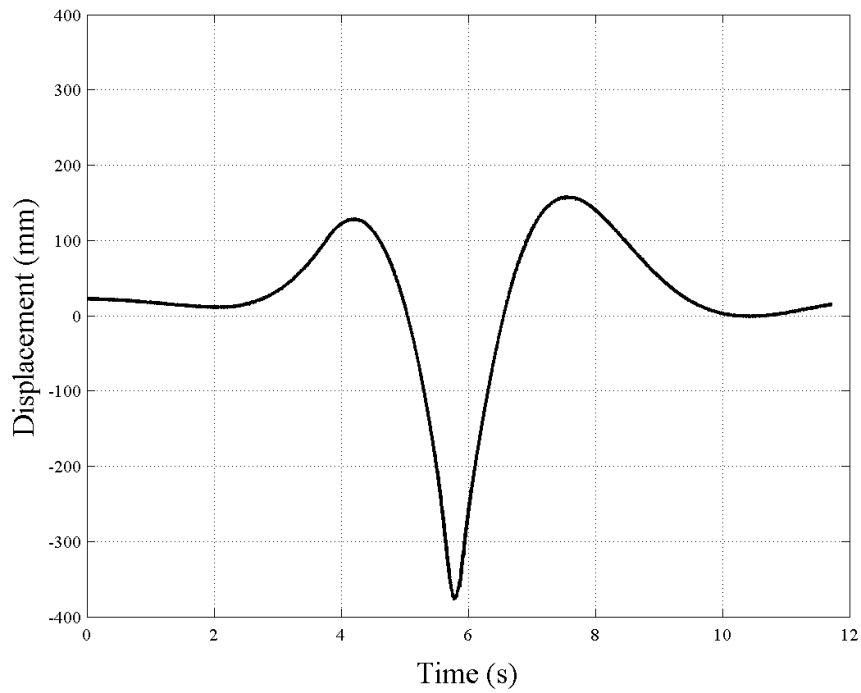


Figure 191. Shake-table Displacement History during test 4.4.

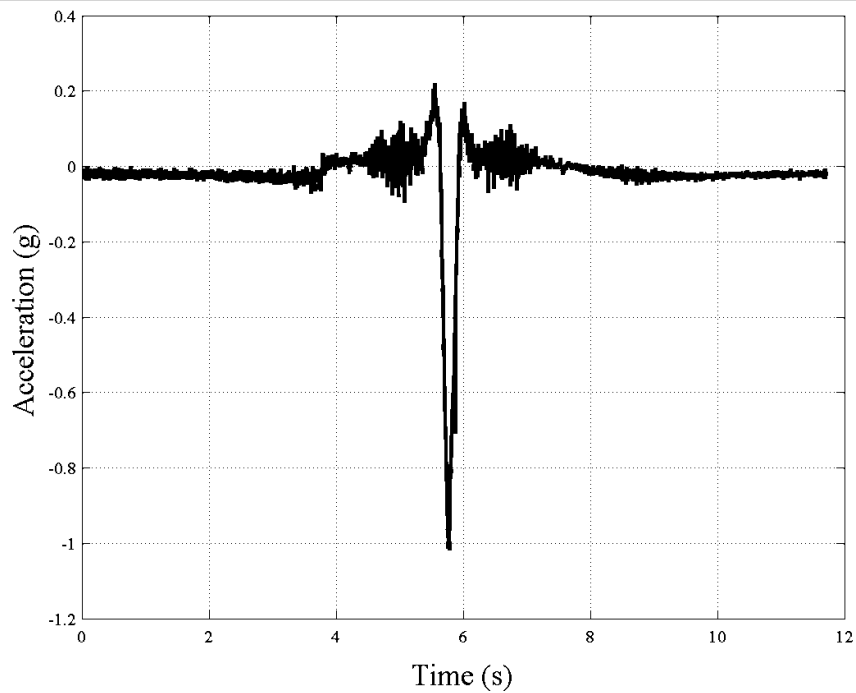


Figure 192. Shake-table Acceleration History during test 4.4.

Figure 193 shows the horizontal mid-height displacement history for the 4.4 test.

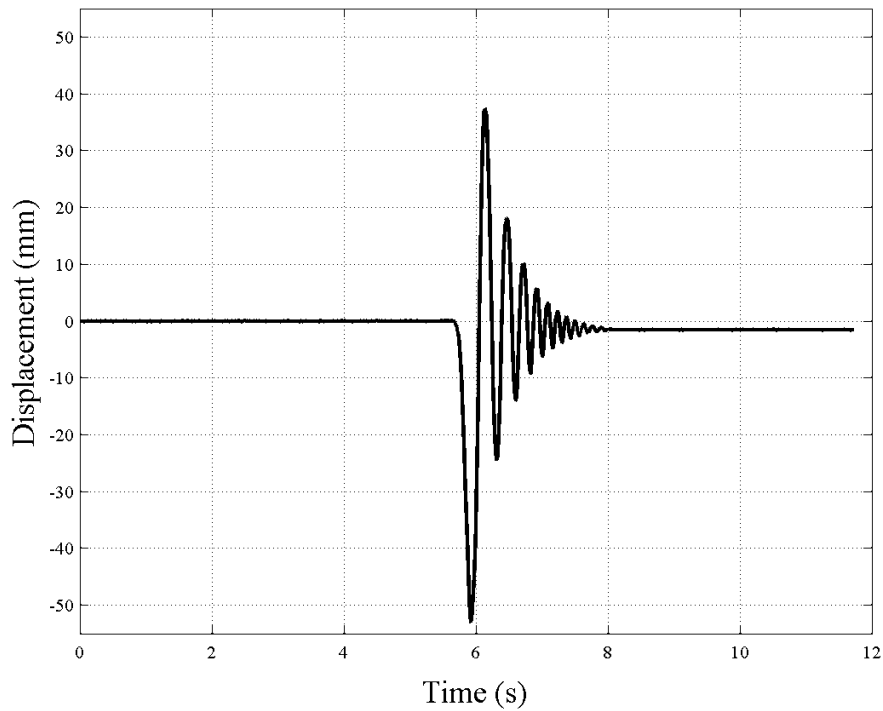


Figure 193. Specimen Horizontal Mid-height Displacement History during test 4.4.

### Testing Phase 5

The testing phase 5 was carried out with an imposed overburden pressure equal to 0.1 MPa. The EC\_COMP\_4 specimen was subjected to incremental experimental test adopting the Gr\_2 input. Figure 194 shows the incremental experimental test results in term of maximum mid-height horizontal displacements achieved by the wall during the testing phase 3. During test 5.3 the specimen exhibits a collapse on the lateral support.

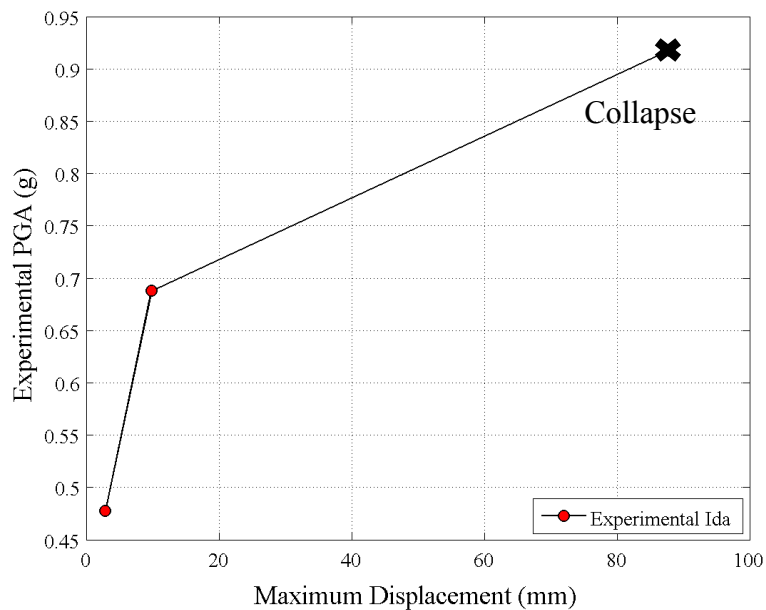
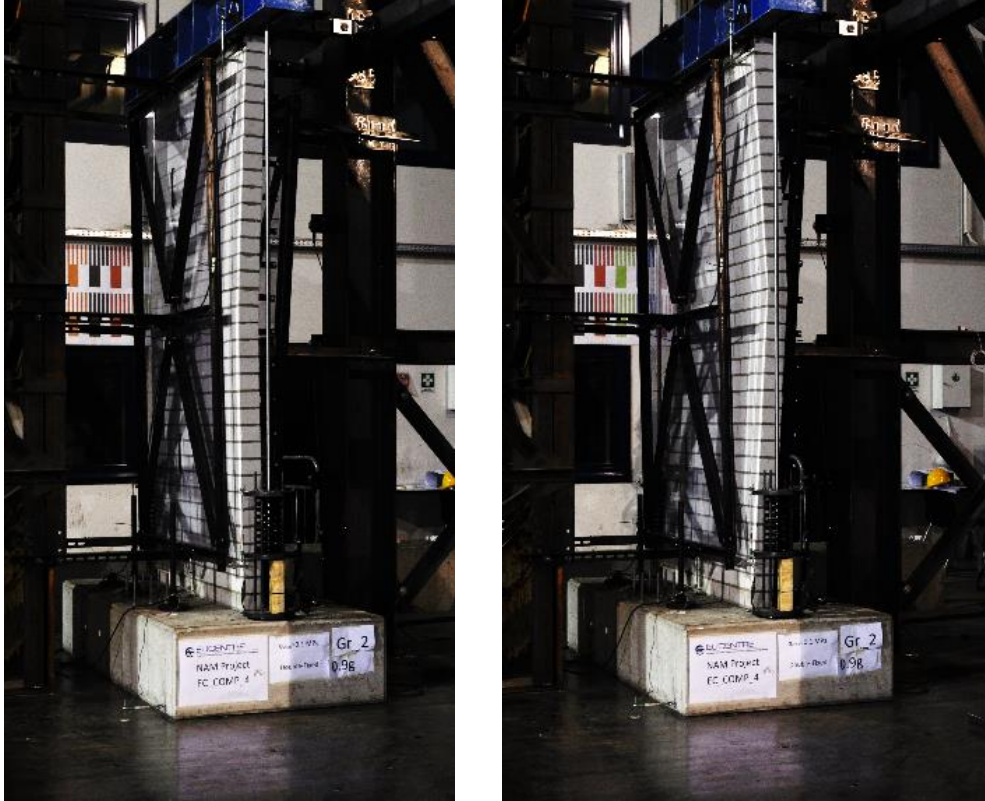


Figure 194. Experimental Tests Gr\_2 (PGA vs. Max response at mid-height).

Figure 195 is composed by two video frames showing the deformed shape of the specimen. The bottom crack appeared at the base, the “mid-height” crack between 19<sup>th</sup> and 20<sup>th</sup> layer, the top crack between 33<sup>rd</sup> and 34<sup>th</sup> as expected. Figure 196 shows a view of the mid-height crack after the test.



*Figure 195. Deformed shape of the EC\_COMP\_4 Specimen (left and right)*



*Figure 196. View of the Mid-height Crack.*

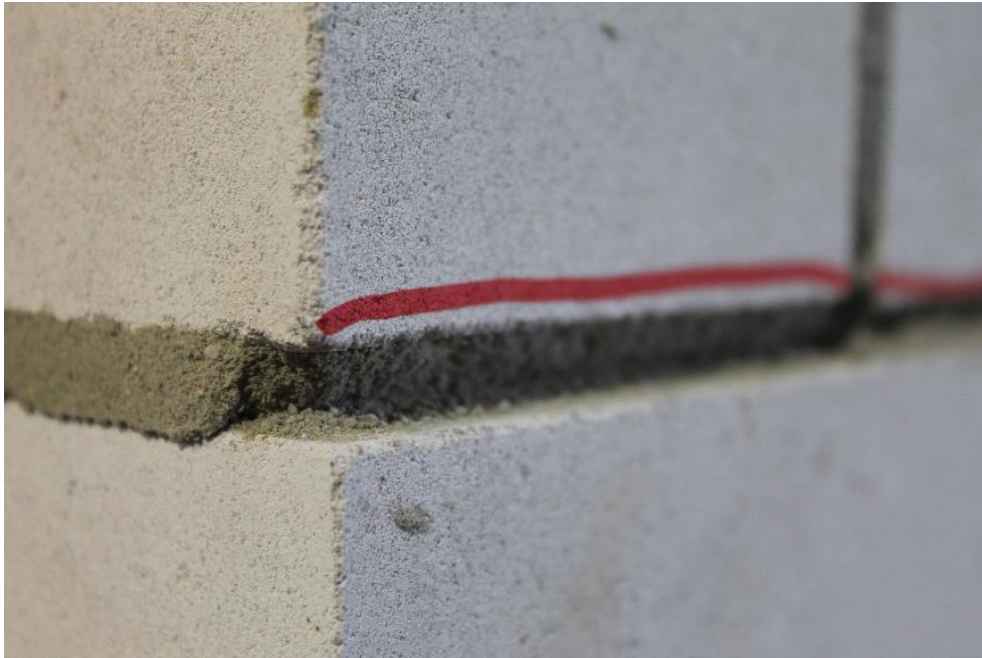


*Figure 197. View of the Cracked Mortar Bed-joint.*



*Figure 198. Decrease in Mortar Bed-joint thickness..*

## 5.4.2 EC\_COMP\_5

### Testing Phase 1

In the testing phase 1 the test specimen have been subjected to Gr\_1 acceleration inputs with opposite sign in order to investigate how the walls response could change with different excitation directions.

The response peaks recorded in this phase were associated always to a deformed shape where the outer leaf tried to increase the gap between the two walls pulling the ties, independently from the input excitation direction. Figure 199 shows the absolute horizontal mid-height response peaks of both walls in the testing phase 1.

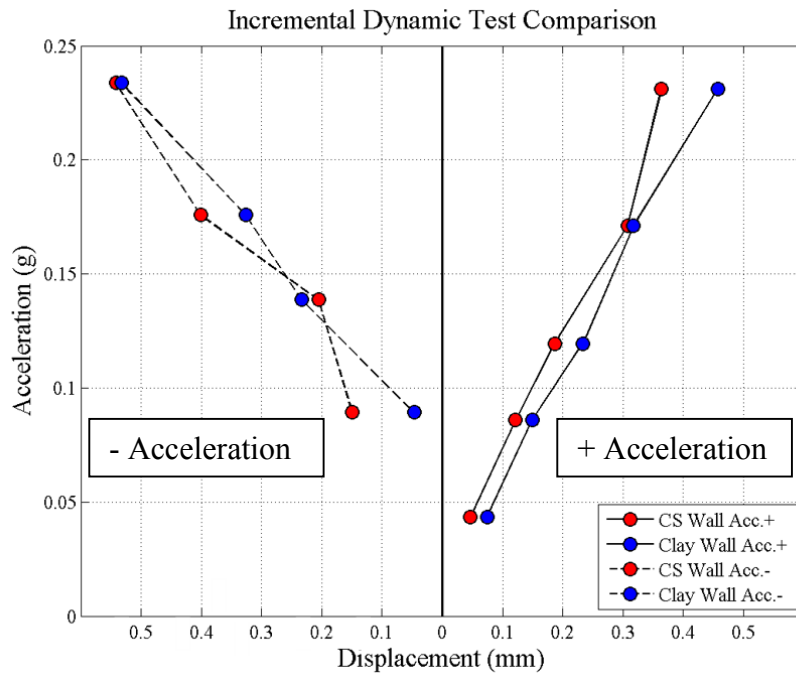


Figure 199. Comparison between mid-height response peaks (absolute values) in positive and negative direction.

### Testing Phase 1&4

Figure 200 shows the entire IDA associated to the Gr\_1 input; it is important to underline as the highest PGA test (4.1) belongs only to a later testing phase (phase 4). The response peaks are the ones associated to both walls horizontal mid-height displacement.

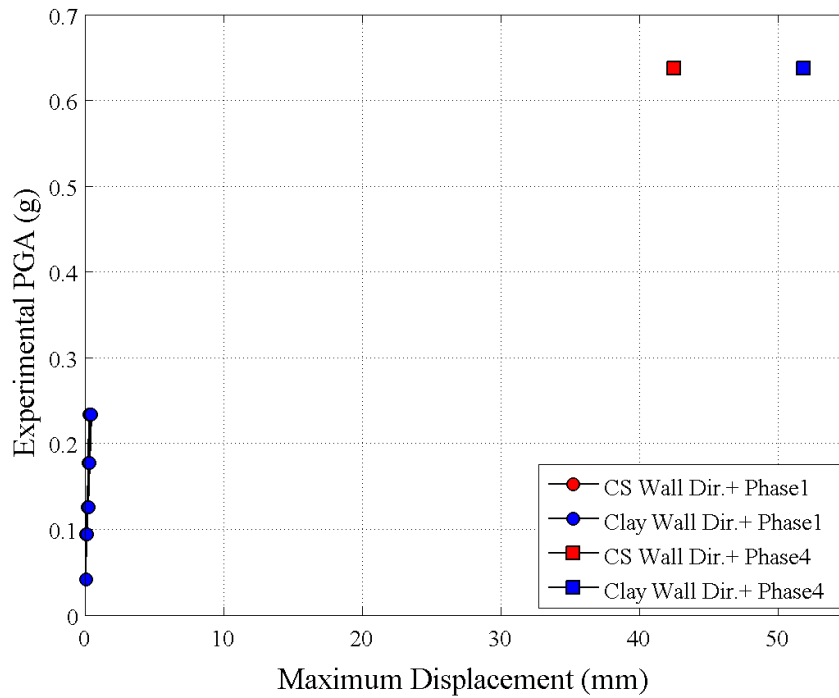


Figure 200. Experimental mid-height response peaks Gr\_1 Tests (PGA vs. Max response at mid-height).

Next figure shows the horizontal mid-height displacement histories of both calcium silicate and clay walls related to the test 4.1 (Gr\_1).

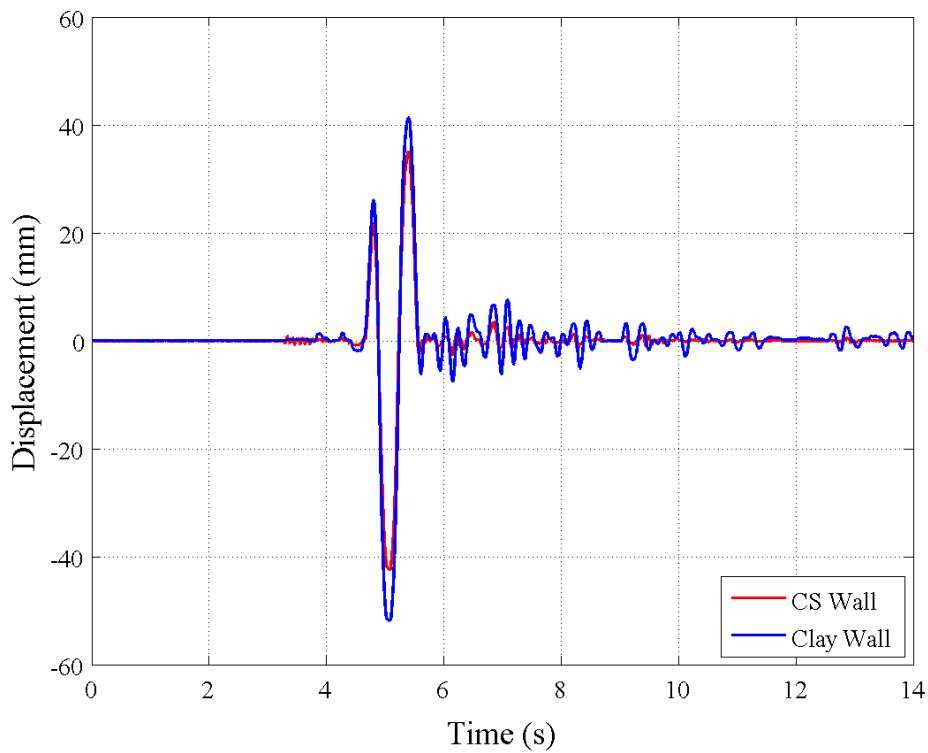


Figure 201. Horizontal mid-height displacement histories comparison between Calcium silicate (CS) and Clay Wall for the 4.1 Test.

The following figures show both walls deformed shapes associated to tests with different acceleration amplitudes. It is worth underlining as the horizontal displacement peaks shown are the ones recorded by the wire potentiometers located at  $\frac{1}{4}$ ,  $\frac{1}{2}$  and  $\frac{3}{4}$  wall height; they represent the response peaks recorded during the overall test duration by each wire potentiometer.

A more refined representation of the deformed shape could be the plot of the horizontal displacement level achieved by each potentiometer at the testing moment where the mid-height clay wall displacement achieves the highest value. In this second way it will be possible to show the deformed shape snap-shot at the instant of the maximum horizontal mid-height displacement.

Figure 202 shows the deformed shapes of both walls associated to the 1.2 test.

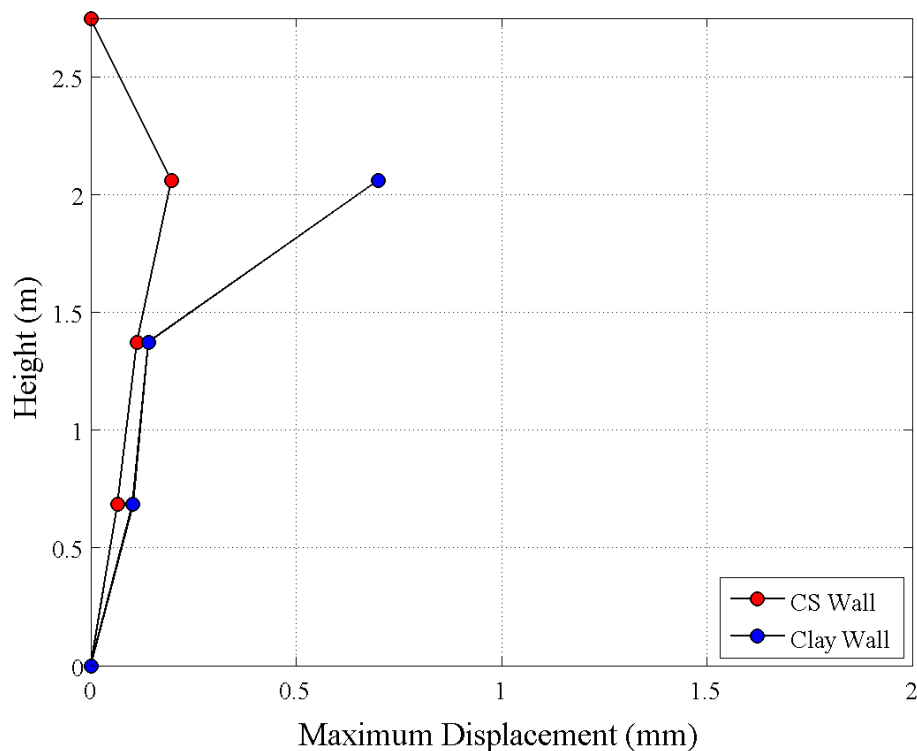


Figure 202. Comparison between maximum displacement profiles of CS and Clay Walls for the Test 1.2.

Figure 203 shows the deformed shapes associated to the 1.6 test.

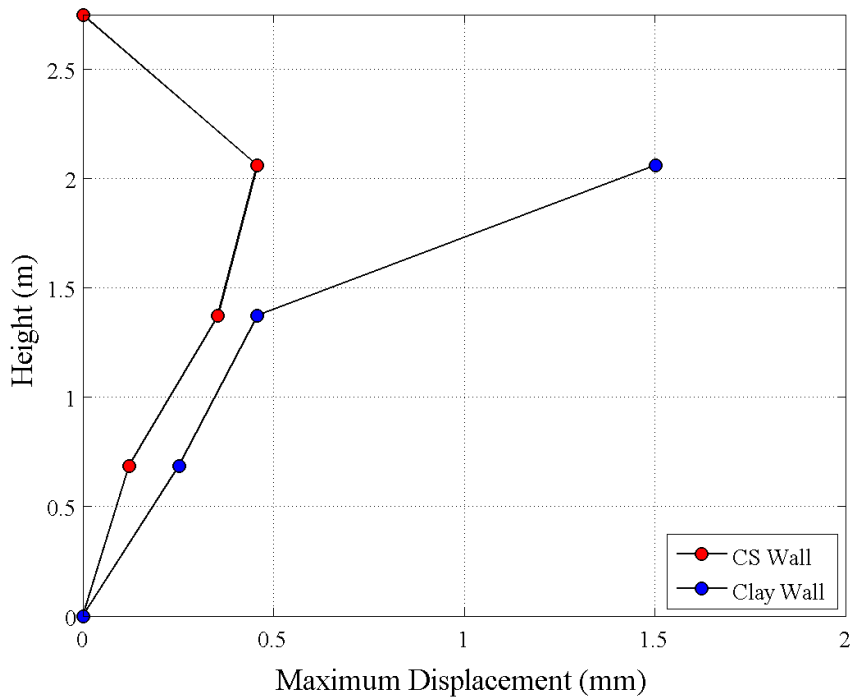


Figure 203. Comparison between maximum displacement profiles of CS and Clay Walls for the Test 1.6.

Figure 204 shows the deformed shapes of both walls associated to the 4.1 test.

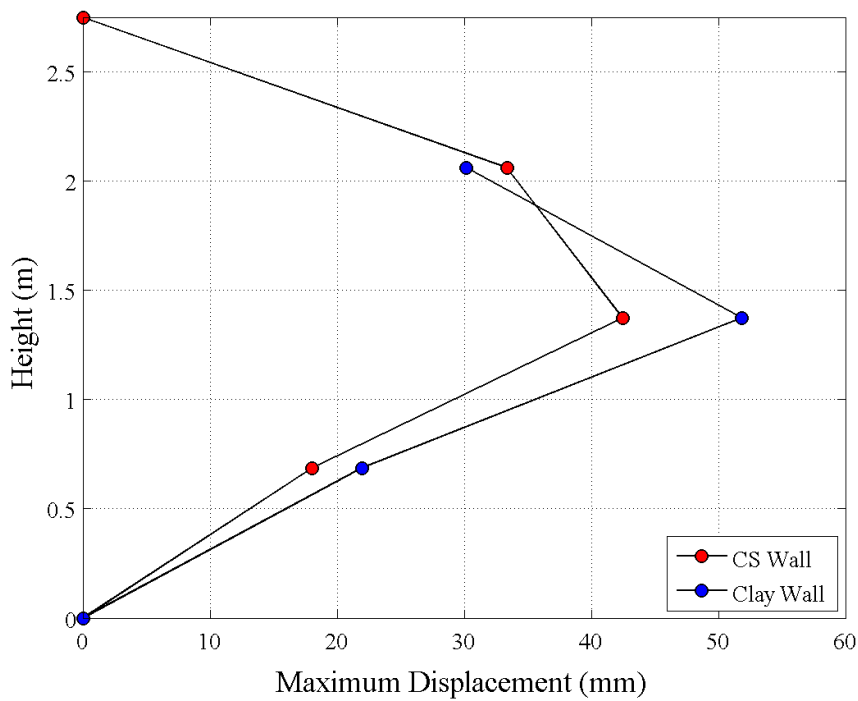


Figure 204. Comparison between maximum displacement profiles of CS and Clay Walls for the Test 4.1.

It is worth noticing as wall deformed shapes vary with the input excitation intensity. For low intensities the calcium silicate wall tend to deform as a classical double fixed beam with the peak response recorded by the wire potentiometer located at  $\frac{3}{4}$  wall height. The clay wall, instead, presents the classical cantilever deformed shape.

For high input intensity (test 4.1) instead, the deformed shape changes significantly with the two walls showing a clear coupled rocking behaviour with the formation of cracks at the walls bottom, top and around mid-height sections.

### Testing Phase 2&5

Next figure shows the horizontal mid-height displacement peaks associated to both walls for RWA inputs associated to different testing phases (phase 2 and phase 5).

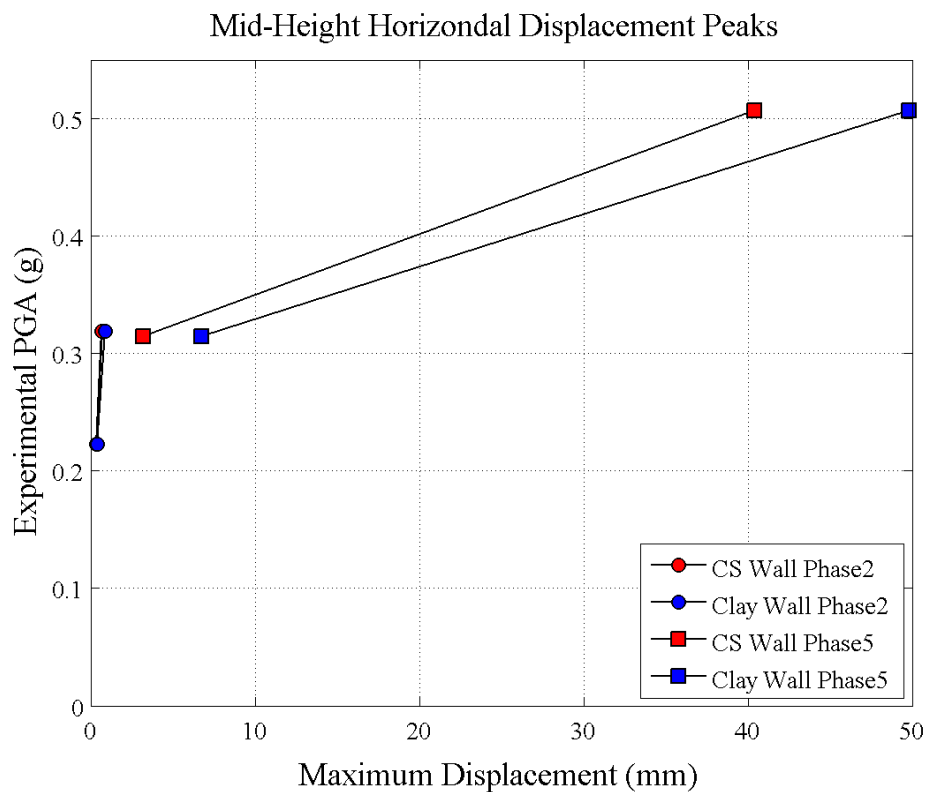


Figure 205. Experimental mid-height response peaks RWA Tests (PGA vs. Max response at mid-height).

Figure 206 shows the acceleration history recorded by the shake-table accelerometer during the 5.2 test.

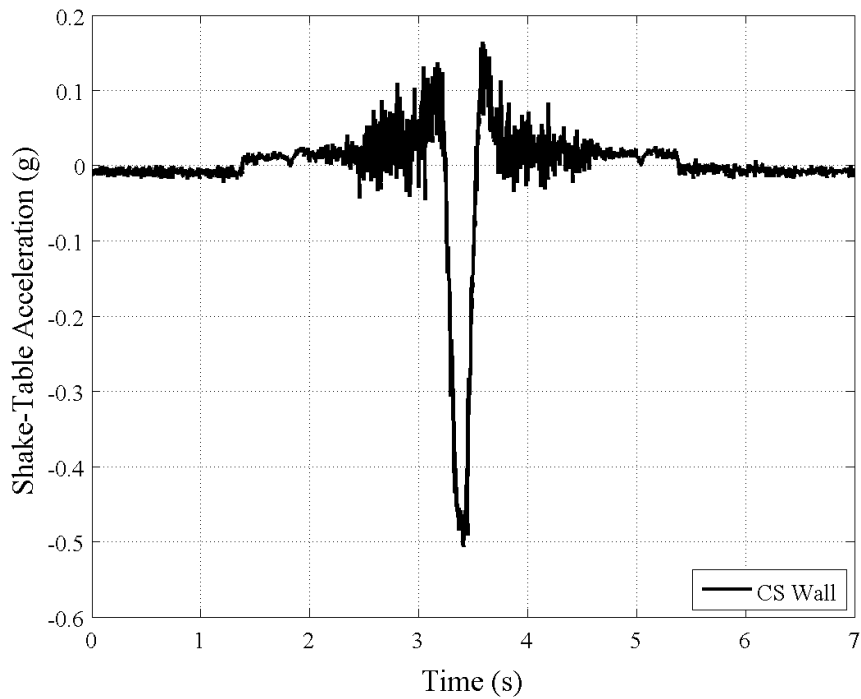


Figure 206. Shake-table Acceleration History during test 5.2.

Figure 207 shows the displacement history performed by the shake-table during the 5.2 test.

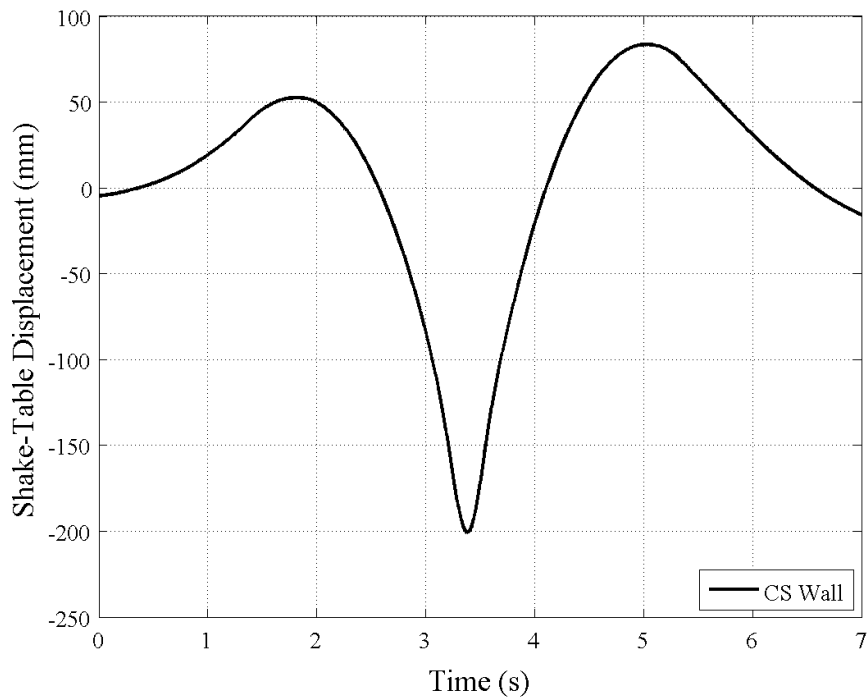


Figure 207. Shake-table Displacement History during test 5.2.

Figure 208 shows horizontal mid-height displacement histories of both walls for the 5.2 test.

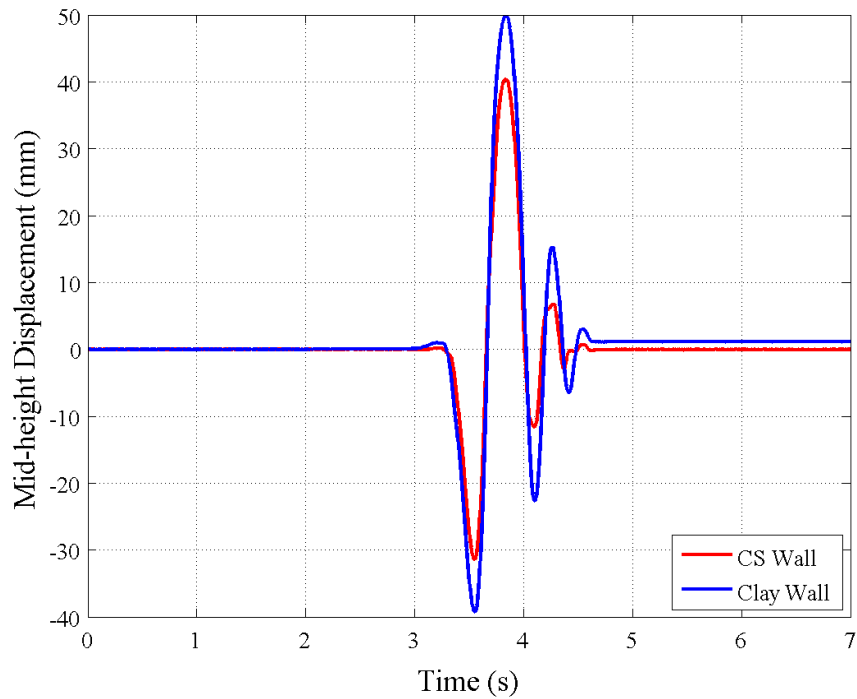


Figure 208. Horizontal mid-height displacement histories comparison between Calcium silicate (CS) and Clay Wall for the 5.2 Test.

### Testing Phase 3&6

Next figure shows the horizontal mid-height response peaks associated to both walls for the Gr\_2 input. During the repetition of Gr\_2 0.7g called test 6.1 (testing phase 6) the specimen collapsed touching and resting on the lateral support.

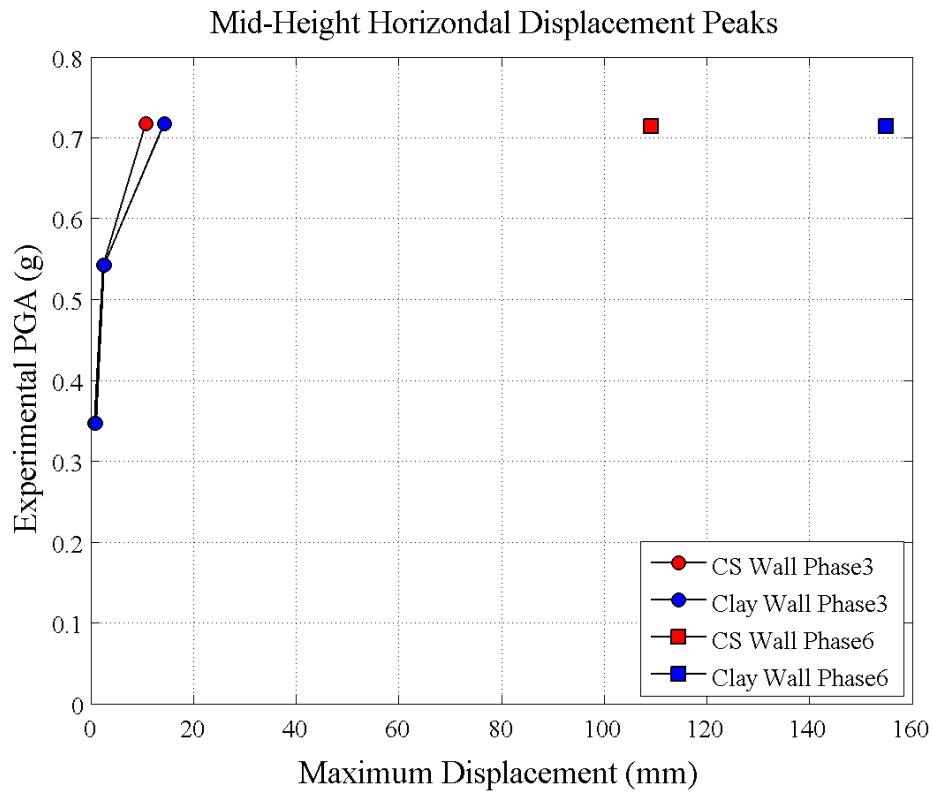


Figure 209. Experimental mid-height response peaks Gr<sub>2</sub> Tests (PGA vs. Max response at mid-height).

Figure 210 shows the deformed shapes of both walls associated to the 3.2 test.

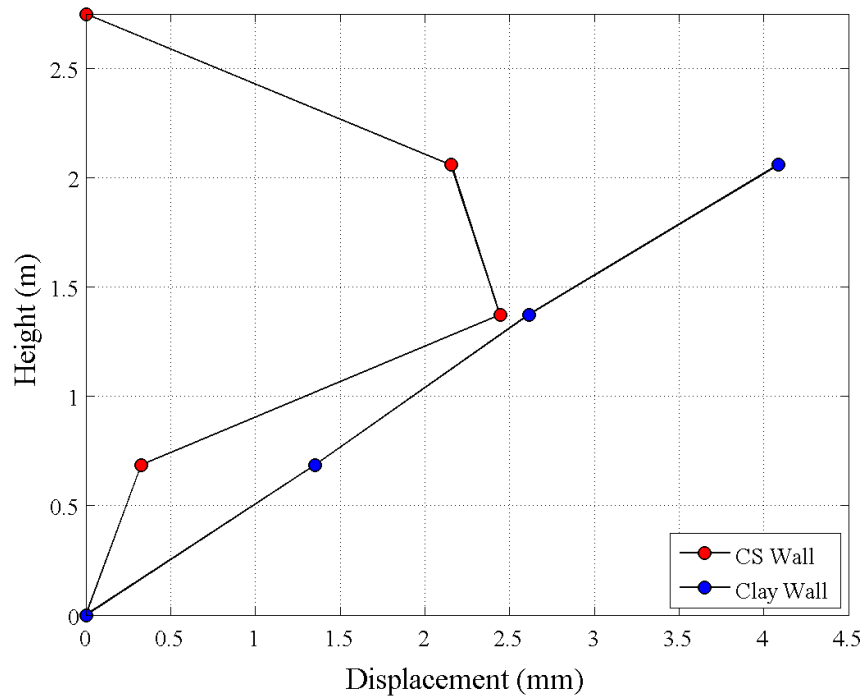
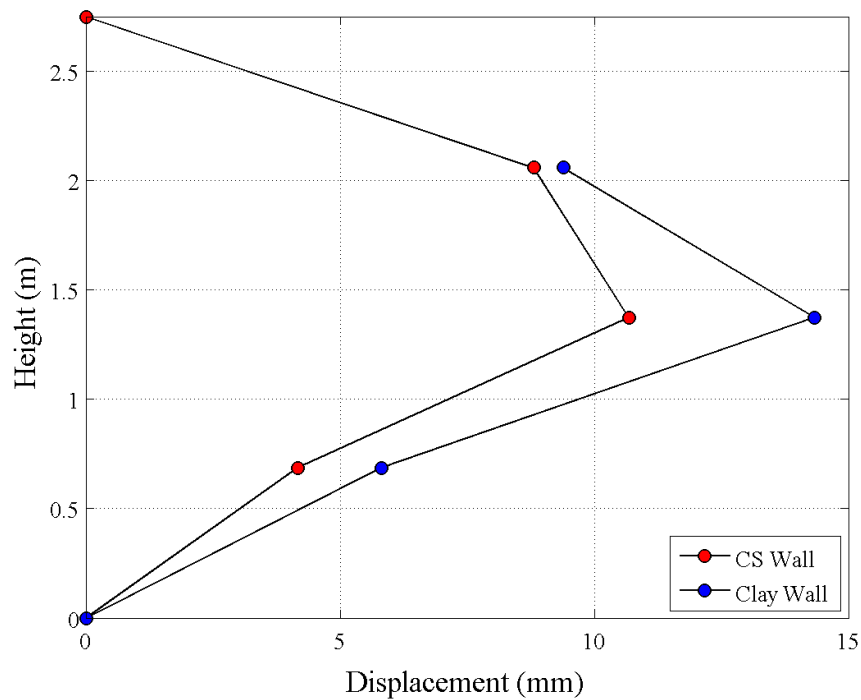


Figure 210. Comparison between maximum displacement profiles of CS and Clay Walls for the Test 3.2.

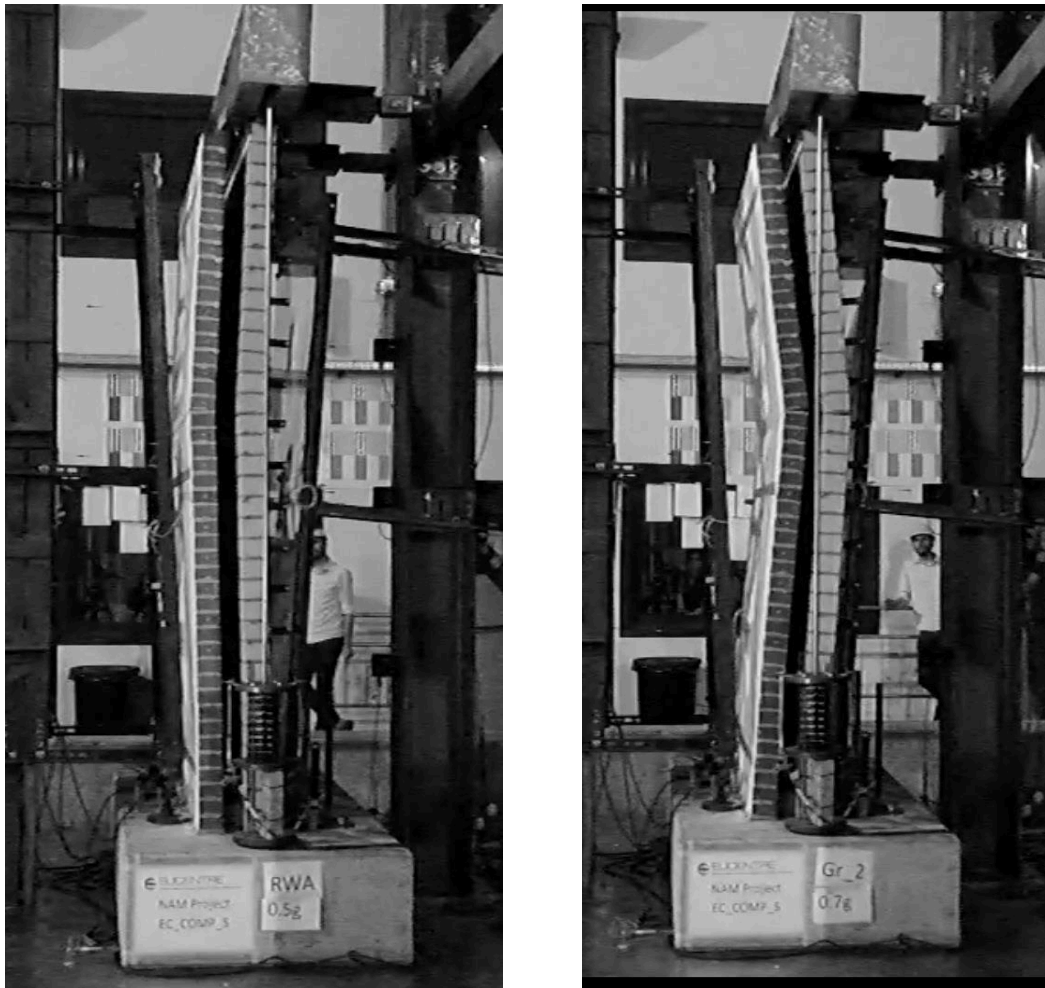
Figure 211 shows the deformed shapes of both walls associated to the 3.3 test.



*Figure 211. Comparison between maximum displacement profiles of CS and Clay Walls for the Test 3.3.*

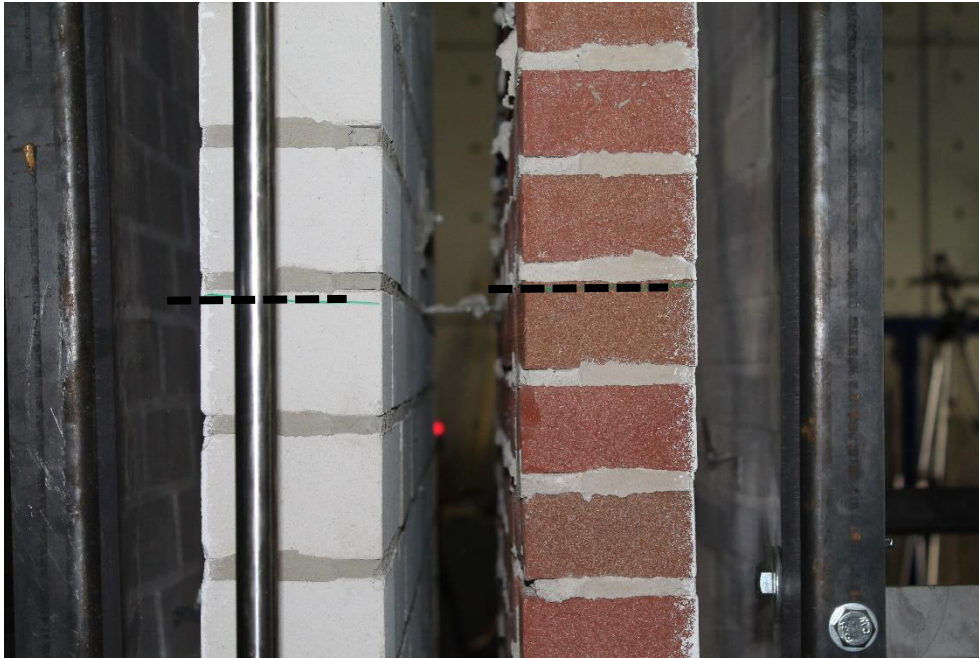
Figure 212 (left) is a snap-shot of the 5.2 test video where the test specimen showed a clear coupled rocking behaviour.

Figure 212 (right) shows the specimen deformed shape during 6.1 test, few instants before the specimen collapse.



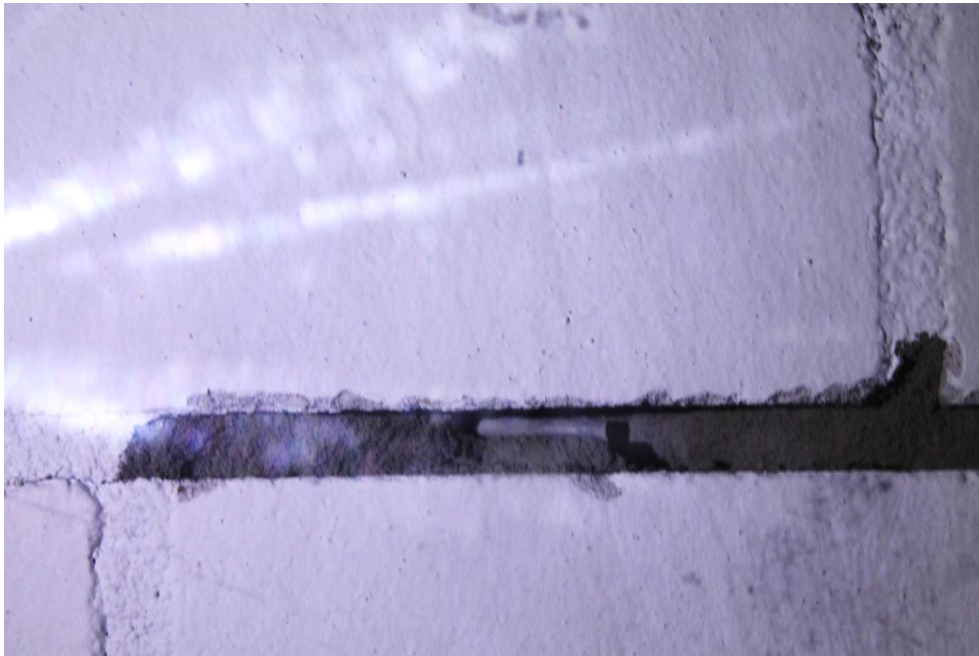
*Figure 212. Deformed shape of the EC\_COMP\_5 Specimen (left and right)*

Figure 213 shows the formation of mid-height cracks at the tie location after the 4.1 test.



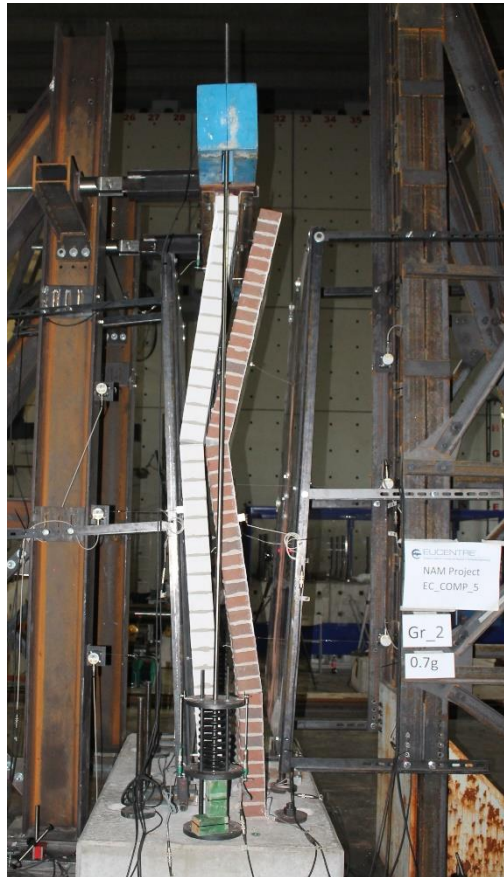
*Figure 213. Formation of mid-height cracks at the tie location*

Figure 214 shows the expulsion of part of the mortar bed joint due to the ties compression force (after 4.1 test).



*Figure 214. Expulsion of part of the mortar bed joint.*

Figure 215 shows the EC\_COMP\_5 specimen collapsed after the 6.1 test.



*Figure 215. Collapse of EC\_COMP\_5 Specimen.*

### 5.4.3 EC\_COMP\_6

#### Testing phase 1

In the testing phase 1 the test specimen have been subjected to Gr<sub>1</sub> acceleration inputs with opposite sign in order to investigate how the walls response could change with different excitation directions.

The response peaks recorded in this phase were associated always to a deformed shape where the outer leaf tried to increase the gap between the two walls pulling the ties, independently from the input excitation direction. The inner leaf deformed shape is the classical deformed shape of a beam in double fixed condition, while the outer leaf, much more flexible, tent to deform like a cantilever. Figure 216 shows the horizontal mid-height response peaks of both walls in the testing phase 1. The values shown represent maximum absolute values.

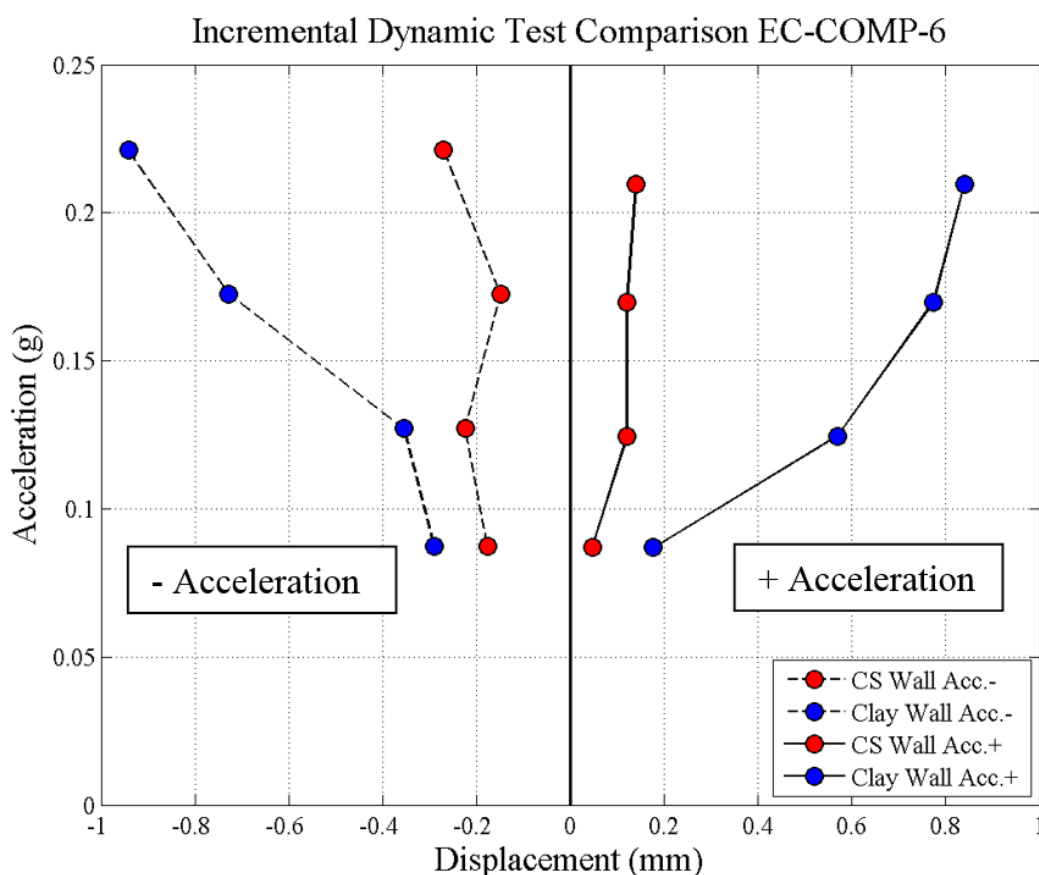


Figure 216. Experimental mid-height response peaks Gr<sub>1</sub> Tests (PGA vs. Max absolute response at mid-height).

The following figures show both walls deformed shapes associated to tests with different acceleration amplitudes. It is worth underlining as the horizontal displacement peaks shown are the ones recorded by the wire potentiometers located at  $\frac{1}{4}$ ,  $\frac{1}{2}$  and  $\frac{3}{4}$  and at

the top of the wall height (only for the clay wall); they represent the response peaks recorded during the overall test duration by each wire potentiometer.

A more refined representation of the deformed shape could be the plot of the horizontal displacement level achieved by each potentiometer at the testing moment where the mid-height clay wall displacement achieves the highest value. In this second way it will be possible to show the deformed shape snap-shot at the instant of the maximum horizontal mid-height displacement.

Figure 217 shows the deformed shapes of both walls associated to the 1.5 test.

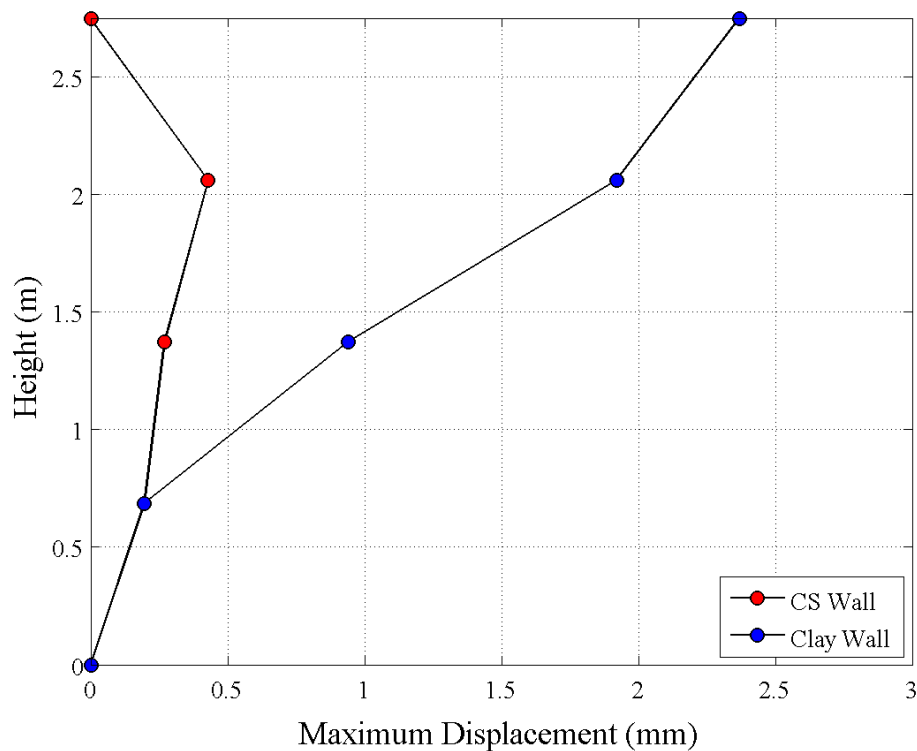


Figure 217. Comparison between maximum displacement profiles of CS and Clay Walls for the Test 1.5.

### Testing Phase 2&4

Next figure shows the horizontal mid-height displacement peaks associated to both walls for RWA inputs associated to different testing phases (phase 2 and phase 4).

RWA inputs with opposite signs have been performed in order to investigate how the walls response could change with different excitation directions.

Figure 218 shows the horizontal mid-height response peaks of both walls in the testing phases 2 and 4.

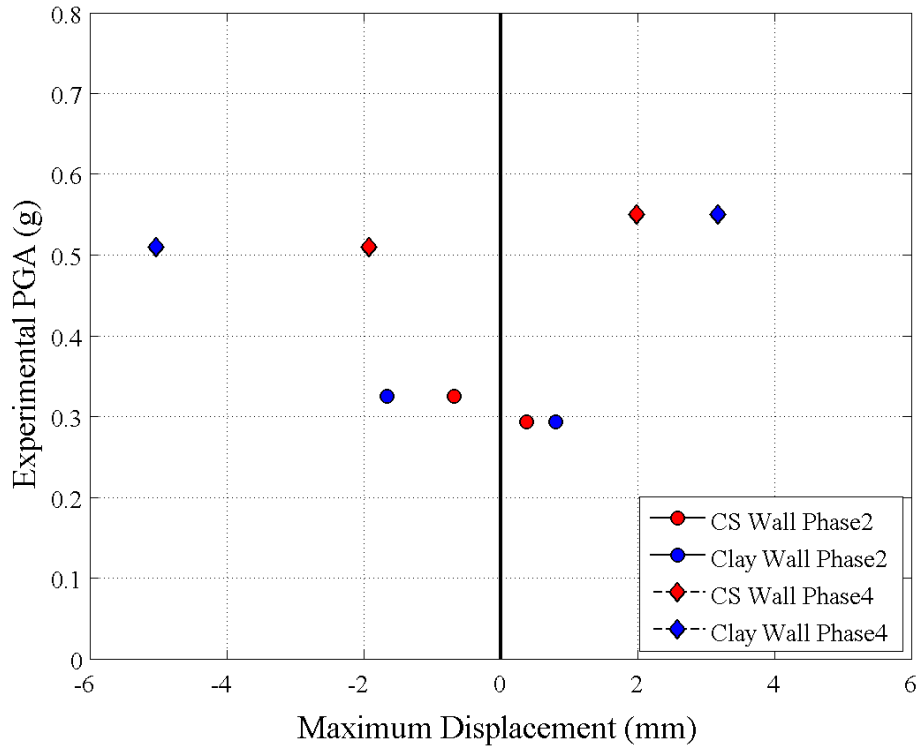


Figure 218. Experimental mid-height response peaks RWA Tests (PGA vs. Max response at mid-height).

Figure 219 shows the acceleration history recorded by the shake-table accelerometer during the 4.2 test.

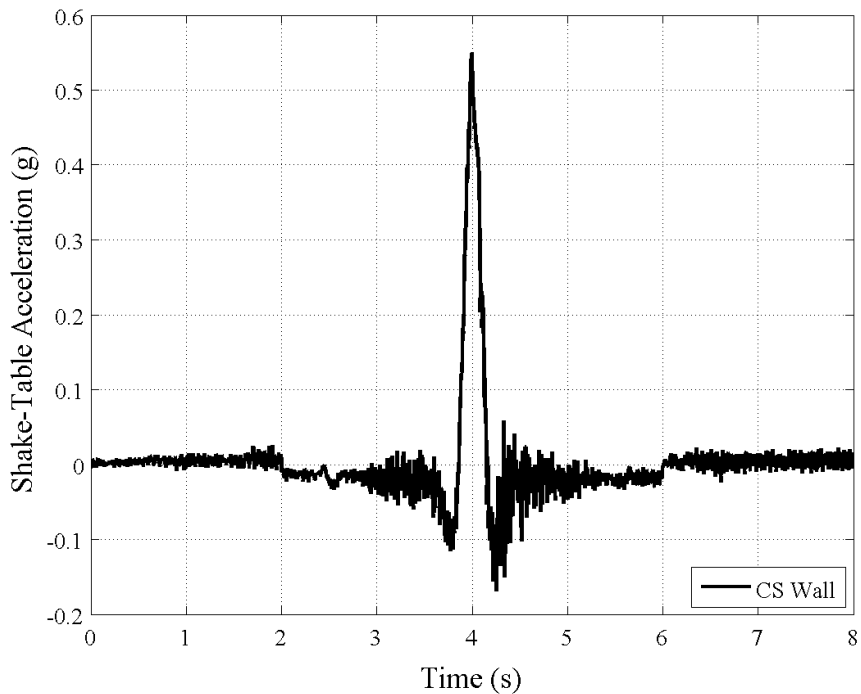


Figure 219. Shake-table Acceleration History during test 4.2.

Figure 220 shows the displacement history performed by the shake-table during the 4.2 test.

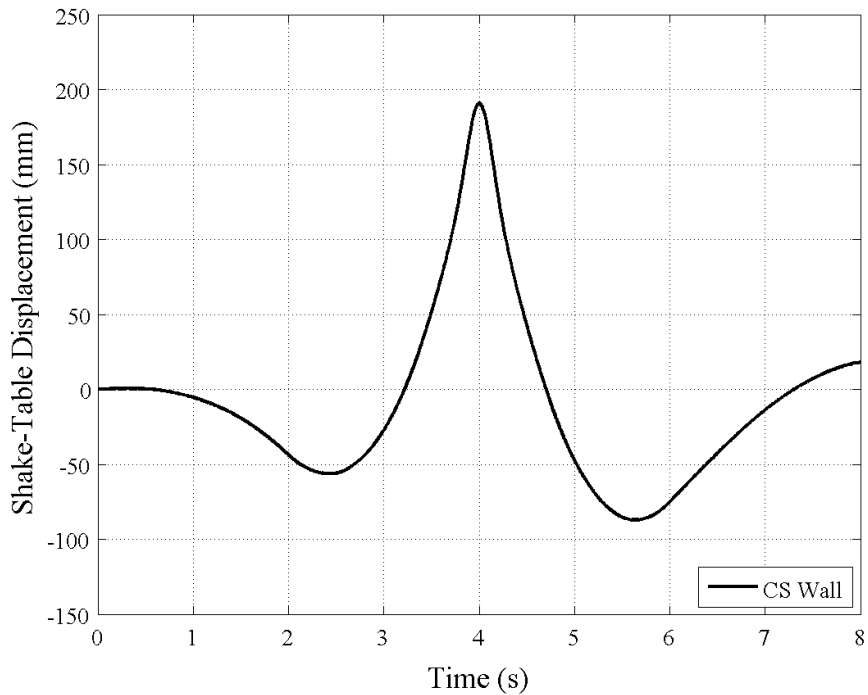


Figure 220. Shake-table Displacement History during test 4.2.

Figure 221 shows horizontal mid-height displacement histories of both walls for the 4.2 test.

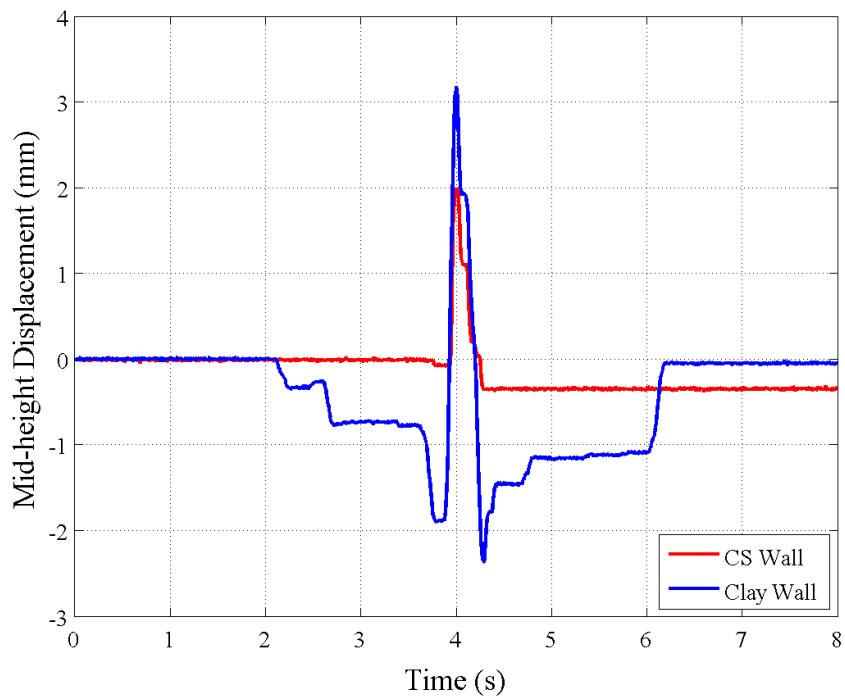


Figure 221. Horizontal mid-height displacement histories comparison between Calcium silicate (CS) and Clay Wall for the 4.2 Test.

Figure 222 shows the deformed shapes of both walls associated to the 4.1 test. In this case the impulse is in the tie pulling direction. It is worth noticing as the deformed shape is still characterised by an inner wall extremely rigid displaying as a double fixed beam element and an outer leaf, which moves almost independently as a cantilever element.

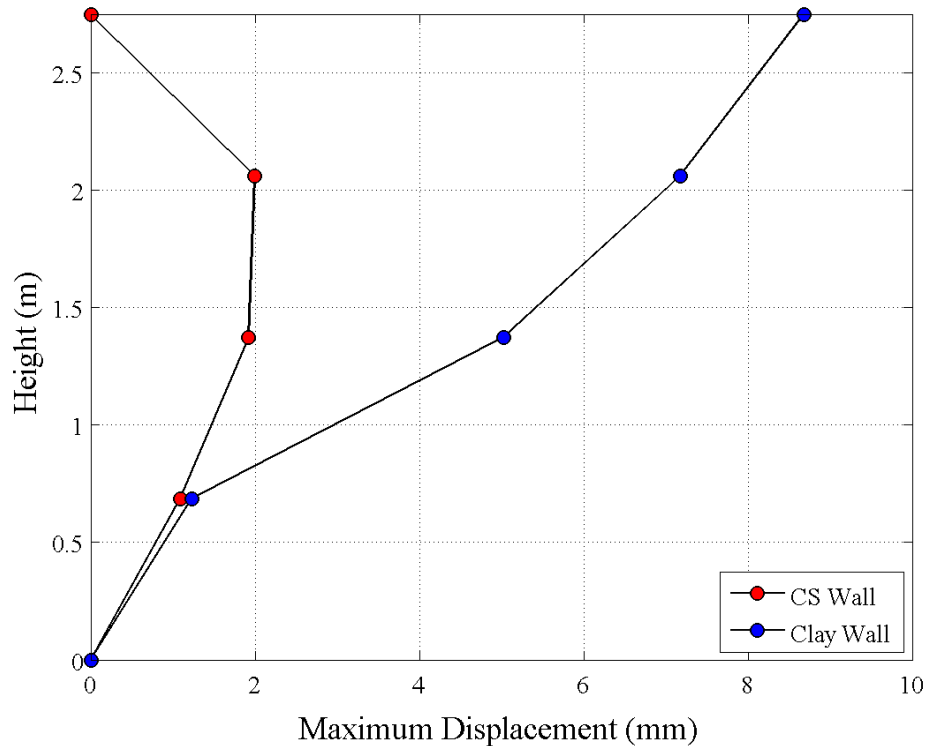


Figure 222. Comparison between maximum displacement profiles of CS and Clay Walls for the Test 4.1.

Figure 223 shows the comparison between top clay wall horizontal displacement histories recorded in each RWA test. The negative tests are the ones where the impulse is in the pulling ties direction. In particular, it can be seen as in test 4.2, although the impulse is in the ties compression direction, there is a significant displacement in the pulling ties direction that can be related to degradation of the anchorage on the clay mortar bed-joint due to test repetitions.

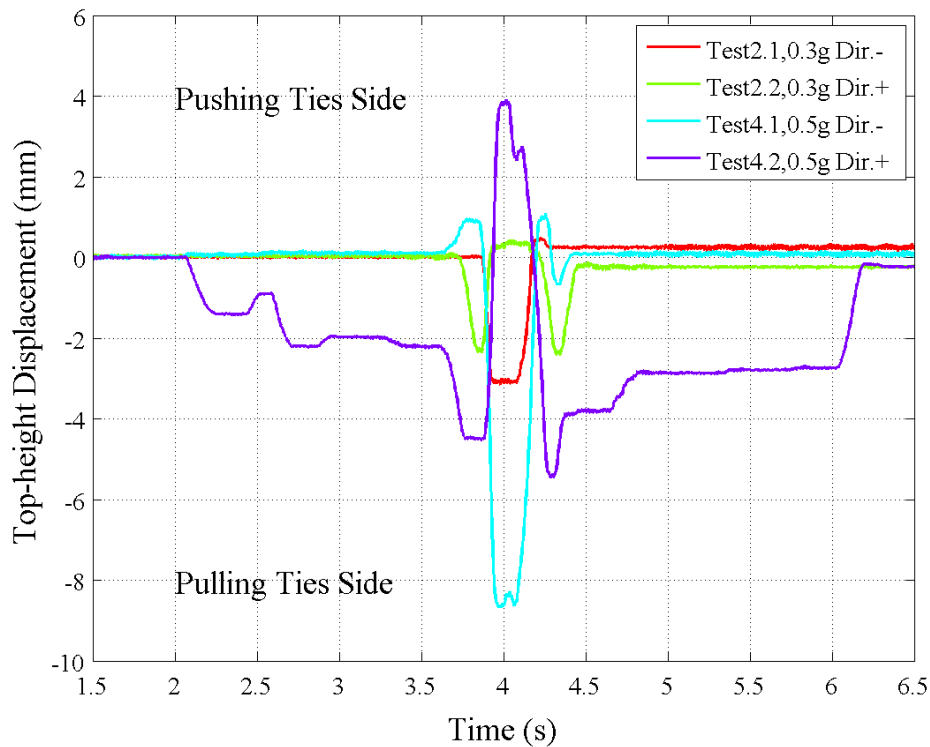


Figure 223. Comparison between top clay wall horizontal displacement histories recorded during each RWA test.

### Testing Phase 3&5

Figure 224 shows the horizontal mid-height response peaks associated to both walls for the Gr\_2 input in testing phases 3 and 5.

During the test 5.2 the walls touched the lateral support installed to prevent the failure of the wall. Although the specimen showed during all the tests a displaced shape characterised by the two walls moving rather independently, the collapse was associated to the activation of the one-way coupled rocking behaviour. The specimen after bouncing on the lateral support exhibited the separation of the two leaves and the failure of the clay wall against the support located in the opposite side. The CS wall instead, came back to its initial position.

Figure 225 shows horizontal mid-height displacement histories of both walls for the 5.1 test. It can be seen as the degradation of the ties anchorage lead to a significant free oscillation phase of the veneer wall at the end of each test. This could be used in order to calculate the degradation of the coupling system.

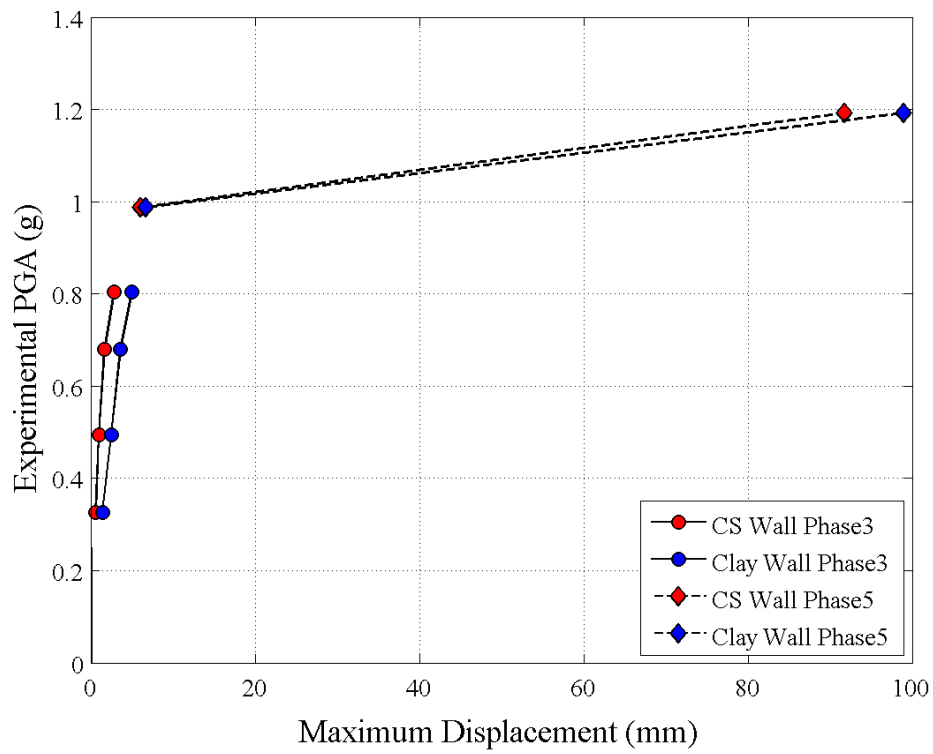


Figure 224. Experimental mid-height response peaks Gr\_2 Tests (PGA vs. Max response at mid-height).

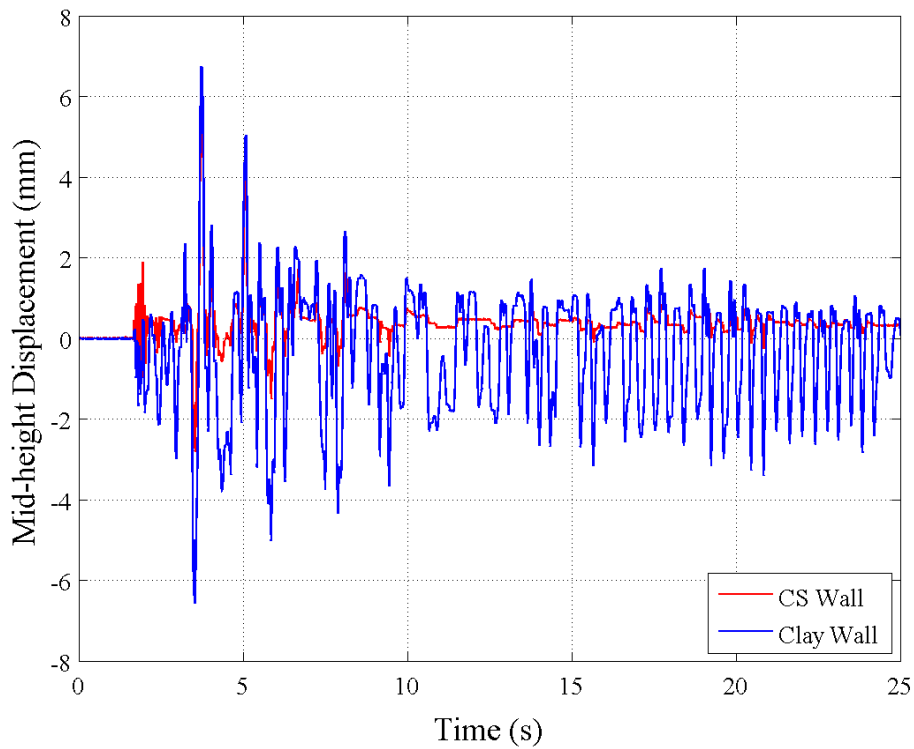


Figure 225. Horizontal mid-height displacement histories comparison between Calcium silicate (CS) and Clay Wall for the 4.2 Test.

Figure 226 shows the deformed shapes of both walls associated to the 5.1 test.

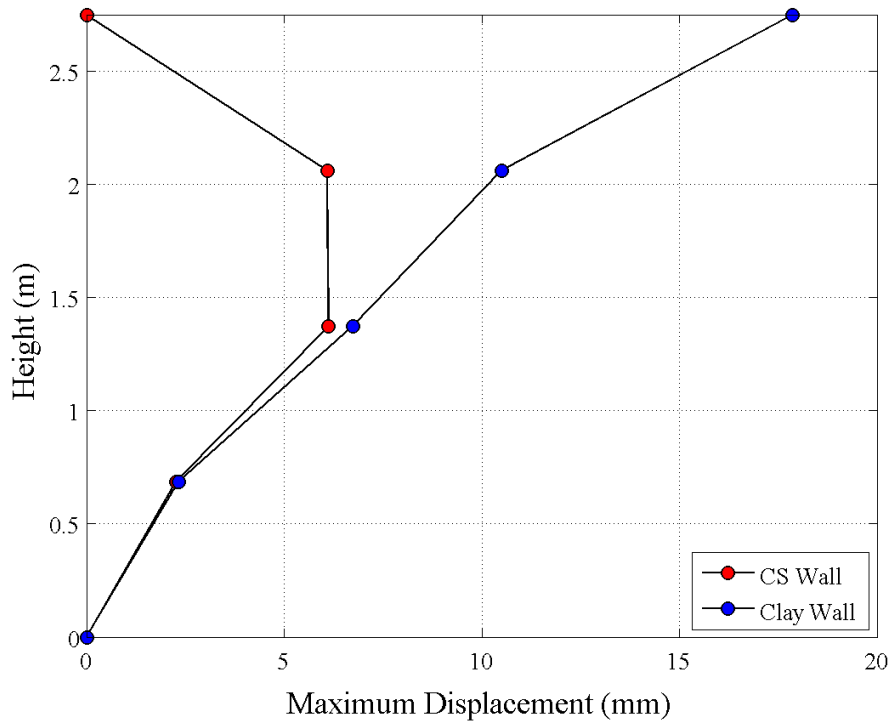


Figure 226. Comparison between maximum displacement profiles of CS and Clay Walls for the Test 5.1.

Figure 227 shows horizontal mid-height displacement histories of the CS wall for the test 5.2. The veneer wall potentiometer was removed to prevent its damage.

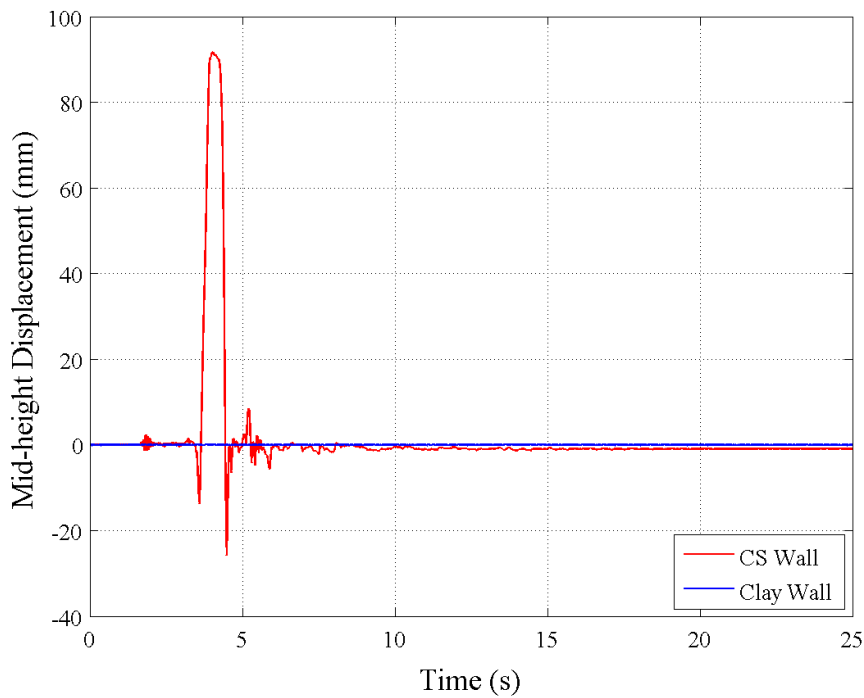


Figure 227. Horizontal mid-height displacement history of Calcium silicate (CS) for the 5.2 Test.

Figure 228 shows a snap-shot of the CS wall deformed shape few instants before the specimen collapse. The deformed shape is clearly the one associated to rocking behaviour already seen for all the others specimens. As previously discussed the veneer wall potentiometers were removed in order to prevent their damage.

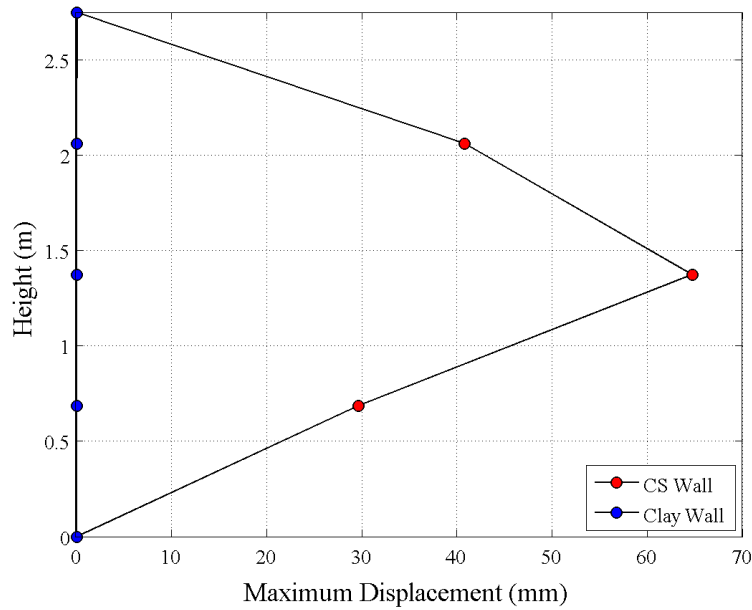


Figure 228. CS Wall Deformed Shape few instants before the collapse (Test 5.2.)

Figure 214Figure 229 shows the damage of the mortar bed joint due to the ties compression force (after 4.1 test).



Figure 229. Damage on the Mortar Bed-joint (after Test 5.1.)

Figure 230 (left) is a snap-shot of the test 5.2 video where the test specimen showed a clear coupled rocking behaviour touching the lateral support. Figure 230 (right) shows the specimen during the end of the test 5.2 and the separation between the two leaves.



*Figure 230. Deformed shape of the EC\_COMP\_6 Specimen (left and right).*

Figure 231 shows the formation of mid-height crack at the end of the test 5.2.



*Figure 231. Formation of mid-height crack (after Test 5.1.).*

Figure 232 shows the collapse of the outer leaf at the end of the test 5.2. It is worth noticing as the clay collapse is associated to the expulsion of the ties from CS wall bed-joints.



*Figure 232. Separation of the two leaves (during Test 5.1.).*

Figure 233 shows the EC\_COMP\_6 specimen collapsed after the 5.2 test.

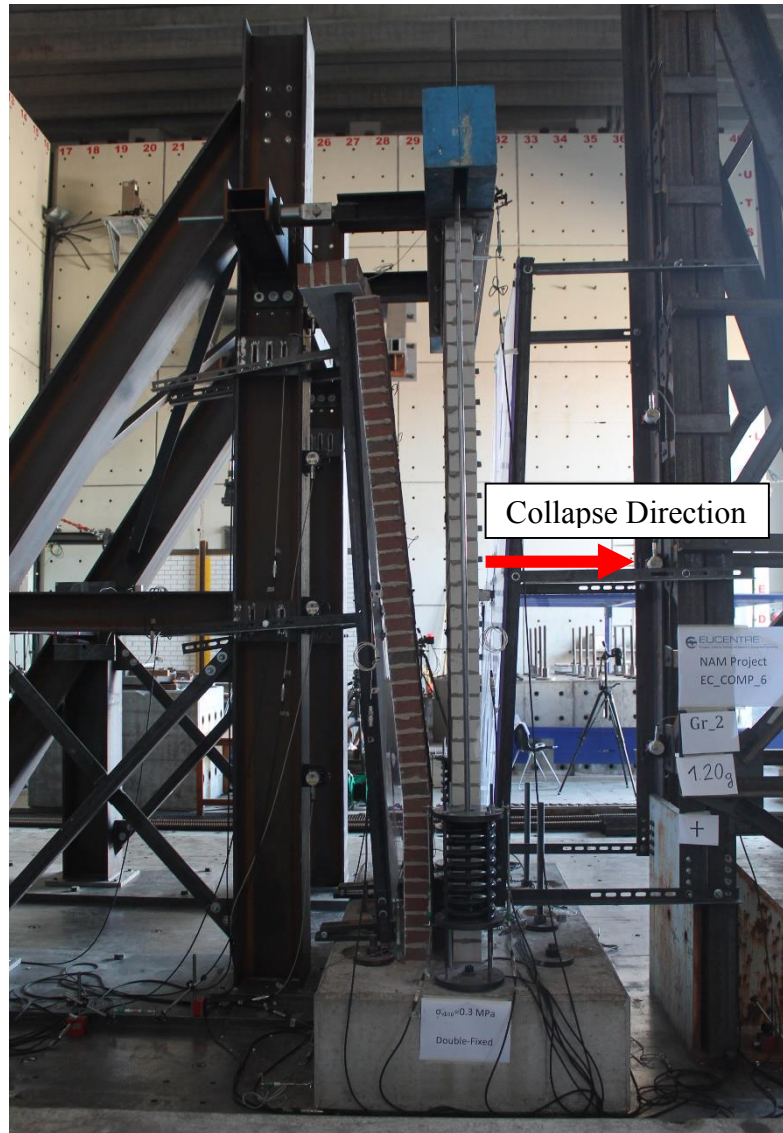


Figure 233. Collapse of EC\_COMP\_6 Specimen (after test 5.2).

## 5.4.4 EC\_COMP\_7

### Testing phase 1

In the testing phase 1 the test specimen have been subjected to incremental Gr<sub>1</sub> acceleration inputs. Figure 234 shows the horizontal mid-height response peaks of both walls in the testing phase 1.

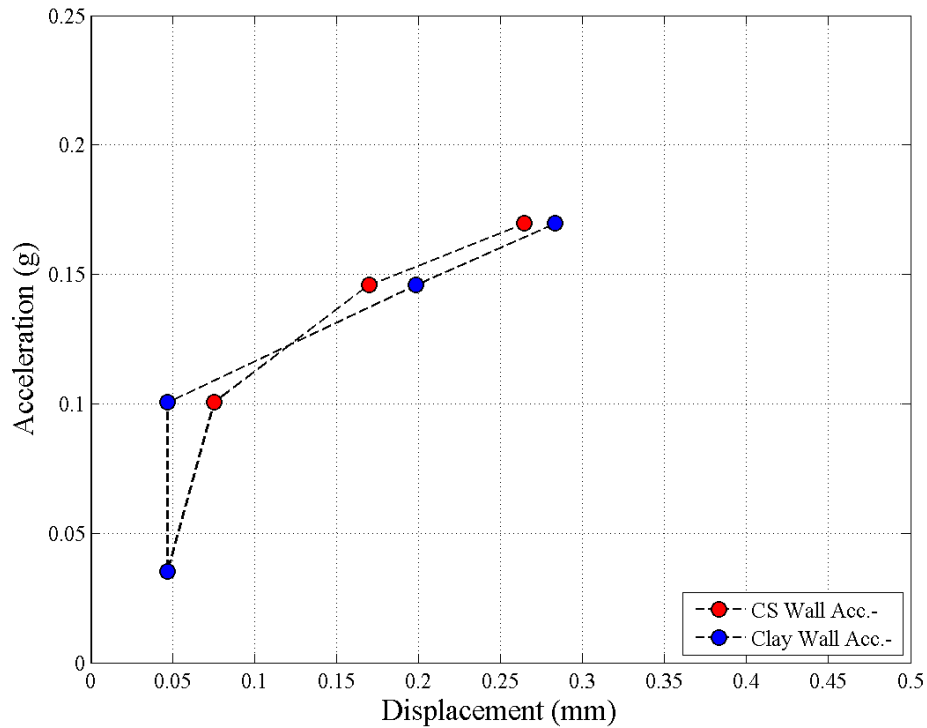


Figure 234. Experimental mid-height response peaks Gr<sub>1</sub> Tests (PGA vs. Max response at mid-height).

The following figures show both walls deformed shapes associated to tests with different acceleration amplitudes. It is worth underlining as the horizontal displacement peaks shown are the ones recorded by the wire potentiometers located at  $\frac{1}{4}$ ,  $\frac{1}{2}$  and  $\frac{3}{4}$  wall height and at the top (only for the clay wall); they represent the response peaks recorded during the overall test duration by each wire potentiometer.

A more refined representation of the deformed shape could be the plot of the horizontal displacement level achieved by each potentiometer at the testing moment where the mid-height clay wall displacement achieves the highest value. In this second way, it will be possible to show the deformed shape snap-shot at the instant of the maximum horizontal mid-height displacement.

Figure 235 shows the deformed shapes of both walls associated to the 1.6 test.

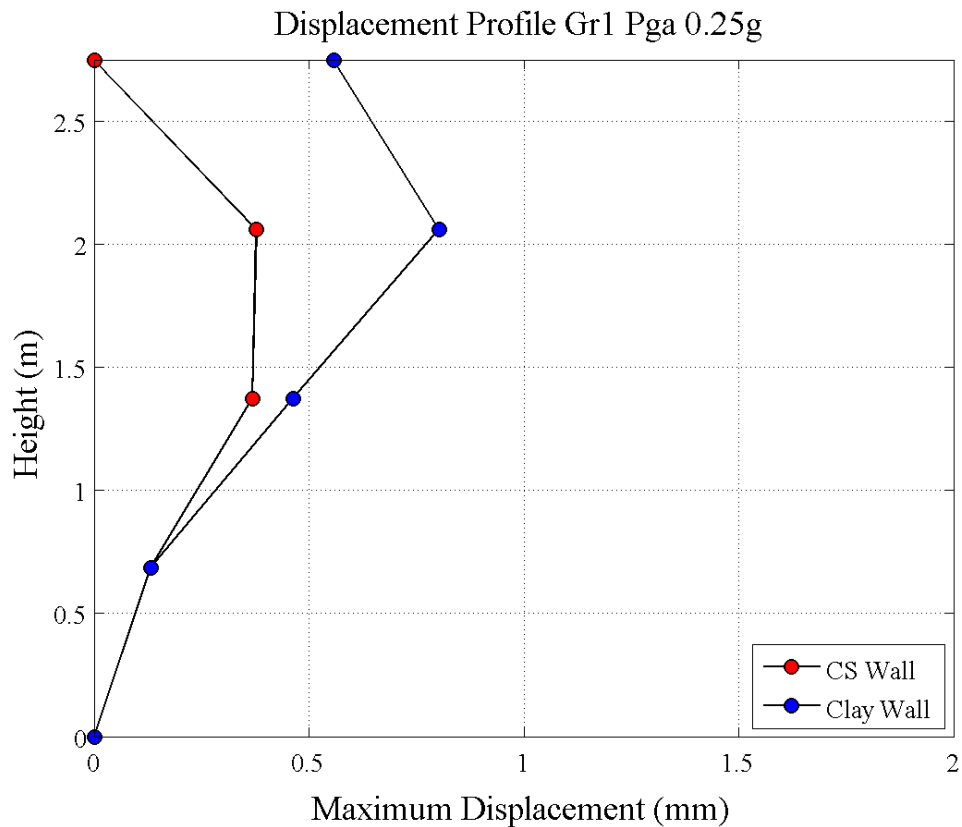


Figure 235. Comparison between maximum displacement profiles of CS and Clay Walls for the Test 1.6.

### Testing Phase 2&4

Next figure shows the horizontal mid-height displacement peaks associated to both walls for RWA inputs associated to different testing phases (phase 2 and phase 4).

RWA inputs with opposite signs have been performed in order to investigate how the walls response could change with different excitation directions.

Figure 236 shows the horizontal mid-height response peaks of both walls in the testing phases 2 and 4 considering the absolute response in negative (right) and positive (left) directions.

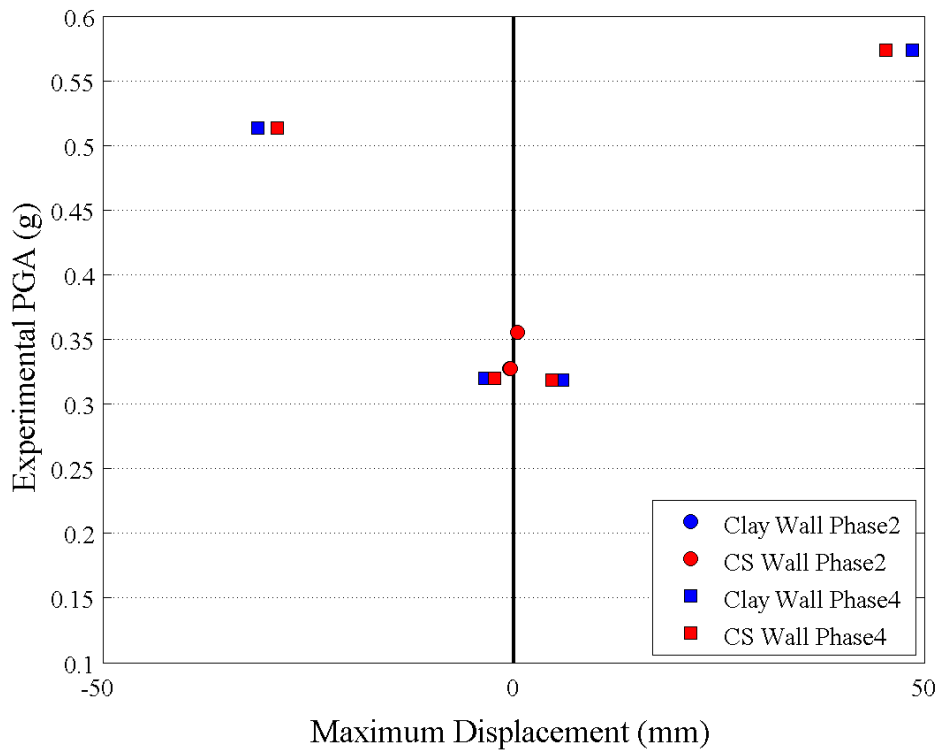


Figure 236. Experimental mid-height response peaks RWA Tests (PGA vs. Max response at mid-height).

Figure 237 shows the acceleration history recorded by the shake-table accelerometer during the 4.5 test.

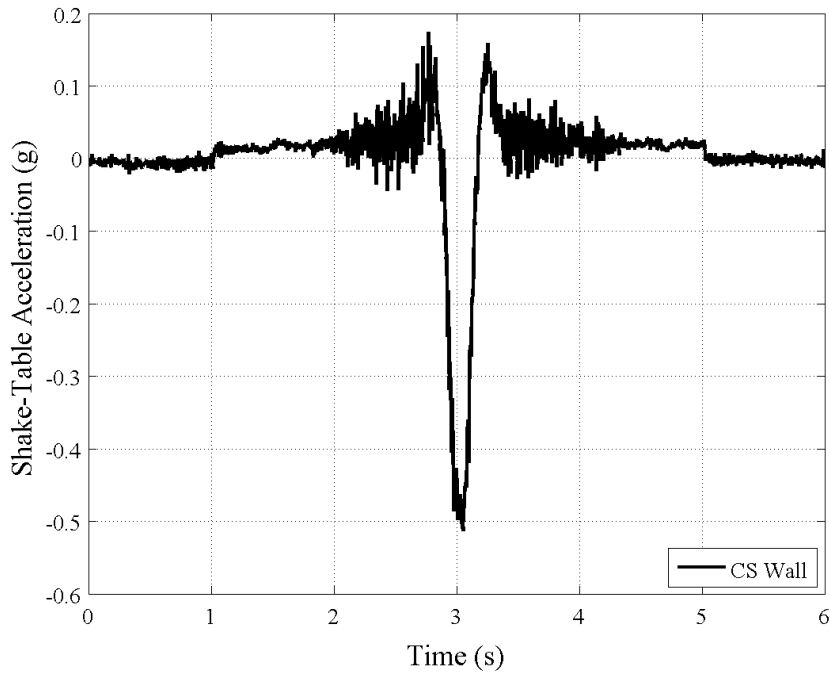


Figure 237. Shake-table Acceleration History during test 4.5.

Figure 238 shows the displacement history performed by the shake-table during the 4.5 test.

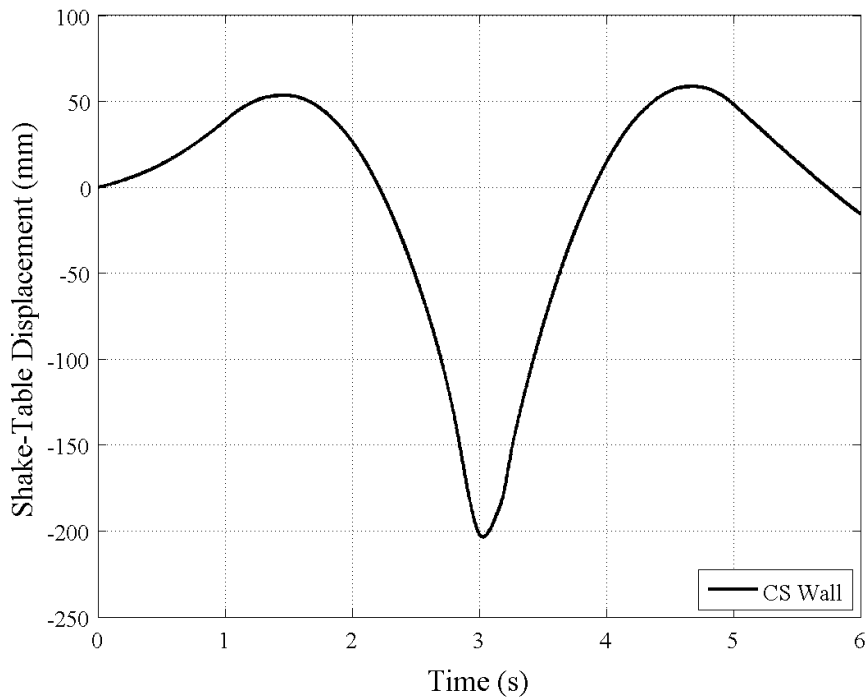


Figure 238. Shake-table Displacement History during test 4.5.

Figure 242 shows horizontal mid-height displacement histories of both walls for the 4.5 test.

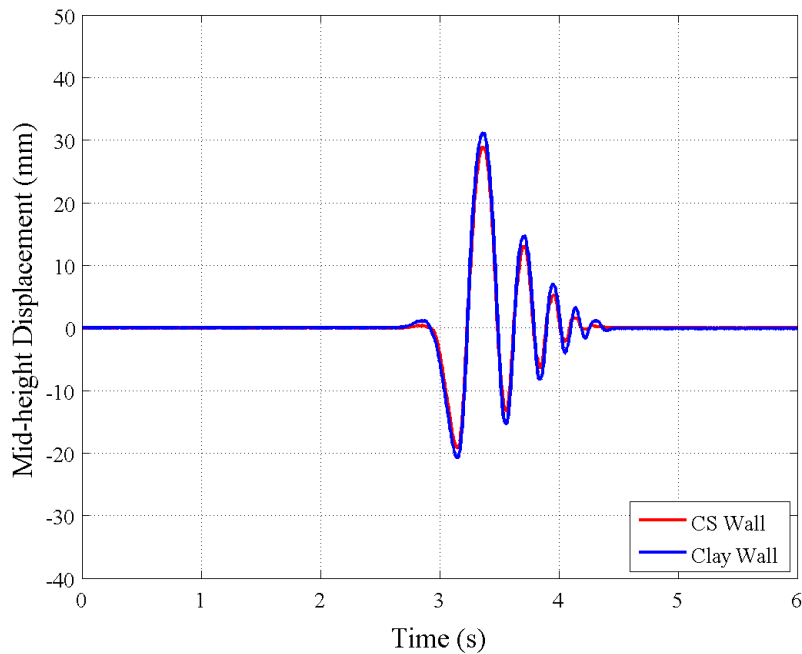


Figure 239. Horizontal mid-height displacement histories comparison between Calcium silicate (CS) and Clay Wall for the 4.5 Test.

Figure 240 shows the acceleration history recorded by the shake-table accelerometer during the 4.6 test.

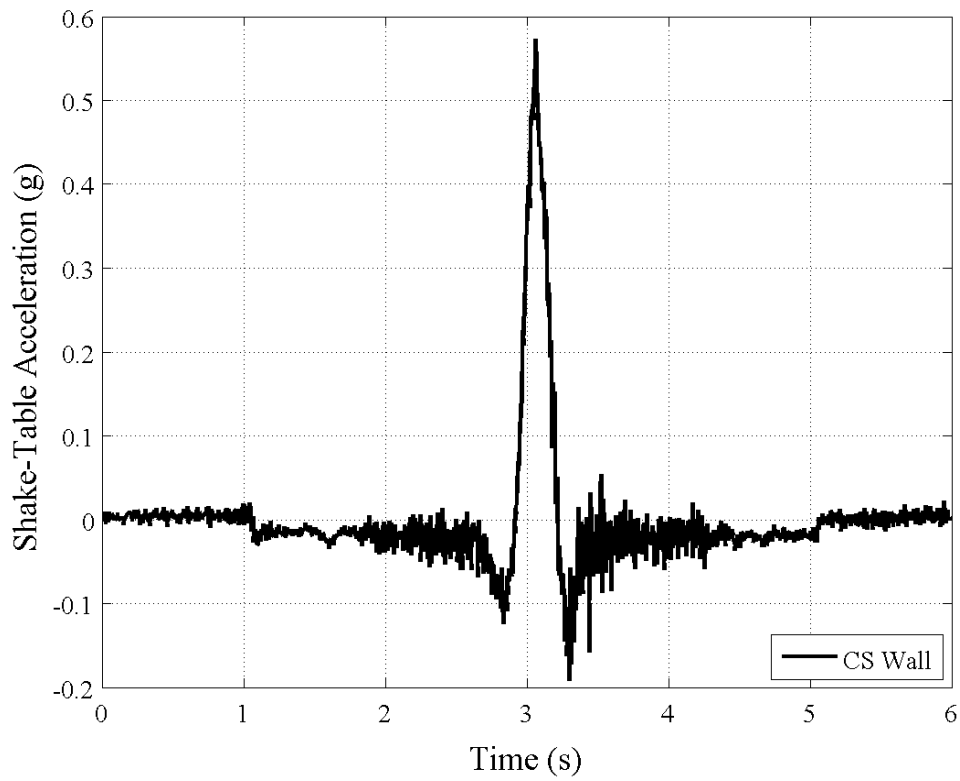


Figure 240. Shake-table Acceleration History during test 4.6.

Figure 241 shows the displacement history performed by the shake-table during the 4.6 test.

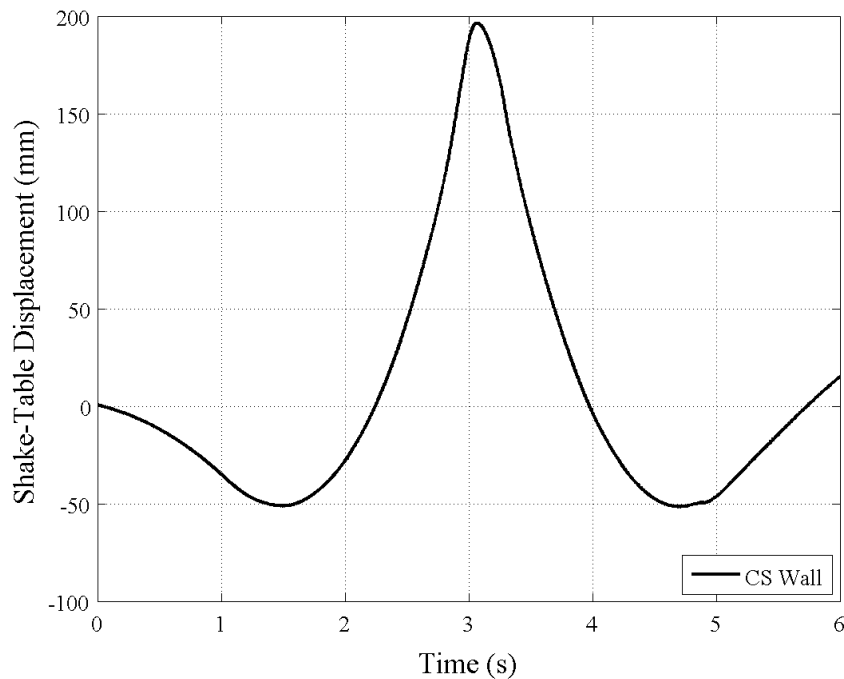
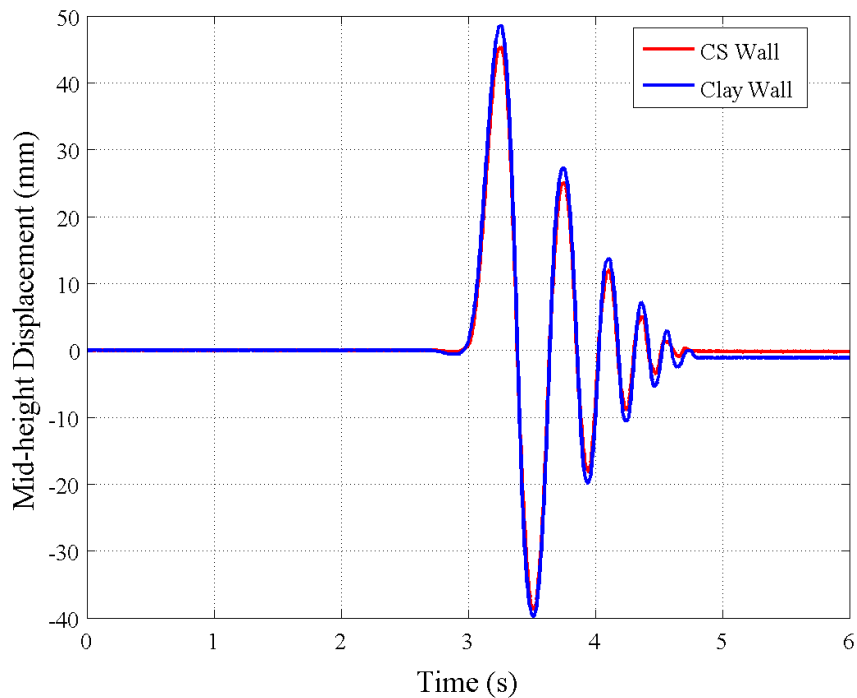


Figure 241. Shake-table Displacement History during test 4.6.

Figure 242 shows horizontal mid-height displacement histories of both walls for the 4.6 test.



*Figure 242. Horizontal mid-height displacement histories comparison between Calcium silicate (CS) and Clay Wall for the 4.6 Test.*

### Testing Phase 3&5

Next figure shows the horizontal mid-height response peaks associated to both walls for the Gr<sub>2</sub> input. Gr<sub>2</sub> inputs with opposite signs have been performed in order to investigate how the walls response could change with different excitation directions. During the test 5.2 the walls showed so high horizontal displacements to touch the lateral support installed to prevent the failure of the wall. Although this further two test (5.3 and 5.4) were then performed.

Figure 243 shows the horizontal mid-height response peaks of both walls in testing phases 3 and 5.

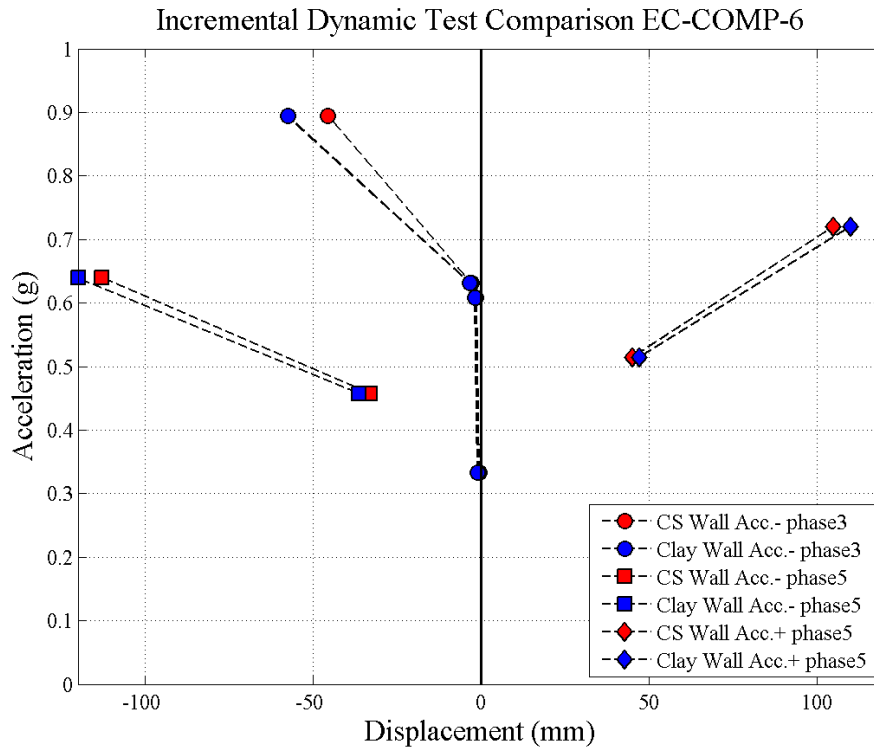


Figure 243. Experimental mid-height response peaks Gr\_2 Tests (PGA vs. Max absolute response at mid-height).

Figure 244 shows horizontal mid-height displacement histories of both walls for the 3.4 test.

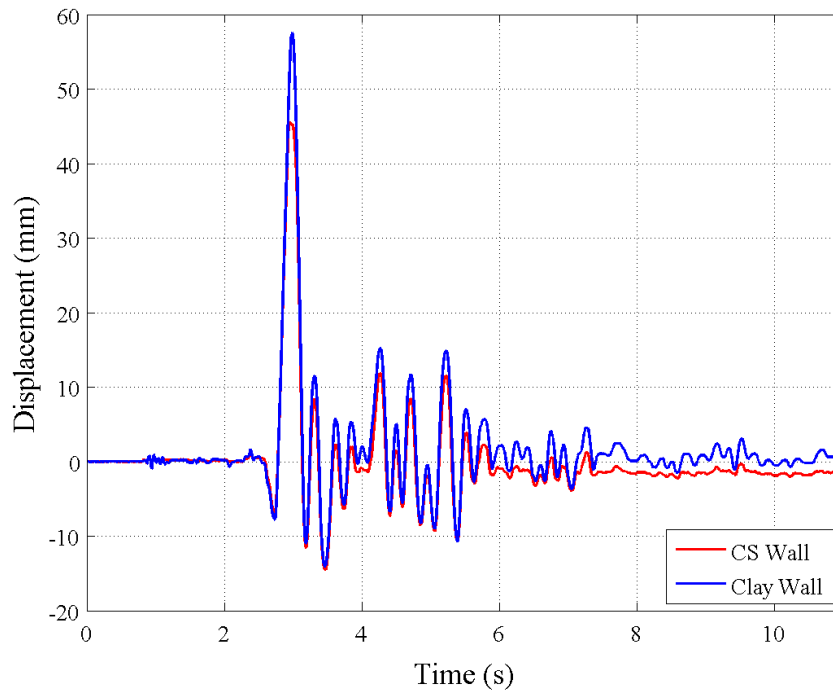


Figure 244. Horizontal mid-height displacement histories comparison between Calcium silicate (CS) and Clay Wall for the 3.4 Test.

For high input intensity (such test 3.4) the two walls showed a clear coupled rocking behaviour with the formation of cracks at the walls bottom, top and around mid-height sections. Figure 245 shows the deformed shapes of both walls associated to the 1.6 test.

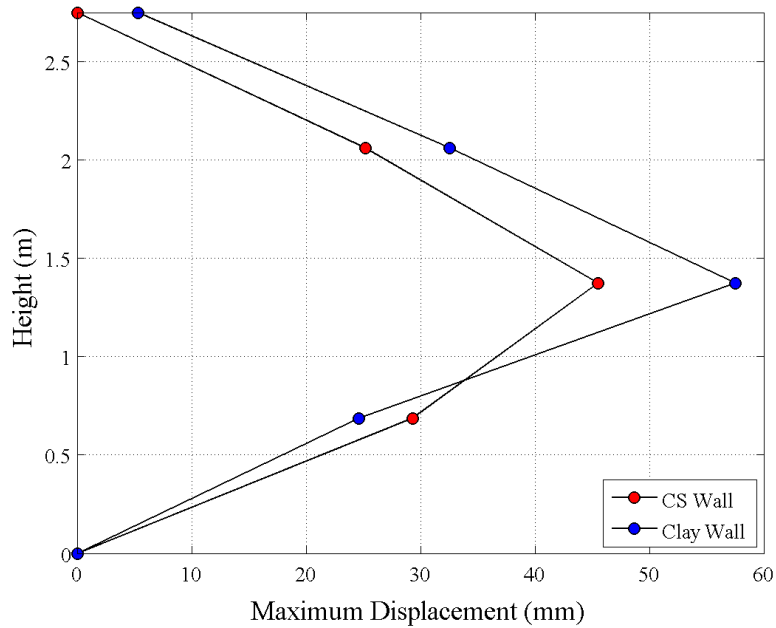


Figure 245. Comparison between maximum displacement profiles of CS and Clay Walls for the Test 3.4.

Figure 246 shows horizontal mid-height displacement histories of both walls for the 5.1 test.

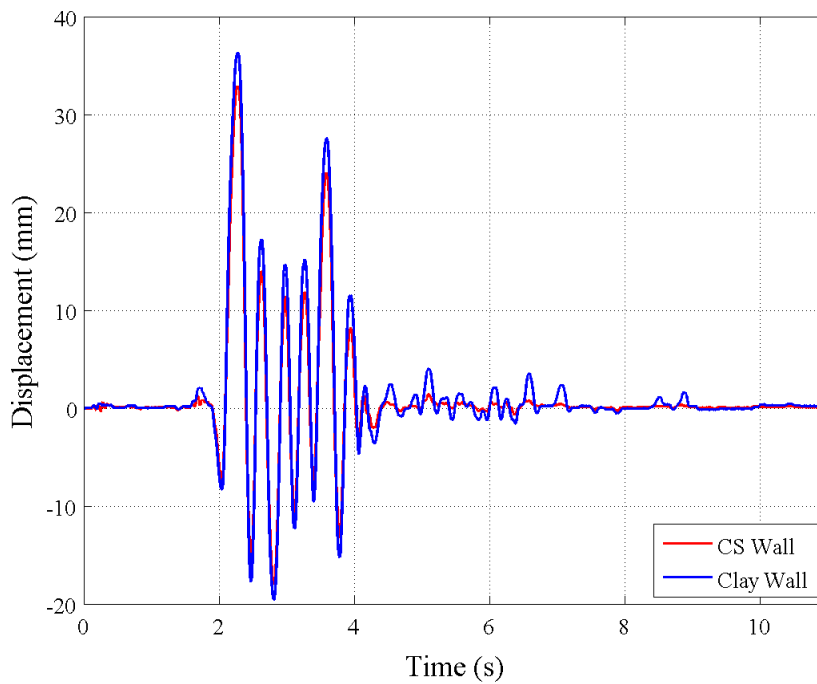


Figure 246. Horizontal mid-height displacement histories comparison between Calcium silicate (CS) and Clay Wall for the 5.1 Test.

Figure 247 shows the deformed shapes of both walls associated to the 5.1 test.

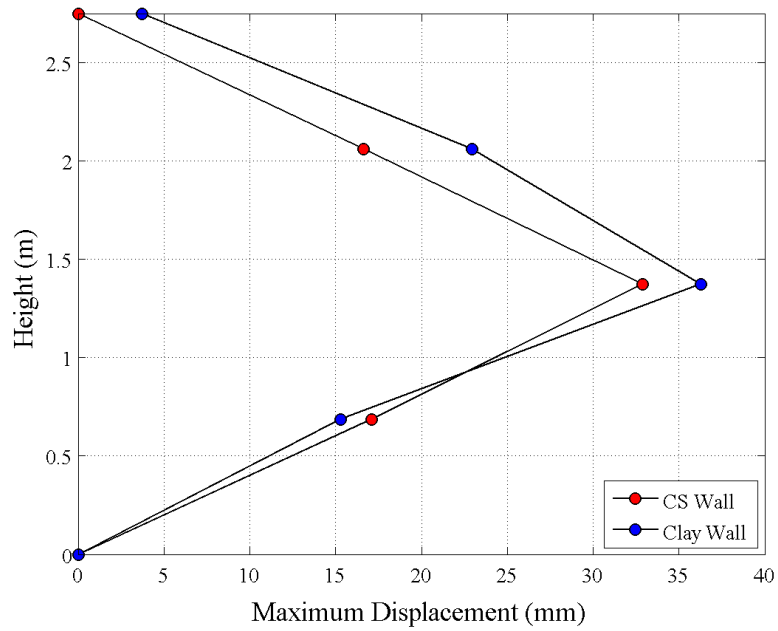


Figure 247. Comparison between maximum displacement profiles of CS and Clay Walls for the Test 5.1.

Figure 248 shows the horizontal mid-height displacement history of the Calcium silicate wall for the 5.3 test. The potentiometer located at the clay wall mid-height was removed to prevent its damage with the forthcoming failure of the wall.

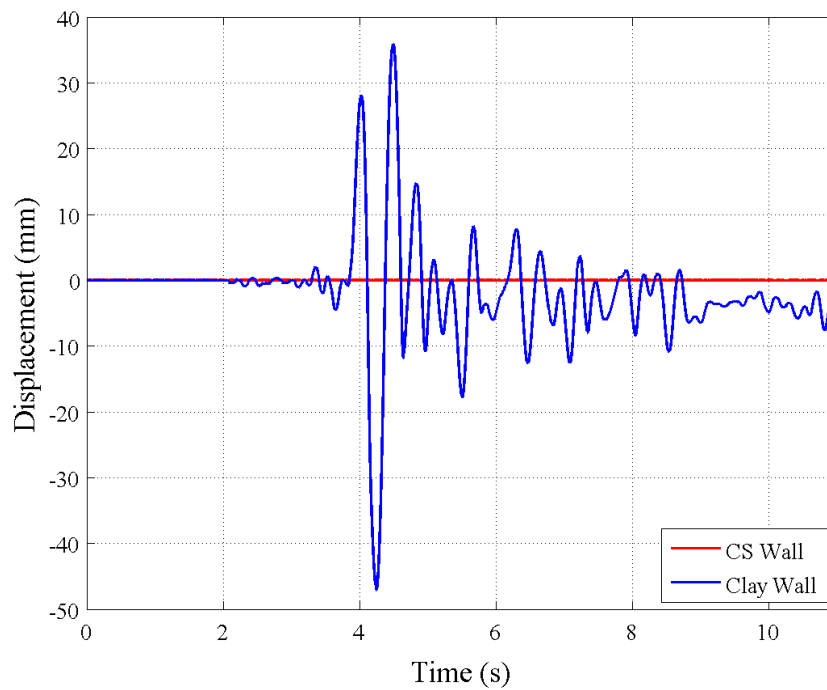
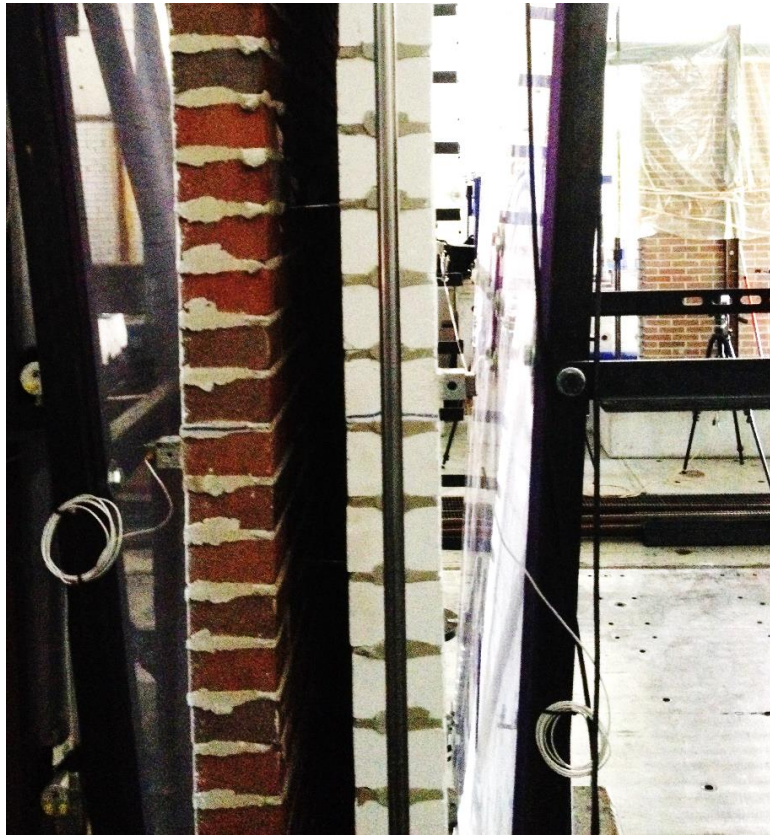


Figure 248. Horizontal mid-height displacement histories comparison between Calcium silicate (CS) and Clay Wall for the 5.3 Test.

Figure 213 shows the formation of mid-height cracks.



*Figure 249. Formation of mid-height cracks.*

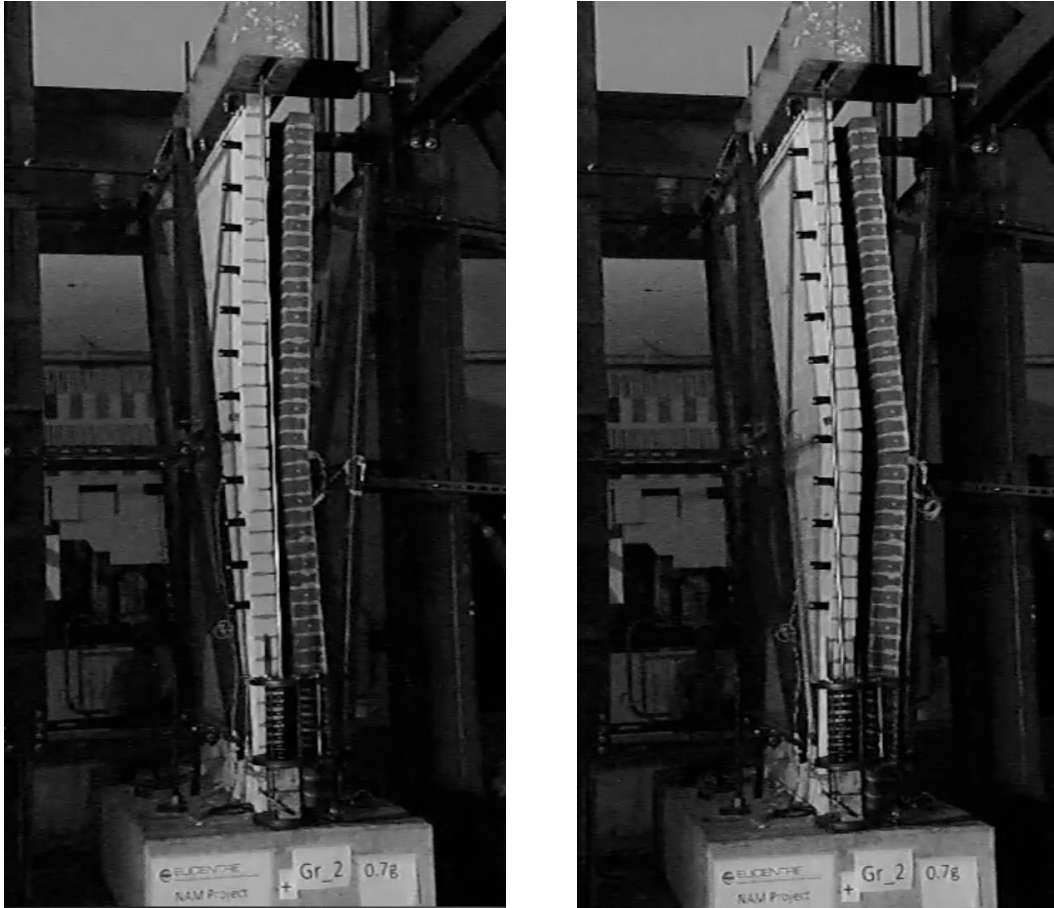
Figure 250 shows the damage of the mortar bed joint due to the ties compression force (after 4.1 test).



*Figure 250. Damage of the mortar bed joint.*

Figure 251 (left) is a snap-shot of the 4.6 test video where the test specimen showed a clear coupled rocking behaviour.

Figure 251 (right) shows the specimen deformed shape during 5.4 test, few instants before the specimen collapse.



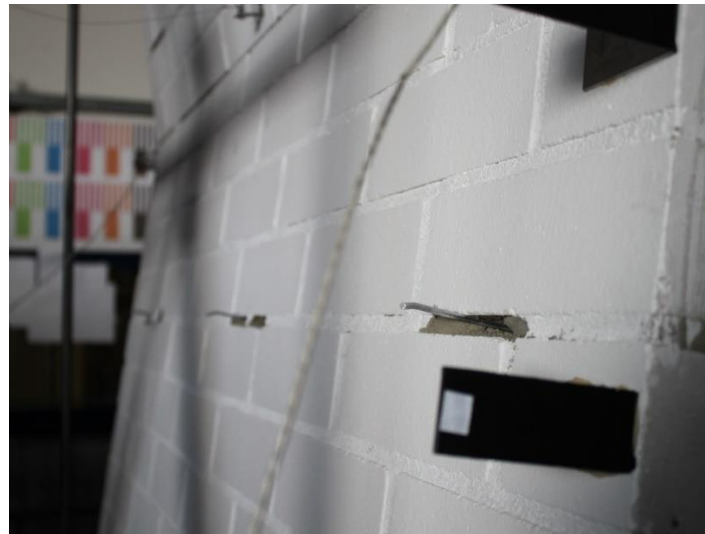
*Figure 251. Deformed shape of the EC\_COMP\_7 Specimen (left and right)*

Figure 252 shows the EC\_COMP\_7 specimen collapsed after the 5.4 test.



*Figure 252. Collapse of EC\_COMP\_7 Specimen.*

Figure 253 shows the expulsion of the ties.



*Figure 253. Damage of the mortar bed joint.*

#### 5.4.5 Deformed shapes

The deformed shapes here in presented have been built according to the horizontal displacement recorded by each wire potentiometer installed on the specimen at the moment of the CS wall mid-height horizontal displacement absolute response peak.

Figure 254 shows the deformed shapes associated to all the specimen for the Gr1-100% test where the peak acceleration direction is towards the positive displacement for the first two specimens and towards the clay wall side for the last three. The CS wall deformed shape is represented by the red line, while the clay wall one by the blue line. The EC-COMP-5 specimen doesn't show any clay wall top displacement because the instrument wasn't installed for such test series.

All the specimen are in their elastic phases, the CS wall tent to deform as a classical double fixed beam with the response peaks recorded by the wire potentiometers located at  $\frac{3}{4}$  and  $\frac{1}{2}$  of the wall height. The clay wall, instead, in cavity wall specimens, tent to display quite independently presenting the classical cantilever deformed shape. As a results, the relative horizontal displacement between the two walls is higher at the top as shown by the EC\_COMP\_5 and EC\_COMP\_6 specimens. Such phenomenon is less evident for the EC\_COMP\_7 specimen where the number of tie for squared metre is higher.

The cavity wall specimens, displaying as previously described, have shown for low intensity levels indeed, a progressive deterioration of the bond of the tie anchoring system.

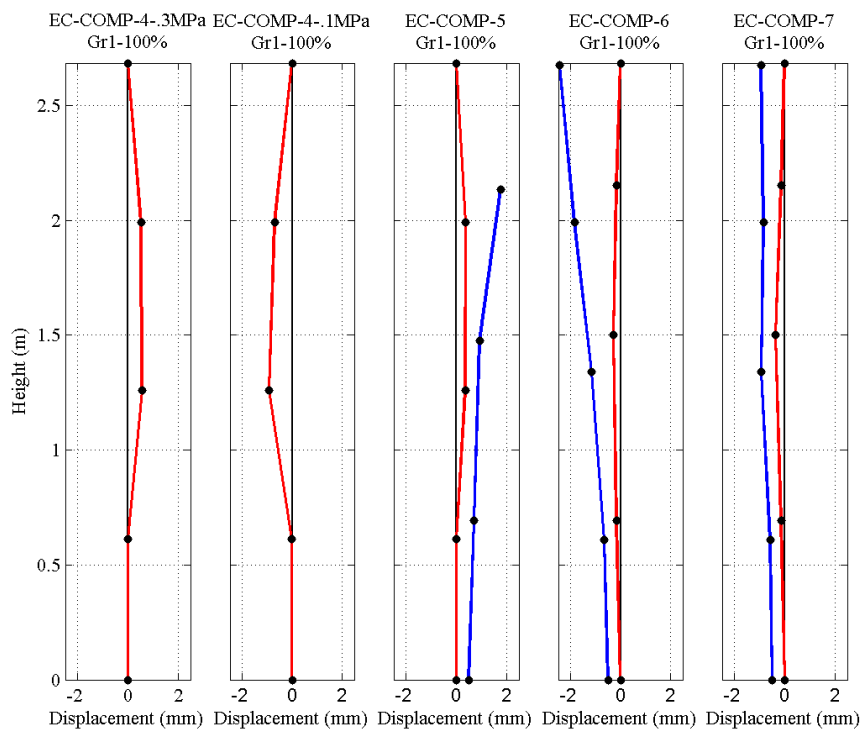


Figure 254. Specimens Deformed Shape Gr1 Input (red for CS Wall, blue for Clay Wall).

Figure 255 shows the deformed shapes associated to all the specimen for different RWA input tests where the peak acceleration direction is towards negative displacements for the first two walls and towards the CS wall side (e.g. pulling the ties) for the cavity specimens.

As the acceleration input and the horizontal displacement consequently, increase the deformed shapes change significantly; the single leaf specimen has shown the formation of cracks at the wall bottom, top and around mid-height sections displaying in rocking behaviour. The two almost rigid bodies above and below the mid-height crack sections rotate around the cracked sections using them as pivot points. This behaviour is particularly evident in the EC\_COMP\_4 specimen with an overburden pressure applied equal to 0.1 MPa.

Also cavity wall specimens exhibit clear coupled rocking behaviours with the formation of cracks at both walls bottom and around mid-height sections. Clearly, the crack at the wall top was detected only on calcium silicate walls, being the clay wall top free of any constraint. It is possible also to appreciate the difference in the response between the cavity wall specimens, where the EC\_COMP\_6 show a considerable lower mid-height deformation when subjected to inputs with similar PGAs.

Figure 256 shows the specimens deformed shape in near collapse conditions. In the EC-COMP-6 specimen case the wire potentiometers installed on the veneer wall have been removed in order to prevent their damage. Again, all the specimens exhibit clear rocking behaviour.

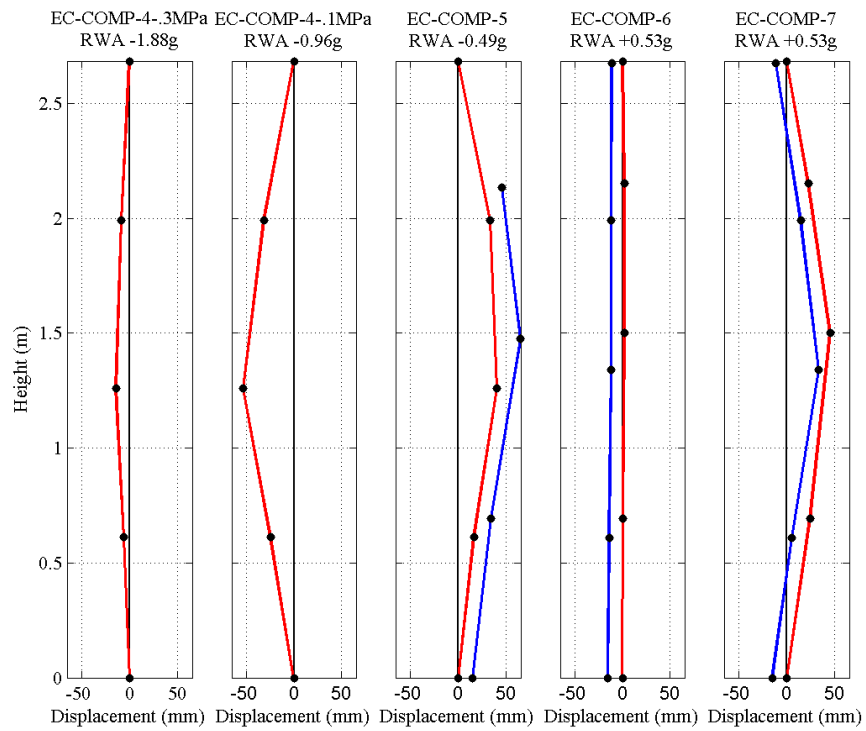


Figure 255. Specimens Deformed Shape RWA Input (red for CS Wall, blue for Clay Wall).

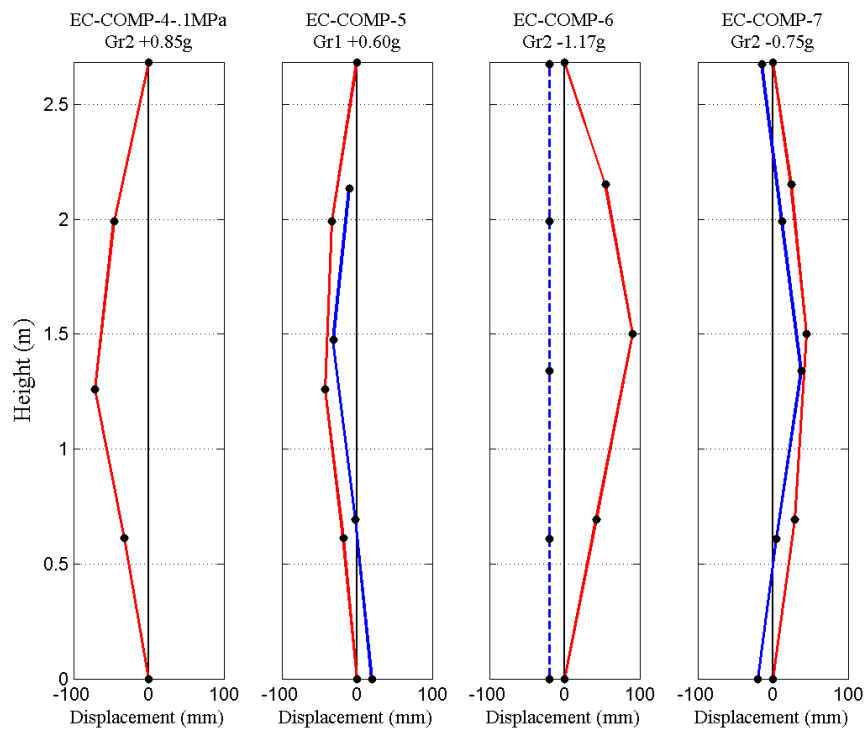
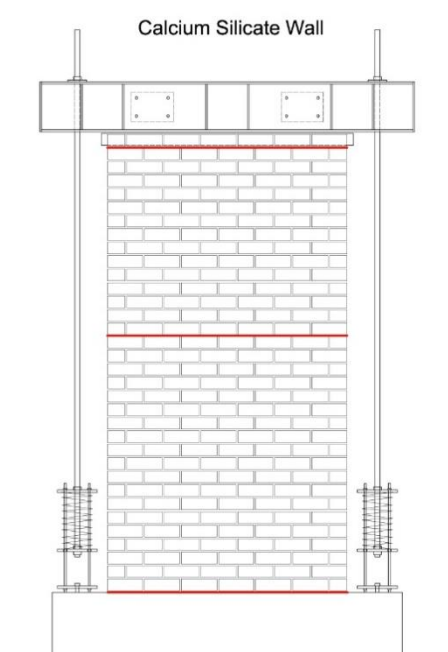


Figure 256. Specimens Deformed Shape near Collapse Limit State (red for CS Wall, blue for Clay Wall).

### 5.4.6 Damage Pattern

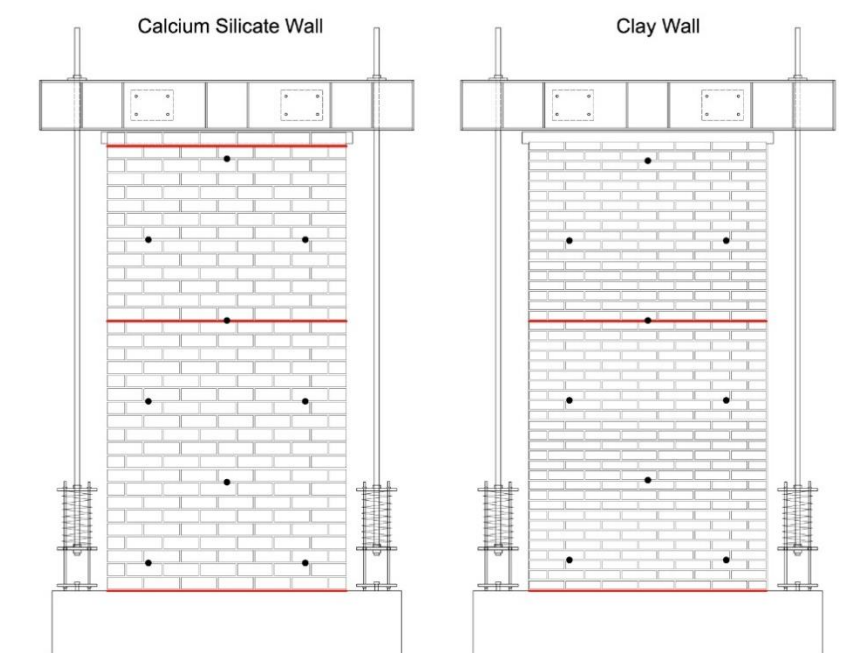
As previously mentioned, all the specimen have shown rocking behaviour with the formation of horizontal cracks at the walls bottom, top and around mid-height sections. The present section identifies the location of cracks for both calcium silicate wall and clay wall for all the specimen tested. The cracks are highlined in red. The metal ties grid is also shown to better understand the position of horizontal cracks with respect to the anchoring system between the two walls.

Figure 257 provides a view of the EC-COMP-4 specimen crack pattern: horizontal cracks have been detected in the mortar bed-joint between the foundation and the first brick layer, between the 19<sup>th</sup> and 20<sup>th</sup> brick layer and between the 33<sup>th</sup> and 34<sup>th</sup> brick layer (the restrained one).



*Figure 257. EC\_COMP\_4 Crack Pattern.*

Figure 258 shows the EC-COMP-5 specimen crack pattern. For what concerns the CS wall, horizontal cracks have been detected in the mortar bed-joint between the foundation and the first brick layer, between the 20<sup>th</sup> and 21<sup>th</sup> brick layer and between the 33<sup>th</sup> and 34<sup>th</sup> brick layer. In the clay wall, horizontal cracks appeared in the mortar bed-joint between the foundation and the 1<sup>st</sup> brick layer and between the 27<sup>th</sup> and 28<sup>th</sup> brick layer, while no cracks developed in clay wall top because it is free of any restrains. Mid-height cracks appeared in both walls at the height of the tie connection between them.



*Figure 258. EC\_COMP\_5 Crack Pattern.*

Figure 259 shows the EC-COMP-6 specimen crack pattern. For what concerns the CS wall, horizontal cracks have been detected in the mortar bed-joint between the foundation and the 1<sup>st</sup> brick layer, between the 20<sup>th</sup> and 21<sup>th</sup> brick layer and between the 33<sup>th</sup> and 34<sup>th</sup> brick layer. In the clay wall, horizontal cracks appeared in the mortar bed-joint between the foundation and the 1<sup>st</sup> brick layer and between the 25<sup>th</sup> and 26<sup>th</sup> brick layer. The mid-height crack in the CS wall appeared at the height of the tie connection between the two walls.

Figure 260 shows the EC-COMP-7 specimen crack pattern. For what concerns the CS wall, horizontal cracks have been detected in the mortar bed-joint between the foundation and the 1<sup>st</sup> brick layer, between the 17<sup>th</sup> and 18<sup>th</sup> brick layer and between the 33<sup>th</sup> and 34<sup>th</sup> brick layer. In the clay wall, horizontal cracks appeared in the mortar bed-joint between the foundation and the 1<sup>st</sup> brick layer and between the 23<sup>th</sup> and 24<sup>th</sup> brick layer. It is worth noticing as in such specimen, which is the one with more ties per m<sup>2</sup>, but mid-height cracks appeared at the exact half height of the specimen.

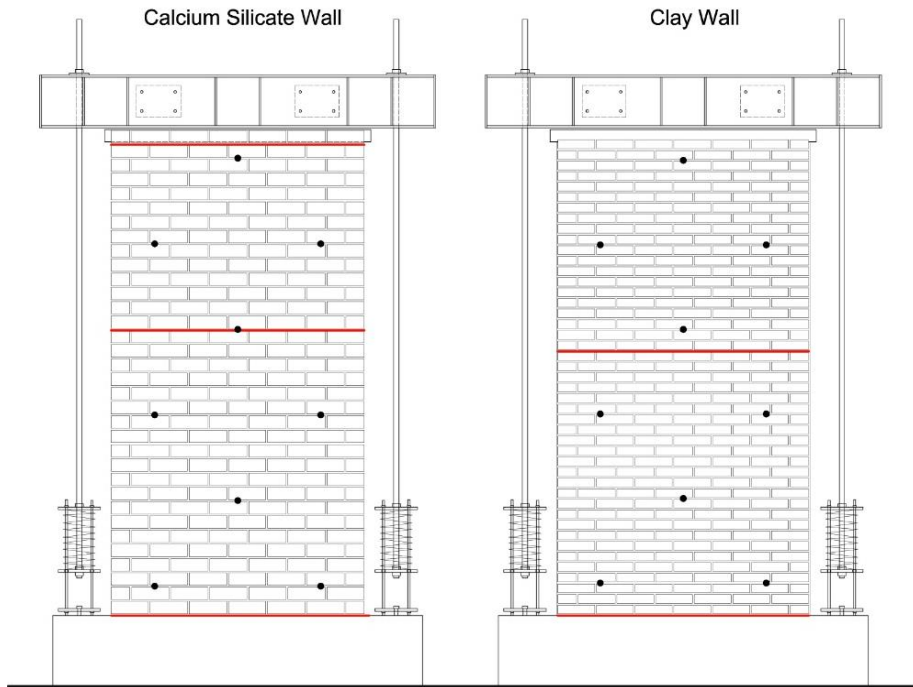


Figure 259. EC\_COMP\_6 Crack Pattern.

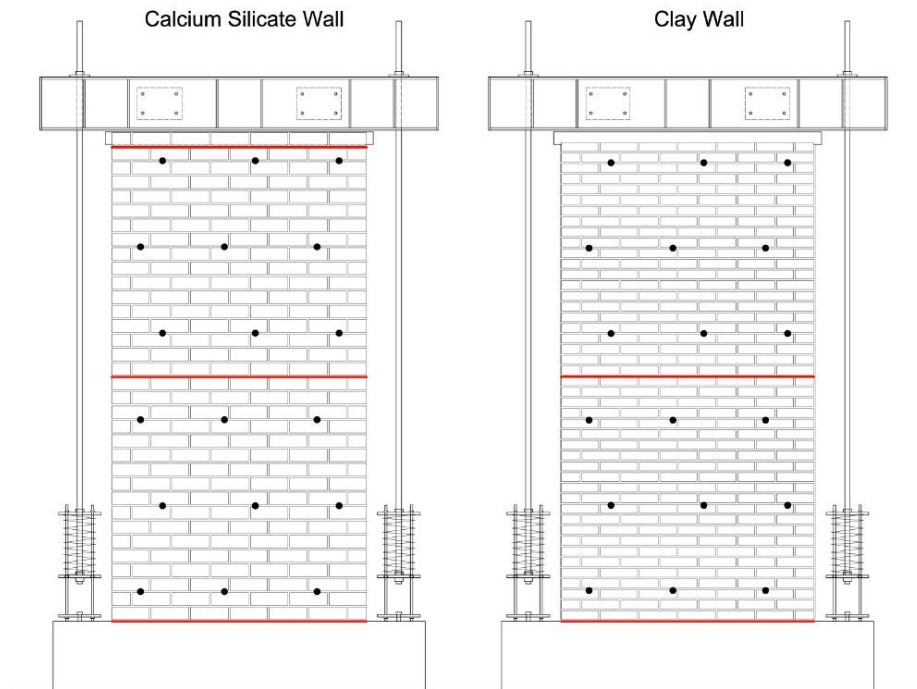


Figure 260. EC\_COMP\_7 Crack Pattern.

### 5.4.7 Summary of the results

The present section provides a comparison between the global responses of all the tested specimen. A detailed report of the experimental response shown by each specimen will follow in previous sections.

The following plots present a comparison between the different specimen responses. Figure 261 shows the incremental dynamic response comparison among all the specimens tested for the initial testing phases (Gr1 input). Clearly, the EC\_COMP\_4 specimen, subjected to an overburden pressure equal to 0.1 MPa, have been already subjected to two testing phases with an applied overburden pressure of 0.3 MPa.

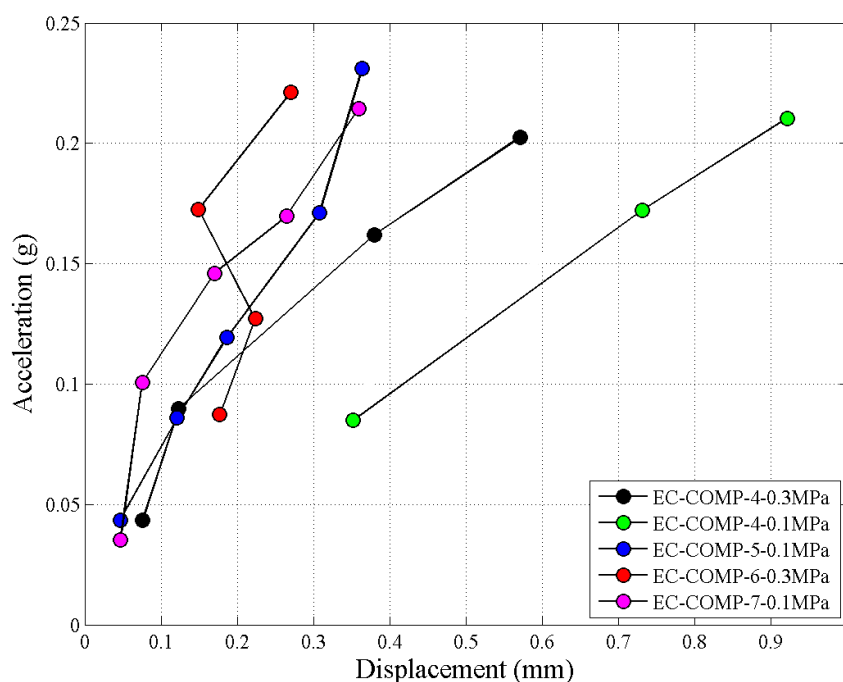


Figure 261. Incremental dynamic response Comparison for Gr1 Input.

Cavity walls are stiffer compared to the single leaf wall. In particular, the EC-COMP-6 specimen seems to be the stiffest, while the EC-COMP-4 with an imposed overburden pressure equal to 0.1 MPa, the more flexible as expected.

Figure 262 shows negative and positive CS and clay walls mid-height displacement response peaks for all the tested specimens associated to RWA acceleration inputs. The position of the black dots identifies the impulse direction. The simplified draws of the specimens on the figure side identify the positions of the walls.

The direction of the wall response peak is in the large number of cases coherent with the RWA input direction. In cavity wall specimens larger mid-height displacements also have been recorded in the opposite direction of the dynamic impulse.

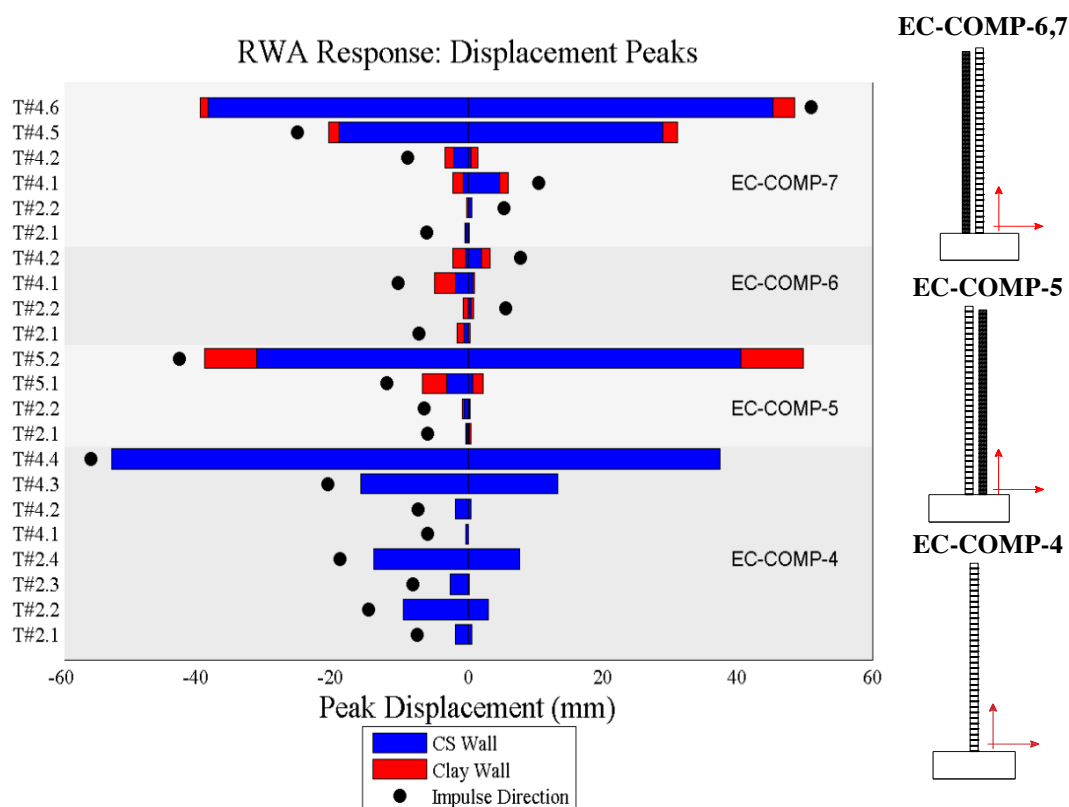


Figure 262. RWA Input: response peaks.

It is possible to observe also as the clay wall exhibits a larger horizontal mid-height displacement response due to the progressive deterioration of the tie anchoring system. Such phenomenon is more evident in EC-COMP-5 and EC-COMP-6 where the tie spacing and number is considerable less than the EC-COMP-7 specimen.

Studying the free oscillation decay phases of the specimens response subjected to RWA input it has been possible to better investigate the relationship between the acting damping and the response frequency. The equivalent viscous damping EVD associated to the logarithmic decay of each oscillation cycle have been computed and plotted with the correspondent frequency. It is worth remembering as EVD takes into account both the energy dissipation due to impacts (in rocking behaviour) and the hysteretic energy dissipation. Figure 263 shows the EC\_COMP\_4 mid-height displacement response during test 4.4 and the frequency variation with the oscillation amplitude. It is largely known as rocking systems do not have a fundamental oscillation period but the response frequency varies with the oscillation amplitude.

It has been observed experimentally that at such variation is associated also a variation in the acting damping in the system.

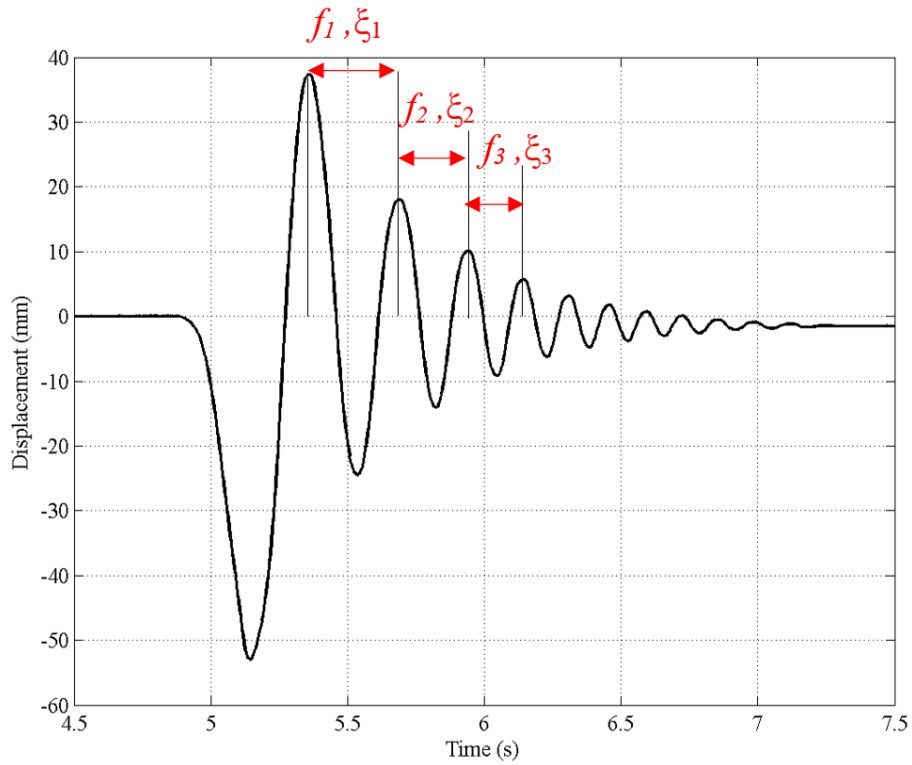


Figure 263. EC\_COMP\_4 Horizontal Mid-height Disp. History during test 4.4.

Figure 264 shows the EVD values associated to each oscillation cycle for different RWA tests performed on the EC\_COMP\_4 specimen.

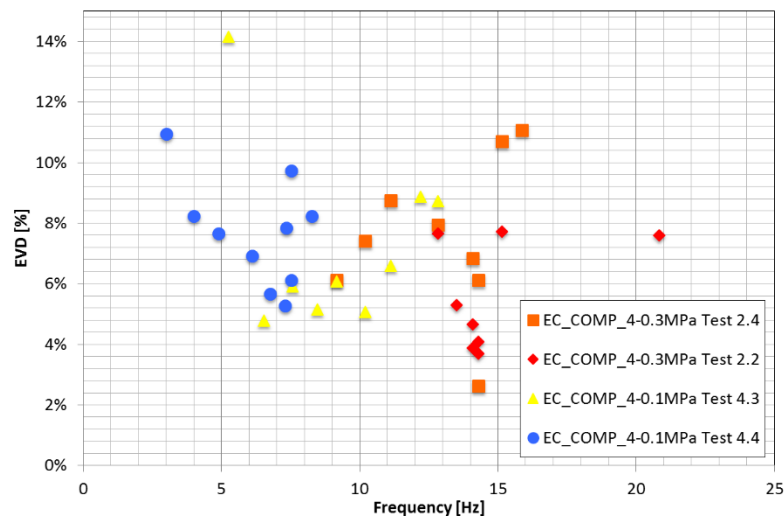


Figure 264. EC\_COMP\_4 Figure 264 EVD-Frequency Relationship.

It is worth noticing as the EVD values found tend to increase with the number of tests and the progressive damage of the specimen.

Figure 265 shows the EVD values associated to each oscillation cycle for different RWA tests performed on EC\_COMP\_5 and EC\_COMP\_7 specimens. The EC\_COMP\_6 wall

specimen did not show appreciable free vibration oscillations in the RWA tests to allow an easy computation of the acting EVD damping. Generally, the damping values computed for the CS walls are slightly higher than the ones found for the clay walls. More data may be extracted, in a future development of the present work, looking at the mid-height acceleration response, which is more affected by higher modes effect.

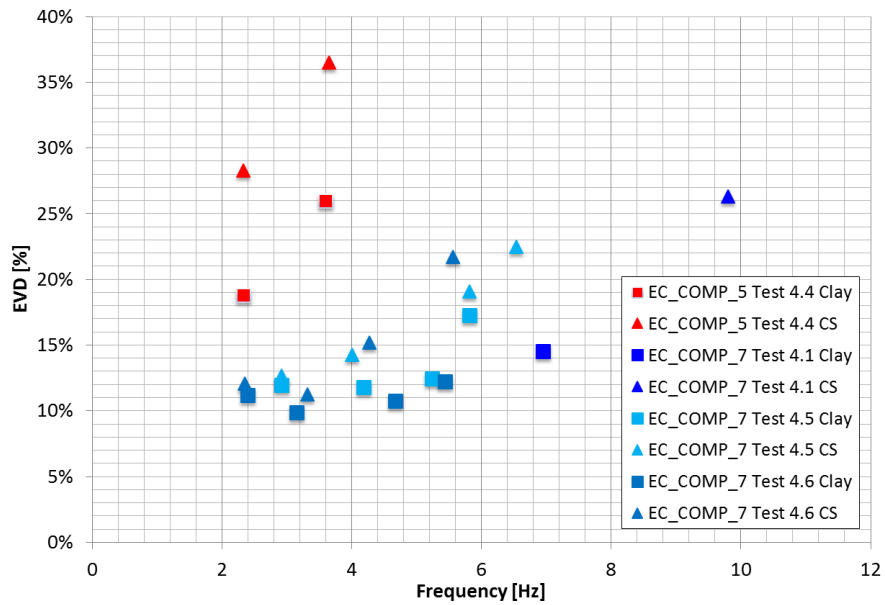


Figure 265. EVD-Frequency Relationship Comparison between Cavity Specimens.



## 6 Full-Scale Building Test, terraced house

This work aims to investigate the seismic behavior of a particular typology of Dutch residential building (terraced house). A shaking table test on a two-story full scale unreinforced masonry building was performed at the EUCENTRE laboratory within a comprehensive research programme on the seismic vulnerability of existing Dutch Unreinforced Masonry (URM) structures. The building specimen was meant to be representative of the end unit of a terraced house system, built with cavity walls and without any particular aseismic design or detailing. Cavity walls are usually composed by an inner loadbearing leaf and an outer leaf having aesthetic and weather-proof functions. In the tested specimen, the loadbearing masonry was composed by calcium silicate bricks sustaining two 6-meters-long reinforced concrete floors. A pitched timber roof was carried by two gable walls. The outer veneer was made by clay bricks connected to the inner masonry by metallic ties as in common construction practice.

An incremental dynamic test was carried out up to the near collapse limit state of the specimen. The input motions were selected to be representative of the dynamic characteristics of induced seismicity ground motions.

The report describes the characteristics of the building and presents the results obtained during the characterization and the shaking table tests, illustrating the response of the structure, the damage mechanism and its evolution during the experimental phases.

Info on the test will be found in the following paper:

- Graziotti F., Tomassetti U., Rossi A., Kallioras S., Mandirola M., Penna A., Magenes G., (2017) *Full scale shaking table test on a URM cavity wall building model*, Proceedings 16<sup>th</sup> World Conference on Earthquake, Santiago, Chile.

Some videos of the described tests could be watched at:

[www.youtube.com/watch?v=h8sZCRUCons&list=PLRDMVFxhFvQm8pxSTPpzHN1AQH0G7sMGk](http://www.youtube.com/watch?v=h8sZCRUCons&list=PLRDMVFxhFvQm8pxSTPpzHN1AQH0G7sMGk)



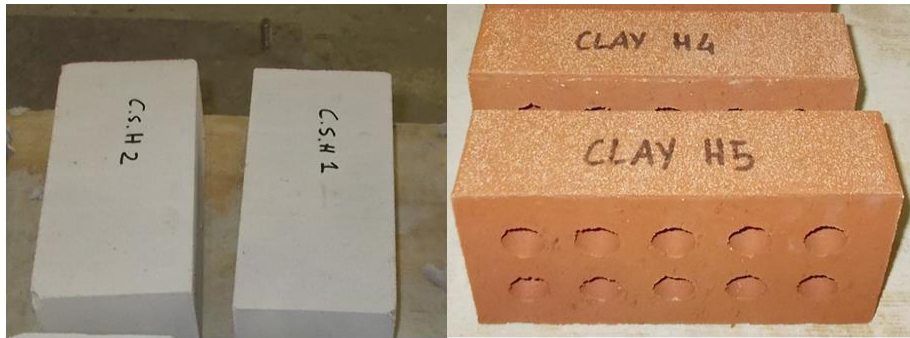


*Figure 267. Calcium silicate bricks and clay bricks.*



*Figure 268. Cavity wall.*

The mortar used for the calcium silicate bricks is different from the one used for the clay bricks. The thickness of the layers were about 1 cm for both masonries. The Figure 269 shows the identification code of these two materials.

Mortar for C.S. bricks	Mortar for clay bricks
 <p>Remix Brickfix BFM Speciaal voor het vermetelen van sterk zulgende stenen met een laaghechtpotentieel en kalkzandsteen Aanmaakwater 3,1 liter/25 kg M3 - voegtype medium - bindmiddel cement - maximale korrel 4 mm - verwerkingstijd ca. 2 uur - verwerkingstemperatuur +5 - 25 °C Ankelnummer: 010921206 Receptcode: BM310 CE Productie: 716105107637</p>	 <p>Remix Droge Mortel BV WWW.REMIX.NL</p>
0920150102 t.h.t.: 19-08-2016 705 ITALY	1401151030 t.h.t.: 28-09-2016 705 BM2 PAVIA/DELFT

Figure 269. Mortar types.

Because the materials are different, the water content is not the same for the two types of mortar used. Table 54 shows the percentage of water, respect to the weight of the mortar, that has to be used.

Table 59. Water content.

	WATER	MORTAR	W/M
	(lt=kg)	(kg) - one bag	(% weight)
<b>Mortar for CS bricks</b>	2.9	25	12%
<b>Mortar for Clay bricks</b>	3.75	25	15%

The following Figures show the geometry of the test-house and its dimension.

- Ground Floor

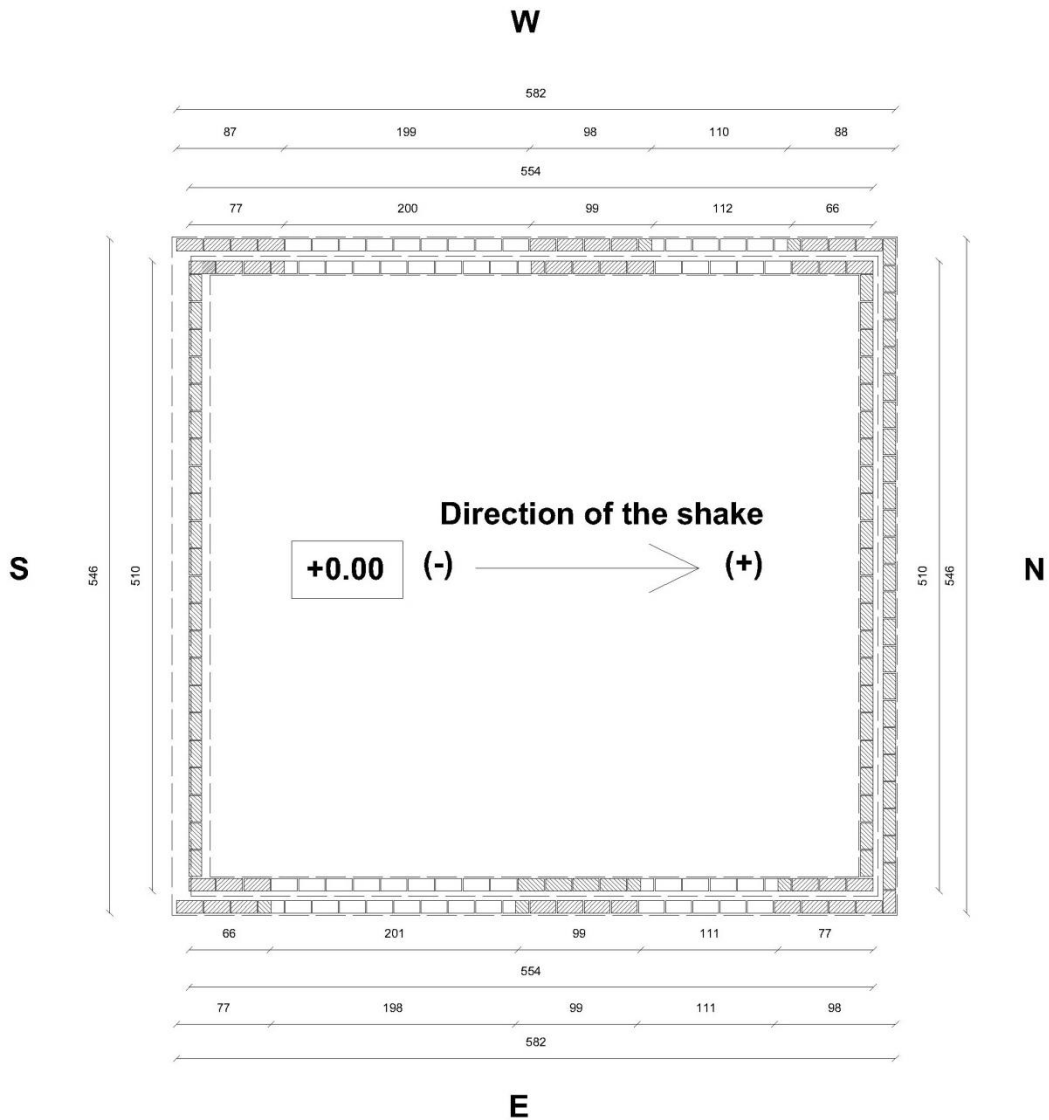


Figure 270. Plan view of the test-house – ground floor.



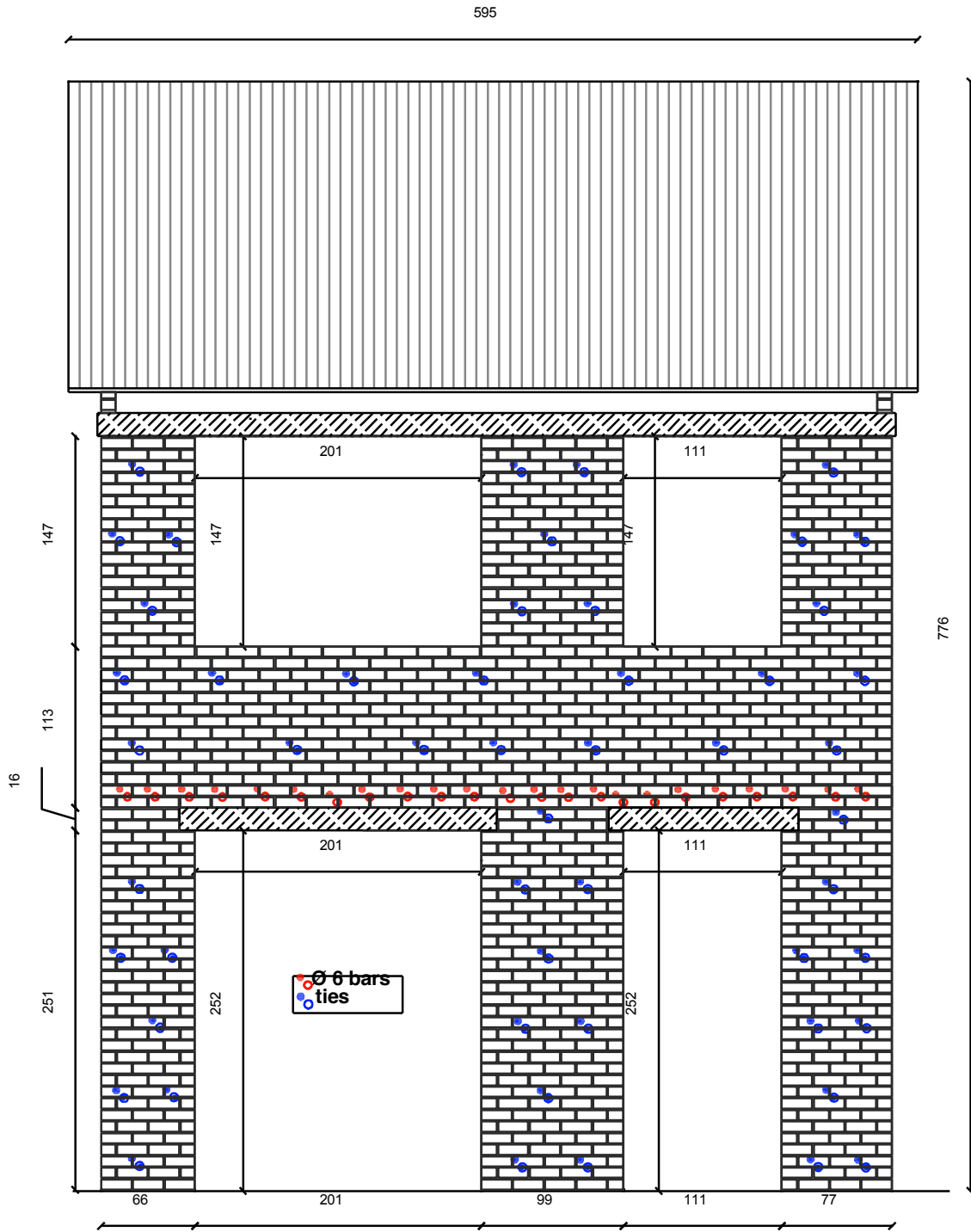


Figure 272. Elevation view of the test-house -inner leaf - east-side.

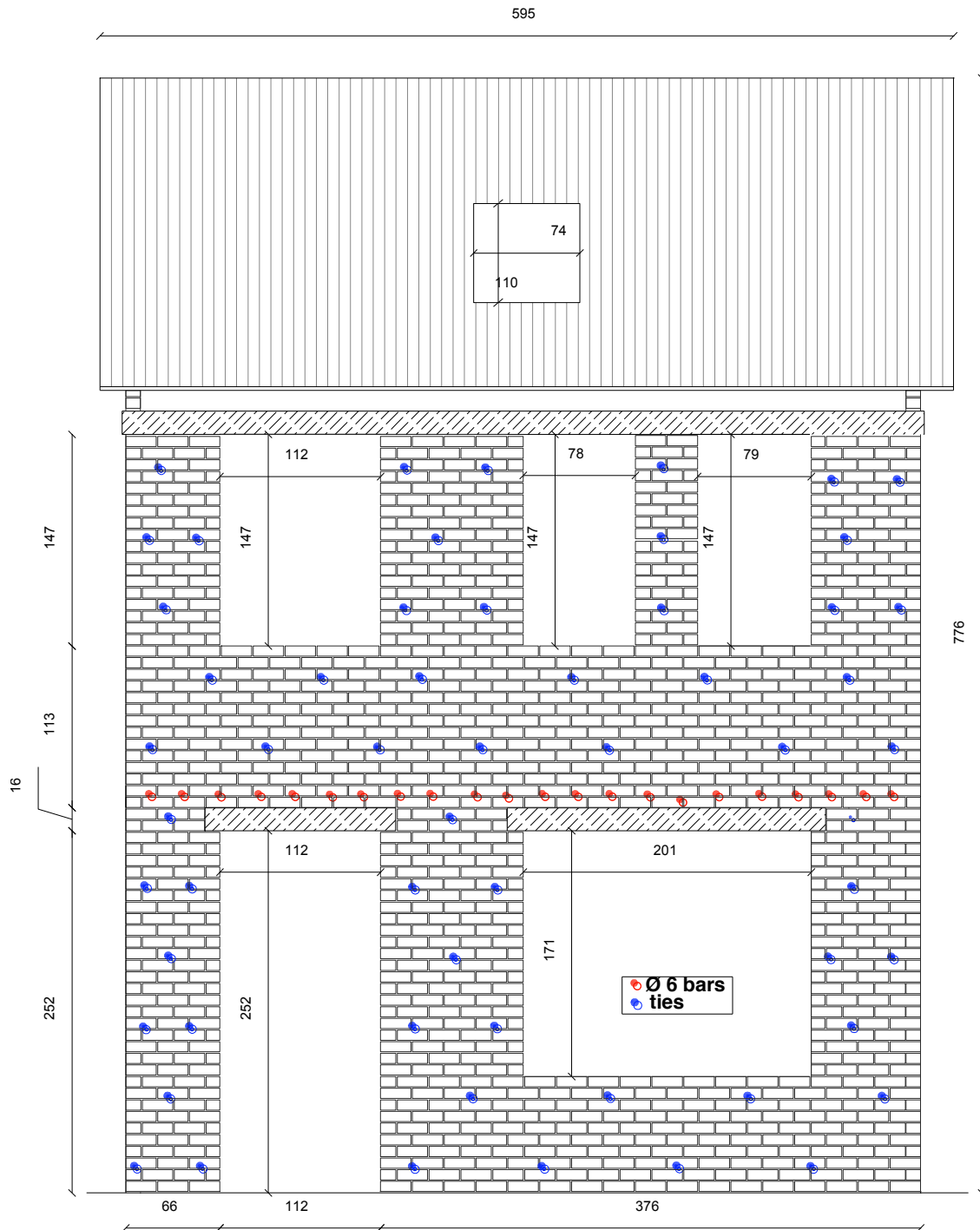


Figure 273. Elevation view of the test-house - inner leaf - west-side.

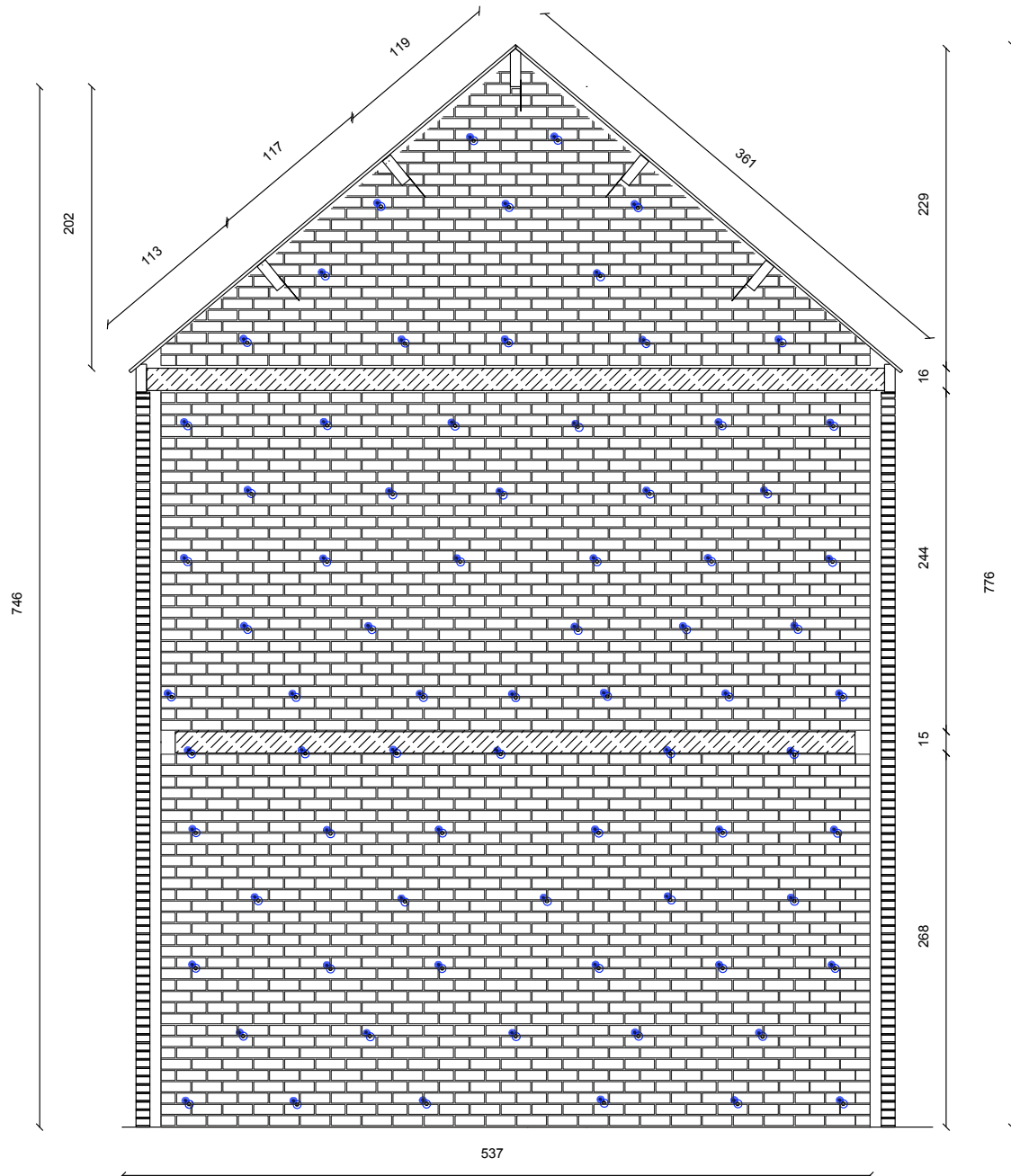


Figure 274. Elevation view of the test-house - inner leaf - north side (with ties) or south side (not considering the ties).

595

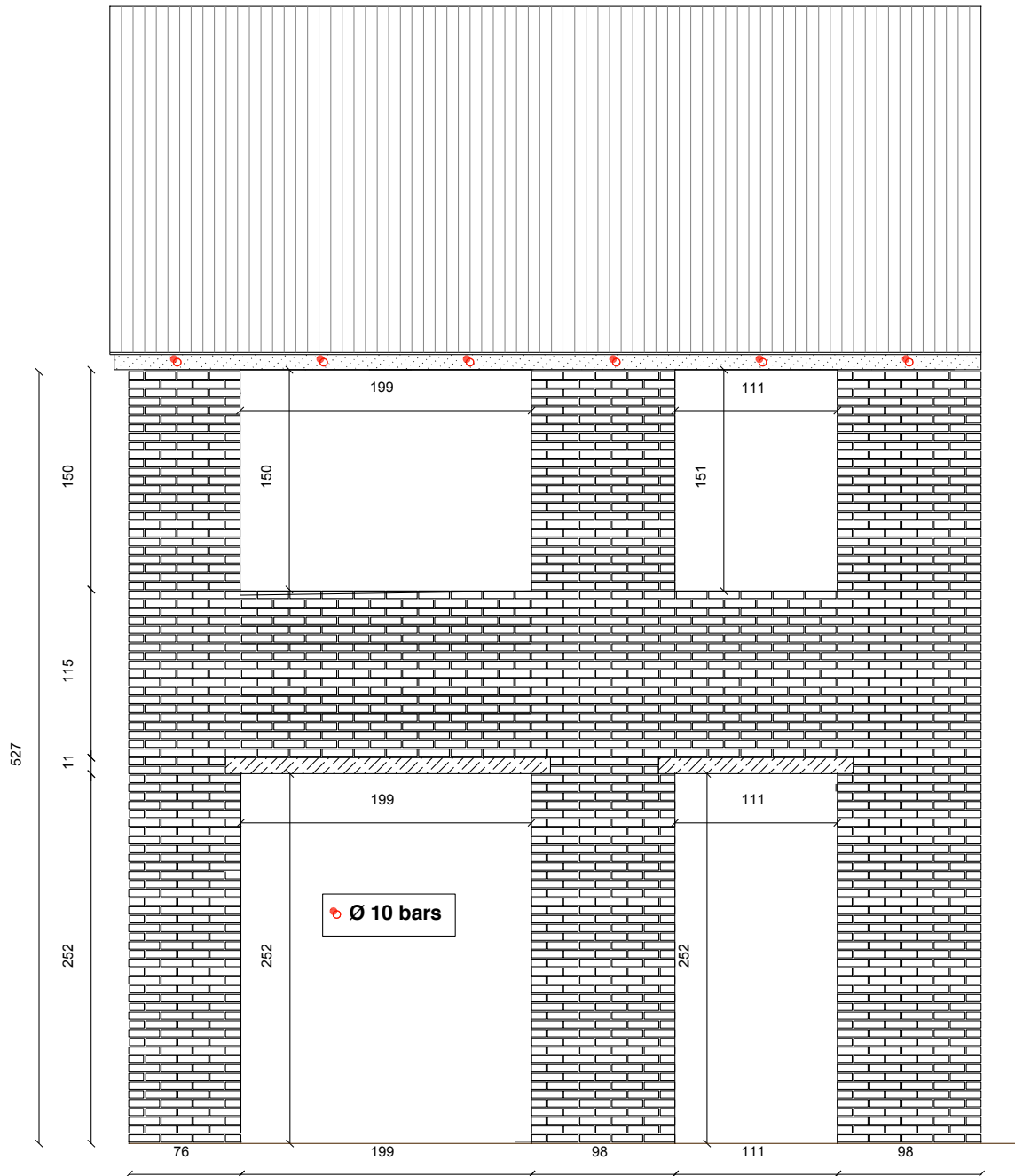


Figure 275. Elevation view of the test-house - outer leaf - east-side.

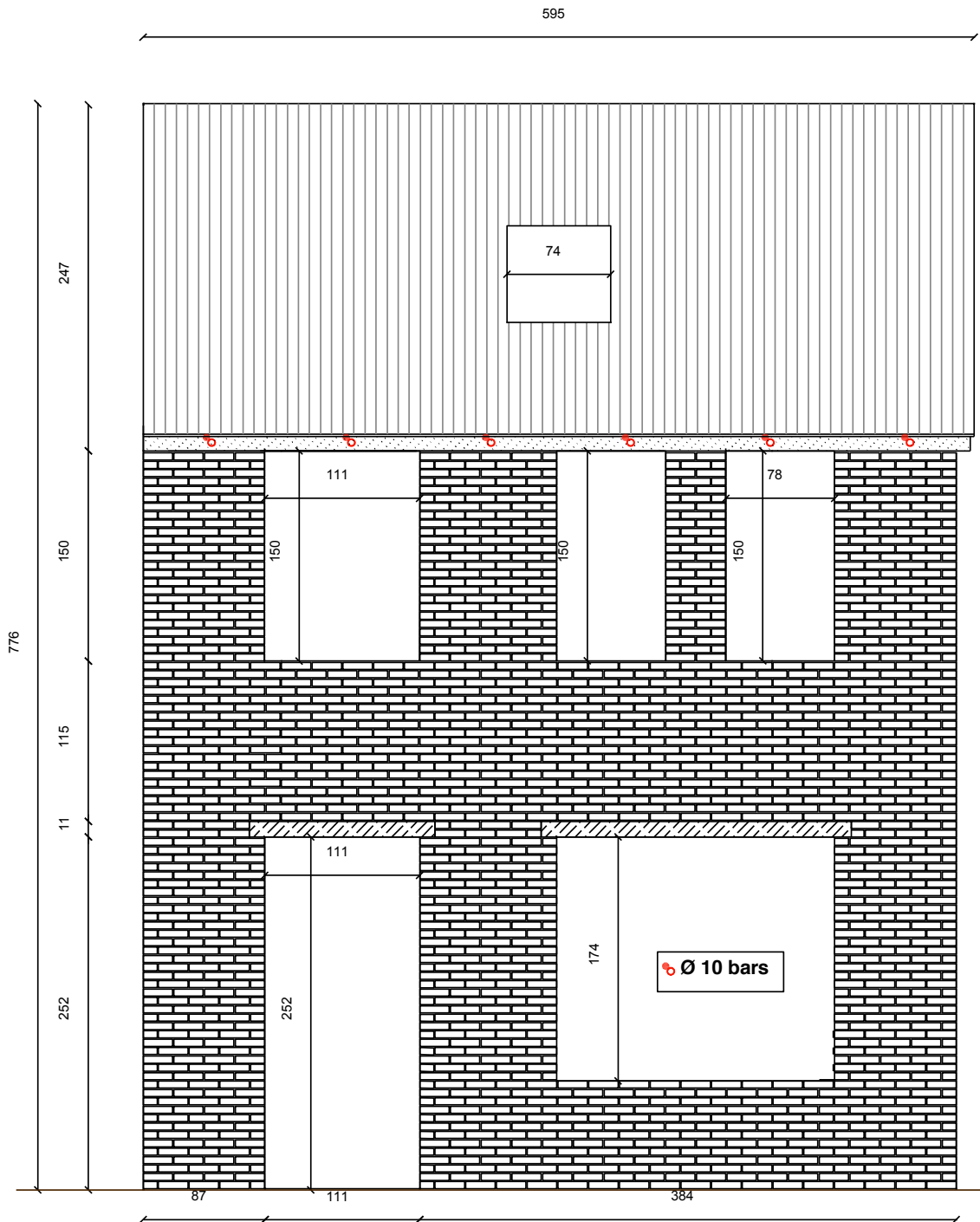


Figure 276. Elevation view of the test-house - outer leaf - west-side.

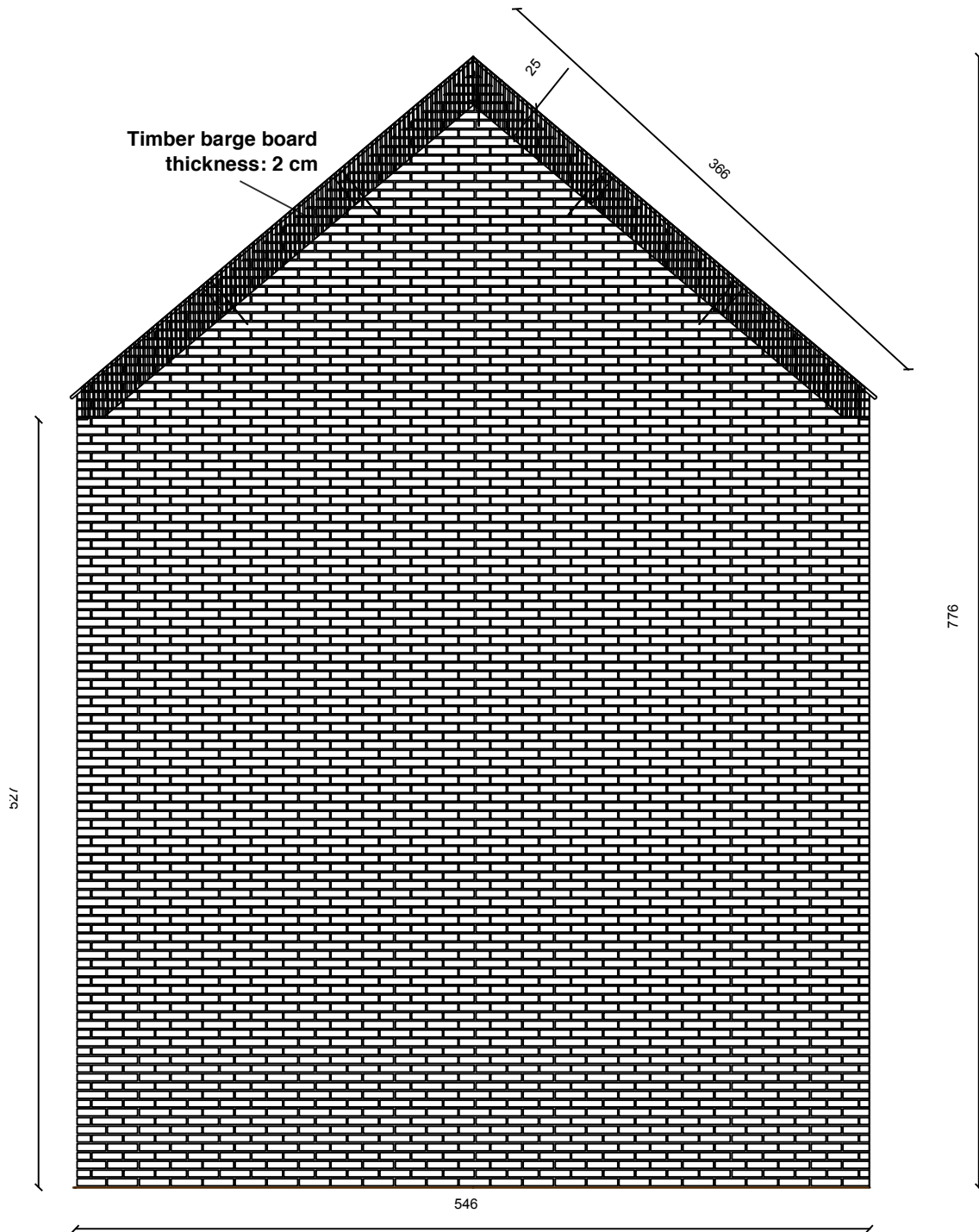


Figure 277. Elevation view of the test-house - outer leaf - north side

## 6.1.1 Construction details

### Ties positioning

The two walls are connected by steel ties, diameter 3.4 mm, length 200 mm. They are inserted in the mortar joint during the laying of the bricks. The mortar was more generally laid on top of the bricks. The edge with the hook is in the inner leaf (calcium silicate bricks), for a length of about 7 cm. 5 cm on the outer leaf.

The following two photos (Figure 278 and Figure 279) show the size and the method of laying those connections.



*Figure 278. Ties dimensions and geometry.*



*Figure 279. Laying of the ties.*

### Characteristic of the slabs

The concrete used has an average strength of  $R_c=29.8$  MPa (this average value was obtained by compression tests of cubic concrete 15x15 cm specimens).

The mass of the slab of the first floor is 10.3 t.

The mass of the slab of the second floor is 11t.

The reinforcements of the slab for the first and second floor are:

- side N-S bottom and top longitudinal reinforcements  $\phi$  12 mm each 150mm.
- side N-S bottom and top transversal reinforcements  $\phi$  8 mm each 250mm.
- side W-E bottom and top longitudinal reinforcements  $\phi$  12 mm each 150mm.
- side W-E bottom and top transversal reinforcements  $\phi$  8 mm each 250mm.

### Detail of the lintel

Above the openings (doors and windows) of the first floor there are lintels, for both inner and outer walls. The lintels were made in reinforced pre-casted concrete. The following Figure 280 shows their geometry.

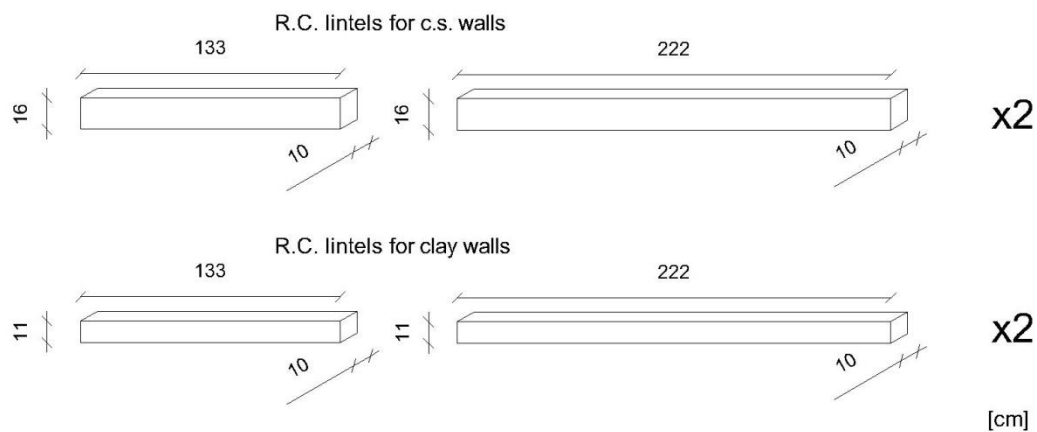


Figure 280. Lintels dimensions and geometry

The steel reinforcement of the lintels is:

- $\phi$  6 mm diameter hoops at 300mm spacing for all lintels.
- $\phi$  10 mm diameter bars top and bottom for all lintels.

### Detail of the connection between the RC slab of the first and second floor and the inner leaf (C.S. walls) - North side

The slabs in reinforced concrete lays only on the north and south inner walls. The N/S walls were built up to a height of 268 cm, then the slab were laid on an approx. 1 cm mortar layer. A series of temporary supports supported the slab during the mortar maturation.

The same procedure is repeated for the slab of the second floor. The vertical distance between the two slabs is 244 cm.

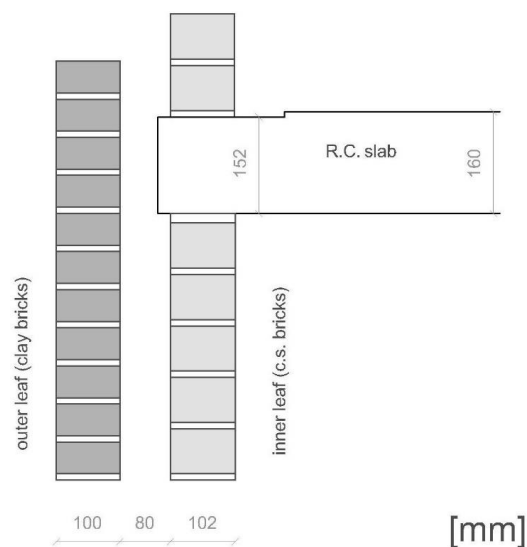


Figure 281. Detail of the connection between the R.C. slab of the first and second floor and the inner leaf (C.S. walls) - North side.

### Detail of the connection between the R.C. slab of the first floor and the inner leaf (C.S. walls) - East and West side

The slab of the first floor is not laying directly on the lateral (east and west) walls, but they are connected with them by means of threaded bars  $\phi$  6 mm, grade 8.8.

The system is shown in the following Figures (Figure 282, Figure 283 and Figure 284).

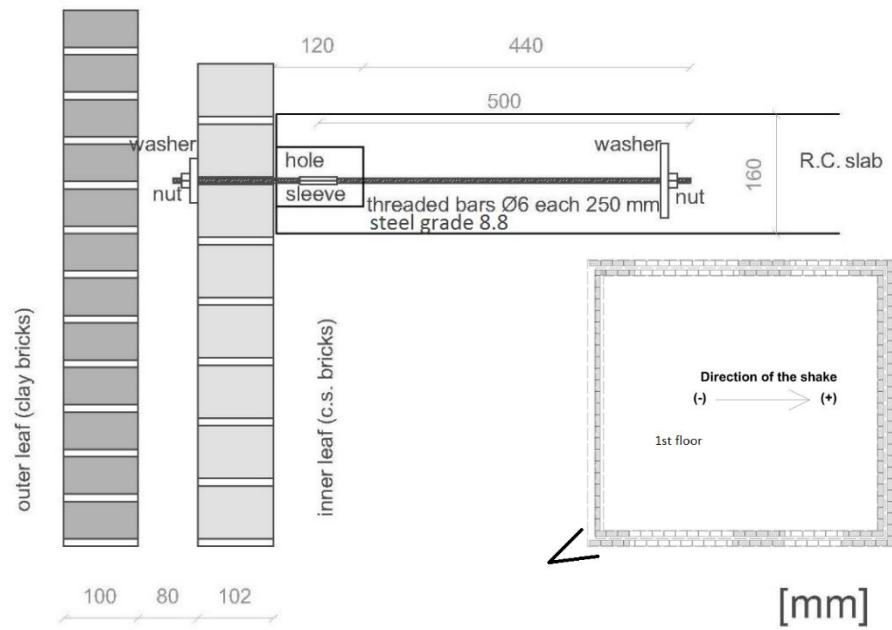
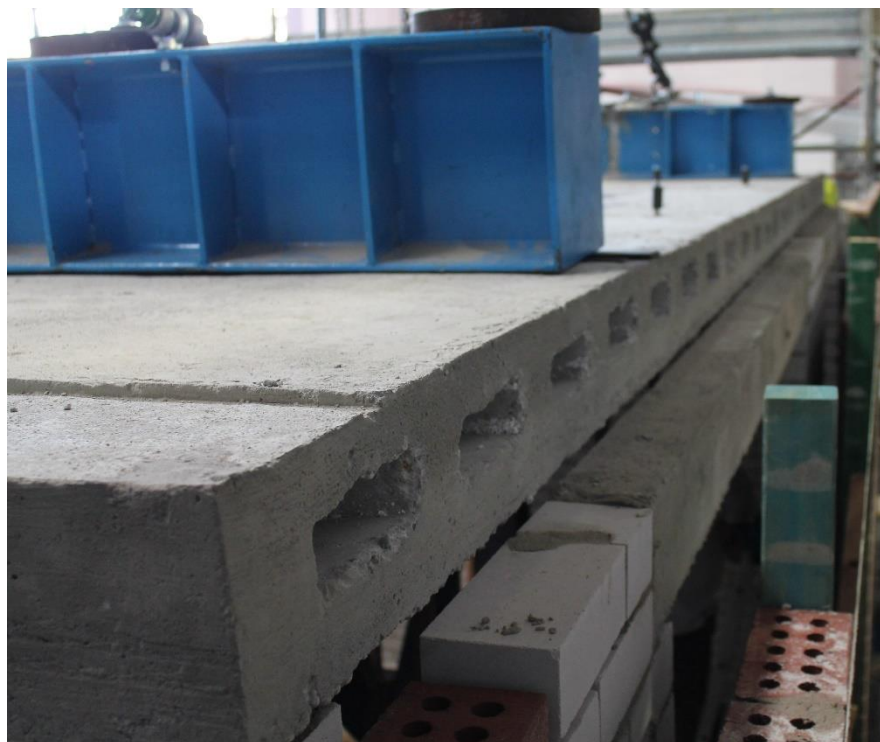


Figure 282. Detail of the connection between the R.C. slab of the first floor and the inner leaf (C.S. walls) - East and West side.



Figure 283. Positioning of the R.C. slab of the first floor - East side



*Figure 284. View of the R.C. slab of the first floor - East side*

**Detail of the connection between the R.C. slab of the second floor and the inner leaf (C.S. walls)**

The slab of the second floor is connected with the lateral timber beams by a series of threaded bars  $\phi$  10, grade steel 8.8. The threaded bars are present each meter. The embedment depth is 10 mm. The connection was made through adhesive: Hilti hit-re 500. Its cohesion capacity is higher than the yielding of the bar.

When the slab is laid, it didn't touch directly the lateral (east and west side) walls but laid only on the south and north inner walls and the temporary supports. The gap between the lateral walls and the slab was filled after the removal of the supports.

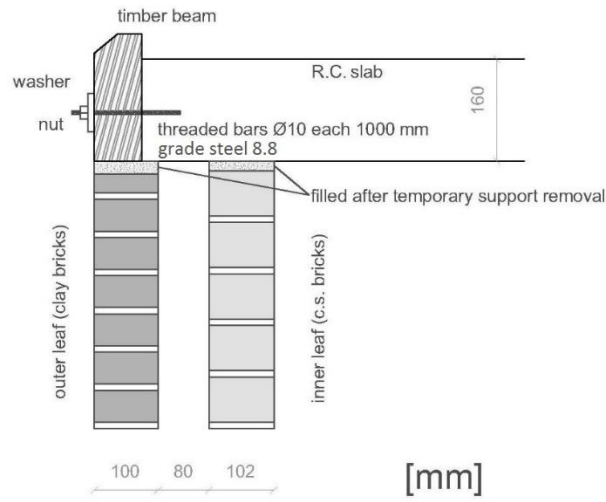


Figure 285. Detail of the connection between the R.C. slab of the second floor and the inner leaf (C.S. walls) - East and West side.

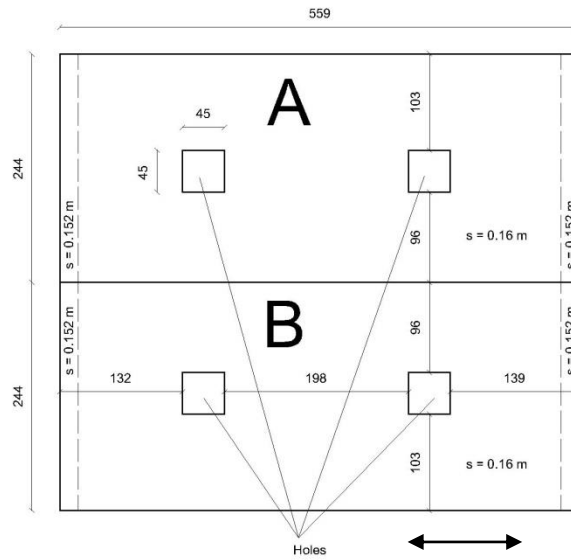


Figure 286. Slab of the first floor.

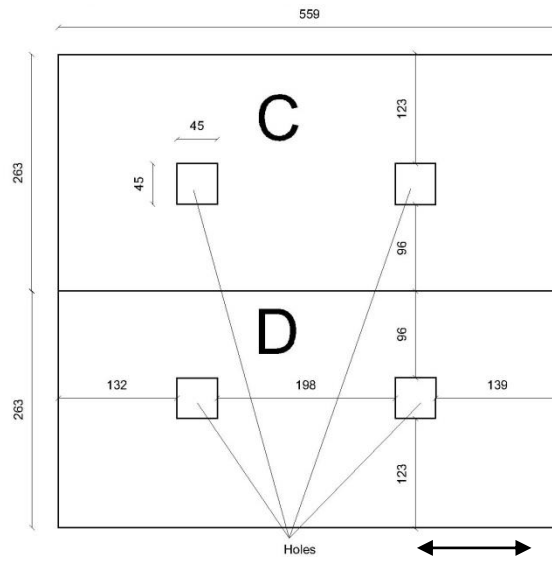


Figure 287. Slab of the second floor.

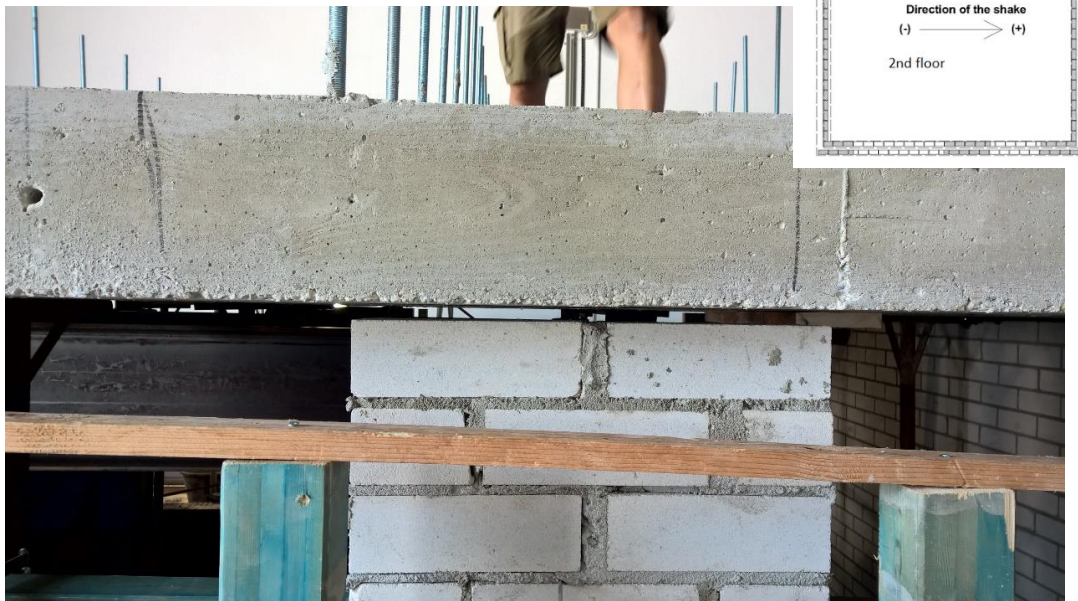


Figure 288. Detail of the connection between the R.C. slab of the second floor and the inner leaf (C.S. walls)- view of the gap filled a posteriori - West side.

### Detail of the roof

The roof was built according Dutch specifications. In particular two 60x2 mm nails each intersection were used to connect each tongue and groove plank with the above timber beams.

The counter and tile battens are shown in next figure.

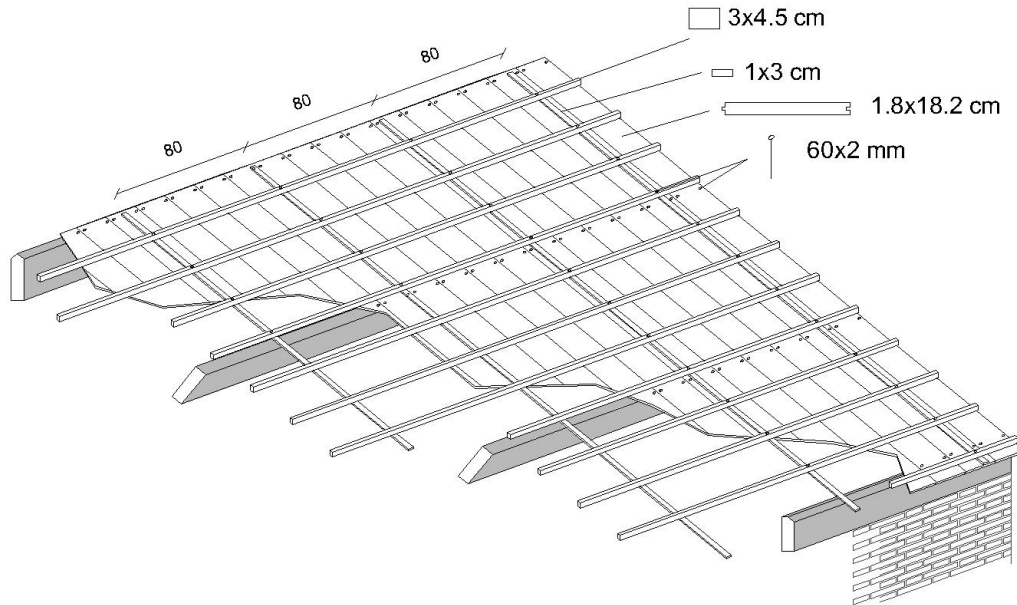
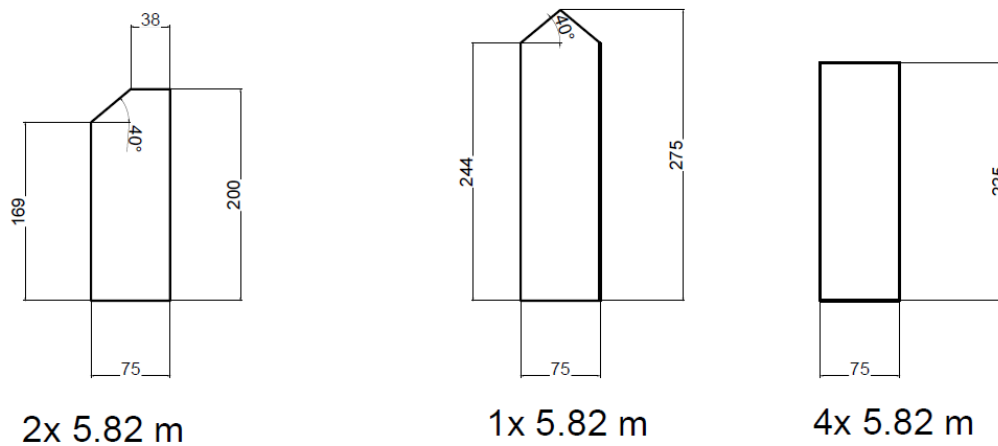


Figure 289. Details of the roof.

The dimensions of the roof beams are reported in following figures:



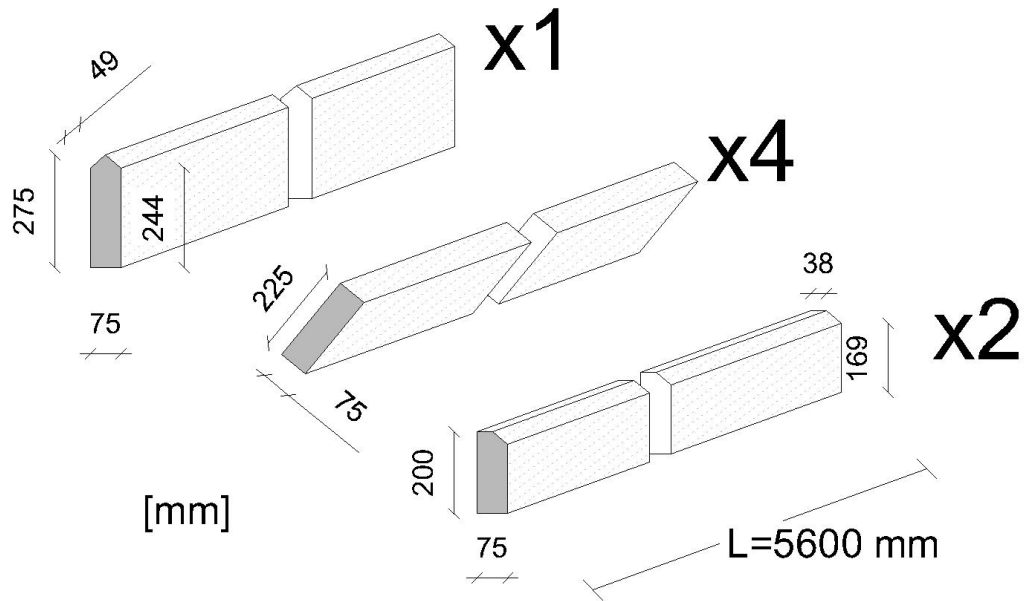
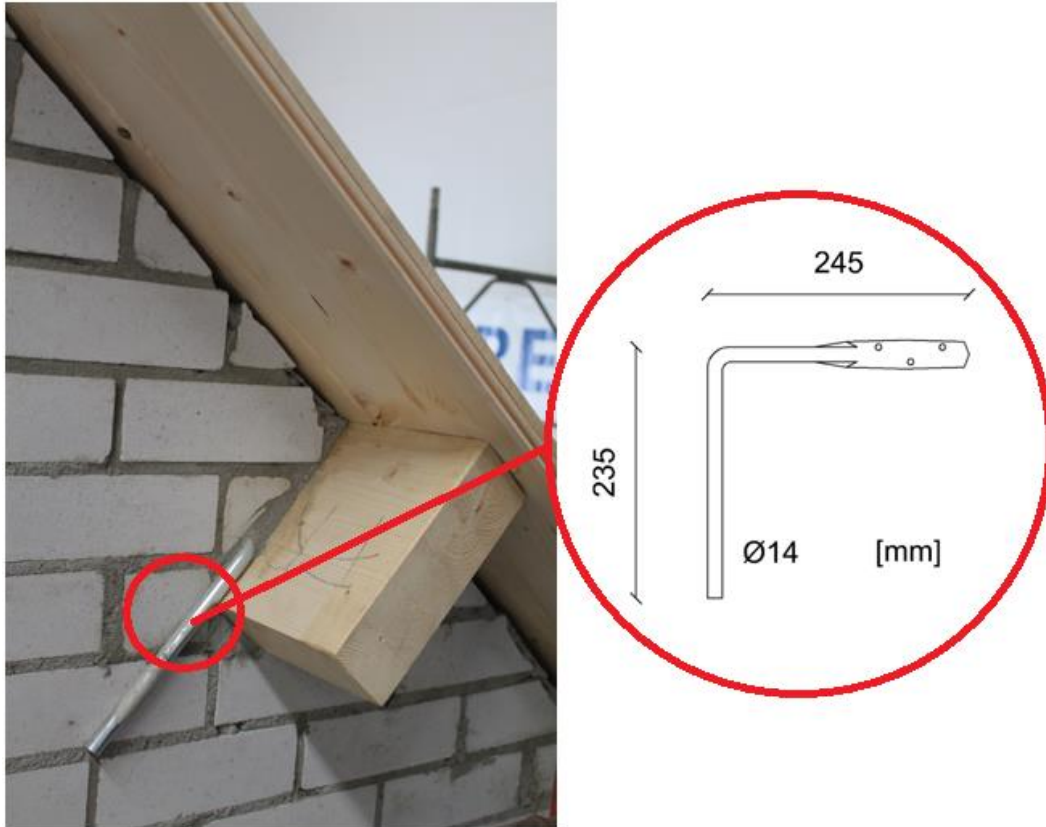


Figure 290. Sections of the girders.



Figure 291. Roof and C.S. gable - South side.

The following image show the detail of the connection with the steel tie, between beam of roof and C.S. gable. The steel tie exist in 5 roof girders (all the ones not connected to the floor in two locations). The nailing of this tie of the roof girder is three "timber" screws 6 cm long.



*Figure 292. Roof and C.S. gable - South side - detail of the connection with the steel tie.*

In the West side of the roof was present an opening, as seen in the following images.

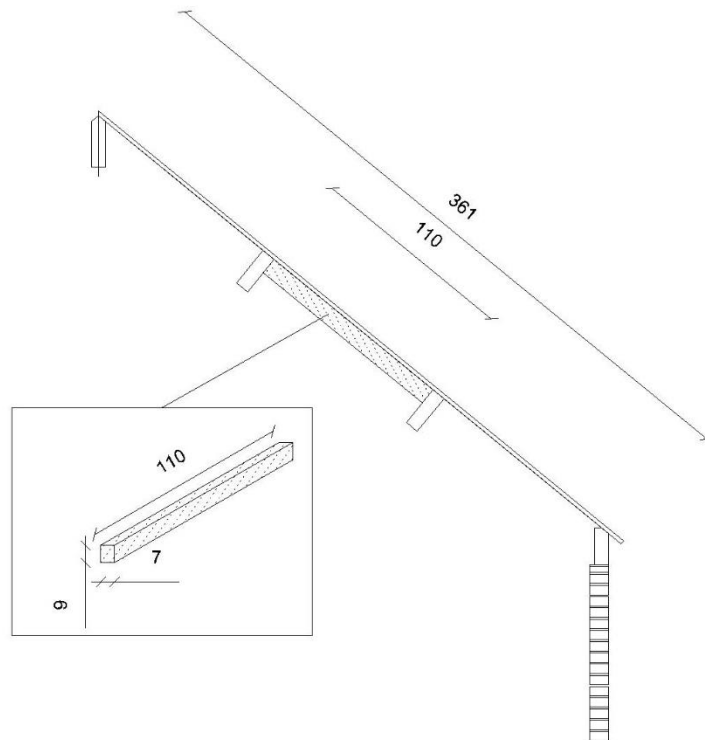
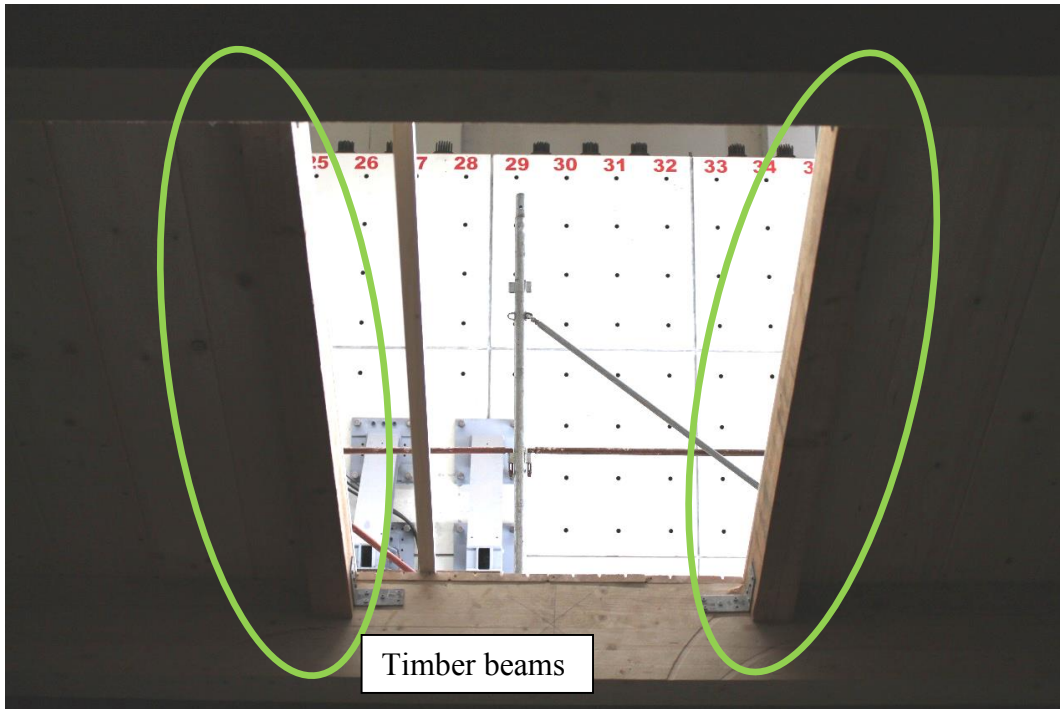


Figure 293. Section of the roof - detail of the opening and the timber beams.



*Figure 294. Roof - West side*



*Figure 295. Detail of the connection between the timber beam of the opening and the girder.*

In the following are a series of images that describe the connection between the beam and the gable clay.



*Figure 296. Detail of the connection between the girder and the clay gable – 1.*



*Figure 297. Detail of the connection between the girder and the clay gable – 2.*



*Figure 298. Detail of the connection between the girder and the clay gable – 3.*

The roof, indeed, has a system of twelve  $\phi 12$  mm rods installed for safety reasons to prevent the local out of plane failure of the specimen gable and the consequently damage of the laboratory. The rods system allows the horizontal out-of-plane displacement of gables till significant displacement level without any force resistance contribution. Applying a tension on the rods it was possible to increase the roof in plane stiffness.



*Figure 299. Detail of two of the rods connecting the second floor to the roof beams.*

The tiles were added on the roof at the end of the construction. The total mass of the roof (tiles+timber) is 2.8t.

The total mass of the house resulted to be 56 t.



*Figure 300. Picture of the specimen at the end of the construction.*

## 6.2 Instrumentation and acquisition system

In order to detect and monitor the structural response under different levels of input motion, several instruments were placed in the building. The location and typology of the instrumentation was determined based on the identification of the position of the critical zones and on the physical quantity to be recorded.

The entire set-up instrumentation consisted in accelerometers, wire potentiometers and traditional potentiometers (measuring the relative displacements).

A rigid steel structure was built and fixed on the shake table with two goals: first of all it was a safety device in order to prevent the global collapse of the structure, secondly it was used as a reference point in order to directly measure the relative displacement of some portions of the house relative to the shake table. The steel structure columns passed through the concrete slabs. Four holes in each slab allowed the independent deformation of the specimen with respect to the rigid frame (see Figure 286 and Figure 287).

### 6.2.1 Identification of the position of the accelerometers

The accelerometers guaranteed an accurate measurement of the following quantities:

- Acceleration of the shake table;
- CS and Clay walls Accelerations along their height;
- Acceleration at 1<sup>st</sup>, 2<sup>nd</sup> and roof levels;
- Acceleration of the Safety steel frame.

Figure 301 shows the position of the accelerometers and the reference system assumed for all the accelerograms. All the acceleration histories are absolute accelerations. For a better illustration, the accelerometers that were installed on the calcium silicate walls are enclosed in circles whereas those installed on the veneer walls are represented by rectangles.

Following lines list the accelerometers installed on the calcium silicate masonry, on the slabs and on the rigid steel frame (see Figure 301):

- # 1 is installed on the slab of the first floor level on the west side to record the accelerations in the x and z direction ;
- # 2 is installed just below the first slab on the east side to record the acceleration in the x, y and z direction;
- # 3 is installed just below the first slab on the east side to record the acceleration in the x, y and z direction
- # 4 is also installed on the first-floor-level RC slab in order on the west side to obtain the accelerations in all three x, y and z directions;
- # 5 is installed on the second slab on the west side. This accelerometer measures the acceleration in the x, y and z direction of the roof ;



- # 6 is installed just below the second slab on the east side to record the acceleration in the x, y and z direction;
- # 7 is installed just below the second slab on the east side to record the acceleration in the x, y and z direction;
- # 8 is installed on the second slab on the west side. This accelerometer measures the acceleration in the x, y and z direction of the roof;
- # 9 is installed at the roof- ridge-level of the south side and recording the acceleration in the x, y and z direction;
- # 10 is installed at the ridge of the gable of the north side and recording the acceleration in the x, y and z;
- # 11 is installed on the ridge of the roof for recording the accelerations in the z direction;
- # 24 is installed at the mid-height of the second storey north recording the accelerations in the x direction;
- # 25 is installed at 2/3 of the height of the north facade gable recording the accelerations in the x direction;
- # 26 which is installed on the base of the building on the west side is used to record the accelerations in the x direction at the foundation level;
- # 27 is installed on the base of the building on the east side to record the accelerations in the x direction at the foundation level;
- # 28 is installed on the steel frame on the first floor level on the west side in order to record the accelerations in the x direction of the frame, which is considered to be fixed at the shaking table;
- # 29 is installed on the steel frame on the second floor level on the west side in order to record the accelerations in the x direction of the frame, which is considered to be fixed at the shaking table;
- # 30 is installed at 2/3 of the height of the south facade gable recording the accelerations in the x direction;
- # 31 is installed at the mid-height of the second storey south recording the accelerations in the x direction;
- # 32 is attached on the inner steel frame on the west side to record the accelerations in the x direction. The steel frame is considered to be fixed at the shaking table;
- # 33 is installed on the inner steel frame on the east side to record the acceleration in the x direction. The frame is considered to be fixed at the shaking table;

The accelerometers installed on the veneer walls were (see Figure 301):



- # 12 is installed on the first floor level of the south side and recording the acceleration in the x direction;
- # 13 is installed on the first floor level of the south side and recording the acceleration in the x direction;
- # 14 is installed on the second floor level of the south side and recording the acceleration in the x direction;
- # 15 is installed on the second floor level of the south side and recording the acceleration in the x direction;
- # 16 is installed on the first floor level of the north side and recording the acceleration in the x direction;
- # 17 is installed on the first floor level of the north side and recording the acceleration in the x direction;
- # 18 is installed on the first floor level of the north side and recording the acceleration in the x direction;
- # 19 is installed on the second floor level of the north side and recording the acceleration in the x direction;
- # 20 is installed on the second floor level of the north side and recording the acceleration in the x direction;
- # 21 is installed on the second floor level of the north side and recording the acceleration in the x direction;
- # 22 is installed at the mid-height of the second storey north recording the accelerations in the x direction;
- # 23 is installed at  $2/3$  of the height of the north facade gable recording the accelerations in the x direction;

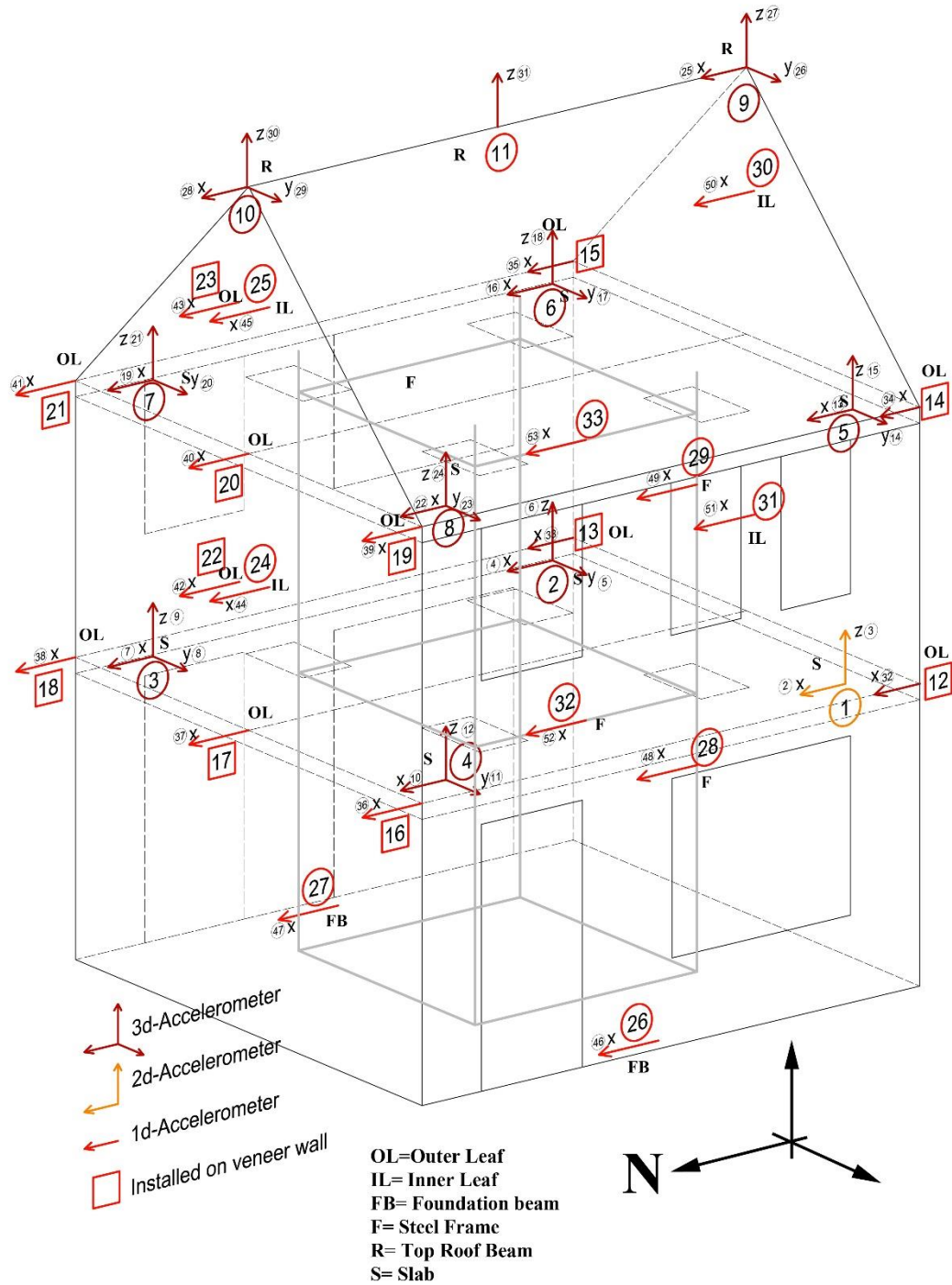


Figure 301. Identification of the accelerometers position.

## 6.2.2 Identification of the position of the displacement transducers

The instrumentation consisted also of a set of wire and traditional potentiometers, which guaranteed a measurement of the displacements of some portions of the building specimen. The wire potentiometers have been installed to monitor the out-of-plane displacement of CS walls (South), cavity walls (North) and the displacement of the roof level. The traditional potentiometer, instead, monitored the X and Y direction displacement of first and second level.

Figure 302 shows the position of the wire and traditional potentiometers. Again, the reference system is shown in the

Figure 302. All the presented displacement are relative to the shake-table (i.e. the rigid steel frame).

The potentiometers installed on the calcium silicate masonry, on the slabs and on the steel frame are the following (see

Figure 302):

- # 1 is a wire potentiometer and is installed at the mid-height of the first storey south recording the displacement of the calcium silicate wall (height +1.34);
- # 2 is a wire potentiometer and is installed at the mid-height of the second storey south recording the displacement of the calcium silicate wall (height +4.09);
- # 3 is a wire potentiometer and is installed at 2/3 of the height of the south facade gable recording the displacement in the x direction (height +6.74);
- # 4 is a wire potentiometer and is installed at the mid-height of the first storey north recording the displacement of the calcium silicate wall (height +1.26);
- # 5 is a wire potentiometer and is installed at the mid-height of the first storey north recording the displacement of the calcium silicate wall (height +4.09);
- # 6 is a wire potentiometer and is installed at 2/3 of the height of the north facade gable recording the displacement in the x direction (height +6.74);
- # 10 is a wire potentiometer and is installed at the ridge of the gable of the north side and recording the displacement of the roof;
- # 11 is attached on the inner steel frame of the first floor on the south-east side to record the X displacements of the slab relative to the steel frame. The frame is considered to be fixed at the shaking table;
- # 12 is attached on the inner steel frame of the first floor on the north-east side to record the X displacements of the slab relative to the steel frame. The frame is considered to be fixed at the shaking table;



- # 13 is attached on the inner steel frame of the first floor on the north-west side to record the X displacements of the slab relative to the steel frame. The frame is considered to be fixed at the shaking table;
- # 14 is attached on the inner steel frame of the first floor on the south-east side to record the Y displacements of the slab relative to the steel frame. The frame is considered to be fixed at the shaking table;
- # 15 is attached on the inner steel frame of the second floor on the south-east side to record the X displacements of the slab relative to the steel frame;
- # 16 is attached on the inner steel frame of the second floor on the north-east side to record the X displacements of the slab relative to the steel frame;
- # 17 is attached on the inner steel frame of the second floor on the north-west side to record the X displacements of the slab relative to the steel frame;
- # 18 is attached on the inner steel frame of the second floor on the south-east side to record the Y displacements of the slab relative to the steel frame;
- # 19 is installed, on the first slab, between the two slab to record the sliding of the two;
- # 20 is installed, on the second slab, between the two slab to record the sliding of the two;
- # 21 which is installed on the foundation on the east side is used to record the displacement and the sliding between the foundation and the building;
- # 22 which is installed on the foundation on the west side is used to record the displacement and the sliding between the foundation and the building;
- # 23 which is installed on the shaking table on the east side is used to record the displacement and the sliding between the foundation and the shaking table;
- # 24 which is installed on the shaking table on the west side is used to record the displacement and the sliding between the foundation and the shaking table;
- # 25 which is installed on the shaking table on the east side is used to record the displacement;
- # 26 which is installed on the ground floor on the east side is used to record the displacement in z direction of the facade;
- # 27 which is installed on the ground floor is used to record the displacement in z direction of the facade;

The potentiometers installed on the clay masonry are the following (Figure 302):

- # 7 is a wire potentiometer and is installed at the mid-height of the first storey north recording the displacement of the clay wall (height +1.33);

- # 8 is a wire potentiometer and is installed at the mid-height of the second storey north recording the displacement of the clay wall (height +4.17);
- # 9 is a wire potentiometer and is installed at 2/3 of the height of the north facade gable recording the displacement in the x direction (height +6.66);

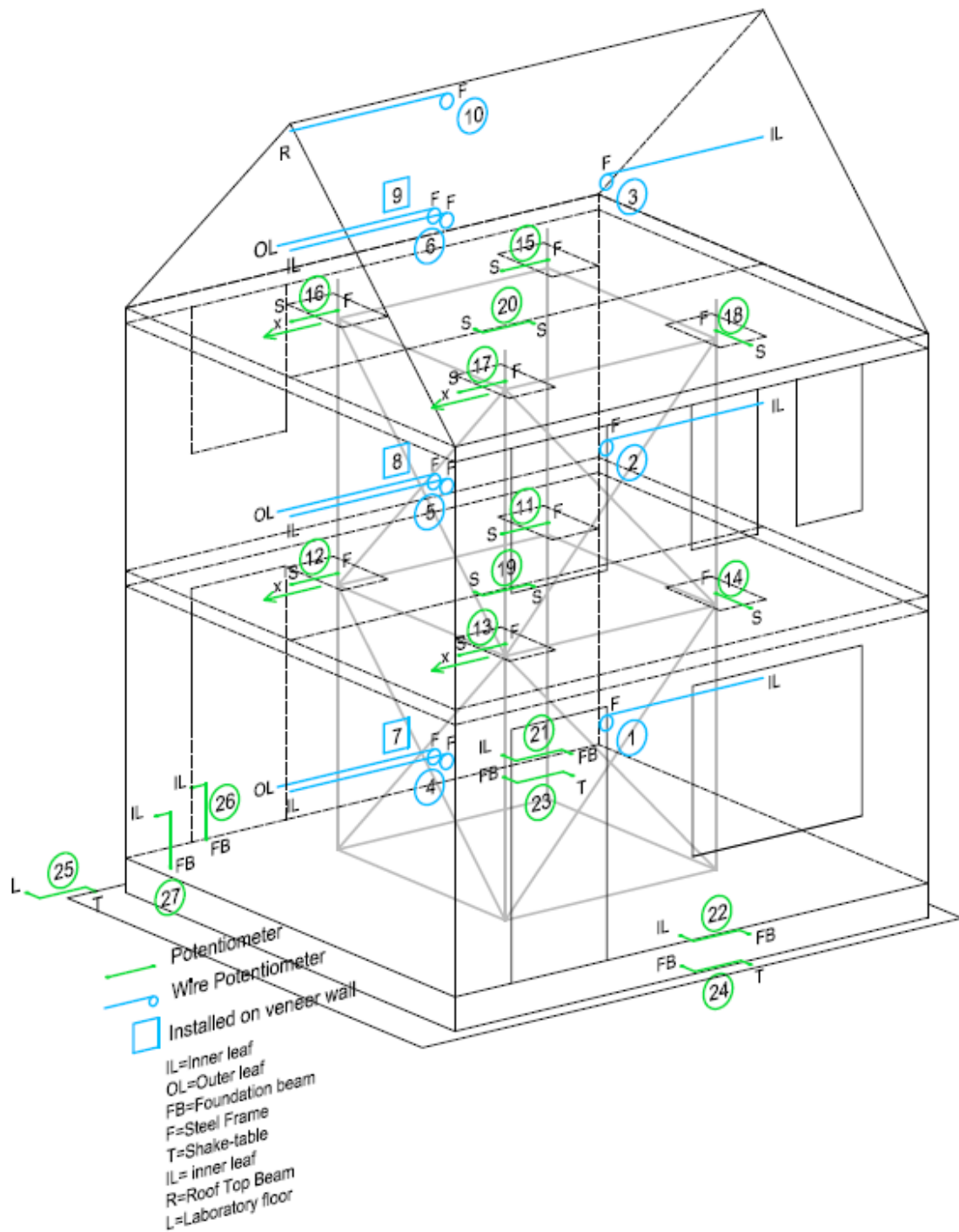


Figure 302. Identification of the potentiometers position.

## 6.3 Test procedure

The building specimen will be subjected to incremental dynamic test runs, namely a series of table motions of increasing intensity. The table input motions will consist of accelerograms aiming to reproduce a realistic simulation of possible ground motions in the study area, corresponding to scenarios with different return periods. A detailed study on the seismic hazard characteristics (Appendix B-2) identified 2 main scenarios. Two records were chosen from those scenarios in order to maximize the outcome of the test, taking into account the final goal: i.e. to develop a solid experimental reference for the development of fragility models for URM buildings in the Groningen area.

### 6.3.1 Dynamic Input Typologies

During the test the specimen was subjected to 3 different typologies of motion: a random white noise (RNDM) (for table calibration and structural identification purposes) and two types of earthquake signals (EQ1, EQ2), each associated to a different scenario. In particular, EQ1-Original (as reported in Appendix B-2) was slightly modified after the first two runs (#2\_25%\_EQ1\_024 and #4\_50%\_EQ1\_050) in order to limit the amplification in acceleration correspondent to the fundamental period of the structure. This was caused by the interaction between the specimen and the shake table. A smooth spectrum (EQ1, Figure 306) was considered to be more representative of the target spectrum.

Table 60. Summary selected report.

Input	PGA [g]	Waveform name	5-75% significant duration [s]
RNDM	0.05	RNDM_00	180
EQ1-Original	-0.0971	00201L	0.375
EQ1	-0.0959	00201L*	0.375
EQ2	0.1596	01703L	1.72

\*Modified by the author of Appendix B-2

Figure 303 to Figure 305 show the acceleration time history of the EQ1-Original, EQ1 and EQ2 respectively. Figure 306 plots a comparison between the three acceleration response spectra.

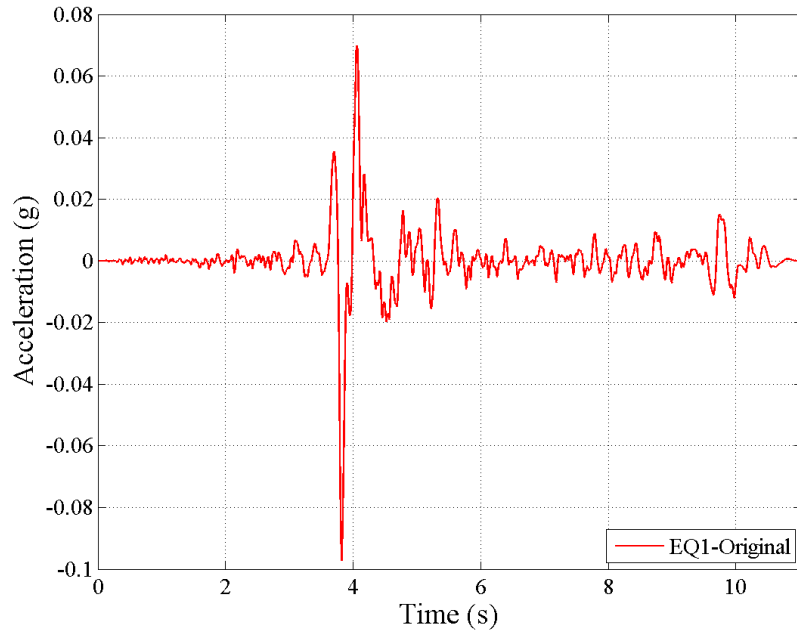


Figure 303. Acceleration time history of EQ1-Original input.

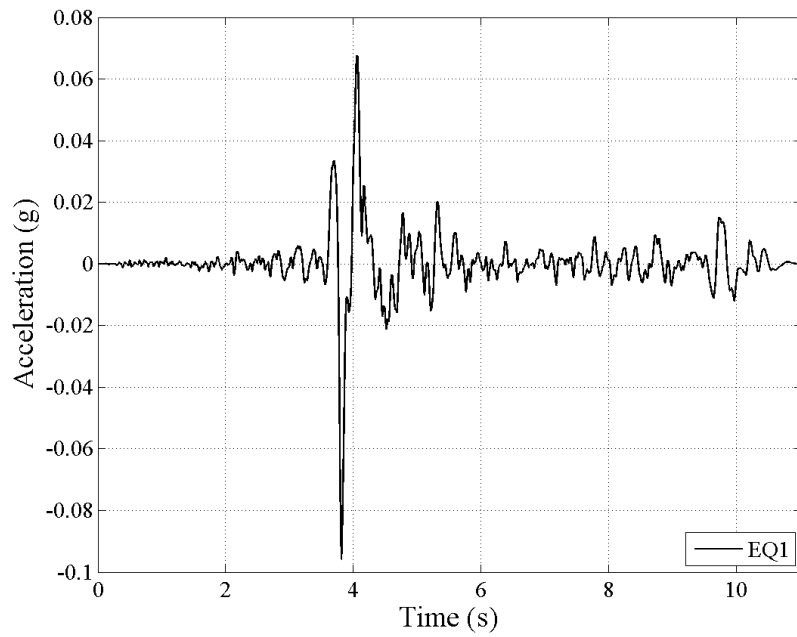


Figure 304. Acceleration time history of EQ1 input.

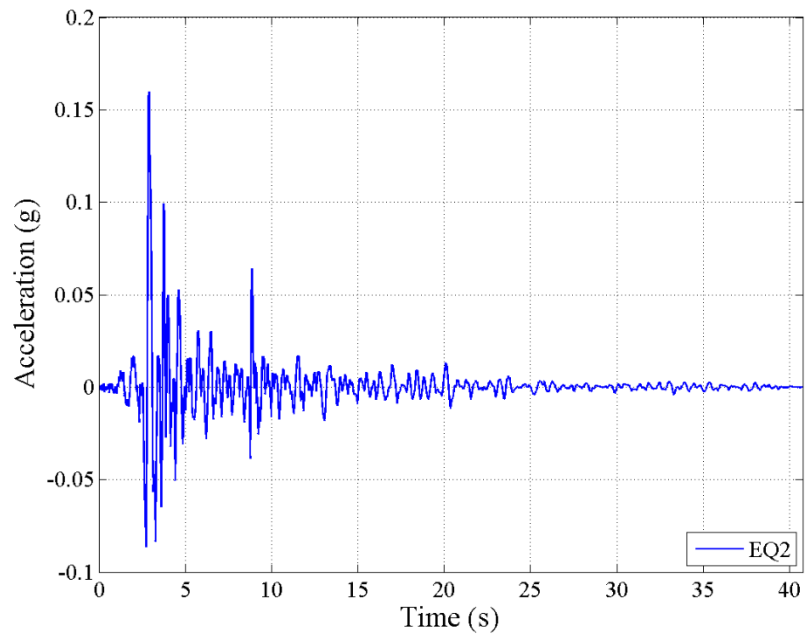


Figure 305. Acceleration time history of EQ2 input.

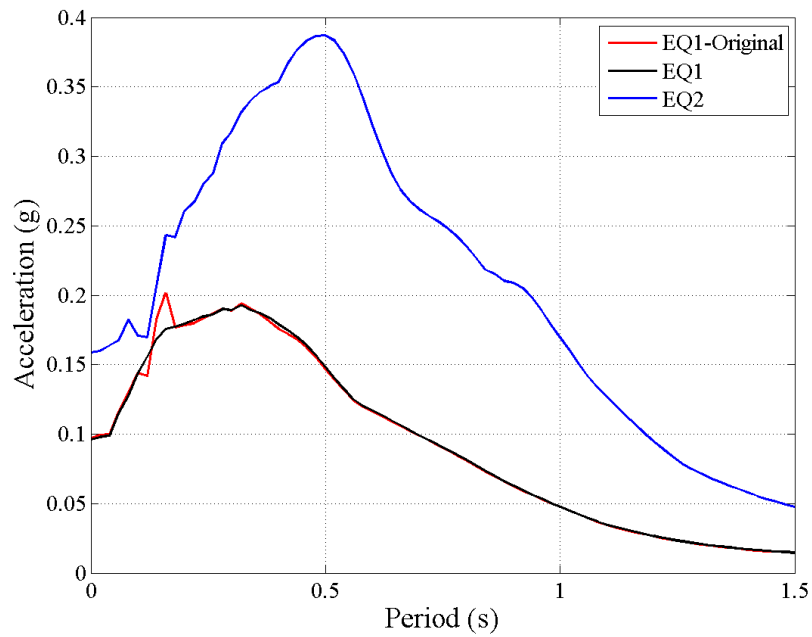


Figure 306. Acceleration response spectra comparison.



### 6.3.2 Applied Dynamic Input Sequence

Table 61 presents the testing sequence applied on the building specimen specifying the input typology, the test name and the roof configuration (some tests have been performed rigid roof configuration in order to prevent further damage of the specimen and the out-of-plane failure of the gables).

Table 61. Summary testing sequence.

<i>Date</i>	<i>Test #</i>	<i>Test Input</i>	<i>Test Name</i>	<i>Recorded PGA [g]</i>	<i>Rods</i>
09/08/2015	1	RNDM	RNDM_01	-	
	2	<i>EQ1-Or</i>	25%_EQ1_024	0.023	
	3	RNDM	RNDM_03	-	
	4	<i>EQ1-Or</i>	50%_EQ1_050	0.050	
09/09/2015	5*	RNDM	RNDM_05	-	V
	6*	<i>EQ1</i>	50%_4xEQ1_050	0.048	V
	7	<i>EQ1</i>	100%_EQ1_100	0.097	
	8	RNDM	RNDM_08	-	
	9	<i>EQ1</i>	150%_EQ1_150	0.138	
09/10/2015	10	RNDM	RNDM_10	-	
	11	<i>EQ2</i>	30%_EQ2_050	0.064	
	12	<i>EQ2</i>	30%_EQ2_050	0.058	
	13	<i>EQ2</i>	30%_EQ2_050	0.055	
	14	<i>EQ2</i>	50%_EQ2_080	0.085	
	15	RNDM	RNDM_15	-	
	16	<i>EQ2</i>	100%_EQ2_160	0.166	
09/12/2015	17	RNDM	RNDM_17	-	
	18	<i>EQ2</i>	50%_EQ2_080	0.114	
	19	<i>EQ2</i>	125%_EQ2_200	0.192	
09/14/2015	20	RNDM	RNDM_20	-	
	21	<i>EQ2</i>	150%_EQ2_240	0.241	
	22	RNDM	RNDM_22	-	
	23	<i>EQ2</i>	200%_EQ2_320	0.305	
	24	RNDM	RNDM_24	-	
09/15/2015	25*	RNDM	RNDM_25	-	V
	26*	<i>EQ2</i>	30%_EQ2_050	0.070	V
	27*	<i>EQ2</i>	30%_EQ2_050	0.058	V
	28*	<i>EQ2</i>	30%_EQ2_050	0.055	V
	29*	<i>EQ2</i>	60%_EQ2_100	0.112	V
	30*	RNDM	RNDM_30	-	V



## 6.4 Test Results

### 6.4.1 Damage pattern evolution

The following sections describe the damage evolution during the entire test. After each table motion, the building was inspected and the damage (*e.g.* cracks) were identified, noted and measured. The evolution was reported on specimen drawings for all the dynamic inputs and then reported in this section.

#### **Observed Damage after Test # 14, 50%\_EQ2\_80**

The survey carried out immediately after the test performed at a nominal peak ground acceleration of  $0.8 \text{ m/s}^2$  did not indicate the formation of any crack.

#### **Observed Damage after Test # 16, 100%\_EQ2\_160**

During the test performed at 100% of EQ2 ( $1.6 \text{ m/s}^2$ ) the specimen suffered slight damage and the formation of the first few cracks was observed. On the east side of the calcium silicate masonry, two cracks were developed on the first storey, a few centimeters above the base level of the two corner piers. Crack #6A identified on the leftmost pier (see Figure 307 to Figure 311) was developed horizontally, in contrast to the rest cracks that presented a stair-stepped diagonal pattern. On the west side of the building, the inner leaves presented similar to the eastern side damage. Diagonal cracks were developed on the bottom of the first storey corner piers, while another crack was identified at the lower left corner of the leftmost second storey opening (crack # 8, shown in Figure 309 and Figure 310).

Measuring the width of the cracks at the end of each test allowed monitoring the evolution of the damage induced on the body of the masonry subjected to the sequence of increasing intensity ground motions. The following figures summarize the location as well as the extension of the cracks observed at the end of the test at PGA of  $1.6 \text{ m/s}^2$ . The maximum crack width measured was approximately 1 mm, corresponding to crack #14B, while crack #8 was as wide as 0.1 mm (Figure 310).

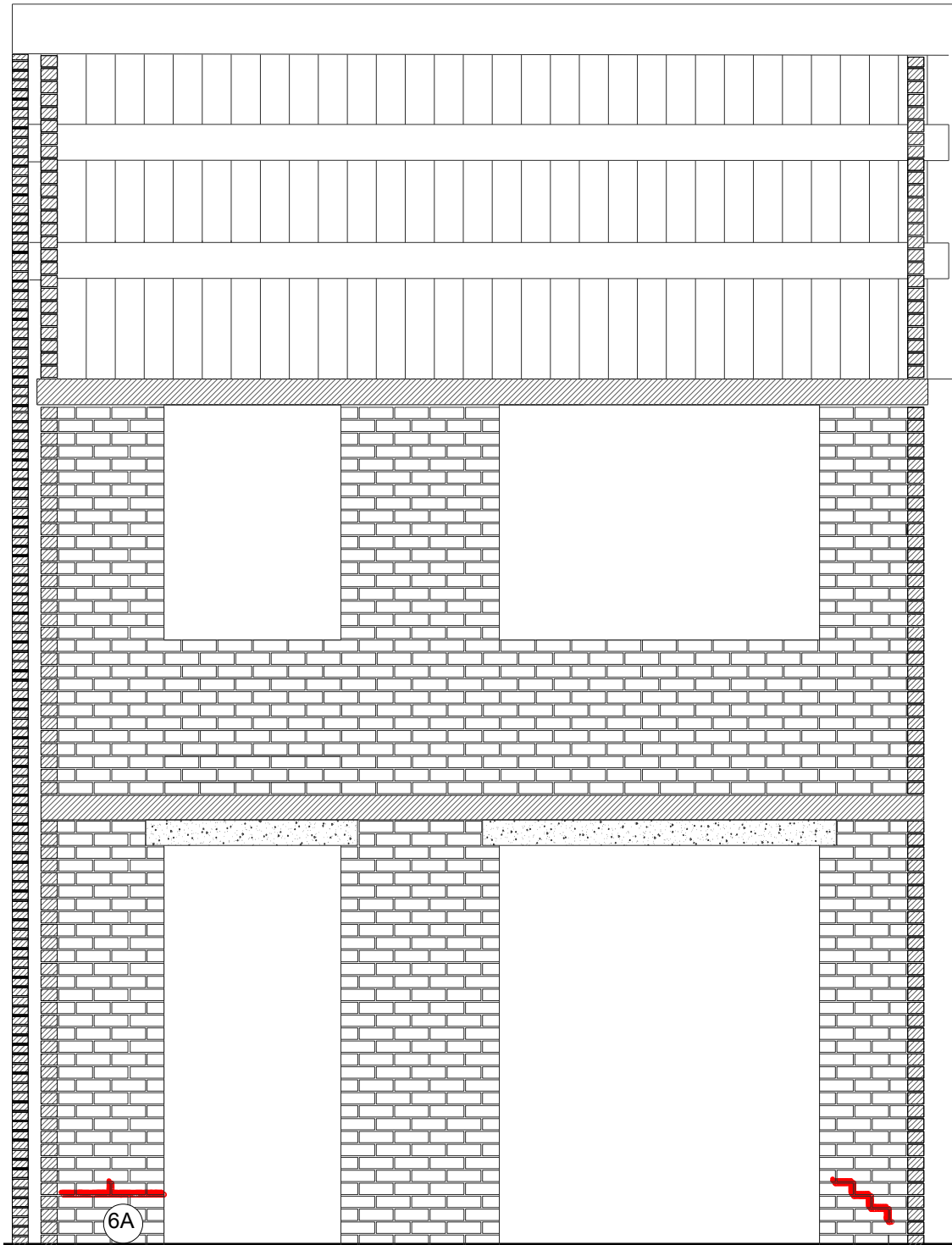


Figure 307. Section of the test-house - inner leaf - east side. Illustration of crack pattern after the test # 16, 100%\_EQ2\_160,  $PGA = 1.6 \text{ m/s}^2$ .



*Figure 308. Crack n 6A after the test # 16, 100%\_EQ2\_160, PGA= 1.6 m/s<sup>2</sup>.*

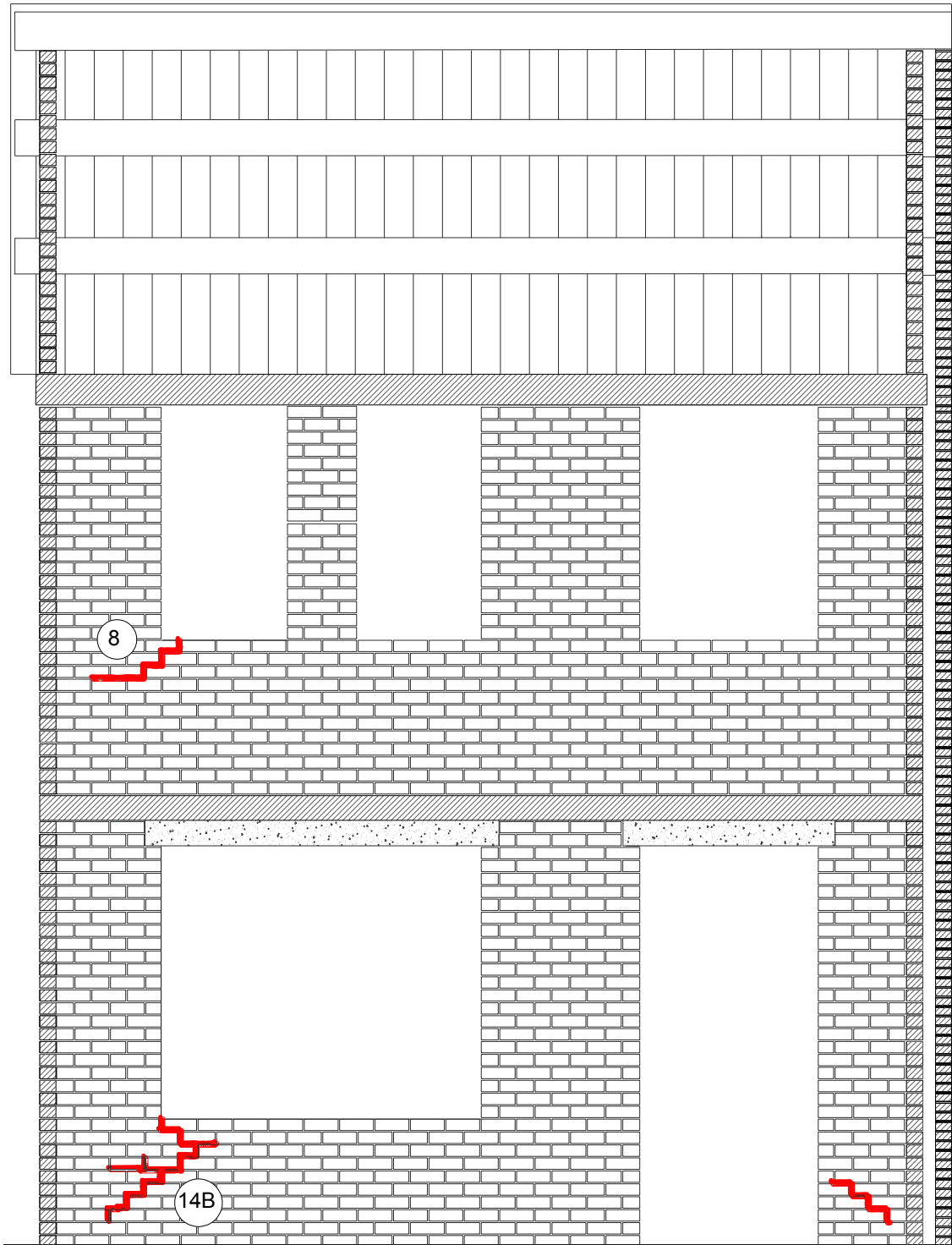


Figure 309. Section of the test - house - inner leaf - west side. Illustration of crack pattern after the test # 16, 100%\_EQ2\_160,  $PGA = 1.6 \text{ m/s}^2$



Figure 310. Crack #8 after the test # 16, EQ2\_160%, PGA= 1.6 m/s<sup>2</sup>

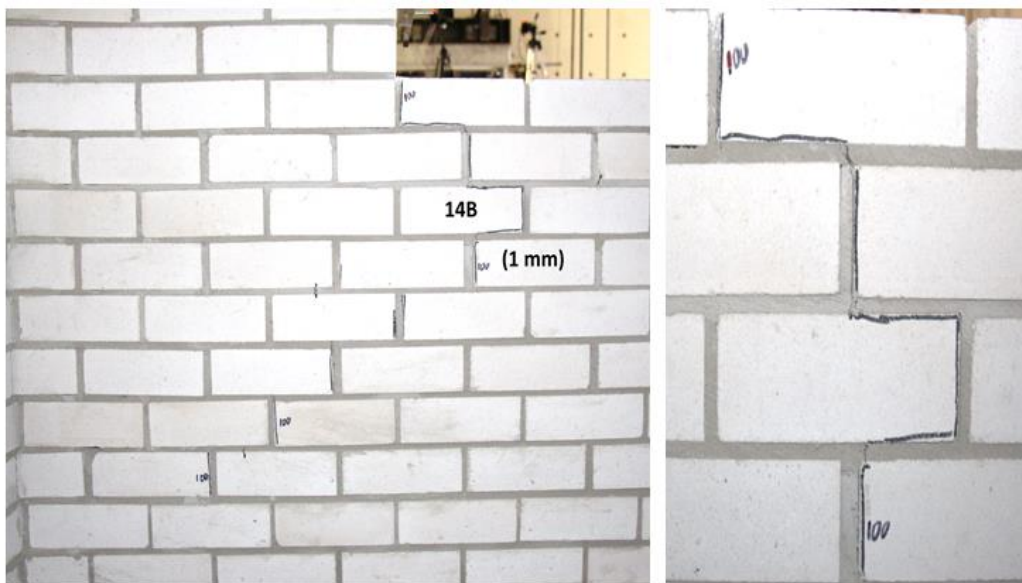


Figure 311. Crack #14B after the test # 16, 100%\_EQ2\_160, PGA= 1.6 m/s<sup>2</sup>.

### Observed Damage after the Test # 19, 125%\_EQ2\_200

At the end of the test performed at nominal PGA of  $2.4 \text{ m/s}^2$  (in this case the recorded PGA was close to  $2 \text{ m/s}^2$ ) the formation of new cracks was evident on both longitudinal inner masonry leafs of the structure. The rest cracks were characterized by a horizontal and diagonal stepped cracking pattern (Figure 313).

Concerning the damage observed on the west side, widening of the existing crack #14B occurred, from an opening of 1 mm to that of 2 mm (shown Figure 312). The newly developed crack, # 9, originating from the corner of the second storey central opening, was 1 mm wide, while the width of crack No. 8 did not change, remaining stable at 0.1mm.

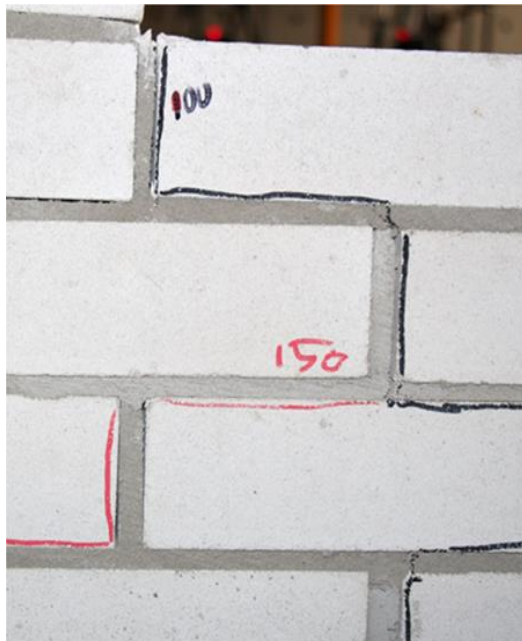
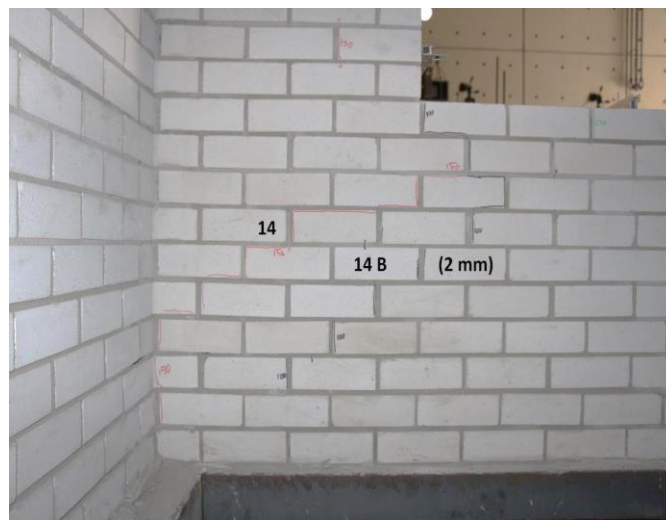
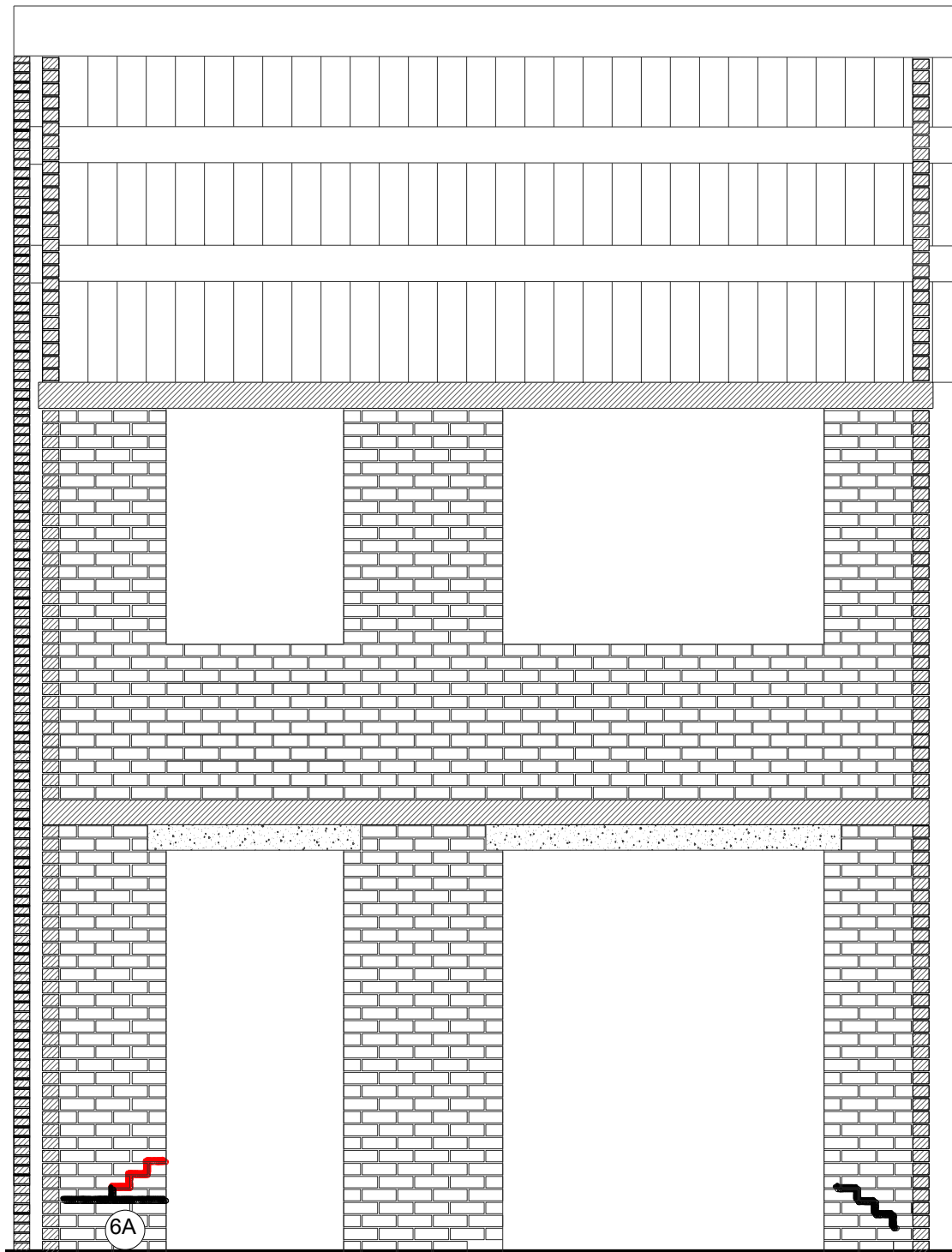


Figure 312. Cracks #14 and #14B after the test # 19, 125%\_EQ2\_200, PGA=  $2 \text{ m/s}^2$ .



*Figure 313. Section of the test-house - inner leaf - East-side. Illustration of crack pattern after the test # 19, 125%\_EQ2\_200,  $PGA = 2 \text{ m/s}^2$ . In red cracks induced at current test and in black the pre-existing cracks.*

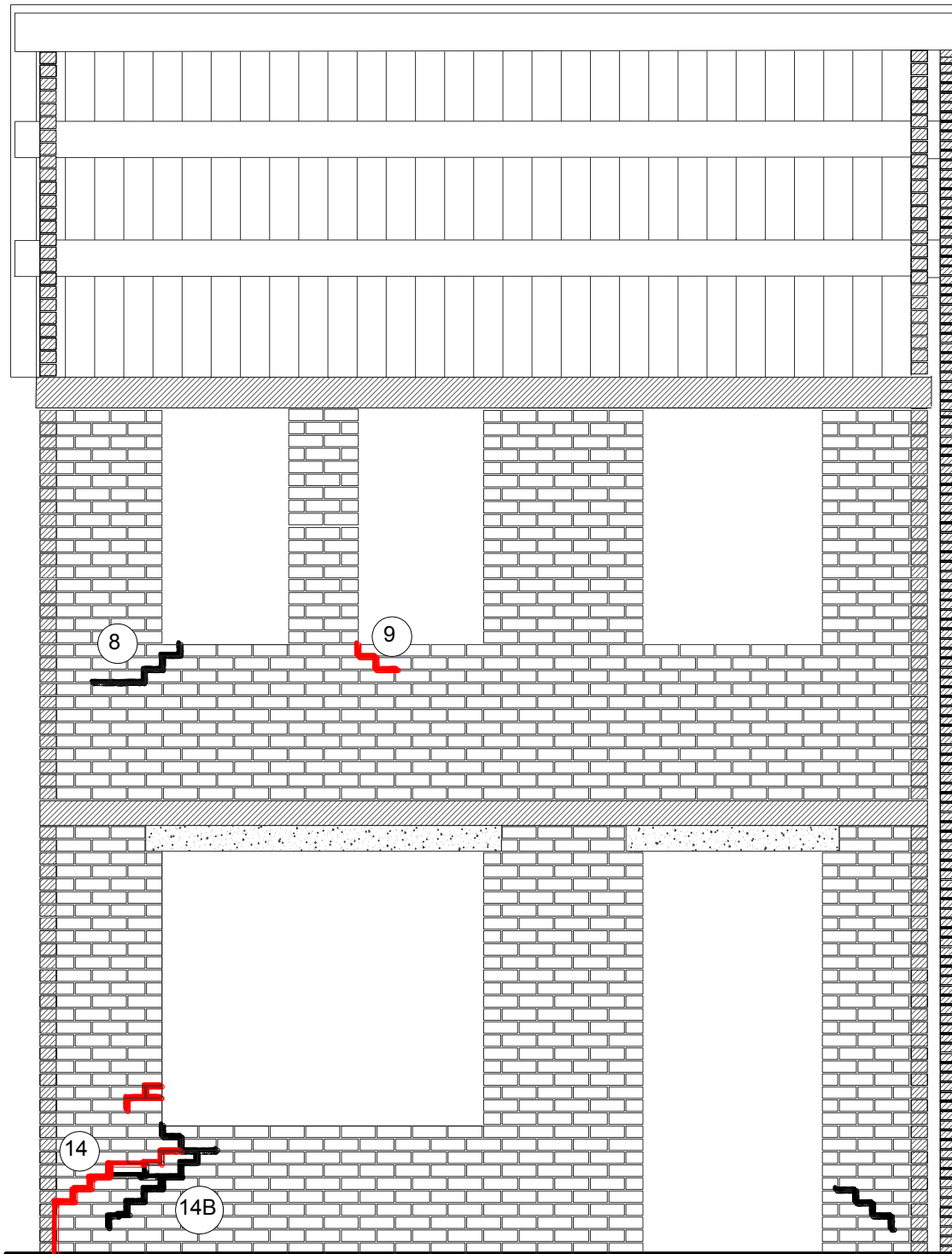


Figure 314. Section of the test-house - inner leaf - west-side. Illustration of crack pattern after the test # 19, 125%\_EQ2\_200,  $PGA = 2 \text{ m/s}^2$ . In red cracks induced at current test and in black the pre-existing cracks.

### Observed Damage After the Test # 21, 150%\_EQ2\_240

As a result of the detailed damage survey of the structure conducted immediately after the shaking table test at nominal PGA of  $2.4 \text{ m/s}^2$ , the formation of new cracks was detected on both storeys of the specimen.

On the east side of the building, the second storey piers presented prevailing horizontal cracks just below the interface between masonry piers and the second floor level slab (Figure 316). In the ground floor a horizontal crack appeared (#6C) a few centimeters above the base level. The width of crack #6C was equal to 2 mm. (shown in Figure 315).

On the west side, the longitudinal calcium silicate wall presented similar to the eastern side sliding on the top of the second storey piers. Furthermore, a horizontal crack was developed along the base of the squat pier of the second storey (exhibiting in-plane rocking response), extending subsequently to the body of the adjacent spandrel (shown in Figure 317).

On the north side, they observe the formation of the first cracks (Figure 318).

At the end of the test performed at PGA of  $2.4 \text{ m/s}^2$ , the width of the previously reported cracks #6 and #14B was equal to 4 mm and 3.5 mm, respectively, while the opening of crack #8 was no wider than 0.2 mm.



*Figure 315. Crack #6C after the test # 21, 150%\_EQ2\_240, PGA=  $2.4 \text{ m/s}^2$ .*

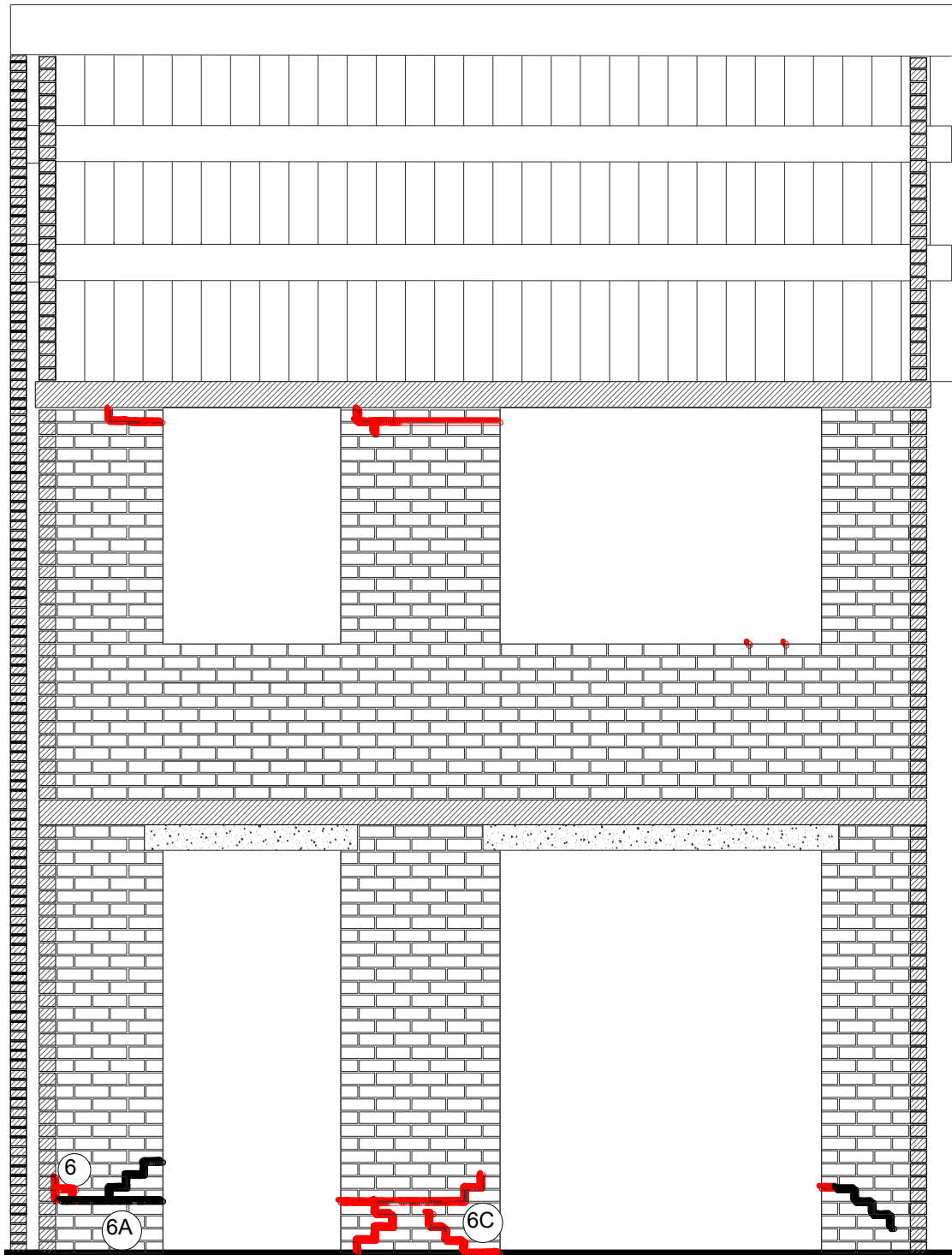


Figure 316. Section of the test-house - inner leaf - east-side. Illustration of crack pattern test after the test #21, 150%\_EQ2\_240,  $PGA= 2.4 \text{ m/s}^2$ . In red cracks induced at current test and in black the pre-existing cracks.

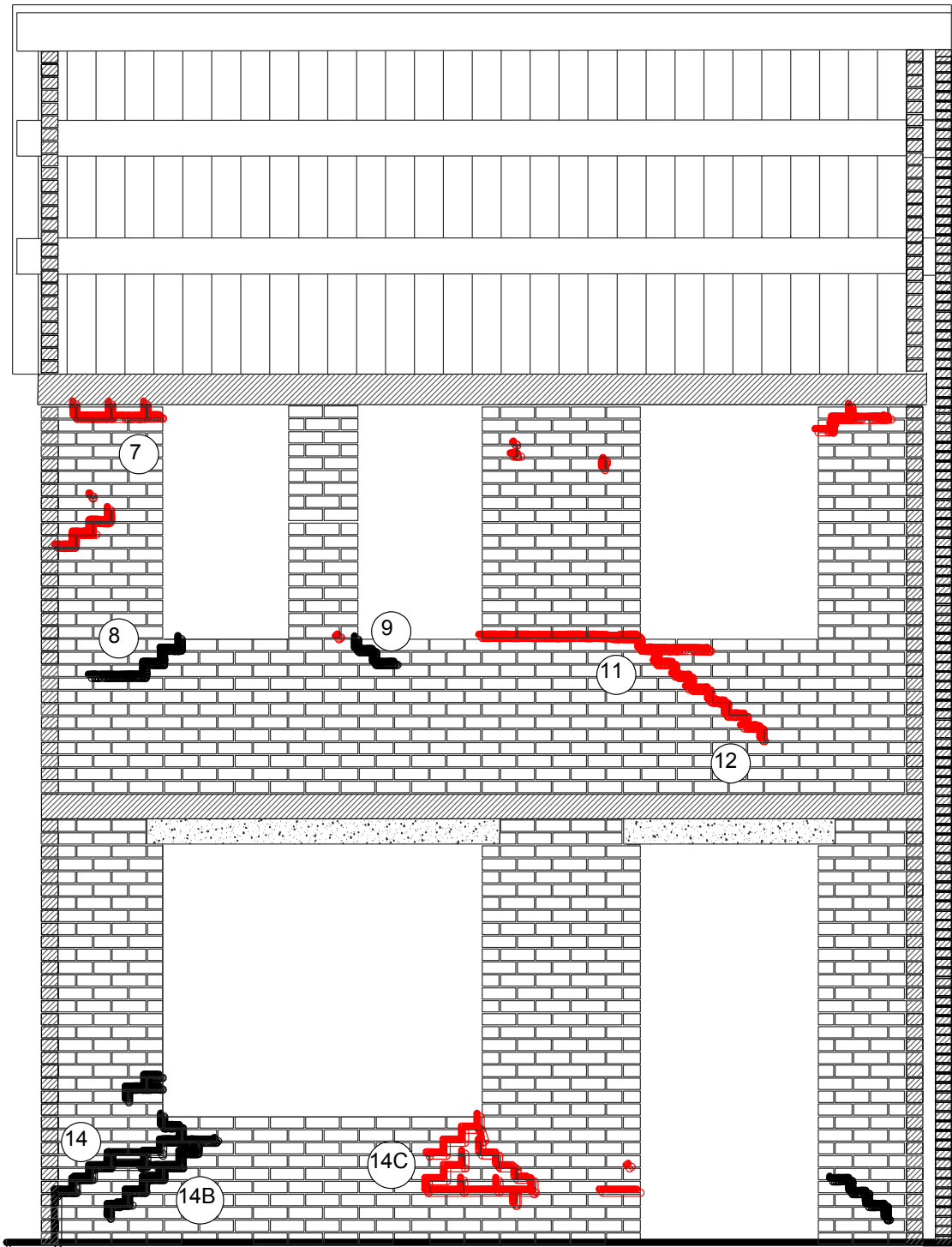
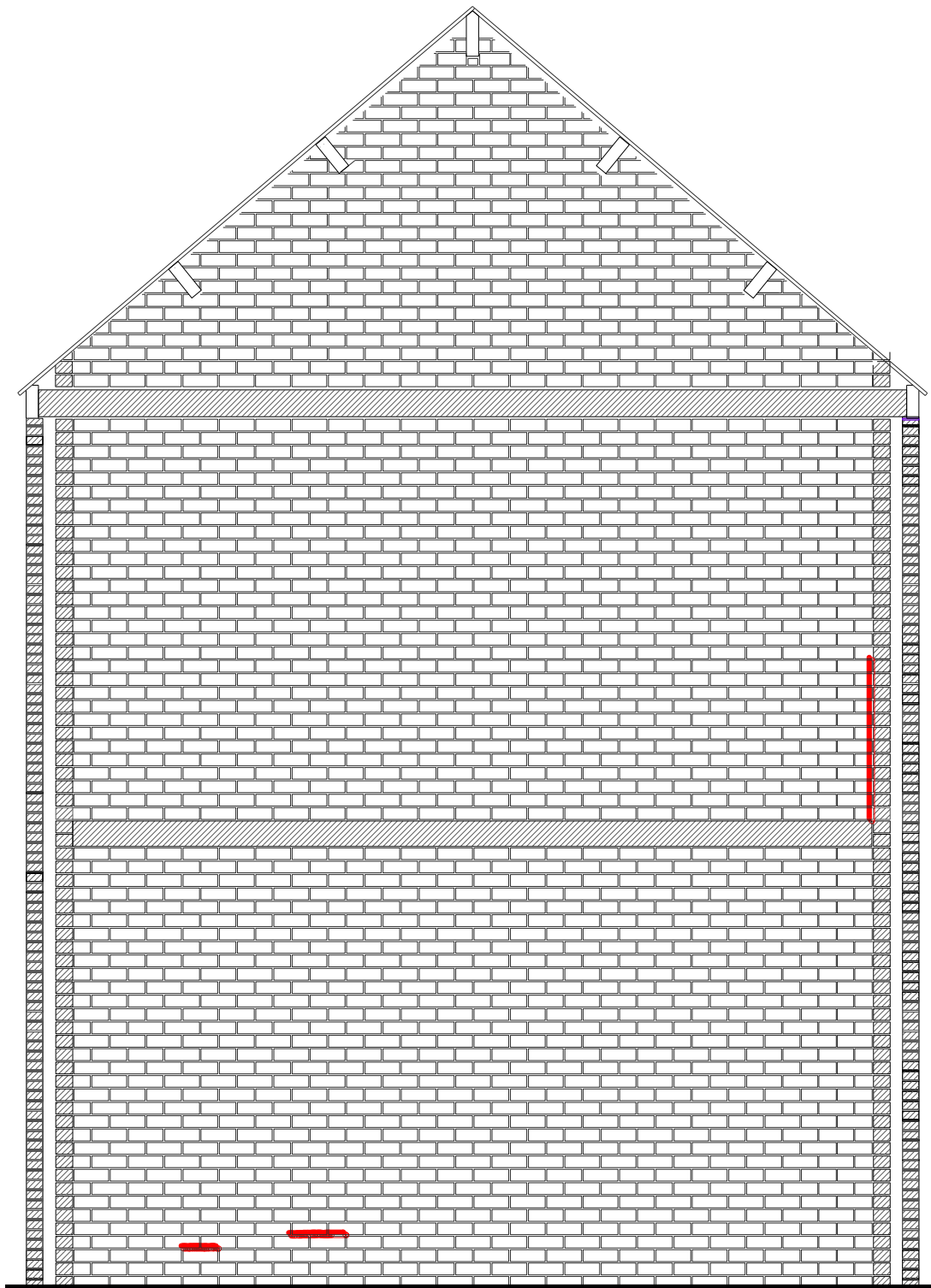


Figure 317. Section of the test-house - inner leaf - west-side. Illustration of crack pattern after the test #21, 150%\_EQ2\_240,  $PGA = 2.4 \text{ m/s}^2$ . In red cracks induced at current test and in black the pre-existing cracks.



*Figure 318. Section of the test-house - inner leaf - north-side. Illustration of crack pattern after the test #21, 150%\_EQ2\_240, PGA= 2.4 m/s<sup>2</sup>. In red cracks induced at current test and in black the pre-existing cracks.*



### **Observed Damage After the Test # 23, 200%\_EQ2\_320**

Because of the relatively high level of acceleration applied, the specimen experienced considerable damage during the test at nominal PGA of  $3.1 \text{ m/s}^2$ , compared to that observed after the lower intensity excitations. In particular, the test performed at this level has been characterized by a global response of the structure, as evidenced by the formation of many new cracks, identified on every one of the specimen walls (both longitudinal and orthogonal, clay and calcium silicate walls), as well as the elongation of pre-existing cracks.

Detailed survey of the structure was conducted revealing extensive damage in the spandrel beams at the first floor level. Cracks starting from the corners of the openings of all walls were reported. De-cohesion of masonry blocks also occurred in the calcium silicate masonry spandrels of both storeys.

Concerning the response of the longitudinal calcium silicate walls, a general widening of the existing cracks, opened during the previous stages of dynamic testing was observed, in particular of those located in the spandrels of the first floor level (cracks #9 and #11, shown in Figure 320). In addition to the above reported cracks, the formation of a new crack (#12) was identified, crossing spandrel W-5 with an angle of about  $45^\circ$  (Figure 320). Extensive damage was also induced in the eastern longitudinal wall spandrels, which had not experienced any damage until this level of excitation, presenting stair-stepped diagonal cracking and sliding of the mortar joints (cracks #1, #2, #3 and #4, shown in Figure 319). The horizontal cracks exhibited at the top of the second storey piers were also enlarged, reaching a maximum residual sliding of 15 mm.

As far as the damage reported in the orthogonal walls is concerned, the formation of diagonal cracks with an angle of approximately  $45^\circ$  with respect to the horizontal plane was clearly observed. Following, a stair-stepped cracking pattern through the mortar joints, with openings no greater than 1.2 mm was observed. This crack pattern is indicative of the flange participation of the orthogonal walls on the in-plane walls response (shown in Figure 322 and in Figure 323).

Focusing on the gables of both north and south side (Figure 322 and Figure 323), horizontal cracks along their base are apparent, just above the second floor level, indicating the out-of-plane overturning mechanism occurring at the gable level. Other cracks are also identified at the locations where the timber beams of the roof are connected with the gable walls. Cracks around these beams are due to pounding of the beams on the supporting masonry gable walls (shown in Figure 322, Figure 323, Figure 331 and Figure 332).

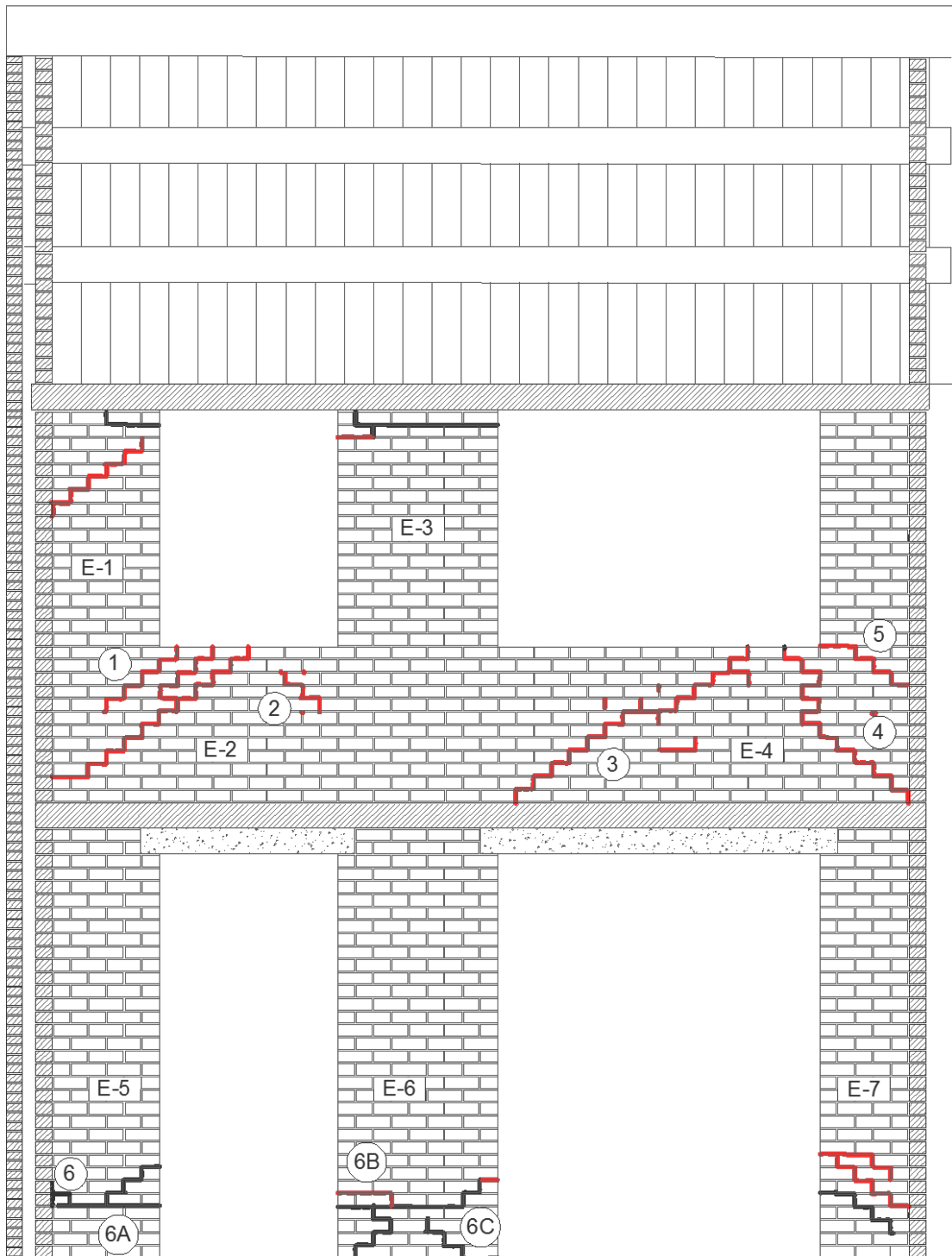


Figure 319. Section of the test-house - inner leaf - east-side. Illustration of crack pattern after the test # 23, 200%\_EQ2\_320,  $PGA = 3.1 \text{ m/s}^2$ . In red cracks induced at current test and in black the pre-existing cracks.

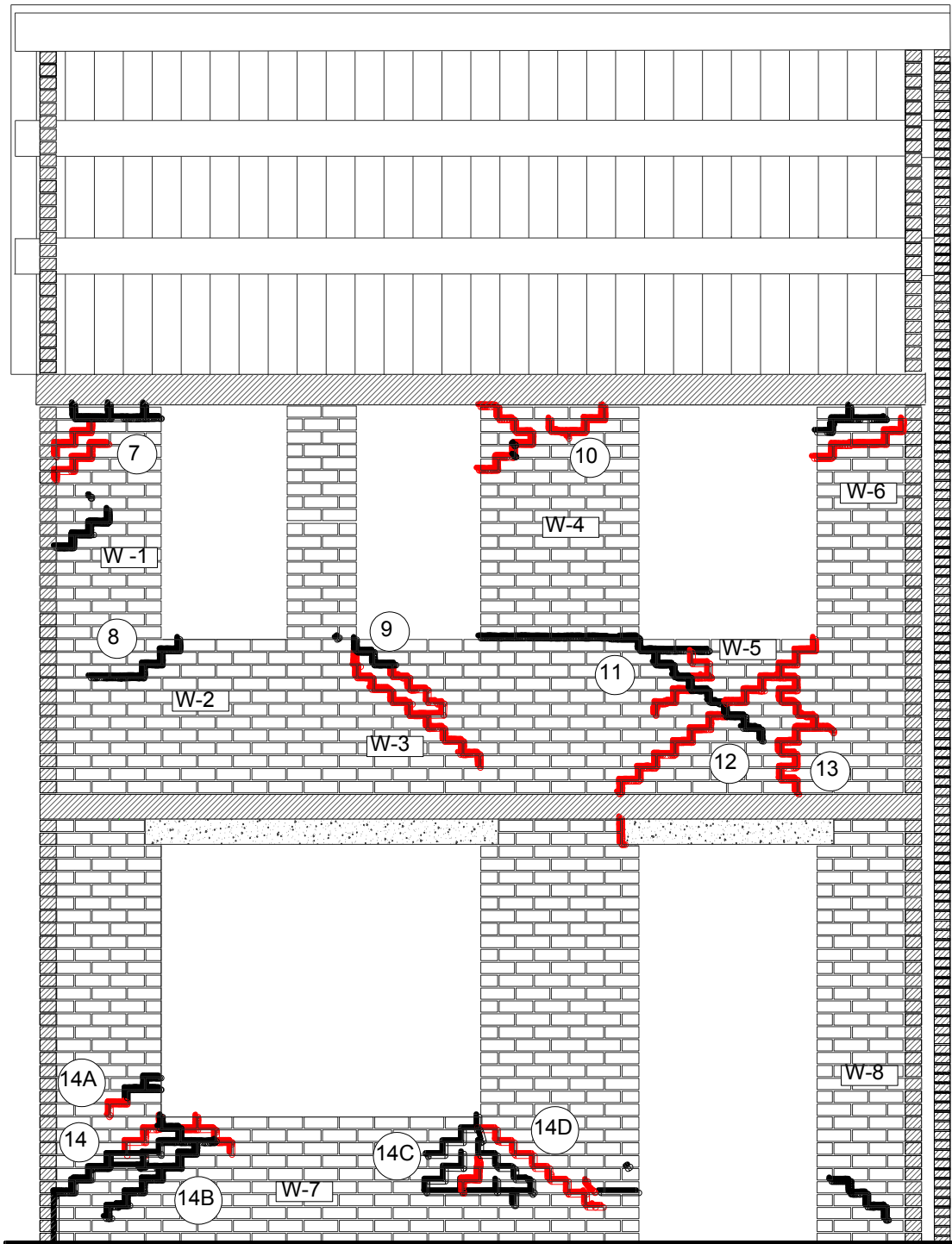


Figure 320. Section of the test-house - inner leaf - west-side. Illustration of crack pattern after the test #23, 200%\_EQ2\_320,  $PGA = 3.1 \text{ m/s}^2$ . In red cracks induced at current test and in black the pre-existing cracks.



Figure 321. Crack #10 after the test # 23, 200%\_EQ2\_320, PGA= 3.1 m/s<sup>2</sup>

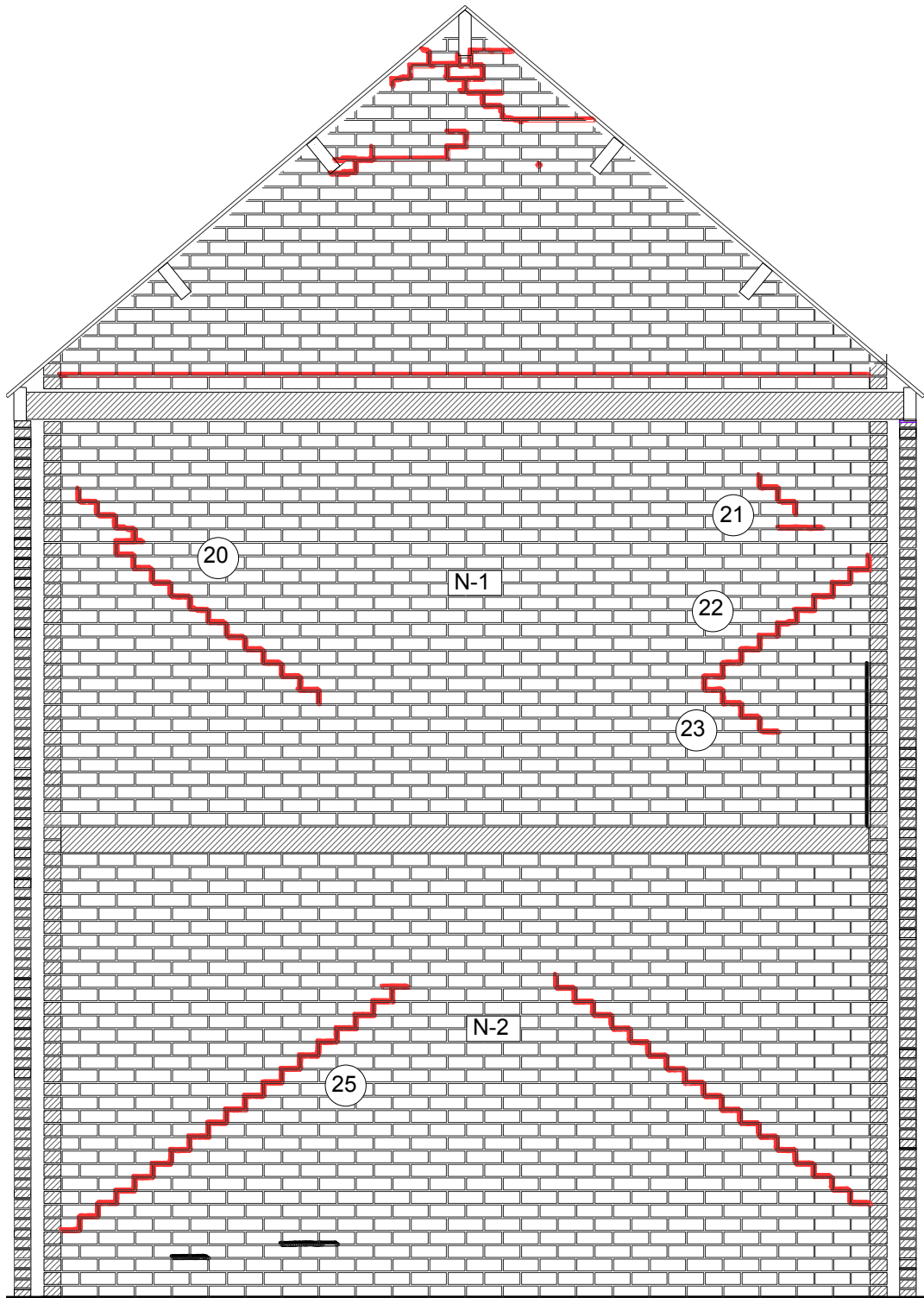


Figure 322. Section of the test-house - inner leaf – north side. illustration of crack pattern after the test # 23, 200%\_EQ2\_320,  $PGA= 3.1 \text{ m/s}^2$ .

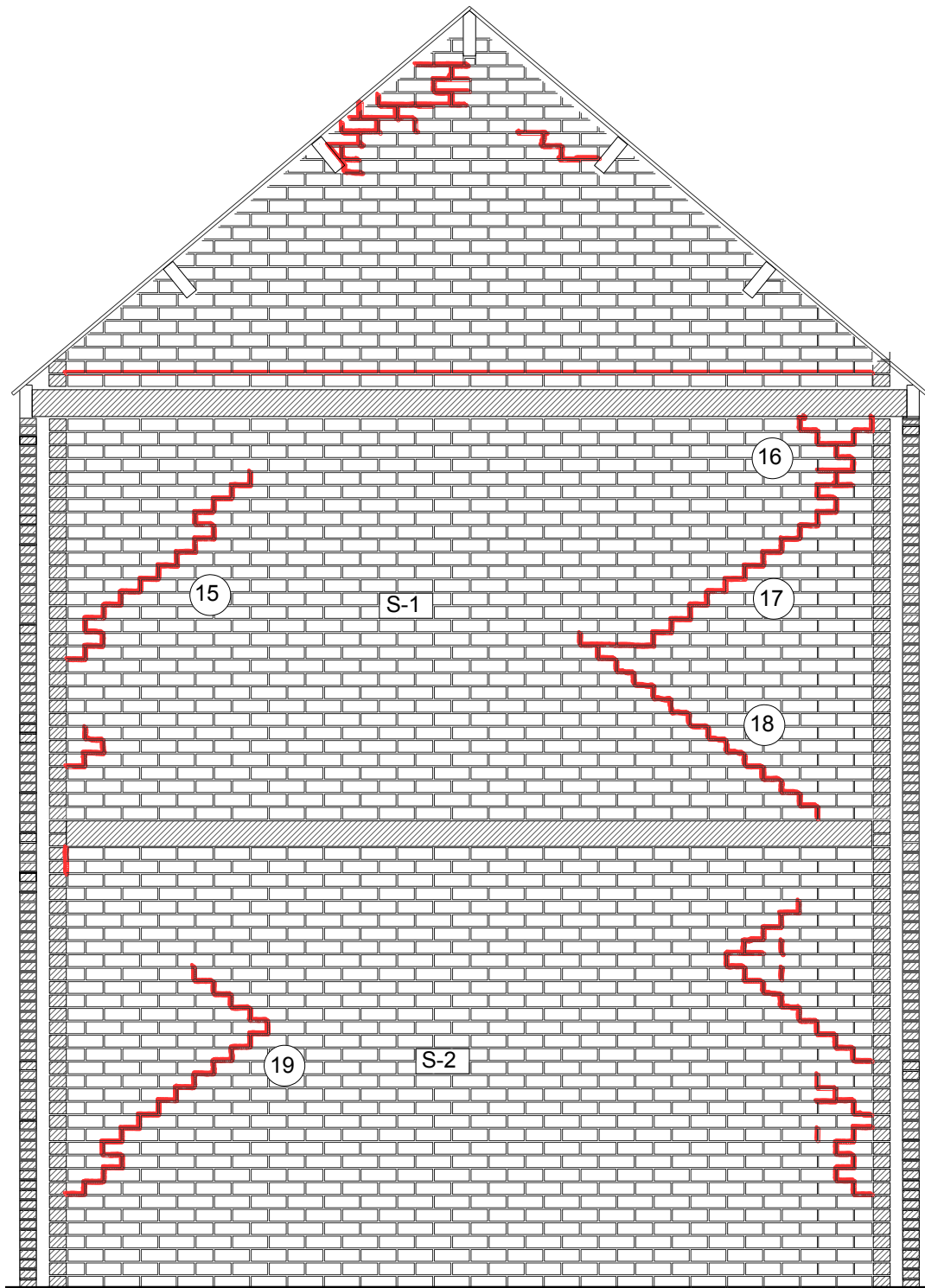


Figure 323. Section of the test-house - inner leaf – south side. illustration of crack pattern after the test # 23, 200%\_EQ2\_320,  $PGA = 3.1 \text{ m/s}^2$ .

In the following are a series of pictures that represent the state of damage after the test #23, 200%\_EQ2\_320,  $PGA= 3.1 \text{ m/s}^2$ .



*Figure 324. Crack after the test # 23, 200%\_EQ2\_320,  $PGA= 3.1 \text{ m/s}^2$ .*



*Figure 325. Crack after the test # 23, 200%\_EQ2\_320,  $PGA= 3.1 \text{ m/s}^2$ .*



*Figure 326. Sliding of the concrete lintel with respect to the masonry support, after the test # 23, 200%\_EQ2\_320,  $PGA = 3.1 \text{ m/s}^2$ .*



*Figure 327. Horizontal crack due to sliding identified on the top of calcium silicate pier, after the test # 23, 200%\_EQ2\_320,  $PGA = 3.1 \text{ m/s}^2$ .*



Figure 328 Increase of the sliding observed on the top of the pier and formation of a new stair-stepped crack, after the test # 23, 200%\_EQ2\_320,  $PGA = 3.1 \text{ m/s}^2$ .



Figure 329. Fracture of brick at the interface between flange and S wall, after the test # 23, 200%\_EQ2\_320,  $PGA = 3.2 \text{ m/s}^2$ .



Figure 330. De-cohesion of masonry blocks observed in the calcium silicate masonry, after the test # 23, 200%\_EQ2\_320,  $PGA = 3.1 \text{ m/s}^2$ .



Figure 331. Cracks around the timber beams due to pounding of the beams on the supporting masonry gable walls, after the test # 23, 200%\_EQ2\_320,  $PGA = 3.1 \text{ m/s}^2$ .



*Figure 332. Cracks around the timber beams due to pounding of the beams on the supporting masonry gable walls, after the test # 23, 200%\_EQ2\_320,  $PGA= 3.1 \text{ m/s}^2$ .*

Regarding the damage observed in the veneer walls, the spandrel E-2 of the eastern façade developed a flexural mechanism with vertical cracks at both ends (crack #32 in Figure 333 and in Figure 334) originating from the concrete lintels, whereas spandrel E-4 presented failure in shear forming the characteristic X-crack pattern. On the western side, large stair-stepped shear cracks were observed, like those crossing the entire spandrel W-2 with an angle of  $45^\circ$  (cracks #26 and #27 in Figure 335). In general, most of the deformations were absorbed by sliding of the concrete lintels with respect to the masonry supports as well as sliding at the interface of the roof timber beams and the second storey masonry piers.

Concerning the northern side veneer wall, the only cracks observed are located at the second floor level, extended along the entire length, is associated to the tendency of the gable wall to develop an out-of-plane overturning mechanism (Figure 338).

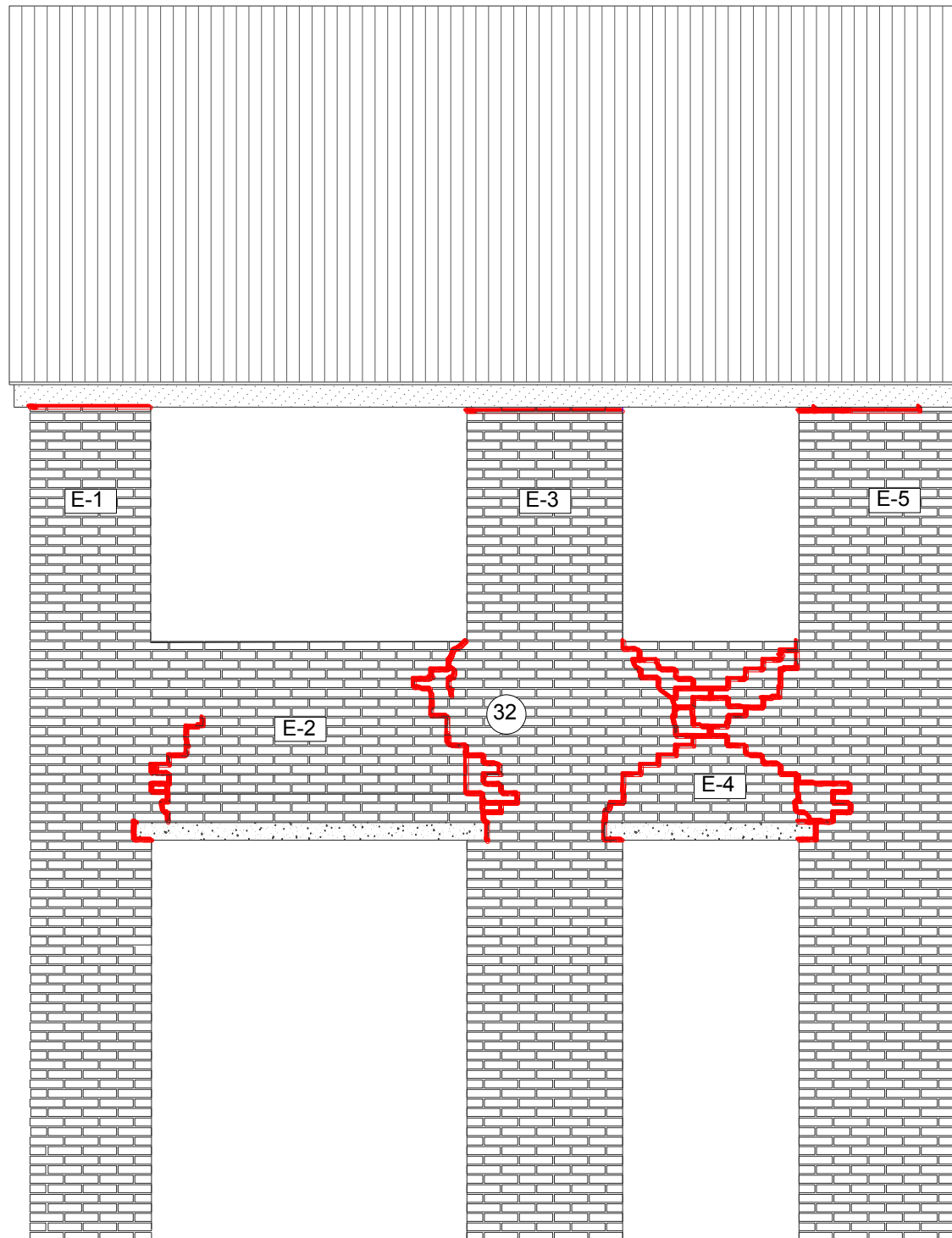


Figure 333. Elevation view of the test-house - outer leaf - east-side. illustration of crack pattern after the test # 23, 200%\_EQ2\_320, PGA= 3.1 m/s<sup>2</sup>.



*Figure 334. Crack after the test # 23, 200%\_EQ2\_320, PGA= 3.1 m/s<sup>2</sup>.*

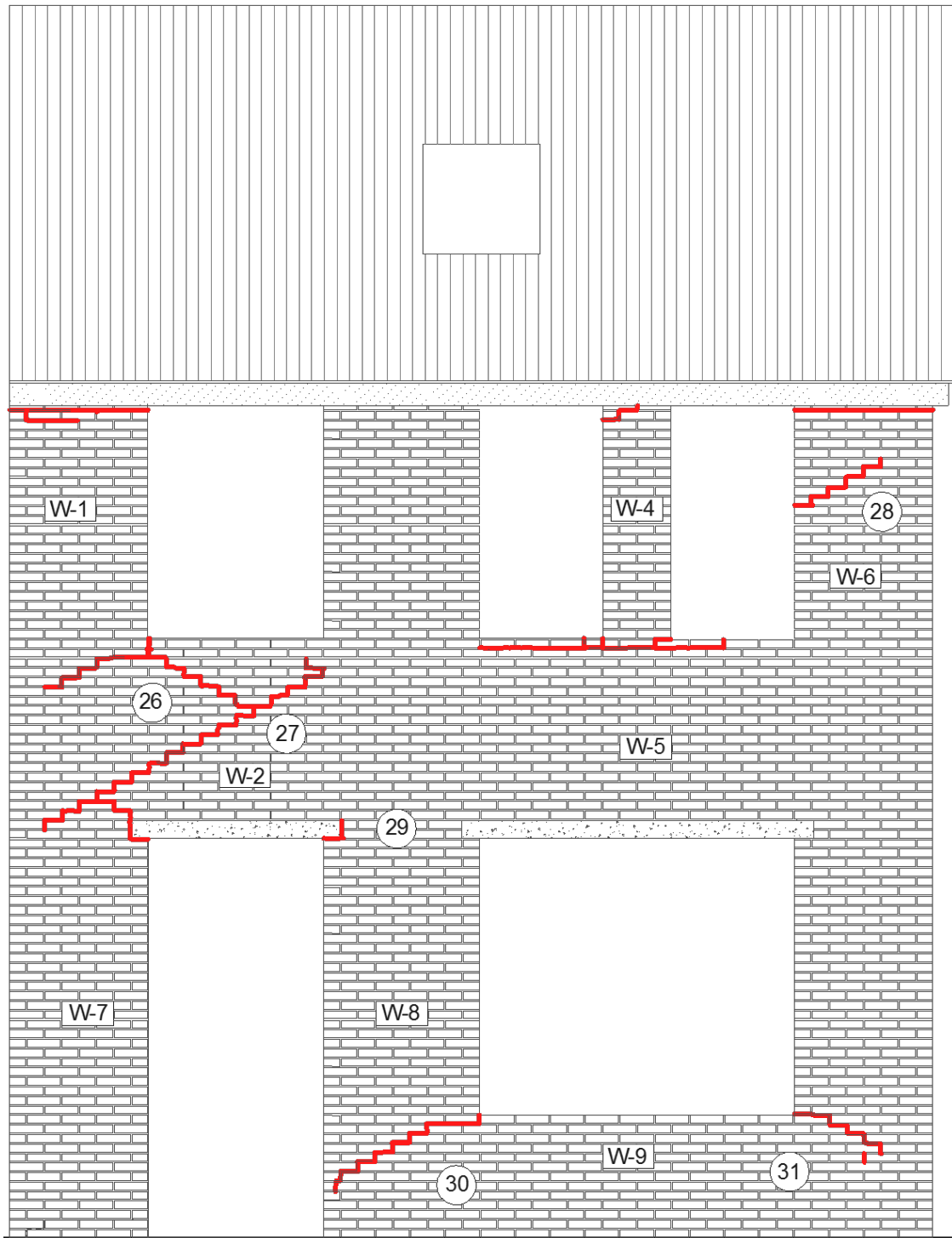


Figure 335. Elevation view of the test-house - outer leaf - west-side illustration of crack pattern after the test # 23, 200%\_EQ2\_320,  $PGA= 3.1 \text{ m/s}^2$ .



Figure 336. Cracks 26, 27 and 29 after the test #23, 200%\_EQ2\_320, PGA= 3.1 m/s<sup>2</sup>.

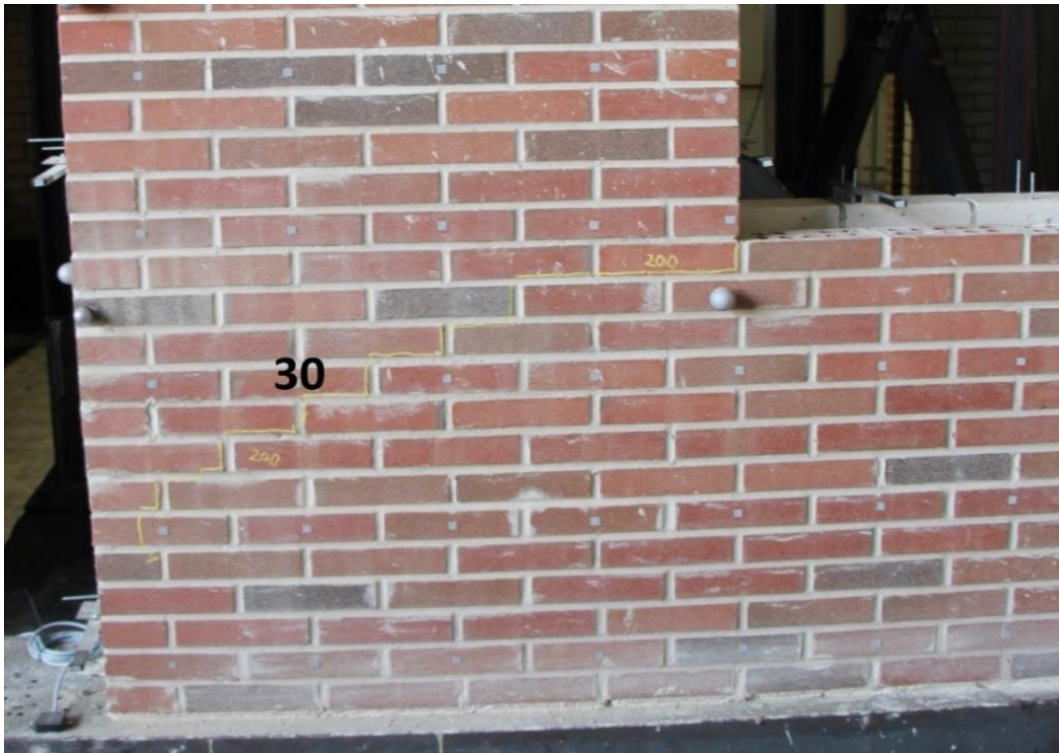
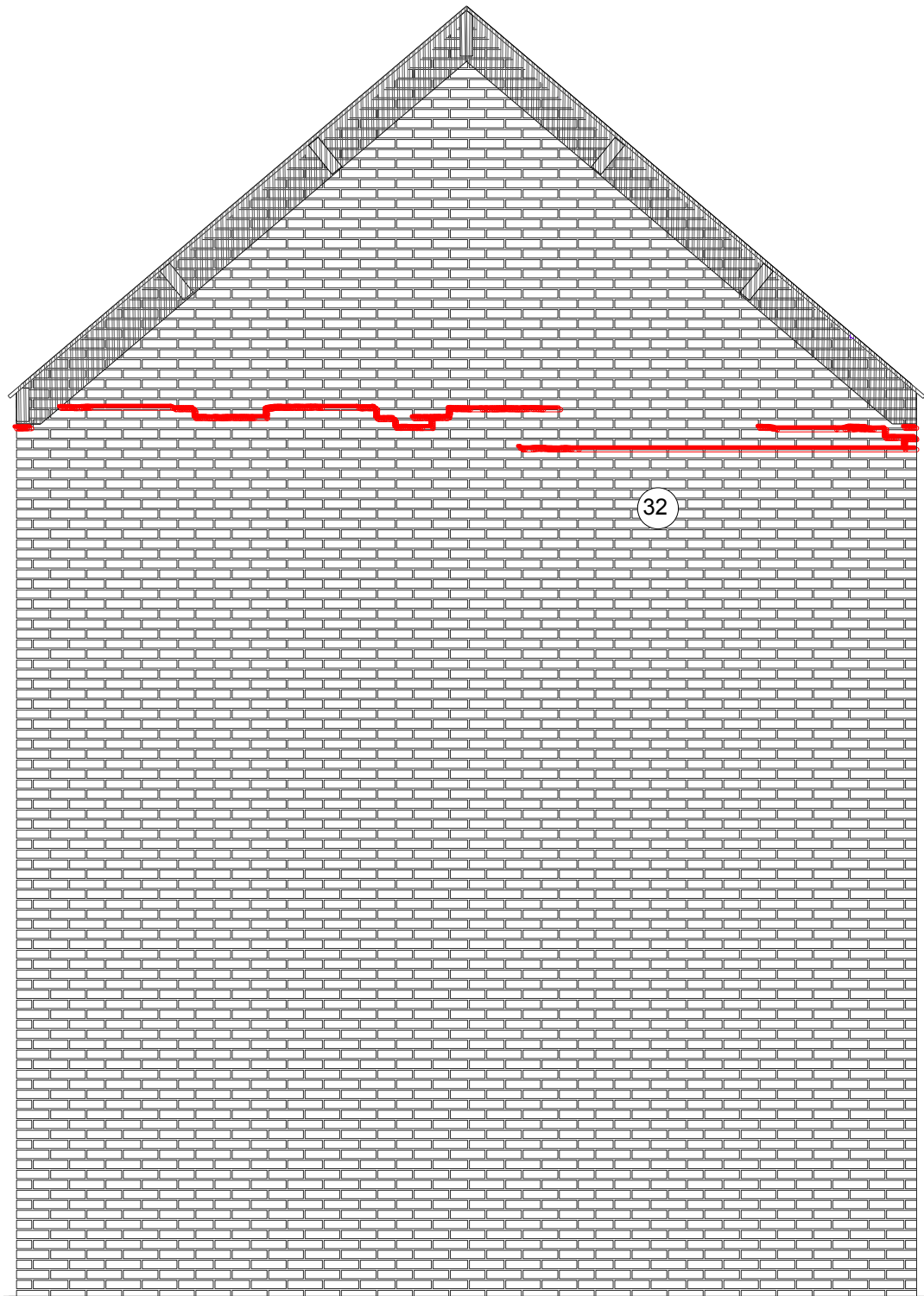


Figure 337. #30 after the test # 23, 200%\_EQ2\_320, PGA= 3.1 m/s<sup>2</sup>.



*Figure 338. Elevation view of the test-house - outer leaf - north side. Illustration of crack pattern after the test # 23, 200%\_EQ2\_320, PGA= 3.1 m/s<sup>2</sup>.*

### Observed Damage After the Test # 29, 60%\_EQ2\_100 (rigid roof).

After the test at PGA of  $3.1 \text{ m/s}^2$ , the building was subjected to a further test at a nominal PGA of  $1 \text{ m/s}^2$ . Before this test the roof rods were tensioned in order to have a rigid diaphragm. Both longitudinal walls were characterized by a moderate widening and elongation of the existing cracks (Figure 341, Figure 342 and Figure 343).

The following figures illustrate the crack patterns reported after the test and described in the preceding paragraphs.

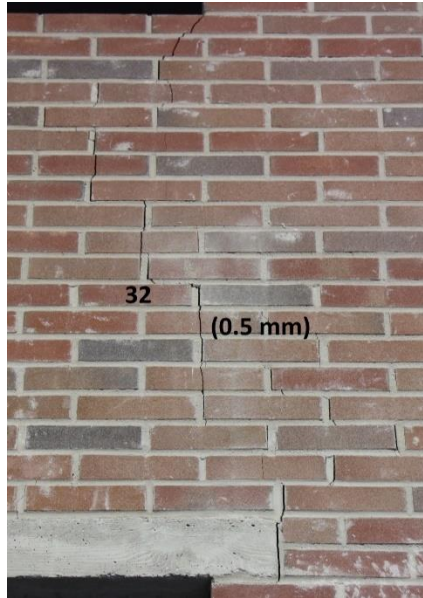


Figure 339. Crack #32 after the test #29, 60%\_EQ2\_100, PGA=  $1.0 \text{ m/s}^2$ .

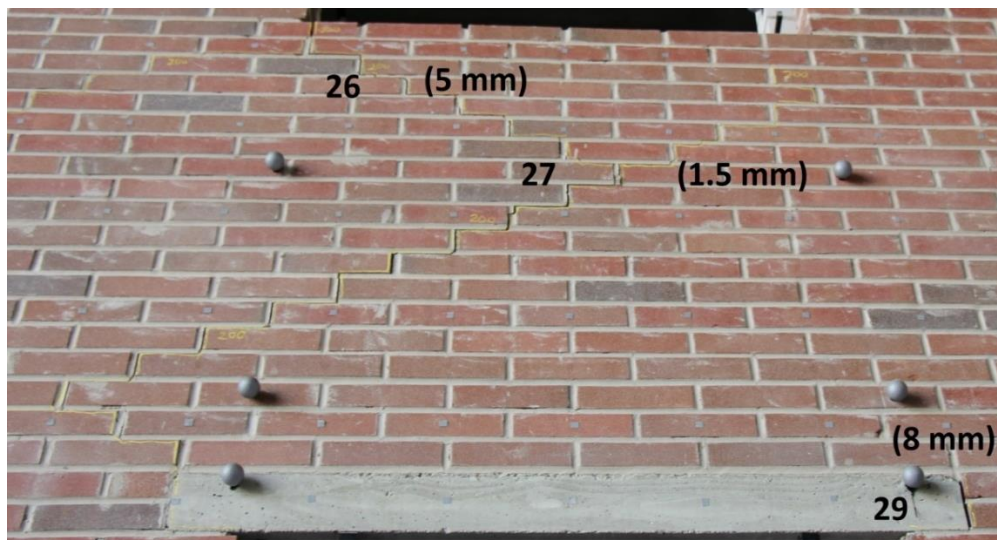


Figure 340. Cracks #26, #27 and #29 after the test #29, 60%\_EQ2\_100, PGA=  $1.0 \text{ m/s}^2$ .

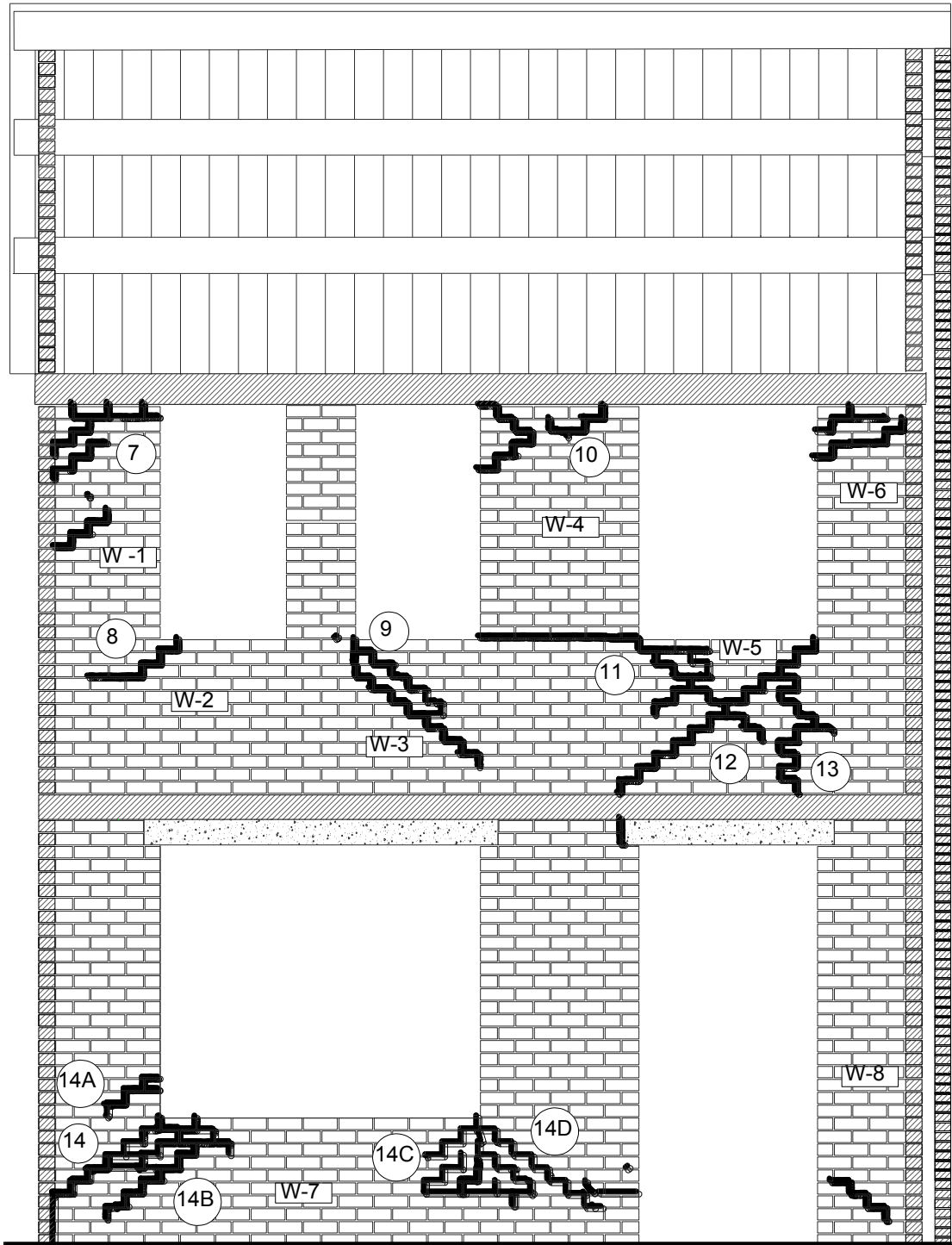


Figure 341. Elevation view of the test-house - inner leaf - east-side. Illustration of crack pattern after the test # 29, 60%\_EQ2\_100,  $PGA= 1,0 \text{ m/s}^2$ .

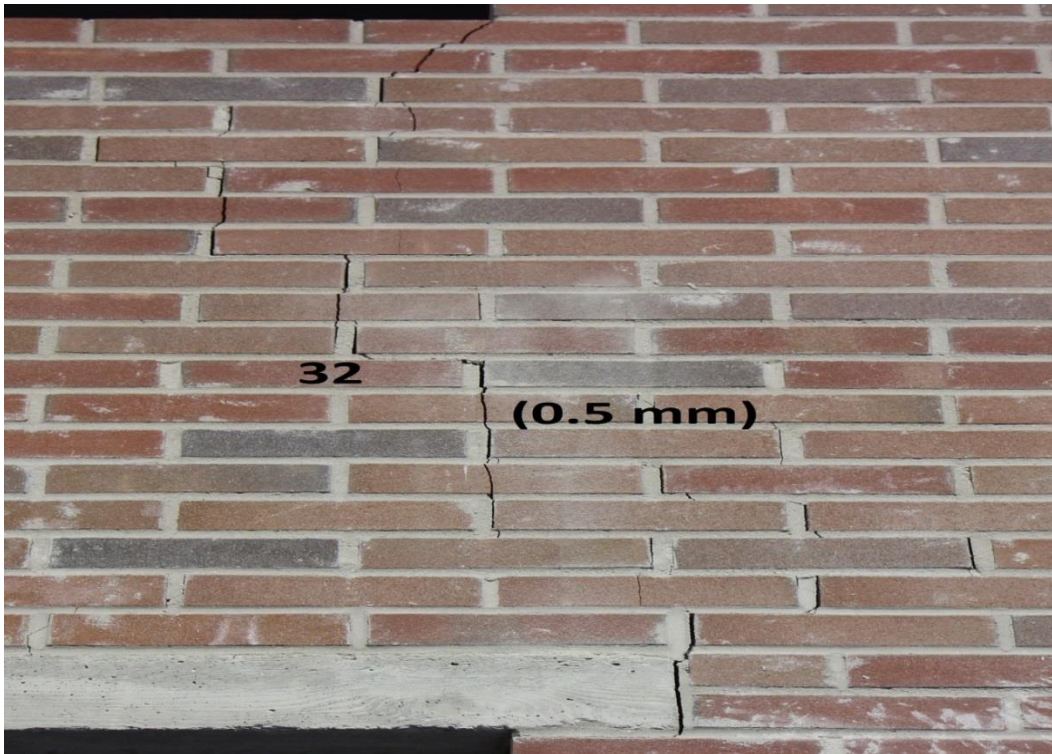


Figure 342. Crack #32 after the test # 29, 60%\_EQ2\_100,  $PGA= 1.0 \text{ m/s}^2$ .

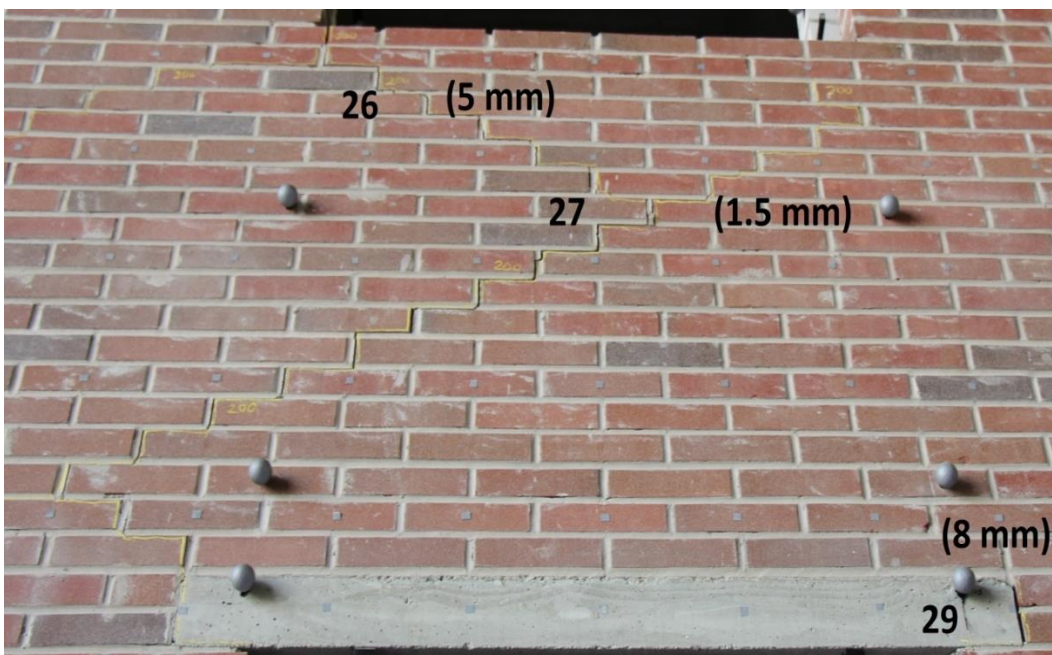


Figure 343. Cracks #26, #27 and #29 after the test # 29, 60%\_EQ2\_100,  $PGA= 1.0 \text{ m/s}^2$ .

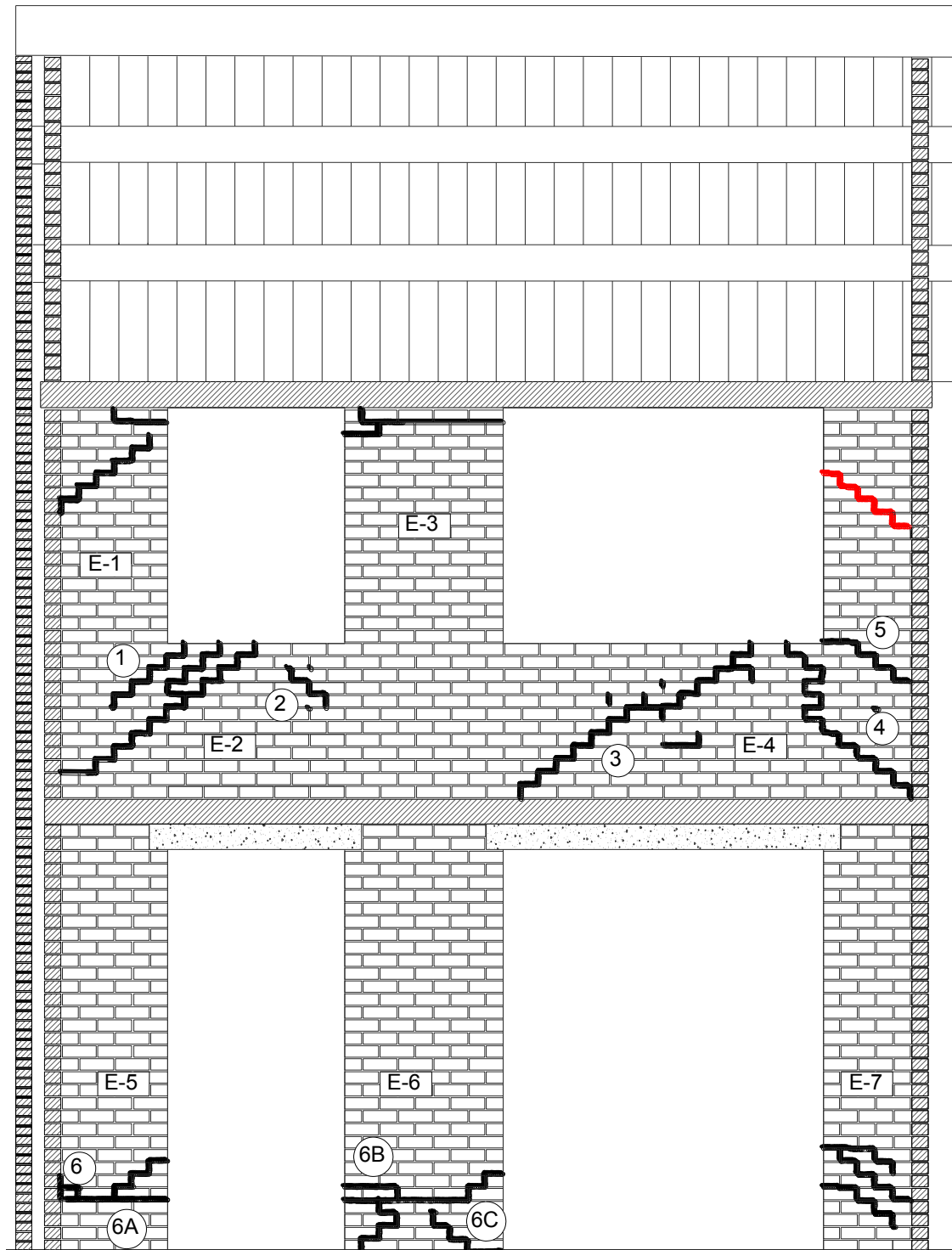


Figure 344. Elevation view of the test-house - inner leaf - west-side. Illustration of crack pattern after the test #29, 60%\_EQ2\_100, PGA= 1.0 m/s<sup>2</sup>. In red cracks induced at current test and in black the pre-existing cracks.

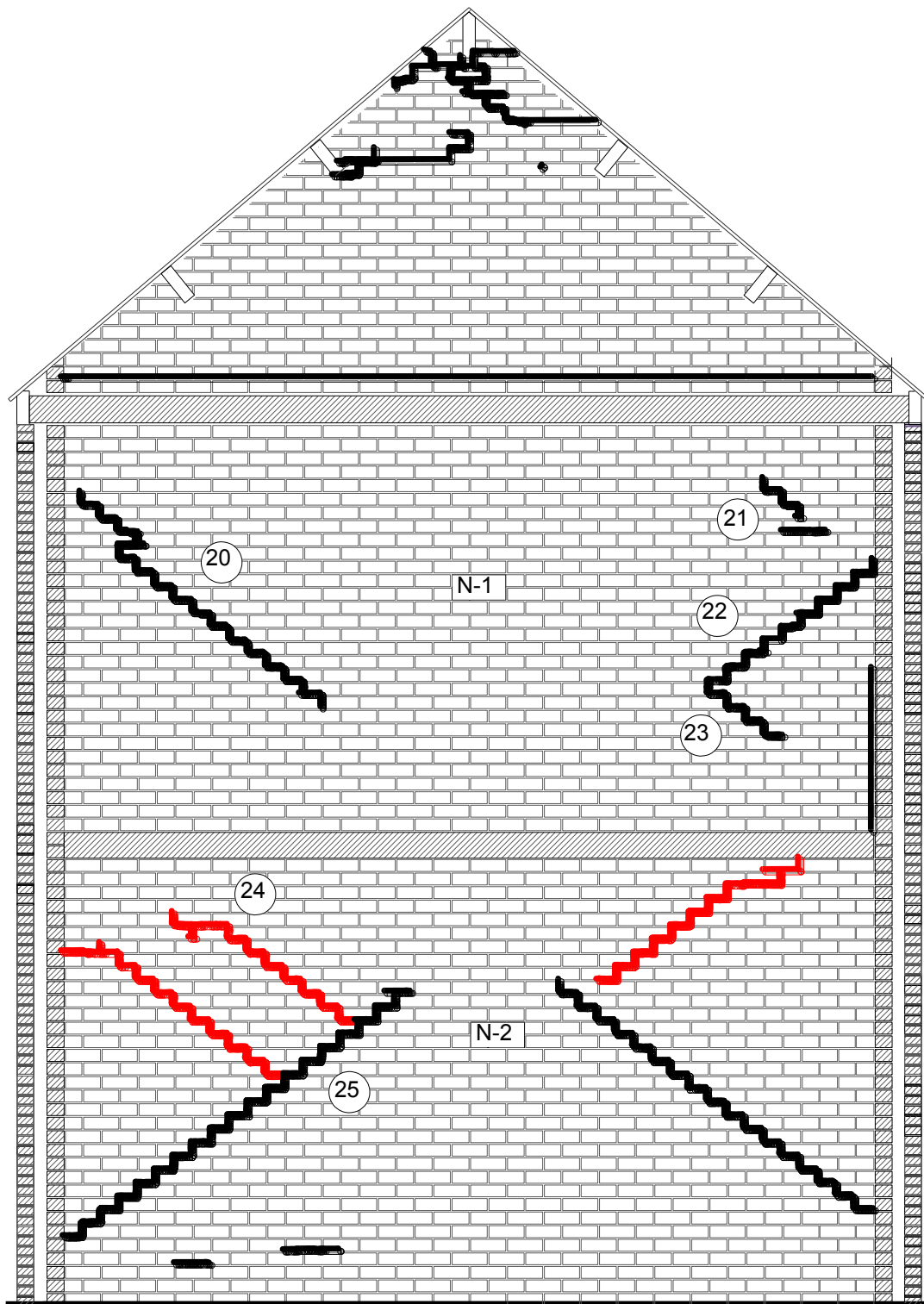


Figure 345. Section of the test-house - inner leaf – north side. Illustration of crack pattern after the test # 29, 60%\_EQ2\_100, PGA= 1.0 m/s<sup>2</sup>. In red cracks induced at current test and in black the pre-existing cracks



*Figure 346. Cracks observed around the ridge timber beam due to pounding (after the test #29, 60%\_EQ2\_100, PGA= 1.0 m/s<sup>2</sup>).*

The following table summarizes the damage induced in the full-scale specimen, in terms of cracks and their corresponding widths observed in the body of the load-bearing as well as the veneer walls, at the end of each shaking table test.



Table 62. Crack Width

Crack Width [mm]					
#	# 16, 100% _EQ2_150	# 19, 125% _EQ2_200	# 21, 150% _EQ2_240	# 23, 200% _EQ2_320	#29*, 60% _EQ2_100
1	/	/	/	-	1.5
2	/	/	/	-	0.2
3	/	/	/	-	2
4	/	/	/	-	1.5
5	/	/	/	-	1
6	/	/	-	-	-
6A	-	-	-	-	6
6B	/	/	/	-	17
6C	/	-	-	-	4
7	/	/	-	-	4
8	0.1	0.1	0.2	0.6	1
9	/	-	-	-	-
10	/	/	/	-	10
11	/	/	-	-	2
12	/	/	-	-	2
13	/	/	/	-	2
14	/	-	-	-	6
14A	/	/	/	-	4
14B	1	2	4	5	10
14C	/	/	-	-	-
14D	/	/	/	-	-
15	/	/	/	0.5	0.5
16	/	/	/	-	1.5
17	/	/	/	-	1
18	/	/	/	-	1
19	/	/	/	1.2	2
20	/	/	/	-	1
21	/	/	/	-	0.5
22	/	/	/	-	0.5
23	/	/	/	-	0.1
24	/	/	/	-	0.4
25	/	/	/	-	2
26	/	/	/	-	5
27	/	/	/	-	1.5
28	/	/	/	-	1.5
29	/	/	/	-	8
30	/	/	/	-	0.2
31	/	/	/	-	1
32	/	/	/	-	0.5
/	The cracks does not exist yes				
-	The cracks has not been measured				



Figure 347 illustrates the evolution of the maximum width of cracks observed in the body of the load-bearing (calcium silicate) masonry on both storeys, during the whole test procedure. It is evident that cracks of greater width were identified on the first storey.

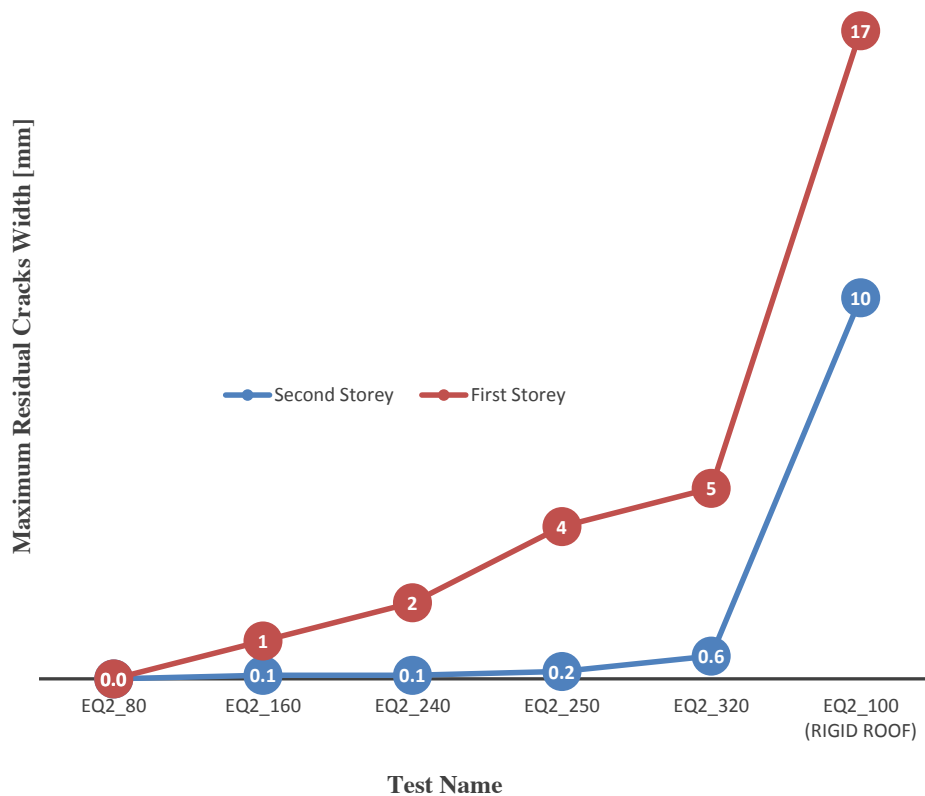


Figure 347. Evolution of maximum width of residual cracks after each test, first and second storey

The following sections analyse the response of the specimen to each input motion. In particular, the response spectrum of the recorded acceleration at the foundation level, the displacement histories of each floor, the force-displacement curve and the deformed shapes are plotted for each run.

The first plot of each section reports also the spectral acceleration and the spectral displacement calculated at a period equal to the one computed by mean of dynamic identification at the previous RNDM run (see 6.4.17 for details).

#### 6.4.2 Test #2\_25%\_EQ1\_024

Figure 348 shows the comparison between theoretical and the experimental acceleration response spectrum; the experimental acceleration time history used for the spectrum comparison is the average of the recorded accelerations on the specimen foundation (#26, #27). As expected, a little difference in all the spectra is noticeable. This is due to the fact that it is more difficult for the controller to replicate the input spectra around the period of resonance of the structure.

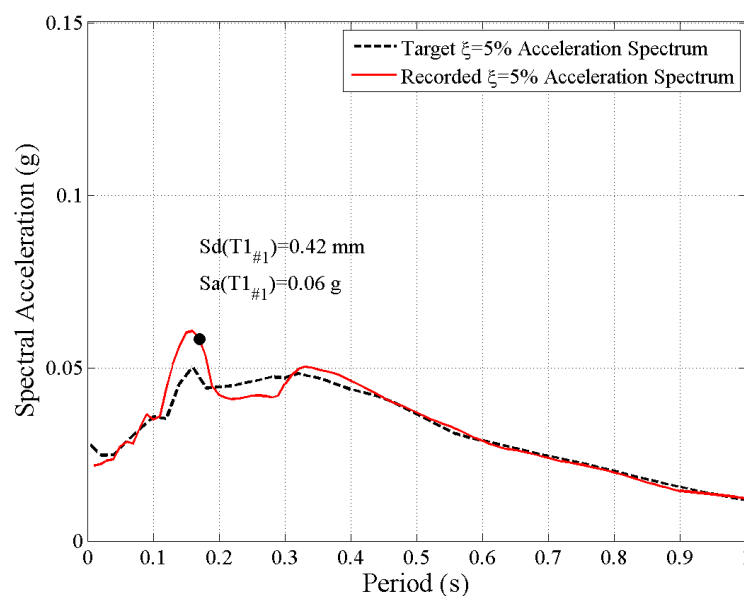


Figure 348. Test#2\_25%\_EQ1\_024: Theoretical-Experimental Spectral Comparison.

Figure 349 shows the displacement time histories of first, second and roof levels; first and second levels displacement histories have been averaged between the three potentiometer installed (#12, #13, #14 and #15, #16, #17). In all the graph the residual displacement of the previous test is taken into account.

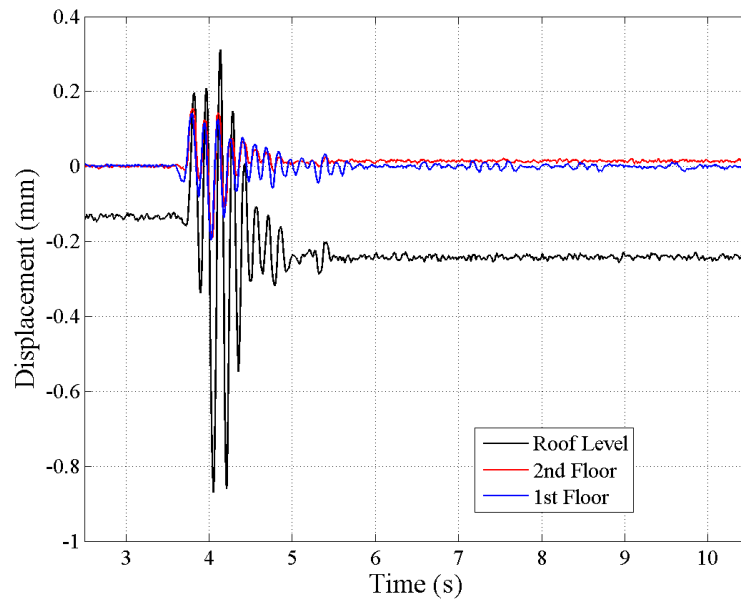


Figure 349. Test #2\_25%\_EQ1\_024: Displacement Histories.

Figure 350 shows the base shear vs 2<sup>nd</sup> floor displacement history plot (positive displacements toward North). The base shear has been obtained by summing the product of each accelerometer installed on the specimen time the related mass portion.

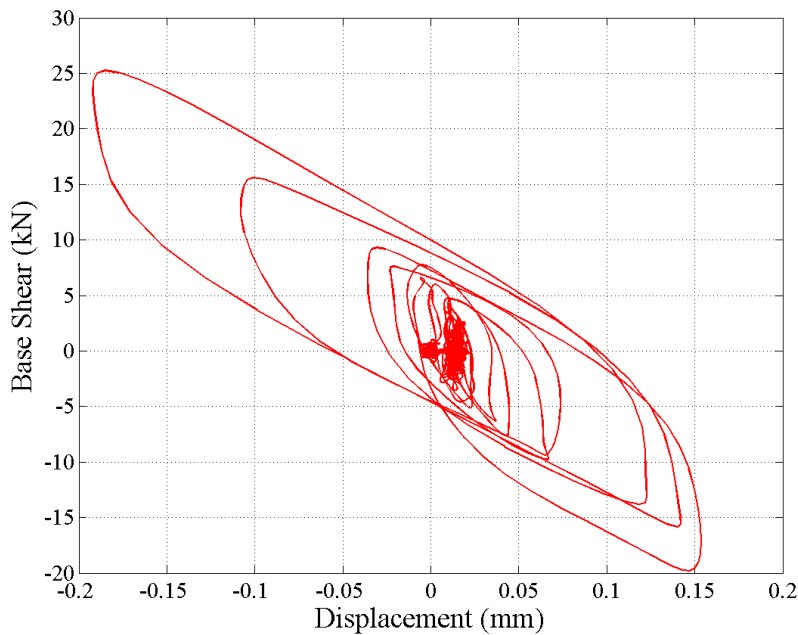


Figure 350. Test #2\_25%\_EQ1\_024: Base Shear vs 2<sup>nd</sup> Floor Displacement.

Figure 351 shows the absolute maximum response recorded at each level. The red line represents the envelope deformed shape while the blue one is the displacement recorded by first and roof levels at the instant of the maximum absolute 2<sup>nd</sup> floor displacement.



Figure 351 plots also the residual displacements measured at the end of the test (taking in this way into account the cumulative residuals of previous tests).

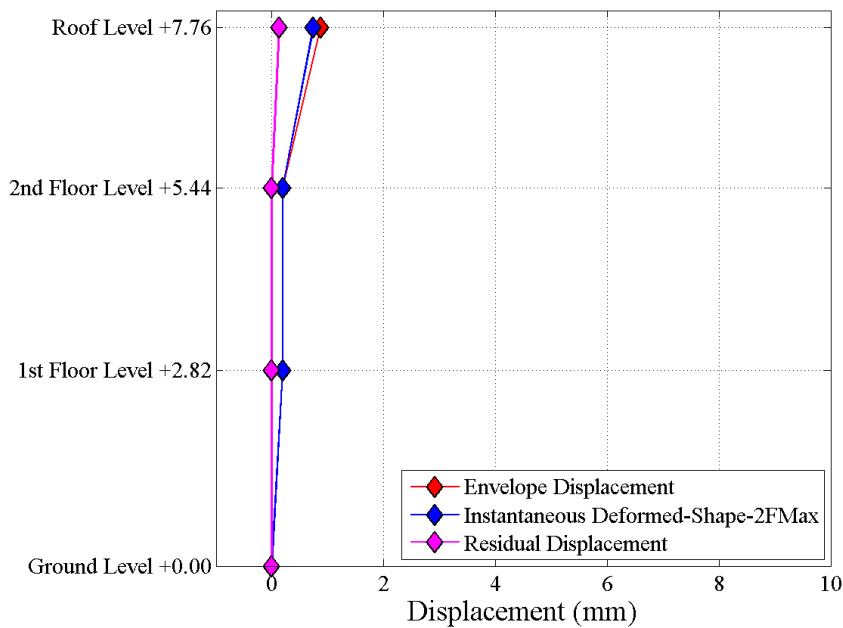


Figure 351. Test #2\_25%\_EQ1\_024: Peak and Residual Displacements.

Figure 352 represents the instantaneous deformed shape of the building at the instant of the peak 2<sup>nd</sup> floor displacement. The response of the OOP potentiometer is also included. The deformation is amplified by a scaling factor equal to 250 as indicated in the figure.

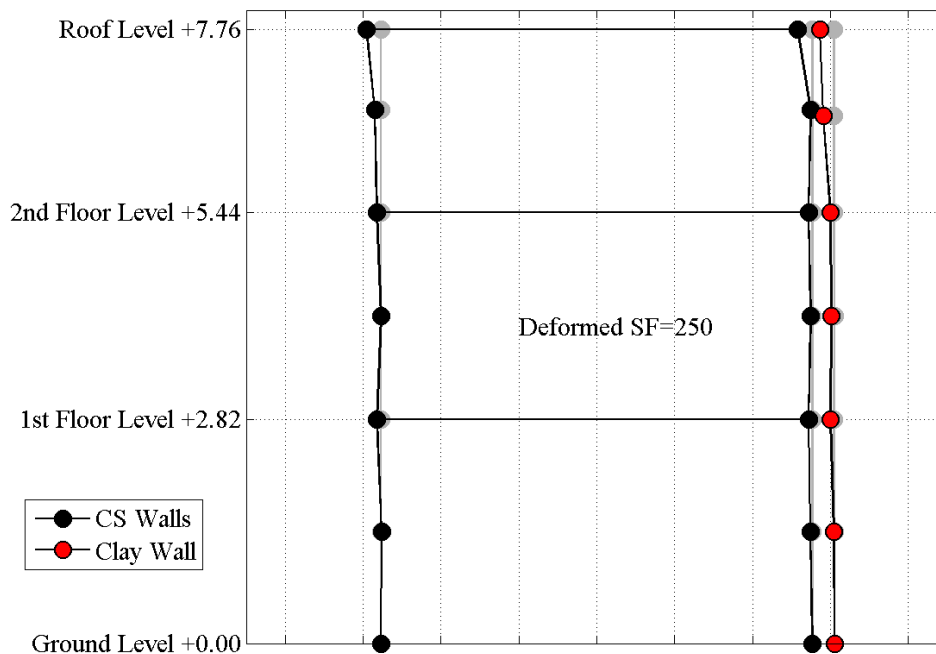


Figure 352. Test #2\_25%\_EQ1\_024: Deformed Shape.



Figure 353 plots the envelope of the maximum drifts recorded during the test. The roof drift has been computed dividing the top gable displacement by the diagonal length from the gable peak to the 2<sup>nd</sup> floor along the roof slope (3.5 m).

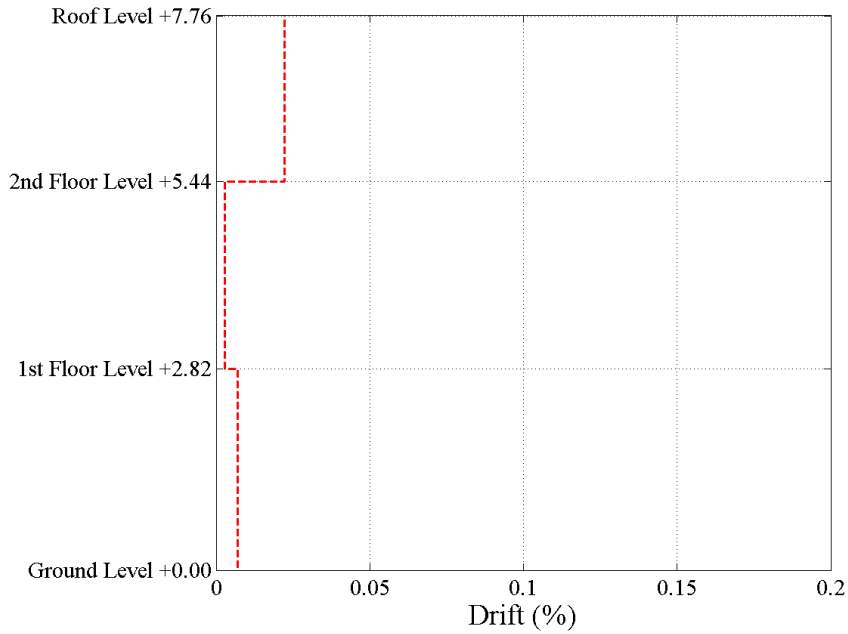


Figure 353. Test #2\_25%\_EQ1\_024: Maximum Absolute Drift.



### 6.4.3 Test #4\_50%\_EQ1\_050

As before, Figure 354 shows the comparison between theoretical and the experimental acceleration response spectrum; the experimental acceleration time history used for the spectrum comparison is the average of the recorded accelerations on the specimen foundation (#26, #27).

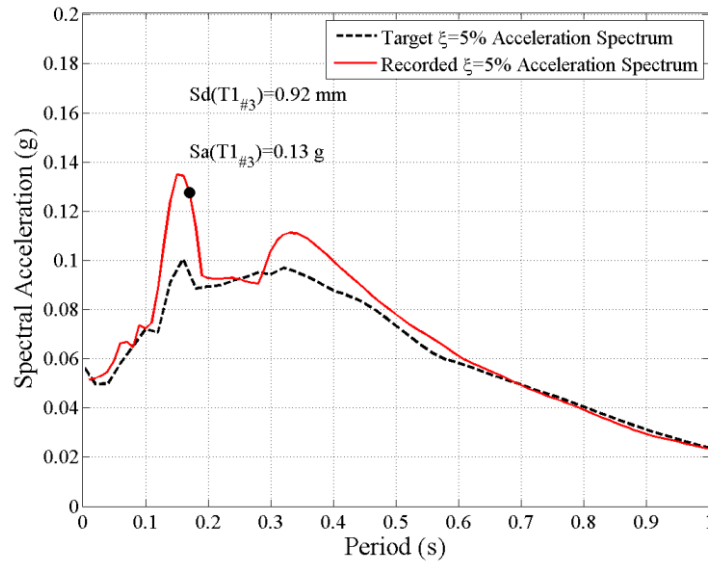


Figure 354. Test #4\_50%\_EQ1\_050: Theoretical-Experimental Spectral Comparison.

Figure 355 shows the displacement time histories of first, second and roof levels; first and second levels displacement histories have been averaged between the three potentiometer installed (#12, #13, #14 and #15, #16, #17).

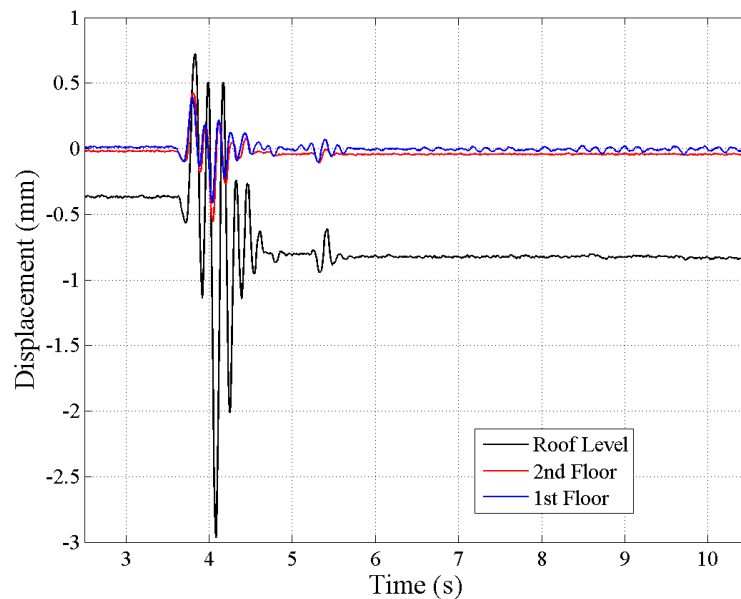


Figure 355. Test #4\_50%\_EQ1\_050: Displacement Histories.



Figure 356 shows the base shear vs 2<sup>nd</sup> floor displacement history plot. The base shear has been obtained by summing the product of each accelerometer installed on the specimen time the related mass portion.

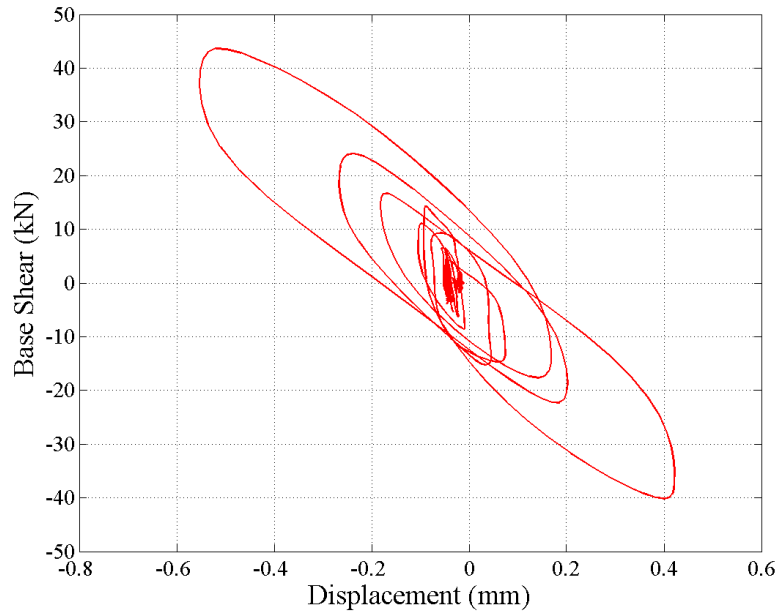


Figure 356. Test #4\_50%\_EQ1\_050: Base Shear vs 2<sup>nd</sup> Floor Displacement.

Figure 357 shows the absolute maximum response recorded at each level. The red line represents the envelope deformed shape while the blue one is the displacement recorded by first and roof levels at the instant of the maximum absolute 2<sup>nd</sup> floor displacement. Figure 351 plots also the residual displacements measured at the end of the test.

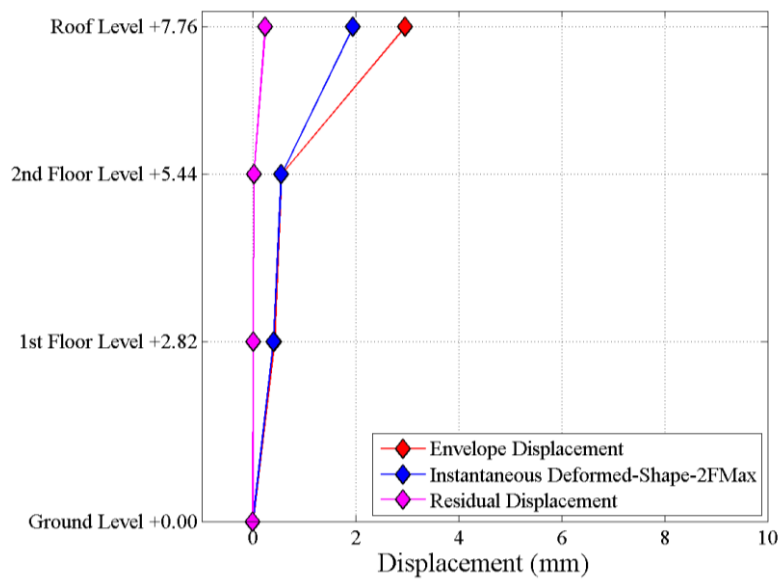


Figure 357. Test #4\_50%\_EQ1\_050: Peak and Residual Displacements.

Figure 358 represents the instantaneous deformed shape of the building at the instant of the peak 2<sup>nd</sup> floor displacement. The response of the OOP potentiometer is also included. The deformation is amplified by a scaling factor equal to 250 as indicated in the figure.

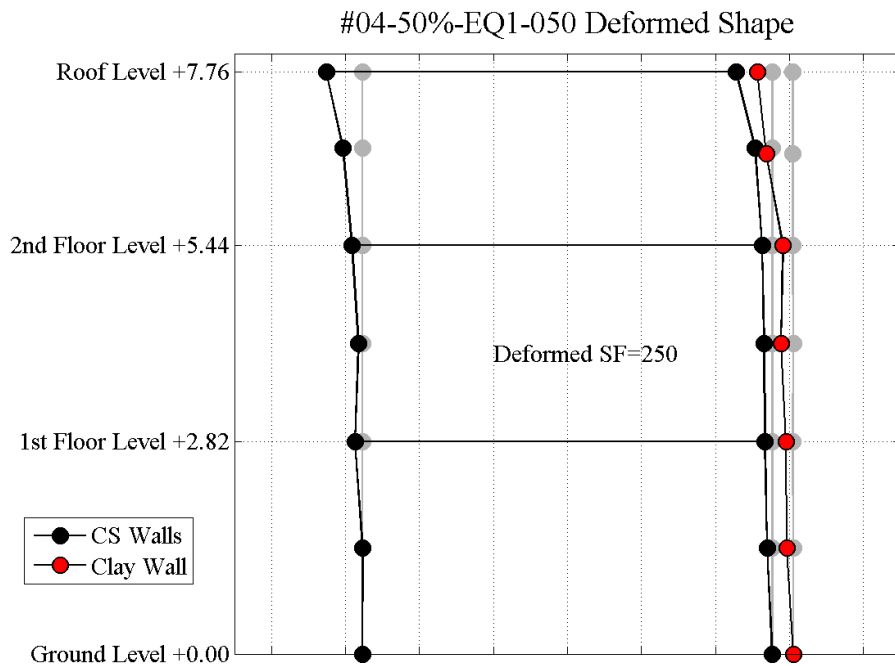


Figure 358. Test #4\_50%\_EQ1\_050: Deformed Shape.

Figure 359 plots the envelope of the maximum drifts recorded during the test. The roof drift has been computed dividing the top gable displacement by the diagonal length from the gable peak to the 2<sup>nd</sup> floor along the roof slope (3.5 m).

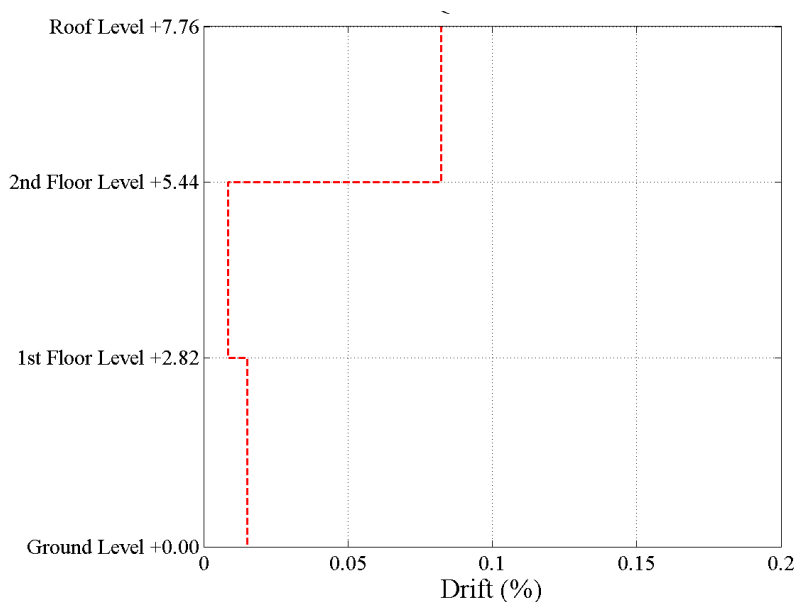


Figure 359. Test #4\_50%\_EQ1\_050: Maximum Absolute Drift.

#### 6.4.4 Test #6\*\_50%\_4xEQ1\_050 (Rigid roof)

The accelerogram EQ1\_050 was repeated 4 times for calibration purpose. For this reason, in order not to damage the roof, it was chosen to activate the rods. Figure 360 shows the comparison between theoretical and the experimental response spectrum; the experimental acceleration time history used for the spectrum comparison is the average of the recorded accelerations on the specimen foundation (#26, #27).

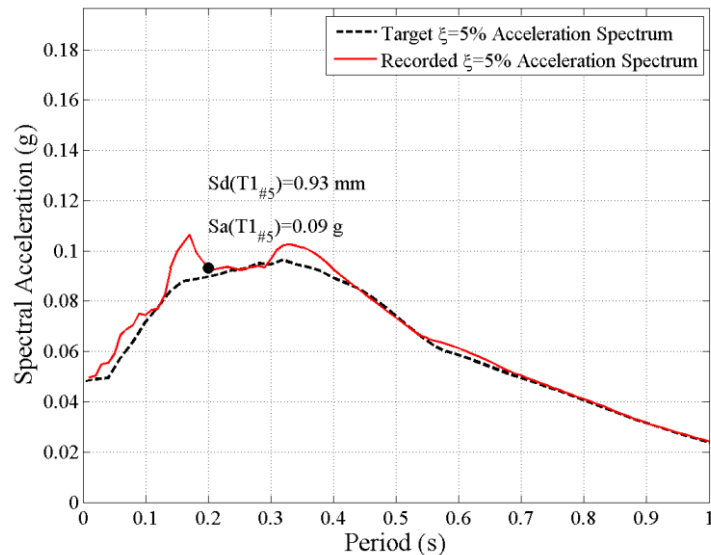


Figure 360. Test #6\*\_50%\_4xEQ1\_050: Theoretical-Experimental Spectral Comparison.

Figure 361 shows the displacement time histories of first, second and roof levels; first and second levels displacement histories have been averaged between the three potentiometer installed (#12, #13, #14 and #15, #16, #17).

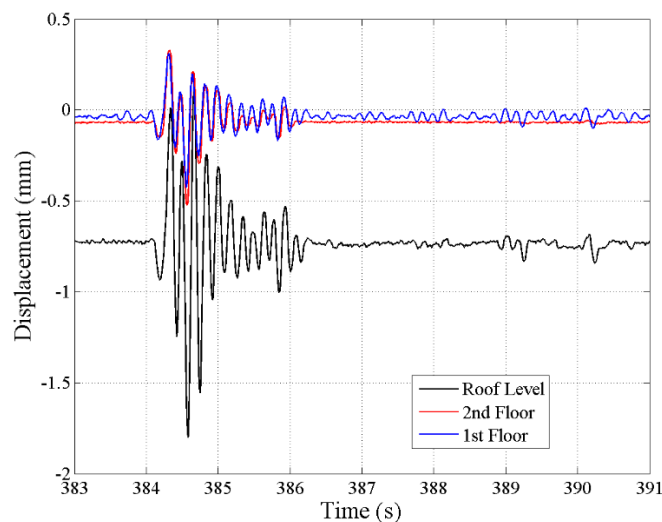


Figure 361. Test #6\*\_50%\_4xEQ1\_050: Displacement Histories.



Figure 362 shows the base shear vs 2<sup>nd</sup> floor displacement history plot. The base shear has been obtained by summing the product of each accelerometer installed on the specimen time the related mass portion. Notice the similar response in the 4 runs of the same ground motion performed.

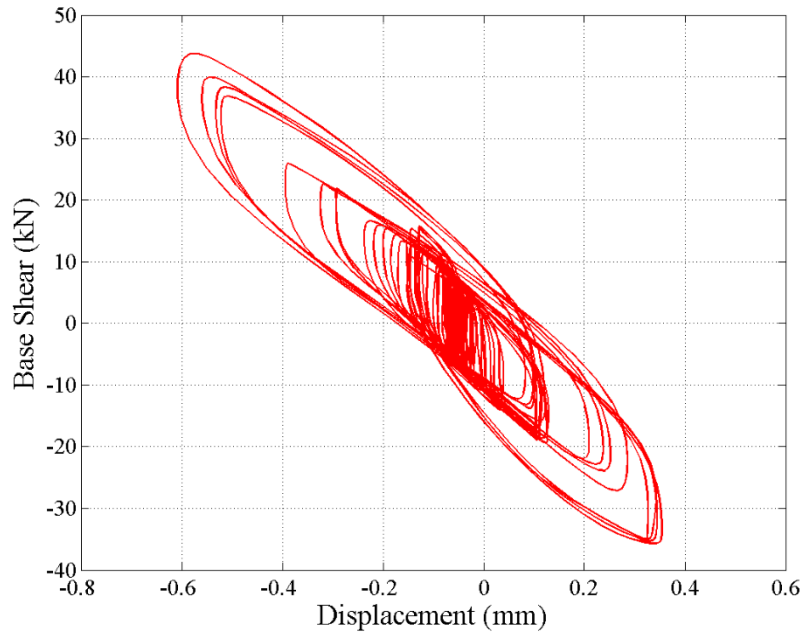


Figure 362. Test #6\*\_50%\_4xEQ1\_050: Base Shear vs 2<sup>nd</sup> Floor Displacement.

Figure 363 shows the absolute maximum response recorded at each level. The red line represents the envelope deformed shape while the blue one is the displacement recorded by first and roof levels at the instant of the maximum absolute 2<sup>nd</sup> floor displacement. Figure 351 plots also the residual displacements measured at the end of the test.

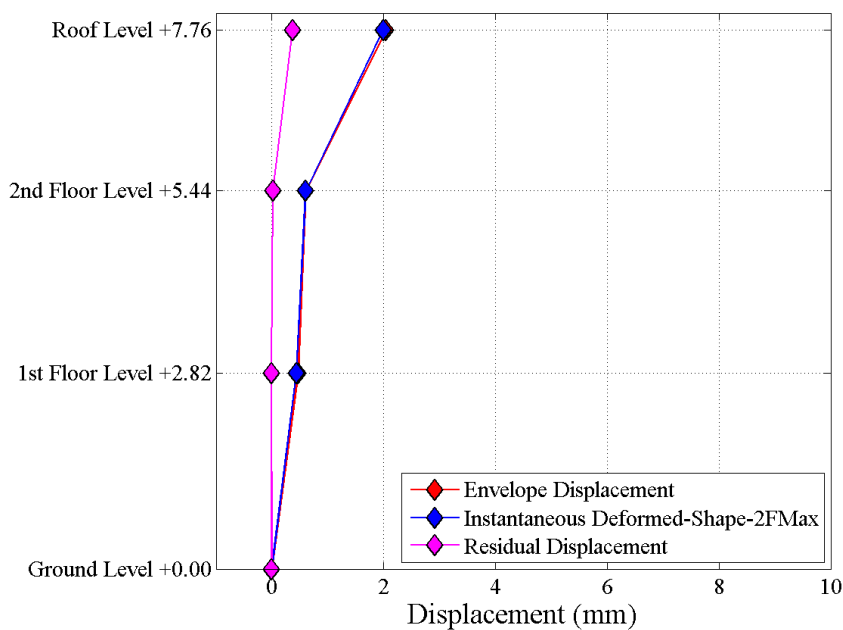


Figure 363. Test #6\*\_50%\_4xEQ1\_050: Peak and Residual Displacements.

Figure 364 represents the instantaneous deformed shape of the building at the instant of the peak 2<sup>nd</sup> floor displacement. The response of the OOP potentiometer is also included. The deformation is amplified by a scaling factor equal to 250 as indicated in the figure.

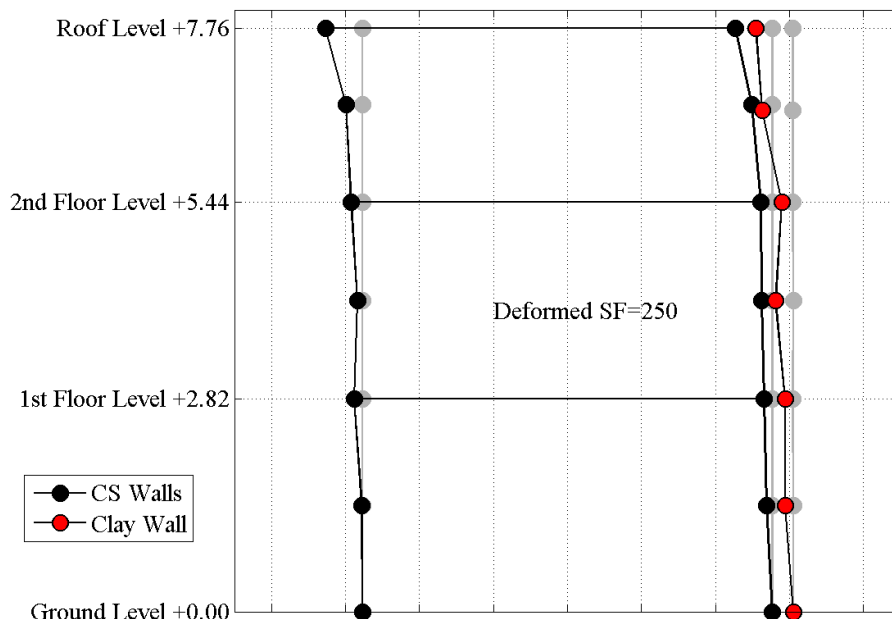


Figure 364. Test #6\*\_50%\_4xEQ1\_050: Deformed Shape.

Figure 365 plots the envelope of the maximum drifts recorded during the test. The roof drift has been computed dividing the top gable displacement by the diagonal length from the gable peak to the 2<sup>nd</sup> floor along the roof slope (3.5 m).

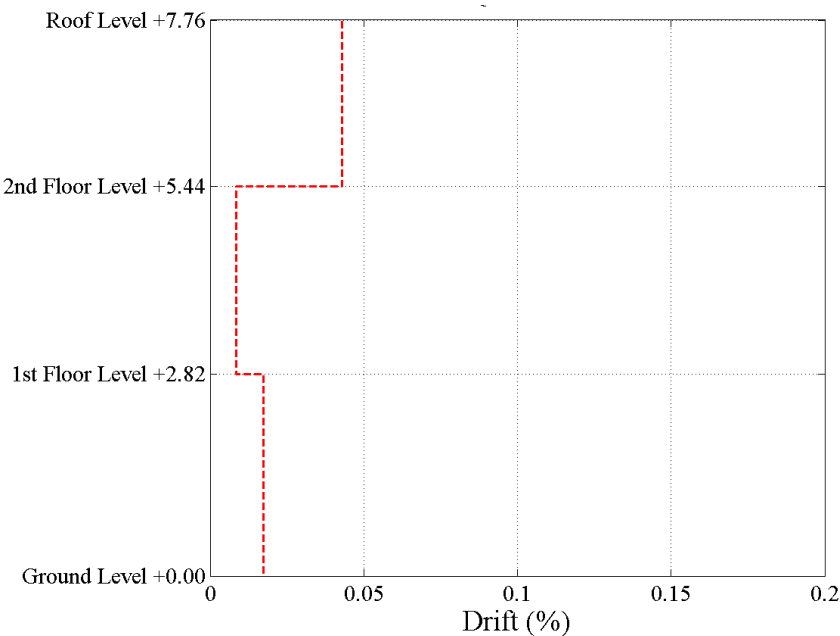


Figure 365. Test #6\*\_50%\_4xEQ1\_050: Maximum Absolute Drift.

### 6.4.5 Test #7\_100%\_EQ1\_100

Figure 366 shows the comparison between theoretical and the experimental response spectrum; the experimental acceleration time history used for the spectrum comparison is the average of the recorded accelerations on the specimen foundation (#26, #27).

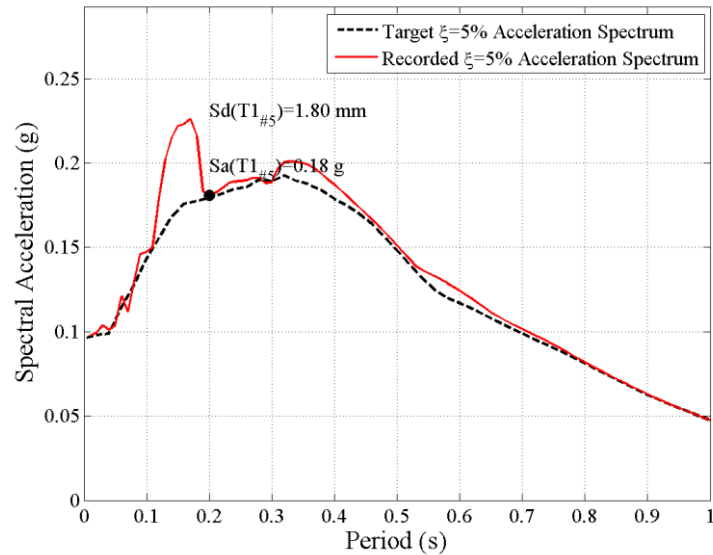


Figure 366. Test #7\_100%\_EQ1\_100: Theoretical-Experimental Spectral Comparison.

Figure 367 shows the displacement time histories of first, second and roof levels; first and second levels displacement histories have been averaged between the three potentiometer installed (#12, #13, #14 and #15, #16, #17).

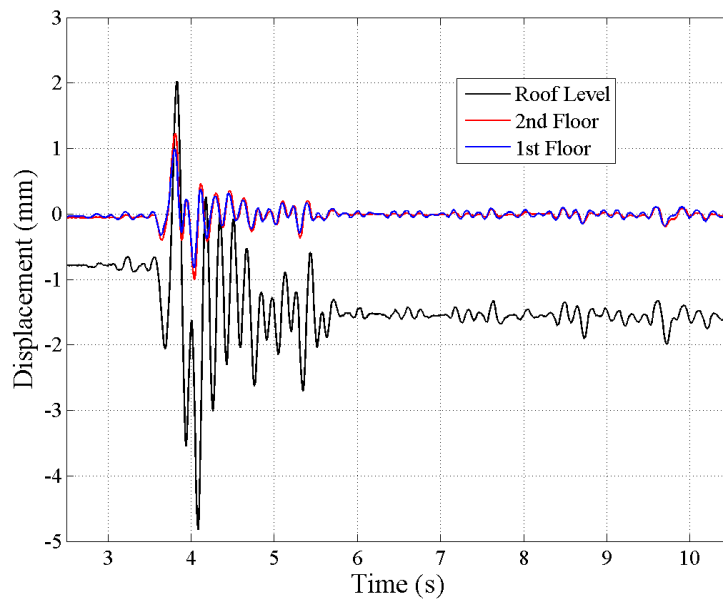


Figure 367. Test #7\_100%\_EQ1\_100: Displacement Histories.



Figure 368 shows a Base shear vs 2<sup>nd</sup> floor displacement history plot. The base shear has been obtained by summing the product of each accelerometer installed on the specimen time the related mass portion.

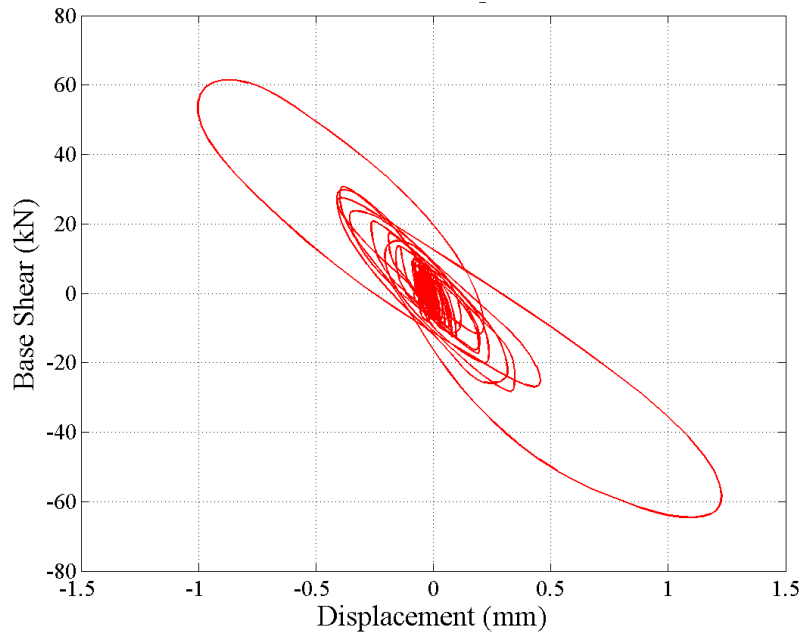


Figure 368. Test #7\_100%\_EQ1\_100: Base Shear vs 2<sup>nd</sup> Floor Displacement.

Figure 369 represents the absolute maximum response recorded at each level. The red line shows the envelope deformed shape while the blue one is the displacement recorded by first and roof levels at the instant of the maximum absolute 2<sup>nd</sup> floor displacement. Figure 351 plots also the residual displacements measured at the end of the test.

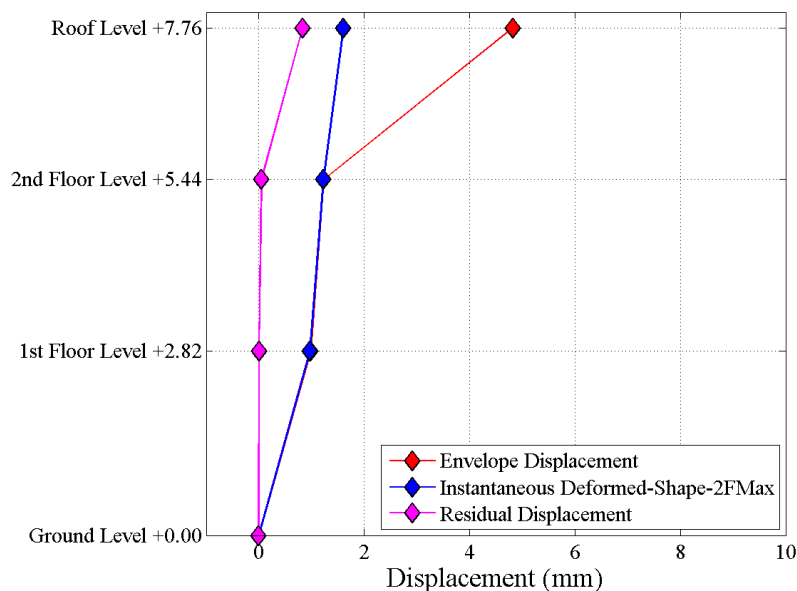


Figure 369. Test #7\_100%\_EQ1\_100: Peak and Residual Displacements.



Figure 370 represents the instantaneous deformed shape of the building at the instant of the peak 2<sup>nd</sup> floor displacement. The response of the OOP potentiometer is also included. The deformation is amplified by a scaling factor equal to 250 as indicated in the figure.

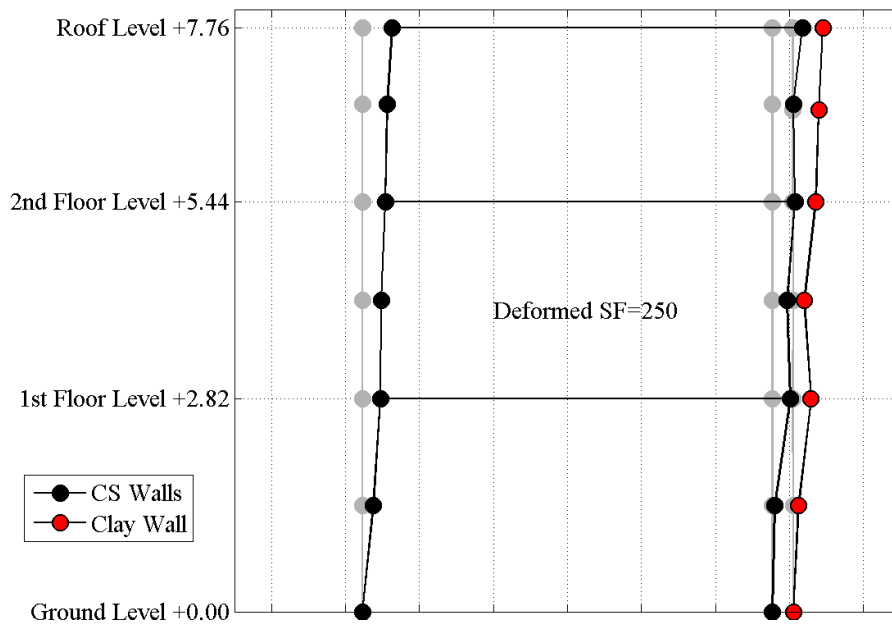


Figure 370. Test #7\_100%\_EQ1\_100: Deformed Shape.

Figure 371 plots the envelope of the maximum drifts recorded during the test. The roof drift has been computed dividing the top gable displacement by the diagonal length from the gable peak to the 2<sup>nd</sup> floor along the roof slope (3.5 m).

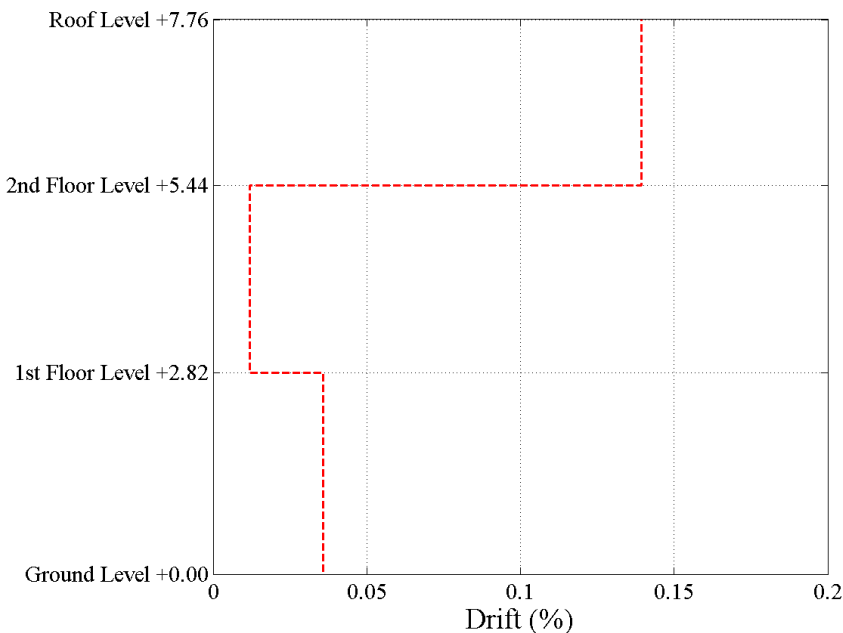


Figure 371. Test #7\_100%\_EQ1\_100: Maximum Absolute Drift.

### 6.4.6 Test #9\_150%\_EQ1\_150

Figure 372 shows the comparison between theoretical and the experimental response spectrum; the experimental acceleration time history used for the spectrum comparison is the average of the recorded accelerations on the specimen foundation (#26, #27).

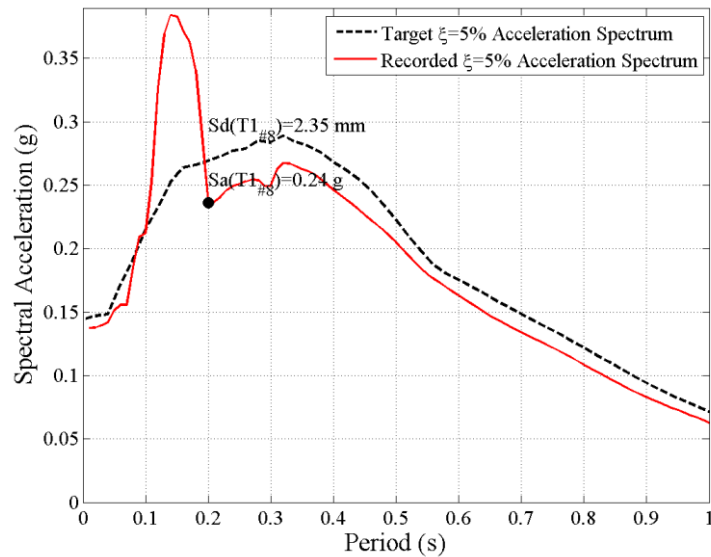


Figure 372. Test #9\_150%\_EQ1\_150: Theoretical-Experimental Spectral Comparison.

Figure 373 shows the displacement time histories of first, second and roof levels; first and second levels displacement histories have been averaged between the three potentiometer installed (#12, #13, #14 and #15, #16, #17).

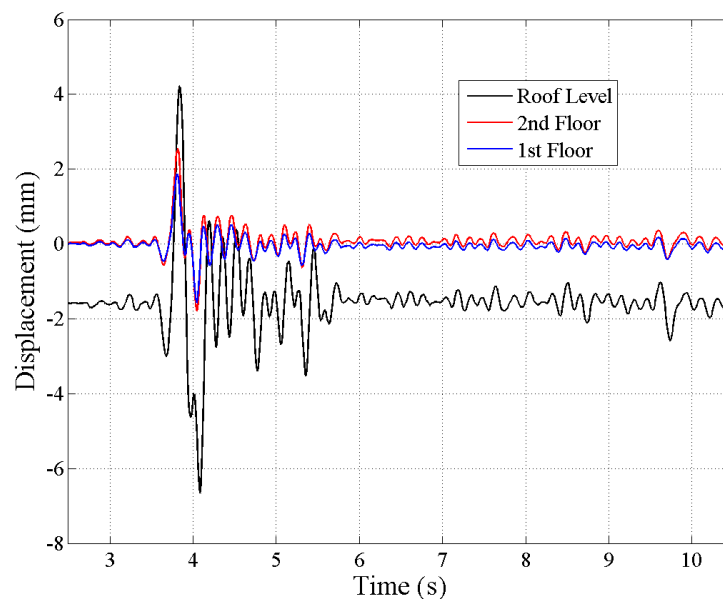


Figure 373. Test #9\_150%\_EQ1\_150: Displacement Histories.

Figure 374 shows a Base shear vs 2<sup>nd</sup> floor displacement history plot. The base shear has been obtained by summing the product of each accelerometer installed on the specimen time the related mass portion.

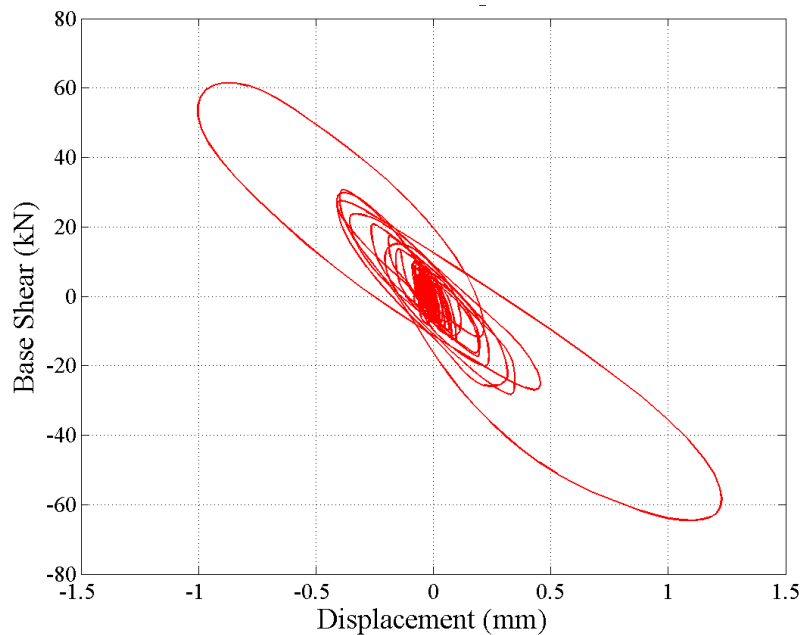


Figure 374. Test #9\_150%\_EQ1\_150: Base Shear vs 2<sup>nd</sup> Floor Displacement.

Figure 375 represents the absolute maximum response recorded at each level. The red line shows the envelope deformed shape while the blue one is the displacement recorded by first and roof levels at the instant of the maximum absolute 2<sup>nd</sup> floor displacement. Figure 375 plots also the residual displacements measured at the end of the test.

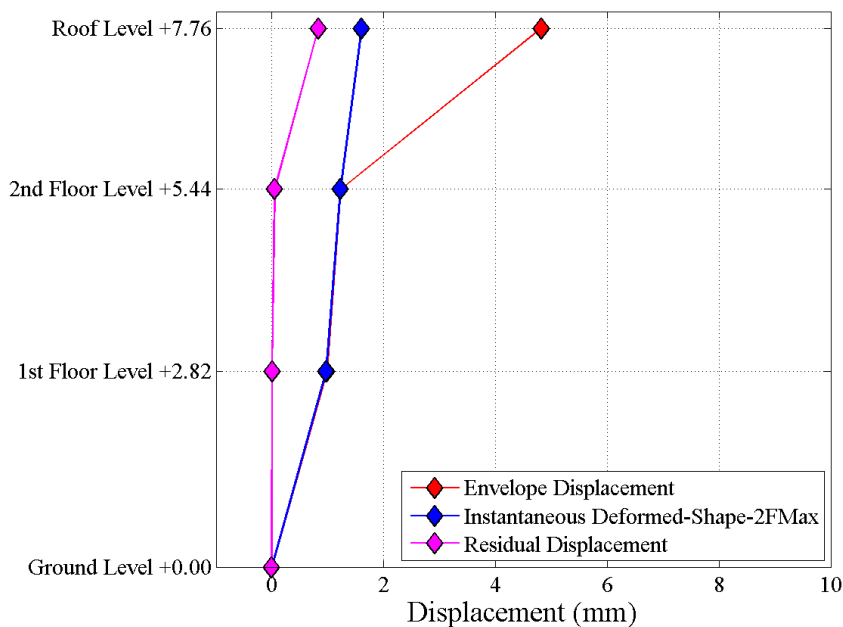


Figure 375. Test #9\_150%\_EQ1\_150: Peak and Residual Displacements.



Figure 376 represents the instantaneous deformed shape of the building at the instant of the peak 2<sup>nd</sup> floor displacement. The response of the OOP potentiometer is also included. The deformation is amplified by a scaling factor equal to 250 as indicated in the figure.

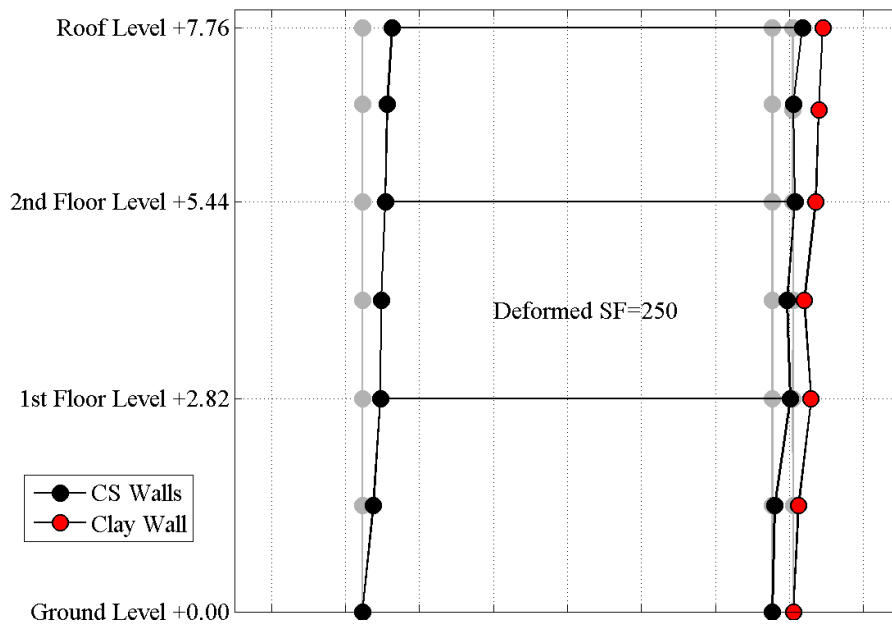


Figure 376. Test #9\_150%\_EQ1\_150: Deformed Shape.

Figure 377 plots the envelope of the maximum drifts recorded during the test. The roof drift has been computed dividing the top gable displacement by the diagonal length from the gable peak to the 2<sup>nd</sup> floor along the roof slope (3.5 m).

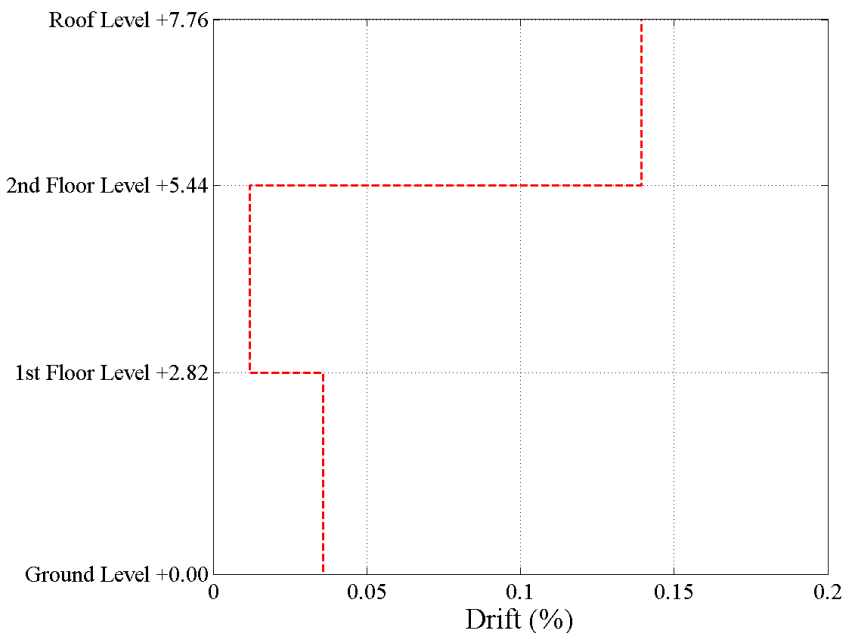


Figure 377. Test #9\_150%\_EQ1\_150: Maximum Absolute Drift.



### 6.4.7 Test #11, #12, #13\_30%\_EQ2\_050

Test #11, #12, #13 were performed in order to calibrate the shaking table. The obtained results are almost the same. In particular, this section provide the results for the last one of the three (#13). Figure 378 shows the comparison between theoretical and the experimental response spectrum; the experimental acceleration time history used for the spectrum comparison is the average of the recorded accelerations on the specimen foundation (#26, #27).

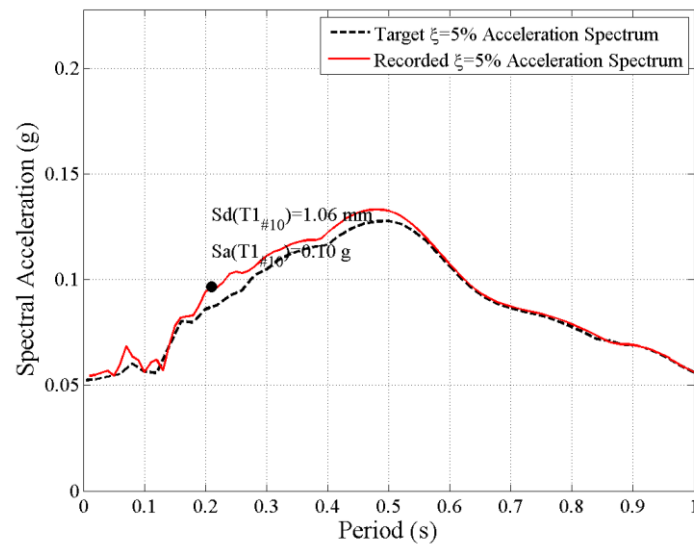


Figure 378. Test #13\_30%\_EQ2\_050: Theoretical-Experimental Spectral Comparison.

Figure 379 shows the displacement time histories of first, second and roof levels; first and second levels displacement histories have been averaged between the three potentiometer installed (#12, #13, #14 and #15, #16, #17).

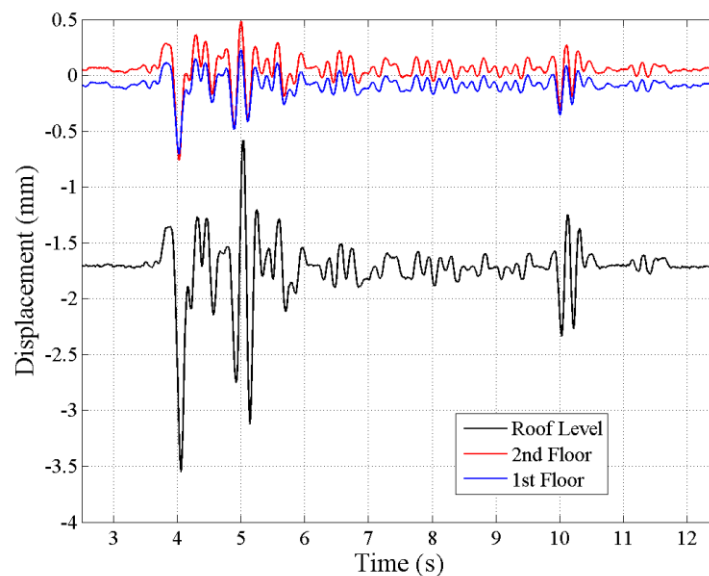


Figure 379. Test #13\_30%\_EQ2\_050: Displacement Histories.

Figure 380 shows the base shear vs 2<sup>nd</sup> floor displacement history plot. The base shear has been obtained by summing the product of each accelerometer installed on the specimen time the related mass portion.

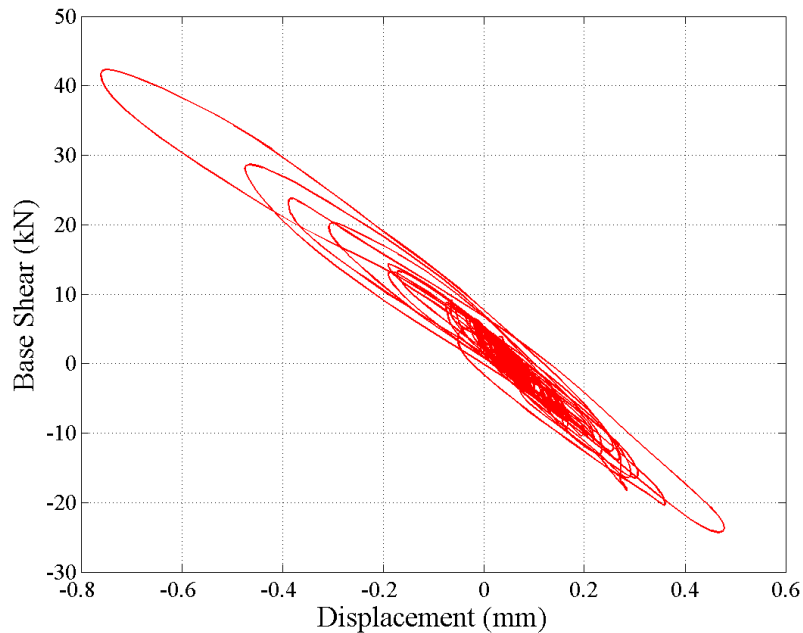


Figure 380. Test #13\_30%\_EQ2\_050: Base Shear vs 2<sup>nd</sup> Floor Displacement.

Figure 381 plots the absolute maximum response recorded at each level. The red line shows the envelope deformed shape while the blue one is the displacement recorded by first and roof levels at the instant of the maximum absolute 2<sup>nd</sup> floor displacement. Figure 381 plots also the residual displacements measured at the end of the test.

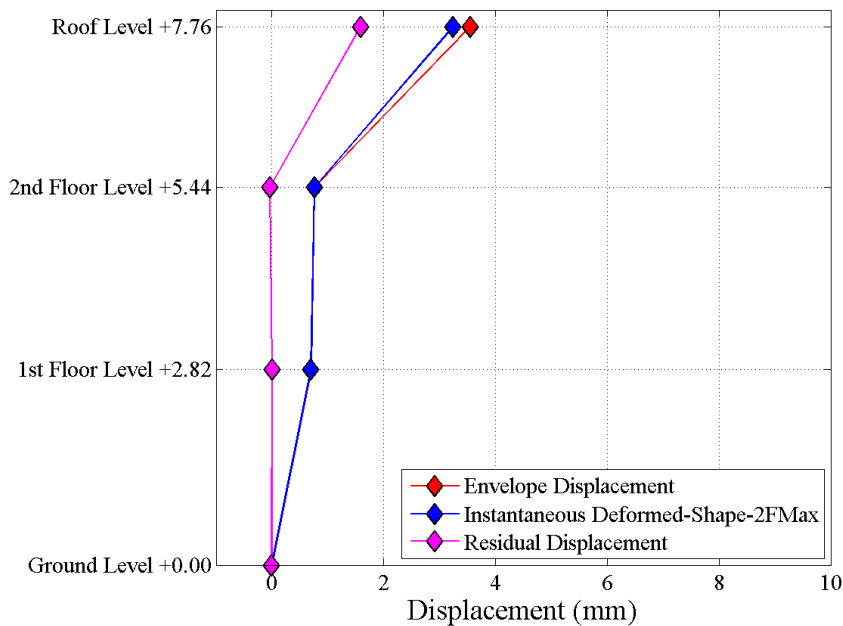


Figure 381. Test #13\_30%\_EQ2\_050: Peak and Residual Displacements.

Figure 382 represents the instantaneous deformed shape of the building at the instant of the peak 2<sup>nd</sup> floor displacement. The response of the OOP potentiometer is also included. The deformation is amplified by a scaling factor equal to 250 as indicated in the figure.

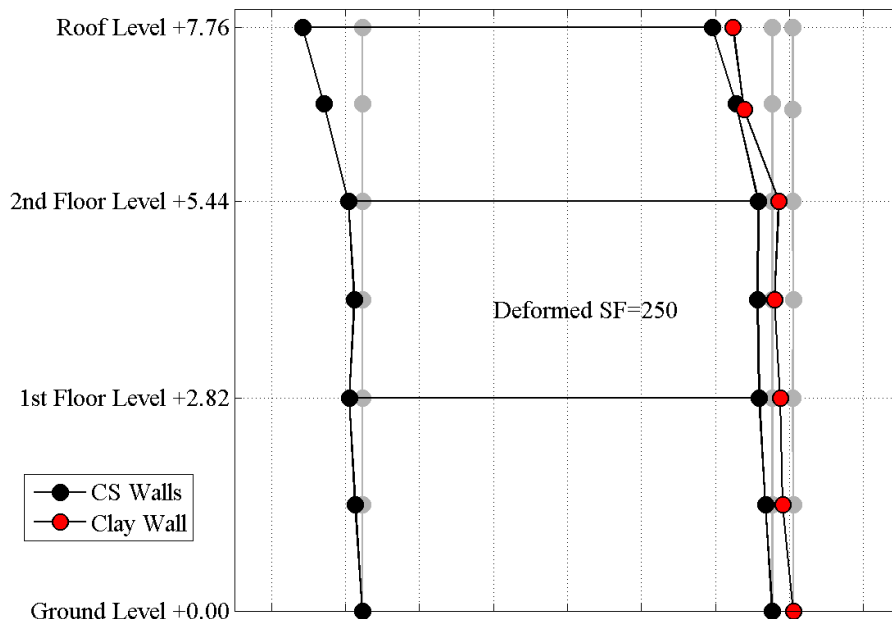


Figure 382. Test #13\_30%\_EQ2\_050: Deformed Shape.

Figure 383 plots the envelope of the maximum drifts recorded during the test. The roof drift has been computed dividing the top gable displacement by the diagonal length from the gable peak to the 2<sup>nd</sup> floor along the roof slope (3.5 m).

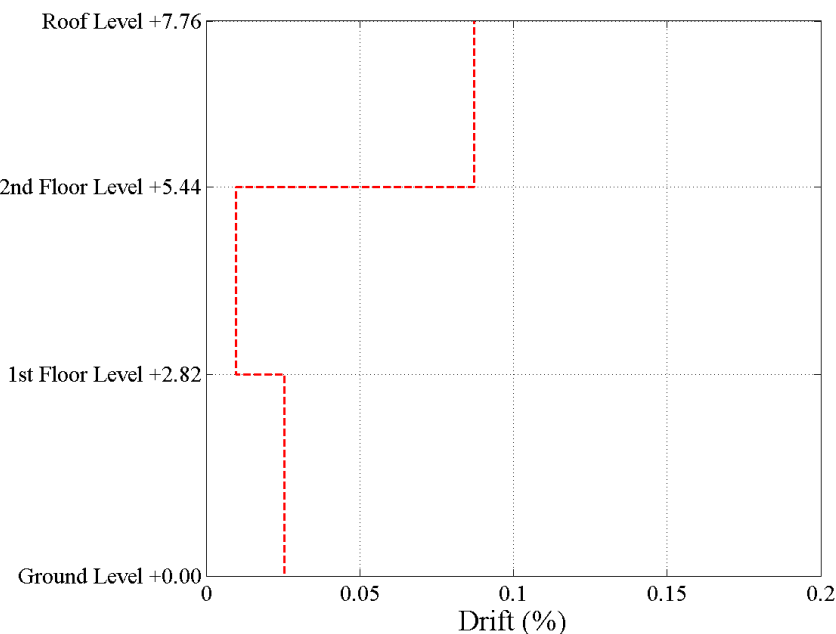


Figure 383. Test #13\_30%\_EQ2\_050: Maximum Absolute Drift.

### 6.4.8 Test #14\_50%\_EQ2\_080

Figure 384 shows the comparison between theoretical and the experimental response spectrum; the experimental acceleration time history used for the spectrum comparison is the average of the recorded accelerations on the specimen foundation (#26, #27).

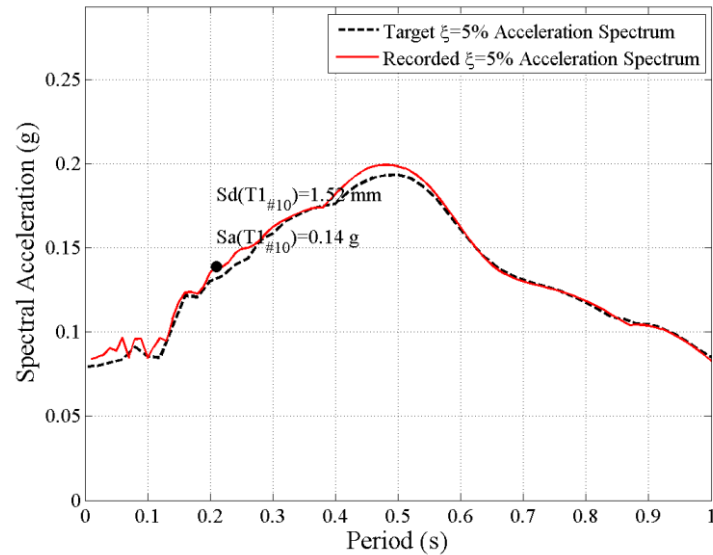


Figure 384. Test #14\_50%\_EQ2\_080: Theoretical-Experimental Spectral Comparison.

Figure 385 shows the displacement time histories of first, second and roof levels; first and second levels displacement histories have been averaged between the three potentiometer installed (#12, #13, #14 and #15, #16, #17).

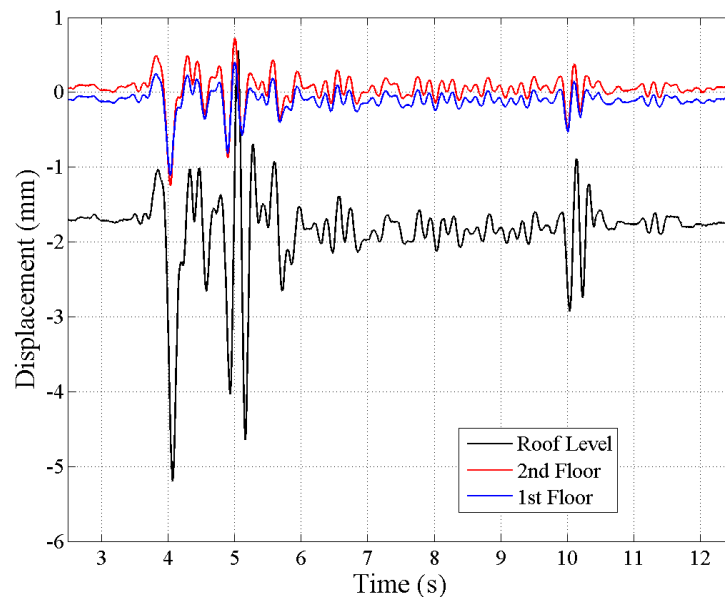


Figure 385. Test #14\_50%\_EQ2\_080: Displacement Histories.

Figure 386 shows the base shear vs 2<sup>nd</sup> floor displacement history plot. The base shear has been obtained by summing the product of each accelerometer installed on the specimen time the related mass portion.

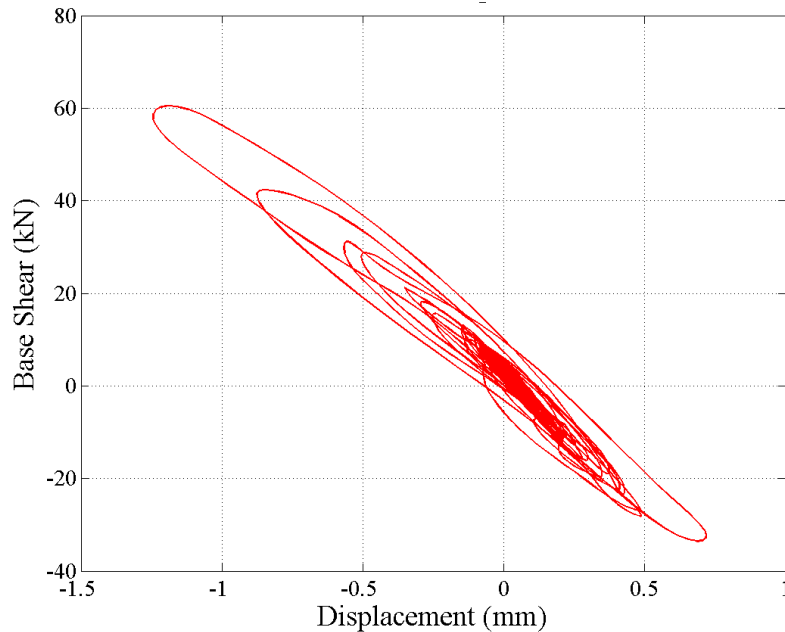


Figure 386. Test #14\_50%\_EQ2\_080: Base Shear vs 2<sup>nd</sup> Floor Displacement.

Figure 387 shows the absolute maximum response recorded at each level. The red line represent the envelope deformed shape while the blue one is the displacement recorded by first and roof levels at the instant of the maximum absolute 2<sup>nd</sup> floor displacement. Figure 387 plots also the residual displacements measured at the end of the test.

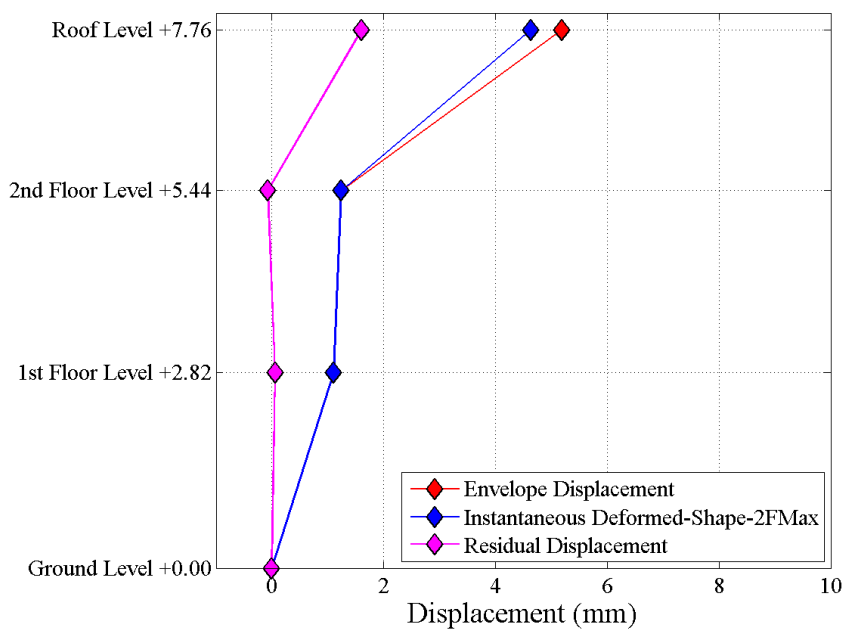


Figure 387. Test #14\_50%\_EQ2\_080: Peak and Residual Displacements.

Figure 388 represents the instantaneous deformed shape of the building at the instant of the peak 2<sup>nd</sup> floor displacement. The response of the OOP potentiometer is also included. The deformation is amplified by a scaling factor equal to 250 as indicated in the figure.

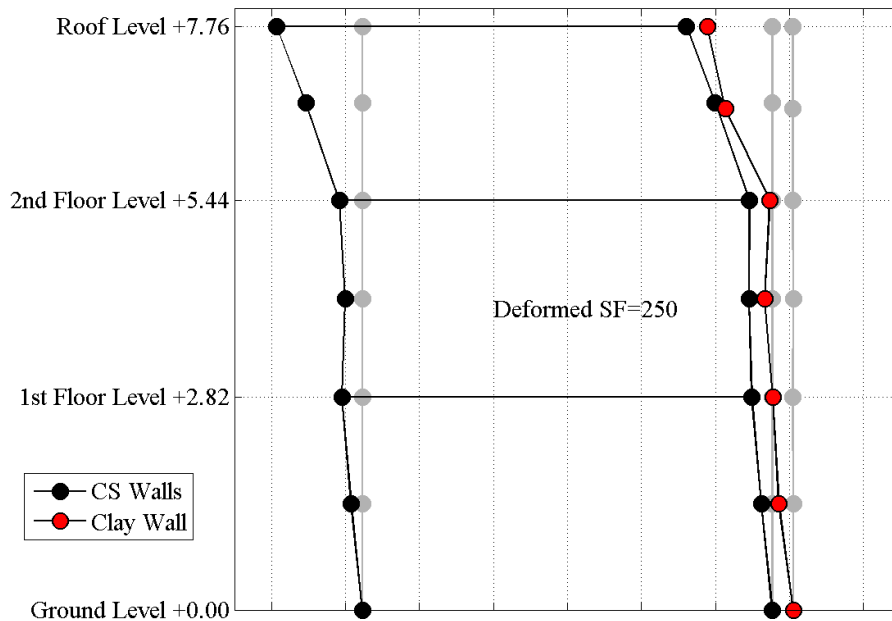


Figure 388. Test #14\_50%\_EQ2\_080: Deformed Shape.

Figure 389 plots the envelope of the maximum drifts recorded during the test. The roof drift has been computed dividing the top gable displacement by the diagonal length from the gable peak to the 2<sup>nd</sup> floor along the roof slope (3.5 m).

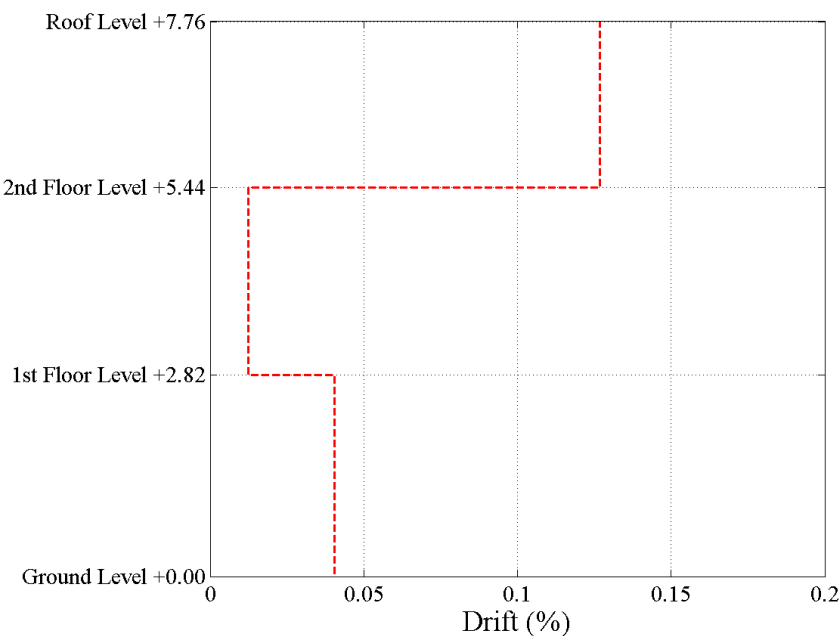


Figure 389. Test #14\_50%\_EQ2\_080: Maximum Absolute Drift.

### 6.4.9 Test #16\_100%\_EQ2\_160

Figure 390 shows the comparison between theoretical and the experimental response spectrum; the experimental acceleration time history used for the spectrum comparison is the average of the recorded accelerations on the specimen foundation (#26, #27).

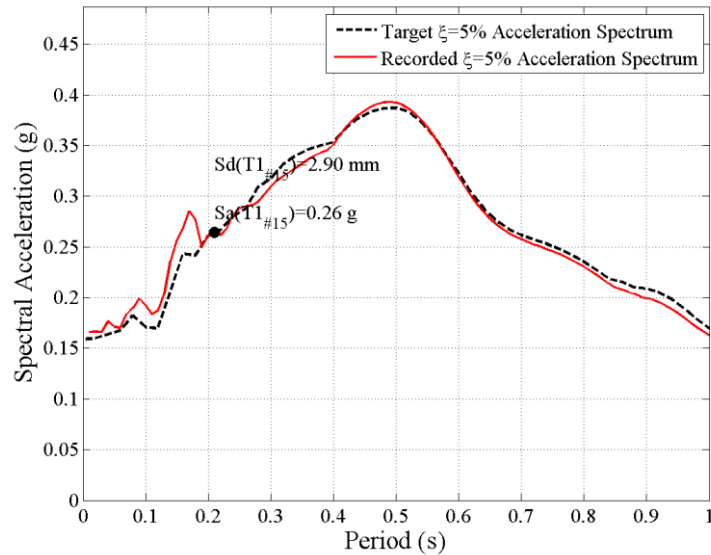


Figure 390. Test #16\_100%\_EQ2\_160: Theoretical-Experimental Spectral Comparison.

Figure 391 shows the displacement time histories of first, second and roof levels; first and second levels displacement histories have been averaged between the three potentiometer installed (#12, #13, #14 and #15, #16, #17).

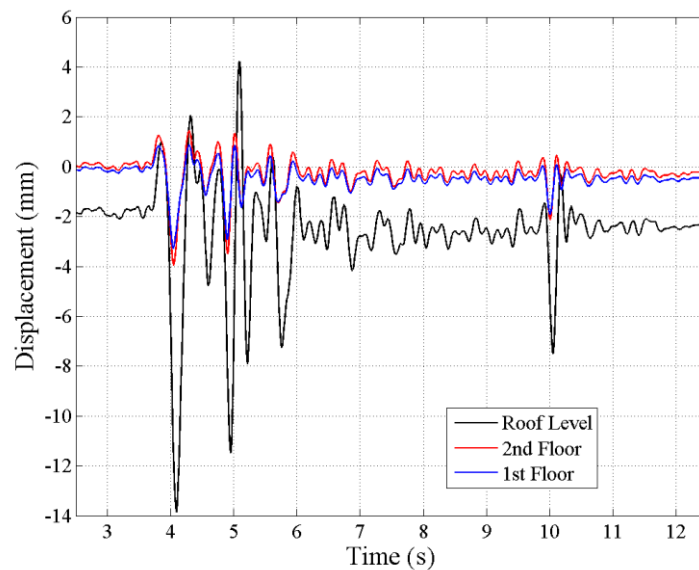


Figure 391. Test #16\_100%\_EQ2\_160: Displacement Histories.

Figure 392 shows the base shear vs 2<sup>nd</sup> floor displacement history plot. The base shear has been obtained by summing the product of each accelerometer installed on the specimen time the related mass portion.

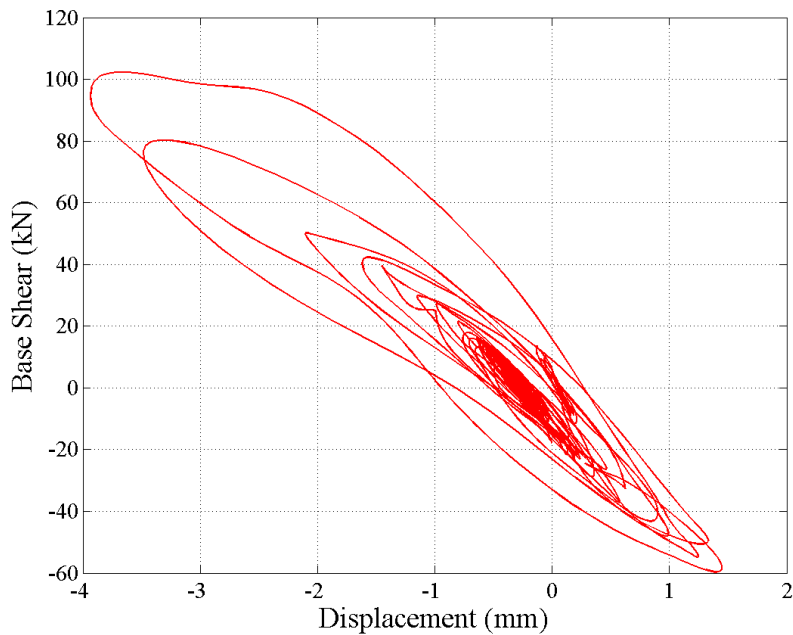


Figure 392. Test #16\_100%\_EQ2\_160: Base Shear vs 2<sup>nd</sup> Floor Displacement.

Figure 393 shows the absolute maximum response recorded at each level. The red line shows the envelope deformed shape while the blue one is the displacement recorded by first and roof levels at the instant of the maximum absolute 2<sup>nd</sup> floor displacement. Figure 393 plots also the residual displacements measured at the end of the test.

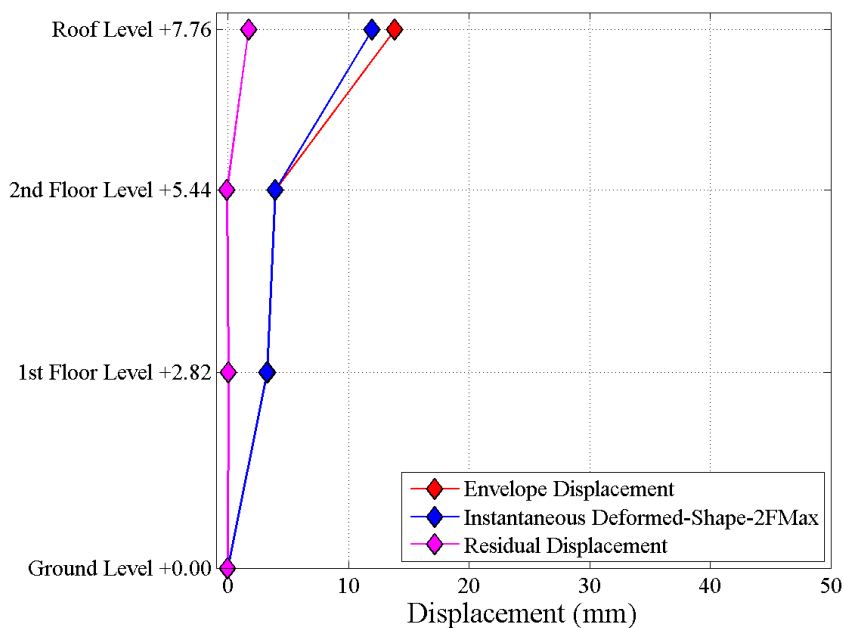


Figure 393. Test #16\_100%\_EQ2\_160: Peak and Residual Displacements.



Figure 394 represents the instantaneous deformed shape of the building at the instant of the peak 2<sup>nd</sup> floor displacement. The response of the OOP potentiometer is also included. The deformation is amplified by a scaling factor equal to 250 as indicated in the figure.

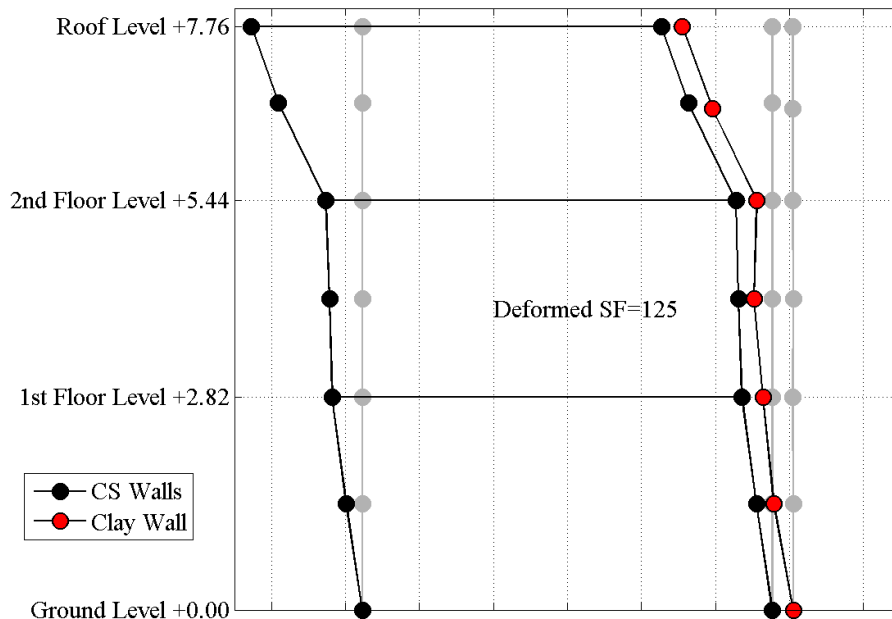


Figure 394. Test #16\_100%\_EQ2\_160: Deformed Shape.

Figure 395 plots the envelope of the maximum drifts recorded during the test. The roof drift has been computed dividing the top gable displacement by the diagonal length from the gable peak to the 2<sup>nd</sup> floor along the roof slope (3.5 m).

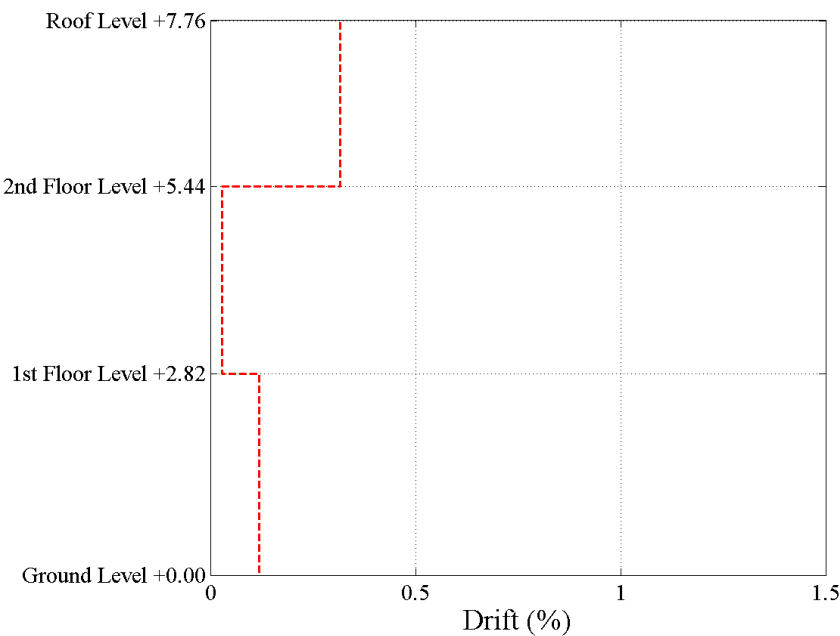


Figure 395. Test #16\_100%\_EQ2\_160: Maximum Absolute Drift.

### 6.4.10 Test #18\_50%\_EQ2\_080

Figure 396 shows the comparison between theoretical and the experimental response spectrum; the experimental acceleration time history used for the spectrum comparison is the average of the recorded accelerations on the specimen foundation (#26, #27).

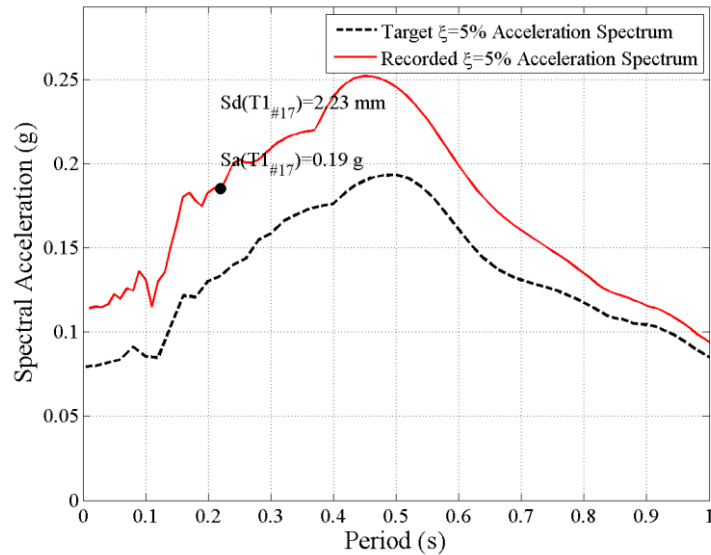


Figure 396. Test #18\_50%\_EQ2\_080: Theoretical-Experimental Spectral Comparison.

Figure 397 shows the displacement time histories of first, second and roof levels; first and second levels displacement histories have been averaged between the three potentiometer installed (#12, #13, #14 and #15, #16, #17).

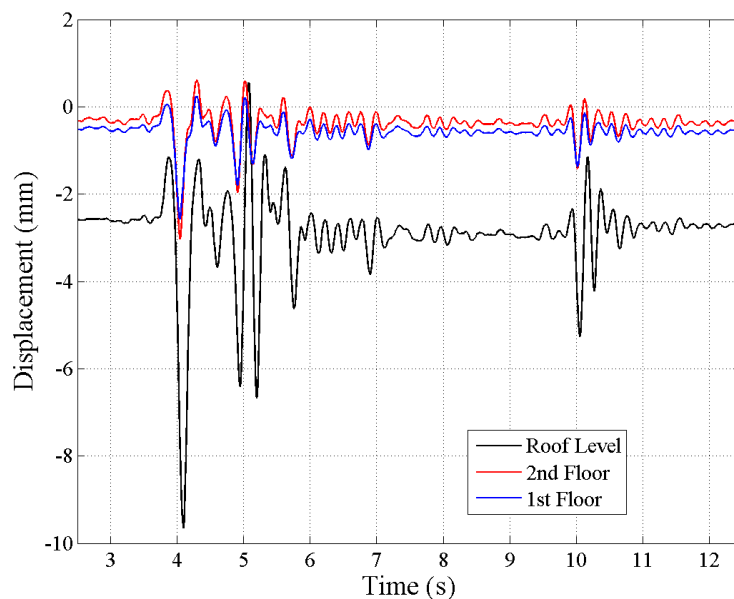


Figure 397. Test #18\_50%\_EQ2\_080: Displacement Histories.

Figure 398 shows the base shear vs 2<sup>nd</sup> floor displacement history plot. The base shear has been obtained by summing the product of each accelerometer installed on the specimen time the related mass portion.

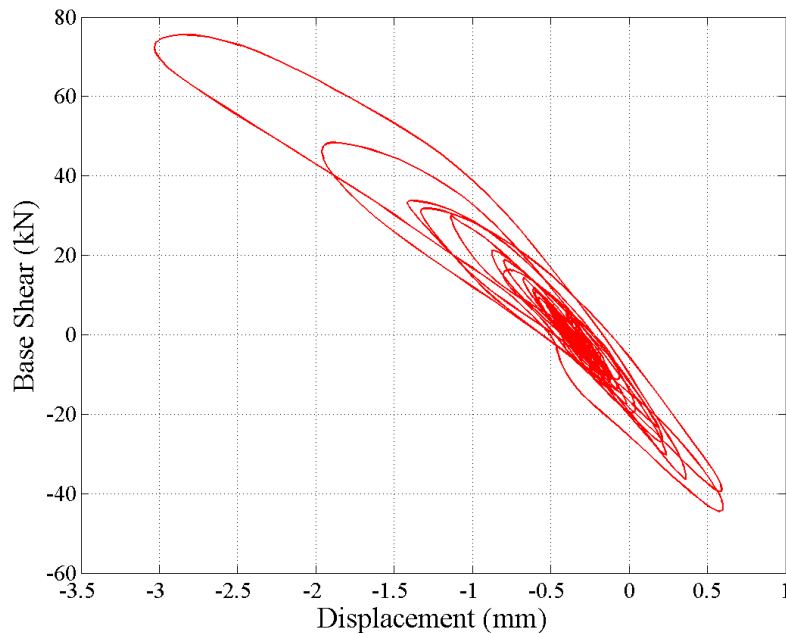


Figure 398. Test #18\_50%\_EQ2\_080: Base Shear vs 2<sup>nd</sup> Floor Displacement.

Figure 399 shows the absolute maximum response recorded at each level. The red line shows the envelope deformed shape while the blue one is the displacement recorded by first and roof levels at the instant of the maximum absolute 2<sup>nd</sup> floor displacement. Figure 399 shows also the residual displacements measured at the end of the test.

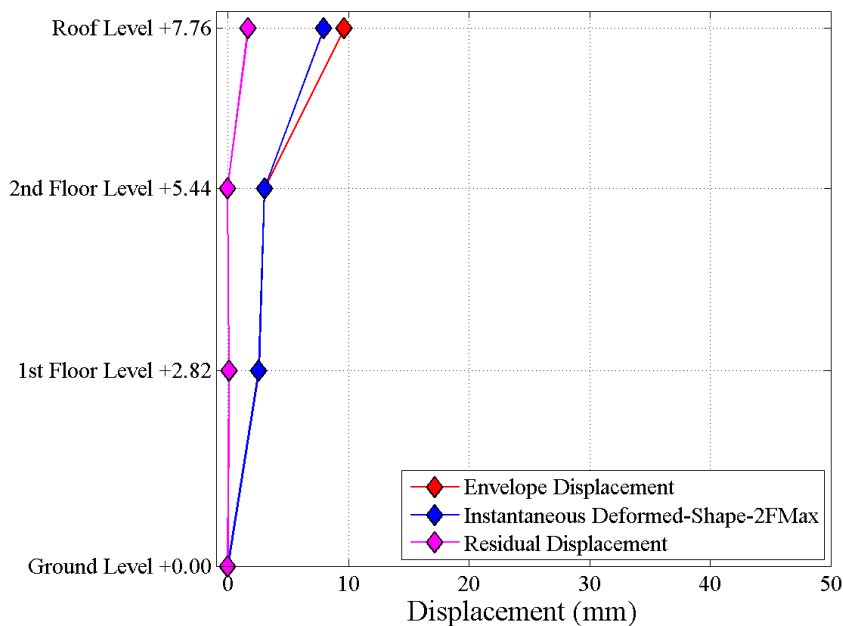


Figure 399. Test #18\_50%\_EQ2\_080: Peak and Residual Displacements.



Figure 400 represents the instantaneous deformed shape of the building at the instant of the peak 2<sup>nd</sup> floor displacement. The response of the OOP potentiometer is also included. The deformation is amplified by a scaling factor equal to 250 as indicated in the figure.

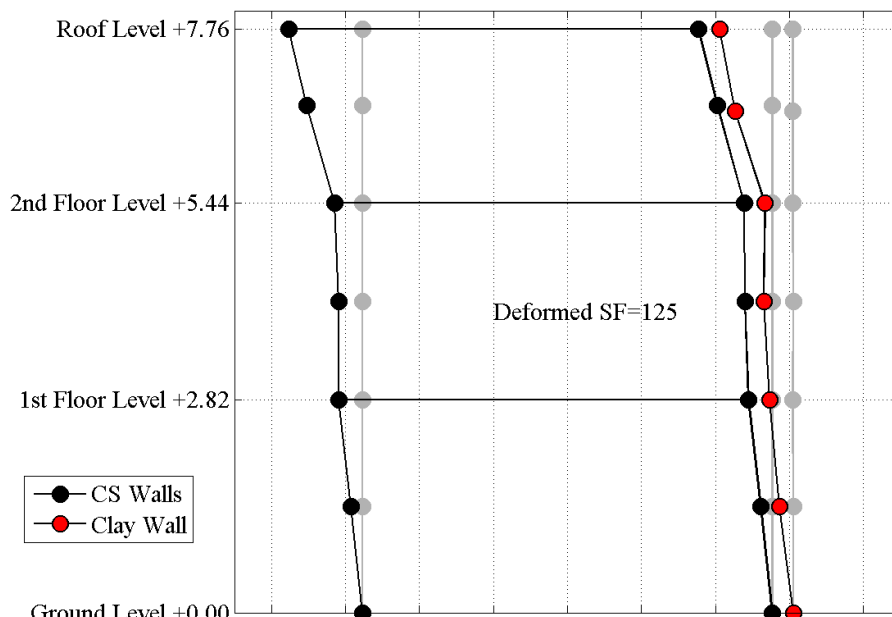


Figure 400. Test #18\_50%\_EQ2\_080: Deformed Shape.

Figure 401 plots the envelope of the maximum drifts recorded during the test. The roof drift has been computed dividing the top gable displacement by the diagonal length from the gable peak to the 2<sup>nd</sup> floor along the roof slope (3.5 m).

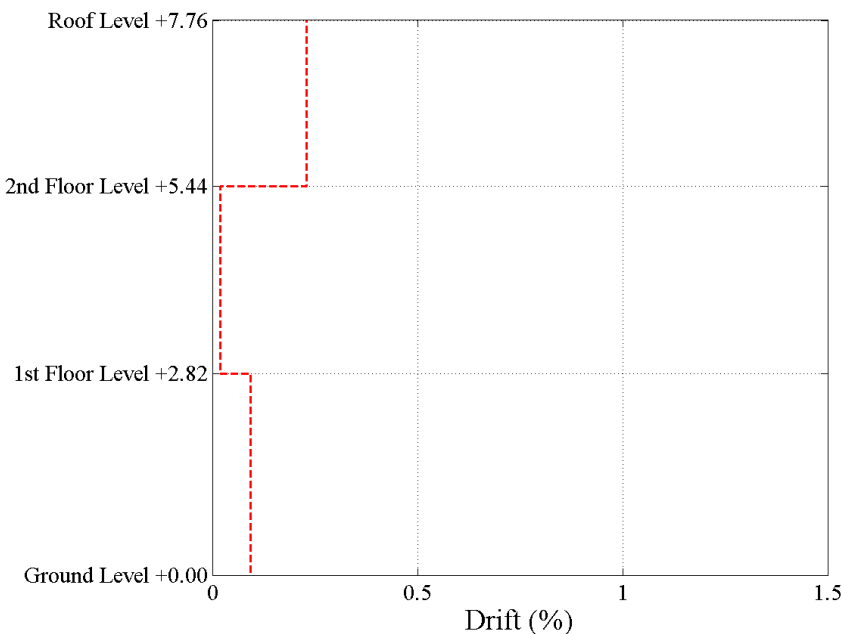


Figure 401. Test #18\_50%\_EQ2\_080: Maximum Absolute Drift.

### 6.4.11 Test #19\_125%\_EQ2\_200

Figure 402 shows the comparison between theoretical and the experimental response spectrum; the experimental acceleration time history used for the spectrum comparison is the average of the recorded accelerations on the specimen foundation (#26, #27).

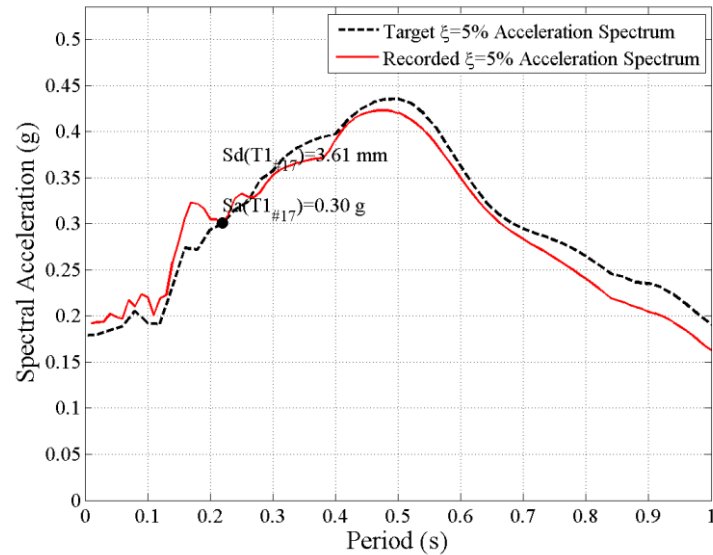


Figure 402. Test #19\_125%\_EQ2\_200: Theoretical-Experimental Spectral Comparison.

Figure 403 shows the displacement time histories of first, second and roof levels; first and second levels displacement histories have been averaged between the three potentiometer installed (#12, #13, #14 and #15, #16, #17).

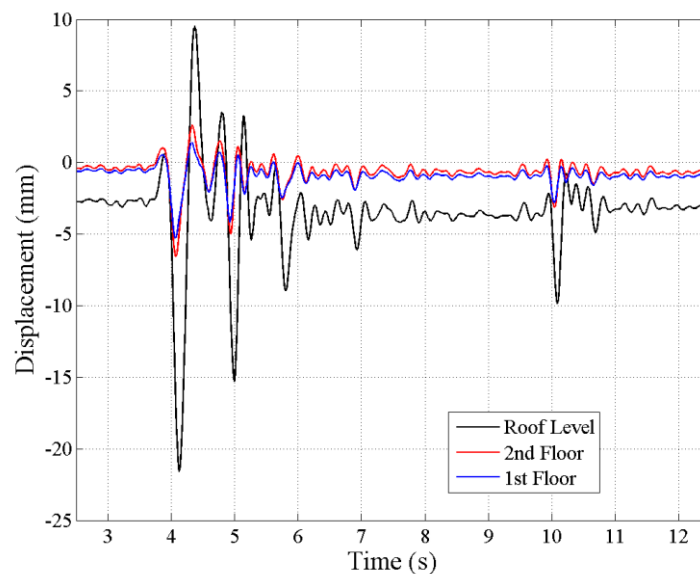


Figure 403. Test #19\_125%\_EQ2\_200: Displacement Histories.

Figure 404 shows the base shear vs 2<sup>nd</sup> floor displacement history plot. The base shear has been obtained by summing the product of each accelerometer installed on the specimen time the related mass portion.

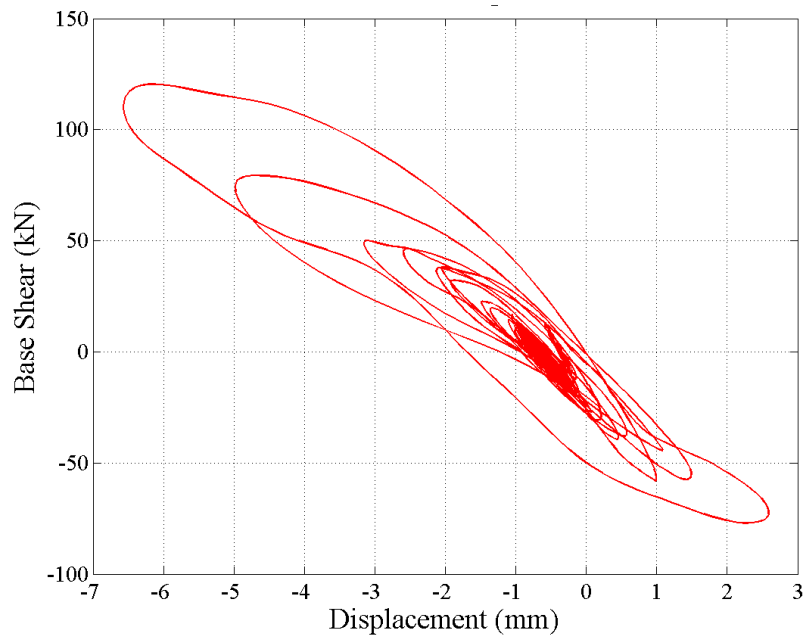


Figure 404. Test #19\_125%\_EQ2\_200: Base Shear vs 2<sup>nd</sup> Floor Displacement.

Figure 405 shows the absolute maximum response recorded at each level. The red line represents the envelope deformed shape while the blue one is the displacement recorded by first and roof levels at the instant of the maximum absolute 2<sup>nd</sup> floor displacement. Figure 405 plots also the residual displacements measured at the end of the test.

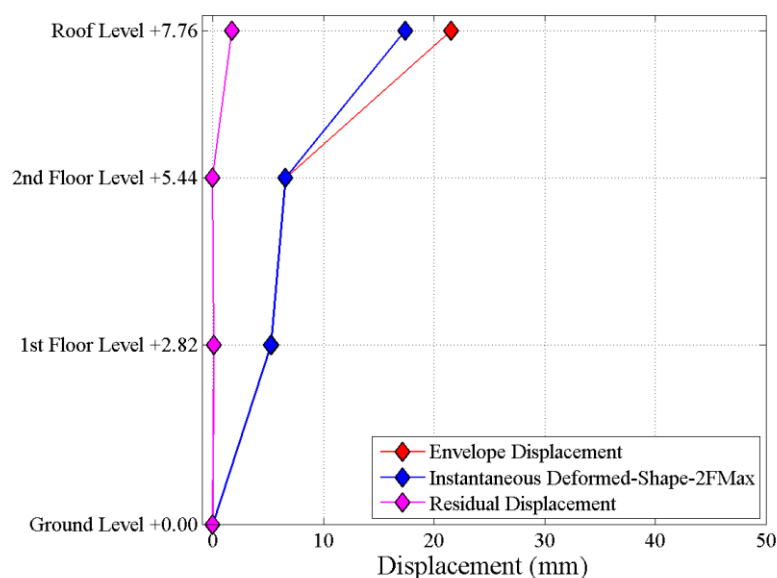


Figure 405. Test #19\_125%\_EQ2\_200: Peak and Residual Displacements.



Figure 406 represents the instantaneous deformed shape of the building at the instant of the peak 2<sup>nd</sup> floor displacement. The response of the OOP potentiometer is also included. The deformation is amplified by a scaling factor as indicated in the figure.

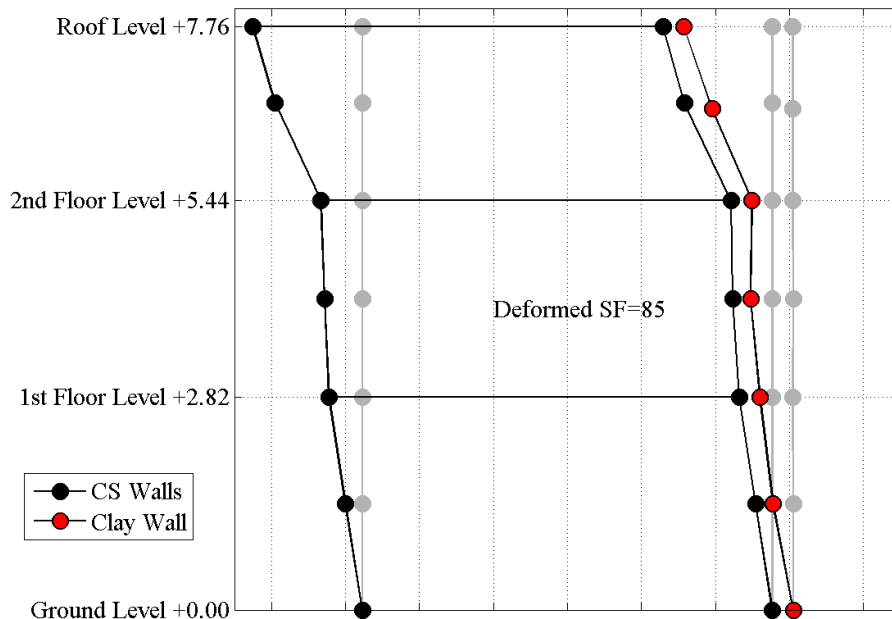


Figure 406. Test #19\_125%\_EQ2\_200: Deformed Shape.

Figure 407 plots the envelope of the maximum drifts recorded during the test. The roof drift has been computed dividing the top gable displacement by the diagonal length from the gable peak to the 2<sup>nd</sup> floor along the roof slope (3.5 m).

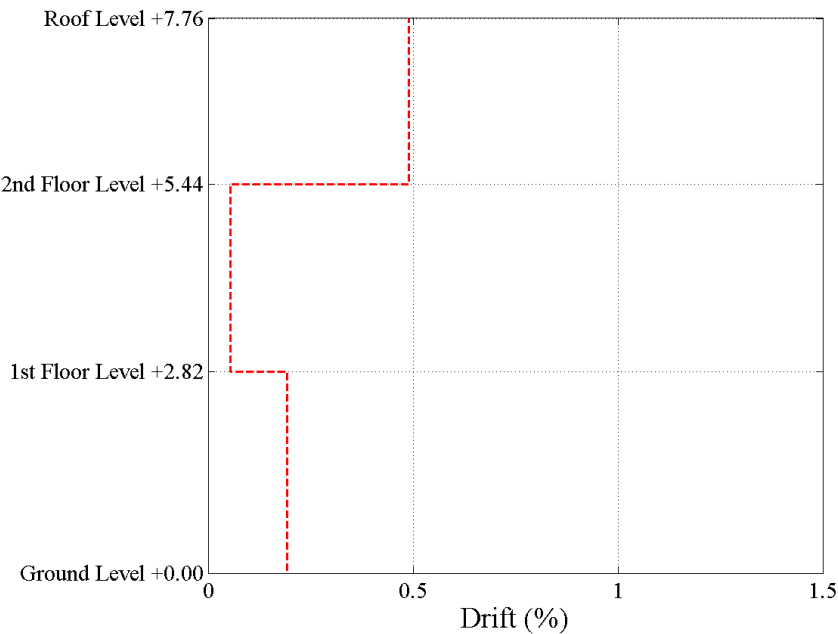


Figure 407. Test #19\_125%\_EQ2\_200: Maximum Absolute Drift.

### 6.4.12 Test #21\_150%\_EQ2\_240

Figure 408 shows the comparison between theoretical and the experimental response spectrum; the experimental acceleration time history used for the spectrum comparison is the average of the recorded accelerations on the specimen foundation (#26, #27).

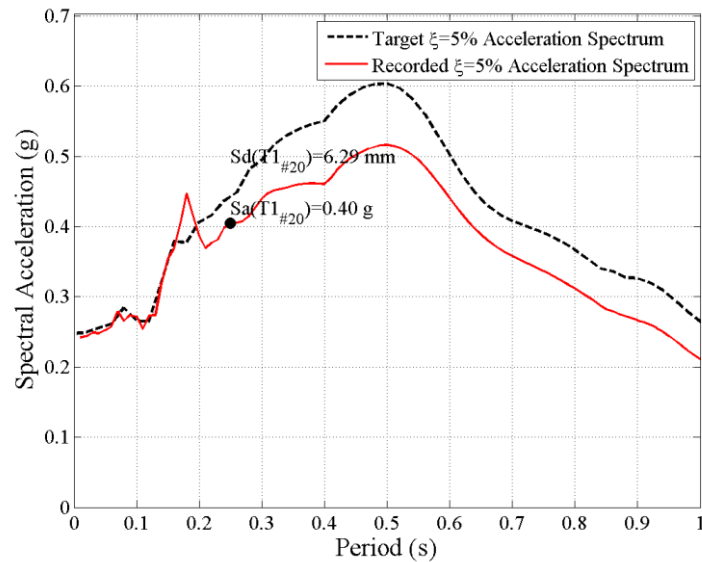


Figure 408. Test #21\_150%\_EQ2\_240: Theoretical-Experimental Spectral Comparison.

Figure 409 shows the displacement time histories of first, second and roof levels; first and second levels displacement histories have been averaged between the three potentiometer installed (#12, #13, #14 and #15, #16, #17).

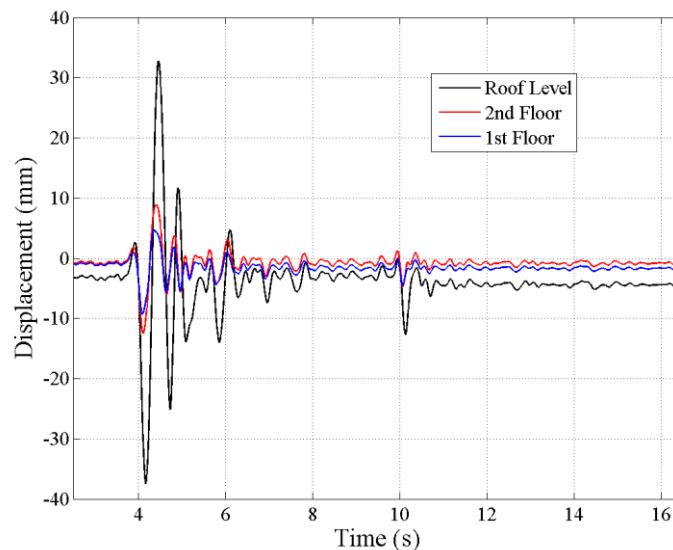


Figure 409. Test #21\_150%\_EQ2\_240: Displacement Histories.

Figure 410 shows the base shear vs 2<sup>nd</sup> floor displacement history plot. The base shear has been obtained by summing the product of each accelerometer installed on the specimen time the related mass portion.

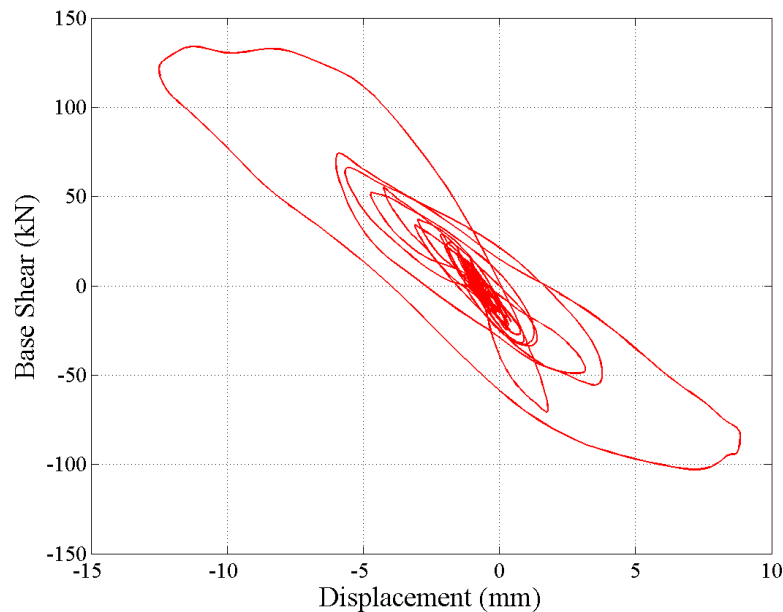


Figure 410. Test #21\_150%\_EQ2\_240: Base Shear vs 2<sup>nd</sup> Floor Displacement.

Figure 411 shows the absolute maximum response recorded at each level. The red line shows the envelope deformed shape while the blue one is the displacement recorded by first and roof levels at the instant of the maximum absolute 2<sup>nd</sup> floor displacement. Figure 411 shows also the residual displacements measured at the end of the test.

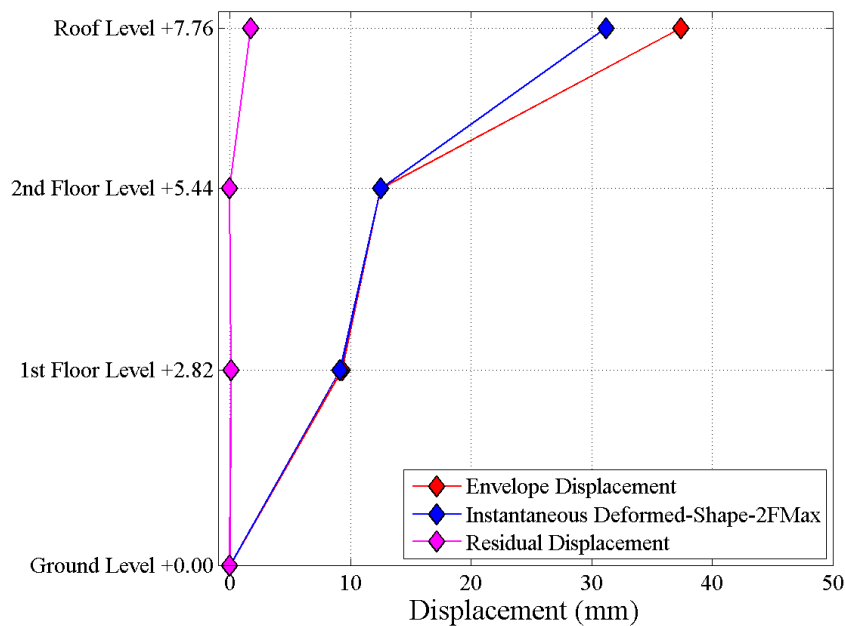


Figure 411. Test #21\_150%\_EQ2\_240: Peak and Residual Displacements.

Figure 412 represents the instantaneous deformed shape of the building at the instant of the peak 2<sup>nd</sup> floor displacement. The response of the OOP potentiometer is also included. The deformation is amplified by a scaling factor as indicated in the figure.

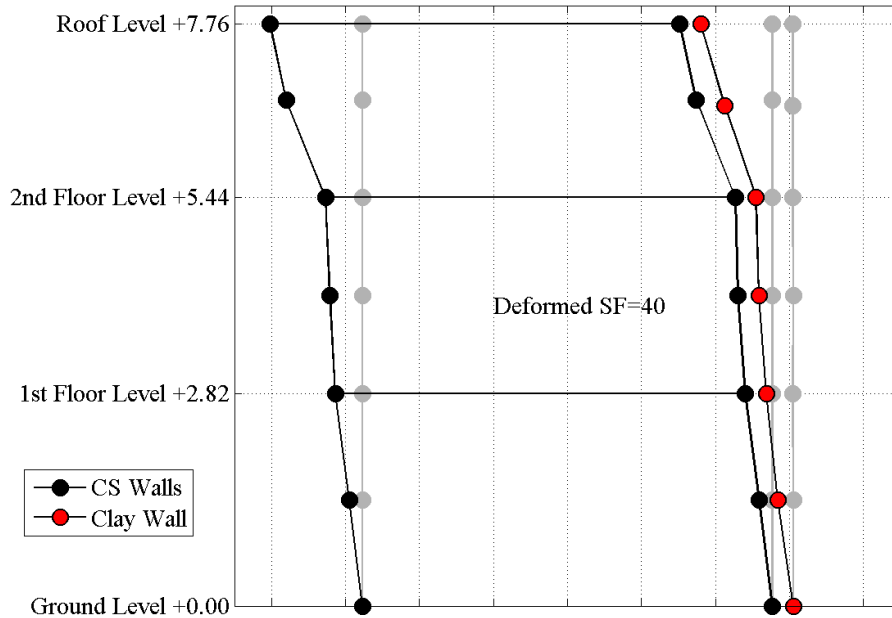


Figure 412. Test #21\_150%\_EQ2\_240: Deformed Shape.

Figure 413 plots the envelope of the maximum drifts recorded during the test. The roof drift has been computed dividing the top gable displacement by the diagonal length from the gable peak to the 2<sup>nd</sup> floor along the roof slope (3.5 m).

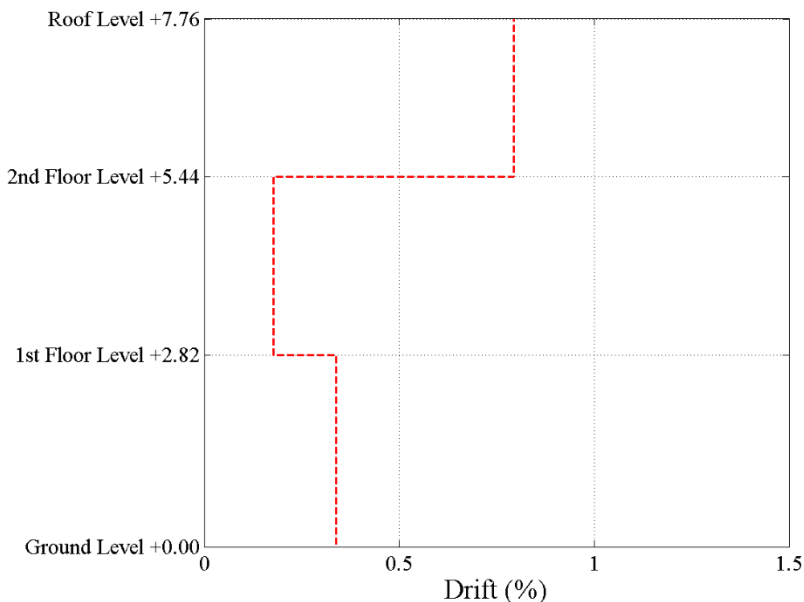


Figure 413. Test #21\_150%\_EQ2\_240: Maximum Absolute Drift.

### 6.4.13 Test #23\_200%\_EQ2\_320

Figure 414 shows the comparison between theoretical and the experimental response spectrum; the experimental acceleration time history used for the spectrum comparison is the average of the recorded accelerations on the specimen foundation (#26, #27).

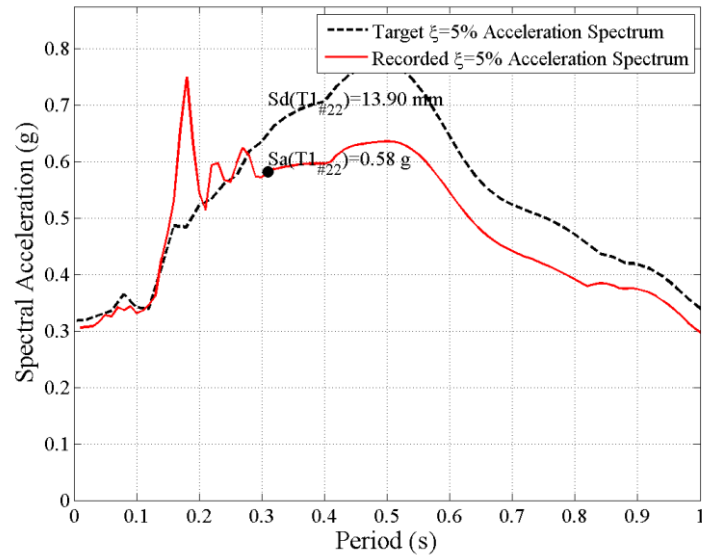


Figure 414. Test #23\_200%\_EQ2\_320: Theoretical-Experimental Spectral Comparison.

Figure 415 shows the displacement time histories of first, second and roof levels; first and second levels displacement histories have been averaged between the three potentiometer installed (#12, #13, #14 and #15, #16, #17).

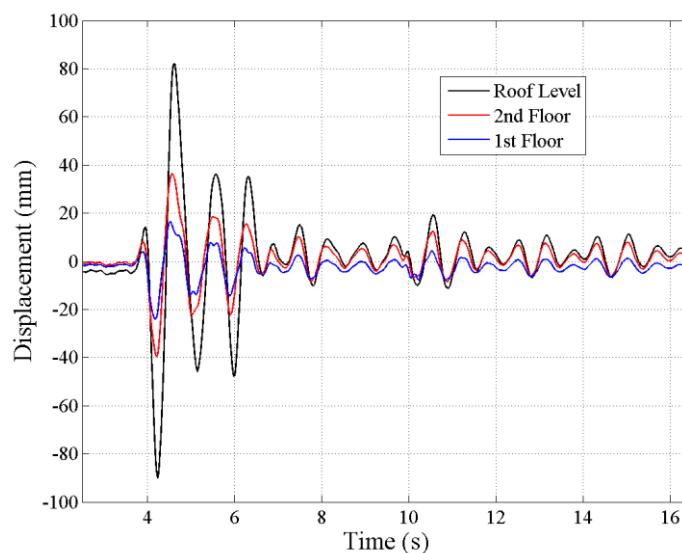


Figure 415. Test #23\_200%\_EQ2\_320: Displacement Histories.

Figure 416 shows the base shear vs 2<sup>nd</sup> floor displacement history plot. The base shear has been obtained by summing the product of each accelerometer installed on the specimen time the related mass portion.

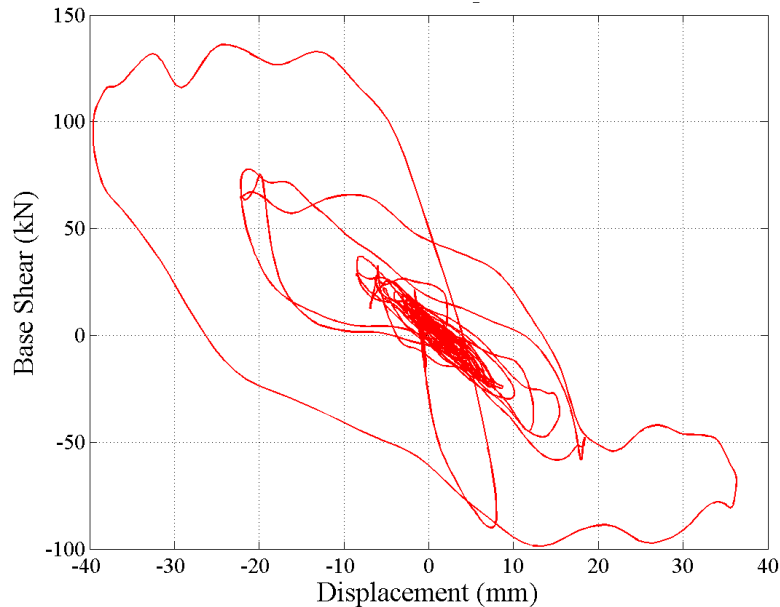


Figure 416. Test #23\_200%\_EQ2\_320: Base Shear vs 2<sup>nd</sup> Floor Displacement.

Figure 417 represents the absolute maximum response recorded at each level. The red line shows the envelope deformed shape while the blue one is the displacement recorded by first and roof levels at the instant of the maximum absolute 2<sup>nd</sup> floor displacement. Figure 417 plots also the residual displacements measured at the end of the test.

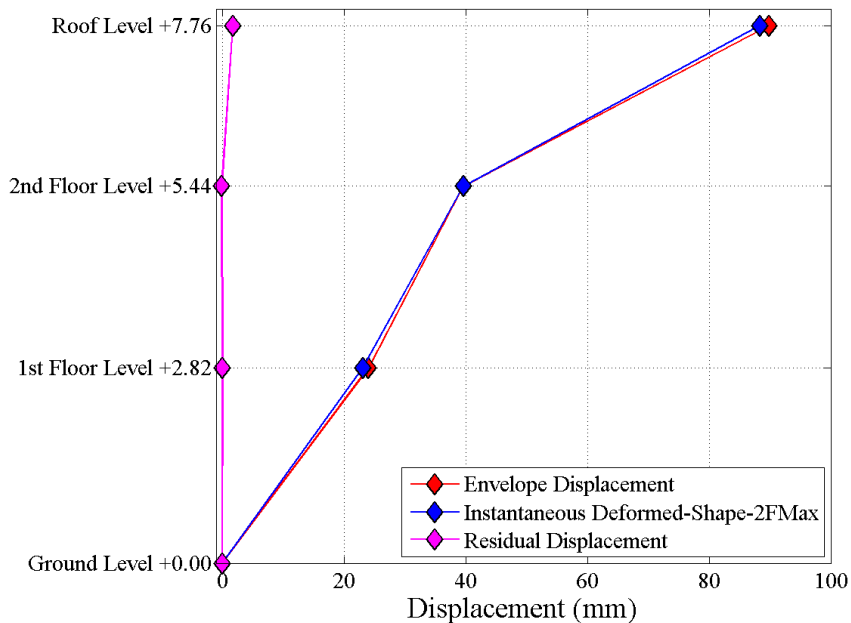


Figure 417. Test #23\_200%\_EQ2\_320: Peak and Residual Displacements.



Figure 418 represents the instantaneous deformed shape of the building at the instant of the peak 2<sup>nd</sup> floor displacement. The response of the OOP potentiometer is also included. The deformation is amplified by a scaling factor as indicated in the figure.

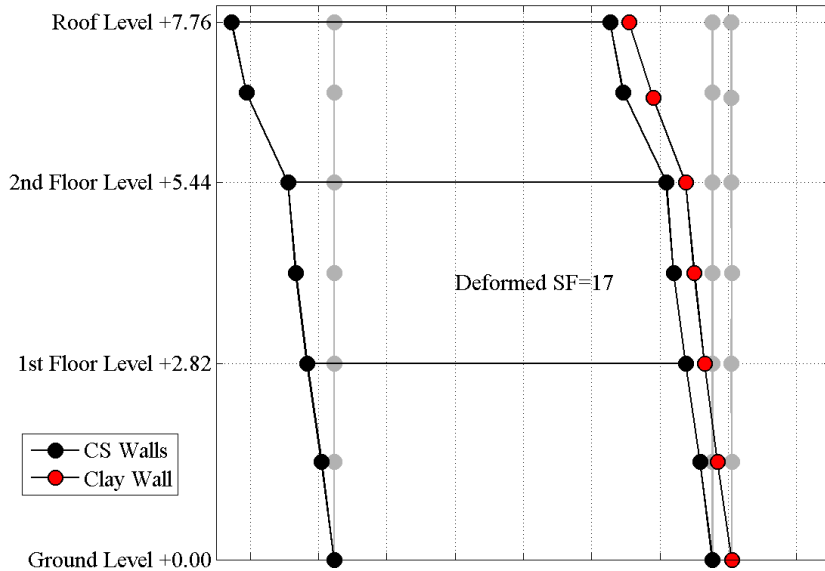


Figure 418. Test #23\_200%\_EQ2\_320: Deformed Shape.

Figure 419 plots the envelope of the maximum drifts recorded during the test. The roof drift has been computed dividing the top gable displacement by the diagonal length from the gable peak to the 2<sup>nd</sup> floor along the roof slope (3.5 m).

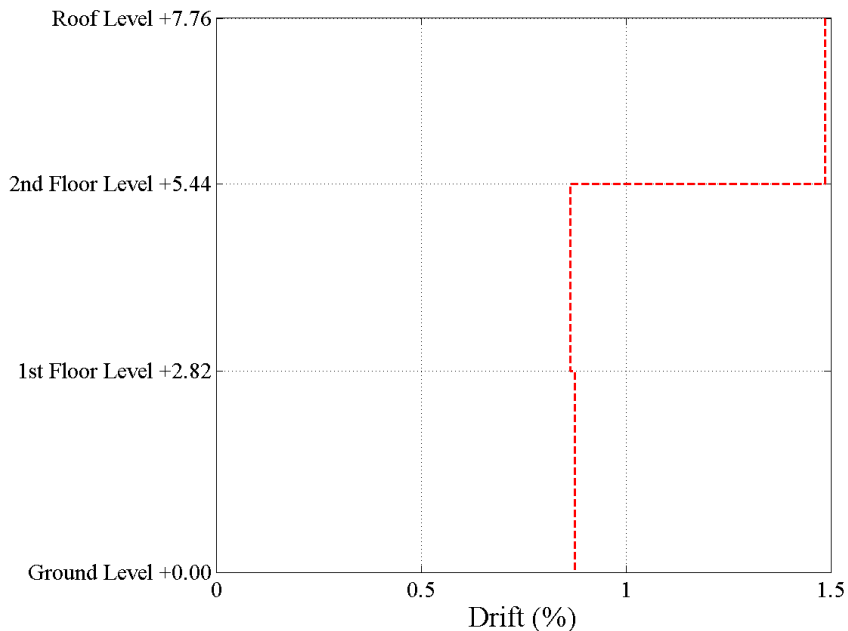


Figure 419. Test #23\_200%\_EQ2\_320: Maximum Absolute Drift.

#### 6.4.14 Test #26\*, #27\*, #28\* \_30%\_EQ2\_050 (Rigid roof)

Test #26\*, #27\*, #28\* were performed in order to calibrate the shaking table. The obtained results are almost the same. In particular this section provide the results for the last one of the three (#28). Figure 420 shows the comparison between theoretical and the experimental response spectrum; the experimental acceleration time history used for the spectrum comparison is the average of the recorded accelerations on the specimen foundation (#26, #27).

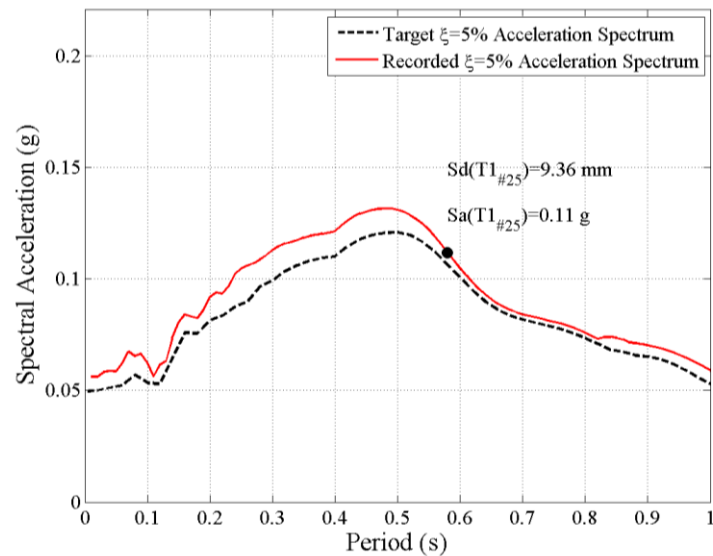


Figure 420. Test #28\*\_30%\_EQ2\_050: Theoretical-Experimental Spectral Comparison.

Figure 421 shows the displacement time histories of first, second and roof levels; first and second levels displacement histories have been averaged between the three potentiometer installed (#12, #13, #14 and #15, #16, #17).

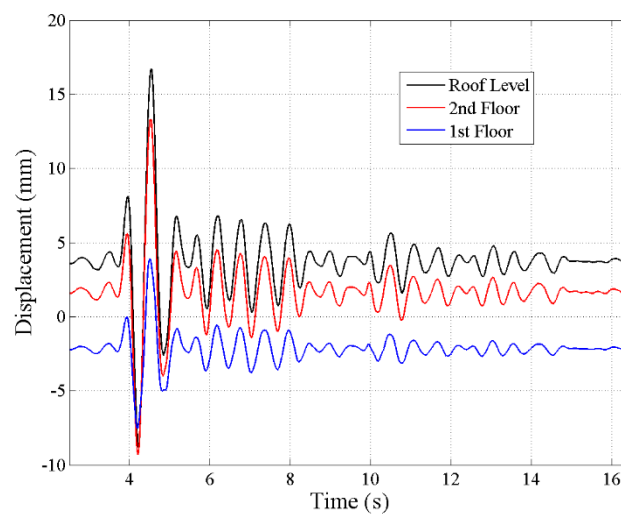


Figure 421. Test #28\*\_30%\_EQ2\_050: Displacement Histories.

Figure 422 shows the base shear vs 2<sup>nd</sup> floor displacement history plot. The base shear has been obtained by summing the product of each accelerometer installed on the specimen time the related mass portion.

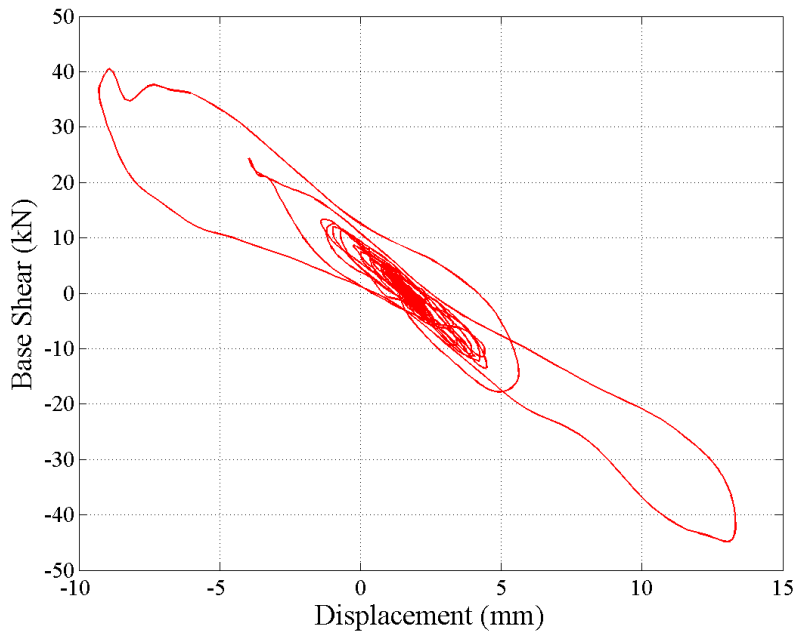


Figure 422. Test #28\*\_30%\_EQ2\_050: Base Shear vs 2<sup>nd</sup> Floor Displacement.

Figure 423 represents the absolute maximum response recorded at each level. The red line shows the envelope deformed shape while the blue one is the displacement recorded by first and roof levels at the instant of the maximum absolute 2<sup>nd</sup> floor displacement. Figure 423 plots also the residual displacements measured at the end of the test.

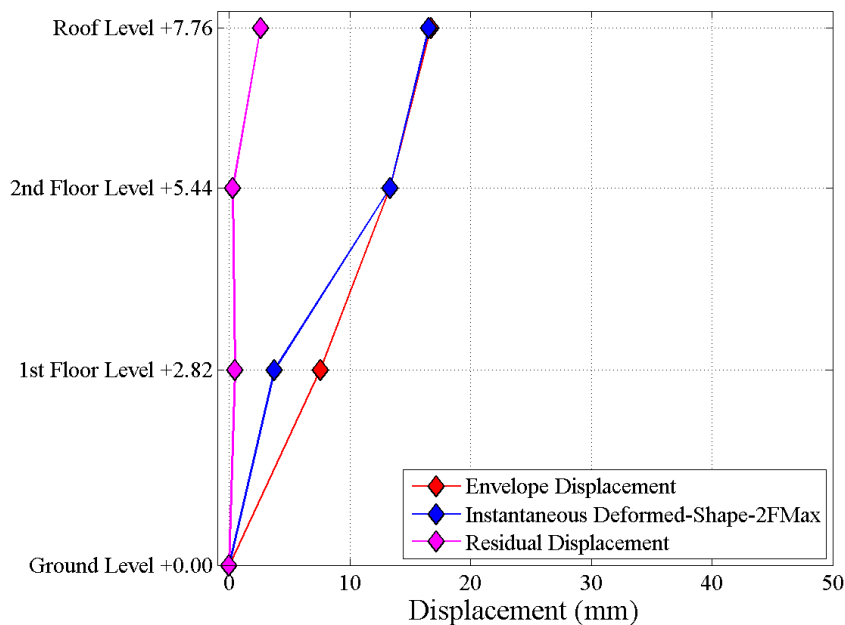


Figure 423. Test #28\*\_30%\_EQ2\_050: Peak and Residual Displacements.



Figure 424 represents the instantaneous deformed shape of the building at the instant of the peak 2<sup>nd</sup> floor displacement. The response of the OOP potentiometer is also included. The deformation is amplified by a scaling factor as indicated in the figure.

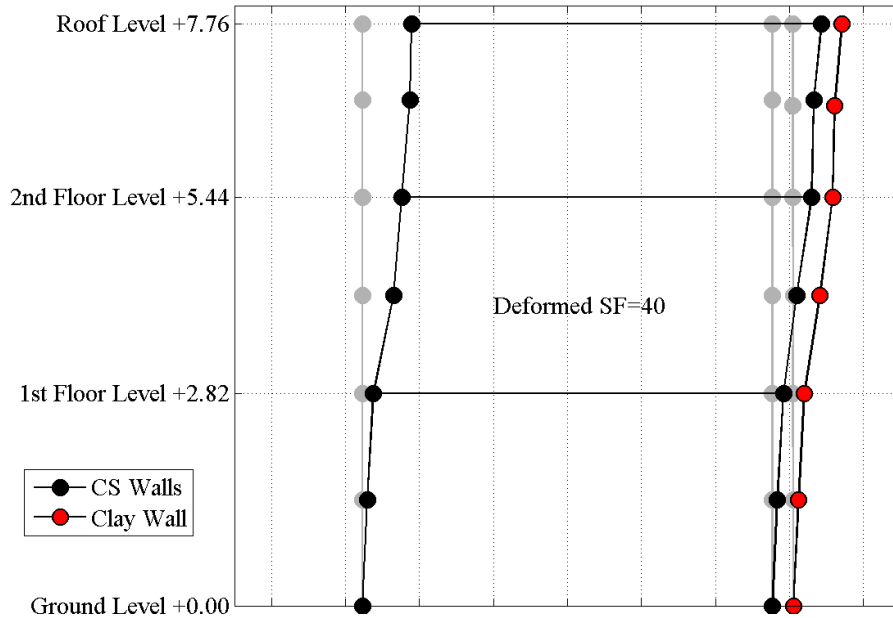


Figure 424. Test #28\*\_30%\_EQ2\_050: Deformed Shape.

Figure 425 plots the envelope of the maximum drifts recorded during the test. The roof drift has been computed dividing the top gable displacement by the diagonal length from the gable peak to the 2<sup>nd</sup> floor along the roof slope (3.5 m).

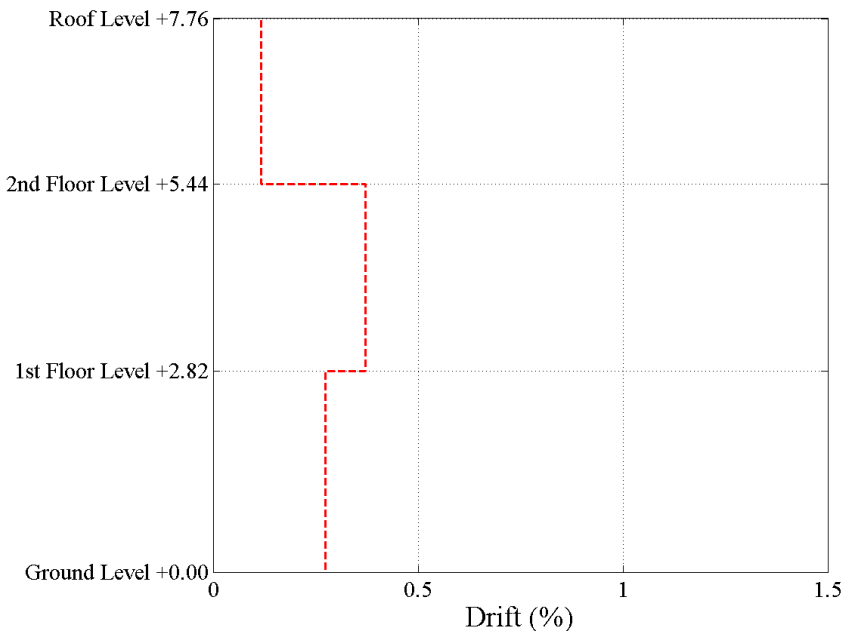


Figure 425. Test #28\*\_30%\_EQ2\_050: Maximum Absolute Drift.

### 6.4.15 Test #29\* \_60%\_EQ2\_100 (Rigid roof)

Figure 426 shows the comparison between theoretical and the experimental response spectrum; the experimental acceleration time history used for the spectrum comparison is the average of the recorded accelerations on the specimen foundation (#26, #27).

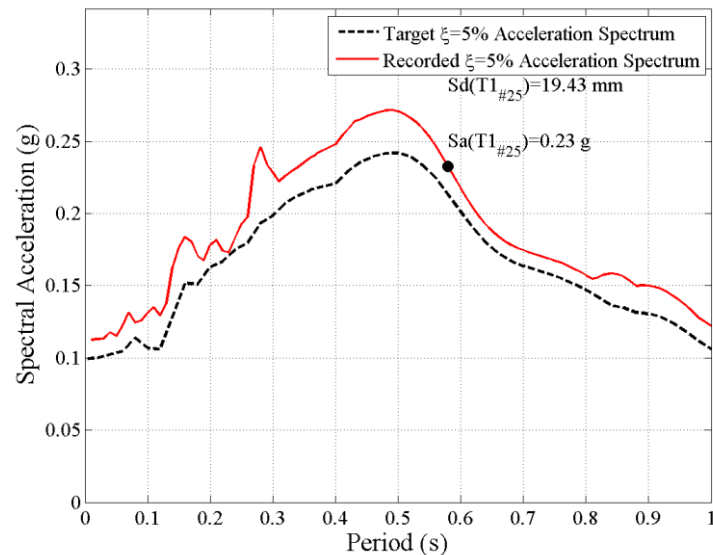


Figure 426. Test #29\* \_60%\_EQ2\_100: Theoretical-Experimental Spectral Comparison.

Figure 427 shows the displacement time histories of first, second and roof levels; first and second levels displacement histories have been averaged between the three potentiometer installed (#12, #13, #14 and #15, #16, #17).

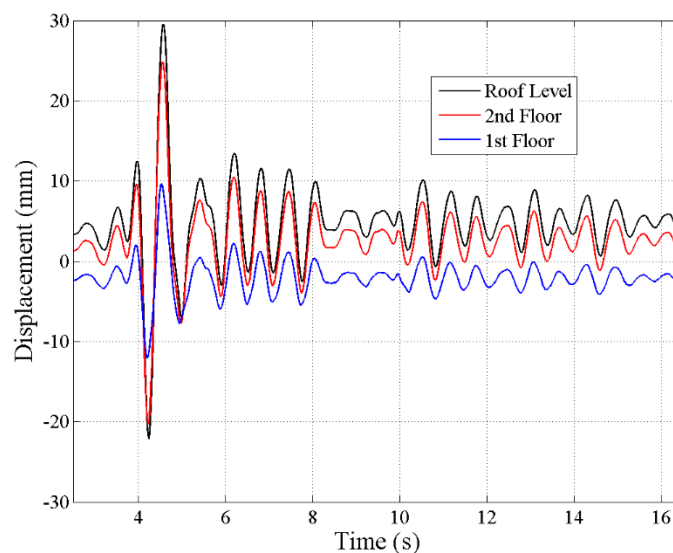


Figure 427. Test #29\* \_60%\_EQ2\_100: Displacement Histories.

Figure 428 shows the base shear vs 2<sup>nd</sup> floor displacement history plot. The base shear has been obtained by summing the product of each accelerometer installed on the specimen time the related mass portion.

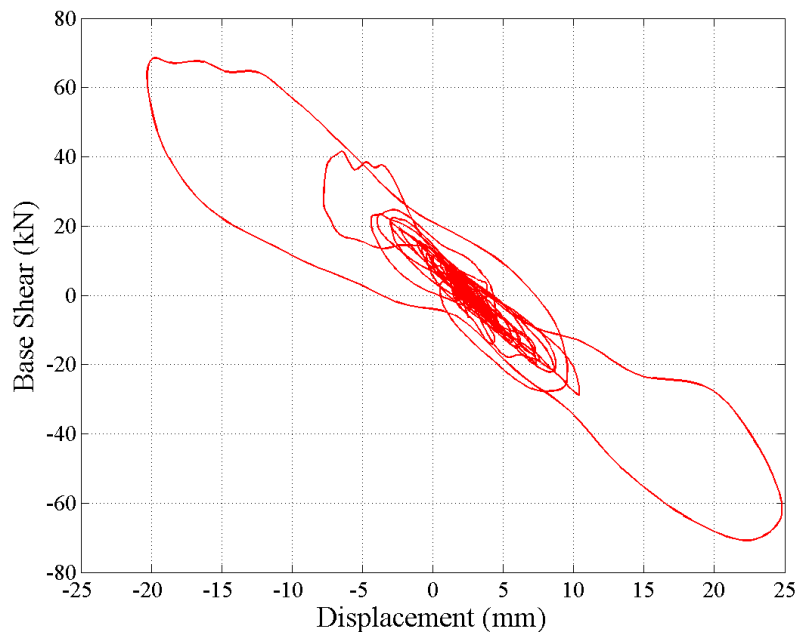


Figure 428. Test #29\*\_60%\_EQ2\_100: Base Shear vs 2<sup>nd</sup> Floor Displacement.

Figure 429 shows the absolute maximum response recorded at each level. The red line represents the envelope deformed shape while the blue one is the displacement recorded by first and roof levels at the instant of the maximum absolute 2<sup>nd</sup> floor displacement. Figure 429 plots also the residual displacements measured at the end of the test.

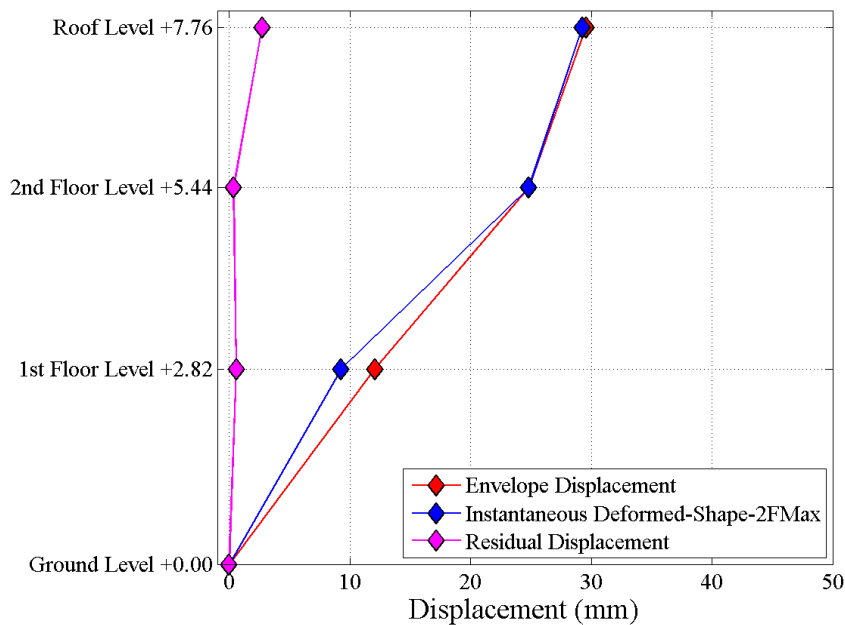


Figure 429. Test #29\*\_60%\_EQ2\_100: Peak and Residual Displacements.



Figure 430 represents the instantaneous deformed shape of the building at the instant of the peak 2<sup>nd</sup> floor displacement. The response of the OOP potentiometer is also included. The deformation is amplified by a scaling factor as indicated in the figure.

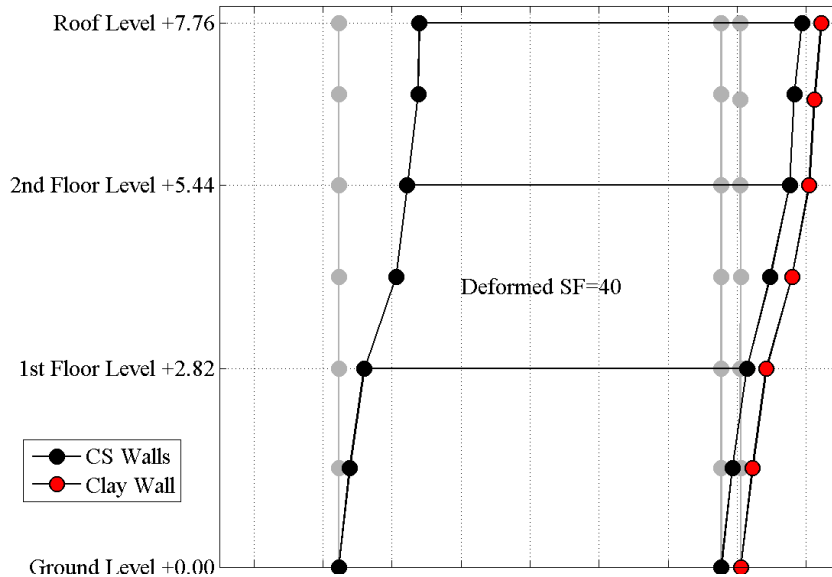


Figure 430. Test #29\*\_60%\_EQ2\_100: Deformed Shape.

Figure 431 plots the envelope of the maximum drifts recorded during the test. The roof drift has been computed dividing the top gable displacement by the diagonal length from the gable peak to the 2<sup>nd</sup> floor along the roof slope (3.5 m).

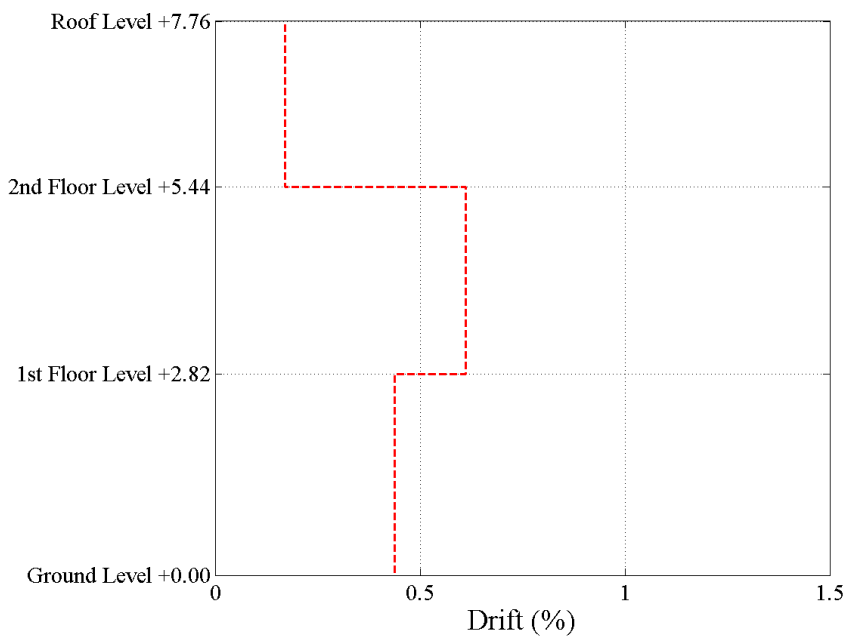


Figure 431. Test #29\*\_60%\_EQ2\_100: Maximum Absolute Drift.

### 6.4.16 Summary of the results

The present section briefly presents the results of the overall experimental campaign. Figure 432 shows the experimental maximum and minimum displacement responses exhibited by first and second floor for all the tests with increasing PGAs.

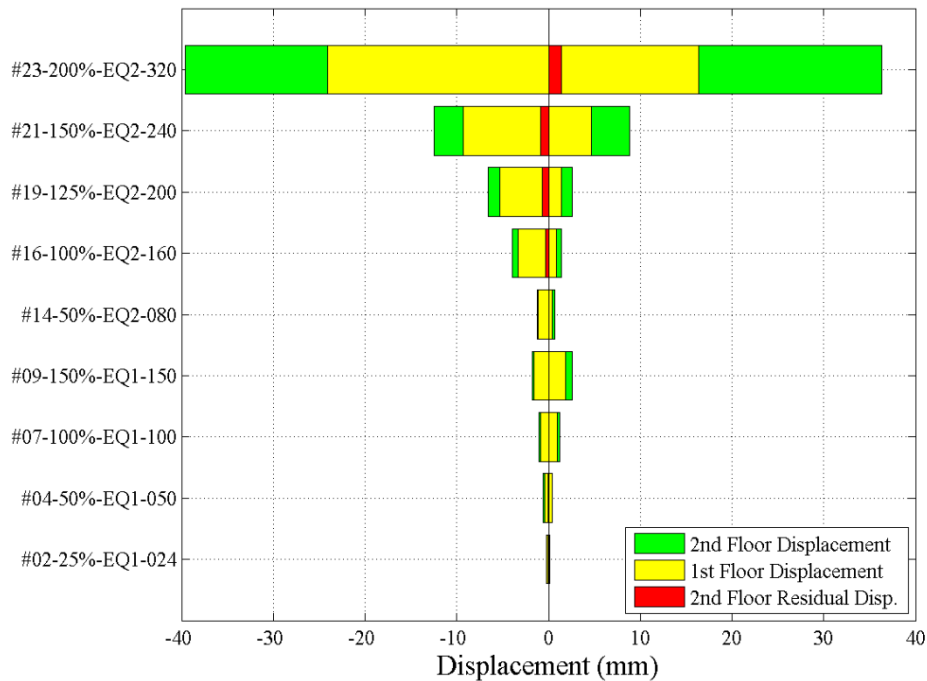


Figure 432. Experimental Displacement Response.

Figure 433 shows the absolute residual displacement of the three levels related to each test performed.

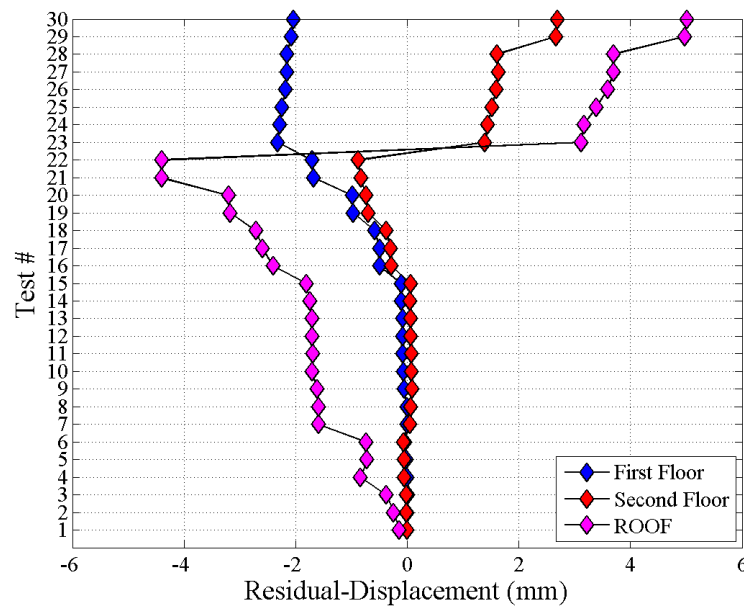


Figure 433. Experimental Residual Displacement Response.



Figure 434 plots the base shear vs the 2<sup>nd</sup> floor displacement related to each test.

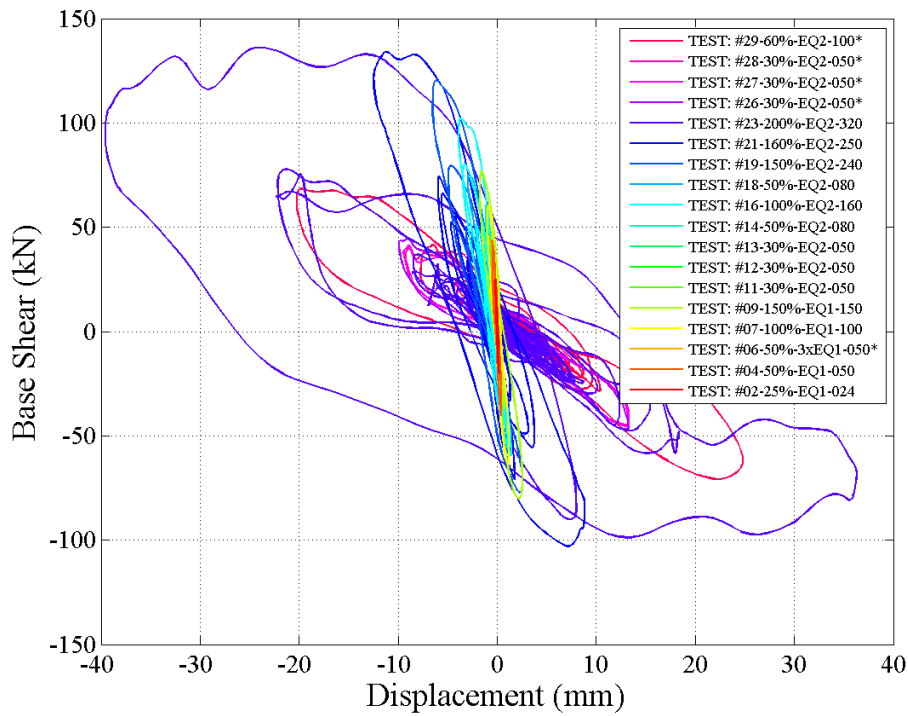


Figure 434. Base Shear vs 2<sup>nd</sup> Floor Displacement.

Figure 435 shows the base shear vs 2<sup>nd</sup> floor displacement envelope identifying the coordinates of the experimental step when the base shear is maximum and when the 2<sup>nd</sup> floor displacement is maximum.

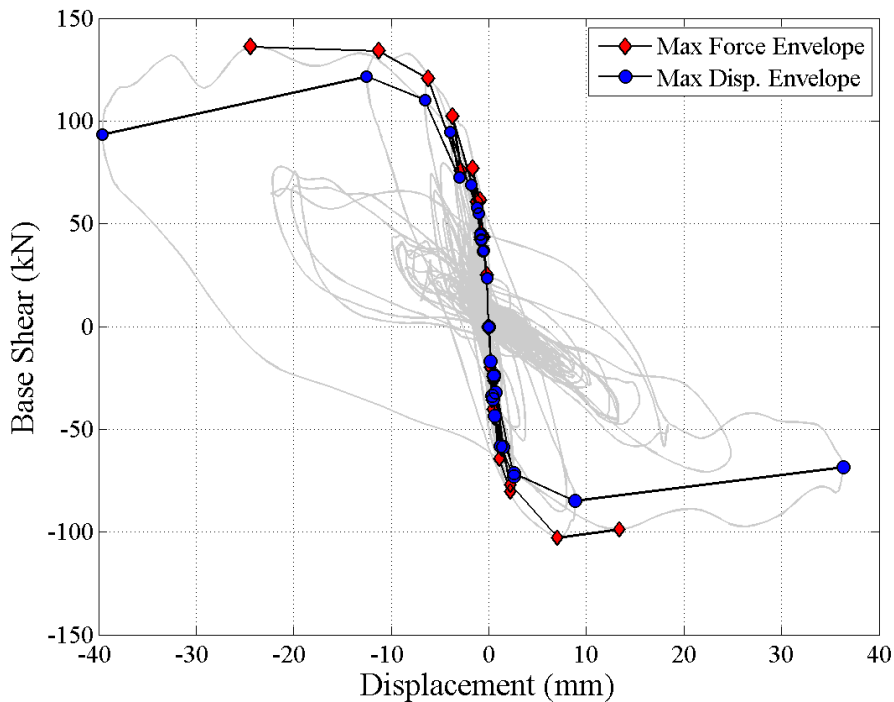


Figure 435. Base Shear vs 2<sup>nd</sup> Floor Displacement: Envelopes.



Table 63 lists the maximum displacement and forces reached during each repetition (i.e. the coordinates of the dots shown in Figure 435).

*Table 63. Base shear and 2<sup>nd</sup> floor displacement Peak Responses.*

TEST #	Peak Base Shear Responses				Peak Displacement Responses			
	Max F [kN]	Disp. [mm]	Min F [kN]	Disp. [mm]	Max D. [mm]	F. [mm]	MinD. [mm]	F. [mm]
25%_EQ1_024	25.3	-0.2	-19.8	0.1	0.2	-17.1	-0.2	23.3
50%_EQ1_050	43.7	-0.5	-40.1	0.4	0.4	-35.3	-0.6	36.8
50%_3xEQ1_050	43.8	-0.6	-35.7	0.3	0.4	-33.9	-0.6	36.7
100%_EQ1_100	61.5	-0.9	-64.5	1.1	1.2	-58.4	-1.0	55.0
150%_EQ1_150	76.9	-1.6	-80.2	2.2	2.5	-73.0	-1.8	68.7
30%_EQ2_050	45.8	-0.8	-26.5	0.5	0.5	-24.5	-0.8	44.6
30%_EQ2_050	43.6	-0.8	-24.6	0.5	0.5	-23.8	-0.8	42.3
30%_EQ2_050	42.4	-0.7	-24.3	0.5	0.5	-23.6	-0.8	41.8
50%_EQ2_080	60.6	-1.2	-33.5	0.7	0.7	-32.1	-1.2	57.7
100%_EQ2_160	102.4	-3.7	-59.7	1.4	1.4	-58.6	-3.9	94.7
50%_EQ2_080	75.6	-2.9	-44.5	0.6	0.6	-43.6	-3.0	72.5
125%_EQ2_200	120.6	-6.2	-77.1	2.3	2.6	-71.4	-6.6	110.2
150%_EQ2_240	134.2	-11.3	-102.9	7.1	8.9	-84.9	-12.5	121.6
200%_EQ2_320	136.3	-24.4	-98.8	13.4	36.3	-68.5	-39.6	93.4
30%_EQ2_050	44.6	-9.0	-46.9	13.0	13.3	-45.6	-9.9	42.0
30%_EQ2_050	41.5	-8.9	-45.5	13.0	13.3	-42.9	-9.5	37.9
30%_EQ2_050	40.6	-8.9	-44.9	13.0	13.3	-41.2	-9.3	36.2
60%_EQ2_100	68.7	-19.7	-70.8	22.2	24.8	-62.1	-20.3	62.5

Figure 436 plots the evolution of the ratio between the second level inertial forces (sum of roof and second storey forces) and the first storey inertial forces at the moment of the peak of base shear response.

It is observable how the two forces are very similar (ratio  $\approx 1$ ) for all the test with no activated rods on roof. This ratio tends to be higher during the test with the stiffened roof (higher inertial force on second slab).

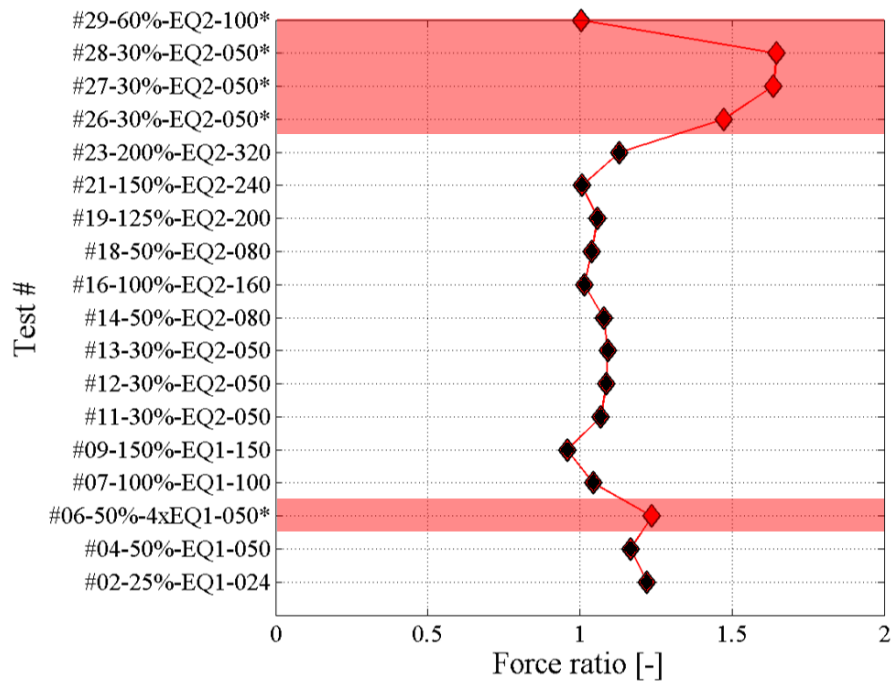


Figure 436. Force Ratio Evolution (test with rigid roof in red).

Figure 437 shows the peak drifts (all three levels) related to each test vs. the peak recorded shake-table acceleration. Only the tests with increasing PGAs are shown (neglecting for simplicity the calibration tests).

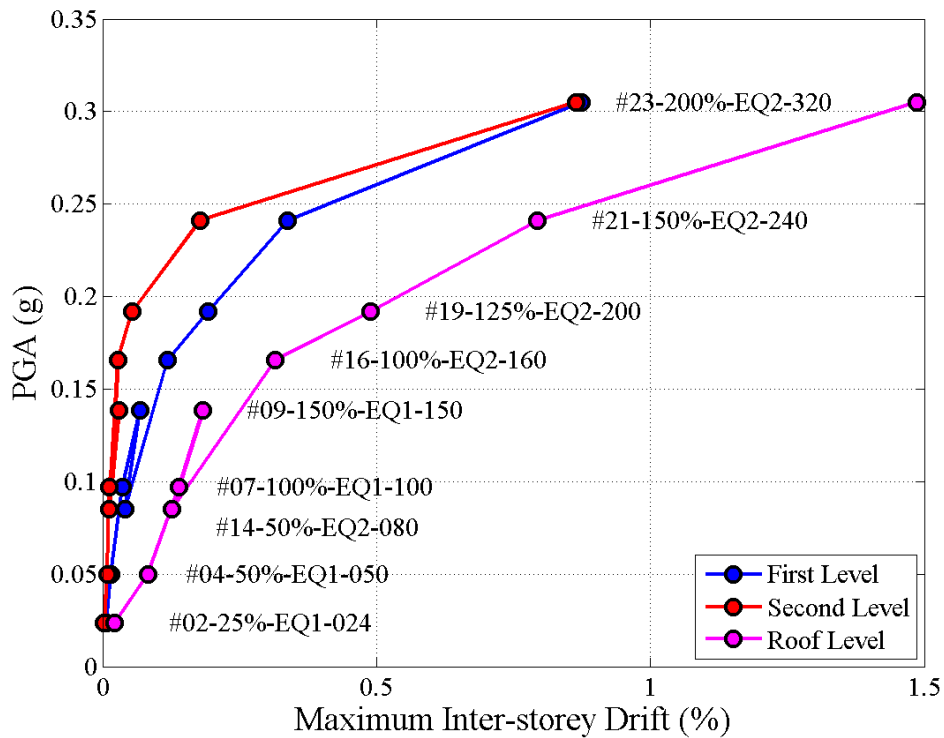


Figure 437. PGA vs Maximum Inter-storey drift.

### 6.4.17 Evolution of dynamic properties

The Output-Only modal identifications techniques, namely Operational Modal Analysis, are based on the dynamic response measurements of a virtual system under natural (ambient or operational) conditions, assuming that the excitations have random nature in time and in the physical space of the structure. Detailed info could be found in Appendix-C.

In the following paragraphs a summary of the results obtained is presented, in terms of singular values, frequencies of vibrations for each mode identified, of mode shapes and damage index for the external veneer and the internal C.S. walls.

Figure 438 and Figure 439 report the results from the Singular Value Decomposition, in particular the blue curves describe the variation of the first singular value in each of the tests while the red lines depict the change of the identified frequencies depending on the cumulating damage, both for the inner walls and the external veneer structural systems.

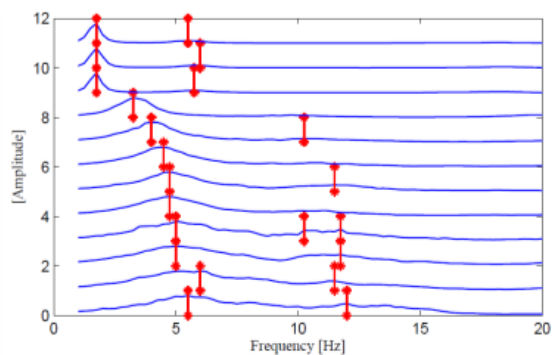


Figure 438. Singular Value Decomposition: inner walls system.

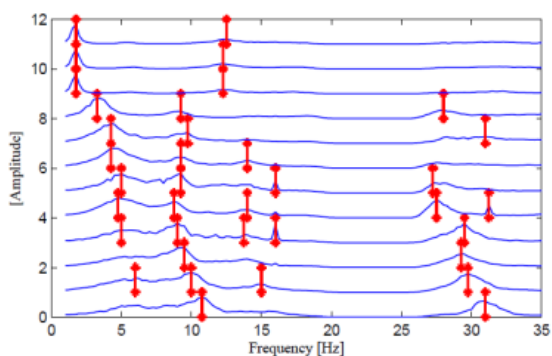


Figure 439. Singular Value Decomposition: external veneer walls system.



The following Table 64 and Table 65 summarise the frequencies of vibration (and periods) of each of the modes identified, applying both the PP and EFDD methods, for the internal C.S. walls and the external veneer walls respectively.

*Table 64. Summary of the frequencies and periods of vibration of the internal calcium silicate system.*

Test #	Test Name	Mode #	EFDD		PP	
			Freq. [Hz]	Period [s]	Freq. [Hz]	Period [s]
1	RNDM_01	1	5.5	0.1818	5.5	0.1818
		2	11.8474	0.0844	12	0.0833
3	RNDM_03	1	6	0.1667	6	0.1667
		2	11.5	0.087	11.5	0.087
5*	RNDM_05	1	5	0.2	5	0.2
		2	11.75	0.0851	11.75	0.0851
8	RNDM_08	1	5	0.2	5	0.2
		2	10.25	0.0976	10.25	0.0976
		3	11.75	0.0851	11.75	0.0851
10	RNDM_10	1	4.75	0.2105	4.75	0.2105
15	RNDM_15	1	4.75	0.2105	4.75	0.2105
		2	11.5	0.087	11.5	0.087
17	RNDM_17	1	4.5042	0.222	4.5	0.2222
20	RNDM_20	1	4	0.25	4	0.25
		2	10.25	0.0976	10.25	0.0976
22	RNDM_22	1	3.25	0.3077	3.25	0.3077
24	RNDM_24	1	1.7187	0.5818	1.75	0.5714
		2	5.75	0.1739	5.75	0.1739
25*	RNDM_25	1	1.7364	0.5759	1.75	0.5714
		2	6	0.1667	6	0.1667
30*	RNDM_30	1	1.7013	0.5878	1.75	0.5714
		2	5.5	0.1818	5.5	0.1818

The variation of the first fundamental period of variation at the different stage of the shaking table testing is depicted in Figure 440, showing a similar trend for both structural system, with values of  $T_1$  increasing as the damage increases, particularly after the test #20.



Table 65. Summary of the frequencies and periods of vibration of the external veneer system.

Test #	Test Name	Mode #	EFDD		PP	
			Freq. [Hz]	Period [s]	Freq. [Hz]	Period [s]
1	RNDM_01	2	10.75	0.093	10.75	0.093
		4	31	0.0323	31	0.0323
3	RNDM_03	1	6	0.1667	6	0.1667
		2	10	0.1	10	0.1
		3	15	0.0667	15	0.0667
		4	29.75	0.0336	29.75	0.0336
5*	RNDM_05	2	9.5	0.1053	9.5	0.1053
		4	29.3729	0.034	29.25	0.0342
8	RNDM_08	1	5	0.2	5	0.2
		2	9	0.1111	9	0.1111
		3	13.75	0.0727	13.75	0.0727
		4	16.0032	0.0625	16	0.0625
		5	29.4054	0.034	29.5	0.0339
10	RNDM_10	1	4.75	0.2105	4.75	0.2105
		2	8.75	0.1143	8.75	0.1143
		3	14	0.0714	14	0.0714
		4	27.7094	0.0361	27.5	0.0364
		5	31.2569	0.032	31.25	0.032
15	RNDM_15	1	5	0.2	5	0.2
		2	9.25	0.1081	9.25	0.1081
		3	16.0156	0.0624	16	0.0625
		4	27.25	0.0367	27.25	0.0367
17	RNDM_17	1	4.25	0.2353	4.25	0.2353
		2	9.25	0.1081	9.25	0.1081
		3	14	0.0714	14	0.0714
20	RNDM_20	1	4.25	0.2353	4.25	0.2353
		2	9.75	0.1026	9.75	0.1026
		3	31	0.0323	31	0.0323
22	RNDM_22	1	3.25	0.3077	3.25	0.3077
		2	9.25	0.1081	9.25	0.1081
		3	28	0.0357	28	0.0357
24	RNDM_24	1	1.7196	0.5815	1.75	0.5714
		2	12.25	0.0816	12.25	0.0816
25*	RNDM_25	1	1.729	0.5784	1.75	0.5714
		2	12.25	0.0816	12.25	0.0816
30*	RNDM_30	1	1.6545	0.6044	1.75	0.5714
		2	12.5	0.08	12.5	0.08

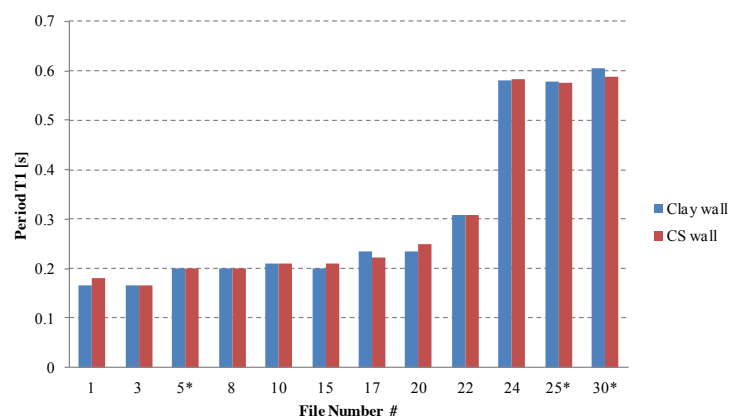


Figure 440. Variation of the fundamental period of vibration  $T_1$ .

A similar description of the effect of cumulative damage on the dynamic properties of the building is given by the index  $id_x$ , obtained as the ratio of the first period of vibration of the damaged structure with respect to that of the undamaged configuration, being equal to 1 when the structure is undamaged. In Figure 441 the variation of the  $id_x$  index for the inner calcium silicate walls is presented.

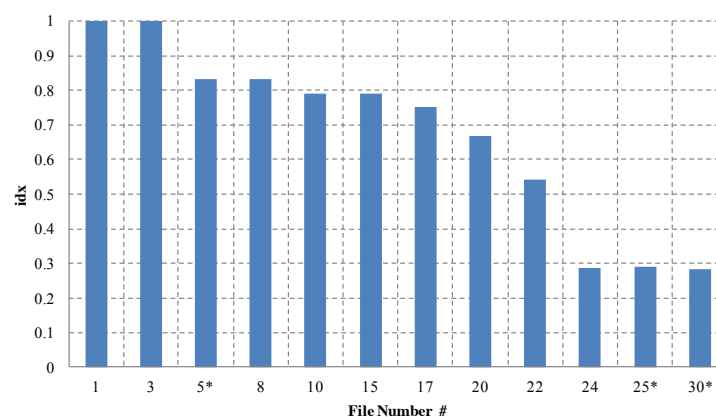


Figure 441. Variation of the damage index  $id_x$  for the internal calcium silicate walls.

The variation of the modal shape of the first mode of vibration is described making reference to the low intensity random vibration tests performed in the following stages of the testing sequence:

- test #1: when the building specimen was in an undamaged condition;
- test #3: after the first test performed with the record EQ1 as input at a PGA of 0.24  $m/s^2$ ;
- test #10: after the sequence of test with the record EQ1 as input;
- test #24: after the testing stages with EQ2 as input, prior to the activation of tie rods.

In Figure 442 the scheme of the geometrical undeformed configuration of the building is presented.

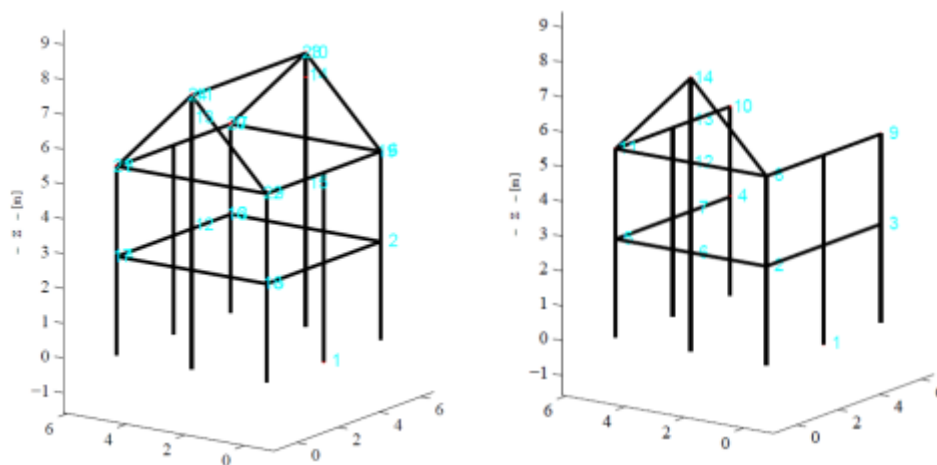


Figure 442. Undeformed configuration: inner walls (left) and external veneer systems (right)

The first mode of vibration of the undamaged building has been identified at a fundamental frequency of 5.5 Hz, for the inner walls system only. The first period of the external veneer walls is assumed to be presumably close to same value. Figure 443 depicts the typical deformed shape of a first mode type of behaviour, with the longitudinal walls responding in-plane and the gable walls overturning out-of-plane, parallel to the direction of the shaking table motion.

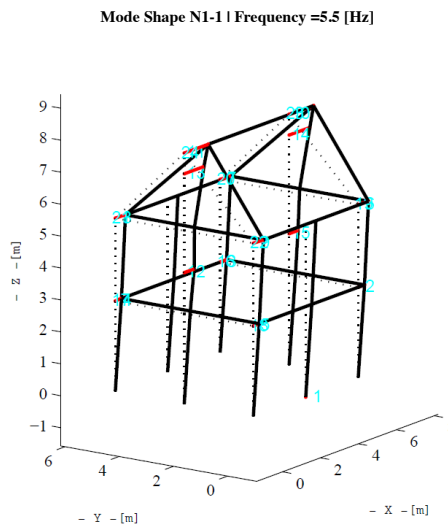


Figure 443. Test #1. Deformed shape of the first mode of vibration: inner walls.

After the first test with EQ1 as input motion, at a PGA of 0.24  $m/s^2$ , the first modes of both the inner and outer walls were identified at a frequency of 6Hz.

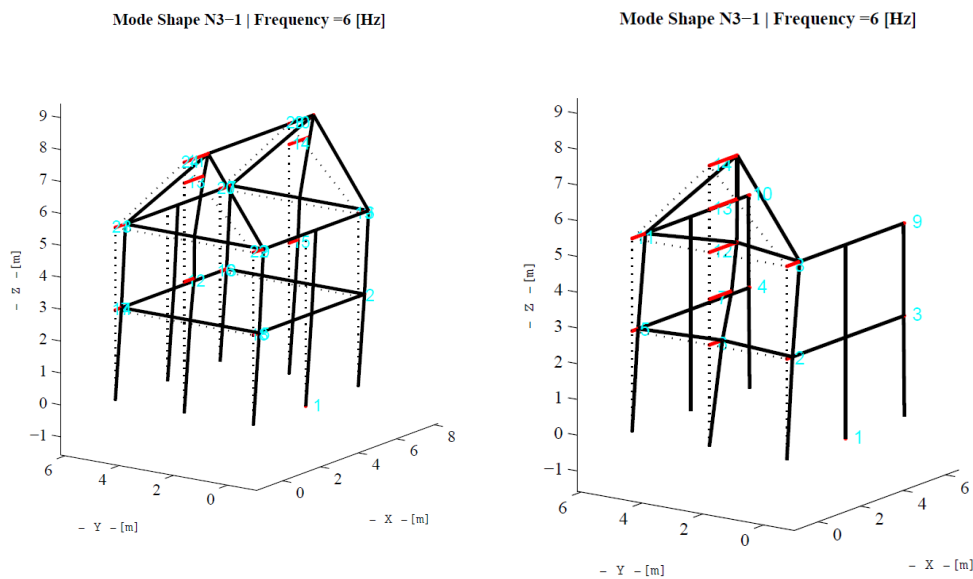


Figure 444. Test #3. Deformed shape of the first mode of vibration: inner walls (left) and external veneer systems (right).

While the deformed shape of the inner walls remains essentially unchanged with respect to that identified during Test #1, the first mode of vibration of the external veneer system shows clearly an out-of-plane response of the North façade with displacement components at mid-span of the wall almost double than the corner ones.

Figure 445 shows the first modes of vibration detected during Test #10: because of the damage level, though limited, the fundamental frequency decreases as expected, albeit the modal shapes remain essentially unvaried.

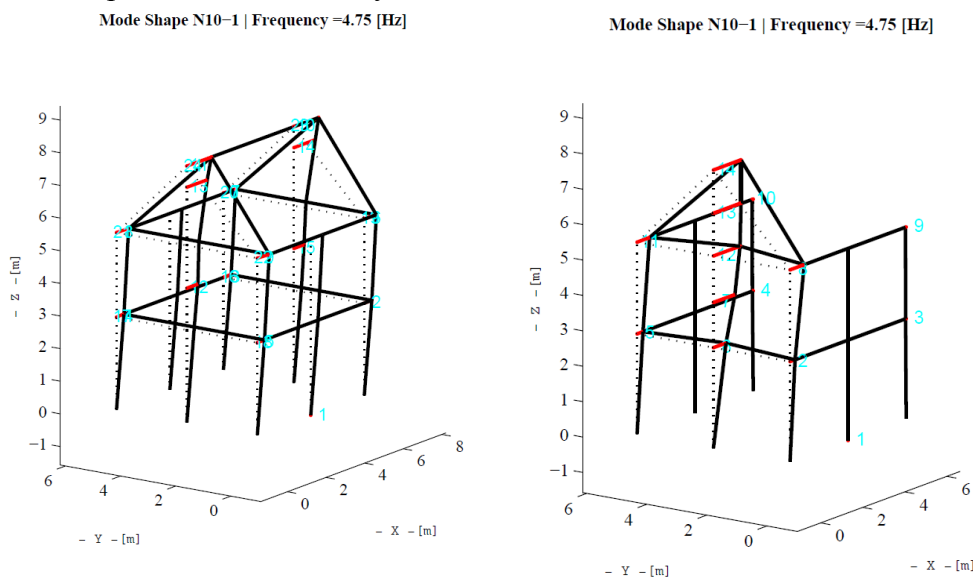
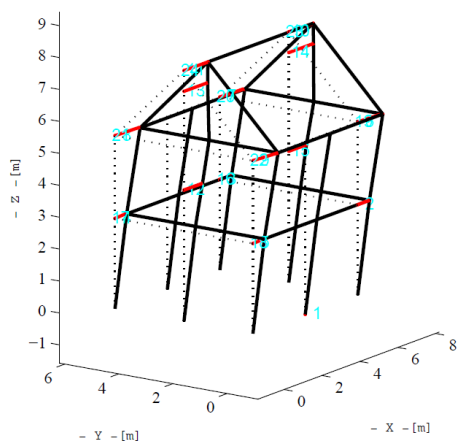


Figure 445. Test #10. Deformed shape of the first mode of vibration: inner walls (left) and external veneer systems (right).

Mode Shape N24-1 | Frequency =1.7187 [Hz]



Mode Shape N24-1 | Frequency =1.7196 [Hz]

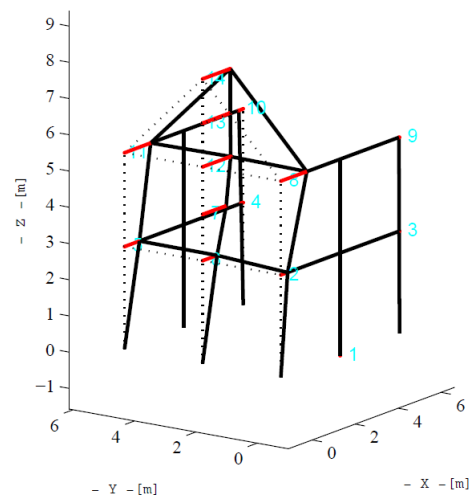


Figure 446. Test #24. Deformed shape of the first mode of vibration: inner walls (left) and external veneer systems (right).

The effect of the cumulated damage on the variation of the dynamic properties is evident in the results of the identification performed during test #24. As already presented in Table 65 and Table 64, the periods associated to each mode of vibration increased significantly (*i.e.* the values of the first period are approximately three times greater than those of the undamaged building prior testing). Regarding the modal shapes associated to the first fundamental frequency, although the mode of vibration is similar to the previous one, the modal displacement components at the second floor level are greater both in the case of the calcium silicate wall system and of the external veneer walls.

## References

---

CEN/TC 125 [1998] "*EN 1052-1:1998 Methods of test for masonry - Determination of compressive strength*"

CEN/TC 125 [1999] "*EN 1015-11:1999 Methods of test for mortar for masonry - Determination of flexural and compressive strength of hardened mortar*"

Brincker, R., Zhang, L., and Andersen, P. [2000] "Modal Identification from Ambient Responses using Frequency Domain Decomposition", Proc.18th International Seminar on Modal Analysis, San Antonio, Texas

Ewins, D. J. [2000] "Modal testing: theory, practice and application", Research Study Press Ltd, England.

Brincker, R., Ventura, C., and Andersen, P. [2001] "Damping Estimation by Frequency Domain Decomposition", Proc. of IMAC XIX, the 19th International Modal Analysis Conference, Kissimmee, USA

CEN/TC 125 [2002], "*EN 1052-3:2002 Methods of test for masonry - Part 3: Determination of Initial shear strength*"

CEN/TC 125 [2005] "*EN 1052-5:2005 Methods of test for masonry - Determination of bond strength by the bond wrench method*"

CEN/TC 125 [2007] "*EN 1052-3:2002/A1:2007 Amendment A1 to European Standard EN 1052-3:2002*"

Crowley, H., Bommer, J., Pinho, R. [2015] "Selection of records for nonlinear dynamic analysis of Groningen buildings" Report, Appendix B-1.

Graziotti F., Tomassetti U., Penna A., Magenes G. (2016), *Out-of-Plane Shaking Table Tests on URM Single Leaf and Cavity walls*, Engineering Structures, (accepted).

Tomassetti U., Graziotti F., Penna A., Magenes G. (2016), *Out-of-plane shaking table test on URM cavity walls*, Proc. 16th IBMAC conference, Padua, Italy.

Graziotti F., Rossi A., Mandirola M., Penna A., Magenes G. (2016) *Experimental Characterization of Calcium-Silicate Brick Masonry for Seismic Assessment*, Proc. 16th IBMAC conference, Padua, Italy.

Graziotti F., Tomassetti U., Rossi A., Kallioras S., Mandirola M., Penna A., Magenes G., (2017) *Full scale shaking table test on a URM cavity wall building model*, Proceedings 16<sup>th</sup> World Conference on Earthquake, Santiago, Chile (submitted).

# Appendix A

## Instructions for the released experimental data

## Guidelines: EC-COMP-2 recorded experimental data

### Traditional acquisition system

The raw experimental data recorded during the test by the traditional acquisition system have been post-processed (filtered, resampled and synchronised) in order to allow any additional study and analyses on the specimens.

The post-processed data are organised in a single 3D matrix (computed with MATLAB) named as “EUCE\_COMP\_2\_traditional.mat”:

**EUCE\_COMP\_2\_traditional = {timestep, instruments, cycles} = {3305, 34, 9}**

In particular, all the instruments are reported in the 34 columns of the matrix according to the following orders:

*Table 1. EUCE\_COMP\_2: Matrix Columns.*

ID Matrix column	1	From 2 to 28
Data recorded	Time	LVDT: from 0 to 26 (see Figure 1 for reference)
Units	sec	mm
*Instrument 21 and 20 are spring-loaded potentiometers		

ID Matrix column	29	30	31	32	33	34
Data recorded	Tempo sonic	F6	D2	F2	D3	F3
Units	mm	kN	mm	kN	mm	kN

During the first cycle (D1\_1, see Table 3 for reference), LVDT number 4 has been out of order.

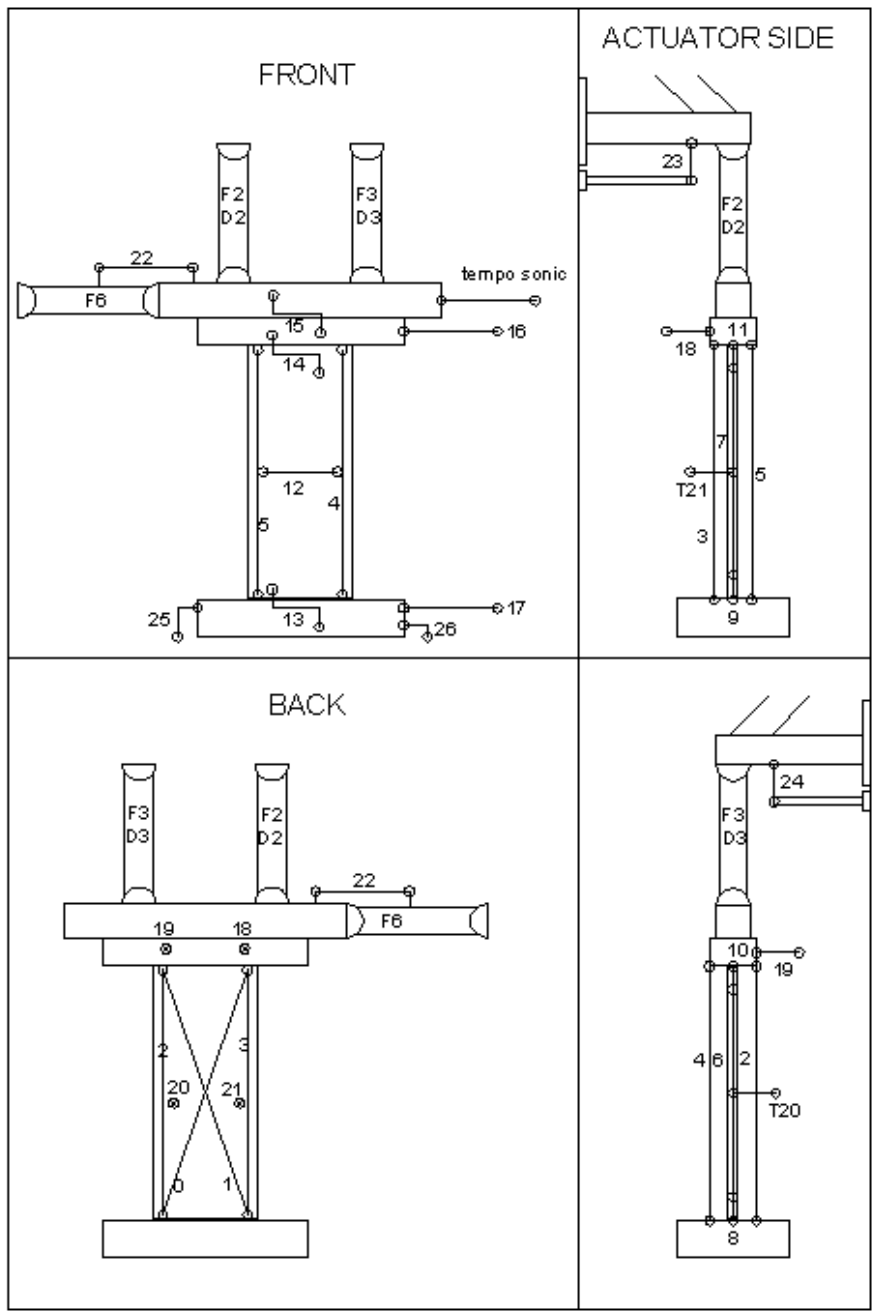


Figure 1. Location of the Instruments

The initial distance between the measure bases of the transducers, are reported in the following table:

*Table 2. EUCE\_COMP\_2: initial distance between the measures bases.*

LVDT	Distance [mm]
0	2825
1	2825
2	2645
3	2640
4	2640
5	2640
6	2510
7	2515
8	205
9	205
10	205
11	205
12	960

The third dimension of the Matrix represents the cycles according to the following order:

*Table 3. EUCE\_COMP\_2: Third dimension of the matrix.*

ID matrix	Cycle
1	D1_1
2	D1_2
3	D1_3
4	1D
5	2D
6	3D
7	4D
8	5D
9	6D

The duration of each cycle (significant row number of the matrix) is summarised in the following table:

*Table 4. EUCE\_COMP\_2: Duration of the cycles.*

Cycle	Row number
D1_1	747
D1_2	1357
D1_3	2016
1D	2673
2D	2649
3D	2653
4D	3182
5D	3305
6D	234

## Guidelines: EC-COMP-1 recorded experimental data

### Traditional acquisition system

The raw experimental data recorded during the test by the traditional acquisition system have been post-processed (filtered, resampled, cut and synchronised) in order to allow any additional study and analyses on the specimens.

The post-processed data are organised in a single 3D matrix (computed with MATLAB) named as “EUCE\_COMP\_1\_traditional.mat”:

**EUCE\_COMP\_1\_traditional = {timestep, instruments, cycles} = {3901, 34, 18}**

In particular, all the instruments are reported in the 34 columns of the matrix according to the following orders:

*Table 5. EUCE\_COMP\_1: Matrix Columns.*

ID Matrix column	1	From 2 to 28
Data recorded	Time	LVDT: from 0 to 26* (see Figure 1 for reference)
Units	sec	mm
*Instrument 21 and 20 are spring-loaded potentiometers		

ID Matrix column	29	30	31	32	33	34
Data recorded	Tempo sonic	F6	D2	F2	D3	F3
Units	mm	kN	mm	kN	mm	kN

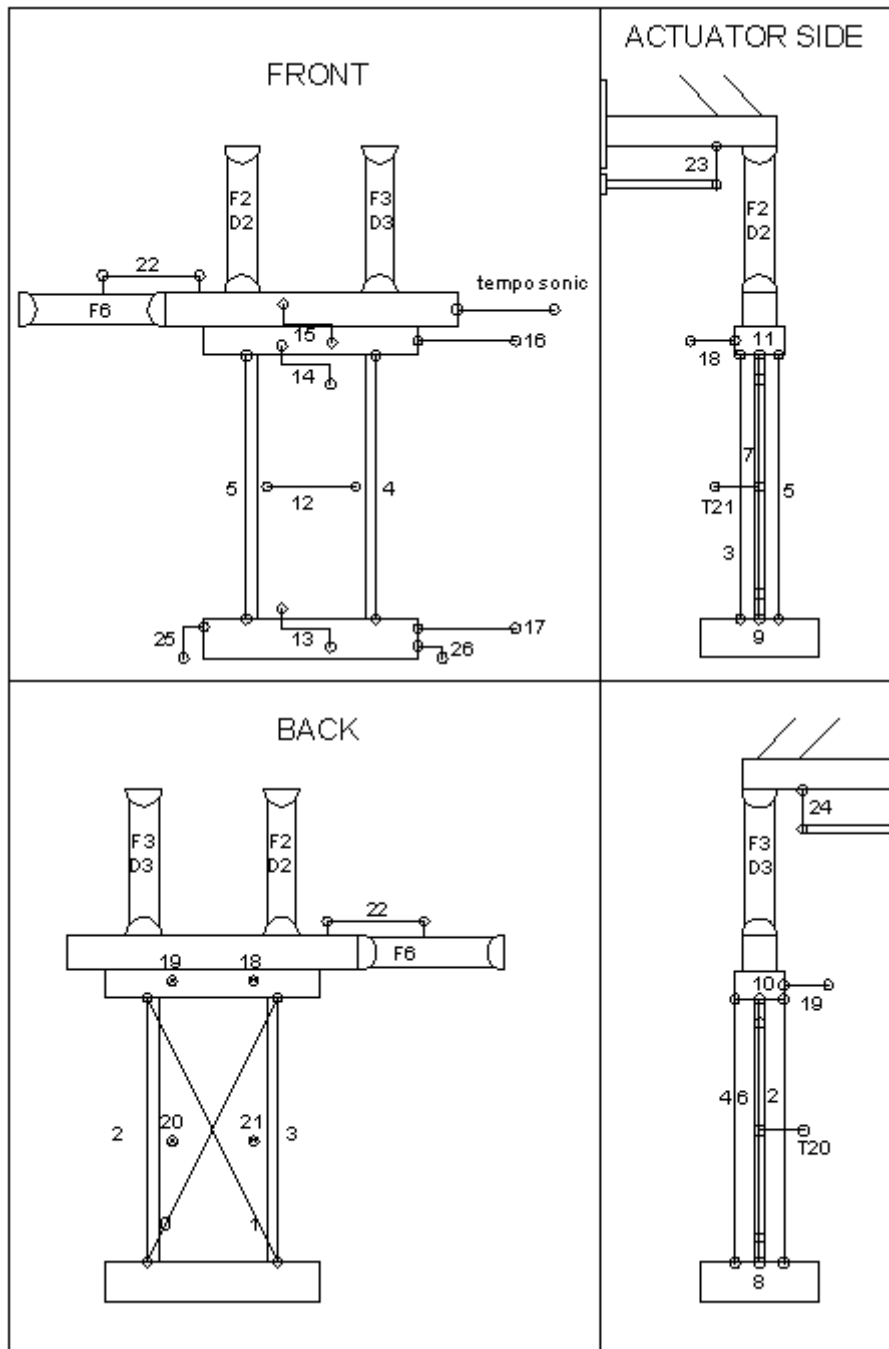


Figure 2. Location of the Instruments

The initial distance between the measure bases of the transducers, are reported in the following table:

*Table 6. EUCE\_COMP\_1: initial distance between the measures bases.*

<b>LVDT</b>	<b>Distance [mm]</b>
0	2965
1	2980
2	2720
3	2720
4	2720
5	2720
6	2510
7	2520
8	125
9	130
10	135
11	125
12	970

The third dimension of the Matrix represents the cycles according to the following order:

*Table 7. EUCE\_COMP\_1: Third dimension of the matrix.*

<b>ID matrix</b>	<b>Cycle</b>
1	D1_1
2	D1_2
3	D1_3
4	1D
5	2D
6	3D
7	4D
8	5D
9	6D
10	7D
11	8D
12	9D
13	10D
14	12D
15	13D
16	14D
17	15D
18	17D

The duration of each cycle (significant row number of the matrix) is summarised in the following table:

*Table 8. EUCE\_COMP\_1: Duration of the cycles.*

<b>Cycle</b>	<b>Row number</b>
D1 1	1262
D1 2	1363
D1 3	2034
1D	2681
2D	2641
3D	2665
4D	3197
5D	3331
6D	3341
7D	3321
8D	2657
9D	2657
10D	2653
12D	2657
13D	2653
14D	3309
15D	3901
17D	2561

## Guidelines: EC-COMP-3 recorded experimental data

### Traditional acquisition system

The raw experimental data recorded during the test by the traditional acquisition system have been post-processed (filtered, resampled, cut and synchronised) in order to allow any additional study and analyses on the specimen.

The post-processed data are organised in a single 3D matrix (computed with MATLAB) named as “EUCE\_COMP\_3\_traditional.mat”:

$$\mathbf{EUCE\_COMP\_3\_traditional} = \{\text{timestep, instruments, cycles}\} = \{4131, 38, 14\}$$

In particular, all the instruments are reported in the 38 columns of the matrix according to the following orders:

*Table 9. EUCE\_COMP\_3: Matrix Columns.*

ID Matrix column	1	From 2 to 32
Data recorded	Time	LVDT: from 1 to 31* (see Figure 1 for reference)
Units	sec	mm
*Instruments 13, 14, 22 and 23 are spring-loaded potentiometers		

ID Matrix column	33	34	35	36	37	38
Data recorded	Tempo sonic	F6	D2	F2	D3	F3
Units	mm	kN	mm	kN	mm	kN

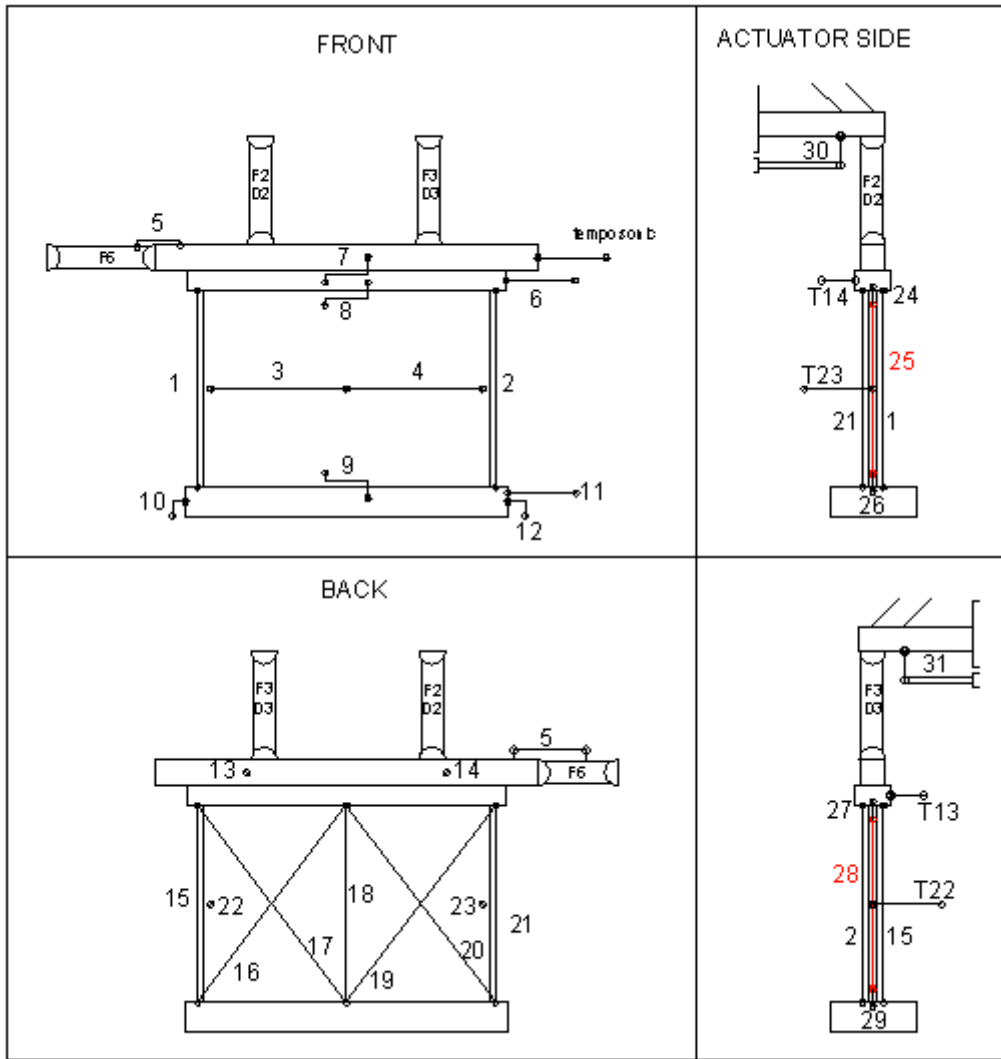


Figure 3. Location of the Instruments

The initial distance between the measure bases of the transducers, are reported in the following table:

*Table 10. EUCE\_COMP\_3: initial distance between the measures bases.*

<b>LVDT</b>	<b>Distance [mm]</b>
1	2710
2	2710
3	1950
4	1950
15	2710
16	3400
17	3400
18	2710
19	3400
20	3400
21	2710
24	230
25	2230
26	240
27	250
28	2220
29	240

The third dimension of the Matrix represents the cycles according to the following order:

*Table 11. EUCE\_COMP\_3: Third dimension of the matrix.*

<b>ID matrix</b>	<b>Cycle</b>
1	F1_1
2	D1_2
3	D1_3
4	D1_4
5	D1_5
6	D1_6
7	D1_7
8	1D
9	2D
10	3D
11	4D
12	5D
13	6D
14	7D

The duration of each cycle (significant row number of the matrix) is summarised in the following table:

*Table 12. EUCE\_COMP\_3: Duration of the cycles.*

<b>Cycle</b>	<b>Row number</b>
F1_1	1082
D1_2	3596
D1_3	717
D1_4	1598
D1_5	1498
D1_6	2247
D1_7	2397
1D	3308
2D	3293
3D	3301
4D	3951
5D	4121
6D	4131
7D	3103

**Example:** in order to obtain the instrument (e.g. 8) record of the cycle (e.g. D1\_3) ->

plot (EUCE\_COMP\_3\_traditional(1:717,9,3))



# Out-of-plane Shake Table Test on Single Leaf Wall and Cavity Walls Results (Eucentre)

## 1. Scope and application field

The aim of this document is to present the experimental results observed during the shake table test on URM single leaf and cavity walls in order to investigate their out-of plane dynamic behaviour. Table 1,2,3 and 4 present the dynamic testing sequence correspondingly to EC\_COMP\_4, EC\_COMP\_5, EC\_COMP\_6 and EC\_COMP\_7 specimens.

Table 1. EC\_COMP\_4 Testing Sequence.

Specimen	Phase #	Test #	Dynamic Input	Input Scaling	PGA [g]
<b>Imposed Overburden Pressure: 0.3 MPa</b>					
EC_COMP_4	1	1.1	Gr 1	20%	+0.04
EC_COMP_4	1	1.2	Gr 1	40%	+0.09
EC_COMP_4	1	1.3	Gr 1	80%	+0.16
EC_COMP_4	1	1.4	Gr 1	100%	+0.20
EC_COMP_4	1	1.5	Gr 1	160%	+0.32
EC_COMP_4	1	1.6	Gr 1	200%	+0.42
EC_COMP_4	1	1.7	Gr 1	250%	+0.53
EC_COMP_4	1	1.8	Gr 1	350%	+0.74
EC_COMP_4	1	1.9	Gr 1	450%	+0.96
EC_COMP_4	2	2.1	RWA 2Hz	-	-1.11
EC_COMP_4	2	2.2	RWA 2Hz	-	-1.63
EC_COMP_4	2	2.3	RWA 2Hz	-	-1.04
EC_COMP_4	2	2.4	RWA 2Hz	-	-1.88
<b>Imposed Overburden Pressure: 0.1 MPa</b>					
EC_COMP_4	3	3.1	Gr 1	40%	+0.08
EC_COMP_4	3	3.2	Gr 1	80%	+0.17
EC_COMP_4	3	3.3	Gr 1	100%	+0.21
EC_COMP_4	3	3.4	Gr 1	160%	+0.34
EC_COMP_4	3	3.5	Gr 1	200%	+0.41
EC_COMP_4	3	3.6	Gr 1	250%	+0.51
EC_COMP_4	3	3.7	Gr 1	300%	+0.60
EC_COMP_4	3	3.8	Gr 1	350%	+0.73
EC_COMP_4	4	4.1	RWA 2Hz	-	-0.25
EC_COMP_4	4	4.2	RWA 2Hz	-	-0.48
EC_COMP_4	4	4.3	RWA 2Hz	-	-0.72
EC_COMP_4	4	4.4	RWA 2Hz	-	-0.96
EC_COMP_4	5	5.1	Gr 2	100%	+0.44
EC_COMP_4	5	5.2	Gr 2	150%	+0.64
EC_COMP_4	5	5.3	Gr 2	200%	+0.85



Table 2. EC\_COMP\_5 Testing Sequence.

Specimen	Phase #	Test #	Dynamic Input	Input Scaling	PGA [g]
EC_COMP_5	0	0.1	Hammering	-	-
EC_COMP_5	0	0.2	White Noise	-	0.1
EC_COMP_5	1	1.1	Gr_1	+20%	+0.04
EC_COMP_5	1	1.2	Gr_1	+40%	+0.09
EC_COMP_5	1	1.3	Gr_1	-40%	-0.09
EC_COMP_5	1	1.4	Gr_1	+60%	+0.12
EC_COMP_5	1	1.5	Gr_1	+80%	+0.17
EC_COMP_5	1	1.6	Gr_1	+100%	+0.21
EC_COMP_5	1	1.7	Gr_1	-60%	-0.13
EC_COMP_5	1	1.8	Gr_1	-80%	-0.17
EC_COMP_5	1	1.9	Gr_1	-100%	-0.23
EC_COMP_5	2	2.1	RWA	-	-0.22
EC_COMP_5	2	2.2	RWA	-	-0.30
EC_COMP_5	3	3.1	Gr_2	+70%	+0.31
EC_COMP_5	3	3.2	Gr_2	+100%	+0.49
EC_COMP_5	3	3.3	Gr_2	+150%	+0.66
EC_COMP_5	4	4.1	Gr_1	+300%	+0.60
EC_COMP_5	5	5.1	RWA	-	-0.30
EC_COMP_5	5	5.2	RWA	-	-0.49
EC_COMP_5	6	6.1	Gr_2	+150%	+0.65

Table 3. EC\_COMP\_6 Testing Sequence.

Specimen	Phase #	Test #	Dynamic Input	Input Scaling	PGA [g]
EC_COMP_6	0	0.1	Hammering	-	-
EC_COMP_6	0	0.2	White Noise	-	0.1
EC_COMP_6	1	1.1	Gr_1	+40%	-0.09
EC_COMP_6	1	1.2	Gr_1	-40%	+0.09
EC_COMP_6	1	1.3	Gr_1	+60%	-0.13
EC_COMP_6	1	1.4	Gr_1	+80%	-0.18
EC_COMP_6	1	1.5	Gr_1	+100%	-0.23
EC_COMP_6	1	1.6	Gr_1	-60%	+0.12
EC_COMP_6	1	1.7	Gr_1	-80%	+0.17
EC_COMP_6	1	1.8	Gr_1	-100%	+0.21
EC_COMP_6	2	2.1	RWA	-	-0.30
EC_COMP_6	2	2.2	RWA	-	+0.29
EC_COMP_6	3	3.1	Gr_2	+70%	-0.32
EC_COMP_6	3	3.2	Gr_2	+100%	-0.47
EC_COMP_6	3	3.3	Gr_2	+150%	-0.66
EC_COMP_6	3	3.4	Gr_2	+170%	-0.77
EC_COMP_6	4	4.1	RWA	-	-0.49
EC_COMP_6	4	4.2	RWA	-	+0.53
EC_COMP_6	5	5.1	Gr_2	+210%	-0.97
EC_COMP_6	5	5.2	Gr_2	+250%	-1.17



Table 4. EC\_COMP\_7 Testing Sequence.

Specimen	Phase #	Test #	Dynamic Input	Input Scaling	Expected PGA [g]
EC_COMP_7	0	0.1	Hammering	-	-
EC_COMP_7	0	0.2	White Noise	-	0.1
EC_COMP_7	1	1.1	Gr_1	+20%	-0.04
EC_COMP_7	1	1.2	Gr_1	+40%	-0.09
EC_COMP_7	1	1.4	Gr_1	+60%	-0.13
EC_COMP_7	1	1.5	Gr_1	+80%	-0.18
EC_COMP_7	1	1.6	Gr_1	+100%	-0.23
EC_COMP_7	2	2.1	RWA	-	-0.31
EC_COMP_7	2	2.2	RWA	-	+0.34
EC_COMP_7	3	3.1	Gr_2	+70%	-0.32
EC_COMP_7	3	3.2	Gr_2	+100%	-0.45
EC_COMP_7	3	3.3	Gr_2	+150%	-0.66
EC_COMP_7	3	3.4	Gr_2	+170%	-0.75
EC_COMP_7	4	4.1	RWA	-	+0.30
EC_COMP_7	4	4.2	RWA	-	-0.31
EC_COMP_7	4	4.3	Hammering	-	-
EC_COMP_7	4	4.4	White Noise	-	-
EC_COMP_7	4	4.5	RWA	-	-0.50
EC_COMP_7	4	4.6	RWA	-	+0.53
EC_COMP_7	5	5.1	Gr_2	+100%	-0.46
EC_COMP_7	5	5.2	Gr_2	+150%	-0.64
EC_COMP_7	5	5.3	Gr_2	-100%	+0.51
EC_COMP_7	5	5.4	Gr_2	-150%	+0.72

Table 5 provides information about the organisation of the Matlab file (Data\_OOP\_Test.mat) in attached with the present document; all the data have been collected in a Matlab structure. Table 5 indicates the Matlab structure coordinates corresponding to each testing session. The N variable represents the number of test performed within each testing session with the same dynamic input. The data, hence, have been collected according to the acceleration input typology rather than chronological sequence. The data have been simply converted from millivolt to millimetres (in the potentiometer case), re-centred in zero and synchronised.

Table 5. Organisation of Experimental Data

Specimen	Gr_1 Input	RWA Input	Gr_2 Input
<b>EUC_COMP_4 0.3 MPa</b>	Struct (1,1) N=9;	Struct (1,2) N=4;	-
<b>EUC_COMP_4 0.1 MPa</b>	Struct (2,1) N=8;	Struct (2,2) N=4;	Struct (2,3) N=4;
<b>EUC_COMP_5</b>	Struct (3,1) N=10;	Struct (3,2) N=4;	Struct (3,3) N=4;
<b>EUC_COMP_6</b>	Struct (4,1) N=8;	Struct (4,2) N=4;	Struct (4,3) N=6;
<b>EUC_COMP_7</b>	Struct (5,1) N=5;	Struct (5,2) N=6;	Struct (5,3) N=8;

Table 6 lists the information recorded during each test and herein presented. The data related to a particular test are presented in matrix form, where each column contains information recorded by a particular instrument. Table 6 describes the instrument typology and the location corresponding to each data column. All the acceleration histories have been filtered by means of a quadratic low pass filter set to a frequency equal to 50 Hz.

*Table 6. Organisation of the Experimental Data Array*

Instrument	Column	Description
-	1	'Time [s]'
Accelerometer	2	'Shake Table Acceleration [g]'
Accelerometer	3	'Foundation Acceleration [g]'
Accelerometer	4	'Frame A Acceleration [g]'
Accelerometer	5	'Frame B Acceleration [g]'
Accelerometer	6	'Top Beam Acceleration [g]';
Accelerometer	7	'Mid-Height CS Wall Acceleration Side A [g]'
Accelerometer	8	'Mid-Height CS Wall Acceleration Side B [g]'
Accelerometer	9	'Mid-Height Clay Wall Acceleration Side A [g]'
Accelerometer	10	'Mid-Height Clay Wall Acceleration Side B [g]'
Potentiometer	11	'Shake Table Displacement 1 [g]'
Table-Output	12	'Shake Table Displacement 2 [g]'
Wire Potentiometer	13	'1/4 CS Wall Height Displacement [mm]'
Wire Potentiometer	14	'1/2 CS Wall Height Displacement [mm]'
Wire Potentiometer	15	'3/4 CS Wall Height Displacement [mm]'
Wire Potentiometer	16	'1/4 Clay Wall Height Displacement [mm]'
Wire Potentiometer	17	'1/2 Clay Wall Height Displacement [mm]'
Wire Potentiometer	18	'3/4 Clay Wall Height Displacement [mm]'
Wire Potentiometer	19	'4/4 Clay Wall Height Displacement [mm]'
Potentiometer	20	'Spring 1 Side A [mm]'
Potentiometer	21	'Spring 2 Side A [mm]'
Potentiometer	22	'Spring 1 Side B [mm]'
Potentiometer	23	'Spring 2 Side B [mm]'
Potentiometer	24	'Rocking CS Bottom [mm]'
Potentiometer	25	'Rocking CS Top [mm]'
Potentiometer	26	'Rocking Clay Bottom [mm]'

During some tests few instruments showed rather high noise; some of them have been removed during the testing session in order to avoid their damage in tests where a significant out-of-plane displacement was expected. Table 7 lists some of these particular cases.

*Table 7. Organisation of the Experimental Data Array*

Specimen	Column	Description
EUC_COMP_4-0.3 MPa	2	Offline
EUC_COMP_4-0.3 MPa	11	Instrument removed in testing phases 2
EUC_COMP_4-0.1 MPa	2	Offline
EUC_COMP_4-0.1 MPa	11	Instrument removed in testing phases 2
EUC_COMP_5	12	Offline
EUC_COMP_5	14	Instrument removed (Gr_2 phase Test N. 4)
EUC_COMP_5	17	Instrument removed (Gr_2 phase Test N. 4)
EUC_COMP_5	25	Rather high noise
EUC_COMP_7	14	Instrument removed (Gr_2 phase Test N. 7,8)
EUC_COMP_7	17	Instrument removed (Gr_2 phase Test N. 6,8)

Figure 1 shows the experimental set-up for all the tested specimens. It clarifies also the location of the instruments listed in table 6 and the data reference system, which is identical for all the tests presented in order to properly compare them.





Table 8 specifies the experimental data organization within a specific structure or testing sequence. The test number (Test #) is coherent with the testing sequence procedure described in the preliminary report (Table 1,2,3 and 4) , while the N variable is the test cell number within the specific Matlab structure (Struct (i,j)). The data, hence, have been collected according to the acceleration input typology rather than chronological sequence. The matlab cell variable containing such experimental data is called “data\_Rf\_filt”. The matlab cell variable “max\_data\_Rf\_filt” contains instead, maximum absolute responses related to each column for each test.

Table 8. Data Cell Number of each Experimental Test

EC COMP 4 0.3 MPa				EC COMP 4 0.1 MPa				EC COMP 5				EC COMP 6				EC COMP 7			
Test #	Input	PGA (g)	N	Test #	Input	PGA (g)	N	Test #	Input	PGA (g)	N	Test #	Input	PGA (g)	N	Test #	Input	PGA (g)	N
1.1	Gr_1	+0.04	1	3.1	Gr_1	+0.08	1	1.1	Gr_1	+0.04	1	1.2	Gr_1	-0.09	1	1.1	Gr_1	-0.04	1
1.2	Gr_1	+0.09	2	3.2	Gr_1	+0.17	2	1.2	Gr_1	+0.09	2	1.6	Gr_1	-0.13	2	1.2	Gr_1	-0.09	2
1.3	Gr_1	+0.16	3	3.3	Gr_1	+0.21	3	1.4	Gr_1	+0.12	3	1.7	Gr_1	-0.18	3	1.3	Gr_1	-0.13	3
1.4	Gr_1	+0.20	4	3.4	Gr_1	+0.34	4	1.5	Gr_1	+0.17	4	1.8	Gr_1	-0.23	4	1.4	Gr_1	-0.18	4
1.5	Gr_1	+0.32	5	3.5	Gr_1	+0.41	5	1.6	Gr_1	+0.21	5	1.1	Gr_1	+0.09	5	1.5	Gr_1	-0.23	5
1.6	Gr_1	+0.42	6	3.6	Gr_1	+0.51	6	1.3	Gr_1	-0.09	6	1.3	Gr_1	+0.12	6	2.1	RWA	-0.31	1
1.7	Gr_1	+0.53	7	3.7	Gr_1	+0.60	7	1.7	Gr_1	-0.13	7	1.4	Gr_1	+0.17	7	2.2	RWA	+0.34	2
1.8	Gr_1	+0.74	8	3.8	Gr_1	+0.73	8	1.8	Gr_1	-0.17	8	1.5	Gr_1	+0.21	8	4.1	RWA	+0.30	3
1.9	Gr_1	+0.96	9	4.1	RWA	-0.25	1	1.9	Gr_1	-0.23	9	2.1	RWA	-0.30	1	4.2	RWA	-0.31	4
2.1	RWA	-1.11	1	4.2	RWA	-0.48	2	4.1	Gr_1	+0.60	10	2.2	RWA	+0.29	2	4.5	RWA	-0.50	5
2.2	RWA	-1.63	2	4.3	RWA	-0.72	3	2.1	RWA	-0.22	1	4.1	RWA	-0.49	3	4.6	RWA	+0.53	6
2.3	RWA	-1.04	3	4.4	RWA	-0.96	4	2.2	RWA	-0.30	2	4.2	RWA	+0.53	4	3.1	Gr_2	-0.32	1
2.4	RWA	-1.88	4	5.1	Gr_2	+0.44	1	5.1	RWA	-0.30	3	3.1	Gr_2	-0.32	1	3.2	Gr_2	-0.45	2
				5.2	Gr_2	+0.64	2	5.2	RWA	-0.49	4	3.2	Gr_2	-0.47	2	3.3	Gr_2	-0.66	3
				5.3	Gr_2	+0.85	3	3.1	Gr_2	+0.31	1	3.3	Gr_2	-0.66	3	3.4	Gr_2	-0.75	4
								3.2	Gr_2	+0.49	2	3.4	Gr_2	-0.77	4	5.1	Gr_2	-0.46	5
								3.3	Gr_2	+0.66	3	5.1	Gr_2	-0.97	5	5.2	Gr_2	-0.64	6
								6.1	Gr_2	+0.65	4	5.2	Gr_2	-1.17	6	5.3	Gr_2	+0.51	7
																5.4	Gr_2	+0.72	8

The data are also available in txt format; each txt file is basically an array which contains all the information listed in table 6 for the specific test.

The txt files are named in the following way ‘Data\_Test\_SP\_TT\_N’, where SP is the specimen number shown in table 9 and TT is the input typology parameter identified in table 10. The N parameter is the variable high lined in red in table 8, which allow identifying the single test.

Table 9. SP variable

Specimen	SP
EUC_COMP_4 0.3 MPa	3
EUC_COMP_4 0.1 MPa	4
EUC_COMP_5	5
EUC_COMP_6	6
EUC_COMP_7	7

Table 10. TT variable

Specimen	TT
Gr-1_input	1
RWA_input	2
Gr-2_input	3



## Appendix A

A Matlab script able to plot and save in txt format only the specific data required by the user is attached. The tool allows also comparing results of different specimens.

It is possible to plot time history responses and maximum absolute responses such as experimental IDA.

In the former case, the script will ask for input column on the x-axis and then for the desired number of lines on the y-axis (according to the column number displayed); the output file will be characterised by a first column constituted by the chosen column for the x-axis (e.g. time) and n-column (according to the chosen number of lines) corresponding to the first specified specimen. The following columns will be filled with the n-columns related to all the others desired specimen.

Col 1	Col 2...n Spec. 1	Col n+1...n+n Spec. 2	Col 2*n+1...2*n+n Spec j
1 desired x axis	1 to n desired lines (y axis)	1 to n desired lines (y axis)	1 to n desired lines (y axis)

The output txt file in the maximum absolute response case is rather different; it will plot for all the desired specimen a first column selected for the y-axis and all the desired n-columns for the x-axis in the following columns.

Col. 1 Spec. 1	Col 2...n Spec 1	Col n+1 Spec. 2	Col n+2...n+2+n Spec2	.....
1 desired y axis	1 to n desired lines (x axis)	1 desired y axis	1 to n desired lines (y axis)	.....

### Instructions Shake-Table Test

Table 1 provide a summary of the testing procedure performed on the Building specimen.

<i>Date</i>	<i>Test #</i>	<i>Test Input</i>	<i>Test Name</i>	<i>Recorded PGA [g]</i>	<i>Rods</i>
09/08/2015	1	RNDM	RNDM_01	-	
	2	EQ1-Or	25%_EQ1_024	0.023	
	3	RNDM	RNDM_03	-	
	4	EQ1-Or	50%_EQ1_050	0.050	
09/09/2015	5*	RNDM	RNDM_05	-	V
	6*	EQ1	50%_4xEQ1_050	0.048	V
	7	EQ1	100%_EQ1_100	0.097	
	8	RNDM	RNDM_08	-	
	9	EQ1	150%_EQ1_150	0.138	
09/10/2015	10	RNDM	RNDM_10	-	
	11	EQ2	30%_EQ2_050	0.064	
	12	EQ2	30%_EQ2_050	0.058	
	13	EQ2	30%_EQ2_050	0.055	
	14	EQ2	50%_EQ2_080	0.085	
	15	RNDM	RNDM_15	-	
	16	EQ2	100%_EQ2_160	0.166	
09/12/2015	17	RNDM	RNDM_17	-	
	18	EQ2	50%_EQ2_080	0.114	
	19	EQ2	125%_EQ2_200	0.192	
09/14/2015	20	RNDM	RNDM_20	-	
	21	EQ2	150%_EQ2_240	0.241	
	22	RNDM	RNDM_22	-	
	23	EQ2	200%_EQ2_320	0.305	
	24	RNDM	RNDM_24	-	
09/15/2015	25*	RNDM	RNDM_25	-	V
	26*	EQ2	30%_EQ2_050	0.070	V
	27*	EQ2	30%_EQ2_050	0.058	V
	28*	EQ2	30%_EQ2_050	0.055	V
	29*	EQ2	60%_EQ2_100	0.112	V
	30*	RNDM	RNDM_30	-	V

All the data related to each test are listed in one .txt file. Following you may find short instruction about how to extract the requested measures.

The following figure shows the position of the accelerometers and the reference system assumed for all the accelerograms. All the acceleration histories are absolute accelerations. It is also indicated the object/component to which the accelerometers are connected.

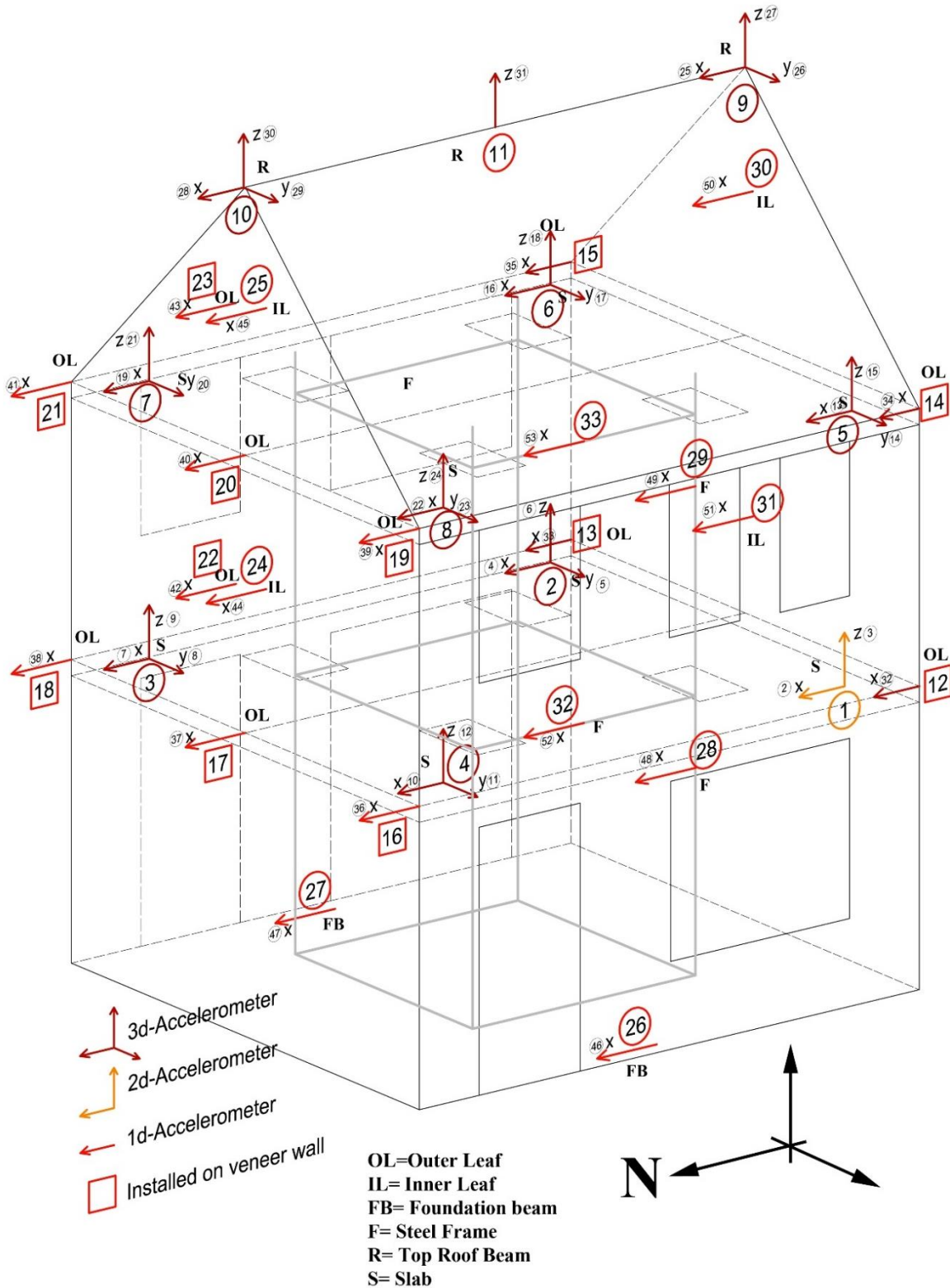


Figure 1 Identification of the position of the accelerometers.

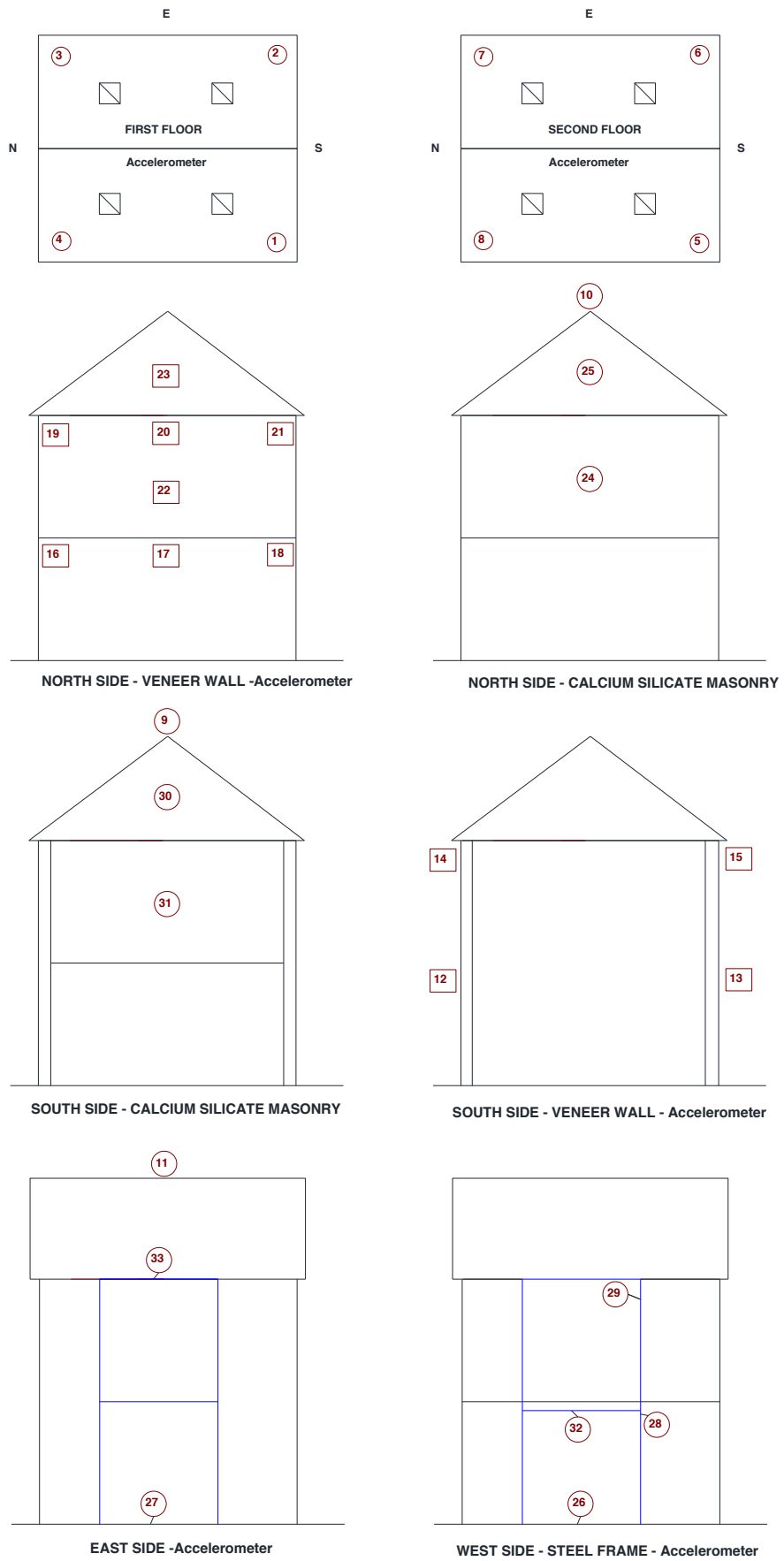


Figure 2 Identification of the position of the accelerometers.

The accelerometers installed on the calcium silicate masonry, on the slabs and on the steel frame are the following:

# 1 is installed on the slab of the first floor level on the west side to record the accelerations in the x and z direction;

# 2 is installed just below the first slab on the east side to record the acceleration in the x, y and z direction;

# 3 is installed just below the first slab on the east side to record the acceleration in the x, y and z direction

# 4 is also installed on the first-floor-level RC slab in order on the west side to obtain the accelerations in all three x, y and z directions;

# 5 is installed on the roof on the west side. This accelerometer measures the acceleration in the x, y and z direction of the second floor;

# 6 is installed just below the second slab on the east side to record the acceleration in the x, y and z direction;

# 7 is installed just below the second slab on the east side to record the acceleration in the x, y and z direction;

# 8 is installed on the roof on the west side. This accelerometer measures the acceleration in the x, y and z direction of the second floor;

# 9 is installed at the roof- ridge-level of the south side and recording the acceleration in the x, y and z direction;

# 10 is installed at the ridge of the gable of the north side and recording the acceleration in the x, y and z;

# 11 is installed on the ridge of the roof for recording the accelerations in the z direction;

# 24 is installed at the mid-height of the second storey north recording the accelerations in the x direction;

# 25 is installed at  $2/3$  of the height of the north facade gable recording the accelerations in the x direction;

# 26 which is installed on the base of the building on the west side is used to record the accelerations in the x direction at the foundation level;

# 27 is installed on the base of the building on the east side to record the accelerations in the x direction at the foundation level;

# 28 is installed on the steel frame on the first floor level on the west side in order to record the accelerations in the x direction of the frame, which is considered to be fixed at the shaking table;

# 29 is installed on the steel frame on the second floor level on the west side in order to record the accelerations in the x direction of the frame, which is considered to be fixed at the shaking table;

# 30 is installed at  $2/3$  of the height of the south facade gable recording the accelerations in the x direction;

# 31 is installed at the mid-height of the second storey south recording the accelerations in the x direction;

# 32 is attached on the inner steel frame on the west side to record the accelerations in the x direction. The steel frame is considered to be fixed at the shaking table;

# 33 is installed on the inner steel frame on the east side to record the acceleration in the x direction. The frame is considered to be fixed at the shaking table;

The accelerometers installed on the veneer walls are:

# 12 is installed on the first floor level of the south-west side and recording the acceleration in the x direction;

# 13 is installed on the first floor level of the south-east side and recording the acceleration in the x direction;

# 14 is installed on the second floor level of the south-west side and recording the acceleration in the x direction;

# 15 is installed on the second floor level of the south-east side and recording the acceleration in the x direction;

# 16 is installed on the first floor level of the north-west side and recording the acceleration in the x direction;

# 17 is installed on the first floor level of the north side and recording the acceleration in the x direction;

# 18 is installed on the first floor level of the north-east side and recording the acceleration in the x direction;

# 19 is installed on the second floor level of the north-west side and recording the acceleration in the x direction;

# 20 is installed on the second floor level of the north side and recording the acceleration in the x direction;

# 21 is installed on the second floor level of the north-east side and recording the acceleration in the x direction;

# 22 is installed at the mid-height of the second storey north recording the accelerations in the x direction;

# 23 is installed at  $2/3$  of the height of the north facade gable recording the accelerations in the x direction;

The following figure shows the position of the wire and traditional potentiometer. The .txt file reports directly the recorded displacement in mm. Again, the reference system is shown in the figure, which is the same for all the measures. It is also indicated the object/component to which the potentiometers are connected.

All the presented displacement are relative to the shake-table.

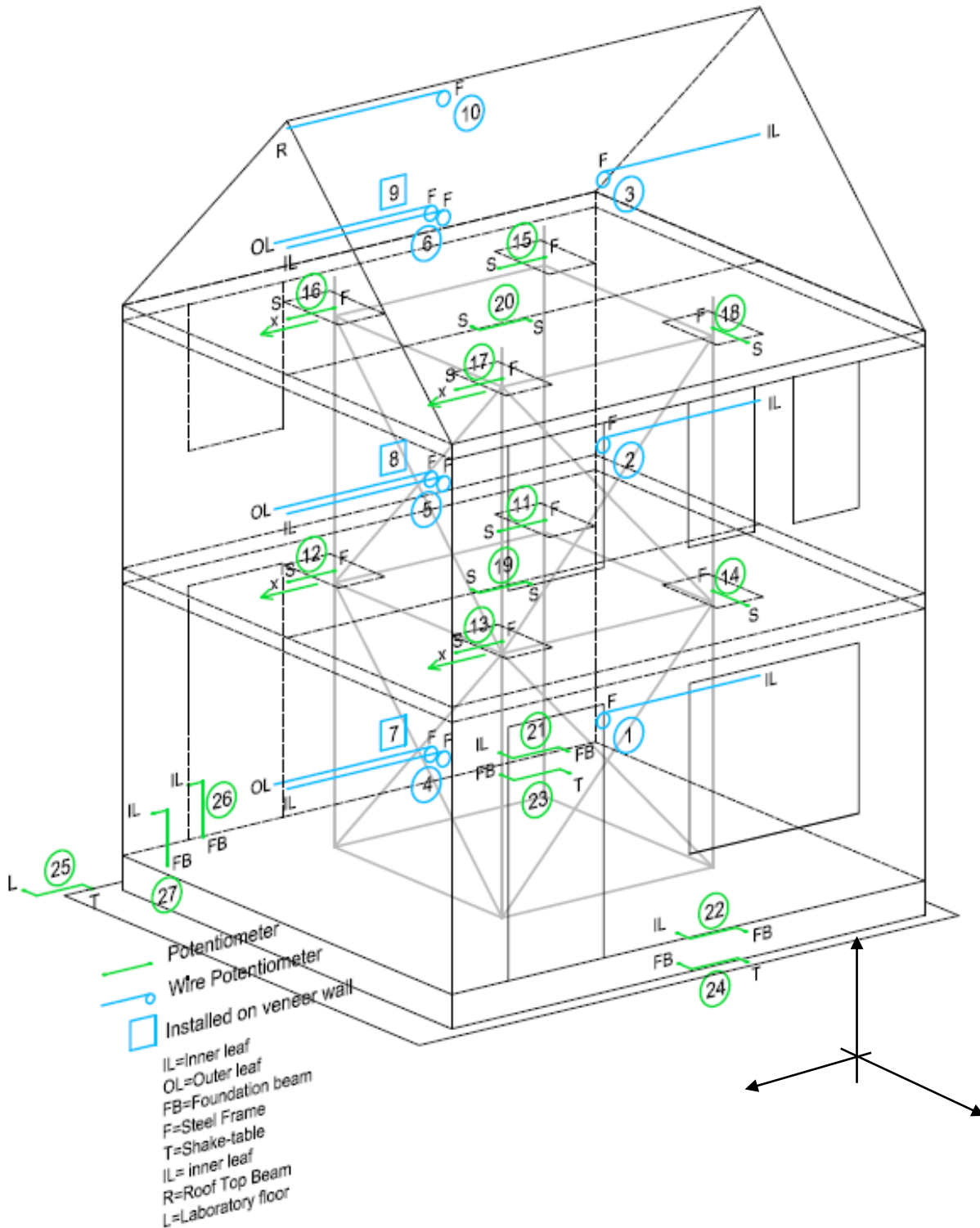
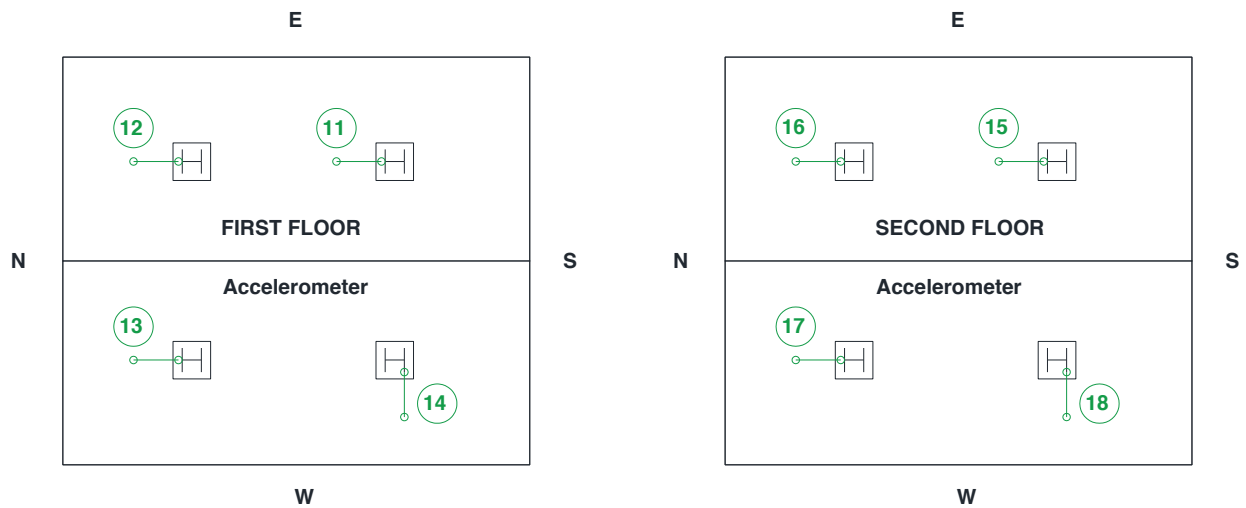


Figure 3 Identification of the position of the potentiometer.



### Section

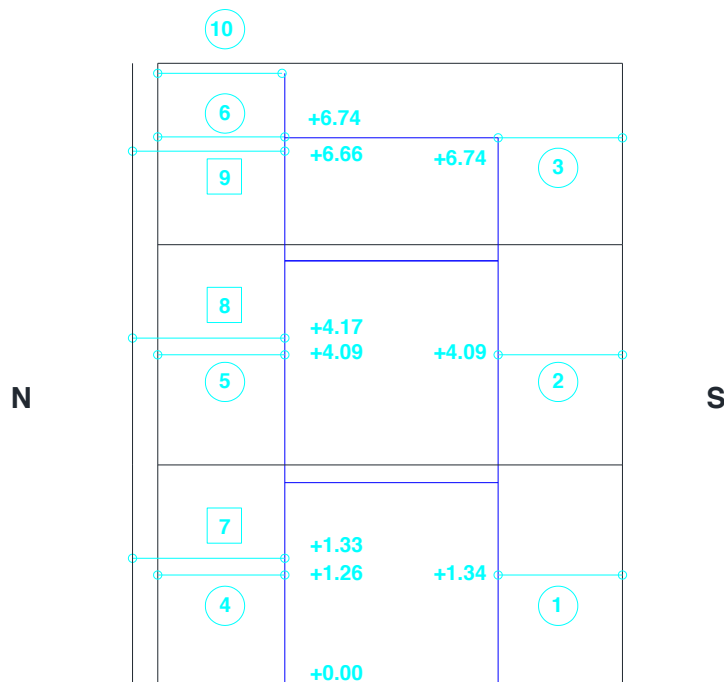


Figure 4 Identification of the position of the potentiometer.

The potentiometers installed on the calcium silicate masonry, on the slabs and on the steel frame are the following:

# 1 is a wire potentiometer and is installed at the mid-height of the first storey south recording the displacement of the calcium silicate wall (height +1.34 m);

# 2 is a wire potentiometer and is installed at the mid-height of the second storey south recording the displacement of the calcium silicate wall (height +4.09 m);

# 3 is a wire potentiometer and is installed at 2/3 of the height of the south facade gable recording the displacement in the x direction (height +6.74 m);

- # 4 is a wire potentiometer and is installed at the mid-height of the first storey north recording the displacement of the calcium silicate wall (height +1.26 m);
- # 5 is a wire potentiometer and is installed at the mid-height of the second storey north recording the displacement of the calcium silicate wall (height +4.09 m);
- # 6 is a wire potentiometer and is installed at 2/3 of the height of the north facade gable recording the displacement in the x direction (height +6.74 m);
- # 10 is a wire potentiometer and is installed at the top of the roof beam north side and recording the displacement of the roof;
- # 11 is attached on the inner steel frame of the first floor on the south-east side to record the x displacements of the slab relative to the steel frame. The frame is considered to be fixed at the shaking table;
- # 12 is attached on the inner steel frame of the first floor on the north-west side to record the x displacements of the slab relative to the steel frame. The frame is considered to be fixed at the shaking table;
- # 13 is attached on the inner steel frame of the first floor on the north-east side to record the x displacements of the slab relative to the steel frame. The frame is considered to be fixed at the shaking table;
- # 14 is attached on the inner steel frame of the first floor on the south-east side to record the displacements of the slab relative to the steel frame (y direction). The frame is considered to be fixed at the shaking table;
- # 15 is attached on the inner steel frame of the second floor on the south-east side to record the x displacements of the slab relative to the steel frame;
- # 16 is attached on the inner steel frame of the second floor on the north-east side to record the x displacements of the slab relative to the steel frame;
- # 17 is attached on the inner steel frame of the second floor on the north-west side to record the x displacements of the slab relative to the steel frame;
- # 18 is attached on the inner steel frame of the second floor on the south-east side to record the displacements of the slab relative to the steel frame (y direction);
- # 19 is installed, on the first floor, between the two slab to record the sliding of the two;
- # 20 is installed, on the second floor, between the two slab to record the sliding of the two;
- # 21 which is installed on the foundation on the east side is used to record the displacement and the sliding between the foundation and the building;
- # 22 which is installed on the foundation on the west side is used to record the displacement and the sliding between the foundation and the building;
- # 23 which is installed on the shaking table on the east side is used to record the displacement and the sliding between the foundation and the shaking table;
- # 24 which is installed on the shaking table on the west side is used to record the displacement and the sliding between the foundation and the shaking table;
- # 25 which is installed on the shaking table on the east side is used to record the x displacement;

# 26 which is installed on the ground floor on the east side is used to record the displacement in z direction of the facade;

# 27 which is installed on the ground floor is used to record the displacement in z direction of the facade;

The potentiometers installed on the clay masonry are the following:

# 7 is a wire potentiometer and is installed at the mid-height of the first storey north recording the displacement of the clay wall (height +1.33 m);

# 8 is a wire potentiometer and is installed at the mid-height of the second storey north recording the displacement of the clay wall (height +4.17 m);

# 9 is a wire potentiometer and is installed at 2/3 of the height of the north facade gable recording the displacement in the x direction (height +6.66 m);

The following table lists the time history contained in each column of the .txt files.

<b>Col #</b>	<b>Instrument / Chanel Description</b>	<b>U.M.</b>	<b>Position</b>
1	Time	[s]	-
2	Accelerometer 1 X Direction	[g]	SW First Floor
3	Accelerometer 1 Z Direction	[g]	SW First Floor
4	Accelerometer 2 X Direction	[g]	SE First Floor
5	Accelerometer 2 Y Direction	[g]	SE First Floor
6	Accelerometer 2 Z Direction	[g]	SE First Floor
7	Accelerometer 3 X Direction	[g]	NE First Floor
8	Accelerometer 3 Y Direction	[g]	NE First Floor
9	Accelerometer 3 Z Direction	[g]	NE First Floor
10	Accelerometer 4 X Direction	[g]	NW First Floor
11	Accelerometer 4 Y Direction	[g]	NW First Floor
12	Accelerometer 4 Z Direction	[g]	NW First Floor
13	Accelerometer 5 X Direction	[g]	SW Second Floor
14	Accelerometer 5 Y Direction	[g]	SW Second Floor
15	Accelerometer 5 Z Direction	[g]	SW Second Floor
16	Accelerometer 6 X Direction	[g]	SE Second Floor
17	Accelerometer 6 Y Direction	[g]	SE Second Floor
18	Accelerometer 6 Z Direction	[g]	SE Second Floor
19	Accelerometer 7 X Direction	[g]	NE Second Floor
20	Accelerometer 7 Y Direction	[g]	NE Second Floor

21	Accelerometer 7 Z Direction	[g]	NE Second Floor
22	Accelerometer 8 X Direction	[g]	NW Second Floor
23	Accelerometer 8 Y Direction	[g]	NW Second Floor
24	Accelerometer 8 Z Direction	[g]	NW Second Floor
25	Accelerometer 9 X Direction	[g]	S Roof
26	Accelerometer 9 Y Direction	[g]	S Roof
27	Accelerometer 9 Z Direction	[g]	S Roof
28	Accelerometer 10 X Direction	[g]	N Roof
29	Accelerometer 10 Y Direction	[g]	N Roof
30	Accelerometer 10 Z Direction	[g]	N Roof
31	Accelerometer 11 Z Direction	[g]	Centre Roof
32	Accelerometer 12 X Direction	[g]	SW Clay Wall First Floor
33	Accelerometer 13 X Direction	[g]	SE Clay Wall First Floor
34	Accelerometer 14 Y Direction	[g]	SW Clay Wall Second Floor
35	Accelerometer 15 X Direction	[g]	SE Clay Wall Second Floor
36	Accelerometer 16 X Direction	[g]	NW Clay Wall First Floor
37	Accelerometer 17 X Direction	[g]	N Clay Wall First Floor
38	Accelerometer 18 Y Direction	[g]	NE Clay Wall First Floor
39	Accelerometer 19 X Direction	[g]	NW Clay Wall Second Floor
40	Accelerometer 20 X Direction	[g]	N Clay Wall Second Floor
41	Accelerometer 21 X Direction	[g]	NE Clay Wall Second Floor
42	Accelerometer 22 X Direction	[g]	N Clay Wall 1 Floor/2 Floor
43	Accelerometer 23 X Direction	[g]	N Clay Gable 2 Floor/Roof
44	Accelerometer 24 X Direction	[g]	N CS Wall 1 Floor/2 Floor
45	Accelerometer 25 X Direction	[g]	N CS Gable 2 Floor/Roof
46	Accelerometer 26 X Direction	[g]	W foundation
47	Accelerometer 27 X Direction	[g]	E foundation
48	Accelerometer 28 X Direction	[g]	Steel Frame First Floor
49	Accelerometer 29 X Direction	[g]	Steel Frame Second Floor
50	Accelerometer 30 X Direction	[g]	S CS Gable 2 Floor/Roof
51	Accelerometer 31 X Direction	[g]	S CS Wall 1 Floor/2 floor
52	Accelerometer 32 X Direction	[g]	Steel Frame First Floor (beam W)
53	Accelerometer 33 X Direction	[g]	Steel Frame Sec. Floor (beam E)

54	Wire Potentiometer 1 X-Direction	[mm]	S CS Wall Ground/1 Floor
55	Wire Potentiometer 2 X-Direction	[mm]	S CS Wall 1 Floor/2 Floor
56	Wire Potentiometer 3 X-Direction	[mm]	S CS Gable 2 Floor/Roof
57	Wire Potentiometer 4 X-Direction	[mm]	N CS Wall Ground/1 Floor
58	Wire Potentiometer 5 X-Direction	[mm]	N CS Wall 1 Floor/2 Floor
59	Wire Potentiometer 6 X-Direction	[mm]	N CS Gable 2 Floor/Roof
60	Wire Potentiometer 7 X-Direction	[mm]	N Clay Wall Ground/1 Floor
61	Wire Potentiometer 8 X-Direction	[mm]	N Clay Wall 1 Floor/2 Floor
62	Wire Potentiometer 9 X-Direction	[mm]	N Clay Gable 2 Floor/Roof
63	Wire Potentiometer 10 X-Direction	[mm]	Top Roof Beam N
64	Potentiometer 11 –X-Direction	[mm]	SE First Floor
65	Potentiometer 12 –X-Direction	[mm]	NE First Floor
66	Potentiometer 13 –X-Direction	[mm]	NW First Floor
67	Potentiometer 14 –Y-Direction	[mm]	SW First Floor
68	Potentiometer 15 –X-Direction	[mm]	SE Second Floor
69	Potentiometer 16 –X-Direction	[mm]	NE Second Floor
70	Potentiometer 17 –X-Direction	[mm]	NW Second Floor
71	Potentiometer 18 –Y-Direction	[mm]	SW Second Floor
72	Potentiometer 19 –Sliding X-Direction	[mm]	First Floor (between slabs)
73	Potentiometer 20 –Sliding X-Direction	[mm]	Second Floor (between slabs)
74	Potentiometer 21 – Sliding Wall-foundation X-Direction	[mm]	Ground level E: Wall-foundation
75	Potentiometer 22 – Sliding Wall-foundation X-Direction	[mm]	Ground level W: Wall-foundation
76	Potentiometer 23 –Foundation-Shake Table X-Direction	[mm]	Ground level E
77	Potentiometer 24 – Foundation-Shake Table X-Direction	[mm]	Ground level W
78	Potentiometer 25 Shake Table–X-Direction	[mm]	Ground
79	Potentiometer 26 –Z-Direction	[mm]	Ground: uplift flange E wall
80	Potentiometer 27 –Z-Direction	[mm]	Ground : uplift flange E wall
81	Shake Table Force X Direction	[kN]	Ground (Actuator horizontal Force)
82	Shake Table Displacement X Direction	[mm]	Ground
83	Shake Table Acceleration X Direction	[g]	Ground

84	Displacement 1 <sup>st</sup> Floor X-direction	[mm]	average
85	Displacement 2 <sup>nd</sup> Floor X-direction	[mm]	average
86	Acceleration Ground Floor X-Direction	[g]	average
87	Acceleration 1 <sup>st</sup> Floor X-Direction	[g]	average
88	Acceleration 2 <sup>nd</sup> Floor X-Direction	[g]	average
89	Acceleration Roof X-Direction	[g]	average
90	Inter-Storey Drift 1st Floor	[%]	average
91	Inter-Storey Drift 2nd Floor	[%]	average
92	Inter-Storey Drift Roof	[%]	average
93	Base Shear	[kN]	calculated
94	Off-line Chanel	[-]	-
95	Off-line Chanel	[-]	-
96	Off-line Chanel	[-]	-
97	Off-line Chanel	[-]	-
98	Off-line Chanel	[-]	-

The following picture shows a view of the specimen.



The following pictures show a view of the North façade (left) and the South façade (left);

On the left it is possible to see accelerometers #16, #17, #18 (first floor level), #22 (mid-height first-floor wall), #19, #20, #21 (second floor level) and #23 (1/2 of the gable). On the right picture it is possible to see accelerometers #12, #13 (first floor level on the veneer wall) and #14, #15 (second floor level on the veneer wall).



The following picture shows a view of accelerometer #9.



The following picture shows a view of accelerometer #6.



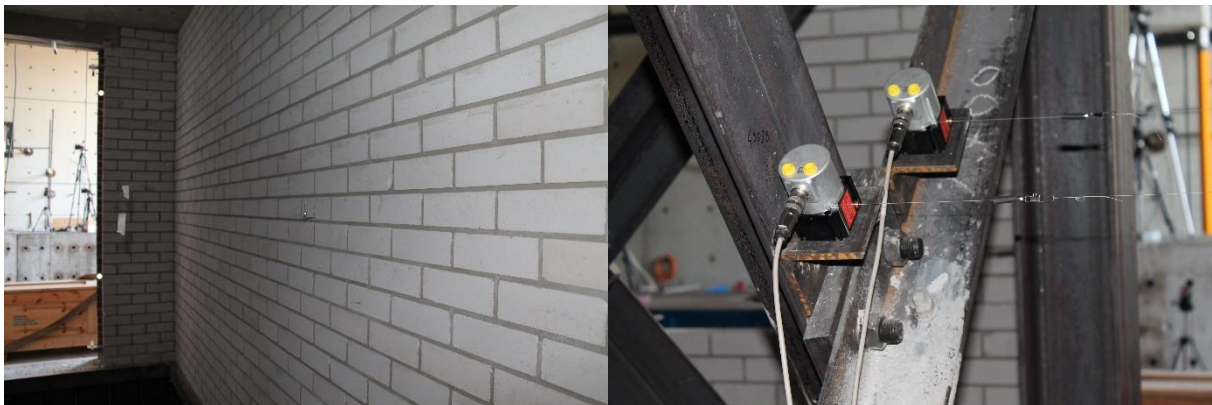
The following picture shows a view of the accelerometer #25 and the wire of the potentiometer #9.



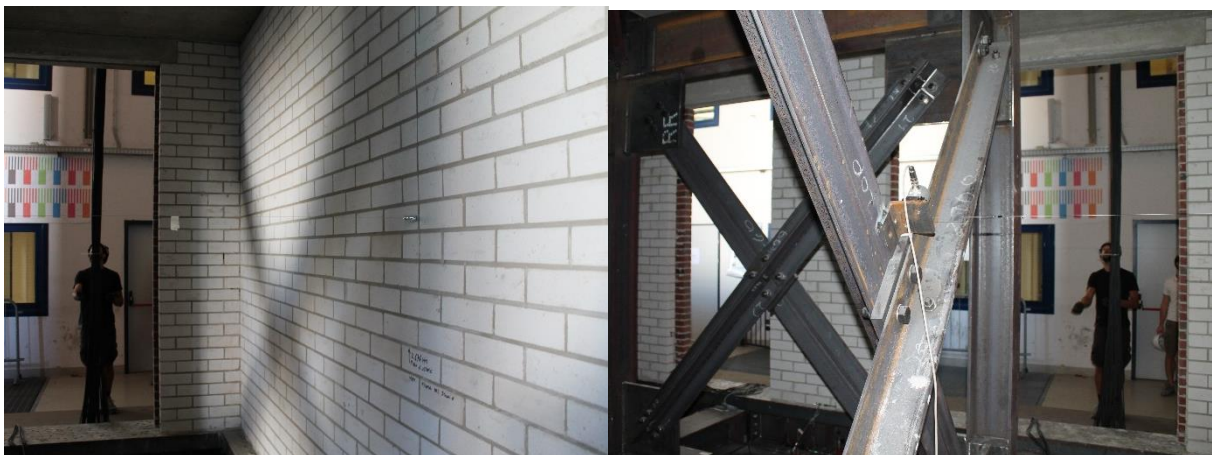
The Following picture shows potentiometers #26 (right) and #27 (left) .



The Following pictures show the wire potentiometers #4 and #7 (passing through the CS walls) .



The Following pictures shows the wire potentiometer #1.



The Following picture shows the potentiometer #25.



The picture below shows the potentiometers #14 and #11 (in the background).



The picture below shows the potentiometers #21 and #23.



In attached you may find the requested plots for each Earthquake test performed and the related .txt.

Name	Description
TestName_AH	Acceleration histories
TestName_DH	Displacement histories
TestName_ID	Inter-storey drift histories
TestName_FD	Force-2nd-Floor Displacement

The following Tables lists the information contained in each .txt file.

TestName_AH	
Column #	Description
1	Time [s]
2	Acceleration Ground Floor X-Direction [g]
3	Acceleration 1st Floor X-Direction [g]
4	Acceleration 2nd Floor X-Direction [g]
5	Acceleration Roof X-Direction [g]

TestName_DH	
Column #	Description
1	Time [s]
2	Displacement 1st Floor X-Direction [mm]
3	Displacement 2nd Floor X- Direction [mm]
4	Displacement Roof [mm]

TestName_FD	
Column #	Description
1	Time [s]
2	Displacement 2nd Floor X- Direction [mm]
3	Base Shear [kN]

TestName_ID	
Column #	Description
1	Time [s]
2	Inter-Storey Drift 1st Floor
3	Inter-Storey Drift 2nd Floor
4	Inter-Storey Drift Roof



## Guidelines: EUCENTRE Building Tests recorded experimental data

### 3D optical acquisition system



The experimental data recorded by the 3D optical acquisition system are provided for all the dynamic tests, summarised in the following table. All the data are organised in .C3D files named as reported in Table 1.

*Table 1. Summary testing sequence.*

<i>Test #</i>	<i>Test Input</i>	<i>Test Name</i>	<i>File Name</i>
2	<i>EQ1-Or</i>	25%_EQ1_024	25%_EQ1_024.c3d
4	<i>EQ1-Or</i>	50%_EQ1_050	50%_EQ1_050.c3d
7	<i>EQ1</i>	100%_EQ1_100	100%_EQ1_100.c3d
9	<i>EQ1</i>	150%_EQ1_150	150%_EQ1_150.c3d
14	<i>EQ2</i>	50%_EQ2_080	50%_EQ2_080.c3d
16	<i>EQ2</i>	100%_EQ2_160	100%_EQ2_160.c3d
19	<i>EQ2</i>	125%_EQ2_200	125%_EQ2_200.c3d
21	<i>EQ2</i>	150%_EQ2_240	150%_EQ2_240.c3d
23	<i>EQ2</i>	200%_EQ2_320	200%_EQ2_320.c3d



Each C3D file can be processed in MATLAB using the following functions (created by GPEM, the acquisition system company), provided in addition to the data:

- [readC3D JA GP.m](#): with this function it is possible to get the frame histories 3D coordinate data from a C3D file. In particular, the most significant output of this function are:
  - *Markers*: 3D matrix with the marker data [NFrames x Nmarkers x Absolute Coordinates(1= X, 2=Y, 3=Z )]
  - *VideoFrameRate*: Frames/sec
  - *ParameterGroup*: Input data of the function "[getVideoLabelsC3D.m](#)", in order to get the marker's label.
- [getVideoLabelsC3D.m](#): this function allows to get the labels of the markers ordered by column in a 1D cell array.
- [getTrajectoriesC3D.m](#): this function allows to import the coordinates of selected marker.

The label and position of each marker is reported in the following figures. During each test, the trajectories of some markers was not reliable and the data has been removed from the matrix. In particular, the missing marker are reported in Table 2.

Table 2. Missing markers.

<i>File Name</i>	<i>Missing markers</i>
25%_EQ1_024.c3d	A056
50%_EQ1_050.c3d	L111B, A056
100%_EQ1_100.c3d	L111B, A056
150%_EQ1_150.c3d	L111B, L23, A056
50%_EQ2_080.c3d	L111B, L23, A056
100%_EQ2_160.c3d	L111B, L23, A056
125%_EQ2_200.c3d	A056, A043B, A093B
150%_EQ2_240.c3d	L111B, A056, A094B
200%_EQ2_320.c3d	L111B, A056

All the marker's coordinates are **absolute [mm]**.

All the displacement time histories have to be considered valid **only** referred to each single test (i.e. the absolute residual displacement could not be computed with this data). On the other hand, one can compute the residual displacement relative to each test. The reason of this issue is that the reference system slightly change every calibration. This do not affect the relative positions of the markers within each run.



The use of all these functions is reported, as an example, in the Matlab routine “*Post\_Process\_EUCENTRE\_Example.m*”:

```
close all;
clc;
clear all;

%% Import 3D-marker data

[Markers,VideoFrameRate,AnalogSignals,AnalogFrameRate,Event,Parameter
Group,CameraInfo,ResidualError]...
    =readC3D_JA_GP('200%_EQ2_320.c3d'); % Getting 3D coordinate data
from a C3D file

%% Import the label of the marker

Label=getVideoLabelsC3D(ParameterGroup); % cell array 1D, with the
labels of the trajectories ordered by column.

%% Import the coordinates of selected marker

A103=getTrajectoriesC3D(ParameterGroup,Markers,'Frontal:A103'); %The
last arguments must have the same name as the marker labels (see
variable "Label" computed above)
A011=getTrajectoriesC3D(ParameterGroup,Markers,'Frontal:A011');
L111A=getTrajectoriesC3D(ParameterGroup,Markers,'Lateral:L111A');

%% Displacement trajectories [mm]

for i=1:size(Markers,3)
    for j=1:size(Markers,1)
        Second_Floor(j,i)=A103(j,i)-(A103(1,i)); %Second Floor
displacement
        base(j,i)=A011(j,i)-(A011(1,i)); %Base displacement
        roof(j,i)=L111A(j,i)-(L111A(1,i)); %Roof displacement
    end
end

%% Figures

figure
hold on
plot(Second_Floor(:,1),'b','linewidth', 0.7)
grid on
xlabel('frame','FontName','Times New Roman','FontSize', 10,
'FontWeight','bold')
ylabel('X Displacement [mm]','FontName','Times New Roman',
'FontSize', 10, 'FontWeight','bold')
h=get(gcf,'CurrentAxes');
set(h,'FontName','Times New Roman','FontSize', 10)
l=legend('Second Floor');
```

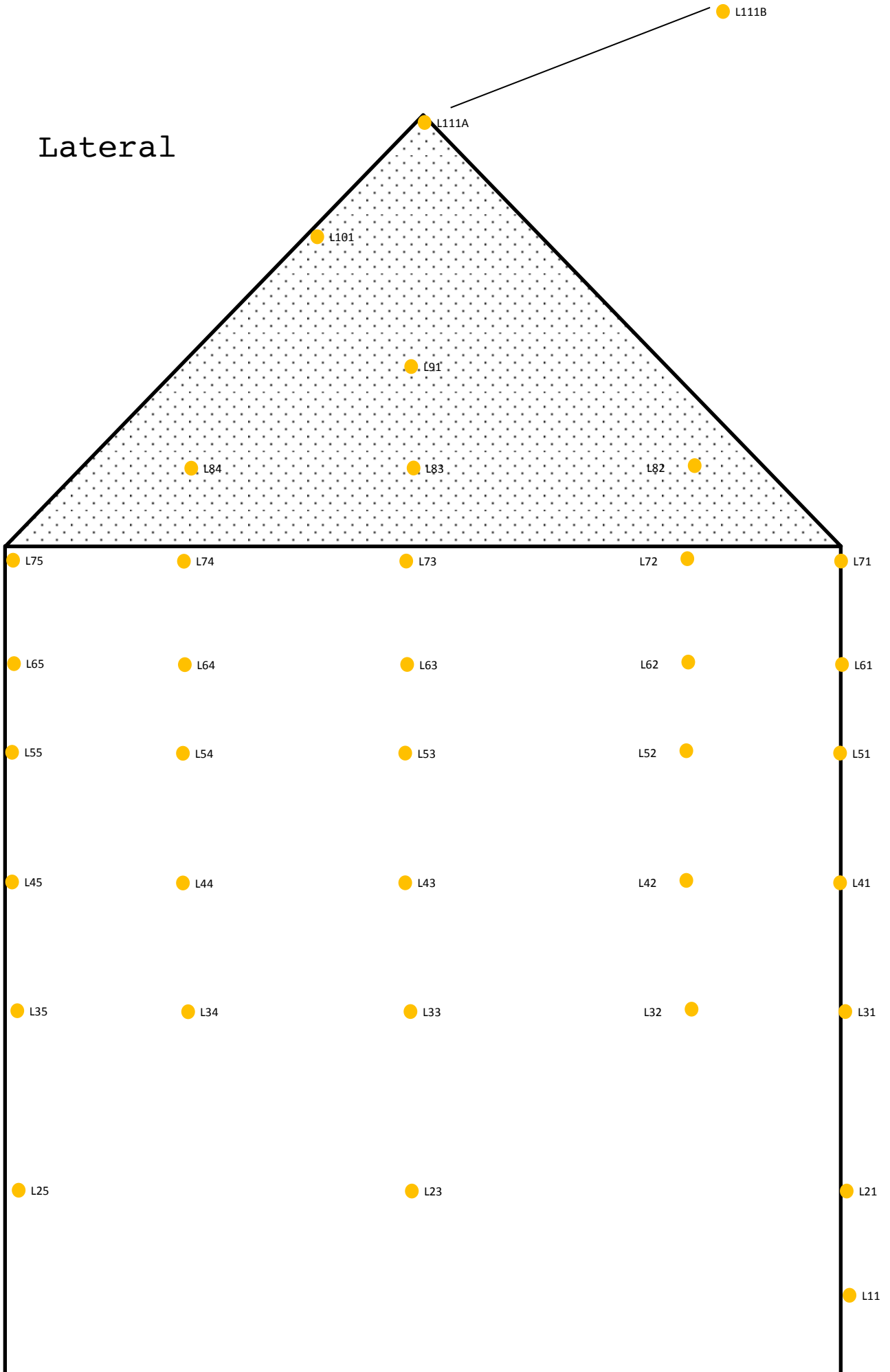


```
set(l, 'Location', 'Best', 'FontName', 'Times New Roman', 'FontSize',  
10)  
grid on
```

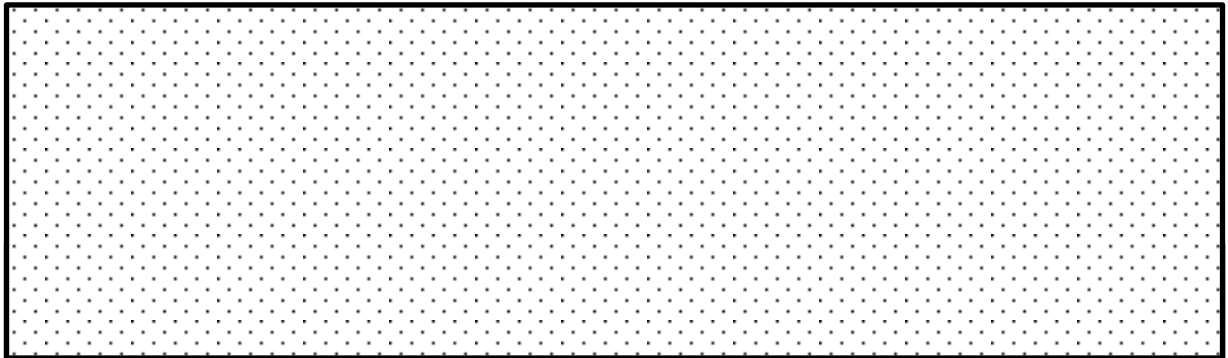
```
figure  
plot(base(:,1), 'k', 'linewidth', 0.7)  
grid on  
xlabel('frame', 'FontName', 'Times New Roman', 'FontSize', 10,  
'FontWeight', 'bold')  
ylabel('X Displacement [mm]', 'FontName', 'Times New Roman',  
'FontSize', 10, 'FontWeight', 'bold')  
h=get(gcf, 'CurrentAxes');  
set(h, 'FontName', 'Times New Roman', 'FontSize', 10)  
l=legend('base');  
set(l, 'Location', 'Best', 'FontName', 'Times New Roman', 'FontSize',  
10)  
grid on
```

```
figure  
plot(roof(:,1), 'k', 'linewidth', 0.7)  
grid on  
xlabel('frame', 'FontName', 'Times New Roman', 'FontSize', 10,  
'FontWeight', 'bold')  
ylabel('X Displacement [mm]', 'FontName', 'Times New Roman',  
'FontSize', 10, 'FontWeight', 'bold')  
h=get(gcf, 'CurrentAxes');  
set(h, 'FontName', 'Times New Roman', 'FontSize', 10)  
l=legend('roof');  
set(l, 'Location', 'Best', 'FontName', 'Times New Roman', 'FontSize',  
10)  
grid on
```

Lateral



# Frontal

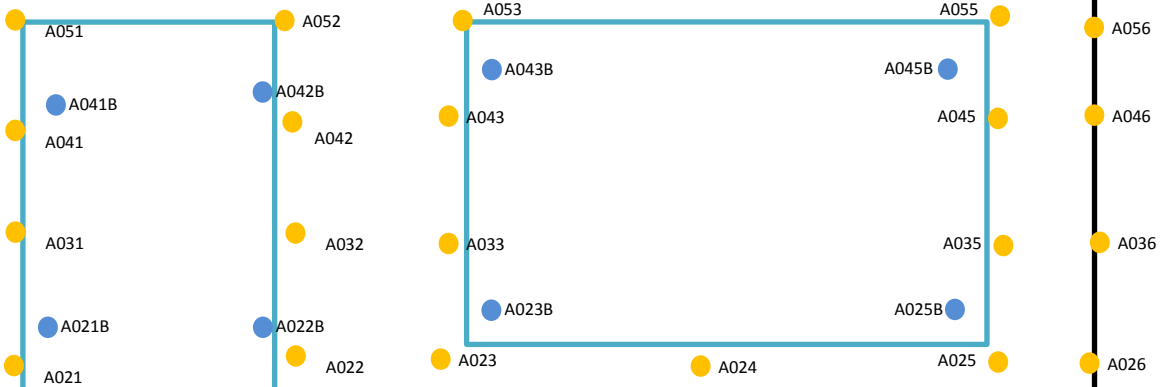


● A101      ● A102      ● A103      A105 ●      ● A106



● A071      ● A072      ● A073      ● A074      A075 ●      ● A076

● A061      ● A062      ● A063      ● A064      A065 ●      ● A066



● A011

- Marker (External Clay)    ○ Marker on the internal steel structure
- Marker (internal CS)

## **Appendix B-1**

### **Selection of records for nonlinear dynamic analysis of Groningen buildings**

# Selection of records for nonlinear dynamic analysis of Groningen buildings

by Helen Crowley, Julian Bommer and Rui Pinho

Version 1.0, 13<sup>th</sup> May 2015

## Introduction

This note outlines the procedure that has been followed to select a set of accelerograms and to match them with current estimations of the seismic hazard in the Groningen field. A total of 7 sets of 3-component records have been selected and matched to the response spectrum and 5–75% Arias intensity significant duration range of the scenario that contributes most to the hazard at a given return period.

## Hazard Characteristics

Version 1 mean hazard curves (for PGA and various spectral ordinates) have been calculated at many sites across the field using the v1 ground-motion prediction equation (GMPE) logic tree (Bommer et al., 2015) – see Figure 1. Disaggregation of the maximum PGA hazard curve has been carried out for various levels of PGA (see Figure 2). A uniform hazard spectrum (UHS) at a return period of 475 years, based only on the central branch of the GMPE logic tree, is presented in Figure 3 and compared with a scenario spectrum. The similarity between the scenario spectrum (obtained from disaggregation) and the UHS shows that the scenarios contributing to the hazard do not vary significantly from period to period, which is expected given that there is in effect a single seismic source contributing to the hazard in the Groningen field. Hence, it is assumed that the disaggregation of the hazard at PGA can be assumed to be of relevance also at higher periods of vibration, and that only a single scenario spectrum is required since it is an approximation to the UHS; there does not appear to be any need to develop time-histories matching multiple spectral targets.

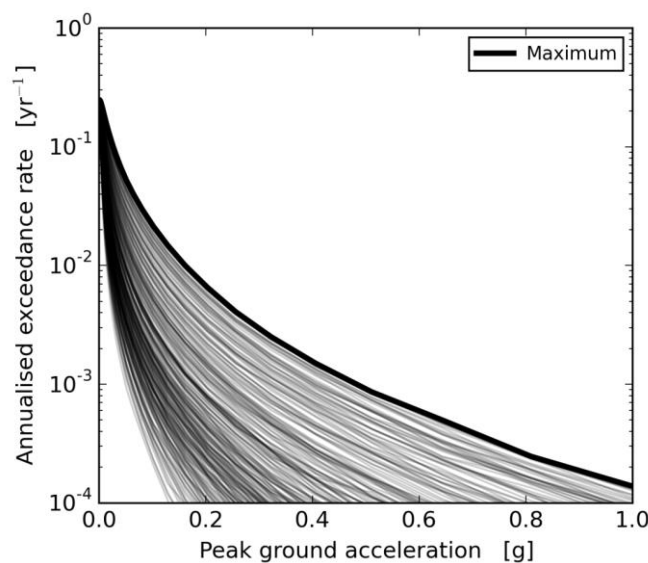


Figure 1. Mean hazard curves across the field in terms of PGA (g) [courtesy of Stephen Bourne]

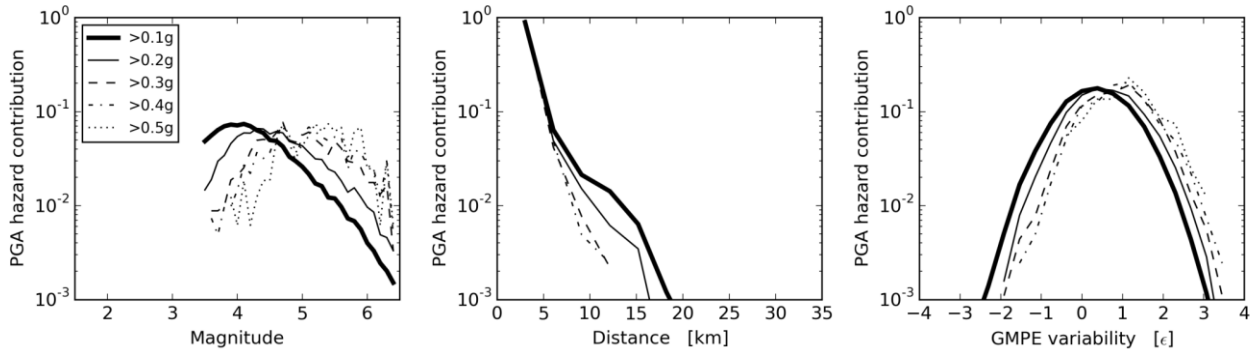


Figure 2. Disaggregation of the maximum PGA hazard curve at different levels of PGA [courtesy of Stephen Bourne]

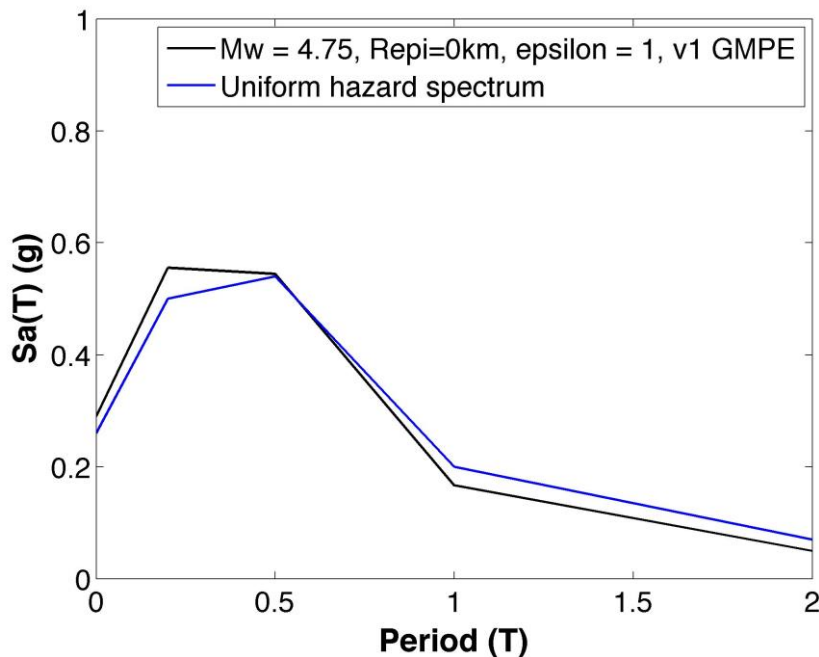


Figure 3. Uniform hazard spectrum based on the central model GMPE at 475-year return period, compared with the modal contributing scenario from disaggregation

The main drawback of the v1 GMPE (and hence the v1 hazard model) is that it currently only incorporates linear site amplification, which leads to an overestimation of the spectral accelerations for scenarios of larger earthquakes at shorter distances, in particular at the lower periods of vibration. An attempt is carried out herein to incorporate nonlinear site amplification in an approximate fashion. It is noted that the inclusion of nonlinear site response may change the return periods of the resulting ground motions but the return periods of ground motions with nonlinear site amplification will not be available until the version 2 GMPEs have been developed and updated estimates of the hazard calculated, which will be completed at the latest by October 2015. For present purposes, it is assumed that the levels of spectral acceleration estimated herein with nonlinear site amplification have the same return period as the original hazard values (i.e., with linear site amplification).

The return period required for the assessment of an existing structure of consequence class CC1B (into which residential housing falls) has been estimated for the Draft 9998

NPR (February 2015) as 800 years (also approximated as 1.2 times the 475-year PGA value) based on the KNMI hazard model, a partial safety factor of 1.1 on the strength side, a fragility function with a logarithmic standard deviation of 0.5, and a local personal risk of  $1.3 \times 10^{-5}$  (TNO, 2013). The calculations undertaken by TNO have been repeated herein under the same assumptions, but using the maximum hazard curve presented in Figure 1. The PGA at 5% probability of collapse is found to be 0.47g, which when divided by the partial safety factor leads to 0.43g. According to the hazard curve in Figure 1, this level of PGA has a return period of 770 years (and can also be estimated as 1.2 times the 475-year PGA value).

The disaggregation of the hazard at 0.43g shows that the modal contribution to this level of hazard is from magnitude 5 earthquakes at 0 km epicentral distance, with an epsilon value approximately equal to 1.2. A response spectrum for this scenario has been calculated with the v1 GMPE, and then nonlinear site amplification has been incorporated using the Sandikkaya et al. (2013) European site amplification model.

As the v1 GMPE already includes linear amplification, based on the same Sandikkaya et al. (2013) model, only the nonlinear amplification needs to be incorporated; the predominant effect for this scenario (**M5**,  $R_{epi}$  0 km,  $\epsilon$  1.2) is to reduce the spectral ordinates.

The PGA on reference rock ( $V_{ref} = 750$  m/s) for the aforementioned magnitude, distance and epsilon has first been estimated, by removing the linear amplification according to the Sandikkaya et al. (2013) model, assuming  $V_{s30} = 200$  m/s as the field-wide average value:

$$\ln(amp_{lin}) = a(T = 0)\ln(V_{s30}/V_{ref}) \quad (1)$$

where  $a(T=0)$  is a regression coefficient provided by the model for PGA. Once the value of reference PGA has been estimated, the nonlinear site amplification term can then be calculated at each period,  $T$ , with the Sandikkaya et al. (2013) model:

$$\ln(amp_{nonlin}) = b(T)\ln\left(\frac{PGA_{ref} + c(V_{s30}/V_{ref})^n}{(PGA_{ref} + c)(V_{s30}/V_{ref})^n}\right) \quad (2)$$

where  $b(T)$ ,  $c$  and  $n$  are regression coefficients provided by the model.

Figure 4 shows the original v1 linear amplified response spectrum and the estimated rock and nonlinear amplified response spectra, according to the Sandikkaya et al. (2013) model, for the aforementioned modal scenario, linearly scaled to the 770-year return period PGA hazard. The nonlinear amplified response spectrum given in Figure 4 has been used as the target horizontal spectrum for the record selection and matching.

The spectra in Figure 4 show a number of interesting features, the first being the very significant site amplification of the rock motions by the soft soil conditions, when only linear response is considered. Equally striking is the very appreciable reduction of this amplification when the nonlinearity in the soil response is invoked; at short period ( $< 0.2$  s) the effect is sufficiently strong to actually lead to a de-amplification of the reference rock motions. This results from the soft soil profile and the onerous loading scenario of a moderate magnitude earthquake directly below the site and motions at approximately the 90-percentile level; the rock PGA is only about 0.24g and for such soft sites nonlinearity may be expected for rock PGA in excess of about 0.05g (see Figure 5).

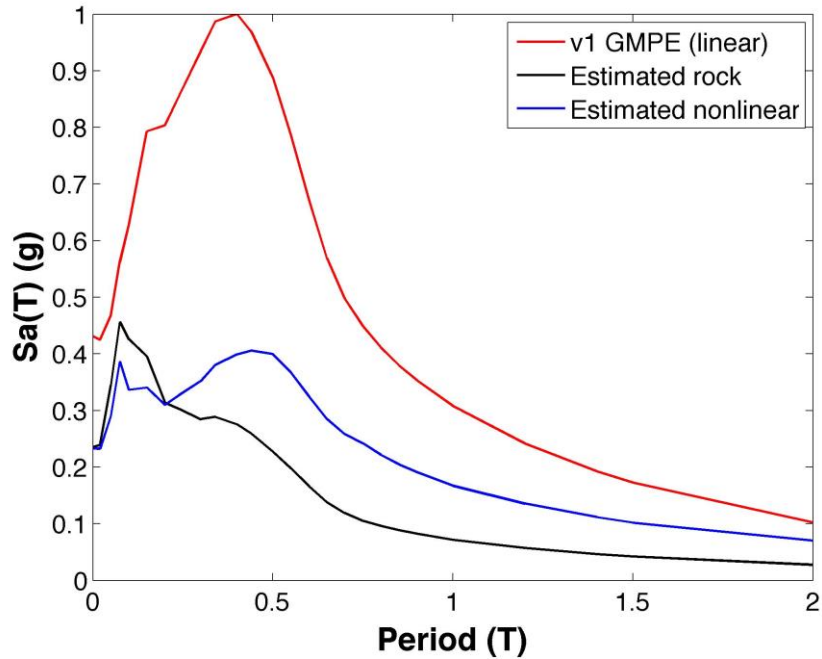


Figure 4. Response spectra from the v1 GMPE (linear), and estimated rock and nonlinear amplified spectra based on the Sandikkaya et al. (2013) model for moment magnitude 5 at an epicentral distance of 0 km, and epsilon = 1.2, scaled to a PGA of 0.43g

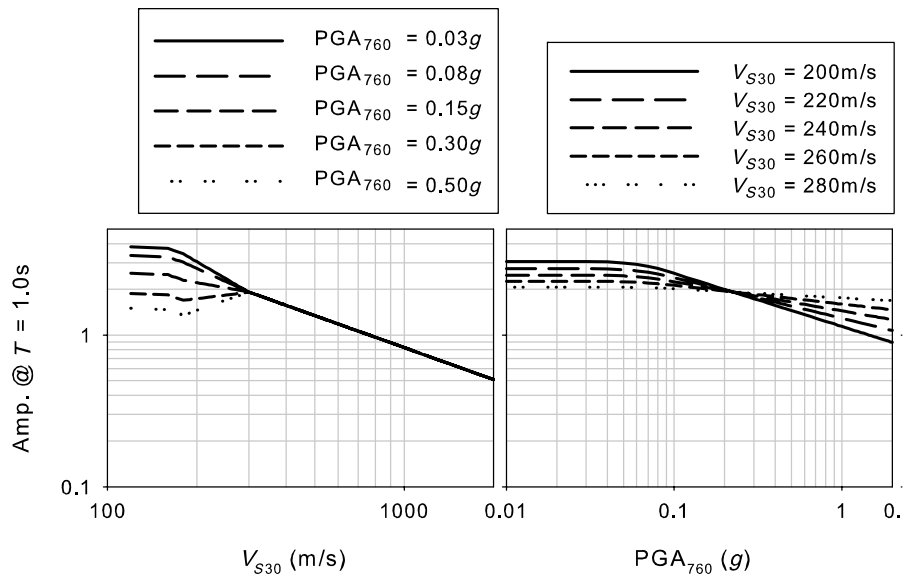


Figure 5. Site amplifications proposed by Boore and Atkinson (2008) for  $T = 1.0$  s. The left column shows the variation of the site amplification with respect to  $V_{s30}$  for different levels of  $PGA_{rock}$  (where  $V_{s30}$  of rock is taken as 760m/s). The right column shows the variation of the site amplifications as a function of  $PGA_{rock}$  for different  $V_{s30}$  values. (Adapted from Sandikkaya et al., 2013)

A vertical target spectrum has also been estimated by applying median vertical-to-horizontal (V/H) ratios at each period obtained from the V/H prediction equation proposed by Akkar et al. (2014), using the parameters described above for the controlling scenario (and thus assuming that there is full positive correlation between the horizontal and vertical spectral ordinates). The vertical target spectrum is shown in Figure 6, and compared with the horizontal target spectrum.

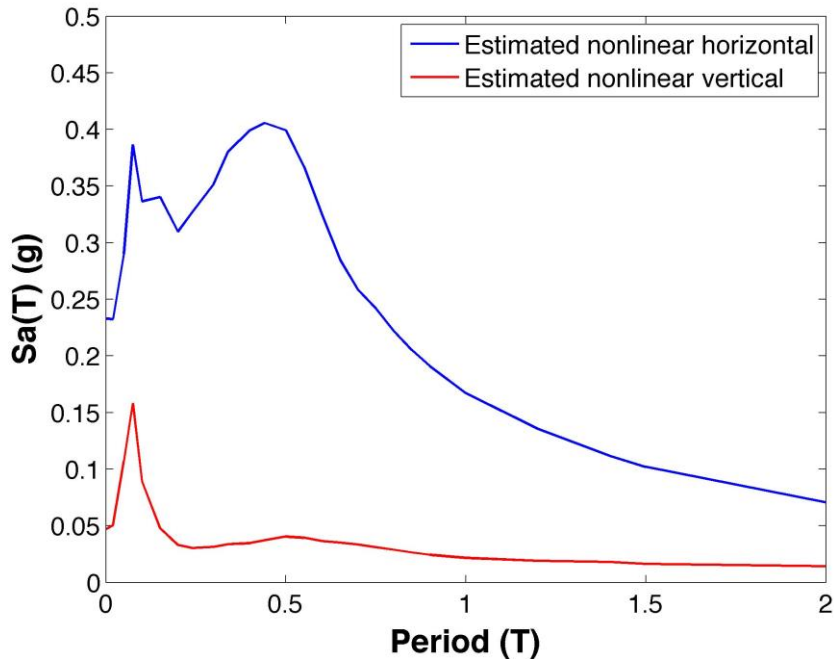


Figure 6. Vertical and horizontal target response spectra

The median 5-75% significant duration for the contributing scenario is 2.84 seconds according to the Kempton and Stewart (2006) prediction equation (that includes the effects of deep soil basins, for which a sediment depth of 600 m has been found to give a reasonable approximation to the durations measured in the Groningen field). The plus and minus one standard deviation significant durations are found to be 1.7 and 4.8 seconds, respectively. However, given that the residuals of spectral ordinates and significant durations have been found to be negatively correlated (see discussion in Chapter 7 of Bommer et al., 2015), and the target spectrum is based on an epsilon of 1.2, the conditional expected duration would actually be lower than 2.84 s. To account for this, an asymmetric window centred on 2.84 s will be used to select the ground motions, from -1 sigma (1.7 s) to +0.5 sigma (3.7 s). The Kempton and Stewart GMPE actually tends to over-estimate the durations of Groningen motions at very short distances, hence for the target scenario it could be appropriate to use even lower durations but for this exercise—and to avoid search criteria that would yield too few results—it was decided to stay with the asymmetric search window of 1.7 to 3.7 s.

### Selection and Linear Scaling of Records

A pre-selection of records from the v1 GMPE database (Bommer et al., 2015) has been undertaken by identifying triaxial sets of records that have a geometric mean 5-75% significant duration (based on the two horizontal components) between 1.7 and 3.7 seconds, ensuring that the maximum usable period is greater than or equal to 2 seconds. Using this reduced set of 269 waveforms, the final selection is made by first calculating the geometric mean horizontal spectrum of the two horizontal components of each triaxial set and linearly scaling it to minimize the difference with respect to the target horizontal response spectrum, across the 0.05 to 2 second period range. The absolute sum of squared errors (SSE) is used to quantify the match between the response spectral ordinates of the geometric mean of the individual components and the target spectrum over the period range of interest. The waveforms have been ordered in terms of the SSE,

and the top 15 horizontal pairs with the lowest SSE are then selected for spectral matching (along with their vertical components), as discussed in the next section.

In order to include also a recording from the Groningen field, the 5-75% significant durations of the 12 strongest recordings to date have been checked, and one waveform was found to fall within the identified range (with 10 falling below the lower bound of the range and one falling above the upper bound). The triaxial set from this recording was thus also selected for spectral matching.

## **Spectral Matching**

The two horizontal components of each ground motion set have been linearly scaled and then spectrally matched to the target horizontal spectrum, and the vertical component has been scaled (to at least a vertical PGA of 0.045g) and then matched to the target vertical spectrum, using the spectral matching algorithm described in Hancock et al. (2006) and embedded within the SeismoMatch software (Seismosoft, 2015). In order to avoid dramatic modifications to the frequency content of the original records, a maximum of 50 iterations have been applied in the matching algorithm. There may thus still be appreciable mismatches between the original and matched spectra, but a final check on the matched set of spectra will be undertaken to ensure that the requirements of the Draft NPR 9988 are met, which states that *“no single value of the average elastic spectrum, for 5% damping, calculated on the basis of all of the time series, may be less than 90% of the corresponding value of the elastic response spectrum with 5 % damping”*.

It is noted that by matching both horizontal components to the same target spectrum, the polarization of the components (which has been observed in Groningen records) is lost (though this will be included at a later stage, as discussed below); for current applications, users may simply scale the two horizontal components by factors whose product is unity (so that their geometric mean is unchanged) to obtain polarized versions of the orthogonal components of the horizontal records. Figure 7 shows the relationship between the response spectral ordinates of the two horizontal components from four different events in the Groningen field, which give an indication of the possible range of the aforementioned scaling factors. Derivation of component-to-component ratio distributions is part of the current scope of work of the GMPE development and when these relationships are ready they will be provided in an update of this document.

After matching, the geometric mean of the 5-75% significant duration of each matched pair of horizontal components has been recalculated (given that spectral matching can change the significant duration) and those with the minimum SSE that are still below 3.7 s have been retained, leading to the 7 triaxial sets from the events presented in Table 1. One matched pair of horizontal accelerograms that had a significant duration of 1.4 s, which is below the minimum value of 1.7 s, was retained given that it could be appropriate to use lower durations, as discussed previously.

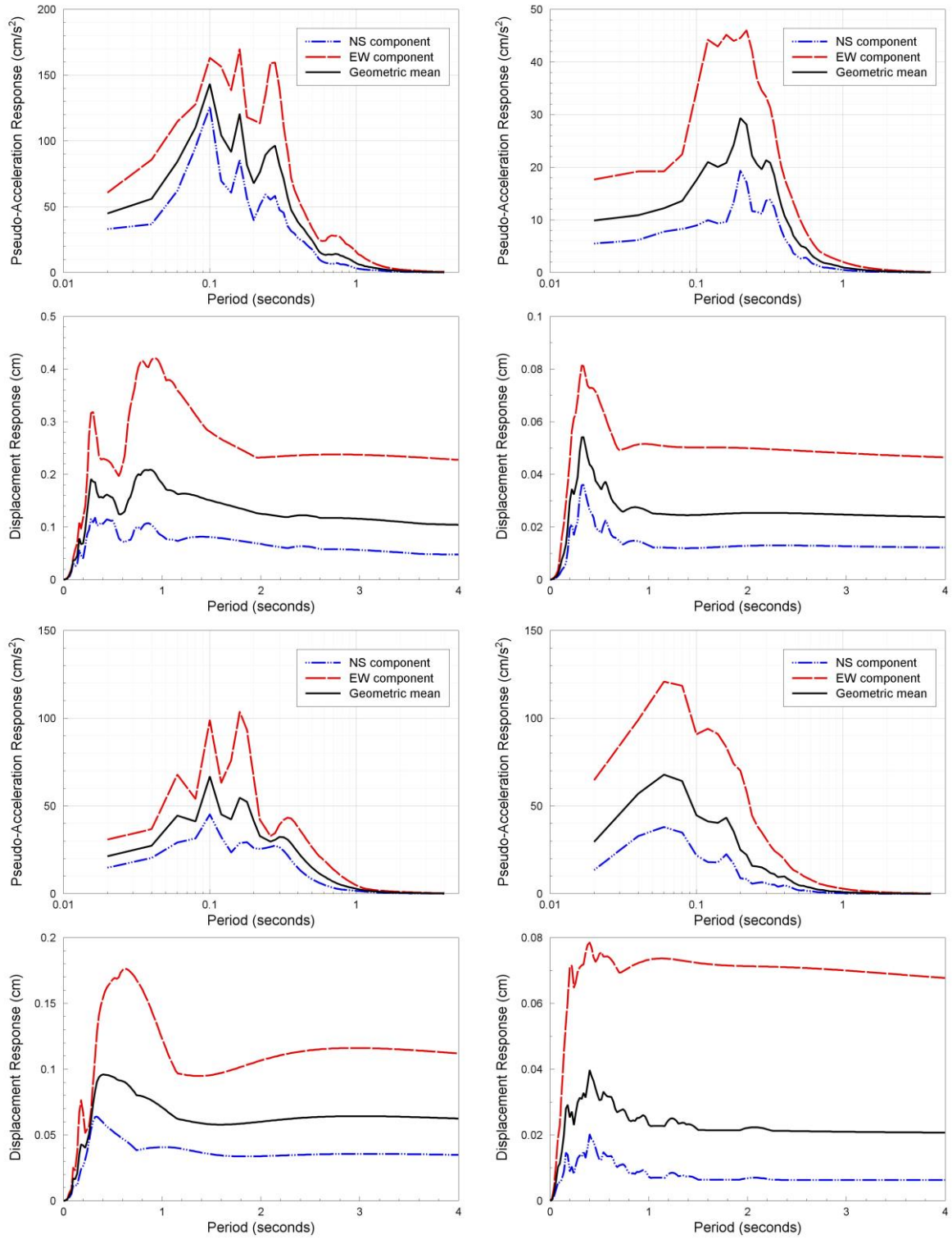


Figure 7. Example response spectra from the Groningen field, illustrating the strong polarization in the horizontal components

Table 1. Summary of events and significant durations of the selected and matched ground motions

No.	Waveform No.	EQ Name	EQ Date	Country	M <sub>w</sub>	R <sub>epi</sub> (km)	5-75% significant duration (s)
1	3443	Ano Liosia (Athens)	1999-09-07	Greece	6	19	2.24
2	3445	Ano Liosia (Athens)	1999-09-07	Greece	6	18	2.50
3	14715	Appenines Umbio-Marchigiano	1997-10-16	Italy	4.3	2	1.43
4	14717	Umbria Marche (aftershock)	1997-11-09	Italy	4.9	22	2.20
5	15887	Duzce 1 (aftershock)	1999-11-19	Turkey	4.9	5	3.00
6	17034	Gran Sasso	2009-04-09	Italy	5.4	13	3.62
7	2-WSE	Groningen	2008-10-30	Netherlands	3.1	1.2	3.04

Appendix A shows the comparison of the matched and original response spectra and time histories for each of the 7 triaxial sets. Figure 8 shows the average response spectra of the horizontal and vertical components, compared with the associated target spectra. As can be seen, the peak at 0.075 seconds on the horizontal and vertical target spectra has not been captured in the matched records but the average spectra are higher than 90% of the target spectra for all other periods, and so these records can reliably be used between 0.1 and 2 seconds. Alternatively, to extend the range of periods from PGA to 2s, the horizontal components provided herein could be further scaled by 1.15, and the vertical components by 1.3, in order to ensure that the average spectrum is always within 90% of the target spectrum.

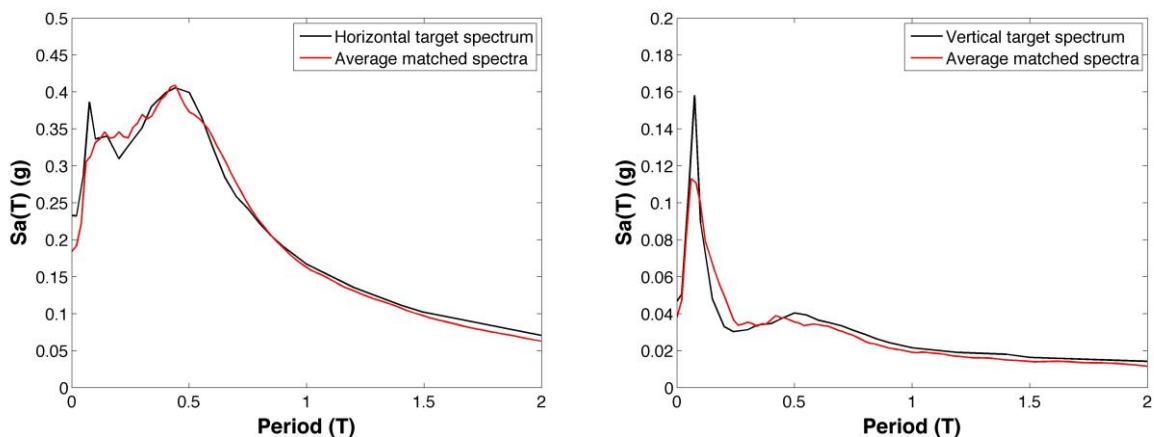


Figure 8. Comparison of horizontal and vertical target spectra and average matched spectra

## Concluding Remarks

This report summarises the selection and adjustment of a suite of acceleration time-histories that are consistent with the current estimates of seismic hazard at the location of greatest hazard in the Groningen field, for a return period consistent with the NEN-NPR design basis for CC1B buildings (dwellings). The final suite of acceleration time-histories consists of 7 tri-axial records, selected from recordings obtained in the Groningen field and throughout Europe and the Mediterranean, with durations consistent with those estimated for the controlling earthquake scenario identified from disaggregation of the hazard. The records have been scaled and spectrally matched to both horizontal and vertical target response spectra.

The current hazard estimates are based on seismological models and GMPEs that are undergoing continuous development towards the preparation of the 2016 Winningsplan. At the current stage of development, the GMPEs do not yet include the effects of soil nonlinearity, which inevitably results in conservative estimates of the stronger levels of ground motion. In developing the target spectra for the selected records an approximate adjustment was made in order to include generic (rather than Groningen-specific) soil nonlinearity, without any adjustment to the return period of the motions. When the v2 GMPEs, including field-specific nonlinear site amplification functions, are ready and the hazard estimates have been revised, this exercise will be repeated, possibly resulting in a revised suite of accelerograms. Furthermore, work is ongoing to estimate the distributions of component-to-component ratios of the Groningen recordings, which will be used to ensure the polarization of the ground motions can be captured in the set of acceleration time-histories, either by correcting the accelerograms presented herein (through the application of such factors, as noted above) or by matching a new set of records to two target horizontal spectra that account for the component-to-component variability. However, it is believed that the current suite of records is perfectly fit for purpose and appropriate for input to dynamic structural analyses.

We would like to invite all users to send any comments, corrections, feedback or suggestions to Jan van Elk ([Jan.Van-Elk@shell.com](mailto:Jan.Van-Elk@shell.com)) so that these considerations can be taken into account in subsequent revisions of this note and associated updates of the suite of accelerograms.

## References

- Akkar, S., M.A. Sandıkkaya & B.Ö. Ay (2014). Compatible ground-motion prediction equations for damping scaling factors and vertical-to-horizontal spectral amplitude ratios for the broader European region. *Bulletin of Earthquake Engineering* **12**(1), 517-547.
- Bommer, J.J., P.J. Stafford, B. Edwards, M. Ntinalexis, B. Dost & D. Kraaijpoel (2015). *Development of Version 1 GMPEs for response spectral accelerations and strong-motion durations*, Version 1, 16 March, 278 pp.
- Boore D.M. and Atkinson G.M. (2008). Ground-motion prediction equations for the average horizontal component of PGA, PGV and 5% damped PSA at spectral periods between 0.01s and 10.0s. *Earthquake Spectra* **24**(1), 99-138
- Hancock, J., J. Watson-Lamprey, N.A. Abrahamson, J.J. Bommer, A. Markatis, E. McCoy & R. Mendis (2006). An improved method of matching response spectra of recorded earthquake ground motion using wavelets. *Journal of Earthquake Engineering* **10**(special issue 1), 67-89.

Kempton, J.J. & J.P. Stewart (2006). Prediction equations for significant duration of earthquake ground motions considering site and near-source effects. *Earthquake Spectra* **22**(4), 985-1013.

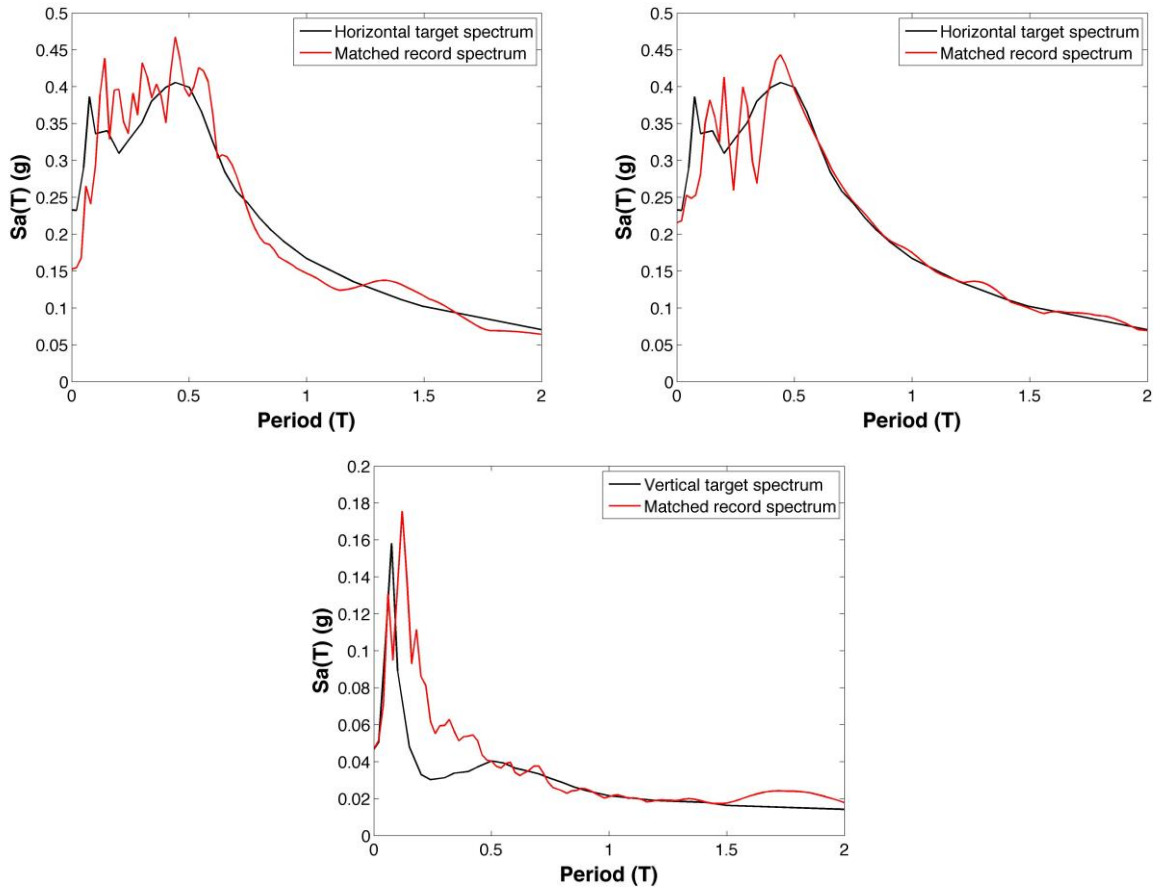
TNO (2013) *R12071: Safety considerations for earthquakes*, NEN Report, 19<sup>th</sup> December 2013.

Sandikkaya, M.A., S. Akkar & P.-Y. Bard (2013). A nonlinear site-amplification model for the next pan-European ground-motion prediction equations. *Bulletin of the Seismological Society of America* **103**(1), 19-32.

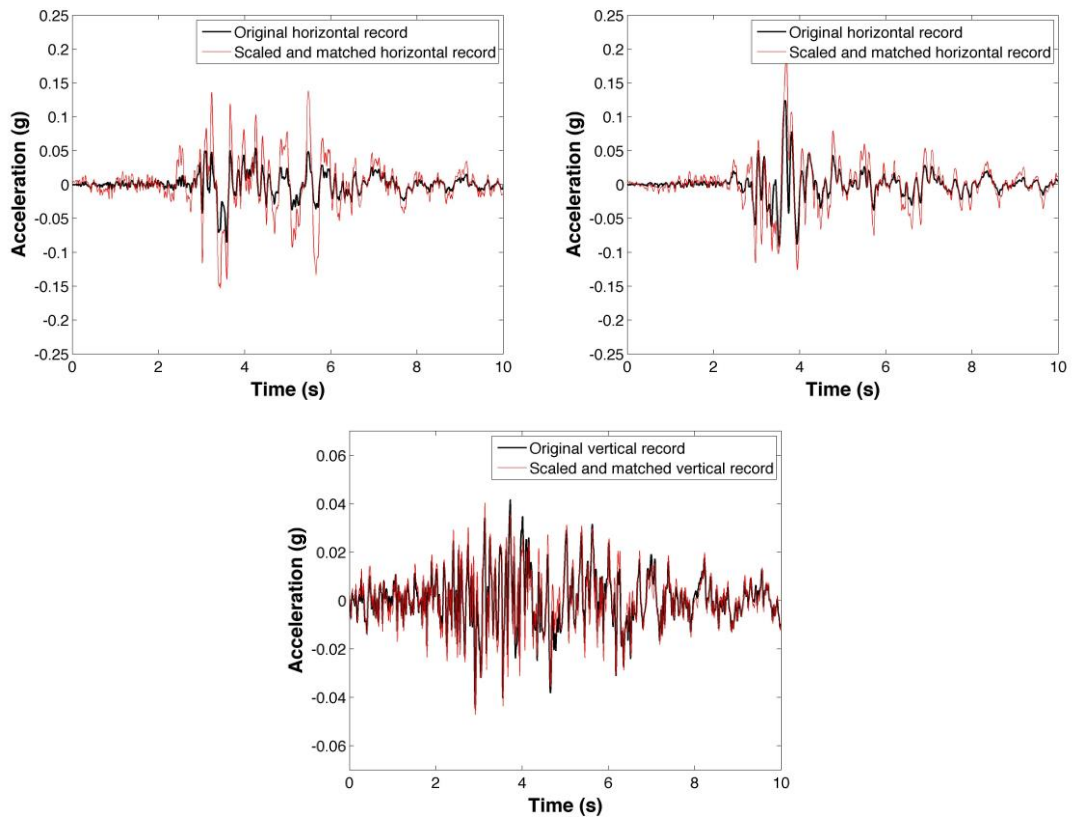
Seismosoft (2015) *SeismoMatch Version 2.1*, Available from URL: <http://www.seismosoft.com/downloads>

## Appendix A

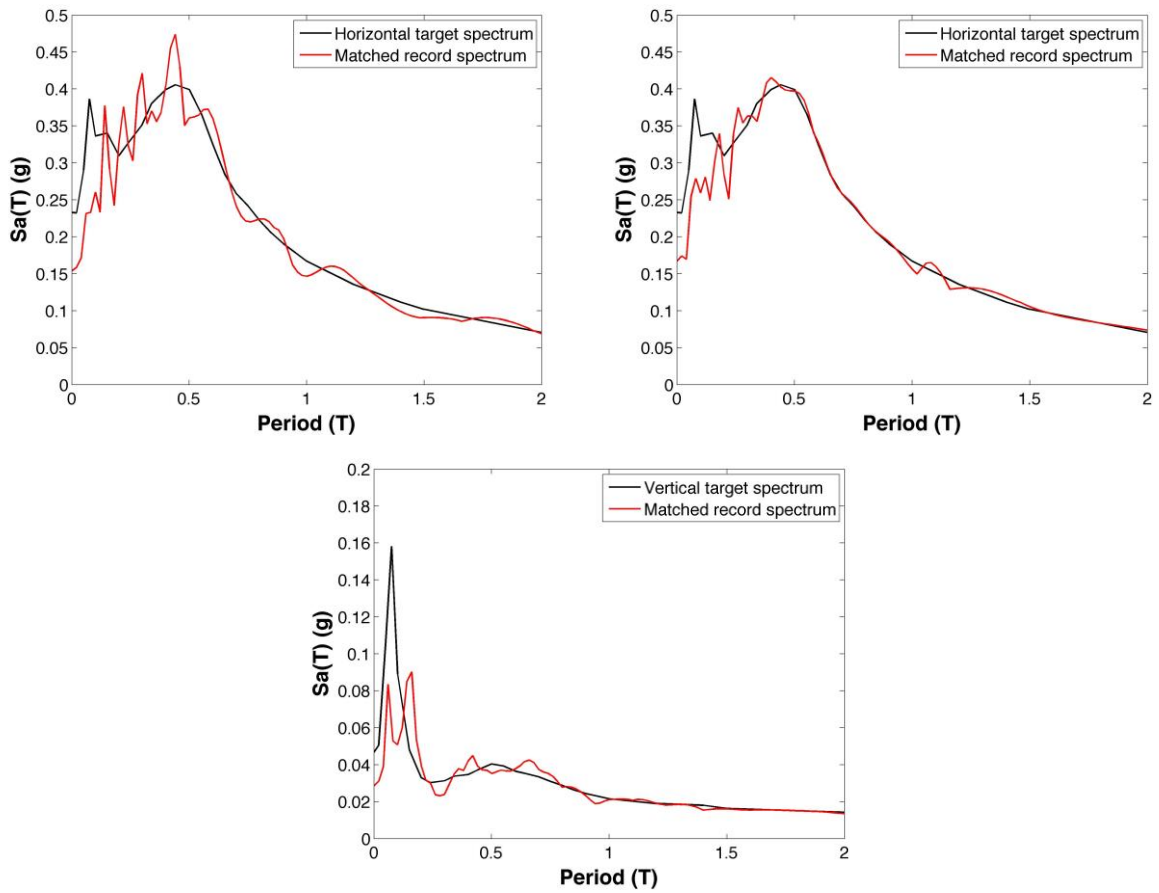
### Triaxial Set 1 Response Spectra



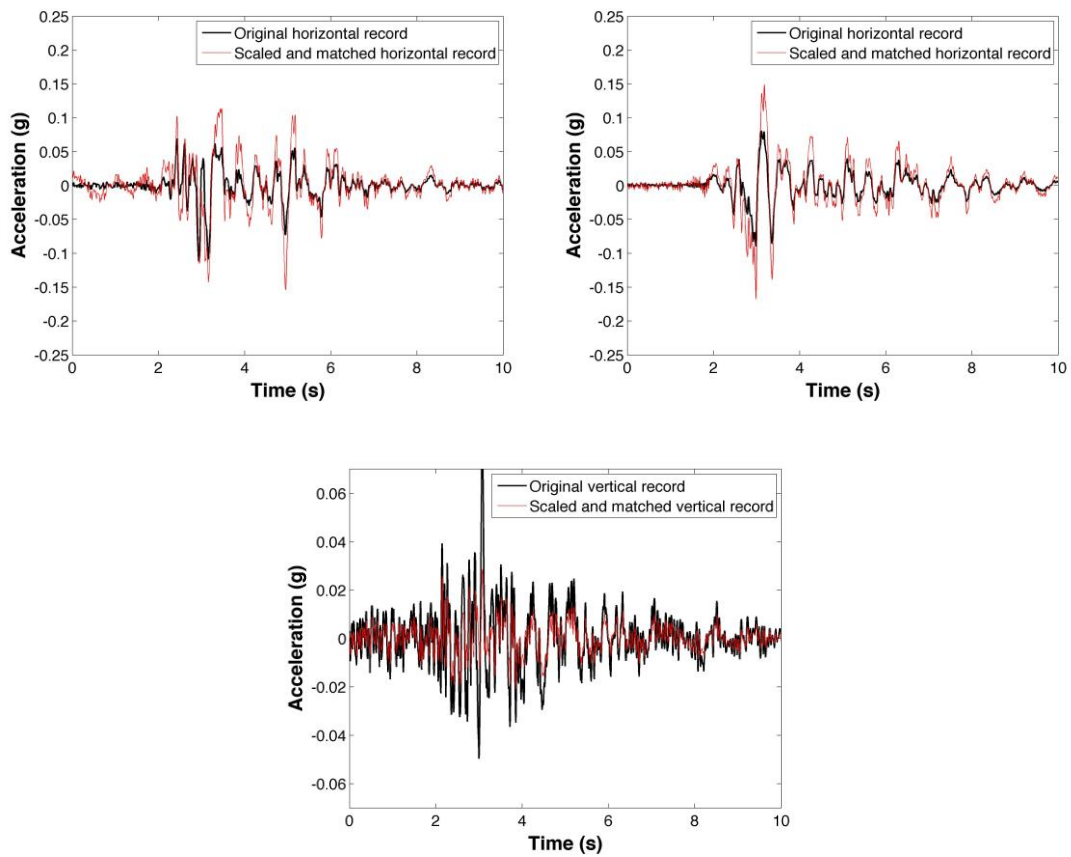
### Triaxial Set 1 Time Histories



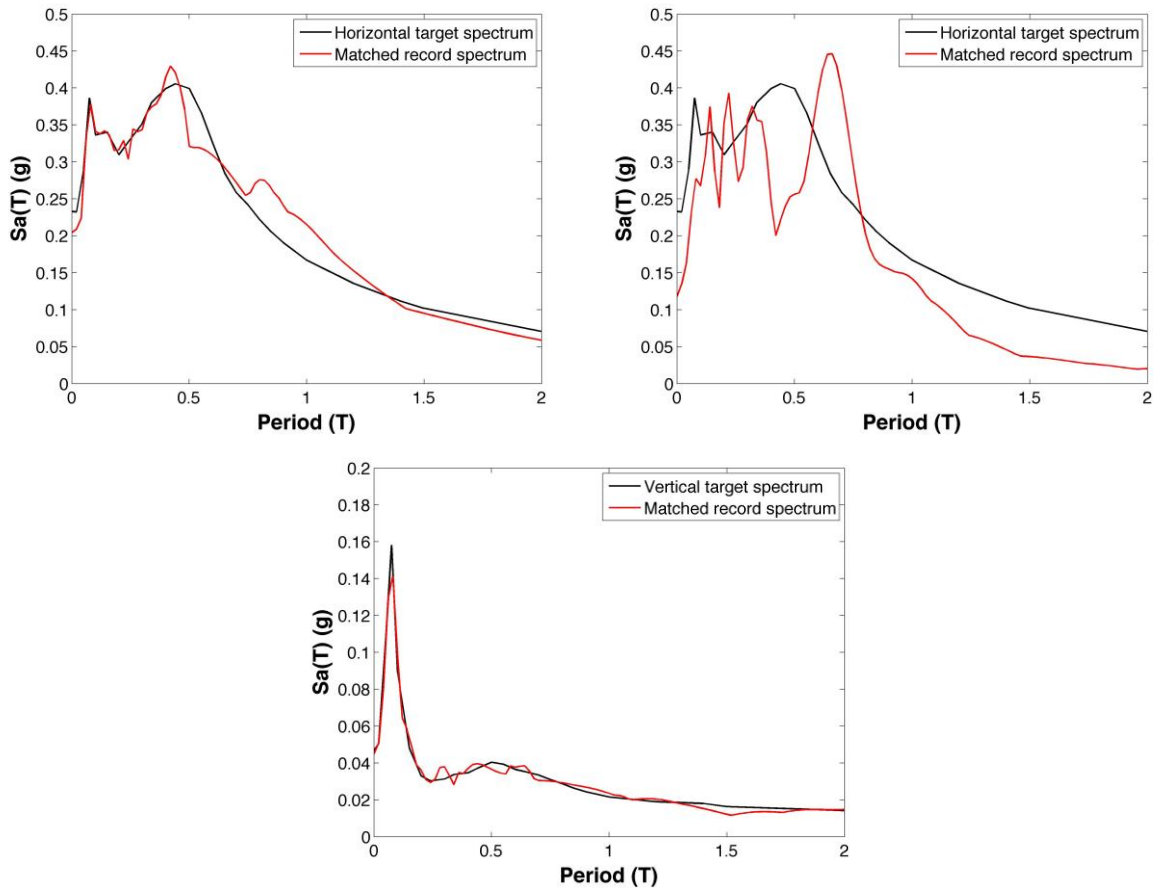
## Triaxial Set 2 Response Spectra



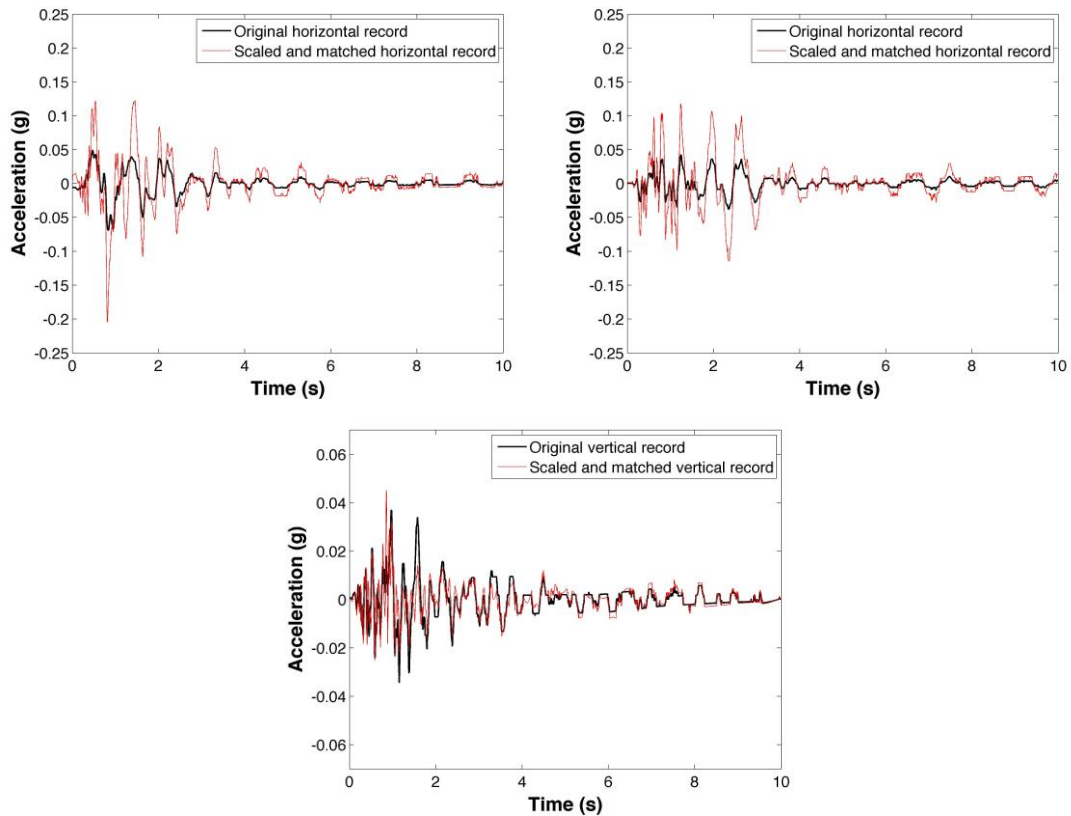
## Triaxial Set 2 Time Histories



### Triaxial Set 3 Response Spectra

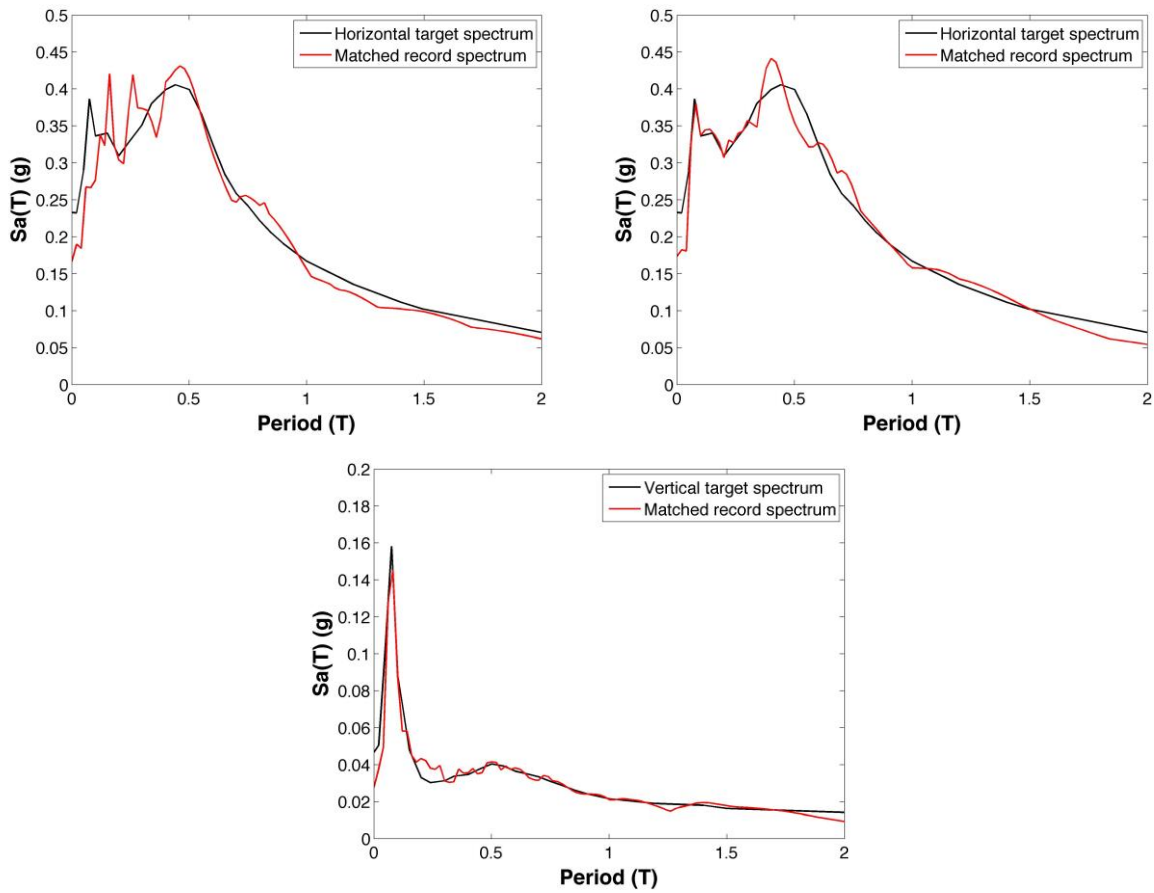


### Triaxial Set 3 Time Histories

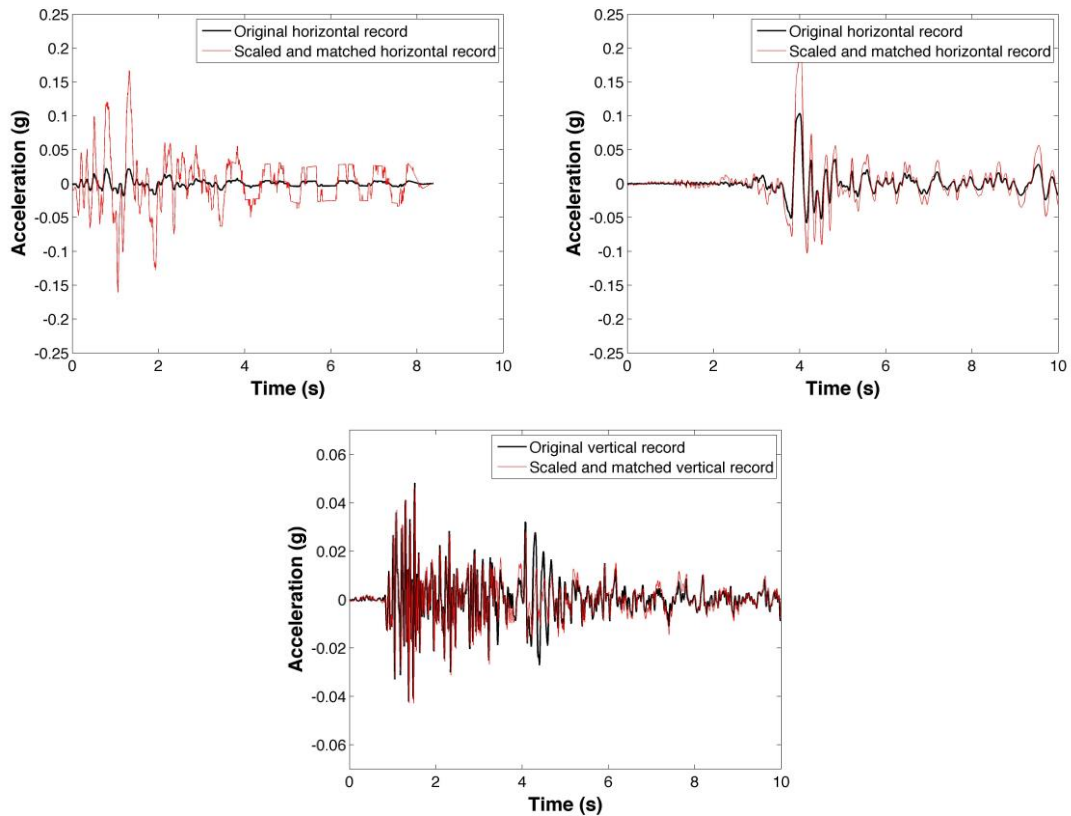


N.B. there is a strange signal in coda that will be investigated and may be replaced in v2.

## Triaxial Set 4 Response Spectra

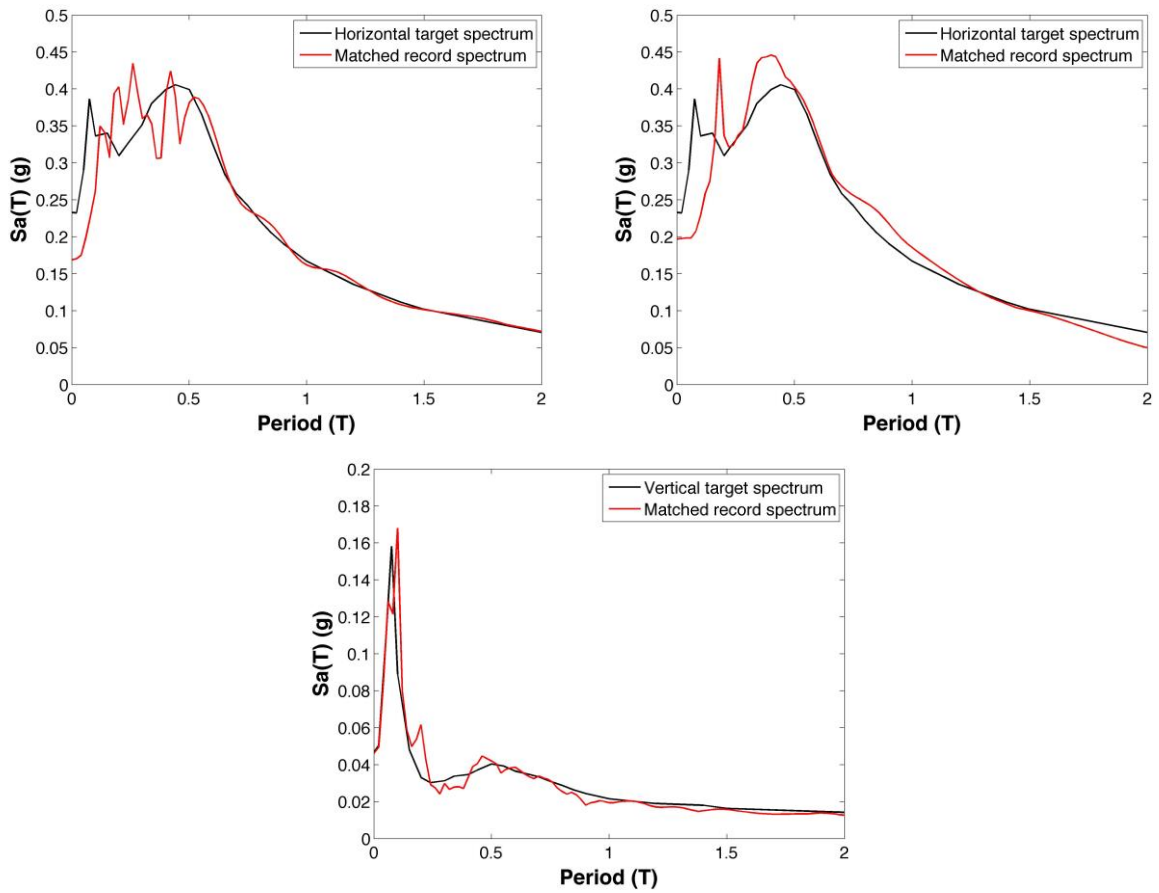


## Triaxial Set 4 Time Histories

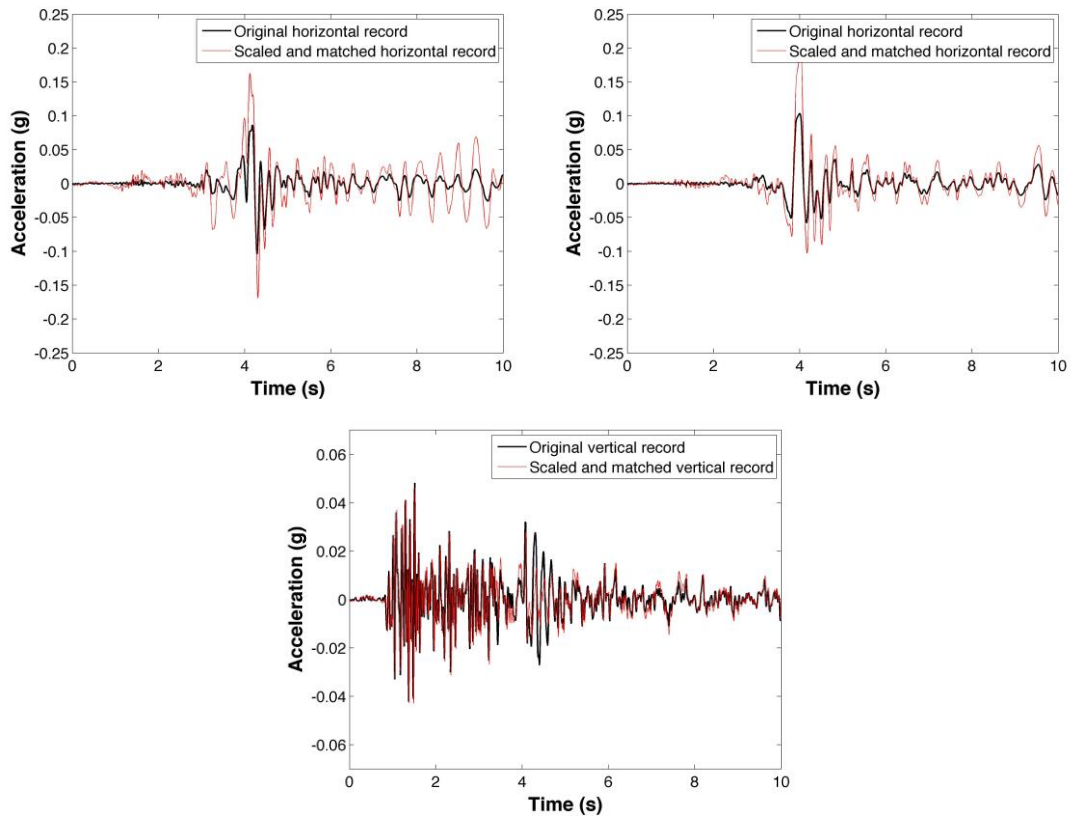


N.B. there is a strange signal in coda that will be investigated and may be replaced in v2.

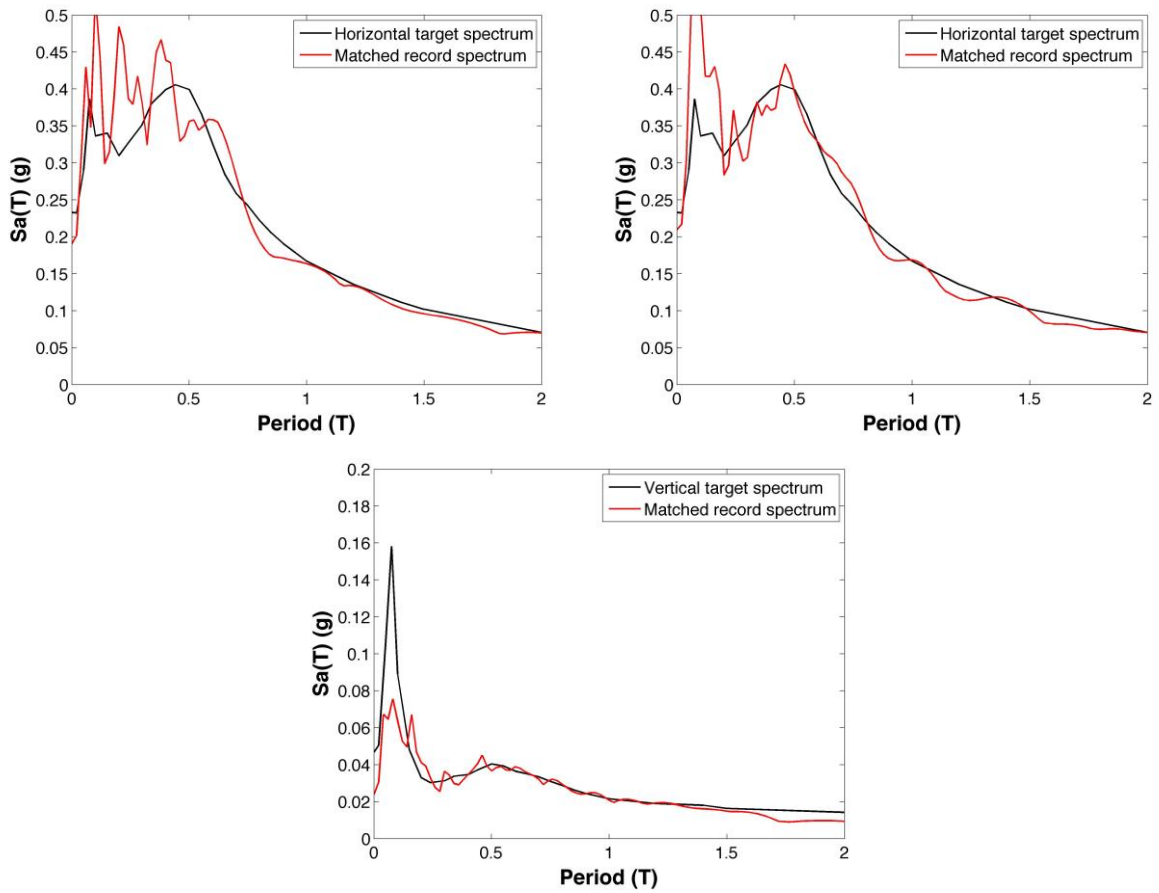
## Triaxial Set 5 Response Spectra



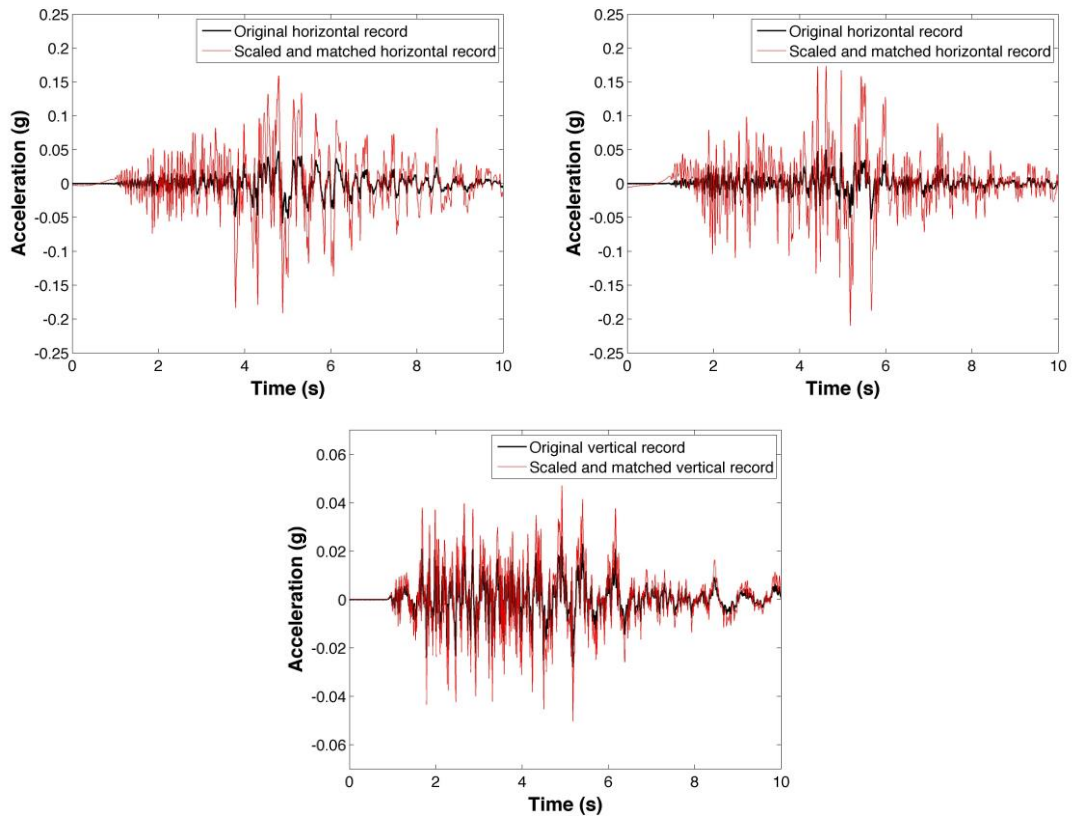
## Triaxial Set 5 Time Histories



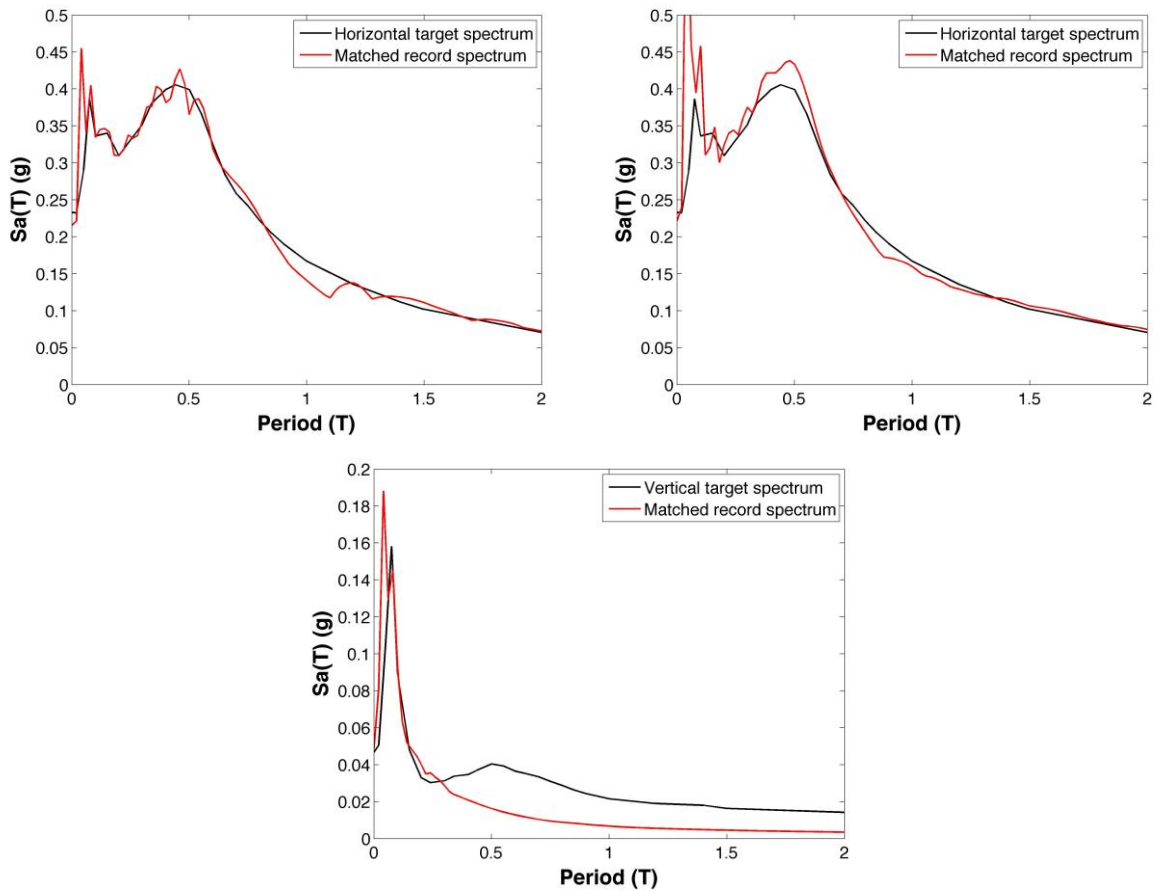
## Triaxial Set 6 Response Spectra



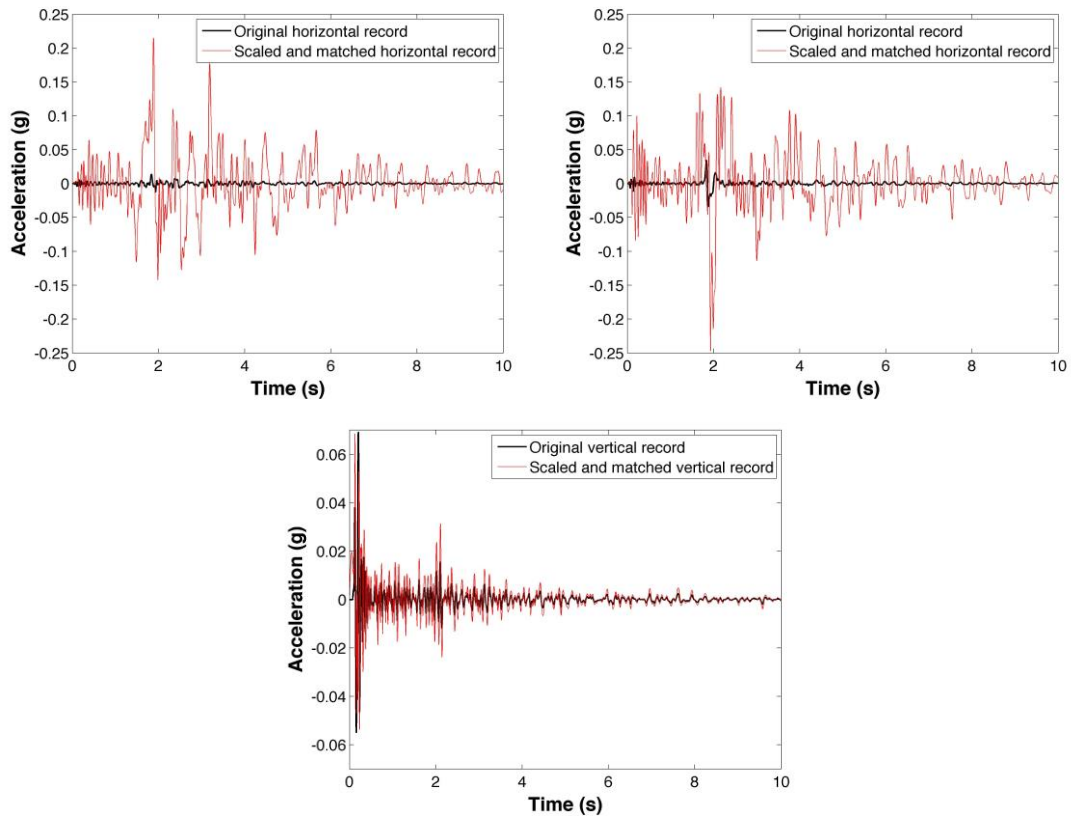
## Triaxial Set 6 Time Histories



## Triaxial Set 7 Response Spectra



## Triaxial Set 7 Time Histories



## **Appendix B-2**

### **Selection of Acceleration Time-Series for Shake Table Testing of Groningen Masonry Building at the EUCENTRE, Pavia**

# **Selection of Acceleration Time-Series for Shake Table Testing of Groningen Masonry Building at the EUCENTRE, Pavia**

Version: 1<sup>st</sup> August 2015

## **Scope**

As part of NAM's data acquisition and analysis programme to develop a seismic hazard and risk model for induced earthquakes in the Groningen gas field, dynamic tests are being performed on structural elements and a full-scale model of a masonry building typical of those encountered in the region. The purpose of this document is to document the selection and preparation of acceleration time-series for the shake table testing on the full-scale model that is scheduled for 10<sup>th</sup> September 2015.

This document is developed jointly by members of the Hazard & Risk Team (Bommer, Crowley, Pinho, Polidoro) and members of the Masonry Structures Group at the EUCENTRE (Magenes, Penna, Graziotti, Mandirola, Bracchi) to ensure that the motions provided for the testing are compatible with the requirements of the testing and also consistent with the seismic hazard in the field.

## **Testing Requirements**

The shake table tests will be performed as uniaxial dynamic loading of the structural model with the objective of ascertaining the ultimate capacity and failure mode of the building but without causing collapse (because of potential collateral damage to the laboratory). The structure is estimated to have a fundamental vibration period of 0.15 seconds in the direction of loading as determined from eigenvalue analyses. However, it is probably more appropriate to use the cracked vibration period of the structure, which has been estimated from bilinear approximations of the capacity curves from pushover analyses to be in the range of 0.25-0.33 s (Figure 1), depending on the assumed lateral force distribution. The yield capacity, in terms of spectral accelerations, has been estimated to be in range of 0.15-0.20g, which is a very important constraint in view of the requirement not to cause collapse. The yield displacement is estimated as 0.0025 m and the ultimate displacement capacity as 0.04 m (Figure 2).

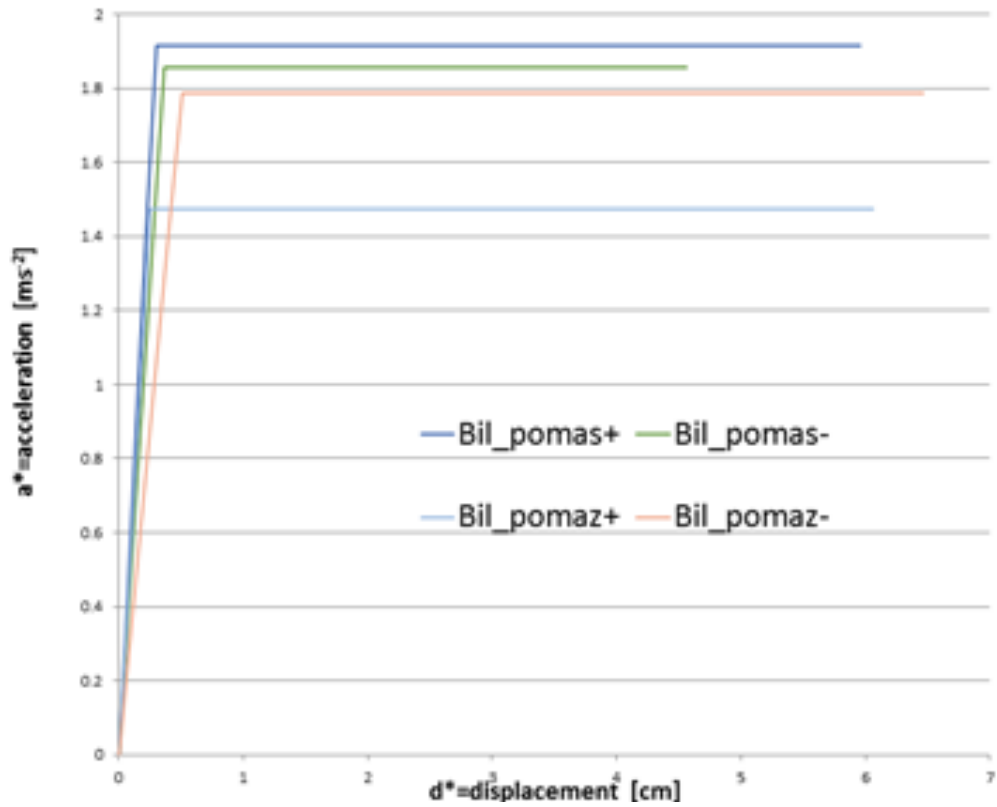


Figure 1. Bilinearised capacity curves for the masonry structure to be tested

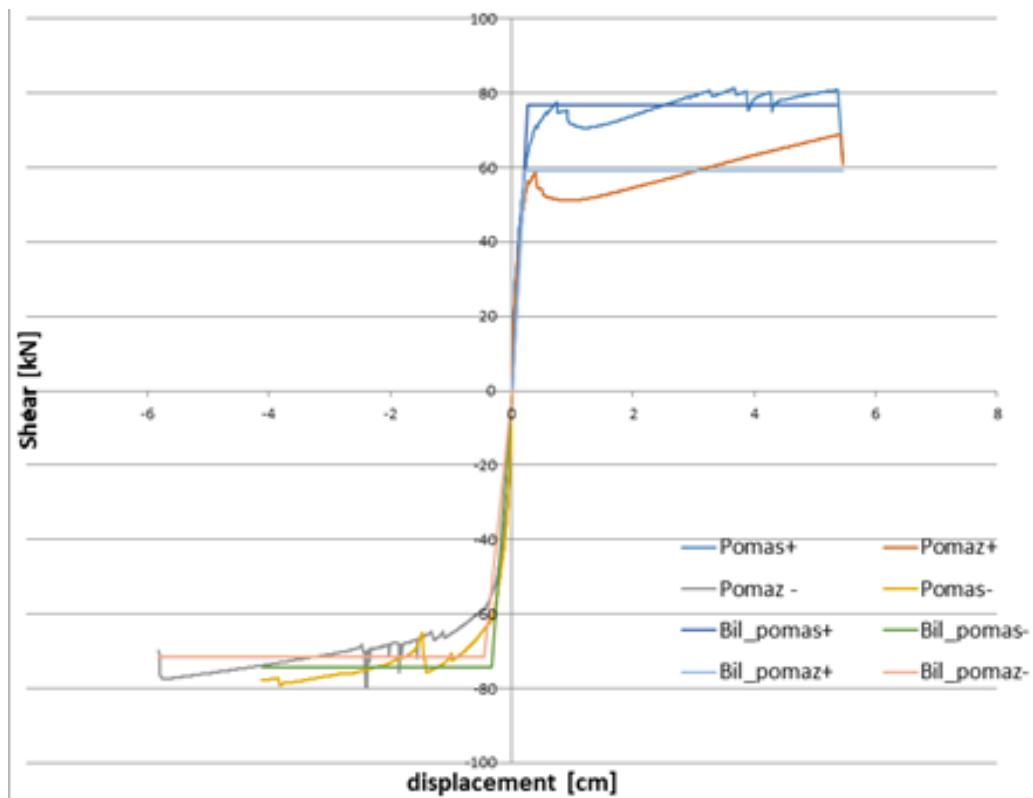


Figure 2. Pushover curves for the masonry structure

There are different requirements in terms of dynamic inputs for the testing:

1. Low-level motions with a broad frequency content for calibration runs
2. A series of realistic motions of increasing amplitude that will eventually lead to failure of the structure

For #1 it is understood that the EUCENTRE will use a generic white-noise signal. For #2, a fundamental choice is whether to use a single acceleration time-history that is scaled through various amplitude levels or to use a series of records that capture not only the increase of amplitude but also other features that may be expected with more severe loading cases. The EUCENTRE requests that no more than two or three records be provided because of the need to re-calibrate for each time-history and the dangers of accumulated damage due to repeated low-level excitation.

Since it is important to avoid total collapse of the structure during the test—or at least at a premature stage of the testing—it is important to estimate *a priori*, from element tests and/or numerical modelling, the intensity levels that would be expected to lead to catastrophic failure of the structure.

## Seismic Hazard Characteristics

In order to identify the controlling earthquake scenarios that dominate the hazard at different annual exceedance probabilities, the hazard was calculated by Dr Stephen Bourne of Shell for Loppersum (the village closest to the current location of highest hazard in the field, with RD coordinates of 245598 X ,594788 Y) using the V1 hazard model and a production period of 5-years (July 2016 to July 2021, consistent with the 2016 Winningsplan). The hazard was calculated in terms of the spectral accelerations at 0.01, 0.2, 0.5, 1 and 2 seconds (Figure 3). The hazard results at selected return periods are listed in Table 1. From the values in the table it can be immediately appreciated that for range of periods defined for the building, yielding can be expected even under the 50-year return period ground motions.

Table 1. Hazard results.

Return Period	Spectral Accelerations (g)				
	0.01 s	0.2 s	0.5 s	1.0 s	2.0 s
50	0.10	0.21	0.16	0.04	0.01
100	0.16	0.32	0.26	0.07	0.02
500	0.36	0.61	0.67	0.22	0.08
1,000	0.48	0.95	0.95	0.33	0.12
2,500	0.69	1.32	1.43	0.53	0.21
5,000	0.89	1.69	1.90	0.70	0.28

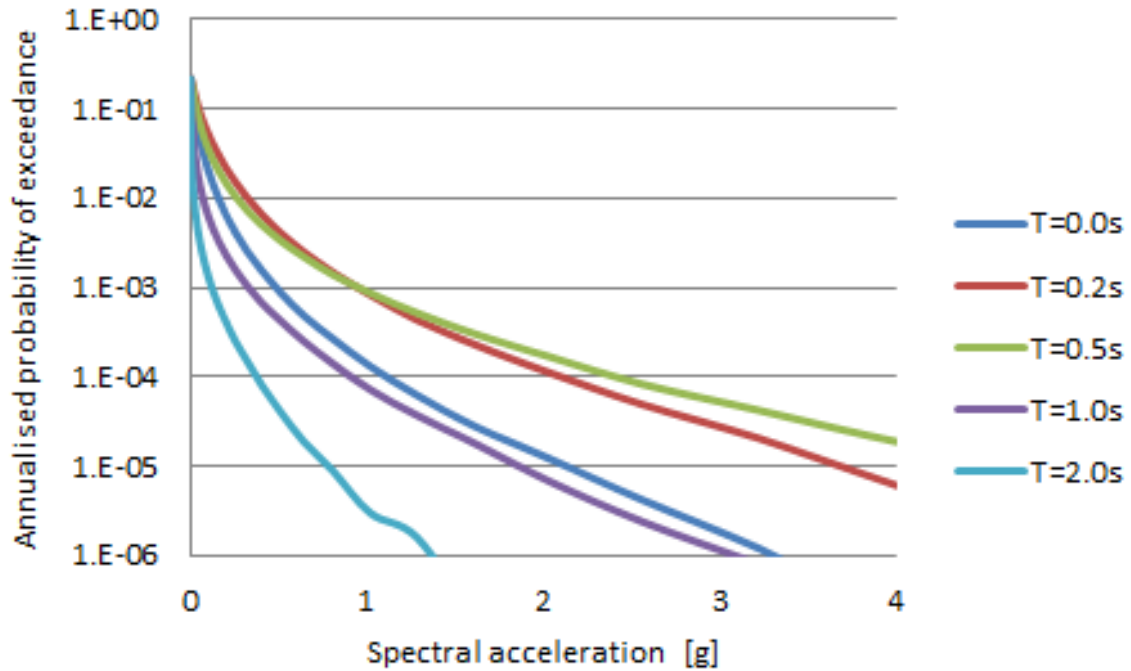


Figure 3. Mean seismic hazards for Loppersum

The hazard estimates were then disaggregated for return periods of 50, 100, 500, 1000, 2500 and 5000 years in terms of contributions by magnitude, distance and epsilon (number of standard deviations above the median prediction). The results show that for the location of highest hazard in the field, the dominant distance is not strongly sensitive to either oscillator period or return period (Figure 4). Although the disaggregation is artificially truncated at a minimum epicentral distance of 3 km, it is clear that for all response periods and return periods the dominant contribution comes from very short distances. This observation simplifies the investigation of the problem because the only parameters of interest become magnitude and epsilon. The disaggregation in terms of contributions by magnitude and epsilon bins are presented graphically in Figures 5 and 6, respectively, and summarised in Table 2. The recurrence of certain values, particularly for epsilon, reflect the resolution at which the disaggregations are performed and the values may therefore be interpreted as indicative approximations rather than exact to three decimal places.

The patterns observed in the results are consistent with expectations, with the values of both the modal magnitude and epsilon increasing with the return period. Additionally, there is an increase in the modal magnitude with the oscillator period. This latter observation highlights the importance of taking into account the natural period of vibration of the structure being tested, although the modal magnitude is more sensitive to return period than to oscillator period.

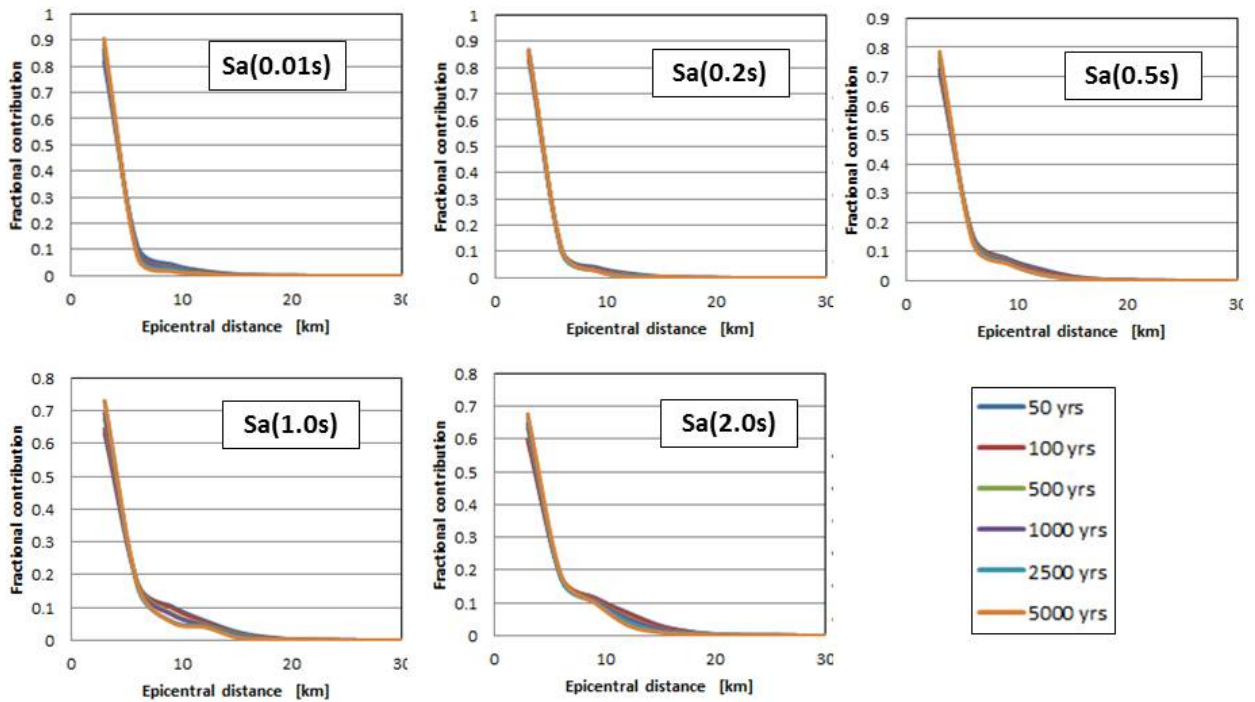


Figure 3. Disaggregation plots for hazard contributions by distance (the truncation at 3 km is unintentional and a result of the software originally being coded for hypocentral distance)

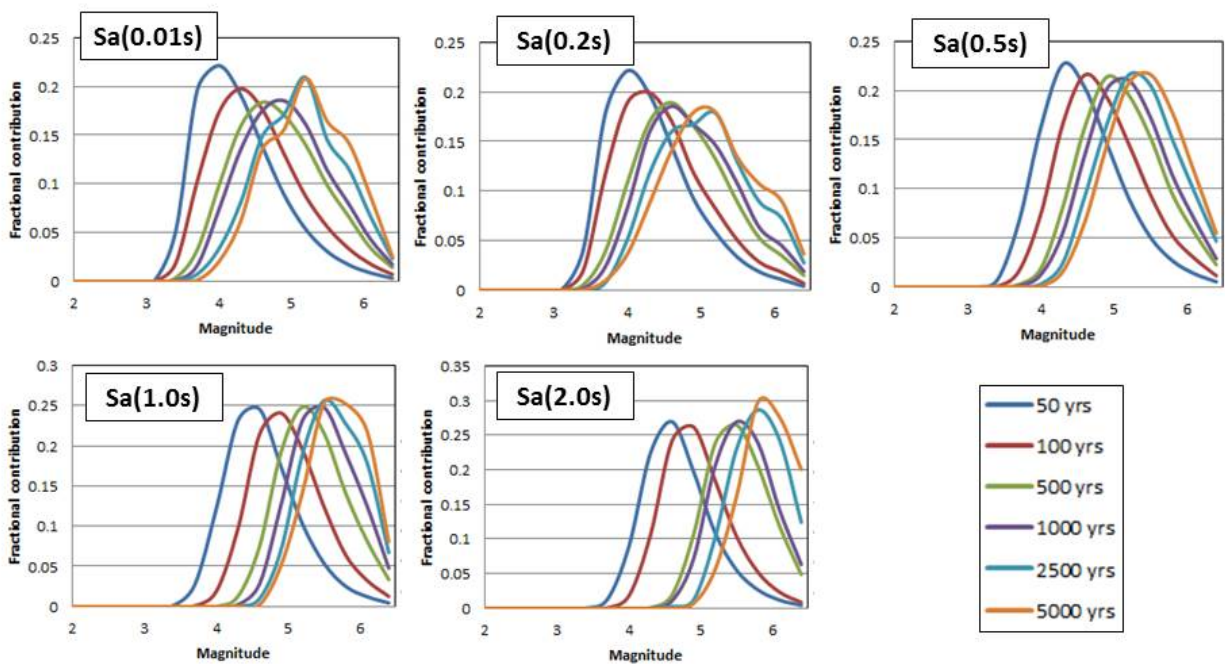


Figure 5. Disaggregation plots for hazard contributions by magnitude

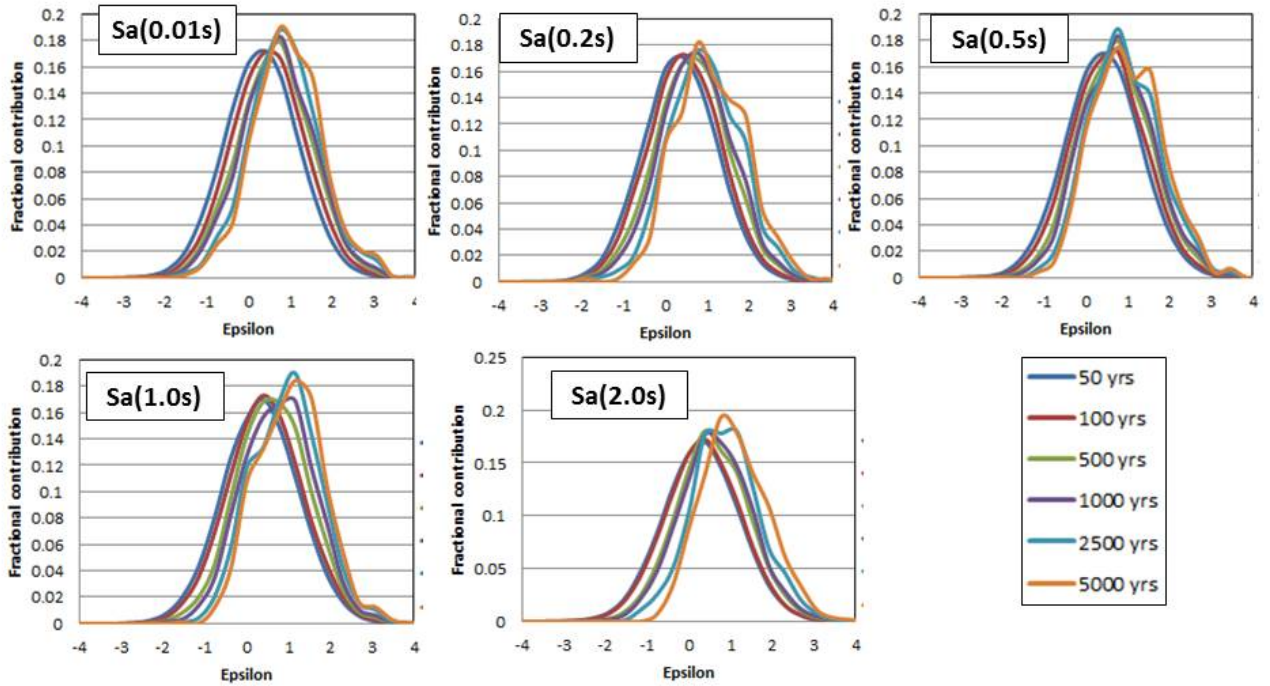


Figure 6. Disaggregation plots for hazard contributions by epsilon

Table 2. Modal contributions of magnitude and epsilon

Return Period	0.01 s		0.2 s		0.5 s		1.0 s		2.0 s	
	M	$\epsilon$	M	$\epsilon$	M	E	M	$\epsilon$	M	$\epsilon$
50	4	0.384	4	0.384	4.3	0.384	4.6	0.384	4.6	0.384
100	4.3	0.384	4.3	0.384	4.6	0.768	4.9	0.384	4.9	0.384
500	4.6	0.768	4.6	0.768	4.9	0.768	5.2	0.384	5.5	0.384
1,000	4.9	0.768	4.6	0.768	5.2	0.768	5.5	1.151	5.5	0.384
2,500	5.2	0.768	5.2	0.768	5.2	0.768	5.5	1.151	5.8	1.151
5,000	5.2	0.768	5.1	0.768	5.5	0.768	5.5	1.151	5.8	0.768

An important observation concerns the epsilon values, which in some cases seem to exhibit somewhat erratic patterns. This appears to be related to convergence issues, as in the case of Sa(2s) and the unusually high value for the 2,500-year return period. As can be appreciated from Figure 4, the disaggregation curve shows a bi-modal behaviour from which it might be inferred that a more appropriate value might lie between the two peaks (which would yield a value similar to that for the 5,000-year return period).

A point worthy of note here is that it has been shown that there is a marked negative correlation between the residuals of spectral accelerations and residuals of durations for the Groningen motions. This fact might allow the selection of a reduced number of accelerograms—which could then be scaled in amplitude as needed—since while the modest increases in modal magnitudes as the return periods increase from 50 to 5,000 years would result in motions of longer durations, this would be at least

partially offset by the smaller durations resulting from the negative correlation coupled with the positive epsilons on accelerations.

A final point that needs to be noted is that the accelerations in Table 1 and the magnitudes in Table 2, especially for the longer return periods, are likely to be over-estimates of the ‘true’ values as a result of the absence of soil non-linearity in the current GMPEs. This means that in reality the increase in dominant magnitude values with increasing return period may actually be smaller than indicated by the values in Table 2.

### Selection and Scaling/Matching Criteria

As already noted, the data in Table 1 show that the yield capacity of the structure is likely to be reached under the action of ground motions with a return period of 50 years, from which it is concluded that only the shorter return periods are relevant. Using the same non-linear static procedures (NSP) that were deployed for the derivation of the V1 fragility functions (Crowley *et al.*, 2015b), it is estimated that under the action of the 50-year UHS, the displacement demand is 0.0047 m—which means that the structure will be responding inelastically—with a corresponding effective period of 0.3 seconds. We make the assumption that the disaggregation information for the acceleration response at 0.2 seconds can be used as a surrogate in this case, which yields a dominant (modal) magnitude of 4.0 and an epsilon of about 0.4 (Table 2). Under the action of the 500-year UHS, the structure has an effective period of 0.5 seconds and displacement demand of 0.034 m, which is a little below the estimated ultimate capacity for the structure. The disaggregation of this scenario yields a modal magnitude of 4.9 and an epsilon of about 0.8 (Table 2). These calculations thus yield two suites of parameters that can be used to define the selection and scaling criteria for the records, as summarised in Table 3.

Table 3. Characteristics of scenarios for record selection

Scenario	Return Period (years)	$T_{\text{eff}}$ (s)	M	$R_{\text{epi}}$ (km)	Epsilon
1	50	0.3	4.0	0.0	0.38
2	500	0.5	4.9	0.0	0.77

The next step is to generate target response spectra for these scenarios. Since the records will be scaled to different amplitudes for input to the shake table tests, it is the spectral shape rather than the absolute amplitudes that are of particular interest. For this reason, it is considered sufficient to generate the scenario spectra using only the central V1 GMPE rather than the weighted average of the three models (lower, central and upper; Bommer *et al.*, 2015a) as used in the hazard calculations presented earlier. Using the full suite of coefficients at multiple response periods

together with the interpolated sigma values, scenario spectra are generated for both scenarios in Table 3. Additionally, using the period-to-period correlations of Akkar *et al.* (2014b), the conditional mean spectra, or CMS (Baker & Cornell, 2006; Baker, 2011), are also generated for both scenarios, conditioned in each case on the spectral acceleration at the effective period. It should be noted that for the scenario of zero epicentral distance, there is no adjustment to be made to the sigma value for geometrical effects of the fault rupture. These four spectra are illustrated in Figure 7. The CMS are presented for interest but in view of the inherent uncertainties in the estimated vibrations periods for the structure, it is considered more appropriate to use the scenario spectra as the targets.

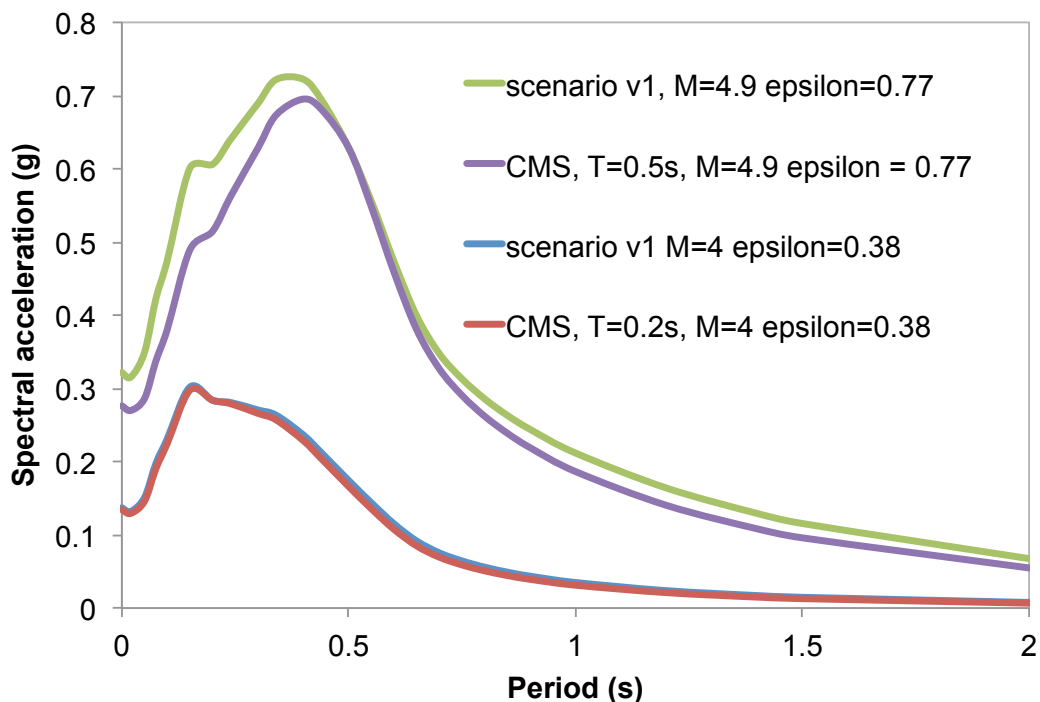


Figure 7. Scenario and conditional mean spectra for the scenarios in Table 3.

An acknowledged shortcoming of the V1 GMPEs is that they only model linear site response; even though the magnitudes of the controlling scenarios in Table 3 are modest, the short source-to-distances mean that the motions may be strong enough to induce non-linear response in the soft soils that cover most of the Groningen field, particularly in the northern parts. Two different approximate adjustments for non-linearity are made by using available non-linear site amplification functions. For both procedures the linear response is firstly removed to transform the motion to some reference baserock horizon, and then the non-linear site amplification functions are applied to bring the baserock motions back to the surface.

In particular, the first approach is the same followed by Crowley *et al.* (2015a) to generate suites of records for structural analyses of Groningen buildings. The

reference rock spectrum is obtained by removing the linear amplification from the v1 linear amplified response spectra according to Sandıkkaya *et al.* (2013). Once the reference spectral acceleration values have been estimated, the nonlinear site amplification term calculated with the same model (Sandıkkaya *et al.*, 2013) is used to define the nonlinear amplified response spectra.

The second approach instead, starting from the v1 linear amplified response spectra, adopts the suite of non-linear site response amplification functions derived for the ground surface at the Groninger Forum site as part of a site-specific assessment of earthquake loads (Bommer *et al.*, 2015b). The amplification function (AF) is defined as in the Equation 1 where  $f_1$ ,  $f_2$  and  $f_3$  are parameters (Bommer *et al.*, 2015b),  $S_{a,rock}$  is the baserock acceleration (g) and  $\varepsilon$  is the zero-mean random variable with standard deviation  $\sigma_{\ln AF}$ .

$$\ln AF = f_1 + f_2 \cdot \ln \left( \frac{S_{a,Rock} + f_3}{f_3} \right) + \varepsilon \quad (1)$$

As in the previous formulation the linear amplification function is represented by the parameter  $f_1$ , the reference rock spectra is obtained by simply dividing the v1 linear spectral accelerations by the exponent of  $f_1$ . Hence, Equation 1 is used to calculate the nonlinear amplified response spectra.

Figure 8 and 9 show the v1 linear amplified response spectra and the nonlinear amplified response spectra (obtained by following the two different approaches) calculated for each scenario respectively. When the second approach is used, nonlinear amplified response spectra are calculated for the two different soil profiles (5a and 6S) described in Bommer *et al.* (2015b).

Given that the Groninger Forum nonlinear response spectra are smoother and are more conservative at longer periods of vibration, and the two soil profiles produce similar results, it has been decided to use their mean, also shown in the same figures, as the target spectra for the record selection and matching. These target spectra are provided in the Excel file appended to this document.

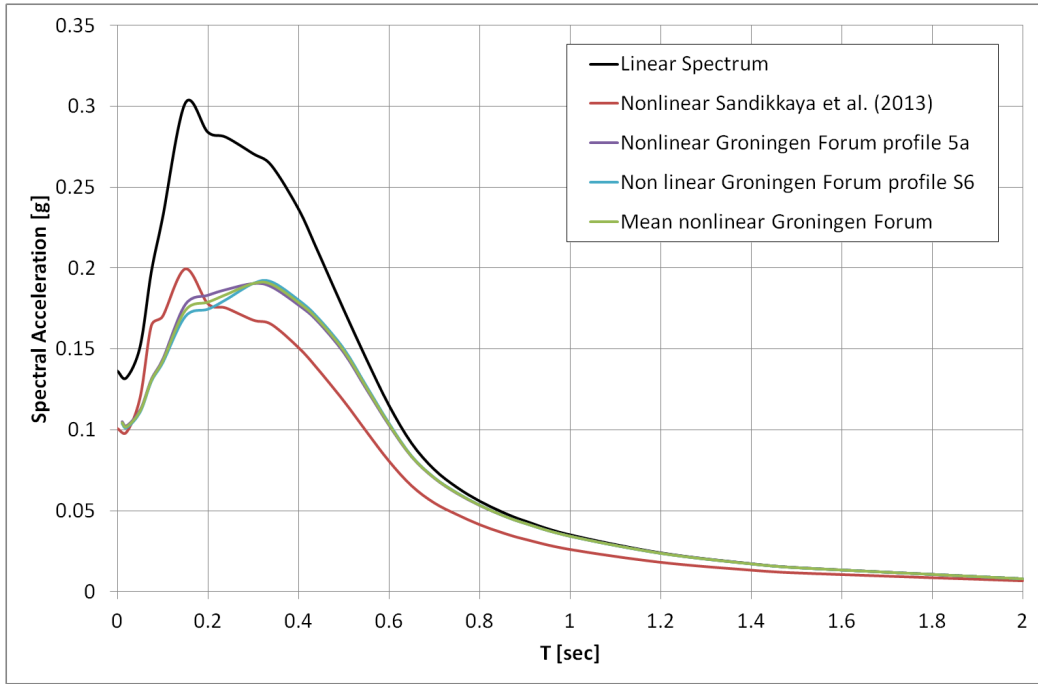


Figure 8. Nonlinear amplified spectra for the scenario 1 based on the Sandikkaya *et al.* (2013) and the non-linear site response amplification functions derived for the ground surface at the Groninger Forum site.

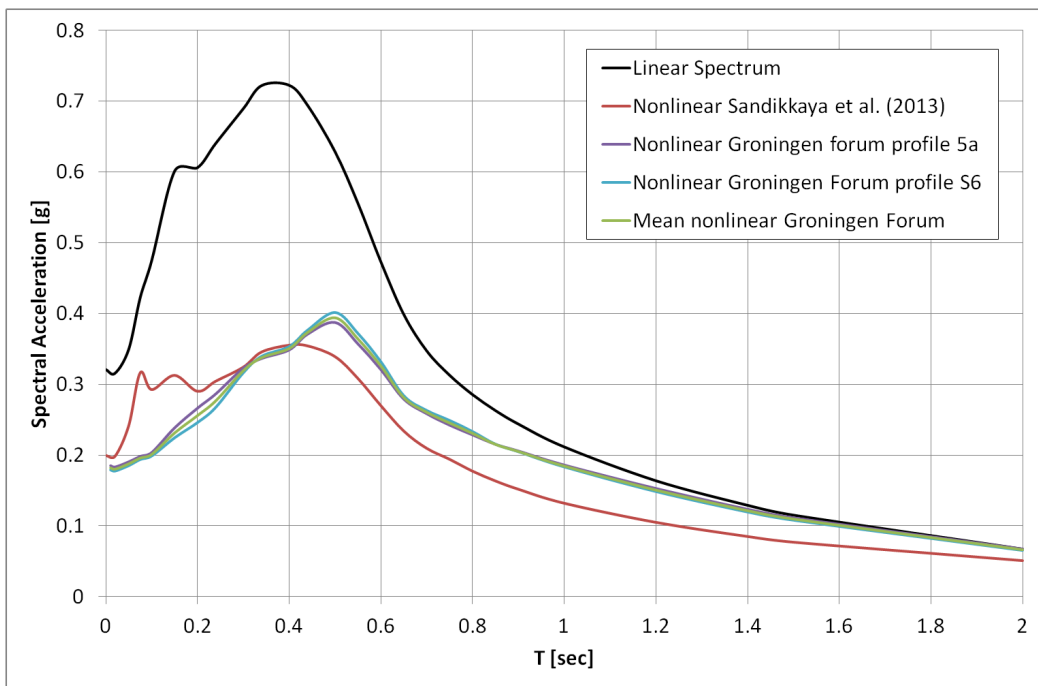


Figure 9. Nonlinear amplified spectra for the scenario 2 based on the Sandikkaya *et al.* (2013) and the non-linear site response amplification functions derived for the ground surface at the Groninger Forum site.

A final consideration in defining the selection criteria is the duration of the ground motion. For the V1 hazard and risk modelling, it was concluded that the predictive equation of Kempton & Stewart (2006) for the significant duration based on the 5-75% accumulation of Arias intensity yielded acceptable approximations to the Groningen data when applied, in the CBL format, with an assumed basin depth ( $Z_{1.5}$ ) of 600 m and an assumed  $V_{S30}$  of 200 m/s;  $R_{rup}$  is approximated by  $R_{hyp}$ , which for the scenarios in Table 3 is 3 km. Equation 2 illustrates the formulation adopted to calculate the duration for the two different scenarios.

$$\ln(D_s) = \ln \left[ \frac{\left( \frac{\exp(6.02)}{10^{1.5M+16.05}} \right)^{\frac{1}{3}}}{1.568 \times 10^7} + 0.07 \cdot R_{rup} + 2.73 - 0.0013(V_{S30}) - 0.00075(Z_{1.5}) \right] \quad (2)$$

However, it was noted by Bommer *et al.* (2015a) that this model does overestimate the durations of the Groningen motions at very short distances, which is a pertinent observation for this application. Moreover, a negative correlation was found between the residuals of spectral acceleration from the V1 GMPEs and the residuals of duration with respect to this adopted model (Bommer *et al.*, 2015a); following the results of Bradley (2011), the correlation coefficient for spectral acceleration at 0.2 s can be used as a substitute for that at 0.3 seconds. Table 4 summarises the calculated  $D_{S5-75}$  values.

Table 4. Calculated durations for the two design scenarios

Scenario	Median $D_{S5-75}$	$\rho[D_{S5-75}, Sa(T_{eff})]$	$\epsilon_{D_{S5-75}}$	$\sigma_{D_{S5-75}}$	Conditional mean $D_{S5-75}$
1	2.25	-0.316	-0.12	0.53	2.11
2	2.28	-0.392	-0.30	0.53	1.96

Noting the observation that at short distances, the Kempton & Stewart (2006) model tends to overestimate durations for small-magnitude Groningen earthquakes, the values in the final column of Table 4 may be treated as upper bounds.

### Selection, Scaling and Matching of Acceleration Records

A pre-selection of records from the NGA database (<http://ngawest2.berkeley.edu>) has been undertaken by identifying horizontal components that have a 5-75% significant duration lower than the conditional mean value defined in Table 4, that is 2.11s for scenario 1 and 1.96s for scenario 2, ensuring that the maximum usable period is greater than or equal to 0.5 seconds.

Using this reduced set of waveforms, the final selection is made by linearly scaling the records to minimize the difference with respect to the target horizontal spectra, across the 0.2 to 0.4 second period range for scenario 1 and 0.3 to 1 second period range for scenario 2. The absolute sum of squared errors (SSE) is used to quantify the match between the response spectral ordinates of the records and the target spectrum over the period range of interest. Hence, the waveforms have been ordered in terms of SSE and the top five records with the lowest SSE values have been selected for the spectral matching.

In order to include a recording from the Groningen field for scenario 1, the database used to develop the v1 GMPEs (Bommer *et al.*, 2015a) has been used. Also in this case a pre-selection of records has been made by identifying horizontal components that have a 5-75% significant duration of less than 2.11s. Hence, the same procedure of linear scaling is applied and the waveforms have been ordered in terms of SSE. The first five records with the lowest SSE plus the record with the lowest SF have been selected for the spectral matching.

Once the horizontal components from the two different databases have been selected for each scenario, accelerograms have been linearly scaled and then spectrally matched to the target horizontal spectra using the spectral matching algorithm described in Hancock *et al.* (2006) and embedded within the SeismoMatch software (Seismosoft, 2015). To avoid dramatic modifications to the frequency content of the original records, a maximum of 30 iterations have been applied in the matching algorithm.

After matching, for scenario 1 two recordings from the NGA database and one from the Groningen database having the best match over a wide period range have been selected, whilst for scenario 2 the top three recordings from the NGA database with the lowest SSE values have been chosen.

Figures 10 and 11 show the target and matched response spectra for the selected recordings, for scenario 1 and 2 respectively, whilst Figures 12 and 13 show the comparison of the original and the scaled/matched time-histories.

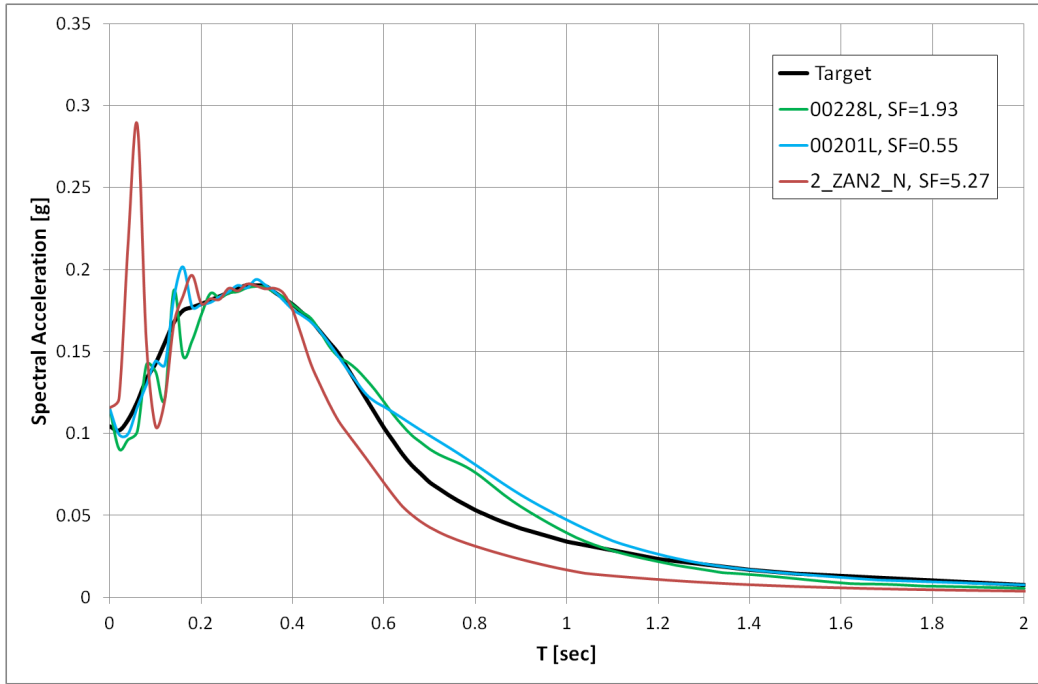


Figure 10. Comparison of target spectrum and matched spectra for scenario 1.

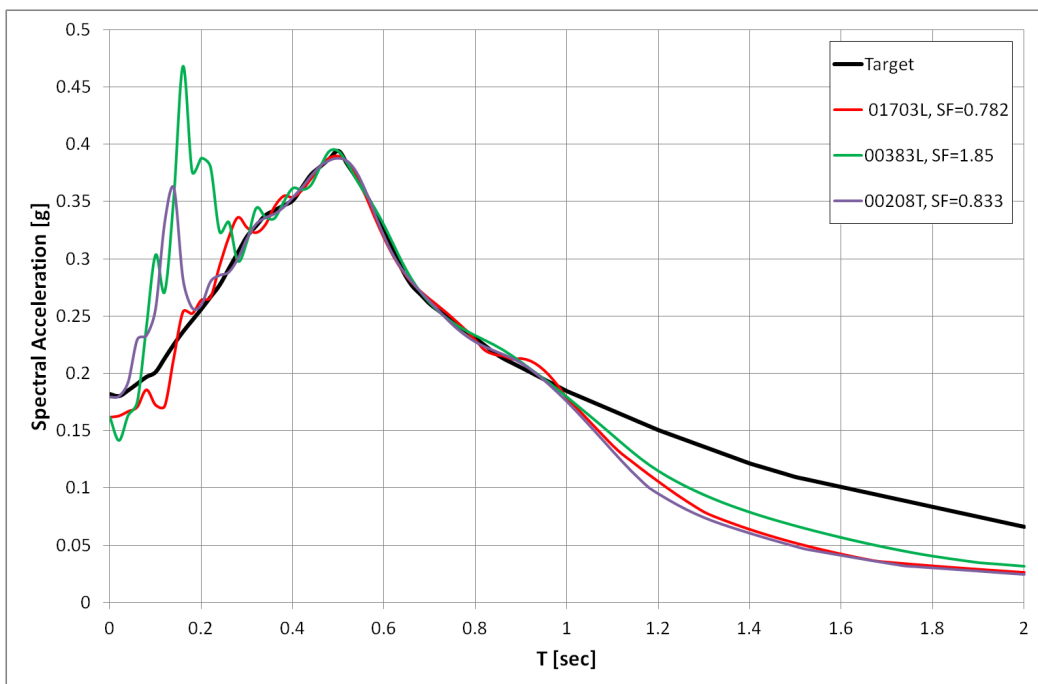


Figure 11. Comparison of target spectrum and matched spectra for scenario 2.

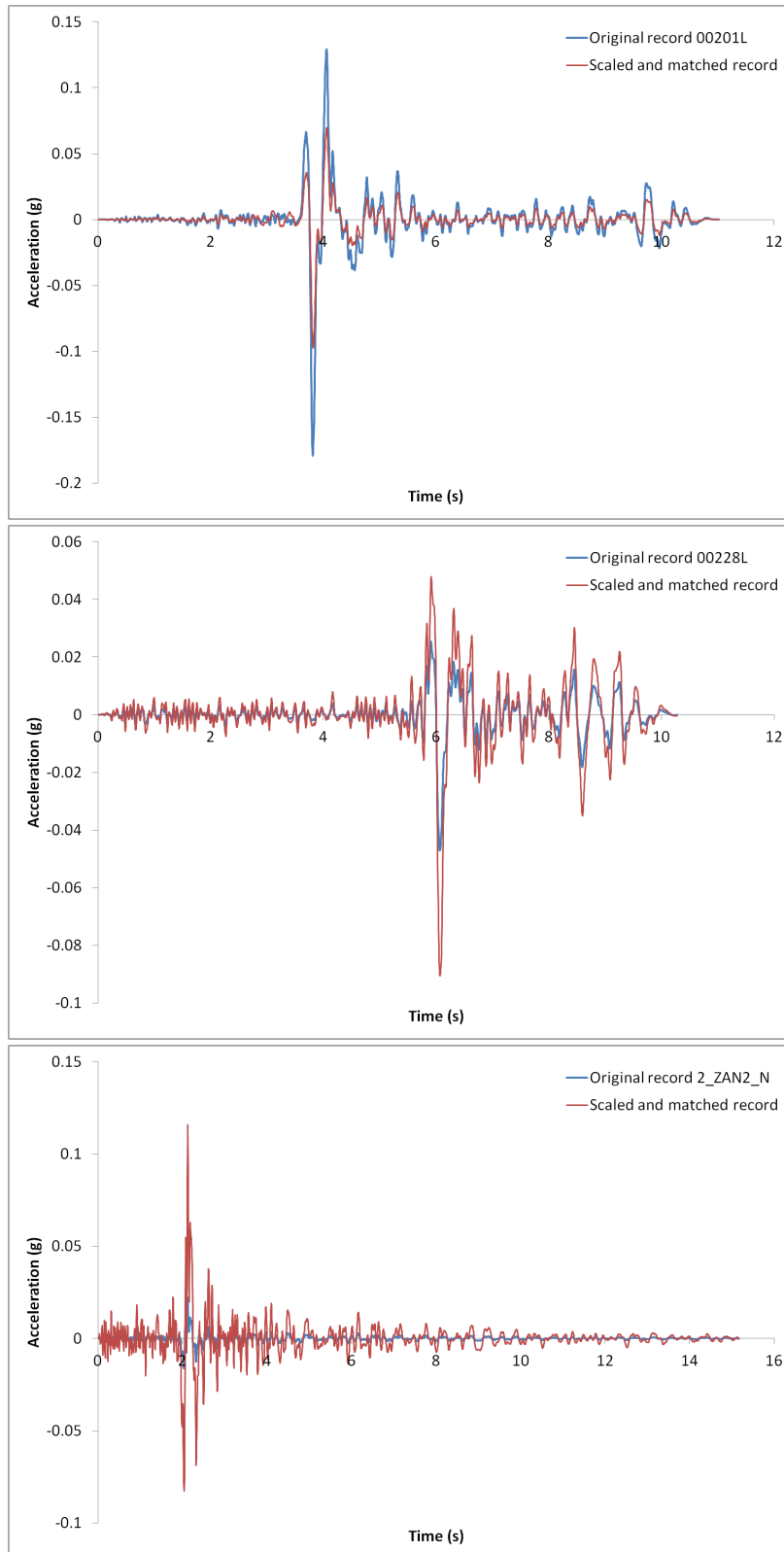


Figure 12. Comparison between the original and scaled and matched records for scenario 1.

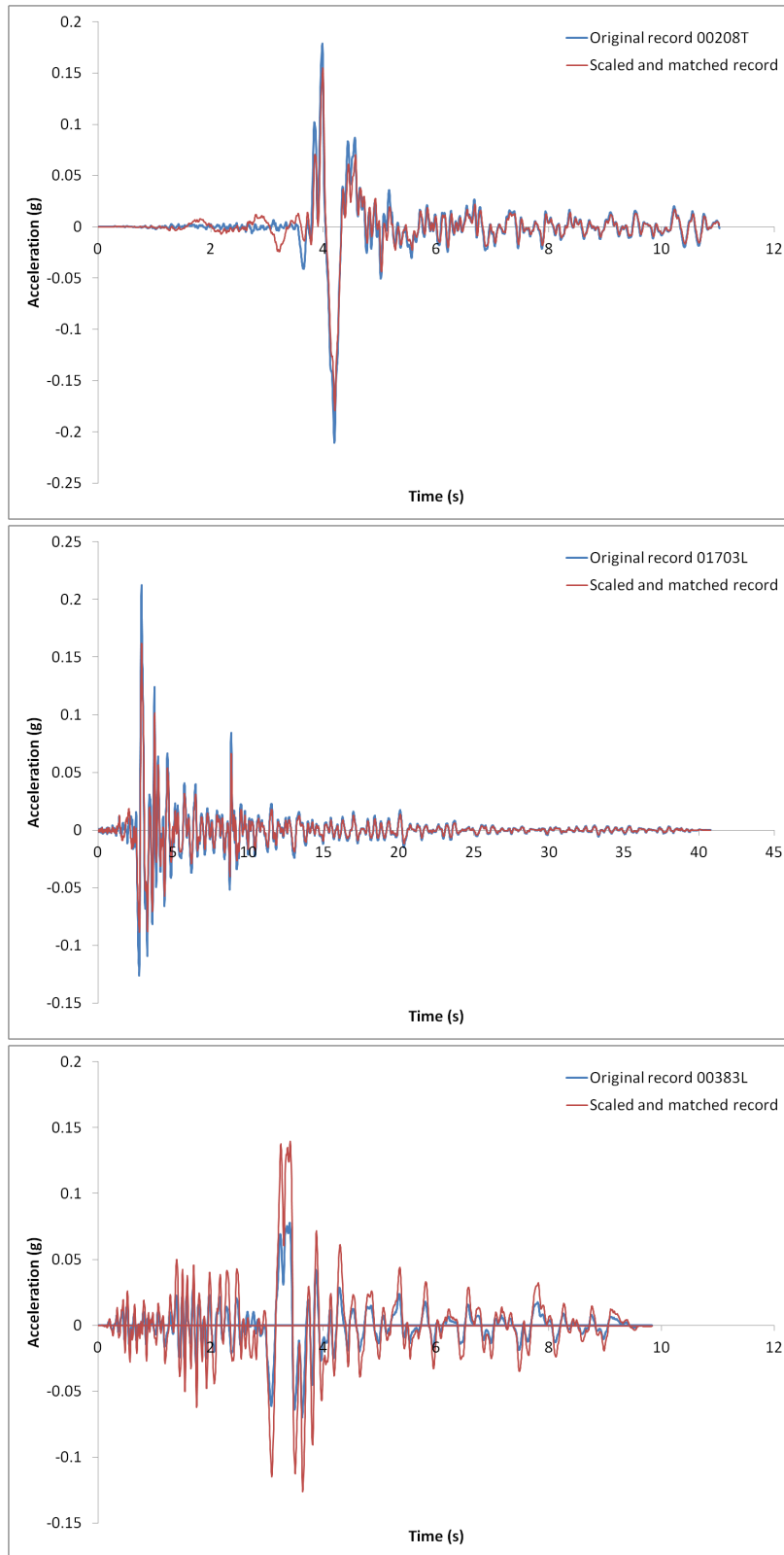


Figure 13. Comparison between the original and scaled and matched records for scenario 2.

As the spectral matching can change the 5-75% significant duration, this has been recalculated for each matched horizontal component to ensure that the value was still lower than the upper bound defined in Table 4.

Information and significant durations of the selected and matched ground motions are reported in Table 5 for scenario 1 and in Table 6 for scenario 2.

Table 5. Summary of records selected for scenario 1.

No.	Waveform No.	Database	EQ Name	EQ Date	Mw	Repi (km)	5-75% significant duration (s)
1	00228L	NGA	Anza (HorseCanyon)	25-02-1980	5.19	41.25	1.05
2	00201L	NGA	Imperial Valley-07	15/10/1979	5.01	15.28	0.375
3	ZAN2_N	Groningen	2	30/10/2008	3.1	3.36	0.395

Table 6. Summary of records selected for scenario 2.

No.	Waveform No.	Database	EQ Name	EQ Date	Mw	Repi (km)	5-75% significant duration (s)
1	01703L	NGA	Northridge-06	20/03/1994	5.28	9.19	1.72
2	00383L	NGA	Coalinga-02	09/05/1983	5.09	8.23	1.97
3	00208T	NGA	Imperial Valley-07	15/10/1979	5.01	7.85	0.40

### Final Selection of Records for Shake Table Test

Accelerograms with a smoother response spectra are preferred for the shake table test, for higher control of both the shake table and the response of the structure, and thus waveforms 00228L, 00201L (scenario 1) and 01703L (scenario 2) are preferred. For scenario 1, it is felt that the shorter duration waveform (00201L) would be more representative of the local hazard, given that it has a significant duration similar to the Groningen recording. Even though this duration is much lower than the target significant duration, it is known that the formula that has been used overestimates the duration of recordings from the field at short distances.

Hence, the waveforms 00201L for scenario 1 and 01703L for scenario 2 have been selected for the shake table test. The shake table test will be an incremental dynamic analysis, with a number of levels of shaking being applied to the structure, as described in the testing protocol. Scenario 1 will be scaled down to 50% to obtain the response of the structure under lower levels of shaking, and scenario 2 will be scaled by up to 2 times for the highest levels of shaking. It has been deemed appropriate to scale scenario 2 by this much given that the disaggregated scenario for spectral

acceleration at 0.5 seconds does not change significantly from 500 to 2500 years. For levels of shaking between scenario 1 and scenario 2, it would be justified to scale either scenario and a practical choice to remain with scenario 1 has been made.

## References

Akkar, S., M.A. Sandıkkaya & J.J. Bommer (2014a). Empirical ground-motion models for point- and extended-source crustal earthquake scenarios in Europe and the Middle East. *Bulletin of Earthquake Engineering* **12**(1), 359-387. *Erratum*: **12**(1), 389-390.

Akkar, S., M.A. Sandıkkaya & B.Ö. Ay (2014b). Compatible ground-motion prediction equations for damping scaling factors and vertical-to-horizontal spectral amplitude ratios for the broader European region. *Bulletin of Earthquake Engineering* **12**(1), 517-547.

Baker, J.W. (2011). Conditional mean spectrum: tool for ground motion selection. *ASCE Journal of Structural Engineering* **137**, 322-331.

Baker, J.W. & C.A. Cornell (2006). Spectral shape, epsilon and record selection. *Earthquake Engineering & Structural Dynamics* **35**, 1077–1095.

Bommer, J.J., S.J. Bourne, H. Crowley, B. Edwards, P. Kruiver, S. Oates & A. Rodriguez-Marek (2015b). *Seismic design loads for the Groningen Forum*. Version 3, 26 June, 88 pp.

Bommer, J.J., P.J. Stafford, B. Edwards, M. Ntinalexis, B. Dost & D. Kraaijpoel (2015a). *Development of Version 1 GMPEs for response spectral accelerations and strong-motion durations*, Version 1, 16 March, 278 pp.

Bradley, B.A. (2011). Correlation of significant duration with amplitude and cumulative intensity measures and its use in ground motion selection. *Journal of Earthquake Engineering* **15**(6), 809-832.

Crowley, H., J.J. Bommer & R. Pinho (2015a). *Selection of records for nonlinear dynamic analysis of Groningen buildings*. Version 1.0, 13 May, 17 pp.

Crowley, H., D. Grant & R. de Vries (2015b). *Development of V1 fragility functions for structural failure*. 1 July, 63 pp.

Hancock, J., J. Watson-Lamprey, N.A. Abrahamson, J.J. Bommer, A. Markatis, E. McCoy & R. Mendis (2006). An improved method of matching response spectra of recorded earthquake ground motion using wavelets. *Journal of Earthquake Engineering* **10**(special issue 1), 67-89.

Kempton, J.J. & J.P. Stewart (2006). Prediction equations for significant duration of earthquake ground motions considering site and near-source effects. *Earthquake Spectra* **22**(4), 985-1013.

Sandıkkaya, M.A., S. Akkar & P.-Y. Bard (2013). A nonlinear site-amplification model for the next pan-European ground-motion prediction equations. *Bulletin of the Seismological Society of America* **103**(1), 19-32.

Seismosoft (2015) SeismoMatch Version 2.1, Available from URL: <http://www.seismosoft.com/downloads>

## **Appendix C**

### **Evolution of dynamic properties, shaking table test on cavity walls terraced house**

The Output-Only modal identifications techniques, namely Operational Modal Analysis, are based on the dynamic response measurements of a virtual system under natural (ambient or operational) conditions, assuming that the excitations have random nature in time and in the physical space of the structure.

The fundamental assumption in this type of identification techniques relates to the fact that the excitation imposed on the structure is comparable to a stationary Gaussian white noise stochastic process in the frequency range of interest. However, the response measured on the structure includes the modal contributions of the ambient forces, the contribution of the structural system and the contribution of the noise signals from undesired sources. Furthermore, the measured response reflects the poles (amplitude peaks from the spectral density functions) from the structural system and from the ambient forces, and consequently the identification techniques must have the ability to separate the different components of the signal.

The techniques can be divided into two main groups, depending on the type of data used, namely frequency or time domains. The first group is based on the signal analysis of each measured point (in frequency domain by the application of the FFTs) and on the correlation between the signals. The techniques are also called non-parametric methods. The second group, constituted by parametric methods, is based on model fitting by the correlation functions or time history series of every measured point in the time domain.

The results relative to the modal identification of the dynamic properties of the full-scale specimen were obtained applying two different methods to the group of techniques performed in the time domain. Among the Output-Only techniques most widely used in the current practice, the Peak Picking method is one of the simplest in terms of computational effort in the Frequency domain. The Peak Picking method is usually applied in case of ambient vibrations and it gives reliable results when structures are characterized by resonant frequencies associated to the modes of vibrations that are sufficiently well separated [Ewins, 2000]. The method is indeed based on the assumption that the peaks of the FRF are reached in the vicinity of the resonant frequency of the structures.

The Peak Picking method was extended by Brincker *et al.* [2000] that introduced the so-called Frequency Domain Decomposition method. The basis of the FDD is the Singular Value Decomposition of the response spectral density matrix into a matrix of singular values and an orthogonal complex matrix containing the mode shape vectors of each spectral peak. The FDD method was further improved by Brincker *et al.* [2001] with the Enhanced Frequency Domain Decomposition technique, which is the second technique applied for the modal identification of the specimen. Because the FDD method evaluates the resonant frequencies with discrete frequency values with limited precision (since it is based on FFT signal analysis) difficulties can occur in presence of close resonant frequencies. The EFDD instead estimates the resonant frequencies and damping coefficients in the time domain through the application of inverse FFT of each spectral density function for each mode shape. In particular, from the discrete Fourier Transform of the single time history recorded and from the relative PSD functions, spectral density matrices are compiled. Such matrices are not directly used for the identification of modal shapes and frequencies of vibration, but are decomposed in singular values (Singular Value Decomposition). The curves depicting the variation of the singular value with respect to the frequency (or period) allows to select spectral bell-shaped portion of the curve in correspondence of peaks (one for each mode of vibration). Such portions are then transformed in the time domain, obtaining auto-correlation functions representative of the dynamic response of a series of single degree-of-freedom system in which the structure is decomposed. By means of appropriate interpolation procedures, it is possible to evaluate natural frequencies and mode shapes of the structure considered. Modes of vibration are identified from singular vectors belonging to suitable intervals near the peak singular value identified.

## EUC-BUILD Modal identification: results summary

In the following paragraphs a summary of the results obtained is presented, in terms of singular values, frequencies of vibrations for each mode identified, of mode shapes and damage index for the external veneer and the internal C.S. walls.

Figure 1 and Figure 2 report the results from the Singular Value Decomposition, in particular the blue curves describe the variation of the first singular value in each of the tests while the red lines depict the change of the identified frequencies depending on the cumulating damage, both for the inner walls and the external veneer structural systems.

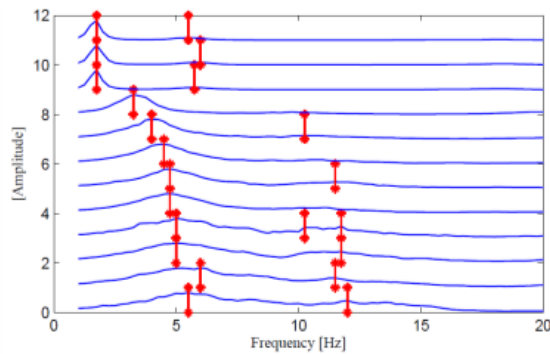


*Figure 1. Singular Value Decomposition: inner walls system.*

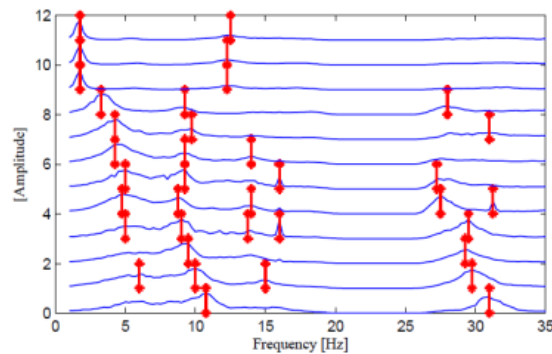


*Figure 2. Singular Value Decomposition: external veneer walls system.*

The following Table 1 and Table 2 summarise the frequencies of vibration (and periods) of each of the modes identified, applying both the PP and EFDD methods, for the internal C.S. walls and the external veneer walls respectively.

*Table 1. Summary of the frequencies and periods of vibration of the internal calcium silicate system.*

Test #	Test Name	Mode #	EFDD		PP	
			Freq. [Hz]	Period [s]	Freq. [Hz]	Period [s]
1	RNDM_01	1	5.5	0.1818	5.5	0.1818
		2	11.8474	0.0844	12	0.0833
3	RNDM_03	1	6	0.1667	6	0.1667
		2	11.5	0.087	11.5	0.087
5*	RNDM_05	1	5	0.2	5	0.2
		2	11.75	0.0851	11.75	0.0851
8	RNDM_08	1	5	0.2	5	0.2
		2	10.25	0.0976	10.25	0.0976
		3	11.75	0.0851	11.75	0.0851
10	RNDM_10	1	4.75	0.2105	4.75	0.2105
15	RNDM_15	1	4.75	0.2105	4.75	0.2105
		2	11.5	0.087	11.5	0.087
17	RNDM_17	1	4.5042	0.222	4.5	0.2222
20	RNDM_20	1	4	0.25	4	0.25
		2	10.25	0.0976	10.25	0.0976
22	RNDM_22	1	3.25	0.3077	3.25	0.3077
24	RNDM_24	1	1.7187	0.5818	1.75	0.5714
		2	5.75	0.1739	5.75	0.1739
25*	RNDM_25	1	1.7364	0.5759	1.75	0.5714
		2	6	0.1667	6	0.1667
30*	RNDM_30	1	1.7013	0.5878	1.75	0.5714
		2	5.5	0.1818	5.5	0.1818

The variation of the first fundamental period of variation at the different stage of the shaking table testing is depicted in Figure 3, showing a similar trend for both structural system, with values of  $T_1$  increasing as the damage increases, particularly after the test #20.

Table 2. Summary of the frequencies and periods of vibration of the external veneer system.

Test #	Test Name	Mode #	EFDD		PP	
			Freq. [Hz]	Period [s]	Freq. [Hz]	Period [s]
1	RNDM_01	2	10.75	0.093	10.75	0.093
		4	31	0.0323	31	0.0323
3	RNDM_03	1	6	0.1667	6	0.1667
		2	10	0.1	10	0.1
		3	15	0.0667	15	0.0667
		4	29.75	0.0336	29.75	0.0336
5*	RNDM_05	2	9.5	0.1053	9.5	0.1053
		4	29.3729	0.034	29.25	0.0342
8	RNDM_08	1	5	0.2	5	0.2
		2	9	0.1111	9	0.1111
		3	13.75	0.0727	13.75	0.0727
		4	16.0032	0.0625	16	0.0625
		5	29.4054	0.034	29.5	0.0339
10	RNDM_10	1	4.75	0.2105	4.75	0.2105
		2	8.75	0.1143	8.75	0.1143
		3	14	0.0714	14	0.0714
		4	27.7094	0.0361	27.5	0.0364
		5	31.2569	0.032	31.25	0.032
15	RNDM_15	1	5	0.2	5	0.2
		2	9.25	0.1081	9.25	0.1081
		3	16.0156	0.0624	16	0.0625
		4	27.25	0.0367	27.25	0.0367
17	RNDM_17	1	4.25	0.2353	4.25	0.2353
		2	9.25	0.1081	9.25	0.1081
		3	14	0.0714	14	0.0714
20	RNDM_20	1	4.25	0.2353	4.25	0.2353
		2	9.75	0.1026	9.75	0.1026
		3	31	0.0323	31	0.0323
22	RNDM_22	1	3.25	0.3077	3.25	0.3077
		2	9.25	0.1081	9.25	0.1081
		3	28	0.0357	28	0.0357
24	RNDM_24	1	1.7196	0.5815	1.75	0.5714
		2	12.25	0.0816	12.25	0.0816
25*	RNDM_25	1	1.729	0.5784	1.75	0.5714
		2	12.25	0.0816	12.25	0.0816
30*	RNDM_30	1	1.6545	0.6044	1.75	0.5714
		2	12.5	0.08	12.5	0.08

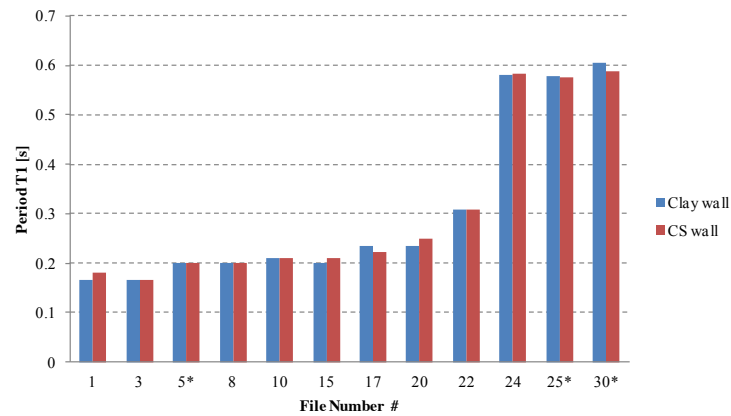


Figure 3. Variation of the fundamental period of vibration  $T_1$ .

A similar description of the effect of cumulative damage on the dynamic properties of the building is given by the index  $id_x$ , obtained as the ratio of the first period of vibration of the damaged structure with respect to that of the undamaged configuration, being equal to 1 when the structure is undamaged. In Figure 4 the variation of the  $id_x$  index for the inner calcium silicate walls is presented.

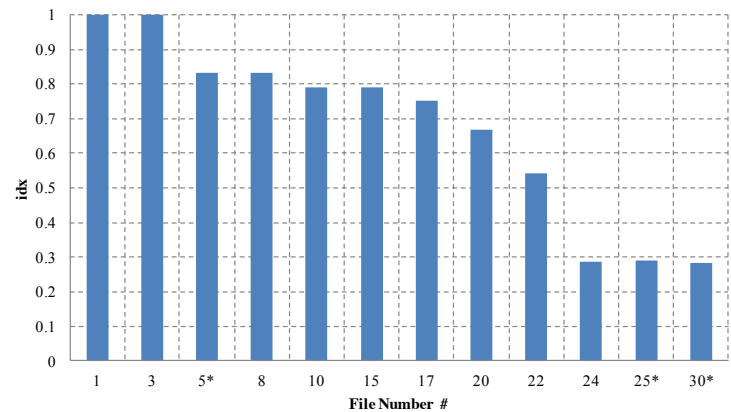


Figure 4. Variation of the damage index  $id_x$  for the internal calcium silicate walls.

The variation of the modal shape of the first mode of vibration is described making reference to the low intensity random vibration tests performed in the following stages of the testing sequence:

- test #1: when the building specimen was in an undamaged condition;
- test #3: after the first test performed with the record EQ1 as input at a PGA of  $0.24 \text{ m/s}^2$ ;
- test #10: after the sequence of test with the record EQ1 as input;
- test #24: after the testing stages with EQ2 as input, prior to the activation of tie rods.

In Figure 5 the scheme of the geometrical undeformed configuration of the building is presented.

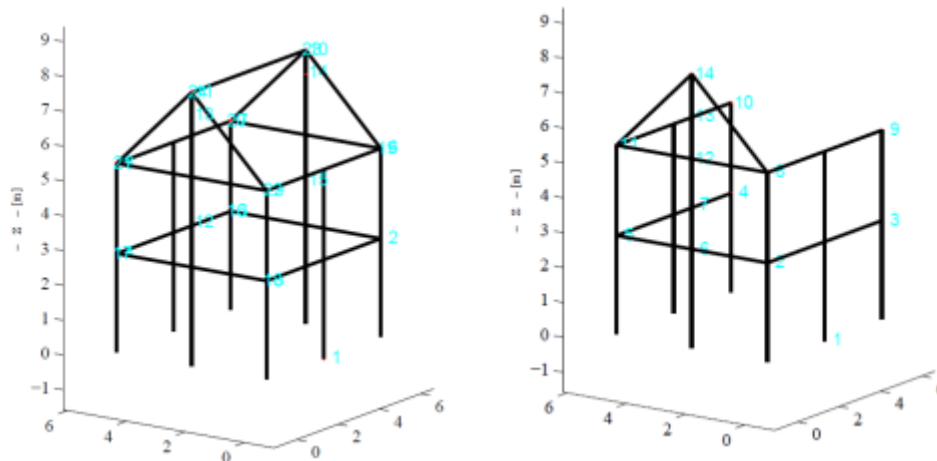


Figure 5. Undeformed configuration: inner walls (left) and external veneer systems (right)

The first mode of vibration of the undamaged building has been identified at a fundamental frequency of 5.5Hz, for the inner walls system only. The first period of the external veneer walls is assumed to be presumably close to same value. Figure 6 depicts the typical deformed shape of a first mode type of behaviour, with the longitudinal walls responding in-plane and the gable walls overturning out-of-plane, parallel to the direction of the shaking table motion.

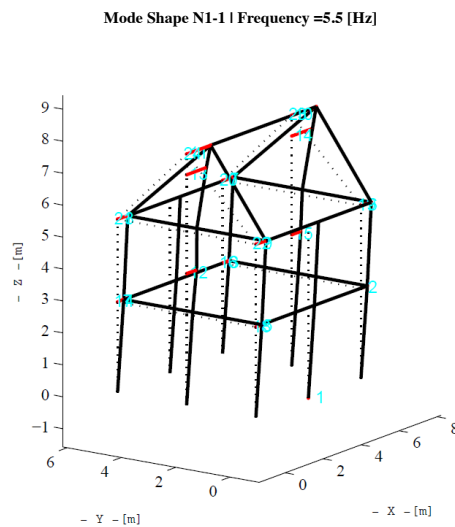


Figure 6. Test #1. Deformed shape of the first mode of vibration: inner walls.

After the first test with EQ1 as input motion, at a PGA of  $0.24 \text{ m/s}^2$ , the first modes of both the inner and outer walls were identified at a frequency of 6Hz.

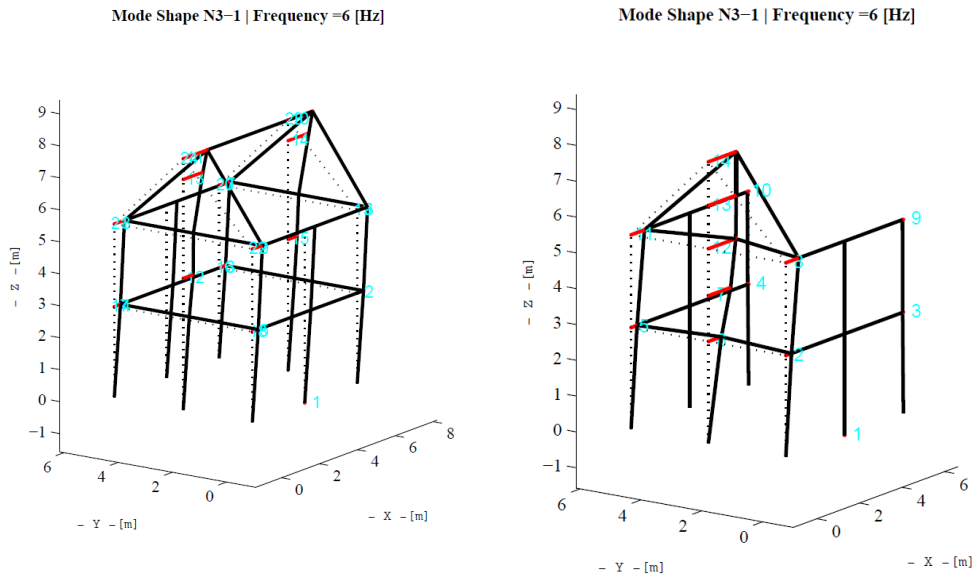


Figure 7. Test #3. Deformed shape of the first mode of vibration: inner walls (left) and external veneer systems (right).

While the deformed shape of the inner walls remains essentially unchanged with respect to that identified during Test #1, the first mode of vibration of the external veneer system shows clearly an out-of-plane response of the North façade with displacement components at mid-span of the wall almost double than the corner ones.

Figure 8 shows the first modes of vibration detected during Test #10: because of the damage level, though limited, the fundamental frequency decreases as expected, albeit the modal shapes remain essentially unvaried.

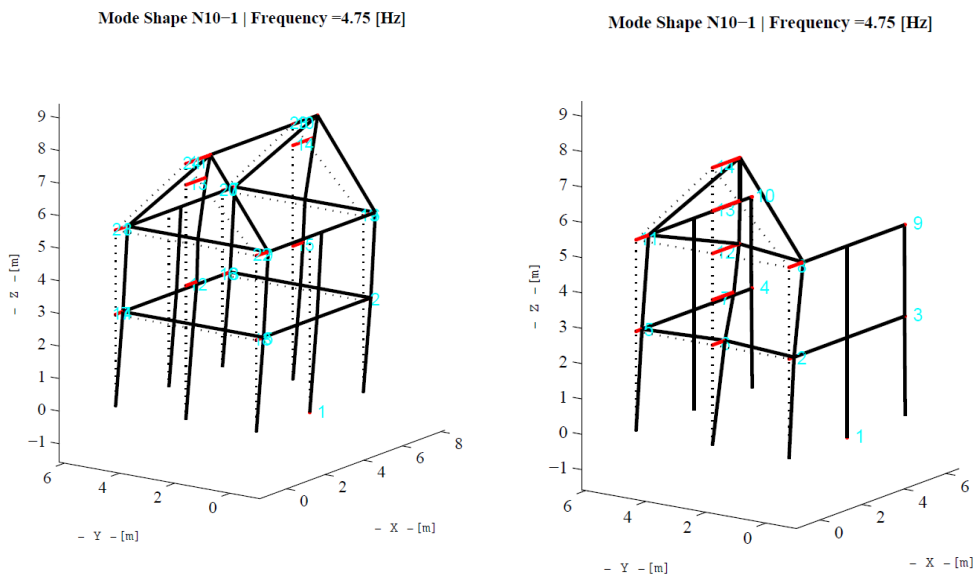
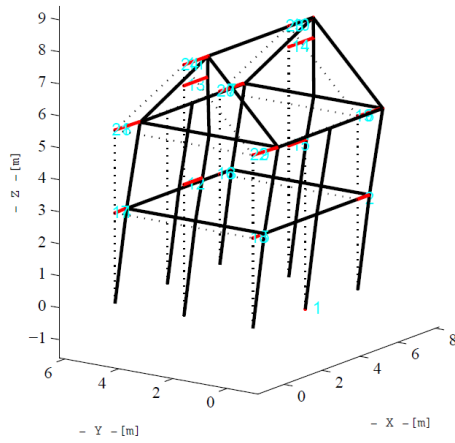


Figure 8. Test #10. Deformed shape of the first mode of vibration: inner walls (left) and external veneer systems (right).

Mode Shape N24-1 | Frequency =1.7187 [Hz]



Mode Shape N24-1 | Frequency =1.7196 [Hz]

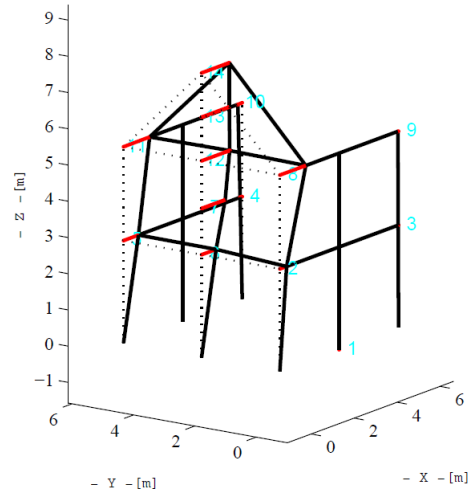


Figure 9. Test #24. Deformed shape of the first mode of vibration: inner walls (left) and external veneer systems (right).

The effect of the cumulated damage on the variation of the dynamic properties is evident in the results of the identification performed during test #24. As already presented in Table 2 and Table 1, the periods associated to each mode of vibration increased significantly (*i.e.* the values of the first period are approximately three times greater than those of the undamaged building prior testing). Regarding the modal shapes associated to the first fundamental frequency, although the mode of vibration is similar to the previous one, the modal displacement components at the second floor level are greater both in the case of the calcium silicate wall system and of the external veneer walls.

## References

---

Brincker, R., Zhang, L., and Andersen, P. [2000] “*Modal Identification from Ambient Responses using Frequency Domain Decomposition*”, Proc.18th International Seminar on Modal Analysis, San Antonio, Texas

Ewins, D. J. [2000] “*Modal testing: theory, practice and application*”, Research Study Press Ltd, England.

Brincker, R., Ventura, C., and Andersen, P. [2001] “Damping Estimation by Frequency Domain Decomposition”, *Proc. of IMAC XIX, the 19th International Modal Analysis Conference*, Kissimee, USA

# Shaking table test on a full scale URM cavity wall building

F. Graziotti<sup>1,2</sup>  · U. Tomassetti<sup>1,2</sup> · S. Kallioras<sup>3</sup> ·  
A. Penna<sup>1,2</sup> · G. Magenes<sup>1,2</sup>

Received: 22 December 2016 / Accepted: 27 June 2017  
© Springer Science+Business Media B.V. 2017

**Abstract** A shaking table test on a two-storey full scale unreinforced masonry (URM) building was performed at the EUCENTRE laboratory within a comprehensive research programme on the seismic vulnerability of the existing Dutch URM structures. The building specimen was meant to represent the end-unit of a terraced house, built with cavity walls and without any particular seismic design or detailing. Cavity walls are usually composed of an inner loadbearing leaf and an outer leaf having aesthetic and weather-protection functions. In the tested specimen, the loadbearing masonry was composed of calcium silicate bricks, sustaining two reinforced concrete floors. A pitched timber roof was supported by two gable walls. The veneer was made of clay bricks connected to the inner masonry by means of metallic ties, as seen in common construction practice. An incremental dynamic test was carried out up to the near-collapse limit state of the specimen. The input motions were selected to be consistent with the characteristics of induced seismicity ground motions. The article describes the characteristics of the building and presents the results obtained during the material characterization and the shaking table tests, illustrating the response of the structure, the damage mechanism and its evolution during the experimental phases. All the processed data are freely available upon request (see <http://www.eucentre.it/nam-project>).

**Keywords** Shaking table test · Full-scale building · URM cavity walls · Induced seismicity · Calcium silicate bricks

---

✉ F. Graziotti  
francesco.graziotti@unipv.it

<sup>1</sup> Department of Civil Engineering and Architecture - DICAr, University of Pavia, via Ferrata 3, 27100 Pavia, Italy

<sup>2</sup> European Centre for Training and Research in Earthquake Engineering - EUCENTRE, via Ferrata 1, 27100 Pavia, Italy

<sup>3</sup> UME School, IUSS Pavia, Piazza della Vittoria 15, 27100 Pavia, Italy

## 1 Introduction

The results presented in this manuscript are part of a wider research project aimed at assessing the vulnerability of buildings typical of the Groningen region (located in the Northeast Netherlands). This area, historically not prone to tectonic ground motions, during the last two decades has been subjected to seismic events induced by reservoir depletion due to gas extraction. The most severe event was an earthquake of local magnitude 3.6 that occurred on August 16th, 2012, near Huizinge, above the central part of the Groningen gas field (Bourne et al. 2015). Buildings not specifically designed for seismic actions are thus now exposed to this type of low intensity shaking. Unreinforced masonry (URM) buildings represent the large majority of the local existing building stock (almost 90%).

Currently, very limited data are available on the seismic response of construction typologies similar to those of the Dutch practice. An experimental campaign, starting in 2015, aimed at investigating the performance of structural components, assemblies and systems typical of building typologies present in the Groningen area. The testing campaign included in situ mechanical characterization tests (Tondelli et al. 2015) and laboratory tests comprising: characterisation tests performed on bricks, mortar and small masonry assemblies; in-plane cyclic shear-compression (Graziotti et al. 2016a) and dynamic out-of-plane tests on full-scale masonry piers (Graziotti et al. 2016b). Two full-scale shaking table tests have been conducted in 2015 and 2016 on two different URM building typologies on the testing facilities of the EUCENTRE laboratory. The first one is described in this manuscript, while information on the second one are available in Graziotti et al. (2016c, 2017).

The shaking table test presented in this article was designed to address several open questions related to the seismic behaviour of terraced houses that constitute the majority of the Dutch URM building stock, mainly with residential purposes. They are usually two-storey buildings with openings on only two of their sides, consisting of several structurally independent side-by-side units (4–6). The greatest part of this architectural typology is built with cavity walls, a construction system that became widespread after World War II.

A cavity wall building is a type of construction where an air gap is left between the two leaves of bricks. Sometimes insulating material is inserted in the cavity. The external leaf of a cavity wall is often a brick veneer wall without any load bearing function, while the internal leaf is the loadbearing one, carrying the vertical loads transmitted by the floors and the roof. It is common for the inner leaf to be constructed with different materials than the outer leaf. In several European countries, an example of this solution is to have the inner wall made of calcium silicate brick/blocks, while the outer wall uses clay bricks. Wythes on either side of a cavity wall are typically connected by regularly spaced metal cavity ties, which can vary in material, shape and spacing. Because of their relatively light weight, good thermal insulation properties and effective protection against driving rain, cavity walls are widely used in Central and Northern Europe countries, especially for residential construction. Information on the seismic behaviour of cavity walls is quite limited, and mostly related to earthquakes occurring in Australia (Newcastle, 1989) and New Zealand (Christchurch sequence, 2010–2011) (Ingham and Griffith 2011). Furthermore, a shaking table test on a cavity-wall building specimen with loadbearing concrete blocks was performed by Degée et al. (2008).

The shaking table test presented in this manuscript aims at studying the seismic response of this type of building. In particular, relevant results of the experimental study

are: drift limits for different performance levels, damage evolution for increasing shaking levels; storey accelerations amplified along the building height, and displacement/drift profiles for increasing shaking intensity. In particular, specific attention was paid to the dynamic performance of the roof structure and on the possible activation of gable out-of-plane mechanisms. With the aim of reproducing the seismic behaviour of an existing URM terraced house, an incremental dynamic test was carried out up to the near collapse conditions of the specimen. This work presents the geometric and mechanical characteristics of the specimen (Sect. 2), the input motions applied to the shaking table, the testing protocol and the instrumentation (Sect. 3). Section 4 discusses the performance of the building under ground motion excitation, the test results in terms of damage evolution, hysteretic responses, performance of the roof structure and the identification of the local and global limit states (Sect. 4).

## 2 Specimen characteristics

The building specimen was intended to represent the end-unit of a URM cavity-wall terraced house of the late '70s. This residential typology is characterised by wide openings on the front and back sides. The transverse walls, that separate units, are double-wythe cavity walls without any openings. Internal transverse walls are composed of a couple of loadbearing walls, carrying most of the vertical loads coming from floors and roof and, therefore, they are capable of resisting significant in-plane lateral forces. Houses built with this common configuration are expected to be characterised by two very different seismic behaviours in the two principal directions. These structures are generally more flexible and vulnerable in the longitudinal direction. For this reason, a unidirectional shaking table test was carried out by applying base excitations along this direction. Figure 1 shows the front view of a classic terraced house and its plan view.

Adjacent units are generally structurally detached, and the discontinuous slabs rest only on the loadbearing walls of the individual units. Each unit is therefore completely self-supported by transverse walls and structurally independent from the other units. The only common walls are the outer veneer walls. For this reason, it was possible to test on the shaking table a representative sub-volume (one end-unit) of an entire terraced house (as shown in the coloured part of Fig. 1a). The first floor is generally made of a reinforced concrete (RC) slab, while the second floor is either a RC or timber diaphragm.

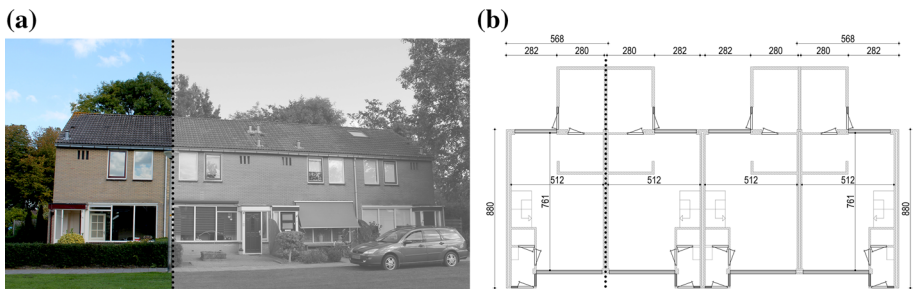


**Fig. 1** A typical terraced house in Loppersum, Groningen, NL: **a** illustration of the front façade; **b** plan view

The presence of a timber roof usually dominates over other typical roofing solutions for this building typology.

## 2.1 Geometry of the specimen

The test-house was a full-scale two-storey building, with a timber roof and RC slabs. The specimen was built directly on the shaking table of the EUCENTRE laboratory (Fig. 2a). It was 5.82 m long, 5.46 m wide (slightly reduced compared to the typical width found in the building stock, due to the shaking table dimensions) and 7.76 m high with a total mass  $M$  of 56.4 t. The walls, supported by a steel–concrete composite foundation, consisted of two unreinforced masonry leaves. The inner loadbearing leaf was made of calcium silicate (CS) bricks whereas the external leaf was a clay brick veneer without any loadbearing function. The two pre-cast RC floor slabs (with a mass of 10.3 t and 11 t for the first and second floor, respectively) were supported only by the two transverse (North and South) inner CS walls. The inner CS masonry was continuous along the entire perimeter of the house, while the outer clay brick leaf was not present in the South façade, simply because the specimen was meant to represent the end-unit of a system of row houses. Pictures of the specimen after the end of the construction are shown in Fig. 2, while Fig. 3 depicts the ground and first floor plan views of the specimen.

An air gap of 80 mm was left between the two leaves, as usually seen in common practice. L-shaped steel ties with a diameter of 3.1 mm and a length of 200 mm were inserted in the 10-mm-thick mortar bed-joints during the laying of the bricks, ensuring the connection between the two masonry leaves (the location of the steel ties is showed by blue dots in Fig. 4). The L hook side was embedded in the inner CS walls for a length of 70 mm, while the “zig-zag” extremity was embedded in the clay masonry for a length of 50 mm (Fig. 5a, d). Two gable walls in the transverse façades (North and South) supported a 43° pitched timber roof. In the ground storey, pre-cast reinforced concrete lintels were placed above the openings on both inner and outer walls. The dimensions of the lintels were 160 × 100 mm for CS walls and 110 × 100 mm for clay walls. Lintels were 1.33 and 2.22 m long for shorter and wider openings, respectively.

A rigid steel-frame was installed in the interior of the test-house. This structure served mainly as a safety system, providing support for the two slabs in case of partial or global collapse of the specimen, as well as a rigid reference system for a direct measure of the floors, walls and roof displacements (Fig. 5f). The frame was not in contact with the

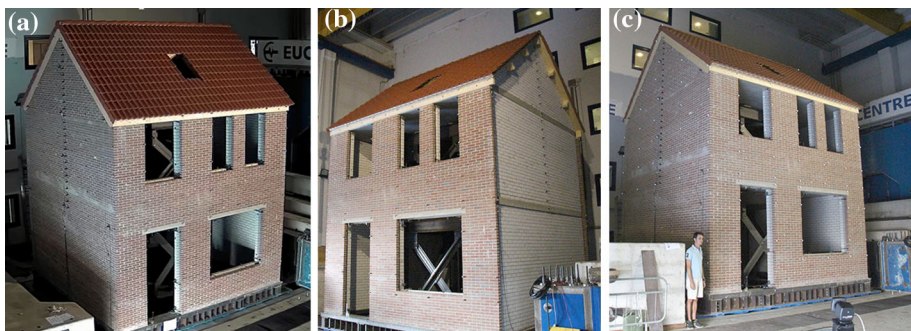


**Fig. 2** Views of the full-scale specimen: **a** North-West (from top); **b** South-West; **c** North-West (from bottom)

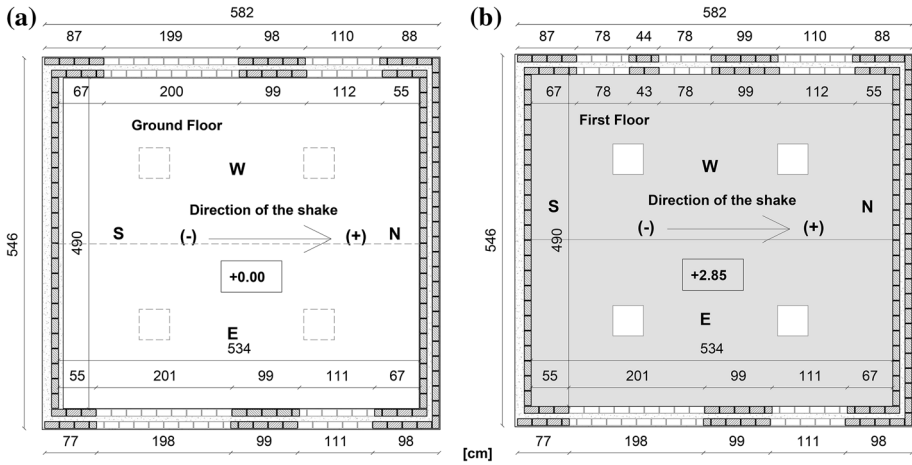


**Fig. 3** a Plan view of the ground floor, and b the first floor of the specimen. Arrows indicate the assumed positive direction of the shaking table motion. Units of cm

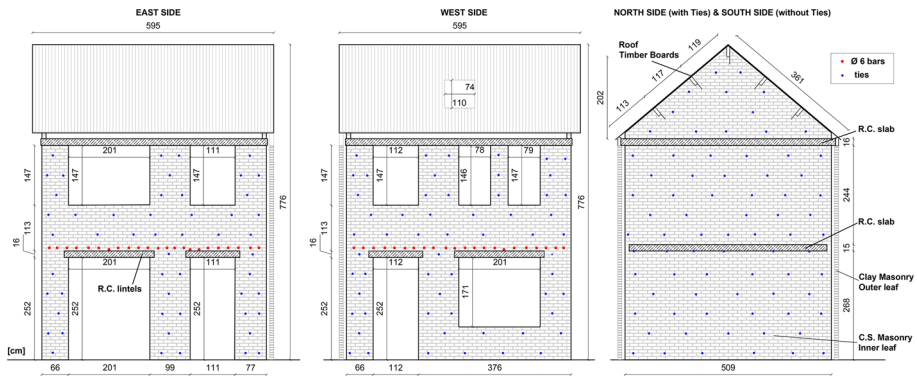


**Fig. 4** Elevation views of the specimen's inner CS leaf. Units of cm

building, since its columns passed through 450-mm-square holes in the two slabs, large enough to accommodate significant lateral displacements of the specimen (Fig. 3c).

### 2.2 Building construction details

It is well known among the engineering community that construction details can significantly affect the seismic response of a structure, especially a URM building. Observation of damage caused by major earthquakes, as well as laboratory tests (Tomažević et al. 1991; Magenes et al. 2014) have shown that the role of the connections between horizontal and vertical structural elements is of primary importance for ensuring a good structural performance. The construction details of the specimen were representative of the Dutch common practice of the '60s and '70s. Figure 5 presents pictures captured during the construction phase of the specimen.

The connection between the first floor slab and the inner CS longitudinal leaves (East and West walls) was ensured by means of 6-mm-diameter threaded bars, the position of



**Fig. 5** Construction details of the specimen: **a** positioning of cavity steel ties; **b** building phase of inner CS leaf; **c** laying of the second floor slab; **d** geometry of steel tie; **e** construction of CS leaves at second floor level; **f** safety steel frame

which is indicated by red dots in Fig. 4. Details of this connection are also shown in Fig. 5c, d. This solution was meant to represent a common technique associated with a cast-in situ RC slab where the bars were embedded in the masonry before casting the slab. Since the construction in the laboratory environment required the slabs to be precast, the connectors were pre-inserted in the concrete and then anchored to the masonry in a second phase. As recurrent in the building stock, an air gap (hole sleeve in Fig. 6c) was left in order to guarantee differential thermal expansion of the components. There was no direct connection between the outer clay veneer wall and the first-floor slab.

The second-floor slab was not directly supported by the longitudinal walls (East and West); the gap between the slab and the inner CS longitudinal walls was filled with mortar

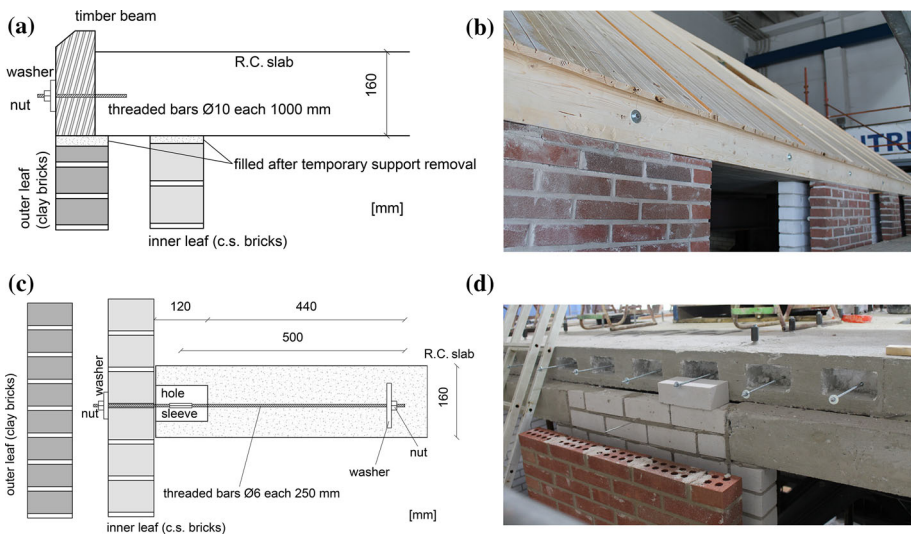


**Fig. 6** Details of the connections between the precast RC slabs and the longitudinal CS walls: **(a, b)** second floor, and **(c, d)** first floor level

after the removal of the temporary supports and the attainment of the deflection of the slab. Similarly, the timber wall plates were not in contact with the longitudinal clay walls (East and West), but they were attached to the edge of the second floor slab by means of 100-cm-spaced 10-mm-diameter threaded bars, while the resulting gap between the beams and the top of the veneer was afterwards filled with mortar (Fig. 6a, b). Such details were adopted in order to reproduce a loading configuration common in the building stock. This solution resulted in almost no vertical load being transmitted to the longitudinal walls under static conditions.

The timber roof was a simple structure consisting of one ridge beam, two wall plates on top of the longitudinal outer leaves and two girders per side between the ridge beam and the wall plates, at approximately every 1.2 m. Tongue and groove planks, with a width equal to 182 mm and a thickness of 18 mm, were nailed on top by means of two  $60 \times 2$  mm nails at each intersection (Fig. 7a). The timber beams of the roof were supported by the transverse inner CS leaves (North and South gables), whereas this connection was further reinforced by the presence of L-shaped steel anchors, as shown in Fig. 7c. The roof was completed by the installation of clay tiles and the total mass of the finished roof was 2.8 t. The in-plane stiffness of the timber diaphragm was essentially provided by the nailed connections between beams and planks, as well as by the effectiveness of the tongue and groove joints.

### 2.3 Mechanical properties of materials

Part of the experimental campaign that was carried out at the laboratory of the University of Pavia, allowed the mechanical properties of the building materials employed for the construction of the specimen to be determined. It comprised strength tests on units and mortar samples, as well as tests on small masonry assemblages, such as compression tests, bond wrench tests and shear tests on triplets. CS and clay units were tested in compression according to EN 772-1 (2000). The dimensions of the CS units were  $212 \times 102 \times 71$  mm. The clay bricks were perforated with ten vertical holes, they had a void ratio of 17% and dimensions of  $211 \times 100 \times 50$  mm. The flexural and compressive strength of the mortar were determined according to the prescriptions of EN 1015-11 (1999). Six masonry wallettes made of CS and clay bricks were tested in compression in the direction perpendicular to the horizontal bed-joints, according to EN 1052-1 (1998). These tests allowed the determination of the compressive strength of masonry ( $f_m$ ), as well as the secant elastic modulus of masonry at 33% of the compressive strength ( $E_m$ ). Bond wrench tests on twenty CS and twenty clay masonry wallettes were performed in order to determine the bond strength of masonry, according to EN 1052-5 (1998). Specimens of both types of masonry were also subjected to

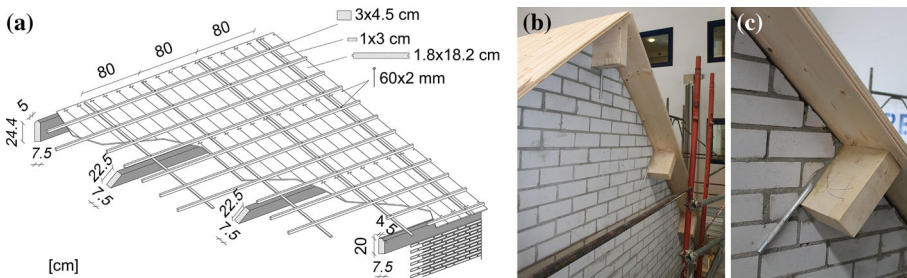


**Fig. 7** Details of the roof structure: **a** geometry of the timber diaphragm; **b** connection between the timber beams and the South gable; **c** steel anchors

**Table 1** Summary of structural masses, units of t

		<i>First storey</i>	<i>Second storey</i>	<i>Gables</i>	<i>Total</i>
<i>Masonry structure</i>	<i>Inner leaf (CS)</i>	8.5	8.7	2.4	19.6
	<i>Veneer (Clay)</i>	5.6	5.9	1.2	12.7
<i>RC slabs</i>		10.3	11.0	-	21.3
<i>Roof (tiles and timber trusses)</i>		-	-	-	2.8
<i>Entire building</i>					<b>56.4</b>

**Table 2** Masonry mechanical properties

Material property	Symbol	U.M.	Calcium silicate		Clay	
			Average	C.o.V.	Average	C.o.V.
Density of bricks	$\rho_b$	kg/m <sup>3</sup>	1900	0.02	1650	0.02
Density of masonry	$\rho$	kg/m <sup>3</sup>	1835	0.01	1905	0.03
Compressive strength of bricks	$f_b$	MPa	17.18	0.14	32.45	0.13
Compressive strength of mortar	$f_c$	MPa	5.71	0.25	6.24	0.09
Flexural strength of mortar	$f_t$	MPa	1.78	0.23	1.48	0.19
Masonry compressive strength	$f_m$	MPa	5.49	0.10	12.72	0.15
Masonry Young's modulus in compression	$E_m$	MPa	1736	0.26	4742	0.17
Flexural bond strength of masonry	$f_w$	MPa	0.056	0.47	0.152	0.65
Masonry (bed joint) initial shear strength	$f_{v0}$	MPa	0.03	-	0.11	-
Masonry (bed joint) shear friction coefficient	$\mu$	-	0.50	-	0.68	-

the shear test for the determination of the initial shear strength ( $f_{v0}$ ) and the friction coefficient ( $\mu$ ), according to the guidelines given by EN 1052-3 (1998).

A parallel testing campaign was conducted at the Delft University of Technology (TU Delft) on specimens built using the same materials (Esposito et al. 2016). In particular, tests that allowed the determination of the tensile load capacity of the steel ties connecting the two masonry leaves were performed by Messali et al. (2016). They found that the pull-in and pull-out strengths of the “zigzag” tie extremity (Fig. 5d) embedded in clay masonry specimens, considering an overburden pressure of 0.3 MPa, was higher than the strengths associated with the hook extremity embedded in CS specimens and subjected to the same imposed pressure. The average pull-out and push-in strengths recorded for CS specimens were approximately 1.46 and 1.09 kN, respectively. Moreover, the tensile ultimate capacity of the steel anchors was approximately 4.3 kN. The concrete used to cast the two slabs had an average compressive strength of 29.5 MPa. The masses of the test unit are summarized in Table 1, while Table 2 lists the masonry mechanical properties resulting from material characterization tests.

### 3 Testing protocol and instrumentation

#### 3.1 Input signals

The specimen was subjected to a sequence of incremental dynamic tests. A series of table motions of increasing intensity were applied with the objective of assessing the

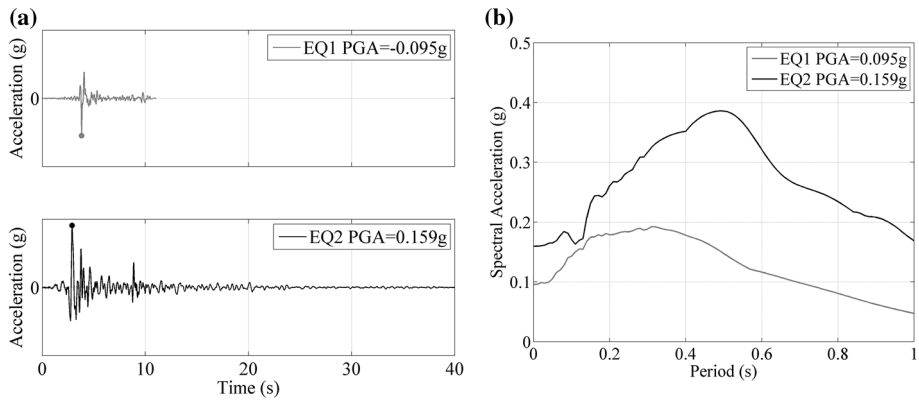


**Fig. 8** EQ1 and EQ2 input signals: **a** acceleration time histories, and **b** acceleration response spectra

ultimate capacity and failure modes of the building. Since the shaking table is uniaxial, the seismic input was applied parallel to the longitudinal direction (North–South) of the tested building, exciting out-of-plane the loadbearing transverse walls (North and South façades). The selected input motions aimed at being representative of expected ground motion in the region of Groningen. A detailed study on the seismic hazard characteristics identified two main scenarios with return periods of 50 and 500 years (see Appendix B2 of Graziotti et al. 2015). Two records EQ1 and EQ2 with 5–75% significant duration of 0.375 s and 1.72 s and a PGA of 0.095 g and 0.159 g, respectively, were finally selected to be representative of the two scenarios. Their smooth response spectra were considered ideal for a higher control of both the shaking table and the response of the structure. Figure 8 shows the theoretical acceleration time-histories of the experimental inputs and their acceleration response spectra.

### 3.2 Testing protocol

The sequence of incremental dynamic tests was performed by gradually increasing the intensity of the two ground motions with EQ1 being applied first, followed by EQ2. Table 3 presents the applied testing sequence specifying the input typology, the intensity and the comparison between nominal and recorded PGAs and 5% elastic spectral accelerations,  $Sa(T_{1,1})$  at the fundamental period  $T_{1,1} = 0.17$  s of the undamaged structure (calculated by means of a dynamic identification test, see further details in Sect. 4.4). Further intensity measures (IMs) listed in Table 3 are the peak ground velocity PGV, the 5%-damping elastic spectral displacement obtained from the recorded base acceleration, and the modified Housner intensity ( $mHI$ ). The  $mHI$  has shown very good correlations with the nonlinear displacement demand induced in short period URM structures (Graziotti et al. 2016d). It is defined as the integral of the pseudo-velocity elastic response spectrum between a structural period of 0.1 s and 0.5 s (which correspond to the range of periods of interest of the tested specimen):

**Table 3** Summary of the testing sequence

Test #	Test Input	Test Name	Nominal PGA [g]	Recorded PGA [g]	Calculated PGV [m/s]	Nominal $Sa(T_{1,i})$ [g]	Calculated $Sa(T_{1,i})$ [g]	Calculated $Sd(T_{1,i})$ [mm]	Calculated mHI [mm]
1	RNDM	RNDM-01	0.050	-	-	-	-	-	-
2	EQ1	EQ1-25%	0.024	0.024	0.015	0.049	0.055	0.4	8.3
3	RNDM	RNDM-03	0.050	-	-	-	-	-	-
4	EQ1	EQ1-50%	0.049	0.050	0.031	0.097	0.126	0.9	18.2
5	RNDM	RNDM-05	0.050	-	-	-	-	-	-
6	EQ1	EQ1-50%C	0.048	0.050	0.031	0.089	0.108	0.8	17.3
7	EQ1	EQ1-100%	0.096	0.099	0.056	0.179	0.229	1.6	34.9
8	RNDM	RNDM-08	0.050	-	-	-	-	-	-
9	EQ1	EQ1-150%	0.144	0.137	0.077	0.268	0.369	2.6	47.7
10	RNDM	RNDM-10	0.050	-	-	-	-	-	-
11	EQ2	EQ2-30%C	0.053	0.064	0.049	0.081	0.096	0.7	23.4
12	EQ2	EQ2-30%C	0.053	0.059	0.045	0.081	0.087	0.6	22.2
13	EQ2	EQ2-30%C	0.053	0.056	0.043	0.081	0.083	0.6	21.5
14	EQ2	EQ2-50%	0.079	0.087	0.067	0.122	0.125	0.9	31.8
15	RNDM	RNDM-15	0.050	-	-	-	-	-	-
16	EQ2	EQ2-100%	0.159	0.170	0.123	0.245	0.286	2.1	62.1
17	RNDM	RNDM 17	0.050	-	-	-	-	-	-
18	EQ2	EQ2-50%C	0.079	0.114	0.088	0.122	0.183	1.3	41.3
19	EQ2	EQ2-125%	0.199	0.194	0.133	0.306	0.324	2.3	69.0
20	RNDM	RNDM-20	0.050	-	-	-	-	-	-
21	EQ2	EQ2-150%	0.239	0.243	0.164	0.367	0.404	2.9	84.4
22	RNDM	RNDM-22	0.050	-	-	-	-	-	-
23	EQ2	EQ2-200%	0.319	0.307	0.218	0.489	0.654	4.7	111.6
24	RNDM	RNDM-24	0.050	-	-	-	-	-	-

$$mHI(5\%) = \int_{0.1}^{0.5} PSV(5\%, T) dT \quad (1)$$

The shaded sections in Table 3 refer to the tests with increasing intensity. It is worth noting that such tests have been often preceded by tests of the same typology, but with reduced intensity for the purpose of shake table calibration (e.g. tests #6, #11, #12, #13 and #18). The intensity level of these calibration tests (labelled with a C in the test name, e.g. EQ1-50%C) has been chosen in order to prevent further damage or deterioration in the specimen. In general, a good agreement between nominal and recorded quantities have been observed, with a slight overshoot of the recorded spectral acceleration corresponding to the initial fundamental period  $T_{1,1}$ . Each test with increasing intensity was alternated by random noise tests (RNDM), which, by means of a dynamic identification procedure, allowed the changes in the dynamic properties of the structure to be detected as the damage level increased. In particular, the following sections report the evolution of the fundamental period denoted as  $T_{1,i}$  (where  $i$  is the test identification number as reported in Table 3). The incremental testing sequence has been stopped after the attainment of a near collapse condition in order to prevent a global collapse of the specimen that could have caused damage to the laboratory facilities.

### 3.3 Instrumentation

In order to detect and monitor the structural response under different levels of input motion, several instruments were installed on the building. The location and typology of the instrumentation was determined based on the identification of the critical zones and on the physical quantity to be recorded. The instrumentation consisted of 33 accelerometers and 30 displacement transducers. Figure 9a shows the locations of the three types of employed accelerometers (uni-, bi- and tri-axial). The accelerometers were installed on both inner and outer leaves, as well as on the two floors and the ridge beam of the roof. Figure 9b shows, instead, the displacement transducers installed on the specimen: 10 wire and 20 linear variable displacement transducers (LVDTs). The displacements measured between the specimen and the rigid frame were considered equivalent to the relative displacements with respect to the shaking table surface. In particular, wire potentiometers were installed in order to record the out-of-plane response of the North and South façades at the mid-height of the first and second storeys and the gable. The LVDTs were, instead, utilized to monitor directly the longitudinal and transverse displacement of the first and second slabs. The displacements of some points of the external façades and internal walls were monitored by a 3D optical acquisition system (see Appendix 2). These data allow to compute the differential displacement between inner and outer leaves.

### 4 Test results

The following sections report the main results of the shaking table tests. In particular, some issues related to the global seismic response of the tested building are discussed, in terms of the observed crack patterns, the deformed shapes and the hysteretic behaviour. To summarise briefly: the building sustained shaking of  $PGA = 0.14 \text{ g}$  (EQ1 150%) with no

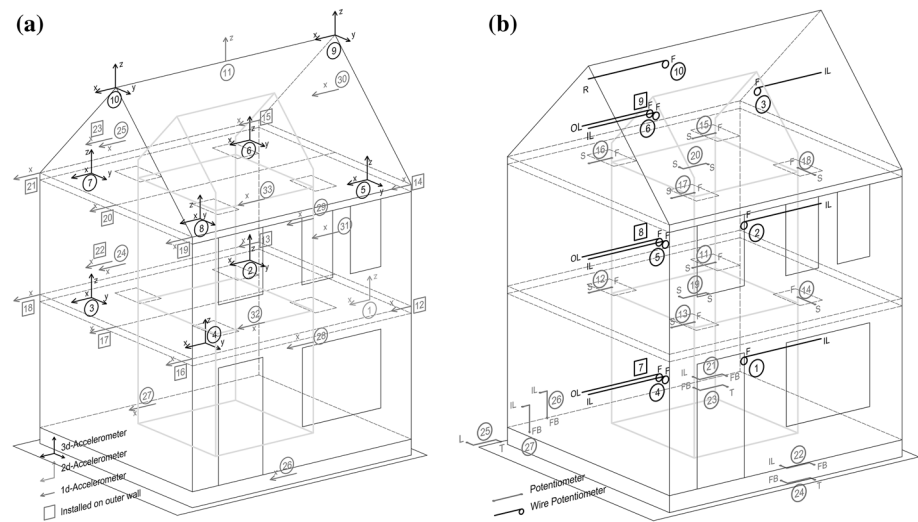


**Fig. 9** Locations of the instrumentation: **a** accelerometers, and **b** displacement transducers (*letters* indicate the component at which the transducers is attached to: *S* slab; *F* frame; *IL* inner leaf; *OL* outer leaf; *FB* foundation beam; *T* shaking table; *R* roof ridge beam; *L* laboratory floor)

visible damage and was in a near-collapse state after testing at  $\text{PGA} = 0.31 \text{ g}$  (EQ2 200%), when the test sequence was stopped. Videos of the applied testing sequence are available online (Eucentre 2015a).

#### 4.1 Shaking table performance

The comparison between the theoretical response spectra and those obtained from the accelerations recorded on the specimen's foundation, shows a general good match. A very slight overshooting of low period spectral ordinates was noticed in all the tests. A 15% undershooting of spectral acceleration in the high period range was observed only in the test EQ2-200%. In the same test a considerable amplification peak occurred at a period of  $T = 0.18 \text{ s}$ . The sudden change of the specimen dynamic characteristics (the fundamental period was doubled), due to its heavy damage and its interaction with the table, did not allow a perfect match of the target spectrum. The comparison of the acceleration response spectra for the tests of EQ2-100% ( $\text{PGA} = 0.17 \text{ g}$ ) and EQ2-200% ( $\text{PGA} = 0.307 \text{ g}$ ) is shown in Fig. 10.

#### 4.2 Damage evolution

At the end of each stage of the shaking table testing sequence, detailed surveys were carried out for the report of every possible evidence of damage having affected the structure (Figs. 11, 12). During the testing under the first scenario seismic excitations (EQ1 scaled from 25%  $\text{PGA} = 0.024 \text{ g}$  to 150%  $\text{PGA} = 0.137 \text{ g}$ ), the building did not experience any noticeable damage. The specimen suffered only slight damage that became visible just after testing under EQ2-100% test ( $\text{PGA} = 0.17 \text{ g}$ ). The formation of a few cracks was observed at the base of the first storey inner-leaf corner piers, associated mainly with their flexural behaviour. The observed damage did not change significantly after testing at EQ2-125% ( $\text{PGA} = 0.194 \text{ g}$ ).

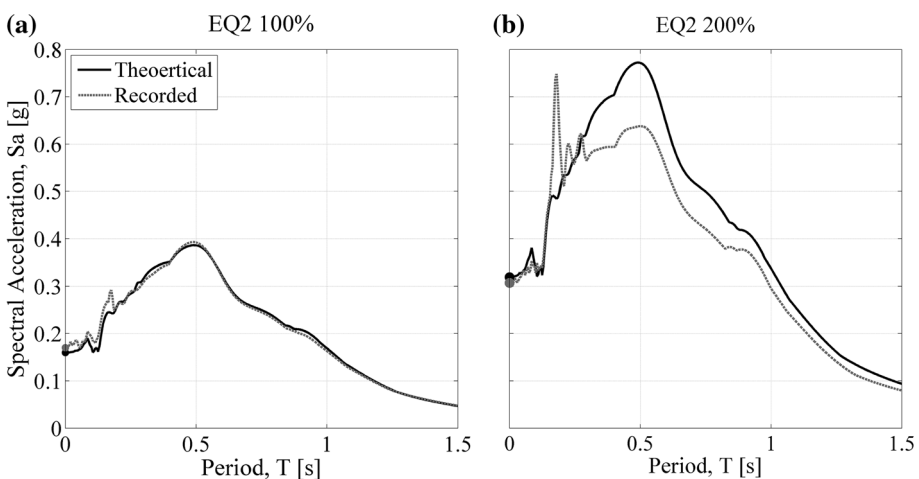


**Fig. 10** Comparison of the acceleration response spectrum of the recorded base acceleration against the target one for testing under **a** EQ2-100% ( $\text{PGA} = 0.17 \text{ g}$ ), and **b** EQ2-200% ( $\text{PGA} = 0.307 \text{ g}$ )



**Fig. 11** Crack pattern evolution of the inner CS walls

The first significant cracks observed in the CS masonry of the second storey were recorded after the test EQ2-150% (PGA = 0.243 g). They were mainly horizontal cracks observed just below the interface between masonry piers and the second floor level slab, as mapped in Fig. 11. A horizontal crack developed along the base of the squat pier of the second storey, on the West side, indicative of the pier’s bending-rocking response. This crack was further extended with a stair-stepped diagonal pattern to the centre of the adjacent spandrel. Until this intensity level no damage in the two transverse walls was detected.

The building experienced a substantial level of damage (compared to that observed under lower intensity shaking) after the test EQ2-200% (PGA = 0.307 g). At this shaking level a global response of the structure was triggered, as evidenced by the formation of new

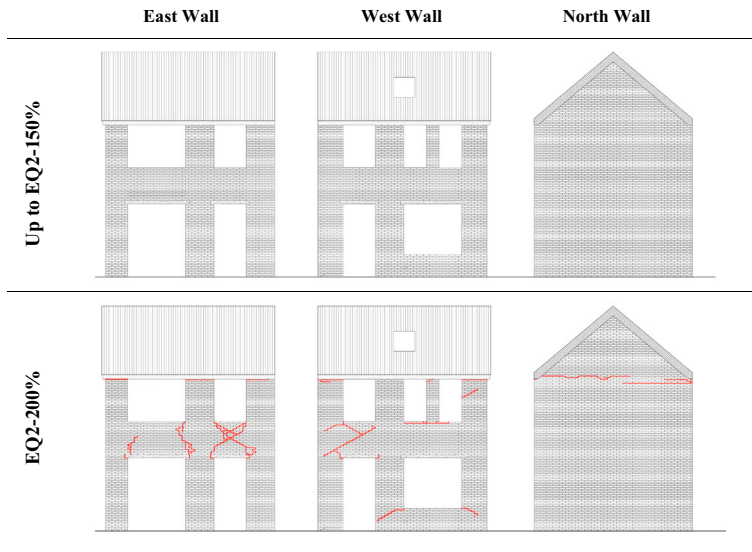


**Fig. 12** Crack pattern evolution of the outer clay walls

cracks or the elongation of pre-existing ones, identified on every one of the piers, as shown in Fig. 11. A detailed survey of the building was conducted and revealed extensive damage in the spandrels of the calcium silicate masonry. In particular, the formation of wide diagonal cracks (starting from the corners of the openings), with sliding of the mortar joints and de-cohesion of blocks were observed (Fig. 13e). In addition, the horizontal cracks located at the top of the second storey piers were extended, reaching a maximum residual sliding of 15 mm.

As far as the damage reported in the transversal walls is concerned, the formation of 45° stair-stepped diagonal cracks (no greater than 1.2 mm) was clearly observed. This could be associated with the activation of an out-of-plane two-way bending mechanism. Focusing on the gables, horizontal cracks along their base were apparent (one or two layers above the second floor level), indicative of an out-of-plane overturning mechanism activated at the gable level. Other cracks were also identified at the locations where the timber beams of the roof were supported on the gable walls. Cracks around these beams were due to interaction of the beams with the supporting masonry gable walls (Figs. 11, 13a).

Regarding the damage noticed in the veneer walls, perceptible cracks developed only during the last test, EQ2-200% (PGA = 0.307 g). In particular, the long spandrel of the eastern façade developed a flexural mechanism with vertical cracks at both ends, originating from the concrete lintels (Figs. 12, 13h), whereas the shorter spandrel presented failure in shear, forming the characteristic X-shape crack pattern (Figs. 12, 13g). On the western side, large stair-stepped shear cracks were observed, such as those crossing the entire short spandrel with an angle of 45°. To a great extent, most of the deformations were absorbed by sliding of the concrete lintels with respect to the masonry supports, as well as sliding at the interface of the roof wall plates and the second storey masonry piers (Fig. 13i). In the northern veneer, the only cracks observed were located at the second floor level. As they extended along the entire length, they were associated with the tendency of the gable wall to develop an out-of-plane overturning mechanism (Fig. 12).

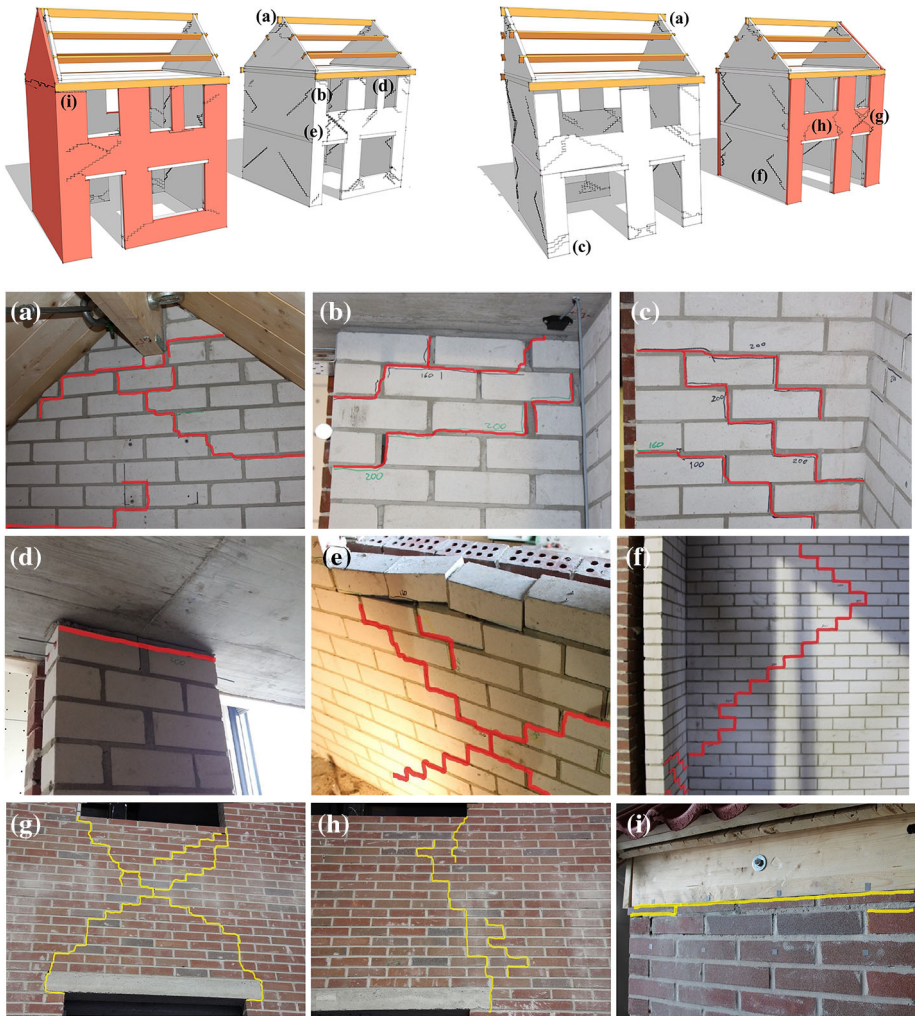


**Fig. 13** 3D view of the observed crack pattern at the instant of attainment of the peak second floor displacement: **a** pounding of the ridge beam on the North CS gable; **b** flexural cracks on the top of the second storey; **c** flexural cracks on the bottom of a first storey pier; **d** sliding at the interface of the second storey pier and the slab; **e** de-cohesion of masonry blocks and diagonal shear cracks through the joints; **f** stair-stepped cracks in the transverse walls; **g** shear failure of the veneer’s short spandrel with the formation of X-shaped crack pattern, **h** flexural cracks in the veneer’s long spandrel; **i** sliding at the interface of the veneer and the timber wall plate

Figure 14 reports the evolution of the maximum residual crack width measured after the end of every test. The same quantity is also plotted versus the peak and residual correspondent inter-storey drift ratio ( $\theta$  and  $\theta_{res}$ , respectively). A higher residual crack width was measured in the ground storey (i.e. 1st storey). This was due to two main factors: the higher drift demand (see Fig. 20) at lower levels and the concentration of the 2nd storey deformation in the interface between the CS wall and the top floor slab. Regarding the first floor, where the slab displacement was completely accommodated by the deformations of

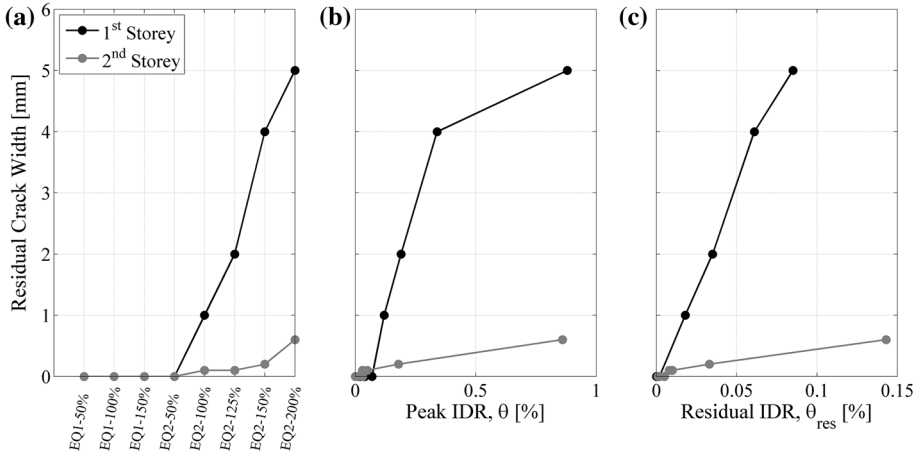


**Fig. 14** Evolution of the maximum residual width of the observed cracks as a function of the: **a** testing sequence, **b** peak IDR, and **c** residual IDR

the piers, a good correlation between  $\theta$  and crack width was observed. The relation between the crack width and the  $\theta_{res}$  was found to be almost linear for both storeys.

### 4.3 Deformed shapes

Deformed shapes in elevation have been generated by plotting the horizontal displacements recorded by the traditional potentiometers mounted on the floors and the wire potentiometers located at the level of the storeys' mid-height and ridge of the roof. Figure 15 represents the out-of-plane deflected shape of a longitudinal cross section of the specimen at the instant of peak second floor displacement for EQ2-100% and EQ2-200%, respectively.

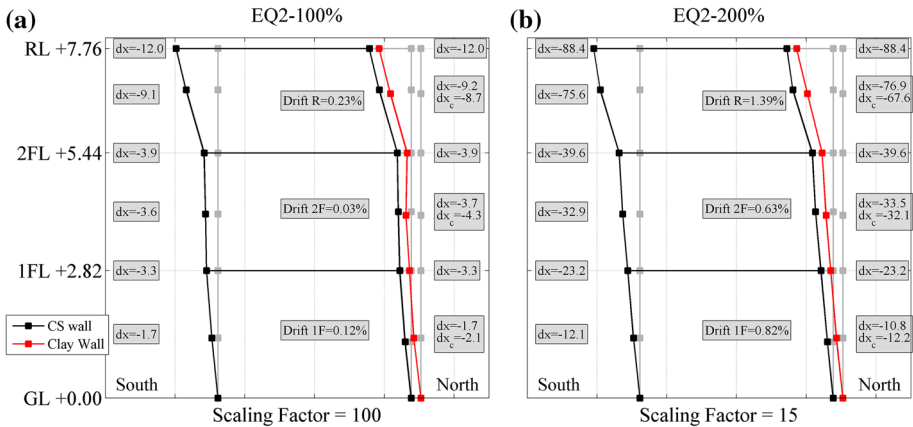


**Fig. 15** Deflected shapes of the specimen during the tests **a** EQ2-100% (PGA = 0.17 g) and **b** EQ2-200% (PGA = 0.307 g). Displacement units of mm

The deformed shapes changed significantly according to the ground motion intensity level and the state of deterioration of the specimen. In both cases, the higher drifts were observed at the roof level. This sub-structure was significantly more flexible. The initial response (similar from EQ1-25% to EQ2-150%, herein represented by the Fig. 15a) was instead characterised by a higher drift demand in the first storey with the second floor remaining almost rigid and experiencing a very low drift demand. During the last test (EQ2-200%), the specimen exhibited similar inter-storey drifts in both storeys, resulting in an almost linear trend (similar to the one corresponding to the first mode of vibration), associated with rocking response of the slender piers over the height of the building, as illustrated in Fig. 15b.

Furthermore, during the EQ2-200% test, after the failure of the interface between the top of the clay wall and the timber wall plates (Fig. 13i), a clear relative displacement was observed between the CS wall and the clay veneer, showing that the presence of cavity ties was not sufficient to ensure their collaboration. Most of the ties were permanently bent at the end of the tests. The inner loadbearing CS structure displaced significantly, while the southern portion of the East and West veneer walls was not involved in such an oscillation. A video of the test shows clearly this phenomenon (Eucentre 2015b).

#### 4.4 Hysteretic responses

The evolution of the specimen's hysteretic response is shown in Fig. 16, in terms of base shear,  $V$ , versus global drift of the first two storeys,  $\tilde{\theta}$ , through all the tests. The global drift is defined as the relative displacement of the second floor slab divided by its distance from the base, given by:

$$\tilde{\theta} = \frac{\Delta_2}{h_1 + h_2} = \frac{\Delta_2}{5440[\text{mm}]} \quad (2)$$

The time histories of the base shear have been computed as the sum of the products of each acceleration recording times the tributary mass of the corresponding accelerometer. Masses are assumed to be lumped at the accelerometer locations. The mass of the masonry body from the foundation level to the mid-height of the ground storey (at 1.38 m from the base) was assigned to the ground floor (and hence multiplied by the base acceleration time history).

The base shear coefficient  $BSC$  is defined as:

$$BSC = \frac{V}{M \cdot g} \quad (3)$$

where  $M \cdot g$  is the total weight of the specimen.

In each plot of Fig. 16, the hysteretic response of preceding tests is reported in grey. The white dots represent the positive and negative peak force responses with the corresponding displacements. The proportion between the two axes of all the plots is the same. In this way, the progressive specimen stiffness degradation and the consequent fundamental period elongation are appreciable.

The EQ2 input induced a more pronounced asymmetry in the specimen response with respect to the EQ1 earthquake. The displacement demand in the negative direction (towards South), indeed, was rather higher than the one in the positive direction. The first significant nonlinearity in the hysteretic response is observed during testing under EQ2-150% ( $PGA = 0.243 \text{ g}$ ), associated with the occurrence of spread flexural cracks in the

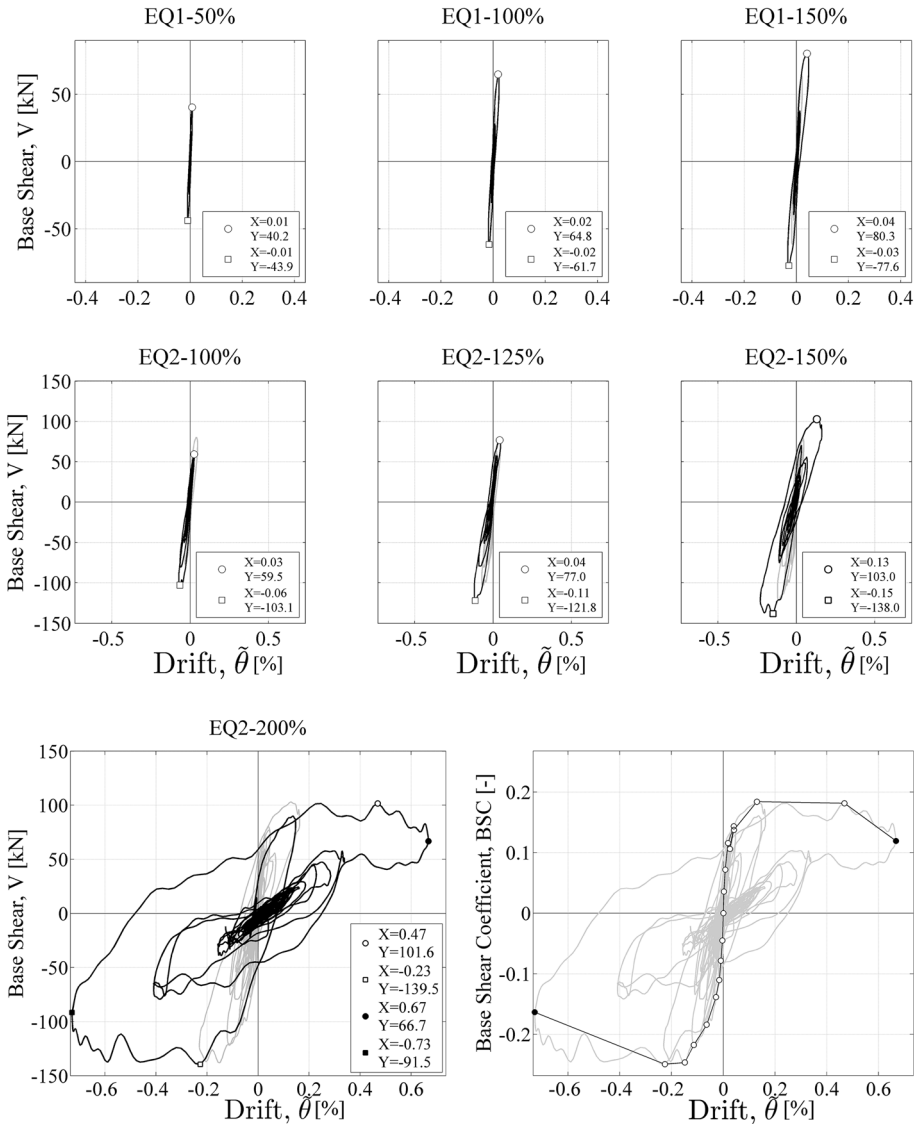


**Fig. 16** Evolution of the global hysteretic response in terms of base shear versus global drift ratio (*left*); Backbone curve in terms of base shear coefficient (*right*)

inner CS walls. During the test at EQ2-200% (PGA of 0.307 g), a large nonlinear behaviour was observed associated with extended damage to the specimen, highlighted by the dramatic enlargement of the hysteresis loops, and the consequent significant increase of the specimen's fundamental period of vibration.

An ultimate global drift ratio  $\tilde{\theta} = 0.7\%$  was reached, while a shear deformation of the roof diaphragm  $\gamma_R = 1.5\%$  was observed for the significantly more flexible roof structure. The maximum base shear  $V_{max}$  attained was approximately 139 kN, corresponding to a base shear coefficient  $BSC_{max} = 0.25$ . The dynamic force–displacement backbone curve

can be obtained by connecting the peak points of the experimental curves. In other words, it is defined as the plot of the maximum resisted base shear,  $V_{max}$ , and the corresponding global drift,  $\tilde{\theta}$ , for each stage of testing. The last point of both the positive and negative branch was obtained as the pair of the maximum drift attained and the corresponding base shear. A force “plateau” in the specimen capacity was reached in both directions. The attainment of the higher base shear occurred for sway towards the negative direction (towards the single-leaf side, South). In particular, the base shear attained for southward motion ( $V_{MAX}^- = 139.5$  kN) was 37% higher than the force reported for motion towards the double-leaf side of the structure ( $V_{MAX}^+ = 101.6$  kN). The asymmetry in the envelope response curve could be attributed to the northward “spike” of the applied accelerogram EQ2 and to the asymmetry of the structure.

#### 4.5 Response of the roof structure

The gable-roof system response was of particular interest for further investigation. The behaviour of the roof was acknowledged as one of the main factors that has driven the response of the substructure during the evolution of the dynamic tests, while the testing procedure ended because of the very large deflections of the gables. The detailed response of the roof in the course of the shaking table testing is illustrated in Fig. 17, in terms of acceleration versus relative displacement curves. The first quantity regards the acceleration,  $a_R$ , recorded by the accelerometers located at the ridge beam level, whereas the second refers to the relative displacement of the ridge,  $\delta_R$ , with respect to the second floor level. The slope of the dashed line is representative of the effective stiffness,  $K_R$ , the gable-roof system, while its ever-decreasing trend indicates that the roof diaphragm undergoes a significant stiffness degradation. Trends for the progressive stiffness degradation, defined as the ratio between the current degraded stiffness,  $K_{Ri}$ , and the initial stiffness,  $K_{R1}$ , can be derived and plotted as a function of the maximum in-plane shear deformation,  $\gamma_{Rmax}$  that the roof diaphragm undergoes during each test, as shown in Fig. 18. The relative roof displacement,  $\delta_R$ , of Figs. 17 and 18 is calculated from the relative ridge displacement (with respect to the second floor) by removing the residual displacements. Similarly, for generating the plots of Fig. 18, the roof shear deformations,  $\tilde{\gamma}_R$ , was computed after subtracting the residual shear deformations,  $\gamma_{R, res}$ , since they resulted in curves biased towards the right, and should not be confused with the roof shear deformations,  $\gamma_R$ , reported in Fig. 20. The roof shear deformation is computed as the relative ridge displacement divided by the inclined length of the roof pitch,  $L_R = 3.61$  m.

The inertia force of the entire roof system,  $F_R$ , system could be estimated by attributing a representative portion of the total mass of the gable-roof system to the ridge beam level. The lumped mass assumed at the top of the roof was equal to one-third of the self-weight of the gable-walls plus half of the weight of the roof, estimated around 2.6 t. Figure 17 reports the force–displacement response of the roof structure, as well as the resulting backbone curve of the system, defined by the peak points of the experimental curves (plot of the maximum attained force,  $F_R$ , against the corresponding relative ridge displacement,  $\delta_R$ , occurring at the same instant, for each stage of testing).

The envelope of the force–displacement responses displays no indication of strength degradation, which confirms diaphragm flexibility and the absence of observable structural failures in the roof. The plots on Fig. 18 show that the roof exhibited an almost linear elastic behaviour up to a displacement of approximately 4 mm, with a stiffness,  $K_a$ , equal to approximately 3.2 kN/mm. Beyond this value the roof entered into a nonlinear phase

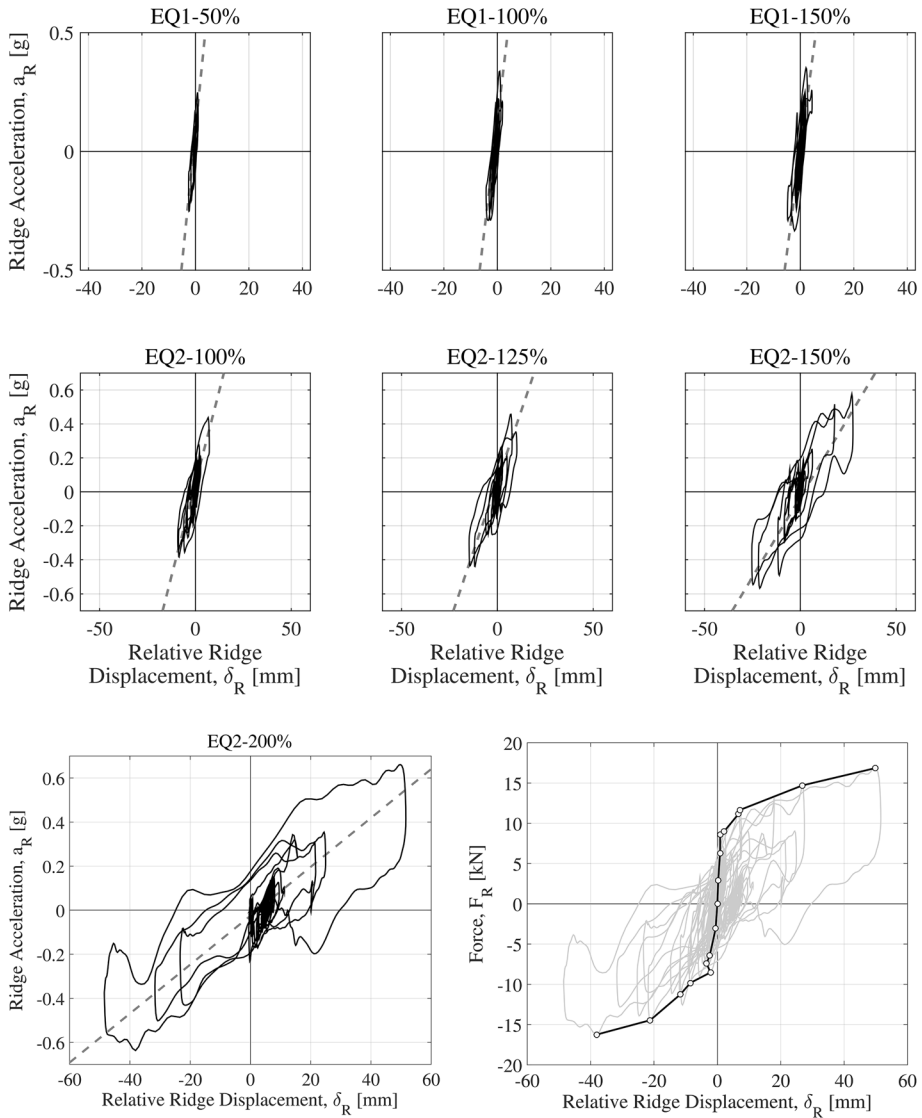


**Fig. 17** Evolution of the roof hysteretic response in terms of acceleration versus relative displacement at the ridge beam level (*left*); Backbone curve (*right*)

characterized by a higher dissipation of energy and a reduced stiffness of  $K_b \approx 0.12$  kN/mm. The wide hysteresis loops demonstrate that the diaphragm is capable of dissipating considerable amounts of energy when subjected to lateral loading.

In order to determine performance parameters of the roof that could be further exploited to investigate its seismic response, it was necessary to appropriately characterize the force-displacement data using a consistent and rational methodology. In the absence of a universally accepted method, the performance of the system could be captured using a bilinear idealization of the backbone response curve. As reported by Peralta et al. (2004) and

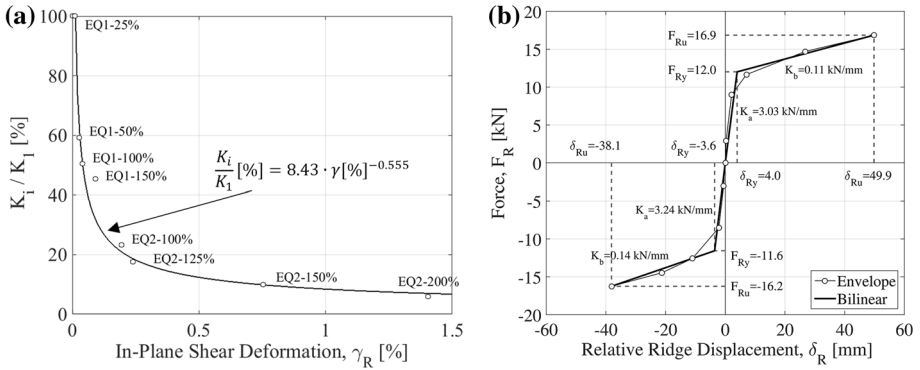


**Fig. 18** **a** Roof stiffness degradation as a function of the maximum attained in-plane shear deformation; **b** Envelope of the force–displacement responses of the roof

Wilson et al. (2014), the response can be approximated by a bilinear representation by applying the principle of hysteretic energy conservation, imposing at the same time the following constraints: the curve should pass through zero load and displacement; the ultimate displacement,  $\delta_u$ , could be taken as the maximum experimental displacement of the secondary linear branch; and the secondary stiffness should be computed as the global gradient of the approximate linear portion of the experimental envelope curve (here, observed for displacement amplitudes above 10 mm). Figure 18 illustrates the key performance parameters for the roof of the tested house, consisting in the initial stiffness,  $K_a$ , the secondary stiffness,  $K_b$ , the effective yield displacement,  $\delta_{Ry}$ , and the corresponding yield load,  $F_{Ry}$ , for both positive and negative displacements.

Because of the composite nature of the roof structure it was difficult to fully single out the experimental response of the timber diaphragm. The experimental data acquired from the tests could only be used to infer conclusions for the roof system response when examined as an ensemble, composed of the gable walls and the timber diaphragm (constructed by boards fastened perpendicular to timber joists).

#### 4.6 Identification of the specimen damage limit states

In this section, the identification of global quantitative thresholds that adequately describe the overall structural damage state of the building, is attempted. The roof sub-structure damage evolution is treated in a separate Sect. 4.2 and not included in this one. The seismic performance of existing buildings is usually evaluated through four damage limit states as proposed, for example, by Calvi (1999): *DL1*: no damage, *DL2*: minor structural damage and moderate non-structural damage (still usable building), *DL3*: significant structural damage and extensive non-structural damage, *DL4*: severe damage leading to demolition. Due to the high non-linearity characterising URM buildings leading to difficulties in distinguish between *DL1* and *DL2*, Calvi (1999) suggested to condense them into a unified damage state. Recently, Lagomarsino and Cattari (2015) proposed a multiscale approach for the definition of the damage thresholds related to each of the four performance levels; at a global scale, the damage levels are identified on the pushover curve according to the fraction of resistant base shear attained, at a sub-system scale such thresholds are defined in terms of inter-storey drift; at the structural element scale, the

seismic performance is evaluated according to the percentage of piers and spandrels exceeding a pre-defined deformation limit condition.

This section compares such damage limits with the actual damage observed through the testing stages of the present experimental test. Difficulties arise in the definition of clear damage states mainly due to two factors: the progressive accumulation of damage and the limited number of tests.

Figure 19 shows the global response of the building in terms of global drift  $\tilde{\theta}$  (Eq. 2) and base shear coefficient  $BSC$  (Eq. 3). The global drift  $\tilde{\theta}$  (as the displacement of the second floor) is not the best engineering demand parameter, EDP, but it could be useful to give a general idea of the specimen performance in terms of deformation achieved. The white dots represent the points of maximum resisted base shear,  $V_{max}$ , and the corresponding global drift,  $\tilde{\theta}$ , for each stage of testing (notice that this point is lower than the maximum global drift achieved in the correspondent test,  $\tilde{\theta}_{max}$ ); the successive corner points of the black solid line are local peaks achieved in the last test EQ2-200%, while the black dot represents  $\tilde{\theta}_{max}$  recorded during the test EQ2-200%. The different limit states, defining the thresholds between damage states, are defined as follows. Figure 19 plots them associated with views of the West side inner CS wall crack patterns.

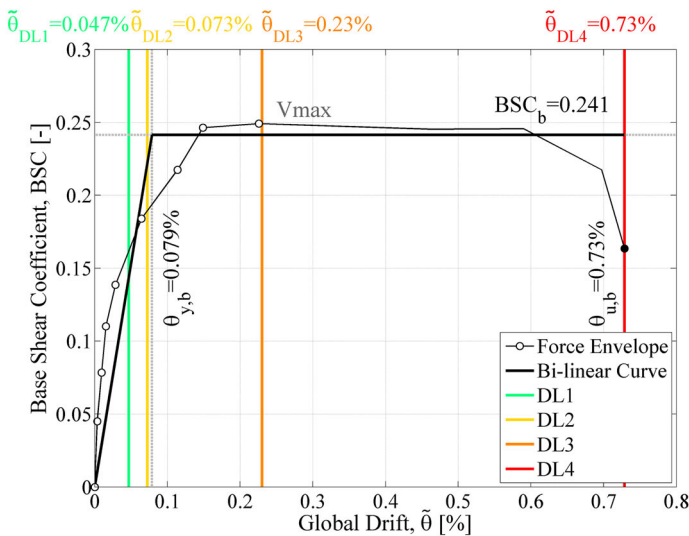
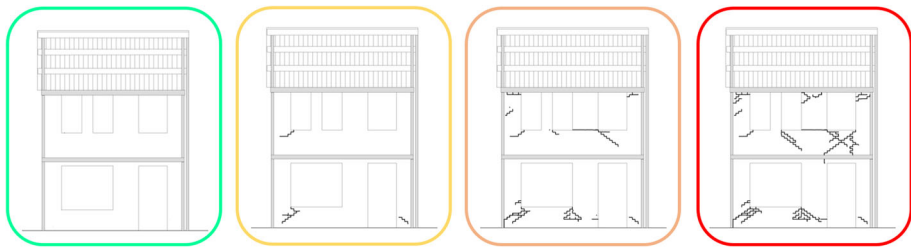


**Fig. 19** Definition of damage limits on the experimental backbone curve, illustration of the corresponding damage extent on the West side inner wall

*DL1* is defined as the maximum achieved level of displacement with no visible damage. The inspection after the execution of test EQ1-150% (PGA = 0.137 g) did not report any cracks. The structure could be considered as fully operational. The maximum recorded global drift was  $\tilde{\theta}_{max} = 0.047\%$ , while the maximum inter-storey drift, recorded at first floor level, was  $\theta_1 = 0.07\%$ .

*DL2* is defined as the maximum achieved level of displacement with minor/slight structural damage. The observed damage could be easily repaired (maximum crack residual not higher than 1 mm, Baggio et al. 2007) for a possible immediate occupancy. In particular, this damage limit was achieved during the test EQ2-100% (PGA = 0.17 g), when the cracks appeared at the bottom of the S-W pier of the first storey ( $\tilde{\theta}_{max} = 0.073\%$ ,  $\theta_1 = 0.12\%$ ). The determination of *DL2* on a global scale is very sensitive to engineering judgment. In this particular case, it was associated with EQ2-100% test because during the following run (i.e. EQ2-125%) the residual crack width reached 2 mm, even though this damage was still limited to the S-W corner of the building.

*DL3* is defined as the maximum achieved level of displacement with moderate structural damage (but still repairable). This state was associated with damage observed in all the piers contributing to the longitudinal resistance of the specimen after test EQ2-150% (PGA = 0.243 g). A posteriori, it was interesting to notice that this run was the first one to demand the full exploitation of the specimen lateral strength. *DL3* could be considered as a life safety limit state. The maximum residual width of the crack was 4 mm. The behaviour was characterized by a peak global drift  $\tilde{\theta} = 0.23\%$ , and a first storey drift  $\theta_1 = 0.34\%$ . Beyond this limit, the house could not be repaired economically.

*DL4* is defined as the maximum displacement reached by the specimen before the decision to stop the test due to a near collapse condition. The definition of a clear near collapse limit state is, hence, not trivial as for the case of the other limit states. The limit could be considered as a collapse-prevention threshold. Moreover, due to the significant reduction of stiffness, small variations in the input intensities could lead to significantly different peak displacements. The observed heavy structural damage (in piers and spandrels of inner and outer leaves) suggests that repairing a house that has reached this limit state may not be convenient. During the last test EQ2-200% (PGA = 0.307 g), a peak global drift  $\tilde{\theta}_{max} = 0.729\%$  and first storey drift  $\theta_1 = 0.88\%$  were achieved. After this test, the maximum residual crack width was 5 mm.

Table 4 compares the experimental and analytical damage limits as proposed by Calvi (1999) and by Lagomarsino and Cattari (2015). In particular, a comparison in terms of sub-system scale variable (i.e. interstorey drift  $\theta_1$ ) and global scale variable (i.e.  $V/V_{max}$  ratio) is proposed for each damage state.

In general, there is a very good agreement between the damage thresholds defined based on the experimental observations and those proposed in the considered analytical approaches. Only the collapse-prevention limit, *DL4*, is underestimated by both criteria. This may be due to the fact that the analytical approaches take into account a possible shear failure, e.g. Calvi (1999) refers to Magenes and Calvi (1997), while the response of the building under examination is dominated by flexural/rocking behaviour, typically associated with a higher displacement capacity (e.g. Graziotti et al. 2016a). As the experimental limit states are associated with a dynamic building response governed by bending/rocking mechanisms the softening which can be observed in the force–displacement envelope (Fig. 19) is much less pronounced than the one assumed in the analytical approach by Lagomarsino and Cattari (2015).

**Table 4** Comparison of the experimental and theoretical damage limits proposed by Calvi (1999) and Lagomarsino and Cattari (2015)

	<i>Scale</i>	<i>Variable</i>	<i>DL1</i>	<i>DL2</i>	<i>DL3</i>	<i>DL4</i>
Calvi (1999)		$\theta_i$		0.1%	0.3%	0.5%
Lagomarsino & Cattari (2015)	Sub-system	$\theta_i$	0.05-0.1%	0.15-0.3%	0.35-0.5%	0.55-0.7%
Experimental		$\theta_1$	0.07%	0.12%	0.34%	0.88%
Lagomarsino & Cattari (2015)		$V/V_{max}$	$\geq 0.5$	0.95-1.0	0.8-0.9	0.6-0.7
Experimental	Global	$V/V_{max}$	0.57	0.76	1.0	0.66
		$\tilde{\theta}$	0.047%	0.073%	0.23%	0.73%

The backbone curve has been further idealised by means of a bilinear approximation based on the equal energy criterion as prescribed by NTC08 (2008). The ultimate strength in terms of base shear coefficient was  $BSC_b = 0.241$  and the ultimate global drift  $\tilde{\theta}_{u,b} = 0.73\%$ , this deformation coincides with the peak global drift  $\tilde{\theta}_{max}$  achieved in the last test EQ2-200%. The bi-linearization procedure proposed by NTC08 (2008) has been developed in order to simply characterize the capacity curve of a building. In this case, the bi-linear idealisation has not been truncated in correspondence to a drop  $V/V_{max} = 0.8$  (as prescribed by NTC08 in case of pushover analysis) but it was extended to the actual maximum displacement achieved (without collapse) during the shaking table test. The “yielding” point corresponds to global drift of  $\tilde{\theta}_{y,b} = 0.079\%$ . It is worth noticing that the quantitative definition of *DL2* almost coincides with the end of the linear elastic range of the bilinear curve whereas *DL3* almost corresponds to the maximum lateral force.

#### 4.7 Derivation of engineering demand parameters according to the specimen performance

EDPs, such as peak inter-storey drift ratio (IDR), residual inter-storey drift ratio (RIDR) or peak floor acceleration (PFA) are important synthetic measures of the seismic behaviour of a building under a given earthquake. The selection of proper EDPs is a crucial point in order to characterize the performance of a structure. The analysis of data derived from shaking table tests, as those herein presented, is a good chance to directly correlate the physical observed damage with EDPs. Figure 20 shows a series of parameters related to the building performance. It is worth remarking that the specimen performance has been influenced by the progressive accumulation of damage during the entire testing sequence, since the test was incremental. This should be taken into account when a correlation between EDPs and intensity measures (IM) is formulated.

Figure 20 reports the building performance in terms of peak displacements ( $\Delta_I$ ,  $\Delta_2$  and  $\Delta_R$ ), IDR ( $\theta_I$ ,  $\theta_2$  and roof diaphragm shear deformation  $\gamma_R$ ) usually strictly connected to the in-plane damage occurring in structural elements like piers and spandrels, and RIDR very often associated with a general damage and damage accumulation. The response in terms of PFA/PGA is also shown. This EDP could be correlated with the OOP performance of masonry (or more in general secondary) components or the damage occurring to acceleration sensitive non-structural components.

The evolution of the building fundamental period of vibration during all test phases is also shown. The fundamental period evolution is calculated by means of dynamic modal

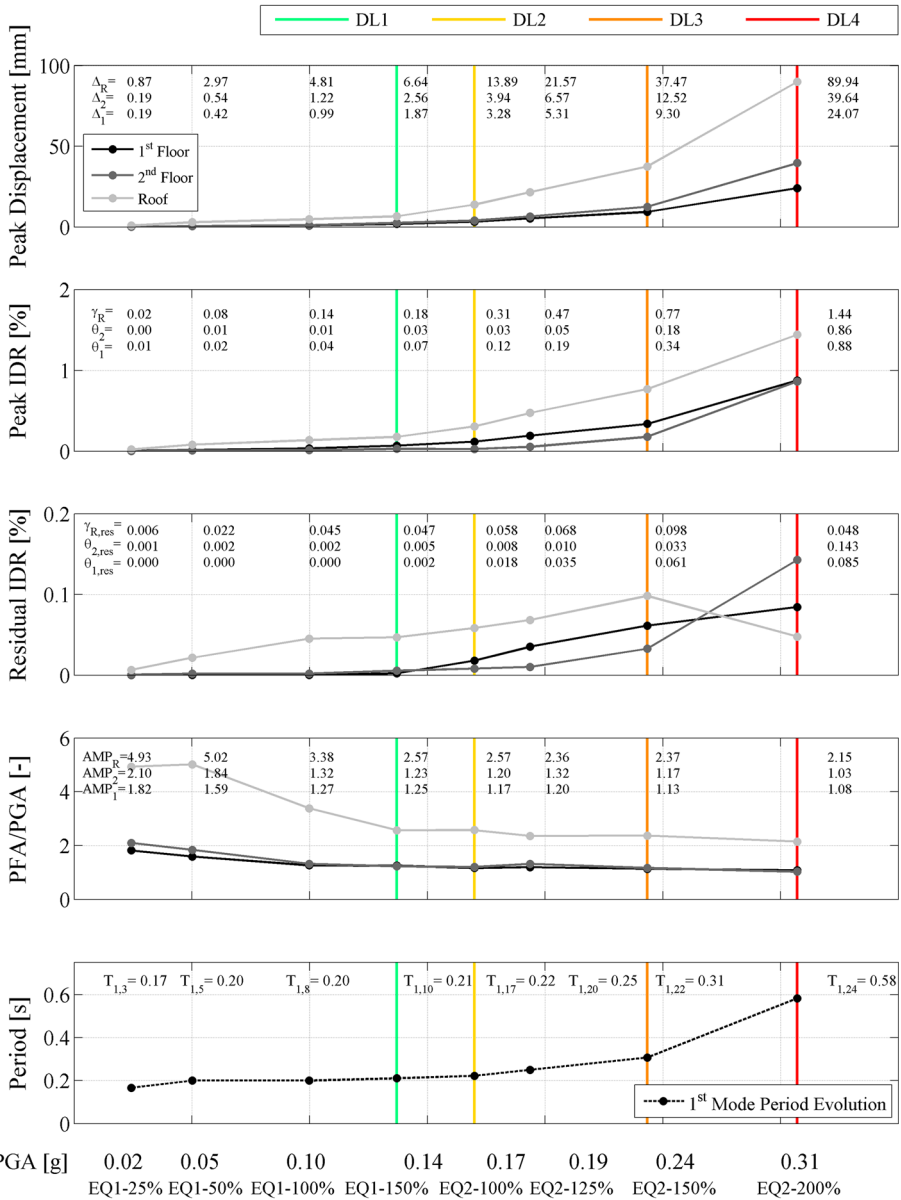


Fig. 20 Summary of the performance of the building specimen

identifications performed before each strong motion by means of low amplitude RDNM excitations (see Table 3). The peaks in the power spectral density can generally be assumed to represent either peaks in the excitation spectrum or normal modes of the structure (Pick Picking method). The normal modes were determined from the identification of the peaks in the power spectral density, the analysis of the phase angles and the computation of the ordinary coherence function. The Peak Picking method used in this

study was the one extended by Brincker et al. (2000, 2001) that introduced the so-called Frequency Domain Decomposition method. The basis of the method is the Singular Value Decomposition of the response spectral density matrix into a matrix of singular values and an orthogonal complex matrix containing the mode shape vectors of each spectral peak. Once the frequencies of vibration were defined, the mode shape components were computed from the amplitude of the cross-spectra normalized to the maximum component, with the direction of motion derived from the phase angles from the cross spectra between channels. The first mode of vibration of the undamaged building has been identified at a fundamental period  $T_{1,1} = 0.17$  s, for the inner walls system only. The first period of the external veneer walls is assumed to be presumably close to the same value. Figure 15, representing the deformed shapes under earthquake-type excitation, also well depicts the calculated deformed shape of a first mode type of behaviour, with the longitudinal walls responding in-plane and the gable walls overturning out-of-plane, parallel to the direction of the shaking table motion. More details regarding the modal identification outcomes are available on Graziotti et al. (2015).

The IDR associated with the first floor,  $\theta_1$ , was systematically higher than the one of the second floor,  $\theta_2$ , up to the test EQ2-200% (PGA = 0.307 g). Attaining the *DLA* condition, they reached a similar maximum value of approximately 0.88%. The first damage limit state (*DL2*), where damage has been observed in the first storey piers, is associated with a first floor drift of  $\theta_1 = 0.12\%$ , while the severe damage limit state (*DL3*) with the exploitation of the specimen full capacity is associated with inter-storey drift ratios  $\theta_1 = 0.34\%$  and  $\theta_2 = 0.18\%$  for the first and second storey, respectively. From the same plot, looking at the evolution of  $\gamma_R$ , it is also noticeable that the roof substructure seems to experience non-linearity starting from early stages of the test (see also Fig. 18a). Residual inter-storey drifts (*RIDR*) have been noticed after the end of the testing phase EQ2-100%, with the attainment of *DL2*.

The plot of the floor acceleration amplification,  $AMP_i$ , shows a progressive decrease, starting from values around 1.5 in the first tests to values close to 1 in the last tests. In accordance to the very limited  $\theta_2$  an almost negligible amplification has been recorded between the first and the second floor. In the EQ2-200% test the observed two-way out-of-plane cracks in all the North and South walls developed after the specimen has been subjected to floor acceleration PFA >0.3 g. This EDP could be considered as a first crack damage state for the OOP walls (further research are ongoing on this topic). The roof structure amplified the ground acceleration by a factor of 5 in the first runs down to a factor of 2 in the last test.

The results of the present experimental tests allow also the EDPs and the observed damage to be related with a seismic intensity measure (i.e. the PGA) for the input motions selected according to the hazard study. This could represent a reference for a sanity check of structural analyses on similar buildings.

## 5 Conclusions

The presented work was part of an extensive experimental campaign aimed at assessing the seismic vulnerability of Dutch URM buildings. It presents results of a unidirectional shaking table test performed on a full-scale specimen representative of a Dutch two-storey URM building with cavity walls and timber roof. The building specimen was intended to represent the end-unit of a terraced house of the late '70s, without any specific seismic

detailing. The loadbearing walls were built with a 10-cm-thick calcium silicate URM, while three out of the four façades were completed by a clay veneer connected to the calcium silicate walls by means of steel ties. The materials were characterized by mechanical characteristics compatible with the ones found in the building stock. The specimen was subjected to incremental input motions representative of two different induced seismicity scenarios characterized by smooth response spectra and a short significant duration. The processing of the recorded signals, both in terms of accelerations and displacements sustained by the tested structure, allowed the evaluation of the seismic resistance and displacement demand at each stage of testing. All the recorded signals (accelerations, displacements, videos) can be requested online (<http://www.eucentre.it/nam-project>).

The loadbearing structure exhibited a box-type global response thanks to the presence of the rigid concrete slabs, which engaged the longitudinal walls and prevented the occurrence of local out-of-plane failure mechanisms in the transverse walls of the 1st and 2nd stories, no torsional effect was recorded. As a consequence, the full in-plane capacity of the longitudinal walls was exploited. Four damage states were identified and compared with some of the theoretical proposals available in literature, with good agreement. In summary, the building withstood the input motion with a PGA of 0.17 g with little damage (maximum first inter-storey drift  $\theta_1 = 0.12\%$ ) and was in the near-collapse state at a PGA of 0.31 g ( $\theta_1 = 0.88\%$ ). No significant shear damage occurred in the masonry piers, which were in general slender, and their response was mainly governed by rocking, whereas sliding occurred at the top of masonry walls parallel to the table motion. A substantial compatibility of displacements was observed between the inner and outer walls up to the near collapse state. During the last run (PGA = 0.31 g), the two substructures moved almost independently and, as the stiffness contribution of the external clay masonry was reduced, the displacement demand of the internal structure increased. The fundamental period of the structure after the tests was almost 3.5 larger than the initial undamaged one. Furthermore, some diagonal stepped cracks were observed in the transversal load bearing walls due to the out-of-plane excitation.

The structure was characterized by a very flexible roof. A study of its dynamic behaviour is proposed in the manuscript. The timber diaphragm was subjected to a maximum shear deformation of almost 1.5%. Values for the amplifications of accelerations are also given herein.

Despite the high flexibility and the consequent vulnerability of roof system, the shaking table tests were able to fully exploit all the strength of the loadbearing structure. The maximum base shear coefficient was almost 0.25. The hysteretic plots, the large amount of experimental data derived from the dynamic tests (available upon request), the series of tests on smaller structural assemblies and characterization tests on materials constitute a useful basis for the development and calibration of numerical models that can reproduce the response of structures with different configurations. These calibrated models, thanks to the identification of different damage limit states herein presented, will be a reference for the vulnerability studies of the Groningen building stock.

**Acknowledgements** This paper describes an activity that is part of the project entitled “Study of the vulnerability of masonry buildings in Groningen” at EUCENTRE, undertaken within the framework of the research program for hazard and risk of induced seismicity in Groningen sponsored by the Nederlandse Aardolie Maatschappij BV. The authors would like to thank all the parties involved in this project: DICAR Lab of University of Pavia and EUCENTRE Lab that performed the test, together with NAM, Arup and TU Delft. The useful advices of R. Pinho, are gratefully acknowledged. Thanks go also to H. Crowley, A. Rossi,

M. Mandirola, E. Cenja, F. Dacarro, S. Peloso, F. Cuppari and E. Mellia for their support in the different phases of the experimental campaign.

## Appendix 1

### List of symbols

$AMP_i$	Acceleration amplification ( $i = 1, 2, R$ for the 1st floor, 2nd floor and ridge beam levels, respectively)
$a_R$	Acceleration at the ridge beam level
$BSC$	Base shear coefficient (Eq. 3)
$BSC_b$	Base shear coefficient of the bilinear approximation
$E_m$	Elastic modulus of masonry
$f_m$	Compressive strength of masonry
$F_R$	Inertia force of the roof
$F_{Ry}$	Yield load of the bilinear response of the roof
$f_{v0}$	Shear strength
$g$	Gravitational acceleration
$h_i$	Height of the $i$ th storey
$K_a$	Initial stiffness of the bilinear curve of the gable-roof system
$K_b$	Secondary stiffness of the bilinear curve of the gable-roof system
$K_{Ri}$	Effective stiffness of the gable-roof system ( $i =$ test identification number)
$L_R$	Inclined length of the roof pitch
$M$	Total mass of specimen
$mHI$	Modified Housner intensity (Eq. 1)
$PSV$	Pseudo spectral velocity
$V$	Base shear
$Sa$	5% elastic spectral acceleration
$T_{1,i}$	Fundamental period ( $i =$ test identification number)
$\gamma_R$	Shear deformation of roof diaphragm (with the residual shear deformations)
$\gamma_{R,res}$	Residual shear deformations of the roof diaphragm
$\tilde{\gamma}_R$	Shear deformation of roof diaphragm (without the residual shear deformations)
$\Delta_i$	Displacement ( $i = 1, 2, R$ for the 1st floor, 2nd floor and ridge beam levels, respectively)
$\Delta_{Rmax}$	Maximum displacement of the roof
$\delta_R$	Relative displacement of the ridge with respect to the second floor level
$\delta_{Ry}$	Yield displacement of the roof bilinear response
$\delta_{Ru}$	Ultimate displacement of the roof bilinear response
$\theta_i$	Peak inter-storey drift ratio ( $i = 1, 2$ for the 1st floor and 2nd floor, respectively)
$\theta_{i,res}$	Residual inter-storey drift ratio ( $i = 1, 2$ for the 1st floor and 2nd floor, respectively)
$\tilde{\theta}$	Global drift (Eq. 2)
$\tilde{\theta}_{DSi}$	Global drift threshold ( $i =$ damage state)
$\tilde{\theta}_{y,b}$	Yield global drift of the bilinear approximation
$\tilde{\theta}_{u,b}$	Ultimate global drift of the bilinear approximation
$\mu$	Friction coefficient

## Appendix 2

The present section provides guidelines for the use of the lab data obtained by the acquisition systems that can be found in the following location: <http://www.eucentre.it/nam-project/>. Photos and videos from all the testing phases can be requested at the same URL.

### Traditional acquisition system

The data are available in files with *.txt* format, organised in matrix form, where the information recorded by each instrument is listed in columns. Each *.txt* file is named after the corresponding shake-table test, in accordance to Table 3. With reference to Fig. 9, Table 5 lists the type of information given in each data column, as well as the associated

**Table 5** Content of the data matrices

Col #	Instrument/chanel description	U.M.	Position/description
1	Time	[s]	–
2	Accelerometer 1 x direction	[g]	South-West First-Floor Slab (m = 4648 kg)
3	Accelerometer 1 z direction	[g]	South-West First-Floor Slab
4	Accelerometer 2 x direction	[g]	South-East First-Floor Slab (m = 4373 kg)
5	Accelerometer 2 y direction	[g]	South-East First-Floor Slab
6	Accelerometer 2 z direction	[g]	South-East First-Floor Slab
7	Accelerometer 3 x direction	[g]	North-East First-Floor Slab (m = 4596 kg)
8	Accelerometer 3 y direction	[g]	North-East First-Floor Slab
9	Accelerometer 3 z direction	[g]	North-East First-Floor Slab
10	Accelerometer 4 x direction	[g]	North-West First-Floor Slab (m = 4316 kg)
11	Accelerometer 4 y direction	[g]	North-West First-Floor Slab
12	Accelerometer 4 z direction	[g]	North-West First-Floor Slab
13	Accelerometer 5 x direction	[g]	South-West Second-Floor Slab (m = 4244 kg)
14	Accelerometer 5 y direction	[g]	South-West Second-Floor Slab
15	Accelerometer 5 z direction	[g]	South-West Second-Floor Slab
16	Accelerometer 6 x direction	[g]	South-East Second-Floor Slab (m = 3961 kg)
17	Accelerometer 6 y direction	[g]	South-East Second-Floor Slab
18	Accelerometer 6 z direction	[g]	South-East Second-Floor Slab
19	Accelerometer 7 x direction	[g]	North-East Second-Floor Slab (m = 4293 kg)
20	Accelerometer 7 y direction	[g]	North-East Second-Floor Slab
21	Accelerometer 7 z direction	[g]	North-East Second-Floor Slab
22	Accelerometer 8 x direction	[g]	North-West Second-Floor Slab (m = 4257 kg)
23	Accelerometer 8 y direction	[g]	North-West Second-Floor Slab
24	Accelerometer 8 z direction	[g]	North-West Second-Floor Slab
25	Accelerometer 9 x direction	[g]	South Side Ridge Beam (m = 839 kg)
26	Accelerometer 9 y direction	[g]	South Side Ridge Beam
27	Accelerometer 9 z direction	[g]	South Side Ridge Beam
28	Accelerometer 10 x direction	[g]	North Side Ridge Beam (m = 839 kg)

Table 5 continued

Col #	Instrument/channel description	U.M.	Position/description
29	Accelerometer 10 y direction	[g]	North Side Ridge Beam
30	Accelerometer 10 z direction	[g]	North Side Ridge Beam
31	Accelerometer 11 z direction	[g]	Centre Ridge Beam
32	Accelerometer 12 x direction	[g]	South-West First Floor on Clay Wall (m = 1483 kg)
33	Accelerometer 13 x direction	[g]	South-East First Floor on Clay Wall (m = 1240 kg)
34	Accelerometer 14 x direction	[g]	South-West Second Floor on Clay Wall (m = 526 kg)
35	Accelerometer 15 x direction	[g]	South-East Second Floor on Clay Wall (m = 495 kg)
36	Accelerometer 16 x direction	[g]	North-West First Floor on Clay Wall (m = 991 kg)
37	Accelerometer 17 x direction	[g]	North First Floor on Clay Wall (m = 1035 kg)
38	Accelerometer 18 x direction	[g]	North-East First Floor on Clay Wall (m = 1174 kg)
39	Accelerometer 19 x direction	[g]	North-West Second Floor on Clay Wall (m = 828 kg)
40	Accelerometer 20 x direction	[g]	North Second Floor on Clay Wall (m = 632 kg)
41	Accelerometer 21 x direction	[g]	North-East Second Floor on Clay Wall (m = 859 kg)
42	Accelerometer 22 x direction	[g]	North mid-height of First Floor on Clay Wall (m = 662 kg)
43	Accelerometer 23 x direction	[g]	North mid-height of Clay Gable Wall (m = 697 kg)
44	Accelerometer 24 x direction	[g]	North mid-height of First Floor on CS Wall (m = 603 kg)
45	Accelerometer 25 x direction	[g]	North mid-height of CS Gable Wall (m = 664 kg)
46	Accelerometer 26 x direction	[g]	Foundation Beam West Side (m = 3738 kg)
47	Accelerometer 27 x direction	[g]	Foundation Beam East Side (m = 3155 kg)
48	Accelerometer 28 x direction	[g]	Steel Frame First Floor
49	Accelerometer 29 x direction	[g]	Steel Frame Second Floor
50	Accelerometer 30 x direction	[g]	South mid-height of CS Gable Wall (m = 664 kg)
51	Accelerometer 31 x direction	[g]	South mid-height of First Floor on CS Wall (m = 603 kg)
52	Accelerometer 32 x direction	[g]	West Beam of the Steel Frame First Floor
53	Accelerometer 33 x direction	[g]	East Beam of the Steel Frame Second Floor
54	Wire Potentiometer 1 x direction	[mm]	South mid-height of Ground Floor on CS Wall (+1.34 m)
55	Wire Potentiometer 2 x direction	[mm]	South mid-height of First Floor on CS Wall (+4.09 m)
56	Wire Potentiometer 3 x direction	[mm]	South mid-height of CS Gable Wall (+6.74 m)
57	Wire Potentiometer 4 x direction	[mm]	North mid-height of Ground Floor on CS Wall (+1.26 m)
58	Wire Potentiometer 5 x direction	[mm]	North mid-height of First Floor on CS Wall (+4.09 m)
59	Wire Potentiometer 6 x direction	[mm]	North mid-height of CS Gable Wall (+6.74 m)
60	Wire Potentiometer 7 x direction	[mm]	North mid-height of Ground Floor on Clay Wall (+1.33 m)
61	Wire Potentiometer 8 x direction	[mm]	North mid-height of First Floor on Clay Wall (+4.17 m)
62	Wire Potentiometer 9 x direction	[mm]	North mid-height of Clay Gable Wall (+6.66 m)
63	Wire Potentiometer 10 x direction	[mm]	Ridge Beam
64	Potentiometer 11 x direction	[mm]	South-East First-Floor Slab
65	Potentiometer 12 x direction	[mm]	North-East First-Floor Slab

**Table 5** continued

Col #	Instrument/channel description	U.M.	Position/description
66	Potentiometer 13 x direction	[mm]	North-West First-Floor Slab
67	Potentiometer 14 y direction	[mm]	South-West First-Floor Slab
68	Potentiometer 15 x direction	[mm]	South-East Second-Floor Slab
69	Potentiometer 16 x direction	[mm]	North-East Second-Floor Slab
70	Potentiometer 17 x direction	[mm]	North-West Second-Floor Slab
71	Potentiometer 18 y direction	[mm]	South-West Second-Floor Slab
72	Potentiometer 19 x direction	[mm]	Sliding between the two First-Floor Slabs
73	Potentiometer 20 x direction	[mm]	Sliding between the two Second-Floor Slabs
74	Potentiometer 21 x direction	[mm]	East Side Sliding between wall-foundation
75	Potentiometer 22 x direction	[mm]	West Side Sliding between wall-foundation
76	Potentiometer 23 x direction	[mm]	E side Sliding between shaking table-foundation
77	Potentiometer 24 x direction	[mm]	W side Sliding between shaking table-foundation
78	Potentiometer 25 x direction	[mm]	Laboratory floor: Shaking table displacement
79	Potentiometer 26 z direction	[mm]	Ground: uplift flange East CS Wall
80	Potentiometer 27 z direction	[mm]	Ground: uplift flange North CS Wall
81	Shaking Table Force x direction	[kN]	Actuator force
82	Shaking Table Disp. x direction	[mm]	Actuator displacement
83	Shaking Table Acc. x direction	[g]	Actuator acceleration
84	Displacement 1st Floor x direction	[mm]	Average columns 64, 65 and 66
85	Displacement 2nd Floor x direction	[mm]	Average columns 68, 69 and 70
86	Acc. Foundation beam x direction	[g]	Average columns 46 and 47
87	Acc. 1st Floor x direction	[g]	Average columns 2, 4, 7 and 10
88	Acc. 2nd Floor x direction	[g]	Average columns 13, 16, 19 and 22
89	Acc. Ridge Beam x direction	[g]	Average columns 25 and 28
90	Inter-storey drift 1st Floor x dir.	[%]	$h_1 = 2.75$
91	Inter-storey drift 2nd Floor x dir.	[%]	$h_2 = 2.60$
92	Inter-storey drift Roof x dir.	[%]	$L_r = 3.61$
93	Base Shear x direction	[kN]	Calculated at the foundation beam level
94	Off-line channels	–	–
95			
96			
97			
98			

instrument location. Some of the accelerometers are accompanied by the portion of the structural mass that was considered in computing the inertial forces. The first column represents the data acquisition time step, while columns 2–53 contain the acceleration time-histories recorded by the accelerometers mounted on the structure. All the data recorded directly by instruments (2–83) are raw data filtered by means of a quadratic low-

pass filter set to a frequency equal to 50 Hz. The displacement histories recorded by wire potentiometers are listed in columns 54–63, while those recorded by traditional potentiometers are found in columns 64–80. Columns 81, 82 and 83 contain the actuator read-out data, in terms of horizontal (x direction) forces, displacements and accelerations. The last columns (84–93) contain quantities that were not directly measured but computed, such as the total base-shear force and the inter-storey drift ratio time-histories (Table 5).

### 3D optical acquisition system

The data obtained by the 3D optical acquisition system (Fig. 21) can be found in the same database. The synchronized data are provided for the shaking-table tests listed in Table 6, organized in *C3D* files.

The *C3D* files can be opened in MATLAB using the *.m* file provided with the data (an example is also available “Post\_Process\_EUCENTRE\_Example.m”).



**Fig. 21** 3D optical acquisition system (markers illustrated with *white dots*)

**Table 6** Summary the data obtained by the 3D optical acquisition system

Test #	Test input	Test name	File name
2	EQ1-Or	25%_EQ1_024	25%_EQ1_024.c3d
4	EQ1-Or	50%_EQ1_050	50%_EQ1_050.c3d
7	EQ1	100%_EQ1_100	100%_EQ1_100.c3d
9	EQ1	150%_EQ1_150	150%_EQ1_150.c3d
14	EQ2	50%_EQ2_080	50%_EQ2_080.c3d
16	EQ2	100%_EQ2_160	100%_EQ2_160.c3d
19	EQ2	125%_EQ2_200	125%_EQ2_200.c3d
21	EQ2	150%_EQ2_240	150%_EQ2_240.c3d
23	EQ2	200%_EQ2_320	200%_EQ2_320.c3d

The label and position of each marker is illustrated in Figs. 22 and 23. In some cases, the trajectories of some markers was not reliably recorded, as a consequence the corresponding data have been removed from the data matrices. In particular, the missing marker are listed in Table 7.

The coordinates of the markers are given in mm. Although the absolute residual displacements can be extracted from the data collected during each individual test, the

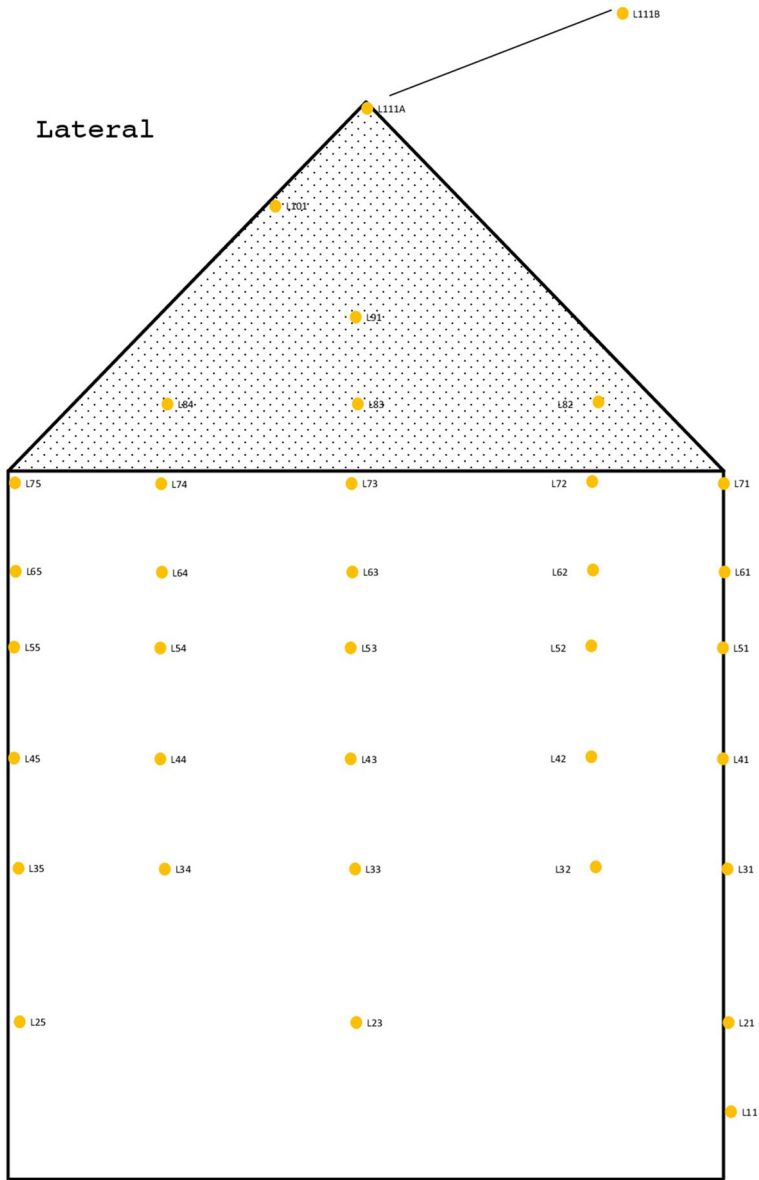


**Fig. 22** 3D optical acquisition system: markers mounted on the North façade of the building specimen

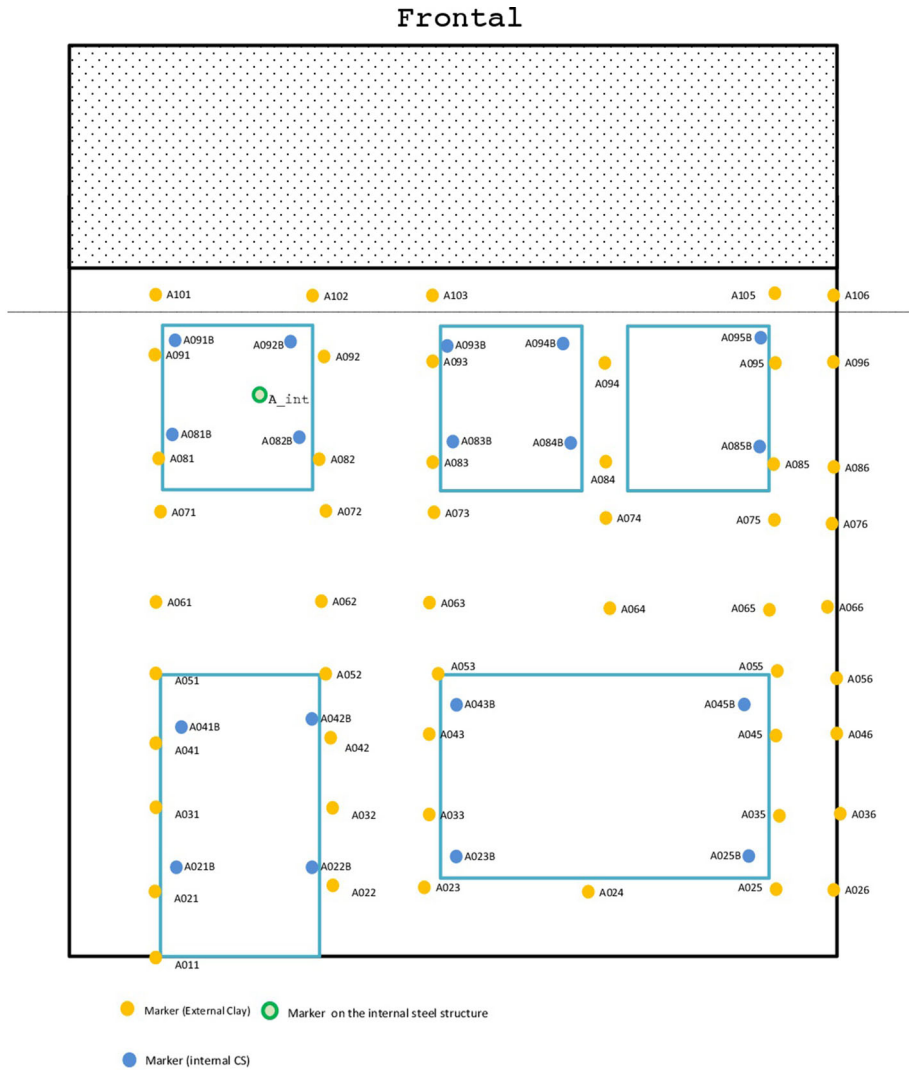


**Fig. 23** 3D optical acquisition system: markers mounted on the West façade of the building specimen

measurements do not include reliable residual displacements resulting from previous tests. This happens due to the slight change of the reference system adopted after the calibration of the 3D optical system performed in the beginning of every test (problem solved in tests conducted after this one). For example, in order to compute the residual displacement of a given marker through various tests, the suggestion is to use relative position (e.g. consider marker A011 as origin of x axis) and sum all the residuals recorded at the end of each test or directly refer to traditional instrumentation data. The relative position of markers (useful for the computation of deformation and the residual deformation) within each test is not affected.

**Table 7** Markers missing from the final provided data matrices

File name	Missing markers
25%_EQ1_024.c3d	A056
50%_EQ1_050.c3d	L111B, A056
100%_EQ1_100.c3d	L111B, A056
150%_EQ1_150.c3d	L111B, L23, A056
50%_EQ2_080.c3d	L111B, L23, A056
100%_EQ2_160.c3d	L111B, L23, A056
125%_EQ2_200.c3d	A056, A043B, A093B
150%_EQ2_240.c3d	L111B, A056, A094B
200%_EQ2_320.c3d	L111B, A056

## References

- Baggio C, Bernardini A, Colozza R, Corazza L, Della Bella M, Di Pasquale G, Dolce M, Goretti A, Martinelli A, Orsini G, Papa F, Zuccaro G (2007) Field manual for post-earthquake damage and safety assessment and short term countermeasures (AeDES). European Commission—Joint Research Centre—Institute for the Protection and Security of the Citizen, EUR, 22868
- Bourne SJ, Oates SJ, Bommer JJ, Dost B, van Elk J, Doornhof D (2015) A Monte Carlo method for probabilistic hazard assessment of induced seismicity due to conventional natural gas production. *Bull Seismol Soc Am* 105(3):1721–1738. doi:[10.1785/0120140302](https://doi.org/10.1785/0120140302)
- Brincker R, Zhang L, Andersen P (2000) Modal Identification from Ambient Responses using Frequency Domain Decomposition. In: Proceedings on 18th international seminar on modal analysis, San Antonio, Texas
- Brincker R, Ventura C, Andersen P (2001) Damping estimation by frequency domain decomposition. In: Proceedings of IMAC XIX, the 19th international modal analysis conference, Kissimmee, USA
- Calvi GM (1999) A displacement-based approach for vulnerability evaluation of classes of buildings. *J Earthq Eng* 3:411–438
- Degée H, Denoel V, Candeias P, Campos-Costa A, Coelho E (2008) Experimental investigation on non-engineered masonry houses in low to moderate seismicity areas. In: 14th world conference on earthquake engineering, Beijing, China
- EN 1015–11 (1999) European standard: methods of test for mortar for masonry—part 11: determination of flexural and compressive strength of hardened mortar. CEN, Brussels
- EN 1052–1, -3, -5 (1998) European standard: methods of test for masonry. CEN, Brussels
- EN 772-1 (2000) European standard: methods of test for masonry units—part 1: determination of compressive strength. CEN, Brussels
- Esposito R, Messali F, Rots JG (2016) Material characterization of replicated masonry and wall ties. Final report 18 April 2016, Delft University of Technology, Delft, The Netherlands
- Eucentre (2015a) Videos of full-scale shaking table test on a URM cavity-wall building model. <https://www.youtube.com/watch?v=h8sZCRUC&list=PLRDMVFxhFvQm8pxSTPpzHN1AQH0G7sMGk>
- Eucentre (2015b) Videos of full-scale shaking table test on a URM cavity-wall building model. <https://www.youtube.com/watch?v=1xw2GqIQrTw>
- Graziotti F, Tomassetti U, Rossi A, Kallioras S, Mandirola M, Cenja E, Penna A, Magenes G (2015) Experimental campaign on cavity-wall systems representative of the Groningen building stock. Technical Report EUC318/2015U, Eucentre, Pavia, Italy. <http://www.eucentre.it/project-nam/>
- Graziotti F, Rossi A, Mandirola M, Penna A, Magenes G (2016a) Experimental characterization of calcium-silicate brick masonry for seismic assessment. In: Brick and block masonry: trends, innovations and challenges—proceedings of the 16th international brick and block masonry conference, IBMAC 2016, pp 1619–1628
- Graziotti F, Tomassetti U, Penna A, Magenes G (2016b) Out-of-plane shaking table tests on URM single leaf and cavity walls. *Eng Struct* 125:455–470. doi:[10.1016/j.engstruct.2016.07.011](https://doi.org/10.1016/j.engstruct.2016.07.011)
- Graziotti F, Tomassetti U, Rossi A, Marchesi B, Kallioras S, Mandirola M, Frangomeli A, Mellia E, Peloso S, Cuppari F, Guerrini G, Penna A, Magenes G (2016c) Shaking table tests on a full-scale clay-brick masonry house representative of the Groningen building stock and related characterization tests. Technical Report EUC128/2016U, Eucentre, Pavia, Italy. <http://www.eucentre.it/project-nam/>

- Graziotti F, Penna A, Magenes G (2016d) A nonlinear SDOF model for the simplified evaluation of the displacement demand of low-rise URM buildings. *Bull Earthq Eng* 14(6):1589. doi:[10.1007/s10518-016-9896-5](https://doi.org/10.1007/s10518-016-9896-5)
- Graziotti F, Guerrini G, Kallioras S, Marchesi B, Rossi A, Tomassetti U, Penna A, Magenes G (2017) Shaking table test on a full-scale unreinforced clay masonry building with flexible diaphragms. In: *Proceedings of 13th Canadian masonry symposium*, Halifax, Canada
- Ingham J, Griffith M (2011) Performance of unreinforced masonry buildings during the 2010 Darfield (Christchurch, NZ) earthquake. *Aust J Struct Eng* 11(3):207–224
- Lagomarsino S, Cattari S (2015) PERPETUATE guidelines for seismic performance-based assessment of cultural heritage masonry structures. *Bull Earthq Eng* 13:13–47. doi:[10.1007/s10518-014-9674-1](https://doi.org/10.1007/s10518-014-9674-1)
- Magenes G, Calvi GM (1997) In-plane seismic response of brick masonry walls. *Earthq Eng Struct Dyn* 26:1091–1112
- Magenes G, Penna A, Senaldi IE, Rota M, Galasco A (2014) Shaking table test of a strengthened full-scale stone masonry building with flexible diaphragms. *Int J Archit Herit Conserv Anal Restor* 8(3):349–375. doi:[10.1080/15583058.2013.826299](https://doi.org/10.1080/15583058.2013.826299)
- Messali F, Esposito R, Maragna M (2016) Pull-out strength of wall ties. Technical Report, TU Delft, NL
- NTC08 (2008) Italian National Building Code, Ministero delle Infrastrutture e dei Trasporti, Decreto Ministeriale del 14 gennaio 2008, Supplemento ordinario alla G.U. n. 29 del febbraio 2008
- Peralta D, Bracci J, Hueste M (2004) Seismic behavior of wood diaphragms in pre-1950s unreinforced masonry buildings. *J Struct Eng* 130(12):2040–2050
- Tomažević M, Weiss P, Velechovsky T (1991) The influence of rigidity of floors on the seismic behaviour of old stone-masonry buildings. *Eur Earthq Eng* 3:28–41
- Tondelli M, Graziotti F, Rossi A, Magenes G (2015) Characterization of masonry materials in the Groningen area by means of in situ and laboratory testing. Technical Report, Eucentre, Pavia, Italy. <http://www.eucentre.it/project-nam/>
- Wilson A, Quenneville P, Ingham J (2014) In-plane orthotropic behavior of timber floor diaphragms in unreinforced masonry buildings. *J Struct Eng* 140(1):04013038. doi:[10.1061/\(ASCE\)ST.1943-541X.0000819](https://doi.org/10.1061/(ASCE)ST.1943-541X.0000819)